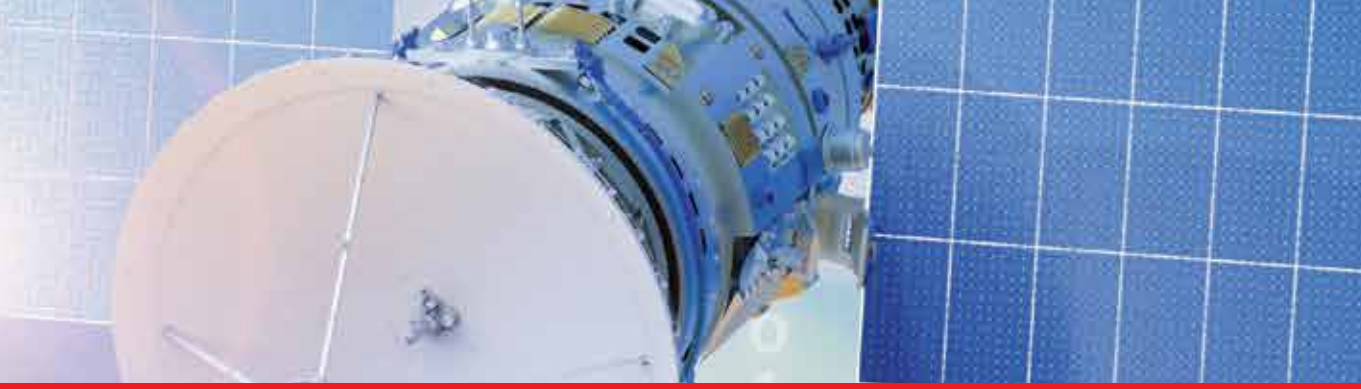

IntechOpen

Ultra Wideband Communications: Novel Trends

System, Architecture and Implementation

Edited by Mohammad Matin

ULTRA WIDEBAND COMMUNICATIONS: NOVEL TRENDS – SYSTEM, ARCHITECTURE AND IMPLEMENTATION

Edited by **Mohammad A. Matin**

Ultra Wideband Communications: Novel Trends - System, Architecture and Implementation
http://dx.doi.org/10.5772/932
Edited by Mohammad Matin

Contributors

Andrey Kistchinsky, Ayman Khalil, Matthieu Crussiere, Jean-François Helard, Shin'ichi Tachikawa, Masatoshi Yokota, Nazih Khaddaj Mallat, Emilia Moldovan, Serioja O. Tatu, Ke Wu, Edward Semyonov, Anton Loschilov, Haruka Suzuki, Ryuji Kohno, Wen Fan, Chiu-Sing Choy, Shinpei Oshima, Kouji Wada, Ryuji Murata, Yukihiro Shimakata, Llorente, BeltrĚÁn, Maria Morant, Antti Anttonen, Aarne Mämmelä, Subbarayan Pasupathy, Nikos Petrellis, Michael Birbas, Owen Casha, Ivan Grech, F. Xavier Moncunill-Geniz, Pere Palà-Schönwälder, Jordi Bonet-Dalmau, Rosa Giralt-Mas, Francisco Del Aguila López, Nazmat Toyin Surajudeen-Bakinde, Xu Zhu, Jingbo Gao, Asoke Nandi, Hai Lin, Lingli Xia, Changhui Hu, Patrick Chiang, Wei Xu, jiaxiang zhao

Notice

First published in Croatia, 2011 by INTECH d.o.o.
eBook (PDF) Published by IN TECH d.o.o.
Place and year of publication of eBook (PDF): Rijeka, 2019.
IntechOpen is the global imprint of IN TECH d.o.o.
Printed in Croatia

Legal deposit, Croatia: National and University Library in Zagreb

Additional hard and PDF copies can be obtained from orders@intechopen.com

Ultra Wideband Communications: Novel Trends - System, Architecture and Implementation
Edited by Mohammad Matin

p. cm.

ISBN 978-953-307-461-0

eBook (PDF) ISBN 978-953-51-5560-7

Meet the editor

Dr. Mohammad A. Matin is currently working at the Department of Electrical Engineering and Computer Science, North South University as an Assistant Professor. He obtained his Ph.D. degree in wireless communications from Newcastle University, UK and M.Sc. degree in digital communications from Loughborough University, UK. Dr. Matin was the visiting lecturer at the National University of Malaysia. He has published over 40 refereed journal and conference papers. He has presented invited talks in Bangladesh, China and Malaysia and has served as a referee of a few renowned journals. He also served as a technical session chair of few international conferences like MIC-CPE 2008, ICCIT 2008, ICCIT 2010, ICMMT 2010 etc. He is currently serving as an editorial board member of IET-WSS, JECE, etc. He has received a number of prizes and scholarships including the Best Student Prize (Loughborough University), Commonwealth Scholarship and Overseas Research Scholarship (ORS). His current research interests include UWB communications, wireless sensor networks, cognitive radio, EM modeling, and antenna engineering.

Contents

Preface

Ultra-Wideband (UWB) is one of the most promising technologies due to its tolerance to multi-path fading, low possibility of interception and high-bit rate capabilities; its main applications include imaging systems, vehicular radar systems, and communications and measurement systems. Following the power constraint and the extremely wide bandwidth of UWB, a fundamental issue arises, that is how to manage the multiple-user access with efficient utilization of bandwidth, support the QoS requirements of multimedia applications and provide coexistence with the existing users. This book has identified few issues as the previous one and covers several research areas including Low noise amplifier (LNA), ADC architectures, UWB filter, high power UWB amplifiers, and UWB low cost transceiver.

Mutli-Band OFDM (MB-OFDM) and Direct-Sequence UWB (DS-UWB) are two main proposals for UWB. Due to incompatiblity of these two proposals, UWB faces huge difficulties in commercialization. On the other hand, Impulse Radio UWB (IR-UWB) has been a hot research area in academia. This book explores UWB RF transceiver architectures, including MB-OFDM UWB, DS-UWB and IR-UWB. In fact, the use of microwave frequencies (3.1–10.6 GHz) for UWB is a subject of intensive research. However, the use of a millimeter-wave carrier for UWB communication is another promising approach as it enables the design of compact and low-cost wireless transceivers , as it is explained in this book.

The investigation of nonlinear distortions of UWB signals runs across considerable difficulties which is shown in chapter 1. This chapter provides a solution as well. The presented solution allows observing nonlinear transformation products of UWB signal against the background of a continuous spectrum of a test signal.

Chapter 2 explains low sampling rate time acquisition schemes and channel estimation algorithms for UWB signals.

A novel Received Response (RR) sequence is presented in chapter 3 to resolve the ISI problem.

Chapter 4 presents a genetic algorithm (GA) based equalization approach for direct sequence ultra-wideband (DS-UWB) wireless communication systems to combat the inter-symbol interference (ISI).

Some recent trends in designing advanced phase-unaware detectors (PUDs) are discussed in chapter 5. These PUDs have created much attention among academic and industrial research communities due to the recent advances in both algorithm and implementation issues.

A low power 3-5 GHz IR-UWB transceiver architecture is presented in chapter 6 with maximum data rate of 100 Mb/s.

Super regenerative receivers are a promising alternative in emerging fields such as wireless sensor networks and medical applications. In chapter 7, the suitability of super regenerative receivers in ultra wideband impulse radio (UWB IR) communications has been analyzed.

Chapter 8 presents a fully integrated, single-chip IR-UWB transceiver with ADC in 90nm CMOS for a typical short-range wireless communication application. A novel pulse-injection-locking method is used for receiver clock synchronization in the receiver demodulation, leading to significant power reduction by eliminating the high-power oversampling ADC and mixer. The complete transceiver could achieve a maximum data rate of 500Mbps, through a 10cm distance, consuming 0.18nJ/bit.

Synchronization issue which includes timing synchronization and frequency synchronization is inevitable in all wireless communication receiver systems and it plays the key role for the system performance. Chapter 9 provides a comprehensive review of the algorithms and architectures for timing and frequency synchronization by considering the real application or implementation.

Designing frequency synthesizers for UWB MB-OFDM alliance applications faces particularly stringent challenges and performance criteria. Chapter 10 focuses the current state of the art in frequency synthesis for UWB MBOA applications.

Commercial GaN discrete transistors and MMICs can be used in constructions of high power UWB amplifiers. Chapter 11 is devoted to considering the developmental process in the technology of GaN microwave power transistors and MMICs and to demonstrate the prospects for the development of this technology as an industrial standard in the nearest future.

In chapter 12, a method for improving out-of-band characteristics of a wideband bandpass filter has been presented, which is suitable for the compact UWB wireless modules. The module consists of an LTCC substrate, integrated circuits, chip components, a shield, and the passive components embedded in the LTCC substrate (e.g. the bandpass filter, coupler and balun).

A number of calibration methods as well as a number of generic error compensation methods based on the processing of the ADC output are presented in chapter 13.

Chapter 14 defines the cross-layer strategy for a distributed multiuser resource allocation scheme under QoS requirements in MB-OFDM systems.

In order to reconcile medical and non-medical applications requirements, an adaptive error controlling mechanism in the form of hybrid ARQ (H-ARQ) has been presented in chapter 15. Such error-controlling system adapts the channel conditions which can optimize the throughput, latency and reliability according to the application specification and channel conditions.

The extension of UWB technology to the optical access network has been discussed in chapter 16. Radio-over-fibre configuration permits the transmission of UWB signals in their native format through fibre-to-the-home (FTTH) access networks.

The principle and the design of six-port 60 GHz transceivers are presented in chapter 17 to be used in future millimeter-wave UWB WLAN.

I hope that this book serves as a comprehensive reference for graduate students and that it will be useful as a learning tool for research in this exciting field.

Mohammad A. Matin
North South University
Bangladesh

Part 1

UWB Communication Systems and Signal Processing

1

Measurements of the Nonlinearity of the Ultra Wideband Signals Transformation

Edward Semyonov[1] and Anton Loschilov[2]
[1]*Tomsk State University of Control Systems and Radioelectronics*
[2]*R&D Company Sibtronika, Ltd.*
Russian Federation

1. Introduction

The linearity is one of the more difficult challenges of receiver in ultra wideband (UWB) communication systems (Green & Roy, 2003). When testing UWB receivers, one should use UWB signals as nonlinear signal distortion caused by a device dependant on the waveform of a signal.

The investigation of nonlinear distortions of UWB signals run across considerable difficulties. They are caused by a continuous spectrum of UWB signals. In this case, it is impossible to observe harmonics or intermodulation products.

In addition, application of UWB signals practically has no alternative in subsurface radars. However, such radars remain linear today. It can be explained by the same reason as stated above (difficulties in observing nonlinear transformation products). The same situation can be observed in reflectometry of wire transmission lines.

Lately Agilent Technologies Company has been using *X*-parameters (Verspecht, 1996; Verspecht & Root, 2006) in Advanced Design System (ADS) and PNA-X measuring devices. It is assumed that object characteristics depend only on the first harmonic of test signal and dc bias. Therefore, *X*-parameters are adequate only when narrow-band test signals are used.

The methods described, which allow using the UWB test signals, have some failings. There is a method, which allows identifying parameters of nonlinear object model by means of testing the object by pulse signal with level sweep (Sobhy et al., 1996). However, such model includes recursive (or nonrecursive) filter and the order of this filter is prespecified. Therefore, if complexity of the object transfer function is not limited, the method is not suitable.

The equivalent gain concept (Arnstein, 1979; Arnstein et al., 1992; Chen et al., 1996) implies finding the difference between the object response and the test signal. In this case it is required that the effective width of the test-signal spectrum should be inside the horizontal segment of the frequency response of the object under test. Otherwise, it is necessary to compensate linear distortions of the test signal produced by the object. In practice, this compensation can be accomplished only for time-independent linear distortions with simple frequency dependence.

The problem of observing nonlinear transformation products of UWB signals can be solved by using the test signal with local null (or nulls) of spectrum (E. Semyonov, 2002, 2004; Lipshitz et al., 2002) or by means of rejection of narrow frequency band in the test-signal

spectrum (Snezko & Werner, 1997). In this case, it is possible to observe only nonlinear transformation products adjacent to nulls.
In the given work, we consider some examples and peculiarities of practical use of our method, which allows observing nonlinear transformation products of UWB signal against the background of a continuous spectrum of a test signal. The advantages of methods proposed (including experimental results) in comparison with the analysis of harmonics and intermodulation products are shown.

2. Method of nonlinear objects testing using ultra wideband signals

The essence of our method (E. Semyonov, 2005; E. Semyonov & A. Semyonov, 2007) is the following. The object linearly transforms signals if

$$u(t) = h(t) * x(t), \tag{1}$$

where $h(t)$ is the impulse response of the object and the equality sign indicates the identity for $x(t)$.
When investigating nonlinearity transformation of narrowband signals, usually there are points or intervals of observed frequency band for which

$$\left.\begin{array}{l} X(\omega) = 0 \\ U(\omega) \neq 0 \end{array}\right\}, \tag{2}$$

where $X(\omega)$ and $U(\omega)$ are the spectra of the test signal and the object response, respectively. In this case there is no necessity to place emphasis on identity (1) for $x(t)$. Indeed, if (2) holds at least for some ω, then it is clear that transformation of signal by an object is nonlinear, even if we take into consideration just one test impact.
Ultra wideband signals have usually a continuous spectrum. Here we can establish the nonlinearity of signals transformation using several test impact. The equality (1) should be held for all impacts (i.e., it should be identical for $x(t)$), otherwise the transformation of signals is nonlinear. Thus, at least two test signals with different waveforms and/or amplitudes are required.
The receiver is assumed to have two (reference and measurement) channels that process, respectively, the test signals generated at the generator output and the object responses. Here there is no need to use test signals with prescribed waveforms. (In particular, nonlinear signal distortions in the generator are acceptable.) This circumstance enables us to investigate, for example, the nonlinearity of signal transformation in communications systems using the fragments of real signals transmitted in these systems (including signals with nonoverlapping spectra). Test signals can be realizations of a random process.
Nonlinearity characteristic is defined by the following relationship

$$\varepsilon^*(t) = S_u[u_1(t)] - F^{-1}\left[\frac{F\{S_u[u_2(t)]\}}{F\{S_x[x_2(t)]\}}\right] * S_x[x_1(t)], \tag{3}$$

where F is the Fourier transform; F^{-1} is the inverse Fourier transform; S_u is the nonlinear operator of the measurement channel that changes the time function of the object response at the input of the receiver's measurement channel to the time function at the output of

this channel; S_x is the nonlinear operator of the reference channel; $u_1(t)$ and $u_2(t)$ are the object responses to signals $x_1(t)$ and $x_2(t)$, respectively; and the asterisk designates convolution.

When an object transforms signals linearly, and the receiver's channels are linear, $\varepsilon^*(t) \equiv 0$. If $\varepsilon^*(t) \neq 0$ at least for some values of time t, signals transformation by the object is nonlinear.

The method of nonlinear time domain reflectometry is known (Bryant, 2007), in which the series of test signals are used as well. However, only "changing the one or more pulse transmission parameter values" (such as dc bias and amplitude) is considered. The waveform of test signal remains invariable. In some cases, such restriction in a choice of test signals is inappropriate. The maximum amplitude of a nonlinear echo is usually observed at the maximum difference between amplitudes of test signals. Thus, small amplitude of the second test signal is desirable, but without energy decrease of that signal. Therefore, the waveform of the second test signal should differ from the waveform of the first. In addition, under this method (Bryant, 2007) only echo signals are registered. (The test signals generated at the generator output are not registered.) In this case, small nonlinearity of the generator should be ensured.

3. Modelling nonlinear distortion of ultra wideband signals. Virtual nonlinear impulse network analyzer

It is important to predict nonlinear distortions of signals in UWB communication and radar systems at design stage.

The task of investigation of nonlinear signals distortions should not be confused with the tasks of investigation of nonlinear objects characteristics, synthesis of nonlinear objects models and identifications of parameters of these models. Even if we have such models, we still know nothing about nonlinearity of transformation of concrete signals made by an object. Having a nonlinear model of an object, it is possible to compute its response to quite arbitrary (including UWB) signals. However, in this case it is not clear, whether the transformation of signal's waveform is caused by linear or nonlinear distortions. In fact, the investigation of nonlinear signals distortions should answer this question. Such investigation can be carried out for the experimentally registered signals or for signals calculated at a modeling stage.

Separately we note the following. Modeling nonlinear objects responses is invariably associated with using nonlinear models of these objects. However, the nonlinear distortions of signals can be selected by linear means. Moreover, a use of linear means of selection of nonlinear distortions is preferable because such means do not introduce additional nonlinear distortions to object response. As an example, we will mention the measurement of total harmonic distortion by the rejection of the first harmonic with linear band-stop filter.

If nonlinearity characteristic (3) is obtained in computer-aided design (CAD) systems as a result of modeling, then there are some peculiarities. First, we can choose the linear receiver for which $S_{x,u}(x) = x$. In this case, the nonlinearity characteristic (3) is expressed as

$$\varepsilon^*(t) = u_1(t) - F^{-1}\left\{\frac{F[u_2(t)]}{F[x_2(t)]}\right\} * x_1(t)\,. \tag{4}$$

Secondly, the object responses are computed also by CAD system (using SPICE or harmonic balance simulator). Let's express it by the formula $u(t) = S[x(t)]$, where S is the nonlinear operator reflecting the signal's transformation by object under study. Substituting this formula into (4), we obtain

$$\varepsilon^*(t) = S\left[x_1(t)\right] - F^{-1}\left[\frac{F\left\{S\left[x_2(t)\right]\right\}}{F\left[x_2(t)\right]}\right] * x_1(t) \tag{5}$$

Thirdly, the signal $x_2(t)$ can be simply shaped by CAD tools as result of a linear transformation of signal $x_1(t)$:

$$x_2(t) = h_1(t) * x_1(t), \tag{6}$$

where $h_1(t)$ is the impulse response of linear filter. Having substituted formula (6) into (5), we obtain (after transformation)

$$\varepsilon^*(t) = S\left[x_1(t)\right] - F^{-1}\left\{\frac{1}{F\left[h_1(t)\right]}\right\} * S\left[h_1(t) * x_1(t)\right]. \tag{7}$$

In fact, $F^{-1}\{1/F[h_1(t)]\}$ is the impulse response $\bar{h}_1(t)$ of some filter, which satisfies to the condition $\bar{h}_1(t) * h_1(t) = \delta(t)$, where $\delta(t)$ is the Dirac delta function. Therefore, we will represent expression (7) in the form:

$$\varepsilon^*(t) = S\left[x_1(t)\right] - \bar{h}_1(t) * S\left[h_1(t) * x_1(t)\right]. \tag{8}$$

Thus, the used CAD systems should contain: generator of test signal $x_1(t)$, nonlinear simulator (based on SPICE or harmonic balance method), linear filters with impulse responses $h_1(t)$ and $\bar{h}_1(t)$ and delay lines for superposition of object's responses to first and second test signal (these responses are consecutive).

We have developed the virtual nonlinear impulse network analyzer (Semyonov et al., 2009). "Virtual analyzer" means analyzer that is placed in the developed scheme just as other library elements. Currently its version made for AWR Design Environment. The devices for nonlinear time domain reflection (TDR_N) and transmission (TDT_N) measurements are made separate (Fig. 1a). Each device contains two control points, one of which allows the user to display the response of object and the other – the nonlinearity characteristic.

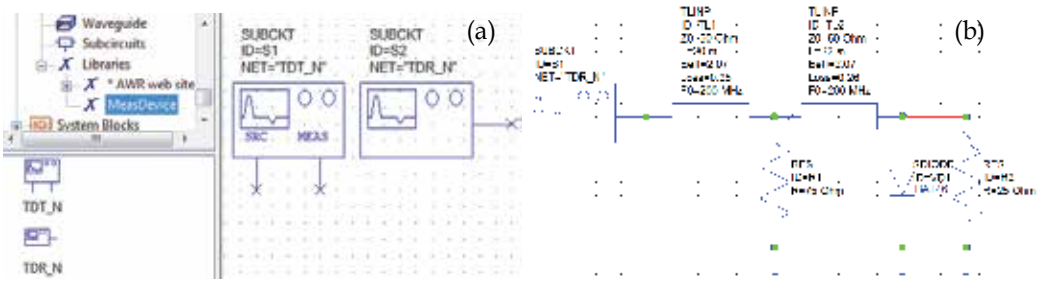

Fig. 1. Impulse time-domain transfer nonlinearity characteristic measurement device (TDT_N) and nonlinear time-domain reflectometer (TDR_N) (a); transmission line with linear (R1) and nonlinear (VD1 и R2) discontinuities (b)

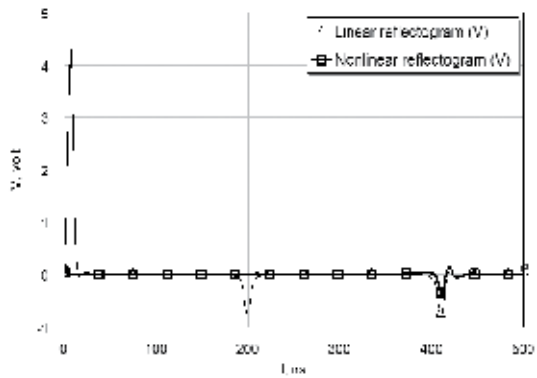

Fig. 2. The results of tests of the transmission line shown in Fig. 1b by virtual nonlinear reflectometer

Fig 1b shows the example of using developed virtual nonlinear reflectometer. It is a fragment of a window of AWR Design Environment. The transmission line with linear and nonlinear discontinuities has been used as the device under test (DUT). Fig. 2 shows the testing results of this line (thin curve is the response of network; thick curve is the nonlinearity characteristic). The extremum of nonlinearity characteristic is observed only at the moment that corresponds to the response of nonlinear discontinuity. Let's draw our special attention to the fact that nonlinearity characteristic does not contain the marks of any linear discontinuities.

4. Baseband nonlinear reflectometer R4-I-01. Wire transmission lines sounding

We have designed a baseband pulsed vector network analyzer R4-I-01 (Fig. 3a) which uses the considered investigation method of the nonlinearity of the signal's transformation (Loschilov et al., 2009). The device works under control of the ImpulseM 2.0 software (Fig. 3b).

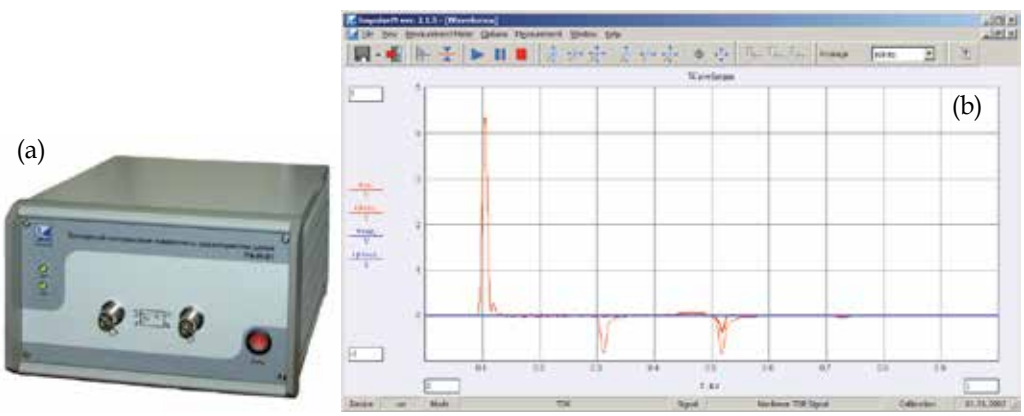

Fig. 3. Baseband pulsed vector network analyzer R4-I-01 (a) and screenshot of the main window of ImpulseM 2.0 software (b). Thin curve shows the response $S_u[u_1(t)]$ of the network which shown in Fig. 1b, thick curve shows the nonlinearity characteristic $\varepsilon^*(t)$ for this network

The device is designed for network analysis in a frequency range 0…25 MHz including wire transmission lines. The amplitude of a test signal can be set up within 0.1…5 V. The minimum pulse width is 10 ns. The detection of nonlinear discontinuities in transmission lines is possible for distance up to 400 m.

The device includes an arbitrary waveform generator (AWG), a two-channel analog-to-digital converter (ADC), a delay line and a hub for universal serial bus (USB). AWG and ADC are connected to the computer with installed software ImpulseM (through USB-hub). The registration of real obtained test signals and object responses by two-channel ADC permits nonlinear distortions of test signals by the generator. The delay line allows separating an incident and reflected wave.

An averaging of last observations of test signals $S_x[x_{1,2}(t)]$ and object responses $S_u[u_{1,2}(t)]$ can be used for noise reduction. The "Averaging" window in the main window of ImpulseM software (Fig. 3b) determines how many observations are averaged. The averaged signals are used for the calculation of nonlinearity characteristic by means of formula (3). The averaged object response $S_u[u_1(t)]$ and the nonlinearity characteristic $\varepsilon^*(t)$ are displayed on the graph (Fig. 3b).

Concerning wire transmission lines, the linear reflectometry with baseband pulse test signals allows to determine the presence of discontinuities in a transmission line, a distance from them and a type of their impedance. However, we cannot determine the nonlinearity of discontinuities. Nonlinear elements are (for example) semiconductor elements and defects of a transmission lines such as metal-oxide-metal (MOM) contacts. To investigate the nonlinearity of signals transformation by discontinuities in a transmission line, one usually use a sinusoidal test signals. However, in this case we have no information about the distance from nonlinear discontinuities. Therefore, the use of baseband pulse test signals for the investigation of signals transformation nonlinearity by discontinuities in wire transmission lines is interesting.

For example, Fig. 3b shows the response $S_u[u_1(t)]$ (thin curve) and the nonlinearity characteristic $\varepsilon^*(t)$ (thick curve) of network shown in Fig. 1b. The nonlinearity characteristic has extremum close to the response of nonlinear discontinuity. Outside of this neighborhood (including the neighborhood of the response of linear discontinuity) extremums of the nonlinearity characteristic are absent. It is possible to recognize the nature of discontinuities (linear or nonlinear) by means of the nonlinearity characteristic (3). Such

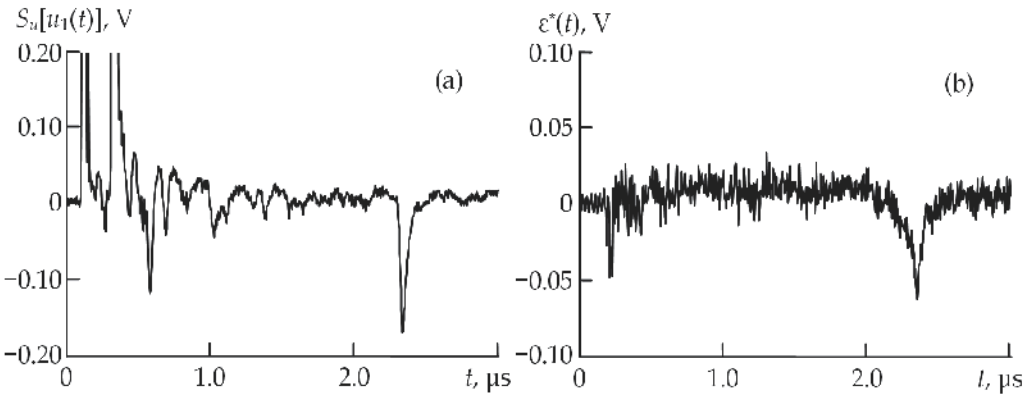

Fig. 4. Usual echo (a) and nonlinear echo (b) of metal-oxide-metal contact

possibility still remains even if the responses of discontinuities are identical (thin curve in Fig. 3b). The nonlinear response has small width. Therefore, it is possible to measure the distance from nonlinear discontinuity.

The comparison of Fig. 2 and 3b shows that results of modeling by virtual nonlinear reflectometer correlate with experimental results quite well.

Other nonlinear object, which can be in wire transmission lines, is metal-oxide-metal contact. Fig. 4 shows the example of detection of such contacts by means of device R4-I-01. We investigated the contact between the steel needle and the oxide coated steel plate. This contact was connected as a short circuit to the end of segment of TRP-0.4 cable. The length of the segment was 230 m. Fig. 4a shows the usual echo and Fig. 4b shows the nonlinearity characteristic (nonlinear echo). The MOM-contact is easily detected and its nonlinear nature is determined definitely.

In addition, we note the advantage of objects detection based on the nonlinearity characteristic.

In the presence of distributed deformations of a line, the response of this line looks like "a noise". For imitation of this quite possible situation, we use unshielded TRP-0.4 cable, which has been winded into a coil. As discontinuity, we used the BAT46 Shottky diode, which has been connected in parallel to the cable. The distance between the measuring device and the diode was 230 m. Fig. 5 shows the response (a) and the nonlinearity characteristic (b) of this network.

The amplitude of the diode response is approximately equal to the amplitude of the response from the distributed deformations of the cable (Fig. 5a). On the contrary, the nonlinearity characteristic has the clear-cut extremum corresponding to an echo-signal from the diode.

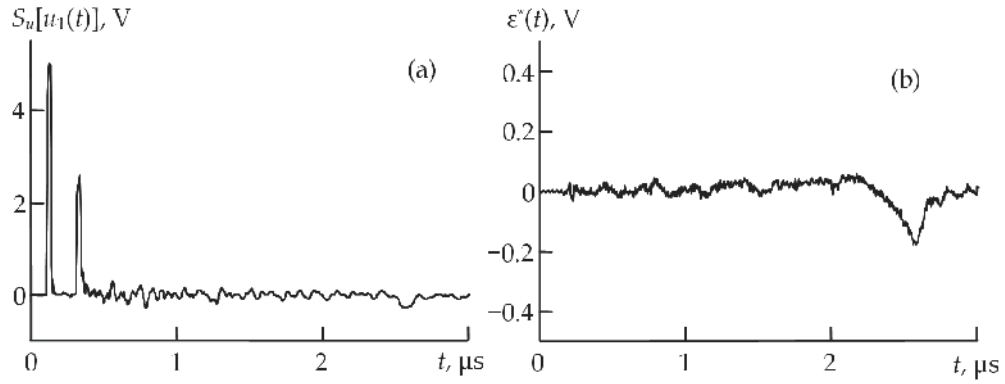

Fig. 5. The response (a) and the nonlinearity characteristic (b) of the BAT46 Shottky diode connected as a parallel discontinuity to the TRP-0.4 cable with distributed deformations

Thus, if the object under test has nonlinear properties, then an object detection based on the nonlinearity characteristic is preferable.

5. Sounding of objects by low-frequency signals with an ultra-wide relative width of spectrum

Selective detection of substances with use of their nonlinear properties is of interest. For this, the field should influence an object material. Concerning a metal, it means that the use of low-frequency signals is needed.

We've done the experimental investigations of 10-mm-dia, 1-mm-thick low-carbon-steel and aluminum disks (E. Semyonov & A. Semyonov, 2007). The objects were placed above the inductor coils with the diameter of 10 mm and at the distance of 2.5 mm from their end surfaces.

Test signal $x_1(t)$ was used in the form

$$x_1(t) = \frac{\sin(2\pi f_{up} t + \pi/2)}{2\pi f_{up} t + \pi/2} - \frac{\sin\left(2\pi f_{up} t - \pi/2\right)}{2\pi f_{up} t - \pi/2}, \tag{9}$$

where f_{up} = 24 kHz is the upper frequency limit of the spectrum of signal $x_1(t)$. The amplitude spectrum of test signal $x_2(t)$ was analogous to the amplitude spectrum of signal $x_1(t)$, and the phase spectrum of the former signal differed from the phase spectrum of $x_1(t)$ by a value that had a quadratic frequency dependence:

$$X_2(\omega) = X_1(\omega)\exp(-jd_2\omega|\omega|), \tag{10}$$

where d_2 is the coefficient that determines a decrease in the amplitude of signal $x_2(t)$ and an increase in the duration of this signal relative to the corresponding parameters of signal $x_1(t)$. The maximum voltage of pulse $x_1(t)$ applied to the transmitting coil with a resistance of 6.3 Ω was 28 V.

To compare the proposed nonlinearity characteristic and the nonlinearity characteristic that was obtained via determination of intermodulation products, a two-frequency (16 and 18 kHz) test signal was used. Its amplitude was equal to the amplitude of signal $x_1(t)$. The necessary frequency resolution was achieved through selection of the duration of the two-frequency signal such that its value was much greater than the duration of signal $x_1(t)$. At a level of 0.1 of the amplitude of the two-frequency signal, its duration was 3.9 ms. Accordingly, the energy of the two-frequency signal was greater than the energy of signal $x_1(t)$.

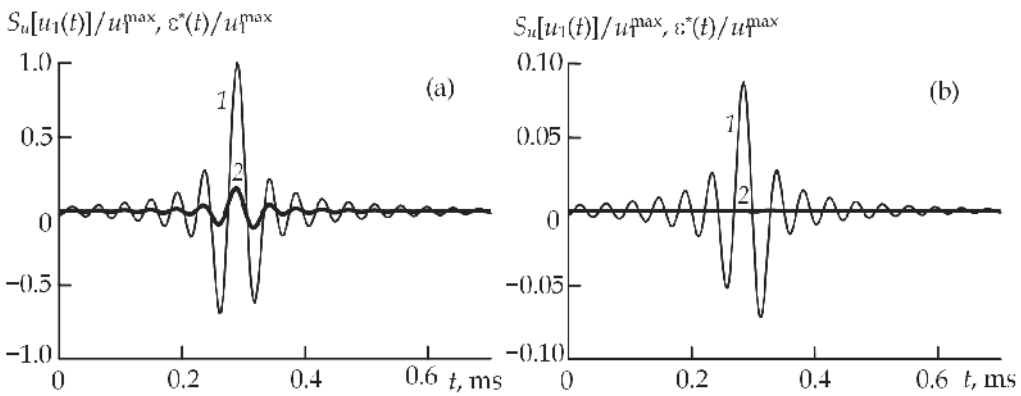

Fig. 6. Normalized response $S_u[u_1(t)]$ (curve *1*) and nonlinearity characteristic $\varepsilon^*(t)$ (curve 2) of a low-carbon-steel object (a) and an aluminum object (b)

For the low-carbon-steel and aluminum objects, responses $S_u[u_1(t)]$ and nonlinearity characteristic $\varepsilon^*(t)$ are shown in Figs. 6a and 6b, where the responses of the objects and nonlinearity characteristics are normalized to amplitude u_1^{max} of response $S_u[u_1(t)]$ of the low-carbon-steel object.

We see a significant nonlinearity of signals transformation by a low-carbon-steel object, while attributes of the nonlinearity of signal transformation performed by an aluminum object were not found. Hence, the proposed nonlinearity characteristic of signals transformation can be used to obtain additional classification attributes of an object.

When the low-carbon-steel object was sensed by a two-frequency test signal with an amplitude equal to the amplitude of $x_1(t)$, the normalized amplitude of the sum of intermodulation products in the object response was 2.2%. This value is 7 times less than the normalized amplitude of nonlinearity characteristic $\varepsilon^*(t)$ that was obtained for this object, although both the sum of intermodulation products and $\varepsilon^*(t)$ can be interpreted as the residuals of the linear equation used to approximate nonlinear transformation.

Fig. 7 additionally shows this relationship (for low-carbon-steel object). Curve *1* shows the amplitude spectrum $E^*(f)$ of the nonlinearity characteristic $\varepsilon^*(t)$. This spectrum is normalized to the maximum U_1^{max} of the amplitude spectrum of the response to the signal $x_1(t)$. Curve *2* shows the intermodulation products $U_{IM}(f)$ in the response to the two-frequency signal (spectral components of the test signal are rejected). This spectrum is normalized to the maximum U_s^{max} of the amplitude spectrum of the response to the two-frequency signal. All test signals had the same amplitudes. It is clear that the normalized components of the amplitude spectrum of the nonlinearity characteristic $\varepsilon^*(t)$ is considerably greater than the normalized intermodulation products.

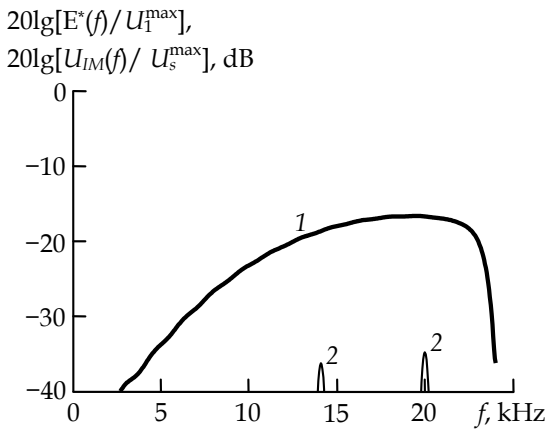

Fig. 7. The amplitude spectrum $E^*(f)$ of the nonlinearity characteristic $\varepsilon^*(t)$ (curve *1*) and the intermodulation products $U_{IM}(f)$ in the response to the two-frequency signal (curve *2*)

This fact means substantial increase of detection range of nonlinear detectors and radars using the considered method.

6. Problems of creation of nonlinear reflectometer with picosecond duration of test signals

If an upper frequency of measuring device exceeds 1 GHz, the formation of a pair of test signals with different forms has considerable difficulties. The upper frequency of up-to-date arbitrary waveform generators is about 10 GHz and they are very expensive. We consider the approach to solve this problem by using analog shaping of signals by passive circuits. The example of sounding of Schottky diode by the 300 ps impulse is described here.

An experimental setup for investigating the characteristics of nonlinear circuits using the considered method of nonlinear reflectometry was developed. Fig. 8 shows block diagram of the experimental setup.

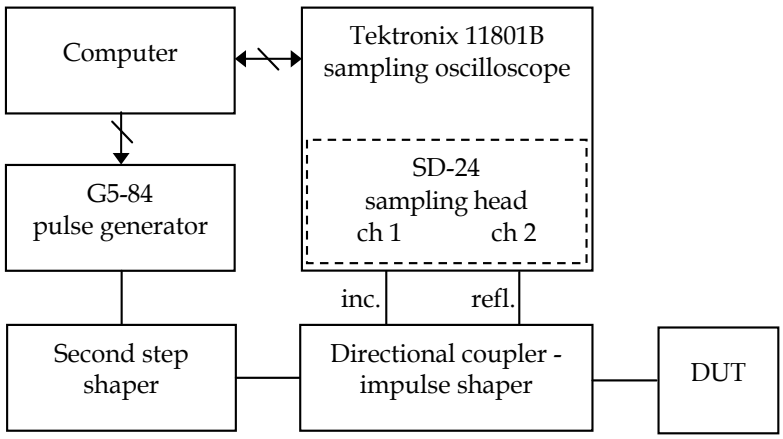

Fig. 8. Block diagram of the experimental setup

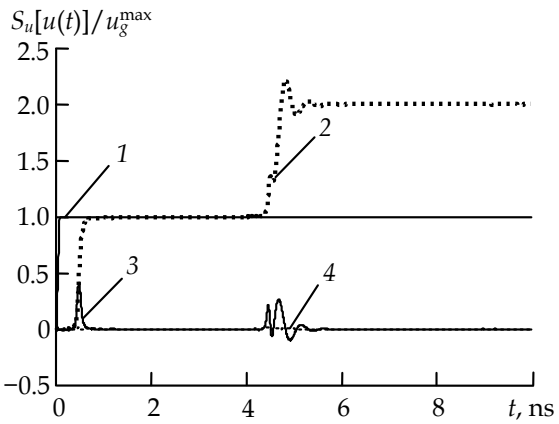

Fig. 9. Examples of waveforms: *1* – G5-84 output waveform; *2* – second step shaper output waveform; *3* – experimental setup output waveform (incident wave); *4* – signal measured on channel *2* (reflected wave)

The experimental setup works as follows. The computer sets the parameters of a test signal, transfers the settings to the generator G5-84 and run generation. Fast voltage step from generator G5-84 comes to the input of the second step shaper, where forms an additional voltage step, delayed relative to the first step at some time T and processed by a linear circuit. After that the signal comes into a directional coupler - impulse shaper, which differentiates the input pair of steps and produces a sequence of pulses arriving at the object under test. An incident component of the test signal comes to the first channel of the sampling oscilloscope. The signal reflected from the DUT comes to the second channel of the sampling oscilloscope. The sampling oscilloscope registers the incident and reflected pulses, and transmits the data to the computer.

Fig. 9 shows some examples of waveforms at the inputs/outputs of blocks of the experimental setup.
The waveforms are presented at the matched mode on the output of the experimental setup. Fig. 9. shows the initial voltage step (curve *1*) produced by the pulse generator G5-84 (the pulse width is much larger than the observation window). After processing by the second step shaper, the signal has additional voltage step with oscillations at the front (curve *2*). Directional coupler - impulse shaper performs three functions: the differentiation of the initial signal (curve *3*); the directional separation of the signal reflected from DUT (curve *4*); the transfer of the incident signal to the first channel of sampling oscilloscope (curve *2*). All signals are normalized to the amplitude $u_g^{\max}$ of the pulse generator output signal.
The experimental investigations were performed with the use of the designed setup. Two types of objects were investigated: a linear object (the 38 Ω chip resistor) and a nonlinear object in which the microwave Schottky diode HSMS-8202 and the 51 Ω chip resistor were connected in parallel. For both objects, linear and nonlinear reflectograms were measured. Fig. 10 shows the results of the experimental investigations.

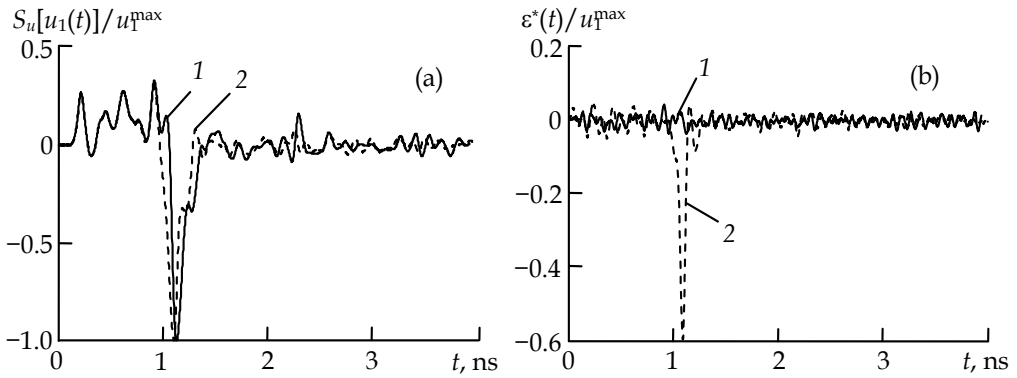

Fig. 10. Experimentally registered linear reflectograms $S_u[u_1(t)]$ (a) and nonlinear reflectograms $\varepsilon^*(t)$ (b). Curve *1* – linear object; curve *2* – nonlinear object. All signals are normalized to the amplitude of signal $S_u[u_1(t)]$

As seen from Fig. 10a, measured reflectograms of linear (curve *1*) and nonlinear objects (curve *2*) have similar forms and amplitudes. (A negative polarity of the responses indicates that the impedance of objects is lower than 50 Ω.) Comparison of the responses cannot indicate nonlinear properties of any objects.
As seen from Fig. 10b, the results obtained by nonlinear reflectometry is different for linear and nonlinear objects. Nonlinear objects trace (curve *2*) has a pronounced extremum in the neighborhood of 1.1 ns, whereas in the trace of a linear object (curve *1*) there are no extremums greater than the noise level. Extremum time position corresponds to the point of connection with a nonlinear element.
The experimental investigations performed illustrate that nonlinear reflectometry can be effectively realized at the width of incident and reflected pulses about 300 ps.

7. Measurement of nonlinearity of ultra wideband receivers

The considered method permits nonlinear distortions of test signals by the generator. Therefore, if the channel between the generator and the receiver is linear, then we measure nonlinear signals distortions only by the receiver (E. Semyonov & A. Semyonov, 2007).

In this case

$$u_{1,2}(t) = h(t) * x_{1,2}(t), \tag{11}$$

where $h(t)$ is the impulse response of this channel. If the impulse response $h(t)$ is Dirac delta function then $u_1(t) = x_1(t)$ and $u_2(t) = x_2(t)$. In this case $\varepsilon^*(t) \equiv 0$ even if transformation of signals by the receiver is nonlinear. Therefore it is necessary to choose $h(t)$ so that the signals $u_1(t)$ and $x_1(t)$ would have different waveforms and/or amplitudes. (The same apply to signals $u_2(t)$ and $x_2(t)$.)

To use the nonlinearity characteristic (3) the receiver should be two-channel. However, quite often it is required to investigate the single-channel receiver (or the separate channel of the multichannel receiver). In this case the same channel of the receiver should register signals $x_{1,2}(t)$ and $u_{1,2}(t)$ (which are the result of transformation of signals $x_{1,2}(t)$ according to (11)). This is possible, if signals $u_{1,2}(t)$ come to the same point in which signals $x_{1,2}(t)$ are registered (similarly how it occurs in reflectometers).

Thus, the channel between the generator and the receiver should contain a delay line (for consecutive transmission of $x_{1,2}(t)$ and $u_{1,2}(t)$ to receiver's input) and a linear filter which provides some difference between the waveforms of signals $u_{1,2}(t)$ and $x_{1,2}(t)$.

If we have a single-channel receiver, then $S_x = S_u = S_r$, where S_r is the operator of the investigated single-channel receiver. Therefore, the formula (3) will become:

$$\varepsilon^*(t) = S_r[u_1(t)] - F^{-1}\left[\frac{F\{S_r[u_2(t)]\}}{F\{S_r[x_2(t)]\}}\right] * S_r[x_1(t)] \cdot \tag{12}$$

If equality (11) holds and $\varepsilon^*(t) \neq 0$ at least for some values of time t, S_r is nonlinear. (The receiver distorts the signals nonlinearly.)

Fig. 11a shows the nonlinearity of transformation of baseband pulse by the Tektronix TDS1012B oscilloscope. Here are shown: signal $S_r[u_1(t)]$ (curve *1*) and nonlinearity characteristic (curve *2*). Both curves are normalized to amplitude $u_1^{\max}$ of signal $S_r[u_1(t)]$. At the same amplitude of the test signal the harmonic distortion has been measured. Fig. 11b shows the results of this measurement. (The frequency of test signal $x_s(t)$ is 50 MHz.) Let us notice that the amplitude of the nonlinearity characteristic of baseband pulse's transformation (1%) is 5 times more than total harmonic distortion (0.2%).

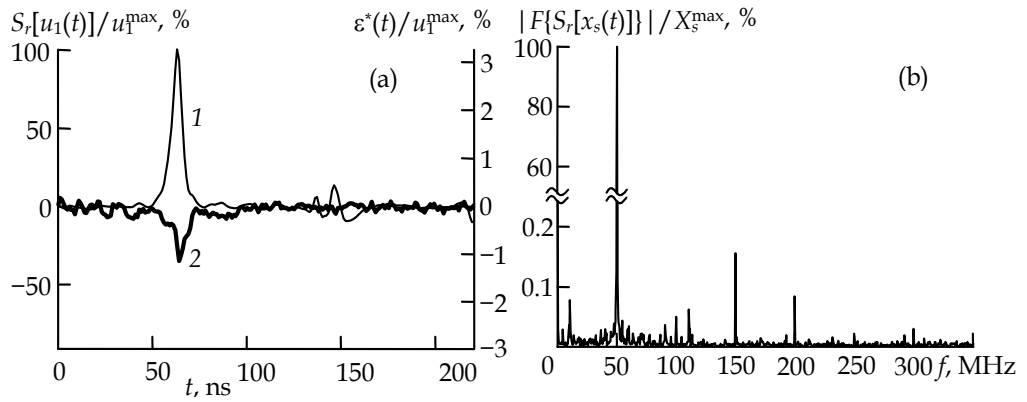

Fig. 11. Receiver-registered baseband pulse ($S_r[u_1(t)]$, curve *1*) and nonlinearity characteristic ($\varepsilon^*(t)$, curve *2*) (a). Spectrum module $|F\{S_r[x_s(t)]\}|$ of the receiver-registered sinusoidal signal (b). (Spectrum is normalized to the amplitude of the first harmonic $X_s^{\max}$.)

This example illustrates special importance of linearity in UWB receivers. Besides, it is clear that for UWB receivers testing one should use UWB signals. In nonlinear radars and nonlinear reflectometers such measurements are necessary to observe the nonlinear response of the object against the background of nonlinear distortions in the receiver (E. Semyonov & A. Semyonov, 2007).

8. Conclusion

The considered method is effective for the following tasks.

1. Investigation of devices (for example, receivers) for ultra wideband communication systems (including design stage).
2. Detection of imperfect contacts and other nonlinear elements in wire transmission lines.
3. Remote and selective detection of substances with the use of their nonlinear properties.

The main advantages of the considered approach are listed below.

1. Real signals transmitted in UWB systems can be used as test signals.
2. Nonlinear signal distortions in the generator are acceptable.
3. Measurement of distance from nonlinear discontinuity is possible.
4. Nonlinear response is several times greater than the response to sinusoidal or two-frequency signal.

The designed devices and measuring setups show high efficiency for frequency ranges with various upper frequency limits (from 20 kHz to 20 GHz).

The developed virtual analyzers provide corresponding investigations of devices and systems at design stage.

9. Acknowledgment

This study was supported by the Ministry of Education and Science of the Russian Federation under the Federal Targeted Programme "Scientific and Scientific-Pedagogical Personnel of the Innovative Russia in 2009-2013" (the state contracts no. P453 and no. P690) and under the Decree of the Government of the Russian Federation no. 218 (the state contract no. 13.G25.31.0017).

10. References

Arnstein, D. (1979). Power division in spread spectrum systems with limiting. *IEEE Transactions on Communications*, Vol.27, No.3, (March 1979), pp. 574-582, ISSN: 0090-6778

Arnstein, D.; Vuong, X.; Cotner, C. & Daryanani, H. (1992) The IM Microscope: A new approach to nonlinear analysis of signals in satellite communications systems. *COMSAT Technical Review*, Vol.22, No.1, (Spring 1992), pp. 93-123, ISSN 0095-9669

Bryant, P. (2007). Apparatus and method for locating nonlinear impairments in a communication channel by use of nonlinear time domain reflectometry, *Descriptions of Invention to the Patent No. US 7230970 B1 of United States*, 23.02.2011, Available from: http://www.freepatentsonline.com/7230970.pdf

Chen, S.-W.; Panton, W. & Gilmore, R. (1996). Effects of Nonlinear Distortion on CDMA Communication Systems. *IEEE Transactions on Microwave Theory and Techniques*, Vol.44, No.12, (December 1996), pp. 2743-2750, ISSN: 0018-9480

Green, E. & Roy, S. (2003). System Architectures for High-rate Ultra-wideband Communication Systems: A Review of Recent Developments, 22.02.2011, Available from: http://www.intel.com/technology/comms/uwb/download/w241_paper.pdf

Lipshitz, S.; Vanderkooy, J. & Semyonov, E. (2002). Noise shaping in digital test-signal generation, *Preprints of AES 113th Convention*, Preprint No.5664, Los Angeles, California, USA, October 5-8, 2002

Loschilov, A.; Semyonov E.; Maljutin N.; Bombizov A.; Pavlov A.; Bibikov T.; Iljin A.; Gubkov A. & Maljutina A. (2009). Instrumentation for nonlinear distortion measurements under wideband pulse probing, *Proceedings of 19th International Crimean Conference "Microwave & Telecommunication Technology" (CriMiCo'2009)*, pp. 754-755, ISBN: 978-1-4244-4796-1, Sevastopol, Crimea, Ukraine, September 14-18, 2009

Semyonov, E. (2002). Noise shaping for measuring digital sinusoidal signal with low total harmonic distortion, *Preprints of AES 112th Convention*, Preprint No.5621, Munich, Germany, May 10-13, 2002

Semyonov, E. (2004). Method for investigating non-linear properties of object, *Descriptions of* Invention to the Patent No. RU 2227921 C1 of Russian Federation, 23.02.2011, Available from:
from: http://v3.espacenet.com/publicationDetails/biblio?CC=RU&NR=2227921C1&KC=C1&FT=D&date=20040427&DB=EPODOC&locale=en_gb

Semyonov, E. (2005). Method for researching non-linear nature of transformation of signals by object, *Descriptions of Invention to the Patent No. RU 2263929 C1 of Russian Federation,* 23.02.2011, Available from: http://v3.espacenet.com/publicationDetails/biblio?CC=RU&NR=2263929C1&KC=C1&FT=D&date=20051110&DB=EPODOC&locale=en_gb

Semyonov, E. & Semyonov, A. (2007). Applying the Difference between the Convolutions of Test Signals and Object Responses to Investigate the Nonlinearity of the Transformation of Ultrawideband Signals. *Journal of Communications Technology and Electronics*, Vol.52, No.4, (April 2007), pp. 451-456, ISSN 1064-2269

Semyonov, E.; Maljutin, N. & Loschilov, A. (2009). Virtual nonlinear impulse network analyzer for Microwave Office, *Proceedings of 19th International Crimean Conference "Microwave & Telecommunication Technology" (CriMiCo'2009)*, pp. 103-104, ISBN: 978-1-4244-4796-1, Sevastopol, Crimea, Ukraine, September 14-18, 2009

Sobhy, M.; Hosny, E.; Ng M. & Bakkar E. (1996). Non-Linear System and Subsystem Modelling in The Time Domain. *IEEE Transactions on Microwave Theory and Techniques*, Vol.44, No.12, (December 1996), pp. 2571-2579, ISSN: 0018-9480

Snezko, O. & Werner, T. (1997) Return Path Active Components Test Methods and Performance Comparison, *Proceedings of Conference on Emerging Technologies*, pp. 263-294, Nashville, Tennessee, USA, 1997

Verspecht, J. (1996). Black Box Modelling of Power Transistors in the Frequency Domain, In: *Conference paper presented at the INMMC '96, Duisburg, Germany*, 22.02.2011, http://users.skynet.be/jan.verspecht/Work/BlackBoxPowerTransistorsINMMC96.pdf

Verspecht, J. & Root D. (2006). Polyharmonic Distortion Modeling. *IEEE Microwave Magazine*, Vol.7, No.3, (June 2006), pp. 44-57, ISSN: 1527-3342

2

Low Sampling Rate Time Acquisition Schemes and Channel Estimation Algorithms of Ultra-Wideband Signals

Wei Xu and Jiaxiang Zhao
Nankai University
China

1. Introduction

Ultra-wideband (UWB) communication is a viable technology to provide high data rates over broadband wireless channels for applications, including wireless multimedia, wireless Internet access, and future-generation mobile communication systems (Karaoguz, 2001; Stoica et al., 2005). Two of the most critical challenges in the implementation of UWB systems are the timing acquisition and channel estimation. The difficulty in them arises from UWB signals being the ultra short low-duty-cycle pulses operating at very low power density. The Rake receiver (Turin, 1980) as a prevalent receiver structure for UWB systems utilizes the high diversity in order to effectively capture signal energy spread over multiple paths and boost the received signal-to-noise ratio (SNR). However, to perform maximal ratio combining (MRC), the Rake receiver needs the timing information of the received signal and the knowledge of the channel parameters, namely, gains and tap delays. Timing errors as small as fractions of a nanosecond could seriously degrade the system performance (Lovelace & Townsend, 2002; Tian & Giannakis, 2005). Thus, accurate timing acquisition and channel estimation is very essentially for UWB systems.

Many research efforts have been devoted to the timing acquisition and channel estimation of UWB signals. However, most reported methods suffer from the restrictive assumptions, such as, demanding a high sampling rates, a set of high precision time-delay systems or invoking a line search, which severally limits their usages. In this chapter, we are focusing on the low sampling rate time acquisition schemes and channel estimation algorithms of UWB signals. First, we develop a novel optimum data-aided (DA) timing offset estimator that utilizes only symbol-rate samples to achieve the channel delay spread scale timing acquisition. For this purpose, we exploit the statistical properties of the power delay profile of the received signals to design a set of the templates to ensure the effective multipath energy capture at any time. Second, we propose a novel optimum data-aided channel estimation scheme that only relies on frame-level sampling rate data to derive channel parameter estimates from the received waveform. The simulations are provided to demonstrate the effectiveness of the proposed approach.

2. The channel model

From the channel model described in (Foerster, 2003), the impulse response of the channel is

$$h(t) = X \sum_{n=1}^{N} \sum_{k=1}^{K(n)} \alpha_{nk} \delta(t - T_n - \tau_{nk}) \quad (1)$$

where X is the log-normal shadowing effect. N and $K(n)$ represent the total number of the clusters, and the number of the rays in the nth cluster, respectively. T_n is the time delay of the nth cluster relative to a reference at the receiver, and τ_{nk} is the delay of the kth multipath component in the nth cluster relative to T_n. From (Foerster, 2003), the multipath channel coefficient α_{nk} can be expressed as $\alpha_{nk} = p_{nk}\beta_{nk}$ where p_{nk} assumes either $+1$ or -1 with equal probability, and $\beta_{nk} > 0$ has log-normal distribution.
The power delay profile (the mean square values of $\{\beta_{nk}^2\}$) is exponential decay with respect to $\{T_n\}$ and $\{\tau_{nk}\}$, i.e.,

$$\langle \beta_{nk}^2 \rangle = \langle \beta_{00}^2 \rangle \exp(-\frac{T_n}{\Gamma}) \exp(-\frac{\tau_{nk}}{\gamma}) \quad (2)$$

where $\langle \beta_{00}^2 \rangle$ is the average power gain of the first multipath in the first cluster. Γ and γ are power-delay time constants for the clusters and the rays, respectively.
The model (1) is employed to generate the impulse responses of the propagation channels in our simulation. For simplicity, an equivalent representation of (1) is

$$h(t) = \sum_{l=0}^{L-1} \alpha_l \delta(t - \tau_l) \quad (3)$$

where L represents the total number of the multipaths, α_l includes log-normal shadowing and multipath channel coefficients, and τ_l denotes the delay of the lth multipath relative to the reference at the receiver. Without loss of generality, we assume $\tau_0 < \tau_1 < \cdots < \tau_{L-1}$. Moreover, the channel only allows to change from burst to burst but remains invariant (i.e., $\{\alpha_l, \tau_l\}_{l=0}^{L-1}$ are constants) over one transmission burst.

3. Low sampling rate time acquisition schemes

One of the most acute challenges in realizing the potentials of the UWB systems is to develop the time acquisition scheme which relies only on symbol-rate samples. Such a low sampling rate time acquisition scheme can greatly lower the implementation complexity. In addition, the difficulty in UWB synchronization also arises from UWB signals being the ultrashort low-duty-cycle pulses operating at very low power density. Timing errors as small as fractions of a nanosecond could seriously degrade the system performance (Lovelace & Townsend, 2002; Tian & Giannakis, 2005).
A number of timing algorithms are reported for UWB systems recently. Some of the timing algorithms(Tian & Giannakis, 2005; Yang & Giannakis, 2005; Carbonelli & Mengali, 2006; He & Tepedelenlioglui, 2008) involve the sliding correlation that usually used in traditional narrowband systems. However, these approaches inevitably require a searching procedure and are inherently time-consuming. Too long synchronization time will affect

symbol detection. Furthermore, implementation of such techniques demands very fast and expensive A/D converters and therefore will result in high power consumption. Another approach (Carbonelli & Mengali, 2005; Furusawa et al., 2008; Cheng & Guan, 2008; Sasaki et al., 2010) is to synchronize UWB signals through the energy detector. The merits of using energy detectors are that the design of timing acquisition scheme could benefit from the statistical properties of the power delay profile of the received signals. Unlike the received UWB waveforms which is unknown to receivers due to the pulse distortions, the statistical properties of the power delay profile are invariant. Furthermore, as shown in (Carbonelli & Mengali, 2005), an energy collection based receiver can produce a low complexity, low cost and low power consumption solution at the cost of reduced channel spectral efficiency.

In this section, a novel optimum data-aided timing offset estimator that only relies on symbol-rate samples for frame-level timing acquisition is derived. For this purpose, we exploit the statistical properties of the power delay profile of the received signals to design a set of the templates to ensure the effective multipath energy capture at any time. We show that the frame-level timing offset acquisition can be transformed into an equivalent amplitude estimation problem. Thus, utilizing the symbol-rate samples extracted by our templates and the ML principle, we obtain channel-dependent amplitude estimates and optimum timing offset estimates.

3.1 The signal model

During the acquisition stage, a training sequence is transmitted. Each UWB symbol is transmitted over a time-interval of T_{s} seconds that is subdivided into N_{f} equal size frame-intervals of length T_{f}. A single frame contains exactly one data modulated ultrashort pulse $p(t)$ of duration T_{p}. And the transmitted waveform during the acquisition has the form as

$$s(t) \quad = \quad \sqrt{E_{\mathrm{f}}} \sum_{j=0}^{NN_{\mathrm{f}}-1} d_{[j]_{N_{\mathrm{ds}}}} p(t - jT_{\mathrm{f}} - a_{\lfloor \frac{j}{N_{\mathrm{f}}} \rfloor} \triangle) \tag{4}$$

where $\{d_l\}_{l=0}^{N_{\mathrm{ds}}-1}$ with $d_l \in \{\pm 1\}$ is the DS sequence. The time shift $\triangle$ is chosen to be $T_{\mathrm{h}}/2$ with T_{h} being the delay spread of the channel. The assumption that there is no inter-frame interference suggests $T_{\mathrm{h}} \leq T_{\mathrm{f}}$. For the simplicity, we assume $T_{\mathrm{h}} = T_{\mathrm{f}}$ and derive the acquisition algorithm. Our scheme can easily be extended to the case where $T_{\mathrm{f}} \geq T_{\mathrm{h}}$. The training sequence $\{a_n\}_{n=0}^{N-1}$ is designed as

$$\{\underbrace{0,\, 0,\, 0,\, \cdots 0}_{n=0,1,\cdots,N_0-1}\ \underbrace{1,\, 0,\, 1,\, 0,\, \cdots 1,\, 0}_{n=N_0,N_0+1,\cdots,N-1}\}, \tag{5}$$

i.e., the first N_0 consecutive symbols are chosen to be 0, and the rest symbols alternately switch between 1 and 0.

The transmitted signal propagates through an L-path fading channel as shown in (3). Using the first arriving time τ_0, we define the relative time delay of each multipath as $\tau_{l,0} = \tau_l - \tau_0$

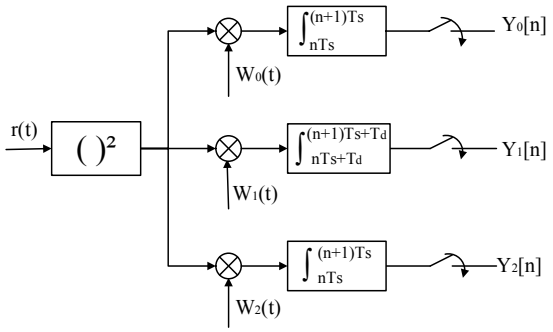

Fig. 1. The block diagram of acquisition approach.

for $1 \leq l \leq L-1$. Thus the received signal is

$$r(t) = \sqrt{E_{\mathrm{f}}} \sum_{j=0}^{NN_{\mathrm{f}}-1} d_{[j]_{N_{\mathrm{ds}}}} p_R(t - jT_{\mathrm{f}} - a_{\lfloor \frac{j}{N_{\mathrm{f}}} \rfloor} \Delta - \tau_0) + n(t) \tag{6}$$

where $n(t)$ is the zero-mean additive white Gaussian noise (AWGN) with double-side power spectral density $\sigma_n^2/2$ and $p_R(t) = \sum_{l=0}^{L-1} \alpha_l p(t - \tau_{l,0})$ represents the convolution of the channel impulse response (3) with the transmitted pulse $p(t)$.
The timing information of the received signal is contained in the delay τ_0 which can be decomposed as

$$\tau_0 \quad = \quad n_{\mathrm{s}} T_{\mathrm{s}} + n_{\mathrm{f}} T_{\mathrm{f}} + \xi \tag{7}$$

with $n_{\mathrm{s}} = \lfloor \frac{\tau_0}{T_{\mathrm{s}}} \rfloor$, $n_{\mathrm{f}} = \lfloor \frac{\tau_0 - n_{\mathrm{s}} T_{\mathrm{s}}}{T_{\mathrm{f}}} \rfloor$ and $\xi \in [0, T_{\mathrm{f}})$.
In the next section, we present an DA timing acquisition scheme based on the following assumptions: 1) There is no interframe interference, i.e., $\tau_{L-1,0} \leq T_{\mathrm{f}}$. 2) The channel is assumed to be quasi-static, i.e., the channel is constant over a block duration. 3) Since the symbol-level timing offset n_s can be estimated from the symbol-rate samples through the traditional estimation approach, we assumed $n_s = 0$. In this chapter, we focus on acquiring timing with frame-level resolution, which relies on only symbol-rate samples.

3.2 Analysis of symbol-rate sampled data $Y_0[n]$

As shown in Fig. 1, the received signal (6) first passes through a square-law detector. Then, the resultant output is separately correlated with the pre-devised templates $W_0(t)$, $W_1(t)$ and $W_2(t)$, and sampled at nT_{s} which yields $\{Y_0[n]\}_{n=1}^{N-1}$, $\{Y_1[n]\}_{n=1}^{N-1}$ and $\{Y_2[n]\}_{n=1}^{N-1}$. Utilizing these samples, we derive an optimal timing offset estimator $\hat{n}_{\mathrm{f}}$.
In view of (6), the output of the square-law detector is

$$\begin{aligned} R(t) \quad &= \quad r^2(t) = (r_{\mathrm{s}}(t) + n(t))^2 = r_{\mathrm{s}}^2(t) + m(t) \\ &= \quad E_{\mathrm{f}} \sum_{j=0}^{NN_{\mathrm{f}}-1} p_R^2(t - jT_{\mathrm{f}} - a_{\lfloor \frac{j}{N_{\mathrm{f}}} \rfloor} \triangle - \tau_0) + m(t) \end{aligned} \tag{8}$$

where $m(t) = 2r_s(t)n(t) + n^2(t)$. When the template $W(t)$ is employed, the symbol rate sampled data $Y[n]$ is

$$Y[n] \quad = \quad \int_0^{T_s} R(t + nT_s)W(t)dt. \tag{9}$$

Now we derive the decomposition of $Y_0[n]$, i.e., the symbol-rate samples when the template $W_0(t)$ defined as

$$W_0(t) \;=\; \sum_{k=0}^{N_f-1} w(t - kT_f), \;\; w(t) = \begin{cases} 1, & 0 \le t < \frac{T_f}{2} \\ -1, & \frac{T_f}{2} \le t < T_f \\ 0, & \text{others} \end{cases} \tag{10}$$

is employed. Substituting $W_0(t)$ for $W(t)$ in (9), we obtain symbol-rate sampled data $Y_0[n]$. Recalling (5), we can derive the following proposition of $Y_0[n]$.

Proposition 1: 1) For $1 \le n < N_0$, $Y_0[n]$ can be expressed as

$$Y_0[n] \quad = \quad N_f I_{\xi,0} + M_0[n], \tag{11}$$

2) For $N_0 \le n \le N-1$, $Y_0[n]$ can be represented as

$$Y_0[n] = \begin{cases} (2\Psi - N_f) I_{\xi,a_{n-1}} + M_0[n], & \xi \in [0, T_\eta) \\ (2\Psi - N_f + 1) I_{\xi,a_{n-1}} + M_0[n], & \xi \in [T_\eta, T_\eta + \frac{T_f}{2}) \\ (2\Psi - N_f + 2) I_{\xi,a_{n-1}} + M_0[n], & \xi \in [T_\eta + \frac{T_f}{2}, T_f) \end{cases} \tag{12}$$

where $\Psi \triangleq n_f - \frac{1}{2}\epsilon$, $\epsilon \in [-\frac{1}{2}, \frac{1}{2}]$ and $T_\eta \in [\frac{T_f}{4}, \frac{T_f}{2}]$. $M_0[n]$ is the sampled noise, and I_{ξ,a_n} is defined as

$$I_{\xi,a_n} \triangleq E_f \int_0^{T_f} \sum_{m=0}^{2} p_R^2(t + mT_f - a_n \triangle - \xi) w(t) dt. \tag{13}$$

We prove the Proposition 1 and the fact that the sampled noise $M_0[n]$ can be approximated by a zero mean Gaussian variable in (Xu et al., 2009) in Appendix A and Appendix B respectively. There are some remarks on the Proposition 1:
1) The fact of $a_{n-1} \in \{0, 1\}$ suggests that $I_{\xi,a_{n-1}}$ in (12) is equal to either $I_{\xi,0}$ or $I_{\xi,1}$. Furthermore, $I_{\xi,0}$ and $I_{\xi,1}$ satisfy $I_{\xi,1} = -I_{\xi,0}$ whose proof is contained in *Fact* 1 of Appendix I.
2) Equation (12) suggests that the decomposition of $Y_0[n]$ varies when ξ falls in different subintervals, so correctly estimating n_f need to determine to which region ξ belongs.
3) *Fact* 2 of Appendix A which states

$$\begin{cases} I_{\xi,0} > 0, & \xi \in [0 \;,\; T_\eta) \bigcup [T_\eta + \frac{T_f}{2} \;,\; T_f] \\ I_{\xi,0} < 0, & \xi \in [T_\eta \;,\; T_\eta + \frac{T_f}{2}) \end{cases} \tag{14}$$

suggests that it is possible to utilize the sign of $I_{\xi,0}$ to determine to which subinterval ξ belongs. However, when $I_{\xi,0} > 0$, ξ could belong to either $[0, T_\eta)$ or $[T_\eta + \frac{T_f}{2}, T_f)$. To resolve this difficulty, we introduce the second template $W_1(t)$ in the next section.

3.3 Analysis of symbol-rate sampled data $Y_1[n]$

The symbol-rate sampled data $Y_1[n]$ is obtained when the template $W_1(t)$ is employed. $W_1(t)$ is a delayed version of $W_0(t)$ with the delayed time T_d where $T_\mathrm{d} \in [0\,,\,\frac{T_\mathrm{f}}{2}]$. Our simulations show that we obtain the similar performance for the different choices of T_d. For the simplicity, we choose $T_\mathrm{d} = \frac{T_\mathrm{f}}{4}$ for the derivation. Thus, we have

$$\begin{aligned} Y_1[n] &= \int_{\frac{T_\mathrm{f}}{4}}^{T_\mathrm{s}+\frac{T_\mathrm{f}}{4}} R(t+nT_\mathrm{s})W_0(t-\frac{T_\mathrm{f}}{4})dt \\ &= \int_0^{T_\mathrm{s}} R(t+nT_\mathrm{s}+\frac{T_\mathrm{f}}{4})W_0(t)dt\,. \end{aligned} \tag{15}$$

Then we can derive the following proposition of $Y_1[n]$.

Proposition 2: 1) For $1 \le n < N_0$, $Y_1[n]$ can be expressed as

$$Y_1[n] = N_\mathrm{f} J_{\xi,0} + M_0[n]\,. \tag{16}$$

2) For $N_0 \le n \le N-1$, $Y_1[n]$ can be decomposed as

$$Y_1[n] = \begin{cases} (2\Psi - N_\mathrm{f} - 1)J_{\xi,a_{n-1}} + M_1[n], & \xi \in [0, T_\eta - \frac{T_\mathrm{f}}{4}) \\ (2\Psi - N_\mathrm{f})J_{\xi,a_{n-1}} + M_1[n], & \xi \in [T_\eta - \frac{T_\mathrm{f}}{4}, T_\eta + \frac{T_\mathrm{f}}{4}) \\ (2\Psi - N_\mathrm{f} + 1)J_{\xi,a_{n-1}} + M_1[n], & \xi \in [T_\eta + \frac{T_\mathrm{f}}{4}, T_\mathrm{f}) \end{cases} \tag{17}$$

where $J_{\xi,0}$ satisfies

$$\begin{cases} J_{\xi,0} < 0\,, & \xi \in [0\,,\, T_\eta - \frac{T_\mathrm{f}}{4}) \bigcup [T_\eta + \frac{T_\mathrm{f}}{4}\,,\, T_\mathrm{f}) \\ J_{\xi,0} > 0\,, & \xi \in [T_\eta - \frac{T_\mathrm{f}}{4}\,,\, T_\eta + \frac{T_\mathrm{f}}{4})\,. \end{cases} \tag{18}$$

Equation (14) and (18) suggest that the signs of $I_{\xi,0}$ and $J_{\xi,0}$ can be utilized jointly to determine the range of ξ, which is summarized as follows:

Proposition 3: $\xi \in [0, T_\mathrm{f}]$ defined in (7) satisfies

1. If $I_{\xi,0} > 0$ and $J_{\xi,0} > 0$, then $\xi \in (\,T_\eta - \frac{T_\mathrm{f}}{4}\,, T_\eta\,)$.
2. If $I_{\xi,0} < 0$ and $J_{\xi,0} > 0$, then $\xi \in (\,T_\eta\,, T_\eta + \frac{T_\mathrm{f}}{4}\,)$.
3. If $I_{\xi,0} < 0$ and $J_{\xi,0} < 0$, then $\xi \in (\,T_\eta + \frac{T_\mathrm{f}}{4}\,, T_\eta + \frac{T_\mathrm{f}}{2}\,)$.
4. If $I_{\xi,0} > 0$ and $J_{\xi,0} < 0$, then $\xi \in (0, T_\eta - \frac{T_\mathrm{f}}{4}) \cup (T_\eta + \frac{T_\mathrm{f}}{2}, T_\mathrm{f})$.

The last case of Proposition 3 suggests that using the signs of $I_{\xi,0}$ and $J_{\xi,0}$ is not enough to determine whether we have $\xi \in (\,0\,, T_\eta - \frac{T_\mathrm{f}}{4}\,)$ or $\xi \in (\,T_\eta + \frac{T_\mathrm{f}}{2}\,, T_\mathrm{f}\,)$. To resolve this difficulty, the third template $W_2(t)$ is introduced. $W_2(t)$ is an auxiliary template and is defined as

$$W_2(t) = \sum_{k=0}^{N_\mathrm{f}-1} v(t - kT_\mathrm{f}),\; v(t) = \begin{cases} 1, & T_\mathrm{f} - 2T_v \le t < T_\mathrm{f} - T_v \\ -1, & T_\mathrm{f} - T_v \le t < T_\mathrm{f} \\ 0, & \text{others} \end{cases} \tag{19}$$

where $T_v \in (0\,,\, T_\mathrm{f}/10]$. Similar to the proof of (14), we can prove that in this case, either $K_{\xi,0} > 0$ for $0 < \xi < T_\eta - \frac{T_\mathrm{f}}{4}$ or $K_{\xi,0} < 0$ for $T_\eta + \frac{T_\mathrm{f}}{4} < \xi < T_\mathrm{f}$ is valid, which yields the information to determine which region ξ belongs to.

3.4 The computation of the optimal timing offset estimator $\hat{n}_{\mathrm{f}}$

To seek the estimate of n_{f}, we first compute the optimal estimates of $I_{\xi,0}$ and $J_{\xi,0}$ using (11) and (16). Then, we use the estimate $\hat{I}_{\xi,0}$,$\hat{J}_{\xi,0}$ and Proposition 3 to determine the region to which ξ belongs. The estimate $\hat{\Psi}$ therefore can be derived using the proper decompositions of (12) and (17). Finally, recalling the definition in (12) $\Psi = n_{\mathrm{f}} - \frac{\epsilon}{2}$ with $\epsilon \in [-\frac{1}{2}, \frac{1}{2}]$, we obtain $\hat{n}_{\mathrm{f}} = [\hat{\Psi}]$, where $[\cdot]$ stands for the round operation.

According to the signs of $\hat{I}_{\xi,0}$ and $\hat{J}_{\xi,0}$, we summarize the ML estimate $\hat{\Psi}$ as follow:

Proposition 4:

- When $\hat{I}_{\xi,0} > 0$ and $\hat{J}_{\xi,0} > 0$, $\hat{\Psi} = \frac{1}{A} \sum_{n=N_0}^{N-1} [Z_n + N_{\mathrm{f}}(I_{\xi,0}^2 + J_{\xi,0}^2)]$.
- When $\hat{I}_{\xi,0} < 0$ and $\hat{J}_{\xi,0} > 0$, $\hat{\Psi} = \frac{1}{A} \sum_{n=N_0}^{N-1} [Z_n + (N_{\mathrm{f}} - 1) I_{\xi,0}^2 + N_{\mathrm{f}} J_{\xi,0}^2]$.
- When $\hat{I}_{\xi,0} < 0$ and $\hat{J}_{\xi,0} < 0$, $\hat{\Psi} = \frac{1}{A} \sum_{n=N_0}^{N-1} [Z_n + (N_{\mathrm{f}} - 1)(I_{\xi,0}^2 + J_{\xi,0}^2)]$.
- When $\hat{I}_{\xi,0} > 0$ and $\hat{J}_{\xi,0} < 0$,

$$\hat{\Psi} = \begin{cases} \frac{1}{A} \sum_{n=N_0}^{N-1} [Z_n + N_{\mathrm{f}} I_{\xi,0}^2 + (N_{\mathrm{f}} + 1) J_{\xi,0}^2] & , \hat{K}_{\xi,0} > 0 \\ \frac{1}{A} \sum_{n=N_0}^{N-1} [Z_n + (N_{\mathrm{f}} - 2) I_{\xi,0}^2 + (N_{\mathrm{f}} - 1) J_{\xi,0}^2] & , \hat{K}_{\xi,0} < 0 \end{cases}$$

where $A \triangleq 2(N - N_0)(I_{\xi,0}^2 + J_{\xi,0}^2)$ and $Z_n \triangleq Y_0[n] I_{\xi,a_{n-1}} + Y_1[n] J_{\xi,a_{n-1}}$. The procedures of computing the optimal ML estimate $\hat{\Psi}$ in Proposition 4 are identical. Therefore, we only present the computation steps when $\hat{I}_{\xi,0} > 0$ and $\hat{J}_{\xi,0} > 0$.

1) Utilizing (11) and (16), we obtain the ML estimates

$$\hat{I}_{\xi,0} = \frac{1}{(N_0 - 1) N_{\mathrm{f}}} \sum_{n=1}^{N_0 - 1} Y_0[n], \; \hat{J}_{\xi,0} = \frac{1}{(N_0 - 1) N_{\mathrm{f}}} \sum_{n=1}^{N_0 - 1} Y_1[n] . \tag{20}$$

2) From 1) of Proposition 3, it follows $T_\eta - \frac{T_{\mathrm{f}}}{4} < \xi < T_\eta$ when $\hat{I}_{\xi,0} > 0$ and $\hat{J}_{\xi,0} > 0$.

3) According to the region of ξ, we can select the right equations from (12) and (17) as

$$Y_0[n] = (2\Psi - N_{\mathrm{f}}) I_{\xi,a_{n-1}} + M_0[n] \tag{21}$$

$$Y_1[n] = (2\Psi - N_{\mathrm{f}}) J_{\xi,a_{n-1}} + M_1[n] . \tag{22}$$

Thus the log-likelihood function $\ln p(y\,; \Psi, I_{\xi,a_{n-1}}, J_{\xi,a_{n-1}})$ is

$$\sum_{n=N_0}^{N-1} \left\{ [Y_0[n] - (2\Psi - N_{\mathrm{f}}) I_{\xi,a_{n-1}}]^2 + [Y_1[n] - (2\Psi - N_{\mathrm{f}}) J_{\xi,a_{n-1}}]^2 \right\} .$$

It follows the ML estimate $\hat{\Psi} = \frac{1}{A} \sum_{n=N_0}^{N-1} [Z_n + N_{\mathrm{f}}(I_{\xi,0}^2 + J_{\xi,0}^2)]$.

3.5 Simulation

In this section, computer simulations are performed. We use the second-order derivative of the Gaussian pulse to represent the UWB pulse. The propagation channels are generated

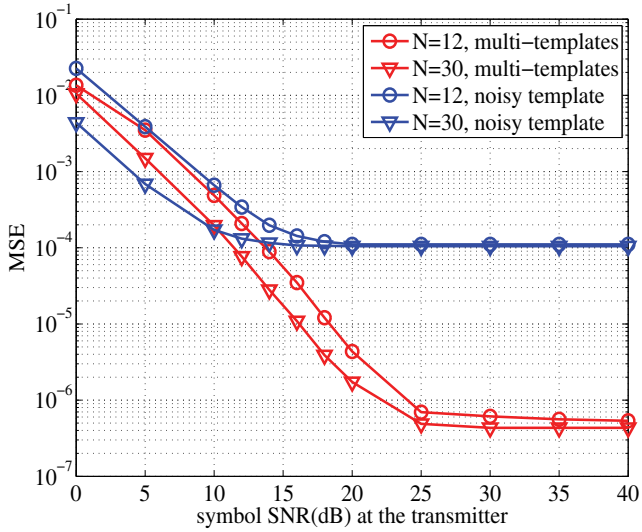

Fig. 2. MSE performance under CM2 with $d = 4m$ ..

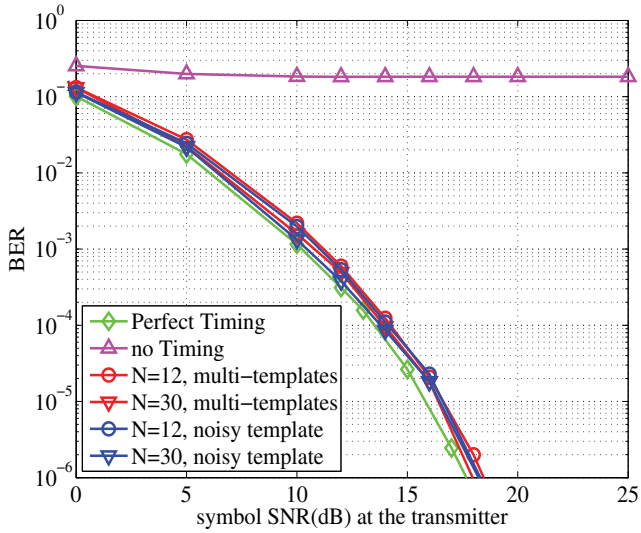

Fig. 3. BER performance under CM2 with $d = 4m$ ..

by the channel model CM2 described in (Foerster, 2003). Other parameters are selected as follows: $T_p = 1$ns, $N_f = 25$, $T_f = 100$ns, $T_v = T_f/10$ and the transmitted distance $d = 4m$. In all the simulations, we assume that n_f and ξ are uniformly distributed over $[0, N_f - 1]$ and $[0, T_f]$ respectively. To evaluate the effect of the estimate $\hat{n}_f$ on the bit-error-rates (BERs) performance, we assume there is an optimal channel estimator at the receiver to obtain the perfect template for tracking and coherent demodulation. The signal-to-noise ratios (SNRs)

in all figures are computed through E_s/σ_n^2 where E_s is the energy spread over each symbol at the transmitter and σ_n^2 is the power spectral density of the noise.
In Fig. 2 present the normalized mean-square error (MSE:$E\{|(\hat{n}_{\rm f} - n_{\rm f})/N_{\rm f}|^2\}$) of the proposed algorithm in contrast to the approach using noisy template proposed in (Tian & Giannakis, 2005). The figure shows that the proposed algorithm (blue curve) outperforms that in (Tian & Giannakis, 2005) (red curve) when the SNR is larger than 10dB. For both algorithms, the acquisition performance improves with an increase in the length of training symbols N, as illustrated by the performance gap among $N = 12$ and $N = 30$. Fig. 3 illustrates the BER performance for the both algorithms. The BERs corresponding to perfect timing (green curve) and no timing (Magenta curve) are also plotted for comparisons.

4. Low sampling rate channel estimation algorithms

The channel estimation of UWB systems is essential to effectively capture signal energy spread over multiple paths and boost the received signal-to-noise ratio (SNR). The low sampling rate channel estimation algorithms have the merits that can greatly lower the implementation complexity and reduce the costs. However, the development of low sampling rate channel estimation algorithms is extremely challenging. This is primarily due to the facts that the propagation models of UWB signals are frequency selective and far more complex than traditional radio transmission channels.
Classical approaches to this problem are using the maximum likelihood (ML) method or approximating the solutions of the ML problem. The main drawback of these approaches is that the computational complexity could be prohibitive since the number of parameters to be estimated in a realistic UWB channel is very high (Lottici et al., 2002). Other approaches reported are the minimum mean-squared error schemes which have the reduced complexity at the cost of performance (Yang & Giannakis, 2004). Furthermore, sampling rate of the received UWB signal is not feasible with state-of-the-art analog-to-digital converters (ADC) technology. Since UWB channels exhibit clusters (Cramer et al., 2002), a cluster-based channel estimation method is proposed in (Carbonelli & Mitra, 2007). Different methods such as subspace approach (Xu & Liu, 2003), first-order cyclostationary-based method (Wang & Yang, 2004) and compressed sensing based method (Paredes et al., 2007; Shi et al., 2010) proposed for UWB channel estimation are too complex to be implemented in actual systems.
In this section, we develop a novel optimum data-aided channel estimation scheme that only relies on frame-level sampling rate data to derive channel parameter estimates from the received waveform. To begin with, we introduce a set of especially devised templates for the channel estimation. The received signal is separately correlated with these pre-devised templates and sampled at frame-level rate. We show that each frame-level rate sample of any given template can be decomposed to a sum of a frequency-domain channel parameter and a noise sample. The computation of time-domain channel parameter estimates proceeds through the following two steps: In step one, for each fixed template, we utilize the samples gathered at this template and the maximum likelihood criterion to compute the ML estimates of the frequency-domain channel parameters of these samples. In step two, utilizing the computed frequency-domain channel parameters, we can compute the time-domain channel parameters via inverse fast transform (IFFT). As demonstrated in the simulation example,

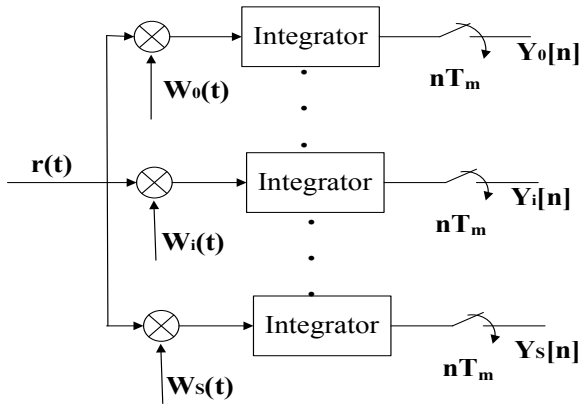

Fig. 4. The block diagram of channel estimation scheme.

when the training time is fixed, more templates used for the channel estimation yield the better (BER) performance.

4.1 The signal model

During the channel estimation process, a training sequence is transmitted. Each UWB symbol is transmitted over a time-interval of T_s seconds that is subdivided into N_f equal size frame-intervals of length T_f, i.e., $T_s = N_f T_f$. A frame is divided into N_c chips with each of duration T_c, i.e., $T_f = N_c T_c$. A single frame contains exactly one data modulated ultrashort pulse $p(t)$ (so-called monocycle) of duration T_p which satisfies $T_p \leq T_c$. The pulse $p(t)$ normalized to satisfy $\int p(t)^2 dt = 1$ can be Gaussian, Rayleigh or other. Then the waveform for the training sequence can be written as

$$s(t) = \sqrt{E_f} \sum_{n=0}^{N_s-1} \sum_{j=0}^{N_f-1} b_n p(t - nT_s - jT_f) \tag{23}$$

where E_f represents the energy spread over one frame and N_s is the length of the training sequence; b_n denotes data, which is equal to 1 during training phase.
Our goal is to derive the estimate of the channel parameter sequence $\mathbf{h} = [h_0, h_1, \cdots, h_{L-1}]$. Since from the assumption L is unknown, we define a N_c-length sequence $\mathbf{p}$ as

$$\mathbf{p} = [h_0, h_1, \cdots, h_{L-1}, h_L, h_{L+1}, \cdots, h_{N_c-1}] \tag{24}$$

where $h_l = 0$ for $l \geq L$. The transmitted signal propagates through an L-path fading channel as shown in (3). Thus the received signal is

$$r(t) = \sqrt{E_f} \sum_{n=0}^{N_s-1} \sum_{j=0}^{N_f-1} \sum_{l=0}^{N_c-1} h_l p(t - nT_s - jT_f - l\,T_c) + n(t) \tag{25}$$

where $n(t)$ is the zero-mean additive white Gaussian noise (AWGN) with double-side power spectral density $\sigma_n^2/2$.

4.2 The choices of templates

In this section, a novel channel estimation method that relies on symbal-level samples is derived. As shown in Fig. 4, the received signal (25) is separately correlated with the pre-devised templates $W_0(t), W_1(t), \cdots, W_S(t)$, and sampled at nT_{m} where sampling period T_{m} is on the order of T_{f}. Let $Y_i[n]$ denote the n-th sample corresponding to the template $W_i(t)$, that is,

$$Y_i[n] \quad = \quad \int_0^{T_{\mathrm{m}}} r(t+nT_{\mathrm{m}})W_i(t)dt \tag{26}$$

with $i = 0, 1, \cdots, S$. Utilizing these samples, we derive the ML estimate of the channel parameter sequence $\mathbf{p}$ in (24).

First we introduce a set of $S+1$ templates used for the channel estimation. The number S is chosen as a positive integer factor of $N_{\mathrm{c}}/2$ by assuming that N_{c} which represents the number of chips T_{c} in each frame is an even number. That is, we have $N_{\mathrm{c}} = 2SM$ with M also being defined as a positive integer factor of $N_{\mathrm{c}}/2$. The i-th template is defined as

$$W_i(t) = \sqrt{E_{\mathrm{f}}} \sum_{k=0}^{N_{\mathrm{o}}-1} \omega_{N_{\mathrm{o}}}^{ik} \left[p(t-kT_{\mathrm{c}}) + p(t-T_{\mathrm{f}}-kT_{\mathrm{c}})\right] \tag{27}$$

with $N_{\mathrm{o}} = 2S = N_{\mathrm{c}}/M$, $\omega_{N_{\mathrm{o}}}^{ik} = e^{-j\frac{2\pi ik}{N_{\mathrm{o}}}}$ and $i \in \{0, 1, \cdots, S\}$. The duration of each template $W_i(t)$ is equal to the sampling period T_{m} which can be expressed as

$$T_{\mathrm{m}} = (N_{\mathrm{c}} + N_{\mathrm{o}})T_{\mathrm{c}} = T_{\mathrm{f}} + N_{\mathrm{o}}T_{\mathrm{c}}. \tag{28}$$

4.3 The computation of the channel parameter sequence $\mathbf{p}$

In this section, we derive the channel estimation scheme that only relies on frame-level sampling rate data. To begin with, let us introduce some notations. Recalling the equation $N_{\mathrm{o}} = N_{\mathrm{c}}/M$ following (27), we divide the N_{c}-length sequence $\mathbf{p}$ into M blocks each of size N_{o}. Therefore, equation (24) becomes

$$\mathbf{p} \quad = \quad [\mathbf{h}_0, \mathbf{h}_1, \cdots, \mathbf{h}_m, \cdots, \mathbf{h}_{M-1}] \tag{29}$$

where the m-th block $\mathbf{h}_m$ is defined as

$$\mathbf{h}_m \quad = \quad [h_{mN_{\mathrm{o}}} \;\; h_{mN_{\mathrm{o}}+1} \;\; \cdots \;\; h_{mN_{\mathrm{o}}+N_{\mathrm{o}}-1}] \tag{30}$$

with $m \in \{0, 1, \cdots, M-1\}$. Let $\mathbf{F}_i$ denote the N_{o}-length coefficient sequence of the i-th template $W_i(t)$ in (27), i.e.,

$$\mathbf{F}_i \quad = \quad [\omega_{N_{\mathrm{o}}}^0 \; \omega_{N_{\mathrm{o}}}^i \; \omega_{N_{\mathrm{o}}}^{2i} \; \cdots \; \omega_{N_{\mathrm{o}}}^{(N_{\mathrm{o}}-1)i}]. \tag{31}$$

The discrete Fourier transform (DFT) of the N_{o}-length sequence $\mathbf{h}_m = [h_{mN_{\mathrm{o}}} \; h_{mN_{\mathrm{o}}+1} \; \cdots \; h_{mN_{\mathrm{o}}+N_{\mathrm{o}}-1}]$ is denoted as

$$\mathbf{H}_m \quad = \quad [H_m^0, H_m^1, \cdots, H_m^i, \cdots, H_m^{N_{\mathrm{o}}-1}] \tag{32}$$

where the frequency-domain channel parameter H_m^i is

$$H_m^i = \mathbf{F}_i \mathbf{h}_m^T = \sum_{k=0}^{N_o-1} \omega_{N_o}^{ik} h_{mN_o+k} \tag{33}$$

with $m \in \{0, 1, \cdots, M-1\}$ and $i \in \{0, 1, \cdots, S\}$.
Our channel estimation algorithm proceeds through the following two steps.

Step 1: Utilizing the set of frame-level samples $\{Y_i[n]\}_{n=1}^N$ generated from the i-th template, we compute the ML estimates of the frequency-domain channel parameters $\{H_m^i\}_{m=1}^M$ for $i \in \{0, 1, \cdots, S\}$. To do this, we show that the samples $\{Y_i[n]\}_{n=0}^{N-1}$ from the i-th template has the following decomposition.

Proposition 1: Every sample in the set $\{Y_i[n]\}_{n=0}^{N-1}$ can be decomposed into the sum of a frequency-domain channel parameter and a noise sample, that is,

$$\begin{cases} Y_i[qM] = 2E_f H_0^i + Z_i[qM] \\ Y_i[qM+1] = 2E_f H_1^i + Z_i[qM+1] \\ \qquad \vdots \\ Y_i[qM+m] = 2E_f H_m^i + Z_i[qM+m] \\ \qquad \vdots \\ Y_i[qM+M-1] = 2E_f H_{M-1}^i + Z_i[qM+M-1] \end{cases} \tag{34}$$

where $Z_i[n]$ represents the noise sample. The parameter q belongs to the set $\{0, 1, \cdots, Q-1\}$ with $Q = \lfloor \frac{N}{M} \rfloor$.
Performing ML estimation to the $(m+1)$-th equation in (34) for $q = 0, 1, \cdots, Q-1$, we can compute the ML estimate $\hat{H}_m^i$ for the frequency-domain channel parameter H_m^i as

$$\hat{H}_m^i = \frac{1}{2E_f Q} \sum_{q=0}^{Q-1} Y_i[qM+m] \tag{35}$$

with $m \in \{0, 1, \cdots, M-1\}$ and $i \in \{0, 1, \cdots, S\}$.

Step 2: Utilizing the computed frequency-domain channel parameters $\{\hat{H}_m^i\}_{i=0}^S$ from the Step 1, we derive the estimate of the time-domain channel sequence $\mathbf{h}_m$ for $m \in \{0, 1, \cdots, M-1\}$. From the symmetry of the DFT, the time-domain channel parameter sequence $\mathbf{h}_m = [h_{mN_o} \; h_{mN_o+1} \; \cdots \; h_{mN_o+N_o-1}]$ is a real valued sequence, which suggests that the DFT of $\mathbf{h}_m$ satisfies

$$H_m^{N_o-i} = (H_m^i)^* \tag{36}$$

with $i \in \{0, 1, \cdots, S\}$ and $S = N_o/2$.
Utilizing equation (36), we obtain the estimate for the N_o-point DFT of $\mathbf{h}_m$ as

$$\hat{\mathbf{H}}_m = [\hat{H}_m^0, \hat{H}_m^1, \cdots, \hat{H}_m^S, (\hat{H}_m^{S-1})^*, \cdots, (\hat{H}_m^2)^*, (\hat{H}_m^1)^*] \tag{37}$$

The estimate of the time-domain channel parameter $\hat{\mathbf{h}}_m$ can be compute via N_o-point IFFT. In view of equation (29), the estimated channel parameter sequence $\mathbf{p}$ in (24) is given by

$$\hat{\mathbf{p}} \quad = \quad [\hat{\mathbf{h}}_0, \hat{\mathbf{h}}_1, \cdots, \hat{\mathbf{h}}_{M-1}]\,. \tag{38}$$

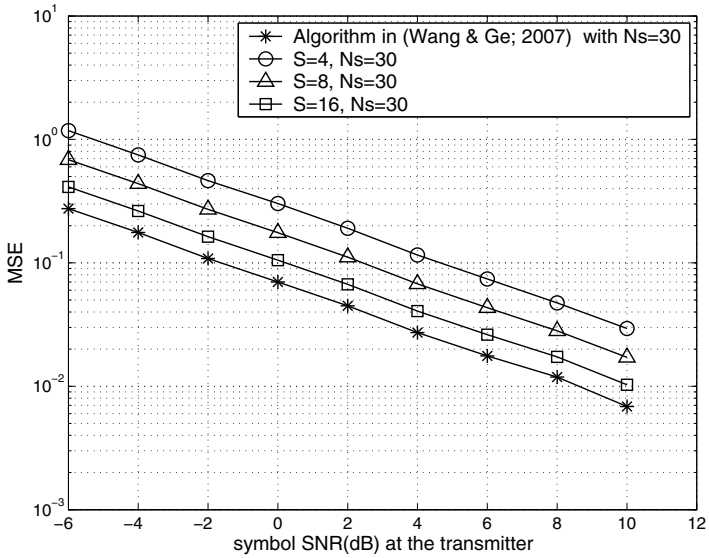

Fig. 5. MSE performance of the algorithm proposed in (Wang & Ge, 2007) and the proposed algorithm with different number of templates ($S = 4\,, 8\,,16$), when the length of the training sequence N_s is 30 .

4.4 Simulation

In this section, computer simulations are performed to test the proposed algorithm. The propagation channels are generated by the channel model CM 4 described in (Foerster, 2003) . We choose the second-order derivative of the Gaussian pulse as the transmitted pulse with duration $T_p = 1$ns. Other parameters are selected as follows: $T_f = 64$ns, $T_c = 1$ns, $N_c = 64$ and $N_f = 24$.

Fig. 5 presents the normalized mean-square error (MSE) of our channel estimation algorithm with different number of templates ($S = 4\,, 8\,, 16$) when the length of the training sequence N_s is 30 . As a comparison, we also plot the MSE curve of the approach in (Wang & Ge, 2007) which needs chip-level sampling rate. Fig. 6 illustrates the bit-error-rates (BERs) performance for the both algorithms. The BERs corresponding to the perfect channel estimation (Perfect CE) is also plotted for comparisons. From these figures, the MSE and BER performances of our algorithm improve as the number of templates increases. In particular, as shown in Fig. 5 and Fig. 6, the MSE and BER performances of our algorithm that relies only on the frame-level sampling period $T_f = 64$ns is comparable to that of the approach proposed in (Wang & Ge, 2007) which requires chip-level sampling period $T_c = 1$ns.

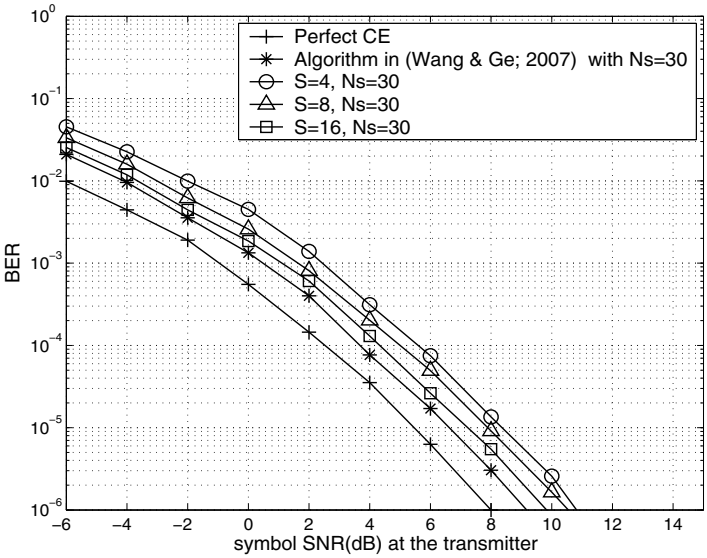

Fig. 6. BER performance of Perfect CE, the algorithm proposed in (Wang & Ge, 2007) and the proposed algorithm with different number of templates ($S = 4, 8, 16$), when the length of the training sequence N_s is 30.

5. Conclusion

In this chapter, we are focusing on the low sampling rate time acquisition schemes and channel estimation algorithms of UWB signals. First, we develop a novel optimum data-aided (DA) timing offset estimator that utilizes only symbol-rate samples to achieve the channel delay spread scale timing acquisition. For this purpose, we exploit the statistical properties of the power delay profile of the received signals to design a set of the templates to ensure the effective multipath energy capture at any time. Second, we propose a novel optimum data-aided channel estimation scheme that only relies on frame-level sampling rate data to derive channel parameter estimates from the received waveform.

6. References

Karaoguz, J. (2001). High-rate wireless personal area networks, *IEEE Commun. Mag.*, vol. 39, pp. 96-102.

Lovelace, W. M. & Townsend, J. K. (2002). The effect of timing jitter and tracking on the performance of impulse radio, *IEEE J. Sel. Areas Commun.*, vol. 20, no. 9, pp. 1646-1651.

Tian, Z. & Giannakis, G. B. (2005). BER sensitivity to mistiming in ultrawideband impulse radios-part I: modeling, *IEEE Trans. Signal Processing*, vol. 53, no. 4, pp. 1550-1560.

Tian, Z. & Giannakis, G. B. (2005). A GLRT approach to data-aided timing acquisition in UWB radios-Part I: Algorithms, *IEEE Trans. Wireless Commun.*, vol. 53,no. 11, pp. IV. 2956-2967.

Yang, L. & Giannakis, G. B. (2005). Timing Ultra-wideband Signals with Dirty Templates,ąś *IEEE Trans. on Commun.*, vol. 53, pp. 1952-1963.

Carbonelli, C. & Mengali, U. (2006). Synchronization algorithms for UWB signals, *IEEE Trans. on Commun.*, vol. 54, no. 2, pp. 329-338.

He, N. & Tepedelenlioglui, C. (2008). Joint Pulse and Symbol Level Acquisition of UWB Receivers, *IEEE Trans. on Wireless Commun.*, vol. 7, no. 1, pp. 6-14.

Carbonelli, C. & Mengali, U. (2005). Low complexity synchronization for UWB noncoherent receivers, in *Proc. 2005 Vehicular Technology Conf.*, vol. 2, pp. 1350-1354.

Furusawa, K.; Sasaki, M.; Hioki, J.; Itami, M.; (2008). Schemes of optimization of energy detection receivers for UWB-IR communication systems under different channel model, *IEEE International Conference on Ultra-Wideband*, pp.157 - 160, Leibniz Universitat Hannover, Germany.

Cheng, X. & Guan, Y. (2008). Effects of synchronization errors on energy detection of UWB signals, *IEEE International Conference on Ultra-Wideband*, pp.161 - 164, Leibniz Universitat Hannover, Germany.

Sasaki, M.; Ohno, J.; Ohno, H.; Ohno, K.; Itami, M. (2010). A study on multi-user access in energy detection UWB-IR receiver, *2010 IEEE 11th International Symposium on Spread Spectrum Techniques and Applications (ISITA)* pp.141 - 146, Taichung, Taiwan.

Xu, W.; Zhao,J.; Wang, D. (2009). A Frame-Level Timing Acquisition Scheme of Ultra-wideband Signals Using Multi-templates, *The 6th International Symposium on Wireless Communication Systems*, pp.61 - 65, Tuscany, Italy.

J. Foerster, Channel modeling sub-commitee report final, *IEEE P802.15-02/490*.

Stoica, L.; Rabbachin, A.; Repo, H.; Tiuraniemi,T.; Oppermann, I. (2005). An ultra-wideband system architecture for tag based wireless sensor networks, *IEEE Trans. on Veh. Technol.*, vol. 54, no. 5, pp. 1632-1645.

Turin, G. L. (1980). Introduction to spread-spectrum antimultipath techniques and their application to urban digital radio, *Proc. IEEE*, vol. 68, pp. 328-353.

Lottici, V; D'Andrea, A. N.; Mengali, U. (2002). Channel estimation for ultra-wideband communications, *IEEE J. Select. Areas Commun.*, vol. 20, no. 9, pp. 1638-1645.

Yang, L. & Giannakis, G. B. (2004). Optimal pilot waveform assisted modulation for ultra-wideband communications, *IEEE Trans. Wireless Commun.*, vol. 3, no. 4, pp. 1236-1249.

Cramer, R. J. M.; Scholtz, R. A.; Win, M. Z. (2002). Evaluation of an ultra wideband propagation channel, *IEEE Trans. Antennas Propagat.*, vol. 50, No. 5.

Carbonelli, C. & Mitra, U. (2007). Clustered ML Channel Estimation for Ultra-Wideband Signals, *IEEE Trans. Wireless Commun.*, vol. 6, No. 7,pp.2412 - 2416.

Paredes, J.L.; Arce, G.R.; Wang, Z. (2007). Ultra-Wideband Compressed Sensing: Channel Estimation, *IEEE Journal of Selected Topics in Signal Processing*, vol. 1, No. 3,pp.383 - 395.

Shi, L.; Zhou, Z.; Tang, L.; Yao, H.; Zhang, J. (2010). Ultra-wideband channel estimation based on Bayesian compressive sensing, *2010 International Symposium on Communications and Information Technologies (ISCIT)*, pp.779 - 782, Tokyo, Japan.

Wang, X. & Ge, H. (2007). On the CRLB and Low-Complexity Channel Estimation for UWB Communications. *IEEE 41st Annual Conference on Information Sciences and Systems*, Baltimore, pp. 151-153.

Xu, Z. & Liu, P. (2003). A subspace approach to blind estimation of ultrawideband channels, in *Proc. IEEE Thirty-Seventh Asilomar Conference on Signals, Systems & Computers*. vol. 2, pp. 1249-1253.

Wang, Z. & Yang, X. (2004). Ultra wide-band communications with blind channel estimation based on first-order statistics, in *Proc. IEEE (ICASSP-04)*. vol. 4, pp. iv-529 - iv-532, Montreal, Canada.

3

A Proposal of Received Response Code Sequence in DS/UWB

Shin'ichi Tachikawa[1] and Masatoshi Yokota[2]
[1]*Nagaoka National College of Technology*
[2]*Nagaoka University of Technology*
Japan

1. Introduction

The demand for a large capacity, high-reliability and high-quality has recently increased in communication systems such as wireless LAN. As a system for this demand, Spread Spectrum (SS) system and Orthogonal Frequency Division Multiplexing (OFDM) system have been studied [1], [2]. Various communication systems are used by the usage for a wireless communication and Ultra Wideband (UWB) has attracted much attention as an indoor short range high-speed wireless communication in the next-generation. Frequency band used of UWB communication is larger than that of a conventional SS communication, and the UWB communication system has high-speed transmission rate [3], [4].

UWB communication has high resolution for multipath to use nano-order pulses, assuming a lot of paths delayed by walls and obstacles in an indoor environment. Furthermore, due to a long delay-path exists, it has known to cause Inter-Symbol Interference (ISI) that influences a next demodulated signal, and the performance of receiver is degraded.

In UWB communications, there is a DS/UWB system applied Direct Sequence (DS) method as one of SS modulated methods. When a binary sequence such as M sequence is adopted as a code sequence, its sequence may cause complicated ISI by a multipath environment. Then, to improve Signal-to-Noise Ratio (SNR), a selective RAKE reception method is adopted at a receiver. A selective RAKE reception method can gather peaks of scattered various signals for one peak [5]-[7]. However, when an interference is too large by a multipath environment, it is difficult to gather receive energy efficiently.

In this chapter, to resolve the ISI problem caused by a multipath environment, a novel Received Response (RR) sequence that has better properties than a M sequence is proposed, and its generation method is shown. The RR sequence is generated by using estimated channel information at a transmitter. Furthermore, the properties of the RR sequence are evaluated for the number of pulses of the RR sequence and the number of RAKE fingers in UWB system, and the effectiveness of RR sequence is shown.

The main contents of this chapter are presented in the below Sections. The explanation of the DS/UWB system and the RR sequence is presented in Section 2. The explanation of the generation method of the RR sequence will be explained in Section 3. In Section 4, simulation conditions and results are shown and discussed. Conclusion of this chapter is presented in Section 5. Refferences are added in Section 6.

2. DS/UWB and Received Response sequence

A Direct Sequence Spread Spectrum (DS/SS) system, in which the bandwidth is spread by using extremely short duration pulses, has high resolution for paths. A DS/UWB system is applied UWB to DS/SS system. Only short duration pulse is used, that system is basically the same one as DS/SS. In a UWB system, a method for getting large SNR is needed to secure reliability of communication at a receiver though power spectrum density of transmitted signals is less than noise level. However, due to transmitting signals are reflected by walls and obstacles and ISI is caused by long delayed multipath in a UWB receiver. Therefore, for multipath in wideband signal, RAKE reception method has been known, which separates paths from an output of Matched Filter (MF) of received signals in some interval and gathers them as path diversity.

When signals continue in one code sequence, a multipath environment causes complicated ISI. Therefore, when such a binary code sequence as a conventional M sequence is used under a multipath environment, the received energy can not be gathered efficiently if RAKE reception method is used at a receiver.

In this chapter, we propose Received Response (RR) sequence that the time which signals dare not to be transmitted is made, and ternary sequence of +1, 0, -1 is used. In using RR sequence, channel information is estimated at a transmitter, and the ISI component known from channel information is used. Then a generation interval of chip and polarity are adjusted, and the delayed chips are composed chips of dominant wave. Therefore, it is possible to made high level peaks from these signal components.

3. A generation method of RR sequence

At a transmitter, RR sequence can be generated in the following procedure (A), (B) and (C).

a. A pulse of UWB and an estimated impulse response are convoluted. Then an ideal received response is obtained before passing of a MF.
b. From the ideal received response like Figure 1, the biggest response is decided as a dominant wave. Then two components of "An estimated position of a selective RAKE finger" and "A polarity of the response of an estimated position (±1)" are obtained within a code length.
c. Its estimated position and polarity are corresponded, and RR sequence is generated.

Furthermore, the position of a selective RAKE finger and the polarity are corresponded with information of Proc. (B), that is, with RR sequence. The shorter an interval of estimated position of a selective RAKE finger, the better the performance. In this chapter, we determine that the interval is one-tenth a chip time.

As an example of using an impulse response of a Non Line of Site (NLOS) environment more than 10 meters in a multipath channel model (named as CM4) adopted IEEE802.15.3a [8], 6RR sequence is generated. Information estimated position of the 6 RAKE fingers is obtained in Figure 1, then Figure 2 shows 6RR sequence of 6 pulses (a code length of 15[ns] is assumed here). If the number of pulse for RR sequence is changed, it had better change the number of information estimated position of the selective RAKE finger in Proc. (B).

Next, a construction and effect of RR sequence is shown using a simplistic ideal received response and RR sequence obtained from its response. Figure 3 shows a received response

and an example RR sequence (4RR sequence is assumed here for simplicity) obtained from its response. Then using 4RR sequence that showed in Figure 3, Figure 4 shows a combined transmitting signal after passing multipath channel and before passing a matched filter when RR sequence is transmitted actually.

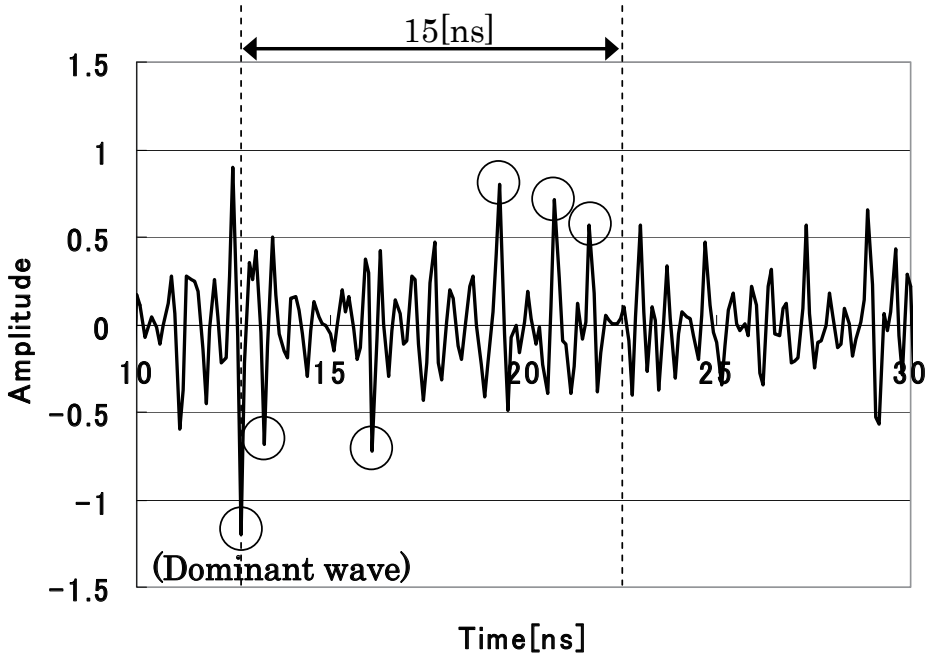

Fig. 1. An example of an ideal received response under the CM4 environment

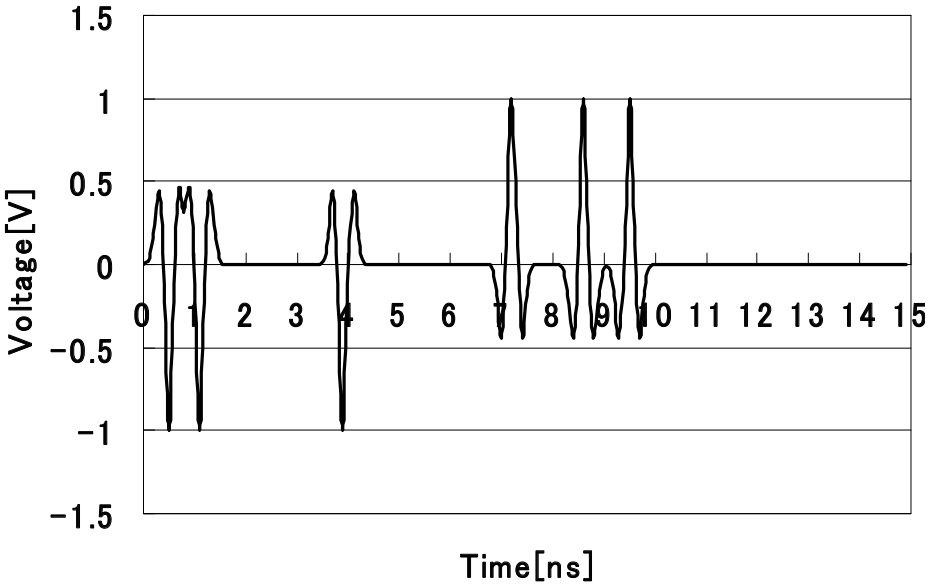

Fig. 2. An example of 6RR sequence

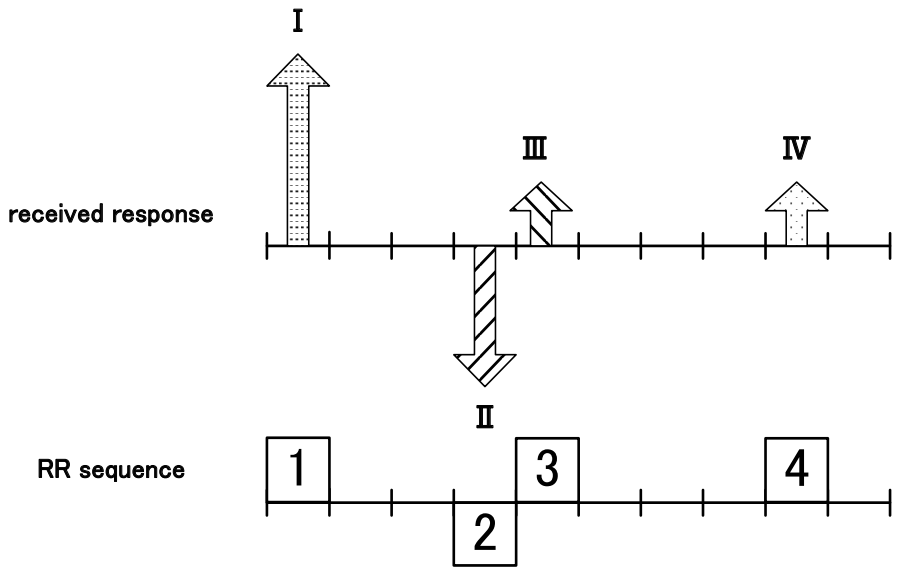

Fig. 3. An example of an ideal received response and RR sequence

In Figure 4, when (I) component is paid attention as a dominant wave, it can be confirmed that 2nd, 3rd and 4th pulse of (I) component combined with each 1st pulse of components except (I) component delayed from dominant wave (where (II), (III) and (IV) components are shown). The delayed components emphasize the pulse of (I) component on In-phase, and besides the 4th pulse of (I) component is combined with the 3rd pulse of (III) component on In-phase except 1st pulse of (IV) component. This cause is to be combined on In-phase accidentally by the type of received response, and to be combine reversed phase too. These can be similarly said even other components. For example, when (III) component is paid attention, it can be confirmed that 1st, 2nd and 4th pulse of (III) component combined with each 3rd pulse of components except (III) component. The components except (III) emphasize the pulse of (III) component on In-phase.
By intentionally combining delayed components with received signals like emphasizing each other, when RR sequence is transmitted instead of a code sequence like simple M sequence, components at finger positions selecting RAKE can be emphasized and properties of receiver can be improved. In this example, although the simple example is showed, the actual selecting paths for the selective RAKE reception are selected sequentially from large one in many paths. Therefore, combining signals is large, and properties of receiver are improved greatly.

4. Simulation results

By the MF reception, the Bit Error Rate (BER) characteristics of proposed RR sequence are compared with that of conventional M sequence. Then BER characteristics when the number of RAKE finger is changed are shown in the selective RAKE reception. For the selective RAKE reception method, a LMS RAKE reception method [9] that has an effect in a channel existing ISI is adopted. For the channel, CM4 of NLOS environment and CM1 of LOS environment [8] are adopted.

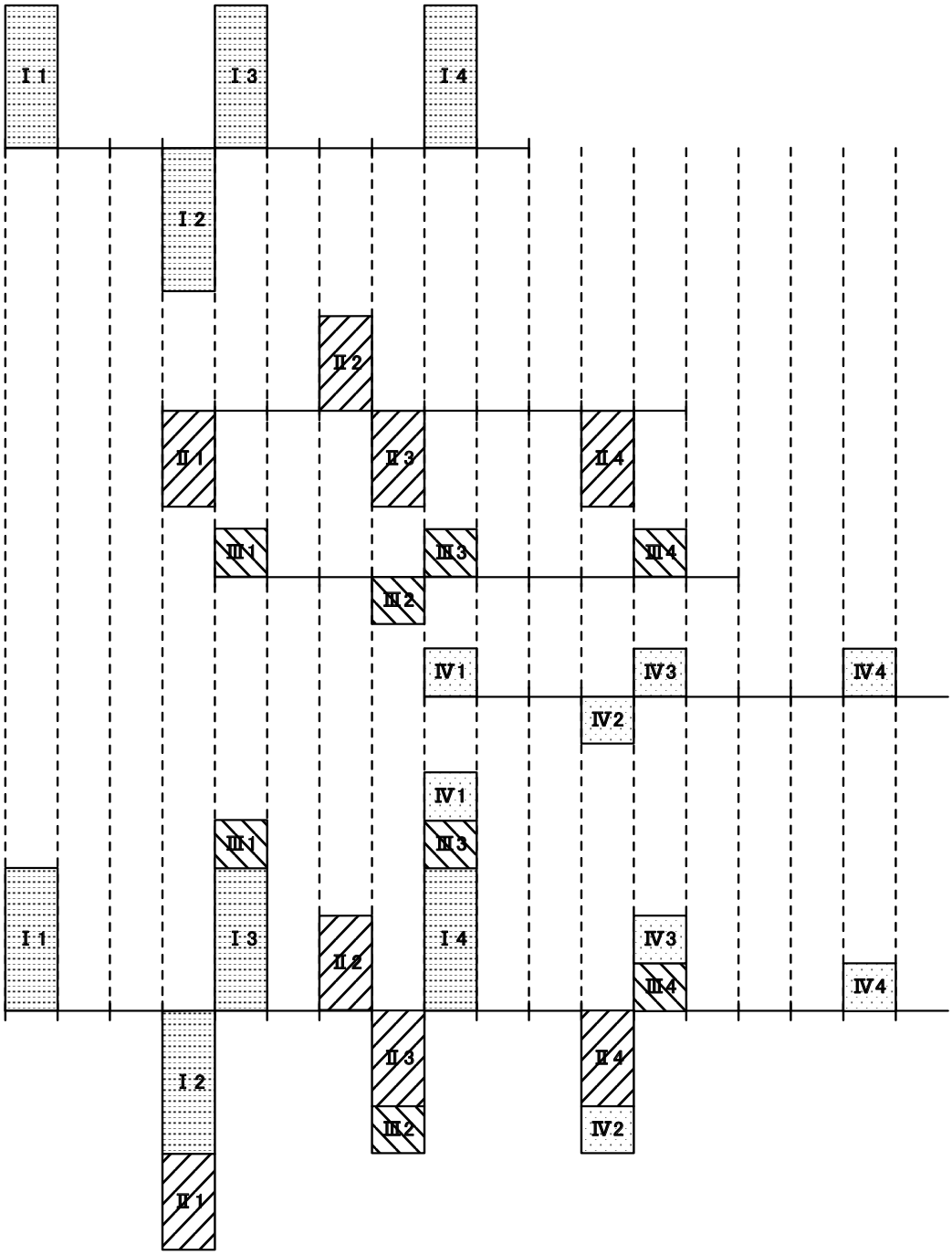

Fig. 4. An example of a combined transmitting signal

To compare superiority or inferiority of the BER characteristics for digital communication method, the BER characteristics are compared and discussed by using E_b/N_0. And E_b originally shows received bit energy at the receiver. However E_b is greatly changed by the various channels in UWB systems. So that, when the channel is changed, the BER characteristics are not compared correctly. Therefore in this chapter, in the between transmitter and receiver, as the received energy when a only dominant wave arrived in the receiver under a channel condition having no delayed wave, that is to say, E_b' of transmission output, BER characteristics are compared and discussed by using E_b'/N_0. By using E_b', E_b' is not changed for the change of the channel models, so the superiority or inferiority of BER characteristics can be compared.

4.1 Comparisons of characteristics for the number of transmitted pulses

To confirm the effect of RR sequence of receiving performance against multipath environments, by using the BER characteristics in the MF reception, RR sequence is compared with M sequence that is used as spread sequence of a conventional DS system. And the effect is confirmed when the number of pulses is changed.

Figure 5 shows an example of an ideal received response under the CM1 environment (LOS environment). Table 1 shows the specification of simulations 1. Figure 6 (1) - (5) shows the transmitted sequences adopting the channel of CM4 in which the received response like Figure 1 can be obtained. And Figure 7 shows its BER characteristics. Then Figure 8 (1)-(5) shows the transmitted sequences adopting the channel of CM1 in which the received response like Figure 5 can be obtained. And Figure 9 shows its BER characteristics.

At first, in Figure 7 of the BER characteristics adopting CM4, as the number of pulses in RR sequence is increased to 6RR sequence using 6 pulses, the good BER characteristics can be obtained. However, when the number of pulses is increased to 15RR sequence using 15 pulses from 6RR sequence, the BER characteristics becomes degraded. From the above, it can be confirmed that the suitable number of the pulses exists by the channel model in RR sequences. In this case, 6RR sequence is the best number of the pulses in CM4 using this simulation. And 6RR sequence is best though 5RR sequence and 7RR sequence aren't shown here. When 6RR sequence is compared with M sequence of the code length 15, it is shown that the BER characteristic is improved greatly in 6RR sequence.

Next, in Figure 9 of the BER characteristics adopting CM1, 3RR sequence using 3 pulses becomes the good BER characteristic. And 3RR sequence is best though 2RR sequence and 4RR sequence aren't shown here. Furthermore, if the number of pulses is increased more than 3 pulses, it is confirmed that the BER characteristics is so degraded. As this reason, in CM1, the 3 higher paths occupy the greater part of the energy in the whole received response, therefore, it is considered that the best characteristic is obtained by generating RR sequence using the information of the 3 higher paths. And even if the number of pulses is increased by using the information of paths after them, it is considered that the great change of the characteristics is not appeared because the energy of the rest received paths is small.

Thus, the energy of received response in CM4 can be scattered not only a dominant wave but also delayed waves. Therefore, if RR sequence is generated, it is possible to compose delayed waves like emphasizing the received signal. However, using many pulses might

negatively affect the receiving performance by complicated ISI components, so it is supposed that the suitable number of pulses exists. On the other hand, as CM1 has a few delayed waves and has a few ISI components, too, the RR sequence is generated by using the information of paths in which the energy of the received response is large, even though the pulses are increased by using the information of paths after them, the interference components are not occurred in CM1, which is different from CM4, and the change of the BER characteristics is little in CM1.
The suitable number of pulses for the smallest BER is changed by the channel models like as 6RR sequence in CM4 and 3RR sequence CM1 used in this section.

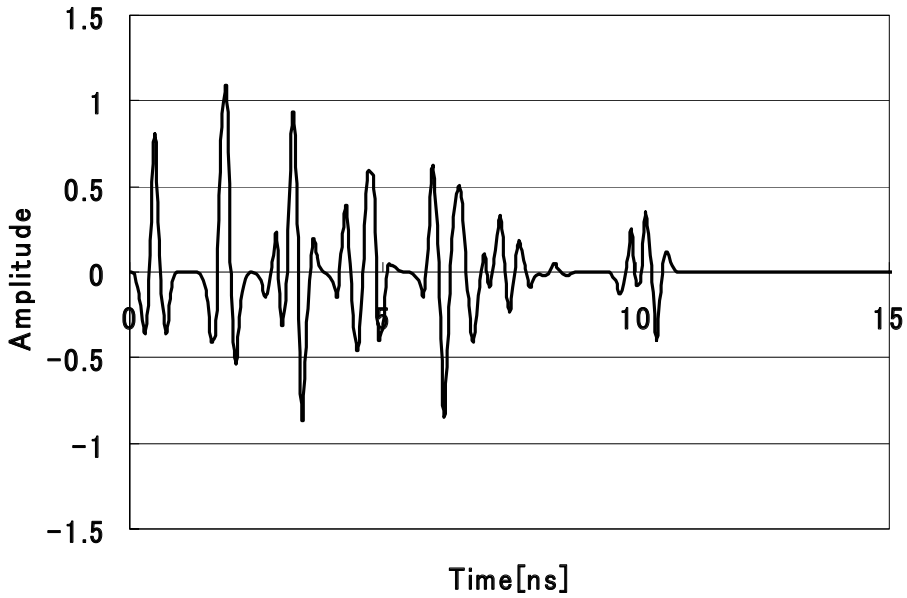

Fig. 5. An example of an ideal received response under the CM1 environment

Primary Modulation	BPSK	
Secondary modulation	DS (1pulse, 4, 6, 15RR seq., M seq.)	DS (1pulse, 3, 6, 13RR seq., M seq.)
Pulse Model	Monocycle Pulse	
Receivers	MF	
Pulse Width [ns]	1	
Transmission Rate [Mbps]	66.7	
Code Length N	15	
Transmission Channel	AWGN + CM4	AWGN + CM1

Table 1. Specification of simulations 1

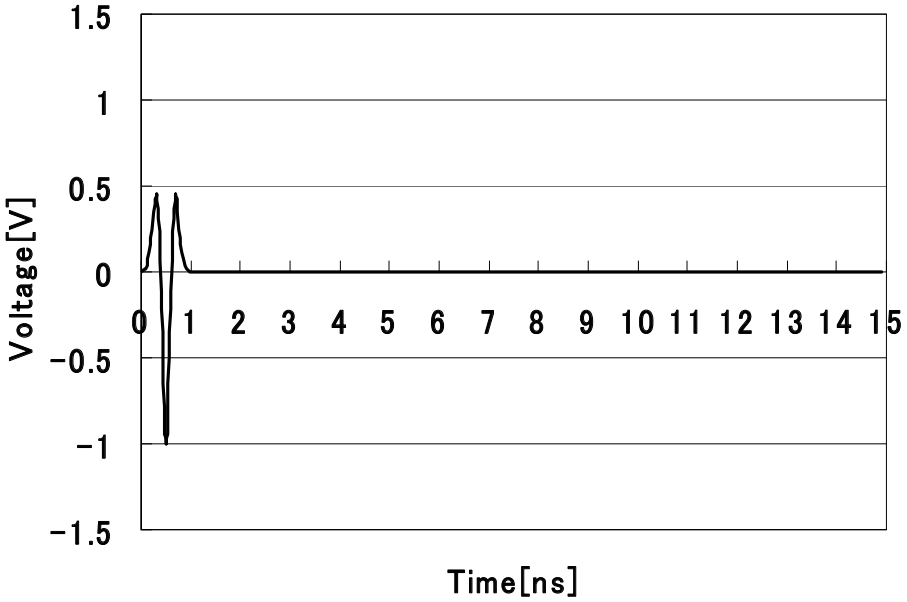

(1) 1 pulse sequence under the CM4 environment

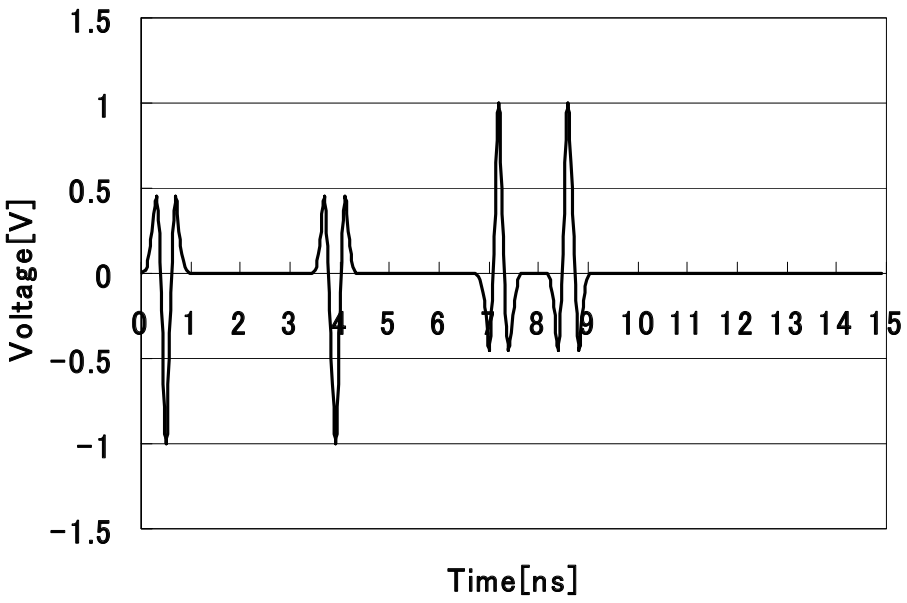

(2) 4RR sequence under the CM4 environment

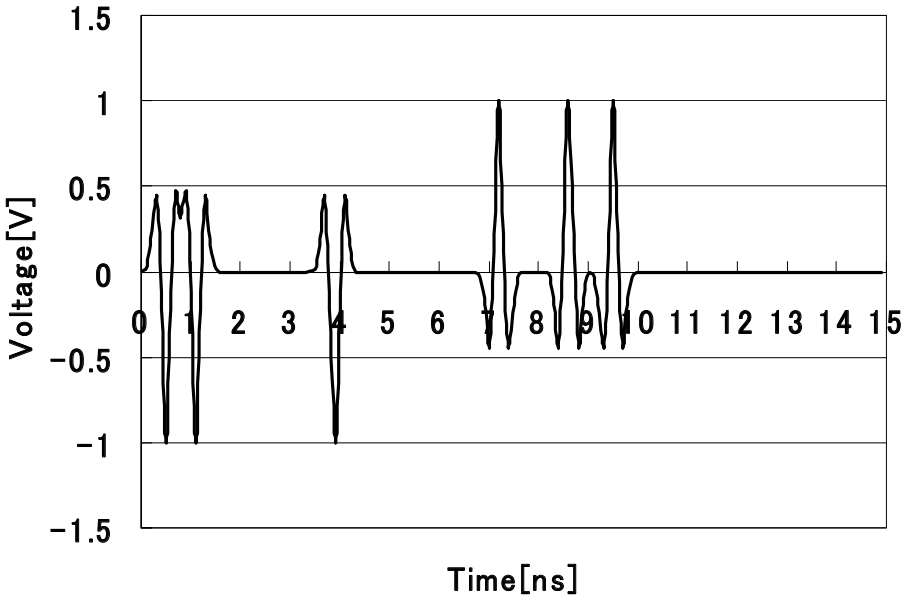

(3) 6RR sequence under the CM4 environment

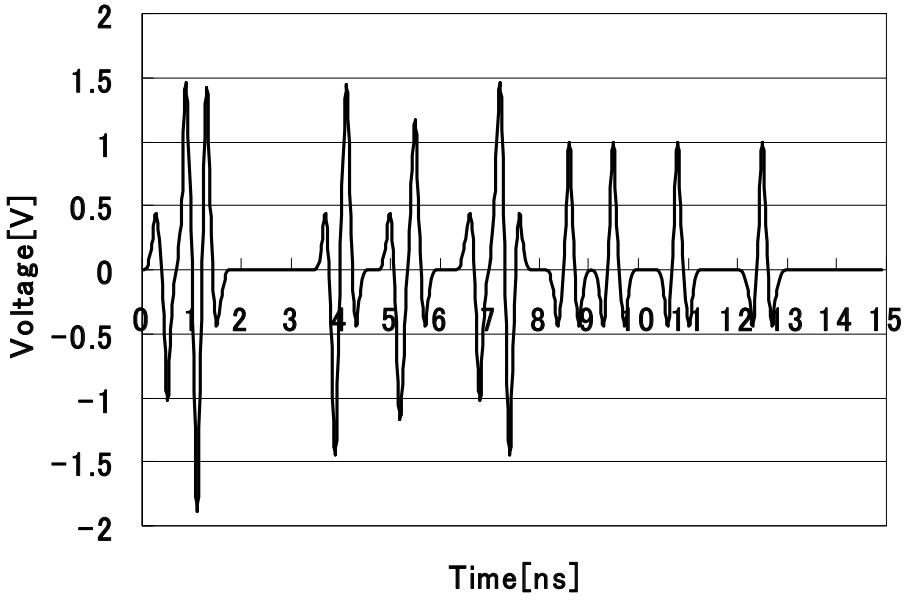

(4) 15RR sequence under the CM4 environment

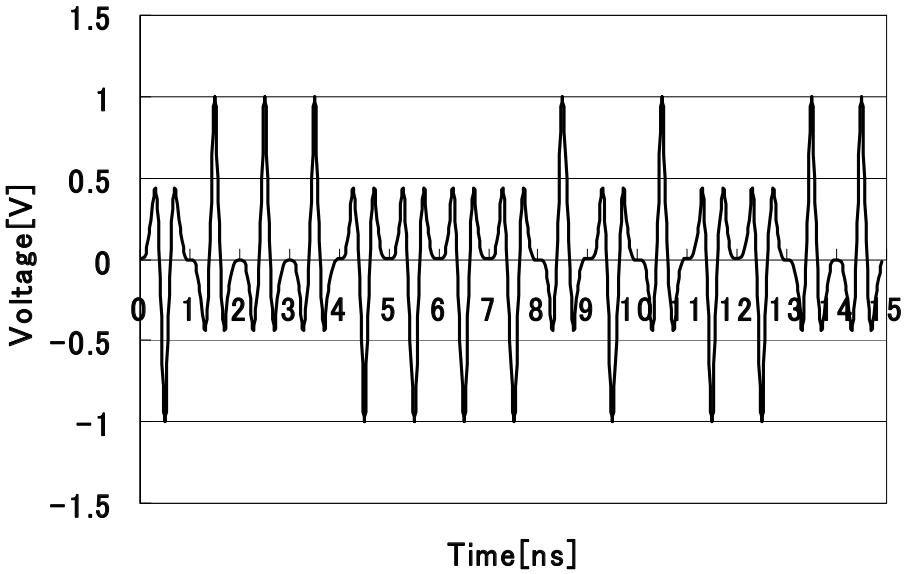

(5) M sequence under the CM4 environment

Fig. 6. Transmitted sequences under the CM4 environment

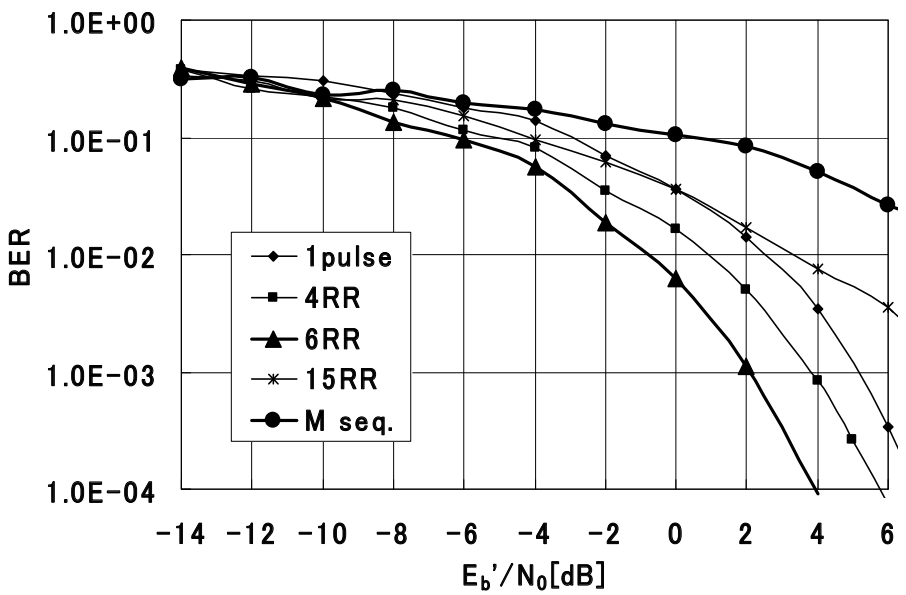

Fig. 7. BER characteristics of MF reception under the CM4 environment

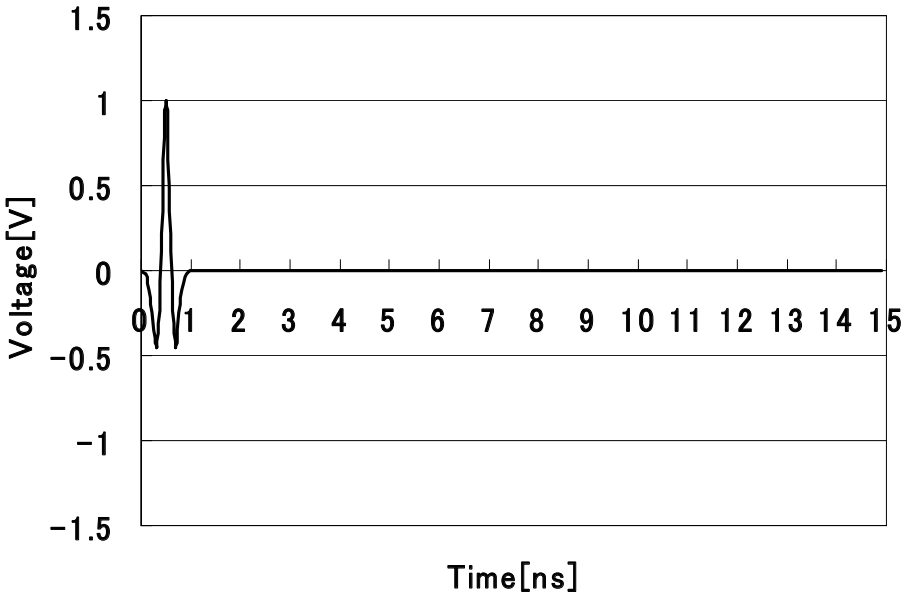

(1) 1 pulse sequence under the CM1 environment

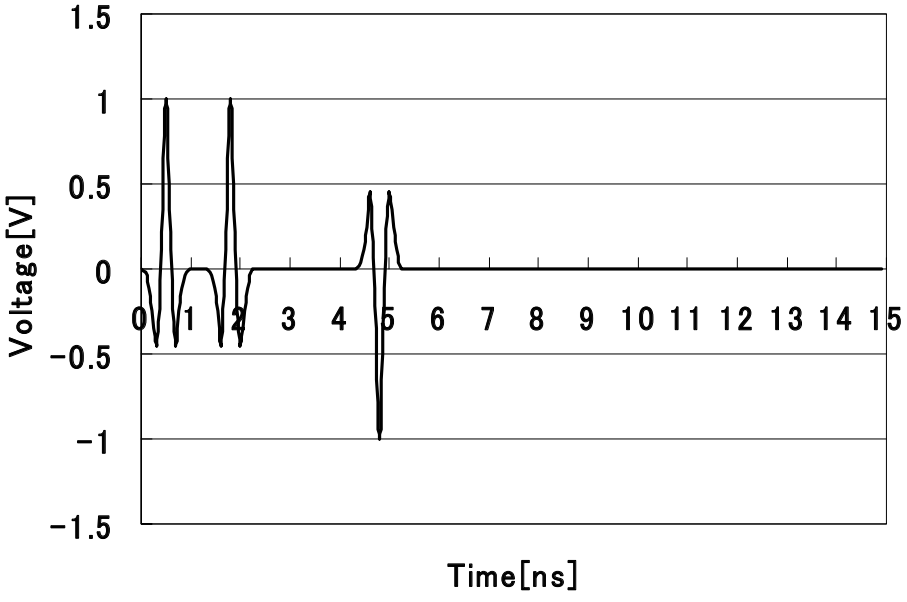

(2) 3RR sequence under the CM1 environment

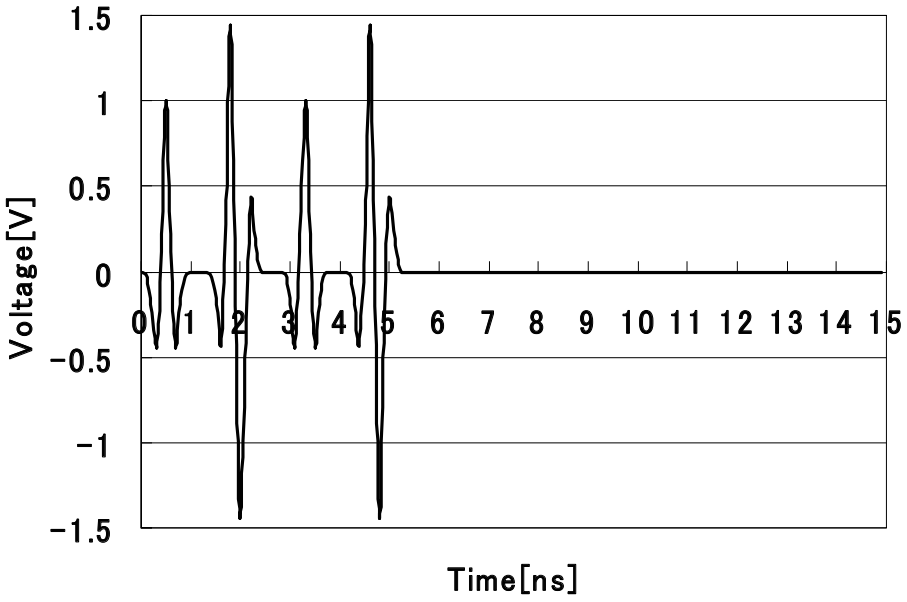

(3) 6RR sequence under the CM1 environment

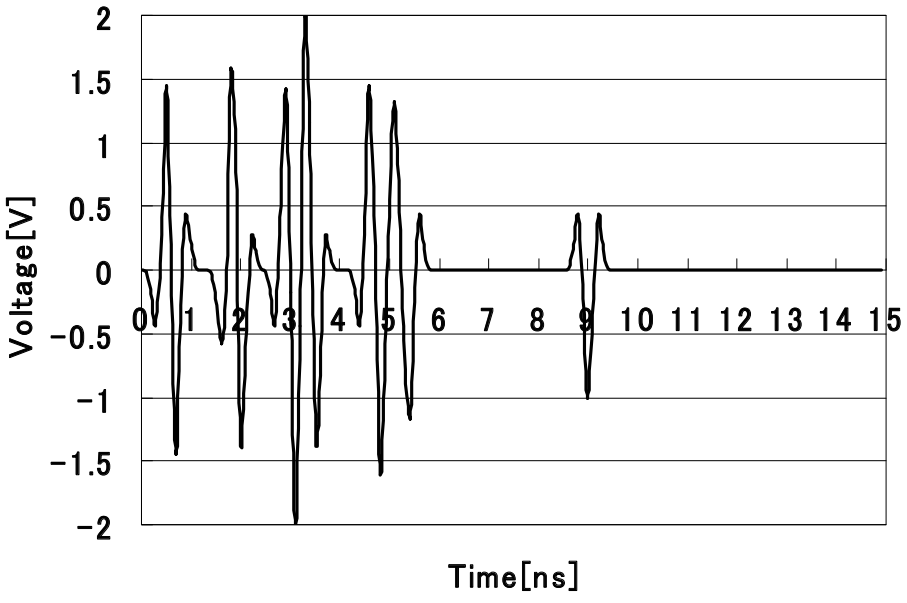

(4) 13RR sequence under the CM1 environment

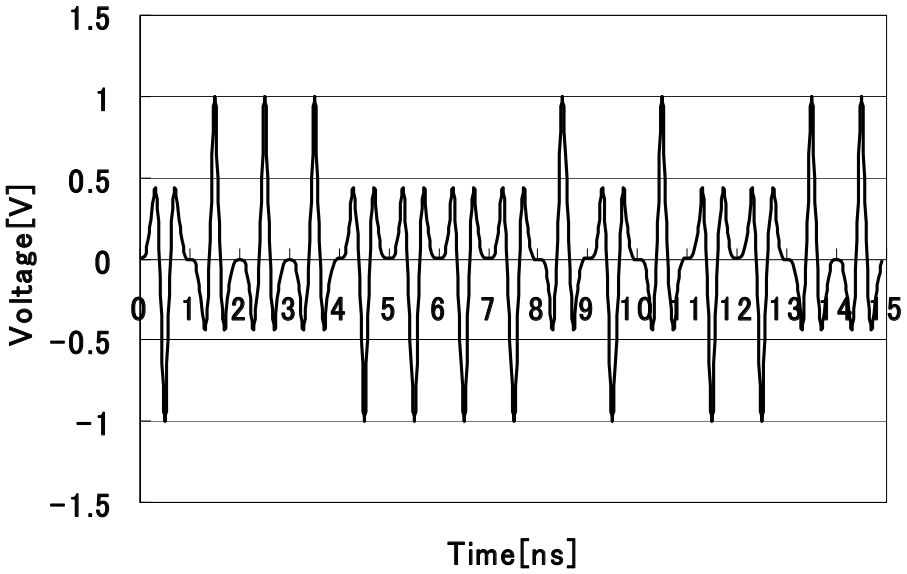

(5) M sequence under the CM1 environment

Fig. 8. Transmitted sequences under the CM1 environment

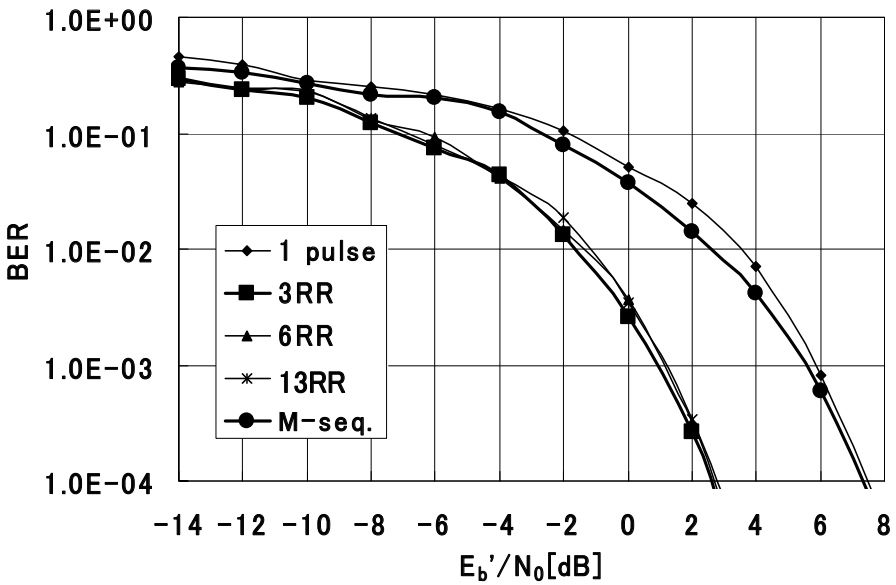

Fig. 9. BER characteristics of MF reception under the CM1 environment

4.2 Comparisons of characteristics for the number of selective RAKE fingers

Under CM4 and CM1 environments, receiving performance for the number of RAKE fingers when RR sequence is combined with LMS-RAKE reception system [9] is discussed by using the BER characteristics. Table 2 shows the specification of simulations 2. Figure 10 shows the BER characteristics when 6RR sequence is used under the CM4 environment. Figure 11 shows the BER characteristics when 3RR sequence is used under the CM1 environment. In this section the BER characteristics using M sequence also is shows for comparison. In each figure, the curve that the number of RAKE fingers is one means that it is the same results with the MF reception.

At first, in Figure 10 of the BER characteristics adopting CM4, as the number of RAKE fingers of 6RR sequence and M sequence is increased, it can be confirmed that the BER characteristics are improved. And an amount of improvement becomes small as the number of RAKE fingers of the combined system is increased. When the number of RAKE fingers is increased from 10 to 20 in 6RR sequence, the BER characteristics are improved only a little. The BER characteristics are saturated. On the other hand, when the number of RAKE fingers is 20 in M sequence, the BER characteristics are not yet saturated. Therefore, it is necessary to increase more the number of RAKE fingers. From the above, the number of RAKE fingers of 6RR sequence has fewer than that of M sequence, so that, the BER characteristics can be improved to a saturated condition. In other words, the energy scattering under the multipath environment is captured efficiently by using RR sequence, and the almost part of the scattering energy can be captured with about 10 fingers.

Next, the BER characteristics under CM1 environment in Figure 11 show similar with that of Figure 10. Even in the case of M sequence, the property approaching the saturated condition is shown according to increment of the number of RAKE fingers. Additionally when BER characteristics of the case of 20 fingers in 3RR sequence, which is approaching the saturated condition, is compared with that in M sequence, the difference of the performance of 3 [dB] can be obtained, that is, the difference of performance between 3RR sequence and M sequence is shown by using the LMS-RAKE reception method.

Consequently, RR sequence has better performances than that of M sequence in the number of a few RAKE fingers. And RR sequence can be approach the saturated condition of the BER characteristics. Therefore, a circuit scale in the receiver is reduced by using RR sequence, and a cost of the system can be reduced.

Primary Modulation	BPSK	
Secondary modulation	DS (6RR seq., M seq.)	DS (3RR seq., M seq.)
Pulse Model	Monocycle Pulse	
Receivers	LMS-RAKE	
Pulse Width [ns]	1	
Transmission Rate [Mbps]	66.7	
Code Length N	15	
Number of RAKE Finger F	1, 10, 20	
Transmission Channel	AWGN + CM4	AWGN + CM1
Step Size Parameter μ	10^{-6}	10^{-5}
Training bit [bits]	200000	200000

Table 2. Specification of simulations 2

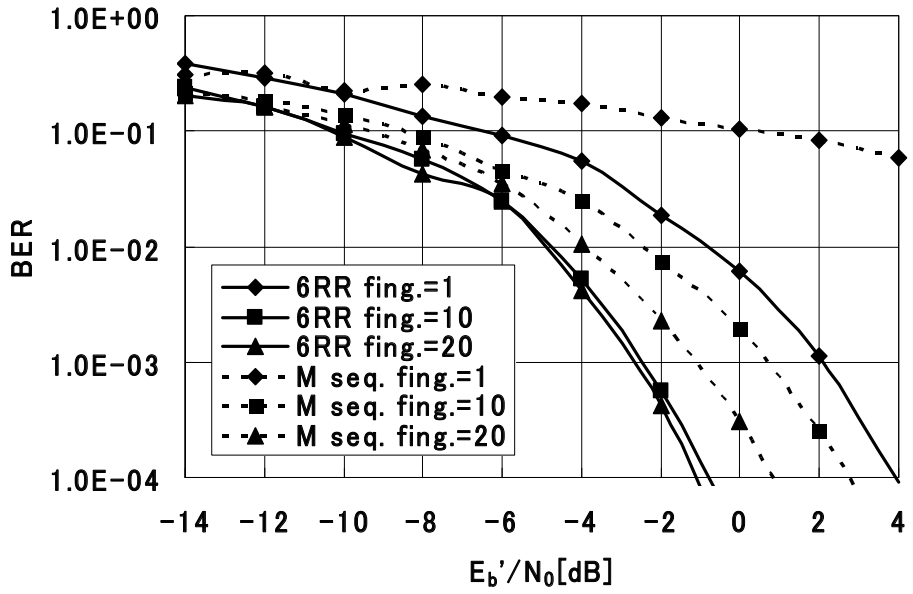

Fig. 10. BER characteristics by the number of RAKE fingers under the CM4 environment

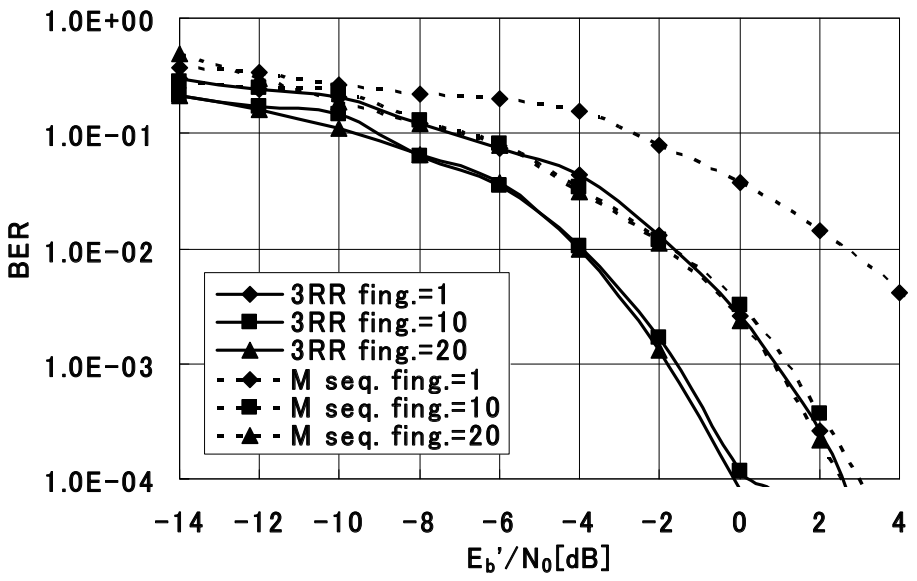

Fig. 11. BER characteristics by the number of RAKE fingers under the CM1 environment

5. Conclusions

In this chapter, in order to solve the ISI problem caused by the multipath environments, we have proposed the received response sequence (ternary code sequence) in DS/UWB which is generated by using the channel information of the multipath environment, and have shown the generating method. By using the proposed sequence, it has been shown that the BER characteristics have been improved greater than that of M sequence in a conventional sequence when the number of pulses has been selected properly. And the receiving energy has been captured efficiently even if the number of selective RAKE fingers has been a few. Therefore, the circuit scale in the receiver has become small and the cost of the system can be reduced.

For further studies, it will be necessary that the effectiveness of the received response is discussed by using a pilot signal which is estimated the channel information in the transmitter practically.

6. References

[1] Marubayashi, G.; Nakagawa, M. & Kohno, R. (1988). Spread Spectrum Communications and its Applications, *The Institute of Electronics, Information and Communication Engineers (IEICE)*, *Corona-sha*, May 1998

[2] Tsuzuku, A. (1999). OFDM Modulation and Demodulation method, *The Journal of The Institute of Electronics, Information and Communication Engineers (J. IEICE)*, Vol.79, No.8, pp.831-834, Aug. 1999

[3] Kohno, R. (2004). Ultra Wideband(UWB) Wireless Technology and Its Contribution in Future Intelligent Wireless Access, *The Journal of The Institute of Electronics, Information and Communication Engineers (J. IEICE)*, Vol.87, No.5, pp396-401, May 2004

[4] Xiao, Z.; Su, L.; Jin, D. & Zeng, L. (2010). Performance Comparison of RAKE Receivers in SC-UWB Systems and DS-UWB Systems, *The Institute of Electronics, Information and Communication Engineers (IEICE) Trans. Communications.*, Vol.E93-B, No.4, pp.1041-1044, April 2010

[5] Win, M. Z.; Chrisikos, G. & Sollenberger, N. R. (2000). Performance of Rake reception in dense multipath channlels:implications of spreading bandwidth and selection diversity order, *IEEE JSAC*, vol.18, pp.1516-1525, August 2000

[6] Terashima, Y.; Sasaki, S.; Rahman, M. A.; Zhou J. & Kikuchi, H. (2005) A study on Rake reception for DS-UWB communications, *The Institute of Electronics, Information and Communication Engineers (IEICE) Technical Report*, WBS2005-3 pp.13-18, June 2005

[7] Rahman, M. A.; Sasaki, S.; Zhou J.; Muramatsu, S. & Kikuchi, H. (2004). Evaluation of Selective Rake Receiver in Direct Sequence Ultra Wideband Communications in the Presence of Interference, *The Institute of Electronics, Information and Communication Engineers (IEICE) Trans. Fundamentals.*, Vol.E87-A, No.7, pp.1742-1746, July 2004

[8] Foerster, J. (2003). Channel modeling sub-committee report final, *IEEE P802.15-02/490r1-SG3a*, Feb. 2003

[9] Yokota, M. & Tachikawa, S. (2006). LMS-RAKE Reception in DS/UWB System against Long Delay-Path Channel, *The Institute of Electronics, Information and Communication Engineers (IEICE) General Conference*, pp.147, Mar. 2006

4

Genetic Algorithm based Equalizer for Ultra-Wideband Wireless Communication Systems

Nazmat Surajudeen-Bakinde, Xu Zhu, Jingbo Gao,
Asoke K. Nandi and Hai Lin
Department of Electrical Engineering and Electronics, University of Liverpool
United Kingdom

1. Introduction

Ultra-wideband (UWB) systems operate in the 3.1 $\sim$ 10.6GHz spectrum allowed by the Federal Communications Commission (FCC) on an unlicensed basis. The ultrawide bandwidth and ultralow transmission power density (-41.25 dBm/MHz for indoor applications) make UWB technology attractive for high-speed, short-range (e.g.,indoor) wireless communications Cai et al. (2006). UWB signal generations for the high-speed, short-range networking is in support of a variety of potential low-cost, low-power multimedia transport applications in home and enterprise environments. Typical scenario is provisioning wireless data connectivity between desktop PC and associated peripherals like keyboard, mouse, printer, etc. Additional driver applications relates to streaming of digital media content between consumer electronics appliances such as TV sets, VCRs, audio CD/DVD and MP3 players Roy et al. (2004).

In an impulse-based DS-UWB system, the transmitted data bit is spread over multiple consecutive pulses of very low power density and ultra-short duration. This introduces resolvable multipath components having differential delays in the order of nanoseconds. Thus, the performance of a DS-UWB system is significantly degraded by the inter-chip interference (ICI) and inter-symbol interference (ISI) due to multipath propagation Liu & Elmirghani (2007).

In a frequency-selective fading channel, a RAKE receiver can be used to exploit multipath diversity by combining constructively the monocycles received from the resolvable paths. Maximum ratio combining (MRC)-RAKE is optimum when the disturbance to the desired signal is sourced only from additive white Gaussian noise (AWGN), therefore it has low computational complexity. However, the presence of multipath fading, ISI, and/or narrowband interference (NBI) degrades the system performance severely Sato & Ohtsuki (2005). The maximum likelihood detection (MLD) is optimal in such a frequency selective channel environment as UWB channel but its computational complexity grows exponentially with the constellation size and the number of RAKE fingers.

The high computational complexity of MLD motivates research for suboptimal receivers with reduced complexity such as linear and non-linear equalizers. In Kaligineedi & Bhargava (2006), performance of non-linear frequency domain equalization schemes viz. decision feedback equalization (DFE) and iterative DFE for DS-UWB systems were studied. Eslami et al in Eslami & Dong (2005) presented the performance of joint RAKE and minimum mean

square error (MMSE) equalizer receiver for UWB communication systems. Parihar et al in two different papers, Parihar et al. (2005) and Parihar et al. (2007) gave thorough analysis of linear and non-linear equalizers for DS-UWB systems considering two different modulation techniques, binary phase shift keying (BPSK) and 4-ary bi-orthogonal keying (4BOK).
Known channel state information (CSI) has been assumed in previous work but practically this is not feasible, because the wireless environment is always changing. Channel estimation is of particular importance in future broadband wireless networks since high data-rate transmissions lead to severe frequency-selective channel fading, which necessitates the use of channel estimation/equalization techniques to combat significant the ISI Sun & Li (2007).
Lots of research work has been done on channel estimation techniques using both the training based and blind approaches. In Sato & Ohtsuki (2005), Mielczarek et al. (2003) and Chu et al. (2008), the pilot-aided channel estimation were carried out. Sato and Ohtsuki in Sato & Ohtsuki (2005) used data-aided approach based on using known pilot symbols to estimate the channel impulse response. The sliding window (SW) and successive cancellation (SC) algorithms were proposed in Mielczarek et al. (2003). Chu et al. also proposed a pilot-channel-assisted log-likelihood-ratio selective combining (PCA-LLR-SC) scheme for UWB systems in Chu et al. (2008). In another set of data-aided approaches based on maximum likelihood (ML) scheme, Wang, Xu, Ji & Zhang (2008) proposes a ML approach to channel estimation using a data-aided simplified ML channel estimation algorithm. In Lottici et al. (2002), Lottici et al. proposed data-aided (DA) and non-data aided (NDA) scenarios based on the ML criterion. Frequency domain channel estimation were reported in Takanashi et al. (2008) where an iterative frequency domain channel estimation technique was proposed for multiple-input multiple-output (MIMO)-UWB communication systems.
The genetic algorithm (GA) works on the Darwinian principle of natural selection called "survival of the fittest". GA possesses an intrinsic flexibility and freedom to choose desirable optima according to design specifications. GA presumes that the potential solution of any problem is an individual and can be represented by a set of parameters regarded as the genes of a chromosome and can be structured by a string of values in binary form Man et al. (1999). GA is a well studied and effective search technique used in lots of work in CDMA communication systems as can be found in Erguin & Hacioglu (2000); Yen & Hanzo (2001) and Al-Sawafi (2004). In Erguin & Hacioglu (2000), a hybrid approach that employs a GA and multistage detector for the multiuser detection in CDMA system was proposed. Yen and Hanzo in Yen & Hanzo (2001) applied GA as a joint channel estimation and multiuser symbol detection in synchronous CDMA systems. A micro GA was developed in Al-Sawafi (2004) as a multiuser detection technique in CDMA system. GA has also been applied to UWB communication systems in Gezici et al. (2005); Wang et al. (2004) and Wang, Yang & Wu (2008). In Gezici et al. (2005), a GA-based iterative finger selection scheme, which depends on the direct evaluation of the objective function, was proposed. T.Wang et al in Wang et al. (2004) formulated an optimization problem aiming to reduce multiband jam interference power on UWB THSS IR system with 2-PPM which belongs to the class of nonlinear combinational optimization. UWB pulse design method was carried out in Wang, Yang & Wu (2008) using the GA optimization. However, to the best of our knowledge, no work has been done, using GA for channel equalization with pilot-aided channel estimation in DS-UWB communication systems.
In this chapter, we propose an equalization approach using GA in DS-UWB wireless communication, where GA is combined with a RAKE receiver to combat the ISI due to the frequency selective nature of UWB channels for high data rate transmission. We also compare our proposed RAKE-GA equalization approach with the MMSE based linear equalization approach and the optimal MLD approach to demonstrate a trade-off between performance

and computational complexity. Moreover, we employ a data aided approach to estimate the channel amplitudes and delays using a sliding window method, which has lower complexity than ML based channel estimation methods Sato & Ohtsuki (2005).
Simulation results show that the proposed GA based structure significantly outperforms the RAKE and RAKE-MMSE receivers. It also provides a very close bit error rate (BER) performance to the optimal RAKE-MLD approach, while requiring a much lower computational complexity. The impact of the number of RAKE fingers on the RAKE-GA algorithm and the speed of convergence in terms of the BER against the number of generations are investigated by simulation, while the number of training overhead, that is the percentage of pilot symbols size compared to the number of transmitted data, is also presented with a plot of BER against the number of training symbols.
Section 2 is the system model. We propose a RAKE-GA equalization approach in Section 3. The data-aided channel estimation for all the receivers are presented in Section 4. Section 5 presents the computational complexity of the RAKE-GA. Simulation results are shown in Section 6. Section 7 draws the conclusion.

2. System model

2.1 Transmit signal

The transmit signal for the DS-UWB can be expressed as

$$x(t) = \sqrt{E_c} \sum_{k=-\infty}^{\infty} d_k v_{\mathrm{TR}}(t - kT_s). \tag{1}$$

where the transmit pulse $v_{\mathrm{TR}}(t)$, is generated by using the ternary orthogonal code sequence as specified in the IEEE standard **?** due to its orthogonality and is of the form given in (2). E_c is the energy per transmitted pulse, $d_k \in \{\pm 1\}$ is the k^{th} transmit symbol, T_s is the interval of one symbol or frame time, each frame is subdivided into N_c equally spaced chips giving $T_s = N_c T_c$.

$$v_{\mathrm{TR}}(t) = \sum_{i=0}^{N_c-1} b_i g(t - iT_c). \tag{2}$$

where $b_i \in \{-1, 0, 1\}$ is the i^{th} component of the spreading code, T_c is the chip width, $g(t)$ represents the transmitted monocycle waveform which is normalized to have unit energy and N_c is the length of the spreading code sequence.

2.2 Channel model

According to Molisch & Foerster (2003), a reliable channel model, which captures the important characteristics of the channel, is a vital prerequisite for system design. Toward this end, the IEEE 802.15.3a task group has evaluated a number of popular indoor channel models to determine which model best fits the important characteristics from realistic channel measurements using UWB waveforms. The goal of the channel model is to capture the multipath characteristics of typical environments where IEEE 802.15.3a devices are expected to operate. The model should be relatively simple to use in order to allow PHY proposers to use the model and, in a timely manner, evaluate the performance of their PHY in typical operational environments.
A log-normal distribution rather than a Rayleigh distribution for the multipath gain magnitude is used because the log-normal distribution fits the measurement data better. In

addition, independent fading is assumed for each cluster as well as each ray within the cluster. Therefore, channel impulse response of this model expressed in a simpler form is given as:

$$h(t) = \sum_{l=1}^{L_{tot}} h_l \delta(t - \tau_l). \tag{3}$$

where L_{tot} is the total number of paths, $\tau_l (= lT_c)$ is the delay of the l^{th} path component and h_l is the l^{th} path gain Foerster (2003).

2.3 Receive signal

The receive signal $r(t)$, which is the convolution of the transmit signal in (1) with the channel impulse responses given in (3) and the addition of noise is shown in (4) as

$$r(t) = x(t) * h(t) + n(t) = \sqrt{E_c} \sum_{k=-\infty}^{\infty} d_k v_{\mathrm{TR}} \sum_{l=1}^{L_{tot}} h_l \left(t - kT_f - \tau_l\right) + n(t). \tag{4}$$

where $n(t)$ is the additive white Gaussian noise (AWGN) with zero mean and a variance of σ^2, $*$ denotes the convolution operator.

3. RAKE-GA based equalization for DS-UWB systems

In this section, we present an equalization approach for DS-UWB systems by using GA. The block diagram of the GA based equalization approach is shown in Fig. 1, where the blocks in the dashed boxing are the initialization of the GA based equalization using RAKE demodulator. The GA is then employed to equalize the output signals from the RAKE demodulator. Compared to the optimal MLD receiver, the proposed RAKE-GA receiver has much lower computational complexity and negligible performance degradation.

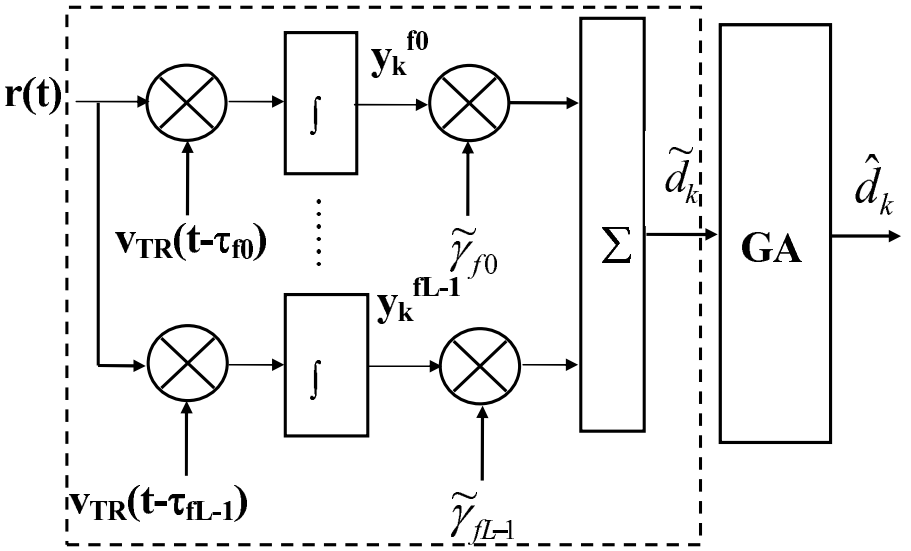

Fig. 1. RAKE-GA for DS-UWB system

3.1 Initialization of RAKE-GA

It is well known that a good initial value is critical in GA based algorithms. For DS-UWB systems, the performance of GA only receiver without proper initialization is even worse than RAKE receiver only due to the frequency selective nature of UWB channels. To this end we obtained our initial population for the GA optimization from the RAKE soft estimates so as to improve the BER performance of our system. A typical RAKE receiver is composed of several correlators followed by a linear combiner, as shown in Fig. 1. The signal received at the RAKE receiver is correlated with delayed versions of the reference pulse, which is the ternary orthogonal spreading sequence, multiplied by the tap weights, the output signals are then combined linearly Siriwongpairat & Liu (2008).

MRC-RAKE combiner, which uses the strongest estimated fingers to select the received signal at the delay times $\tau_{fl}\,(l = 0, ..., L-1)$**?**, was employed in this work. Perfect chip synchronization between the transmitter and the receiver is assumed. The l^{th} correlator's output y_k^{fl} of the RAKE receiver for the k^{th} desired symbol is given by

$$y_k^{fl} = \int_{kT_f+\tau_{fl}}^{(k+1)T_s+\tau_{fl}} r\,(t)\, v_{\mathrm{TR}}\left(t - kT_s - \tau_{fl}\right) dt. \tag{5}$$

Expression (5) in vector notation is expressed as shown in (6)

$$\mathbf{y_k} = \sqrt{E_s} d_k \mathbf{h} + \mathbf{i}_k + \mathbf{n}_k. \tag{6}$$

where $\mathbf{y}_k = \left[y_k^{f1}, ...y_k^{fL}\right]^T$, $\mathbf{h} = \left[h_{f1}, ...h_{fL}\right]^T$, $\mathbf{i}_k = \left[i_k^f, ...i_k^{fL}\right]^T$ with i_k^{fL} denoting ISI of the k^{th} symbol for the l^{th} correlator and $\mathbf{n}_k = \left[n_k^f, ...n_k^{fL}\right]^T$ with n_k^{fL} being the noise component of the k^{th} symbol for the l^{th} correlator. L is the number of RAKE fingers. $E_s = N_c E_c$ which is the energy per symbol. The Selective RAKE receiver output with MRC technique is expressed as

$$\tilde{d_k} = \tilde{\mathbf{fl}}^T \mathbf{y}_k. \tag{7}$$

where $\tilde{\mathbf{fl}} = [\tilde{\gamma}_1, ..., \tilde{\gamma}_L]^T$ is the finger weights of the RAKE receiver estimated from the channel taps, $\tilde{\gamma}_l = \hat{h}_{fl}$ where $\hat{h}_{fl}$=$\left[\hat{h}_{f1}, ...\hat{h}_{fL}\right]^T$ are the channel estimates. The results obtained in (7), which are soft estimates are used as initialization of GA optimization in the following section. The decision function is used to determine the estimated received data as follows:

$$\hat{d}_k = sign\left(\tilde{d_k}\right) \tag{8}$$

3.2 RAKE-GA

The Theory of GA

Despite the intuitive appeal and the symmetry of GAs, it is crucial that we back these fuzzy feelings and speculations about GAs using cold, mathematical facts. The schemata theory will help us to do this.The schemata theory and their net effect of reproduction and genetic operators on building blocks contained within the population for the GA are discussed below Goldberg (1989).

Schema Theory

The design methodology of the GA relies heavily on Holland's notion of schemata. It simply states that schemata are sets of strings that have one or more features in common. A schema is built by introducing a "don't care" symbol, "#," into the alphabet of genes, i.e., #1101#0. A schema represents all strings (a hyperplane or subset of the search space), which match it on

all positions other than "#." It is clear that every schema matches exactly 2' strings, where "r" is the number of don't care symbols, "#," in the schema template. For example, the set of the schema #1101#0 is $\{1110110, 1110100, 0110110, 0110100\}$ Tang et al. (1996).
Effect of Selection
Since a schema represents a set of strings, we can associate a fitness value $f(S,t)$ with schema "S, " and the average fitness of the schema. $f(S,t)$ is then determined by all the matched strings in the population. Using *proportional selection* in the reproduction phase as was done in our RAKE-GA algorithm, we can estimate the number of matched strings of a schema "S" in the next generation.
Let $\zeta(S,t)$be the number of strings matched by schema "S" at current generation. The probability of its selection (in a single string selection) is equal to $f(S,t)/F(t)$. where $F(t)$ is the average fitness of the current population. The expected number of occurrences of S in the next generation is

$$\zeta(S,t+1) = \zeta(S,t) \times \frac{f(S,t)}{F(t)} \tag{9}$$

Let

$$\varepsilon = (f(S,t) - F(t))/F(t) \tag{10}$$

If $\varepsilon > 0$, it means that the schema has an above-average fitness and vice versa.
Substituting (10) into (9) and it shows that an "above average" schema receives an exponentially increasing number of strings in the next generations as presented in (11)

$$\zeta(S,t) = \zeta(S,0)(1+\varepsilon)^t \tag{11}$$

Effect on Crossover
During the evolution of a GA, the genetic operations are disruptive to current schemata; therefore, their effects should be considered. Assuming that the length of the chromosome is P, which is the number of individuals within a population and scattered crossover is applied, in general, a crossover point is selected uniformly among $P-1$ possible positions.
This implies that the *probability of destruction* of a schema S is

$$p_d(S) = \frac{\sigma(S)}{P-1} \tag{12}$$

or the *probability of a schema survival* is

$$p_s(S) = 1 - \frac{\sigma(S)}{P-1} \tag{13}$$

where σ is the *defining length* of the schema S, defined as the distance between the outermost fixed positions. It defines the compactness of information contained in a schema. For example, the *defining length* of #OOO# is 2, while the defining length of 1#OO# is 3.
Assuming the operation rate of crossover is pc, the probability of a schema survival is:

$$p_s(S) \geq 1 - p_c.\frac{\sigma(S)}{P-1} \tag{14}$$

Effect of Mutation
If the bit mutation probability is p_m, then the probability of a single bit survival is $1-p_m$. Defining the *order* of schema S (denoted by $o(S)$) as the number of fixed positions (i.e.,

positions with 0 or 1) present in the schema, the probability of a schema S surviving a mutation (i.e., sequence of one-bit mutations) is

$$p_s(S) = (1 - p_m)^{o(S)} \tag{15}$$

Since $p_m \ll 1$, this probability can be approximated by:

$$p_s(S) \approx 1 - o(S).p_m \tag{16}$$

Schema Growth Equation
Combining the effect of selection, crossover, and mutation, we have a new form of the reproductive schema growth equation:

$$\zeta(S, t+1) \geq \zeta(S, t).\frac{f(S,t)}{F(t)}\left[1 - p_c.\frac{\sigma(S)}{P-1} - o(S).p_m\right] \tag{17}$$

Based on (17), it can be concluded that a high average fitness value alone is not sufficient for a high growth rate. Indeed, short, low-order, above-average schemata receive exponentially increasing trials in subsequent generations of a GA Tang et al. (1996).
Iterations of GA

- **Initialization of Population:** An initial random population was generated by using the soft estimates output of the RAKE receiver as the input to our GA. This was then converted to binary 0 and 1 from the soft estimates obtained from our RAKE receiver. The chromosomes fitness values are evaluated as discussed below.
- **Fitness Function Evaluation:** A fitness value is used to reflect the degree of *goodness* of the chromosome for the problem which would be highly related with its objective value Man et al. (1999). The fitness values of individuals within the population of our GA was evaluated before implementing the GA operations. The GA refine the specified population which consists of the chromosomes, through the selection, reproduction, crossover and mutation operations. The GA minimizes the fitness function in terms of the distance measure criteria. The probability density function of y_k in (6) conditioned on $\mathbf{h}$ *and* $\mathbf{d}$ is

$$p(\mathbf{y}|\,\mathrm{h}, \boldsymbol{d}) = \frac{1}{\left(2\pi\sigma_e^2\right)^{M/2}} \times \exp\left\{-\frac{1}{2\text{œ}_\mathrm{e}^2}\sum_{\mathrm{k}=1}^{\mathrm{M}}\left[\mathrm{y_k} - \sum_{\mathrm{l}=1}^{\mathrm{L_{tot}}}\mathrm{h_l d\,(k-l)}\right]^2\right\} \tag{18}$$

The joint ML estimate of $\mathbf{h}$ *and* $\mathbf{d}$ are obtained by maximizing $p(\mathbf{y}|\mathbf{h}, \mathbf{d})$ over $\mathbf{h}$ *and* $\mathbf{d}$ jointly. Equivalently, the ML solution is the minimum of the cost function **?** . The minimum of the cost function is evaluated to obtain estimate of the transmitted signal, $\hat{\mathbf{d}}$

$$J = \left|\tilde{\mathbf{fl}}^T\mathbf{e}\right| \tag{19}$$

where $\mathbf{e} = [\mathbf{e_1}, ..., \mathbf{e_M}]$, $\mathbf{e_k} = \left(\mathbf{y_k} - \sum_{\mathbf{l}=\mathbf{1}}^{\mathbf{L_{tot}}}\mathbf{h_l d\,(k-l)}\right)$and $k = 1 - M$
where all the terms are as defined in the section for initialization of RAKE-GA . An optimal solution is computationally expensive and so suboptimal solution like GA was adopted for estimating the data, $\hat{\mathbf{d}}$, while data-aided channel estimation approach was used in obtaining the channel estimates, $\hat{\mathbf{h}}$. The GA evaluated the fitness values of individuals by minimizing the cost function in (19).

- **Proportional fitness scaling** was used to convert the raw fitness score returned by the objective function to values in a range that is suitable for the selection function. It makes

the expectation proportional to the raw fitness scores. This is advantageous when the raw scores are in good range. When the objective values vary a little, all individuals have approximately the same chance of reproduction.

- **Stochastic selection** now chooses parents for the next generation based on their scaled values from the fitness scaling function. It lays out a line in which each parent corresponds to a section of the line of length proportional to its scaled value. There is a movement along the line in steps of equal size. At each step, a parent is allocated from the section it lands on. The first step is a uniform random number less than the step size. A certain **elites** are now chosen which are guaranteed to survive to the next generation.
- **Scattered crossover** combines two parents to form a child for the next generation. It creates a random binary vector, rv, then selects the genes where the vector is a 1 from the first parent, $P1$ and the genes where the vector is a 0 from the second parent, $P2$ and combines the genes to form the child. This is illustrated in (20)

$$P1 = [1010010100]$$

$$P2 = [0101101011]$$

$$bv = [1100100101]$$

$$child = [1001001110] \tag{20}$$

- **Gaussian mutation** was used provides genetic diversity and enable the GA to search a broader space, by making small random changes in the individuals in the population. It adds a random number from a Gaussian distribution with mean zero to each vector entry of an individual. The variance of this distribution is determined by the parameters **scale** and **shrink**.

The scale parameter determines the variance at the first generation, that is, it controls the standard deviation of the mutation and it is given by $standard\,deviation = scale \times (v(2) - v(1))$, where $scale = 0 \sim 10$, v is the vector of initial range used to generate the initial population. The initial range is a 2-by-1 vector $v = 0; 1$.

The shrink parameter controls how the variance shrinks as generations go by. That is, it controls the rate at which the average amount of mutation decreases and the variance at the g^{th} generation G is given by $var_k = var_{k-1}\left(1 - shrink.\frac{k}{G}\right)$, where $shrink = -1 \sim 3$. If the **shrink** parameter is 0, the variance is constant, if the **shrink** is 1, the variance shrinks to 0 linearly as the last generation is reached and a negative value of **shrink** causes the variance to grow MATLAB (2007).

- **Stopping criteria** determines what causes the algorithm to terminate. Our algorithm was terminated when the refining of the chromosomes using the operators had been done G times, which is the number of generations.

The RAKE-GA receiver was proposed to reduce the high computational complexity of the RAKE-MLD receiver which is an optimum receiver in a frequency selective channel like UWB. In the MLD scheme, in which the whole search space of possible solutions are utilized, the soft estimate output, of the RAKE receiver is also used as the input to the MLD receiver. The MLD detector searches through all the possible solutions of data bits, $\left(M, 2^M\right)$ and the one close

in distance to the transmitted data based on the distance measure criteria is chosen. The cost function for the RAKE-MLD is also presented in expression (19) thereby making the MLD to spend longer simulation time and even to be more computationally complex.

4. Channel estimation

In this work, a data-aided approach used in Lottici et al. (2002) was also implemented in estimating the channel impulse response. The sliding window correlator method Li et al. (2003); Mielczarek et al. (2003) was used in estimating the channel gains and delays so as to reduce the high computational complexity of the ML approach. A data-aided approach for channel estimation is employed in this work and this implies that the transmitted signal, $x(t)$, is known to the receiver. The ML channel estimation has a very good performance but it is too complicated to be implemented in UWB systems which usually require low complexity receivers Siriwongpairat & Liu (2008). B known pilot symbols are sent for the training $d_k^t, (k = 1, 2..., B)$ in order to estimate the channel. The RAKE receiver gave an output during the training is presented as (21).

$$y_k^{L_{est}} = \int_{kT_f+\tau_{fl}}^{(k+1)T_f+\tau_{fl}} r^t(t)\, v_{\mathrm{TR}}\left(t - kT_f - \tau_{fl}\right) dt. \tag{21}$$

where $y_k^{L_{est}} = \left[y_k^1, y_k^2, ..., y_k^{L_{est}}\right]^T$, $r^t(t)$ is the received training signal for the k^{th} pilot symbol, L_{est} is the number of paths to be estimated and it is assumed that the receiver knows the optimal value of L_{est}(i.e.$L_{est} = L_{tot}$) in (3) Sato & Ohtsuki (2005). All other terms are as already defined in the previous Section.

The estimated path gains of the channel vector $\hat{\mathbf{h}} = \left[\hat{h}_1, \hat{h}_2, ..., \hat{h}_{L_{est}}\right]^T$, can be expressed as follows using the cross-correlation method, where E_s is the energy per symbol Sato & Ohtsuki (2005).

$$\hat{\mathbf{h}} = \frac{1}{B\sqrt{E_s}} \sum_{k=1}^{B} d_k^t y_k^{L_{est}}. \tag{22}$$

5. Computational complexity

We provide a complexity analysis of the proposed RAKE-GA in terms of complex valued floating point multiplication, in comparison with the RAKE, RAKE-MMSE and RAKE-MLD receivers. We assume all the receivers use the same channel estimation as presented in Section 4. Therefore, the complexity of channel estimation is not considered here. The order of complexity, $O(L_{est}M)$ is for the RAKE receiver. The RAKE-MMSE is of the order of $O\left(\left[L_c^3 + L_c^2 M + L_{est}M\right]\right)$. The RAKE-GA has an order of complexity $O\left(\left[GP\left(L_{est}M + logP\right)\right] + L_{est}M^2\right)$. The RAKE-MLD has a complexity of the order of $O\left(\left[M2^M\left(L_{est}M + log2\right)\right]\right)$. L_{est} is the number of paths to be estimated during the channel estimation process, M is the number of symbols per block, N_c is the length of the ternary orthogonal code sequence. G is the number of generations and P is the population size for the RAKE-GA. The computational complexities of the receivers depend on the derivation of the finger weights, the fitness function evaluation and the demodulation of the signal.

Table 1 shows the complexities of the RAKE, RAKE-MMSE, RAKE-GA and RAKE-MLD at $L_{est} = 1024$. The RAKE-MMSE, RAKE-GA and RAKE-MLD were normalized to the RAKE receiver being the least complex receiver but with poor BER performance. The

RAKE-MMSE is five times more complex than the RAKE receiver but has corresponding improved performance. The RAKE-GA is more complex than the other two receivers but obviously with much better BER performance with no error floor as encountered in the other receivers. The RAKE-MLD is the most complex of the four receivers but with the best BER performance. The BER of the RAKE-GA is very close to the RAKE-MLD with a huge reduction in the complexity of the RAKE-GA when compared to the RAKE-MLD.

Receiver	Parameters	Normalized
RAKE Sato & Ohtsuki (2005)	M=100	1
RAKE-MMSE Eslami & Dong (2005)	M=100,Lc=5	5
RAKE-GA	M=10,P=100,G=10	103
RAKE-MLD	M=10	1025

Table 1. Computational Complexity ($L_{est} = 1024$)

6. Simulation results

6.1 Simulation setup

The simulation for the RAKE Sato & Ohtsuki (2005), RAKE-MMSE Eslami & Dong (2005), RAKE-GA and RAKE-MLD receivers were carried out using BPSK modulation at a transmission rate of $R_b = 250$Mbps with symbol duration or frame length of $T_f = 4$ns. Each packet consists of 1000 symbols. A ternary code length of $N_c = 24$ was used for spreading, with a chip width of $T_c = 0.167$ns. The simulated IEEE 802.15.3a UWB multipath channel model with data-aided channel estimation using pilot symbols of $B = 10 \sim 100$ for a single user scenario was employed for the simulation. The channel model 3 (CM3) Foerster (2003) which is a non-line-of-sight (NLOS) environment with a distance of $4 \sim 10$m, mean excess delay of 14.18ns and RMS delay spread of 14.28ns was considered in this work. The number of RAKE fingers used are $L = 5, 10, 15, 20$. The equalizer taps of $L_c = 5$ was used for the RAKE-MMSE.

For the proposed RAKE-GA approach, the population size was $P = 50$ and 100 while the number of generations was $G = 1 \sim 20$. The proportional scaling was employed for the scaling of the fitness values before selection. The crossover of 0.85 was used with an elite count of 0.05. The Gaussian mutation values are $shrink = 1.0$ and $scale = 0.75$. In addition, the unconstrained minimization hybrid function was employed to improve the fitness values of the individuals within the population.

6.2 Performance evaluation

Fig. 2 shows the BER performance of RAKE, RAKE-MMSE, RAKE-GA and RAKE-MLD receivers at $L = 10$ for both known CSI and pilot-aided channel estimation scenarios. The four receivers performed better as expected when the CSI is provided as the channel estimation errors incurred will degrade the performances. The error floors encountered by both the RAKE and RAKE-MMSE receivers were taken care of by the RAKE-GA and RAKE-MLD as explained thus:

- The **RAKE** receiver cannot capture a large signal energy with few number of RAKE fingers and more so a RAKE with MRC weight estimation cannot remove ISI. RAKE receiver also needs very high number of pilot symbols during the channel estimation as the channel estimation error incurred using a few number of pilot symbols resulted in the performance being degraded.

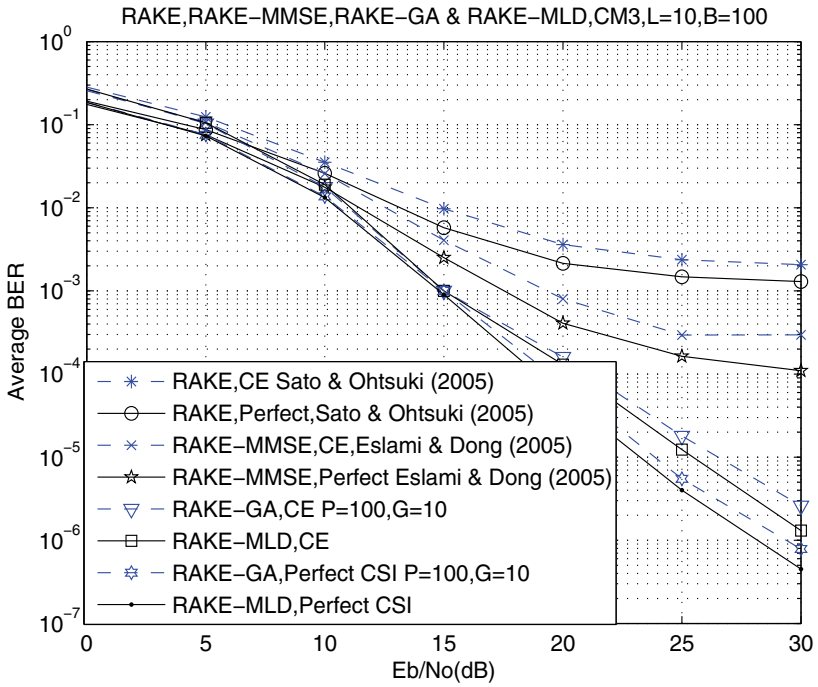

Fig. 2. BER vs. SNR for all receivers

- The **RAKE-MMSE** receiver achieves better BER than RAKE receiver because the equalizer removes the ISI symbol by symbol but the error floor is still encountered since the RAKE receiver output with few RAKE fingers is the input to the equalizer so the RAKE-MMSE cannot capture a large signal energy.
- The **RAKE-GA** receiver on the order hand has no error floor with the same number of RAKE fingers as the other two receivers because it is able to remove the ISI using the distance measure criteria. The soft estimates of the RAKE receiver was a very good initial population choice for the GA and so was the reason for the improvement in performance. The RAKE-GA performs well even with moderate number of pilot symbols.
- The **RAKE-MLD** receiver had the best BER performance as is the optimal receiver which is able to remove the ISI and capture a large signal energy using a few RAKE fingers and not very high pilot symbols since the RAKE receiver output was also the input into the RAKE-MLD receiver.

Fig. 3 shows the BER against SNR for the RAKE-GA receiver at $P = 100$, $G = 10$ at values of $L = 5, 10, 15, 20$. This shows the impact of the number of RAKE fingers on the performance of the scheme. This BER performance improvement is as a result of increase in the number of RAKE fingers. The RAKE-GA at $L = 5$ was of higher BER to the system when $L = 10, 15, 20$ where they were almost of the same BER at all SNR values.
Fig. 4 shows the impact of the number of generations in the BER performance, where $G = 1 \sim 20$ for $P = 100$ and $G = 2 \sim 20$ for $P = 50$ both at $L = 10$ to show the speed of convergence of the algorithm assuming a known CSI. The algorithm at $G = 1 \sim 10$ for $P = 100$ gave better BER generally than at $G = 2 \sim 20$ for $P = 50$. It can thus be concluded that the GA with a

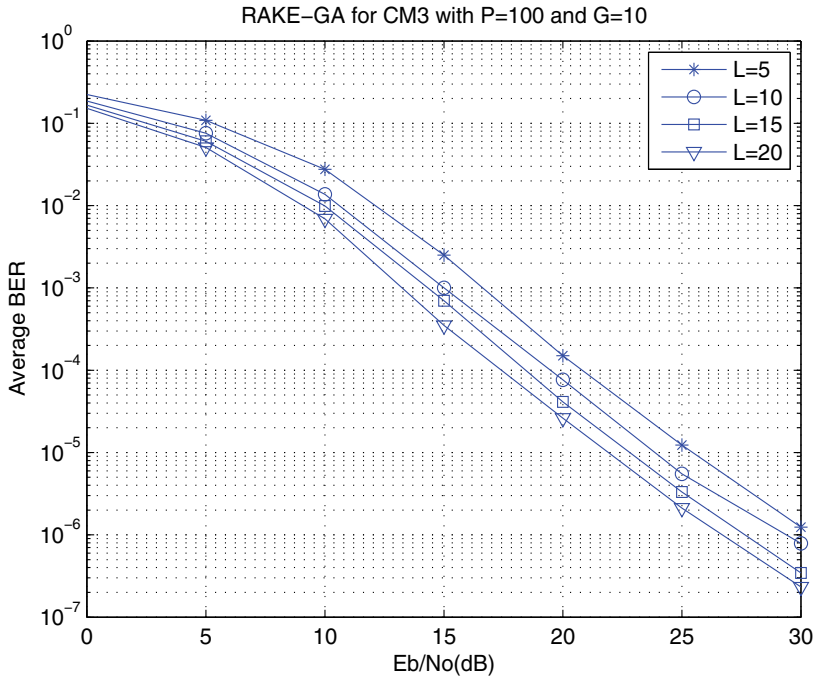

Fig. 3. BER vs. SNR for RAKE-GA

relatively large population size achieves a lower steady state BER than the case with only half the population size at a cost of slightly more generations.
Fig. 5 shows how the BER of the RAKE-GA receiver with channel estimation decreases with increase in the number of pilot symbols giving us the number of training overhead for the pilot-aided channel estimation.

7. Conclusion

We have proposed a GA based channel equalization scheme in DS-UWB wireless communication and compared the results obtained from intensive simulation work with the RAKE, RAKE-MMSE and RAKE-MLD for both known CSI and pilot-aided channel estimation scenarios. Our simulation results show that the proposed RAKE-GA receiver significantly outperforms the RAKE and the RAKE-MMSE receivers. The GA based scheme also gives a very close BER performance to the optimal MLD approach at a much lower computational complexity. Moreover, we have investigated the effect of the number of RAKE fingers, the population size and the pilot overhead on the BER performance. RAKE-GA obtains a good performance with a moderate number of RAKE fingers and a further increase in the number of RAKE fingers has little effect on the performance. GA with a relatively large population size achieves a lower steady state BER than the case with only half the population size at the cost of slightly more generations. And the pilot overhead of 10% is enough for training to obtain comparable performance with the case of perfect CSI.

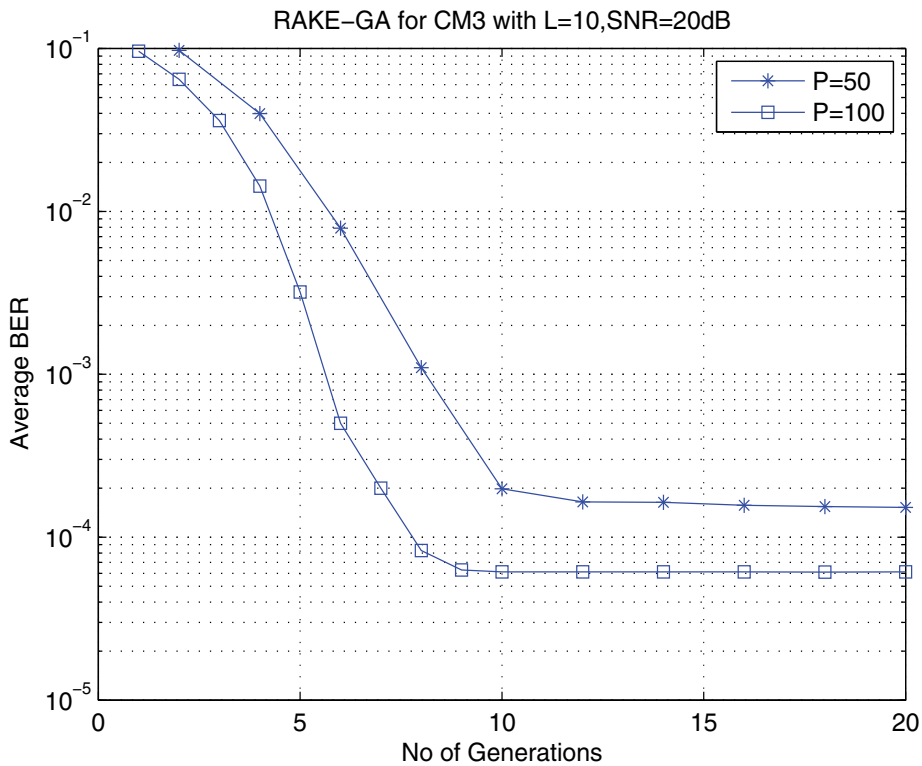

Fig. 4. Convergence speed of RAKE-GA

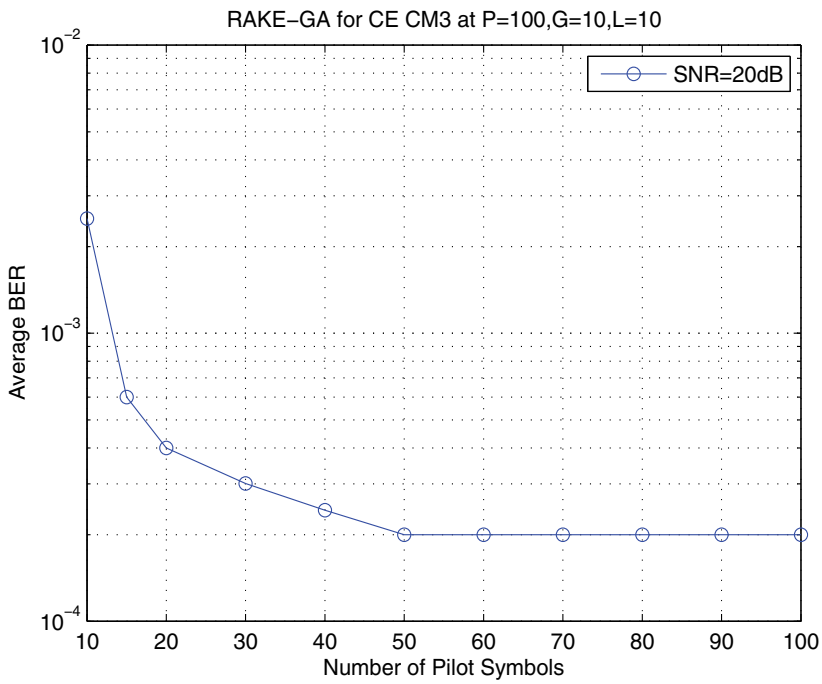

Fig. 5. Impact of Pilot size on RAKE-GA

8. Acknowledgments

This work was supported by the Commonwealth Scholarship Commission, UK, the University of Liverpool, UK and the University of Ilorin, Nigeria

9. References

Al-Sawafi, M. (2004). A micro-genetic algorithm-based CDMA multi-user detector, *Proc. IEEE Conf. Commun. Networks Serv. Res.*, pp. 175–180.

Cai, J., Shen, X., Mark, J. W., Liu, H. & Todd, T. D. (2006). Semiblind channel estimation for pulse-based ultra-wideband wireless communication systems, *IEEE Trans. Veh. Technol.* 55(1): 95–103.

Erguin, K. & Hacioglu, K. (2000). Multiuser detection using a genetic algorithm in CDMA communications systems, *IEEE Trans. Commun.* 48(8): 1374–1383.

Chu, X., Murch, R. D., Liu, J. & Ghavami, M. (2008). Pilot-channel-assisted log-likelihood-ratio selective rake combining for low-rate ultra-wideband communications, *IEEE Trans. Commun.* 56(8): 1313–1323.

Goldberg, E. D. (1989). *Genetic Algorithms in Search, Optimization and Meachine Learning*, Addison Wesley Longman Inc.

Eslami, M. & Dong, X. (2005). Rake-mmse-equalizer performance for UWB, *IEEE Commun. Letters* 9(6): 502–504.

Foerster, J. (2003). Channel modelling sub-committee report final, *Technical report*, IEEE P802.15-02/490r1-SG3a.

Gezici, S., Chiang, M., Poor, H. V. & Kobayashi, H. (2005). A genetic algorithm based finger selection scheme for UWB MMSE rake receivers, *Proc. IEEE Int. Conf. Ultra-Wideband*, pp. 164–169.

Kaligineedi, P. & Bhargava, V. K. (2006). Frequency-domain equalization techniques for DS-UWB systems, *Proc. IEEE Global Telecom. Conf.*, pp. 1–6.

Li, Y., Molisch, A. F. & Zhang, J. (2003). Channel estimation and signal detection for UWB, *Proc. WPMC*, pp. 1–5.

Liu, R. & Elmirghani, J. (2007). Performance of impulse radio direct sequence ultra-wideband system with variable-length spreading sequences, *IET Commun.* 1(4): 597–603.

Lottici, V., D'Andrea, A. & Mengali, U. (2002). Channel estimation for ultra-wideband communications, *IEEE J. Sel. Areas Commun.* 20(9): 1638–1645.

Man, K. F., Tang, K. S. & Kwong, S. (1999). *Genetic algorithms: concepts and designs*, Spriger-Verlag London Ltd.

MATLAB (2007). Genetic algorithm and direct search toolbox 2 user's guide, *Technical report*, The Mathworks,Inc.

Mielczarek, B., Wessman, M.-O. & Svensson, A. (2003). Performance of coherent UWB rake receivers with channel estimators, *Proc. IEEE Veh. Technol. Conf.*, pp. 1880–1884.

Molisch, A. F., & Foerster, J. R. (2003). Channel models for ultrawideband personal area networks, *IEEE Wireless Communi*, 10(6): 14–21.

Parihar, A., Lampe, L., Schober, R. & Leung, C. (2005). Analysis of equalization for DS-UWB systems, *IEEE ICU*, pp. 170–175.

Parihar, A., Lampe, L., Schober, R. & Leung, C. (2007). Equalization for DS-UWB systems - Part II: 4BOK modulation, *IEEE Trans. Commun.* 55(8): 1525–1535.

Roy, S., Foerster, J. R., Somayazulu, S. V. & Leeper, D. G. (2004). Ultra wideband radio design: The promise of high-speed, short-range wireless connectivity, *IEEE Proceedings* 92(2): 295–311.

Sato, H. & Ohtsuki, T. (2005). Computational complexity and performance of RAKE receivers with channel estimation for DS-UWB, *IEICE Trans. Fund. Electron. Commun. Comput Sci* 88(9): 2318–2326.

Siriwongpairat, W. & Liu, K. (2008). *Ultra-Wideband Communications Systems MULTIBAND OFDM APPROACH*, John Wiley & sons,Inc.

Sun, W. & Li, H. (2007). Blind channel estimation and detection for space–time coded CDMA in ISI channels, *Elsevier Digital Signal Processing* 17(1): 280–296.

Takanashi, M., Ogawa, Y., Nishimura, T. & Ohgane, T. (2008). Studies on an iterative frequency domain channel estimation technique for MIMO-UWB communications, *IEICE Trans. Communn.* E91-B(4): 1084–1094.

Tang, K. S., Man, K. F., Kwong, S. & He, Q. (1996). Genetic algorithms and their applications, *IEEE Sig. Processing Mag.* 13(6): 22–37.

Wang, F., Xu, C., Ji, X. & Zhang, Y. (2008). Simplified maximum likelihood channel estimation algorithm for impulse radio UWB, *IEEE Wireless Commun.*

Wang, M., Yang, S. & Wu, S. (2008). A GA-based UWB pulse waveform design method, *Digital Signal Process Rev J* 18(1): 65–74.

Wang, T., Wang, Y. & Chen, K. (2004). Genetic algorithm optimization for ultra wideband impulse radio to mitigate multi-band jam interference, *Proc. World Congr. Intelligent Control Autom. WCICA*, pp. 1429–1433.

Yen, K. & Hanzo L. (2001). Genetic algorithm assisted joint multiuser symbol detection and fading channel estimation for synchronous CDMA systems, *IEEE J. Sel. Areas Commun.* 19(6): 985–998.

5

Low Complexity Phase-Unaware Detectors Based on Estimator-Correlator Concept

Antti Anttonen[1], Aarne Mämmelä[1] and Subbarayan Pasupathy[2]
[1]*VTT Technical Research Centre of Finland*
[2]*University of Toronto*
[1]*Finland*
[2]*Canada*

1. Introduction

Our goal is to present an overview of a class of low complexity detectors working in linear fading multipath channels. In addition, we present briefly a unified theory based on the optimal maximum a posteriori probability (MAP) receiver concept (Woodward & Davies, 1952), which in additive Gaussian noise leads to the estimator-correlator receiver (Price, 1956; Middleton, 1957; Kailath, 1960; Kailath, 1969). The terms receiver and detector are interchangeable. Detectors are estimators where the parameter or symbol set to be estimated is discrete (Kay, 1993; Kay, 1998).

We consider phase-unaware detectors (PUDs) such as differentially coherent detector (DD), noncoherent detector (ND), and energy detector (ED). The term PUD is used to emphasize that the receiver does not have any knowledge of the absolute phase of the received signal although it may have some knowledge of the internal phase structure. We use the term noncoherent to represent a special case of PUD system, and this will be clarified later. PUD detectors are more robust than coherent detectors in a fading multipath channel since the carrier phase of a signal with a wide bandwidth or high carrier frequency may be difficult to estimate with a low complexity. Earlier extensive reviews include (Schwarz et al., 1966; Van Trees, 1971) and more recently (Garth & Poor, 1994; McDonough & Whalen, 1995; Proakis, 2001; Mämmelä et al., 2002; Simon & Alouini, 2005; Witrisal et al., 2009). A summary of the estimator-correlator receiver is presented in (Kay, 1998).

Unless stated otherwise, we exclude equalizers which increase the complexity of the receiver significantly (Lodge & Moher, 1990; Colavolpe & Raheli, 1999). Thus we avoid intersymbol interference (ISI) by signal design and concentrate on the reception of a single symbol, which may include several bits in M-ary communications. It is, however, conceptually straightforward to generalize the single symbol or "one-shot"detectors to symbol sequence detection by replacing the symbols by symbol sequences. The noise is assumed to be additive white Gaussian noise (AWGN). The frequency offset caused by the channel is assumed to be known and compensated. We also assume that the receiver is synchronous in the sense that the start of each symbol interval is known. Estimation of frequency and timing is a highly nonlinear problem, which is studied in (Mengali & D'Andrea, 1997; Meyr et al., 1998), see also (Turin, 1980). Also because of complexity reasons in general we exclude coherent detectors which are such that they assume that the alternative received

symbol waveforms are known including the absolute phase. Obviously, there are also other interesting physical and higher layer aspects we are not able to include due to space limitation.

In our review we emphasize that PUD systems can be derived from the optimal estimator-correlator receiver with suitable simplifying assumptions. In addition, our purpose is to emphasize recent ultra-wideband (UWB) M-ary communications and multiple-input multiple-output (MIMO) diversity systems which enable increase of date rates. One interesting modulation method to consider is the pulse-amplitude modulation (PAM), which has been recently selected for short-range wireless standards such as ECMA-387 and IEEE802.15.3c in which the carrier phase recovery can be a major problem. We also present a historical review of PUDs and summarize the problems in the performance analysis of such systems.

2. Conceptual analysis

General theoretical background is given for example in (Papoulis, 2002; Ziemer & Tranter, 2002; Kay, 1993; Kay, 1998; Proakis, 2001). To make our presentation as compact as possible, we use the complex envelope concept to define the signals as explained in (Franks, 1969). Furthermore, we use some matrix equations, which are explained in (Marple, 1987).

2.1 Coherency

Signal *coherency* is an important concept that leads to several ortogonality concepts, each of which refers to a certain idealized detector structure. The channel is assumed to be a wide-sense stationary uncorrelated scattering (WSSUS) channel with a time-variant impulse response $c(\tau,t)$ and time-variant transfer function $C(f,t) = \alpha(f,t)e^{j\theta(f,t)} = \int_{-\infty}^{\infty} c(\tau,t)e^{-j2\pi f\tau}d\tau$ (Bello, 1963; Proakis, 2001). If the transmitted signal is $s(t)$, the received signal without noise is $h(t) = \int_{-\infty}^{\infty} c(\tau,t)s(t-\tau)d\tau$.

If we transmit an unmodulated carrier or complex exponential $s(t) = e^{j2\pi f_1 t}$ with a unit amplitude and frequency f_1 through the channel, we receive a fading carrier $v(t) = C(f_1,t)e^{j2\pi f_1 t}$ whose amplitude $\alpha(f_1,t)$ and phase $\theta(f_1,t)$ are time-variant. We compare the received signal at two time instants t_1 and t_2 where $\Delta t = t_1 - t_2$. In general, the magnitude of the correlation $E\{h(t_1)h^*(t_2)\}$ between $h(t_1)$ and $h(t_1)$ is reduced when $|\Delta t|$ is increased. In a WSSUS channel, the normalized correlation $|E[h(t_1)h^*(t_2)]|/E[h(t_1)h^*(t_1)] = |E[C(f_1,t_1)C^*(f_1,t_2)]|/E[C(f_1,t_1)C^*(f_1,t_1)]$ does not depend on f_1 or t_1, only on Δt. The minimum positive interval Δt where the normalized correlation is $|E[C(t_1)C^*(t_2)]|/E[C(t_1)C^*(t_1)] = \varepsilon$, where ε is a real constant ($0 \le \varepsilon < 1$), is defined to be the *coherence time* $(\Delta t)_c$. If $|\Delta t| \ll (\Delta t)_c$, the complex samples are correlated in such a way that in general $h(t_1) \approx h(t_2)$. We say that the two samples at t_1 and t_2 are *coherent* with each other, and the fading channel is coherent over the time interval $|\Delta t| \ll (\Delta t)_c$.

If the transmitted signal is modulated and the symbol interval T is so small that $T \ll (\Delta t)_c$, the channel is *slowly fading* and the channel is essentially constant within the symbol interval, otherwise the channel is fast fading. In practice symbol waveforms are often band-limited, for example Nyquist pulses (Proakis, 2001), and their duration may be several symbol intervals. In a slowly fading channel the channel is assumed to be approximately constant during the whole length of the symbol waveform.

In a similar way, if we transmit either $s_1(t) = e^{j2\pi f_1 t}$ or $s_2(t) = e^{j2\pi f_2 t}$, the normalized correlation at time t_1 is $|E[h_1(t_1)h_2^*(t_1)]|/E[h_1(t_1)h_1^*(t_1)] = |E[C(f_1,t_1)C^*(f_2,t_1)]|/$

$E[C(f_1,t_1)C^*(f_1,t_1)]$ which does not depend in a WSSUS channel on t_1 or f_1, only on $\Delta f = f_1 - f_2$. The minimum positive frequency interval Δf where the normalized correlation is $|E[C(f_1,t_1)C^*(f_2,t_1)]|/E[C(f_1,t_1)C^*(f_1,t_1)] = \varepsilon$, where ε is a real constant $(0 \le \varepsilon < 1)$, is defined to be the coherence bandwidth $(\Delta f)_c$. If $|\Delta f| \ll (\Delta f)_c$, the complex samples are correlated in such a way that in general $h_1(t_1) \approx h_2(t_1)$. If this happens over the frequency band B of the modulated signal so that $B \ll (\Delta f)_c$, the channel is frequency-nonselective or flat fading, otherwise it is frequency-selective.

2.2 Classification of detectors

As discussed in (Kay, 1993, p. 12), we must separate optimal detectors, their approximations, and suboptimal detectors. In optimal detectors some parameters related to the channel are assumed to be known. In practice they must be estimated, which leads to an approximation of the optimal detector. A suboptimal detector is not an approximation of any of the known optimal detectors. An example is the discriminator detector when used in a frequency-shift keying (FSK) receiver (Shaft, 1963).

The transmitted complex M-ary symbol is denoted by a and the corresponding symbol waveform as $s(t,a)$. We assume that the receiver knows the symbol set from which a is taken and the waveform $s(t,a)$ for all a. The received signal is then $r(t) = h(t,a) + n(t)$ where $h(t,a) = \int_{-\infty}^{\infty} c(\tau,t)s(t-\tau,a)d\tau$ is the received symbol waveform and $n(t)$ is AWGN.

A *coherent detector* is such a detector where $h(t,a)$ is assumed to be known for each a, and the problem is to estimate a when $r(t)$ is known. Knowledge of $h(t,a)$ implies that we know $c(\tau,t)$. A *partially coherent* or *pseudocoherent detector* is an approximation which estimates $c(\tau,t)$, and there is some error in the estimate. All practical detectors that are called coherent are only partially coherent since $c(\tau,t)$ must be estimated since it is unknown a priori.

A *differentially coherent detector* or *differential detector* is a partially coherent detector, which is based on the assumption of a known pilot symbol in the beginning of the transmission and differential coding in modulation, which observes the received signal over two symbol intervals, and which uses the earlier symbol as a phase reference. The idea can be generalized to several symbol intervals (Leib & Pasupathy, 1988; Divsalar & Simon, 1990). We classify DDs among PUDs since no absolute phase reference is needed. In fact, the equivalence of binary differential phase shift keying (DPSK) detection and noncoherent detection was shown in (Schwartz et al., 1966, pp. 307-308, 522-523) when the observation interval is two symbol intervals. In this case the phase of the channel must remain constant over two symbol intervals.

A *noncoherent detector* is such a detector where the received symbol waveform is assumed to have the form $h(t,a) = v(t,a)\,e^{j\theta}$ where the waveform $v(t,a)$ is assumed to be known and the absolute phase θ is an unknown constant over the reception of the symbol waveform. Thus the received symbol waveforms are known except for the phase term. If the phase θ would change during the reception of the waveform $v(t,a)$, it would be distorted, and the noncoherent detector could not be implemented. The term noncoherent is usually used in this meaning in wireless communications. The term incoherent is usually used in optical communications. Some authors do not want to use the terms noncoherent or incoherent at all because the detector uses the internal phase structure of the signal although an absolute phase reference is missing (Van Trees, 1968, p. 326). The terms are still widely used. Noncoherent detectors have been considered for continuous phase wideband and narrowband signals in (Hirt & Pasupathy, 1981; Pandey et al., 1992).

A *generalized noncoherent detector* is a detector where the received symbol waveform has the form $h(t,a) = \alpha e^{j\theta} v(t,a)$ where $v(t,a)$ is assumed to be known and $\alpha e^{j\theta}$ is an unknown complex gain, which is constant over the duration of the symbol interval. The term "generalized" is used to emphasize that the amplitude gain α is unknown but in a noncoherent detector it is known and for simplicity set to unity.

2.3 Orthogonality of modulated signals

Orthogonality is an important concept since we must avoid as much as possible any crosstalk between signals. In a diversity system crosstalk or interference may appear between diversity channels. An example is multipath diversity where crosstalk is equivalent to interpath interference (Turin, 1980). ISI is another form of crosstalk (Van Etten, 1976). Crosstalk is different from correlation, which is measured by the covariance matrix. There may be correlation although crosstalk is avoided and vice versa. There are different orthogonality concepts for different detectors, including coherent, noncoherent, and energy detectors.

2.3.1 Coherently orthogonal signals

We define the inner product of two deterministic signals $h_1(t)$ and $h_2(t)$ as $< h_1, h_2 > = \int_{-\infty}^{\infty} h_1(t) h_2^*(t) dt$. The signals are *orthogonal* or *coherently orthogonal* (Pasupathy, 1979; Madhow, 2008) if $\mathrm{Re}(< h_1, h_2 >) = 0$. This form of orthogonality is used in coherent detection. As an example we give two complex exponential pulses $h_1(t) = A_1 \exp(j2\pi f_1 t), 0 \le t < T$ and $h_2(t) = A_2 \exp[j2\pi(f_1 + \Delta f)t + \varphi], 0 \le t < T$ with an arbitrary amplitude A_1 or A_2, frequency offset Δf and phase offset φ. The pulses are coherently orthogonal if either 1) $A_1 = 0$ or $A_2 = 0$ or 2) $\Delta f = n/T$ or 3) $\varphi = \pi \Delta f T + (n + 1/2)\pi$ where n is an integer, $n \neq 0$. Signals with $A_1 = 0$ or $A_2 = 0$ are used in on-off keying (OOK) systems. When $\Delta f = n/T, n \neq 0$, the pulses are always orthogonal irrespective of the value of φ. However, for an arbitrary Δf we can always find a phase offset φ for which the pulses are orthogonal. If we set $\varphi = 0$, the pulses are orthogonal if $\Delta f = n/2T$ where $n \neq 0$ is an integer. Such signals are used in coherent FSK systems. If we alternatively set $\Delta f = 0$, the pulses are orthogonal if $\varphi = \frac{\pi}{2} + n\pi, n \neq 0$. Such signals are used in quadrature phase-shift keying (QPSK) systems. The examples were about orthogonality in the frequency domain. Time-frequency duality can be used to find similar orthogonal signals in the time domain, for example by using sinc pulses (Ziemer & Tranter, 2002). Furthermore, some codes are also orthogonal, for example Hadamard codes (Proakis, 2001).

2.3.2 Noncoherently orthogonal signals

The signals $h_1(t)$ and $h_2(t)$ are *noncoherently orthogonal* or *envelope-orthogonal* (Pasupathy, 1979; Madhow, 2008; Turin, 1960) if $< h_1, h_2 > = 0$. This form of orthogonality is used in noncoherent detection. In the previous example, the two complex exponential pulses are noncoherently orthogonal if 1) $A_1 = 0$ or $A_2 = 0$ or 2) $\Delta f = n/T, n \neq 0$. Such signals are used in noncoherent ASK and FSK systems, respectively. In these cases there is no requirement for the phase φ, i.e., it can be arbitrary, but it must be constant during the interval $0 \le t < T$. Noncoherently orthogonal signals are also coherently orthogonal signals.

2.3.3 Disjointly orthogonal signals

Coherently and noncoherently orthogonal signals can be overlapping in time or frequency. To define *disjointly orthogonal* signals $h_1(t)$ and $h_2(t)$, we must first select a window function

$w(t)$ and define the short-time Fourier transform (Yilmaz & Rickard, 2004) $S_k(\tau, f) = \int_{-\infty}^{\infty} w(t-\tau)h_k(t)\, e^{-j2\pi ft}dt, k = 1,2$ which can be interpreted as the convolution of a frequency-shifted version of the signal $h_k(t)$ with a frequency shift $-f$ and the time-reversed window function $w(-t)$. The signals are w-disjoint orthogonal if $S_1(\tau, f)S_2(\tau, f) = 0, \forall \tau, f$. If $w(t) = 1$, the short-time Fourier transform reduces to the ordinary Fourier transform and the w-disjoint orthogonal signals are *frequency disjoint*, which can be implemented in an FSK system. If $w(t) = \delta(t)$, the w-disjoint orthogonal signals are *time disjoint*, which can be implemented in a pulse-position modulation (PPM) system. If two signals are frequency disjoint, they do not need to be time disjoint and vice versa. Time and frequency disjoint signals are called disjointly orthogonal. Our main interest is in the time and frequency disjoint signals. A special case of both of them is OOK. Disjointly orthogonal signals are used in energy detection. Disjointly orthogonal signals are also coherently and noncoherently orthogonal signals.

2.4 Optimal MAP receiver

When defining an optimal receiver, we must carefully define both the assumptions and the optimization criterion. We use the MAP receiver, which minimizes the symbol error probability. A maximum likelihood (ML) receiver is a MAP receiver based on the assumption that the transmitted symbols have identical a priori probabilities. The easiest way to derive the optimal receiver is to use the time-discrete model of the received signal. The received signal $r(t) = h(t, a) + n(t)$ is filtered by an ideal low-pass filter, whose two-sided bandwidth B is wide enough so that it does not distort $h(t, a)$. The output of the filter is sampled at a rate $f_s = B$ that is defined by the sampling theorem. In this case the noise samples are uncorrelated and the time-dicrete noise is white. The sampling interval is normalized to unity.

2.4.1 Optimal MAP receiver

The covariance matrix of a column vector $\mathbf{x}$ is defined as $\mathbf{R}_{xx} = E\{[\mathbf{x} - E(\mathbf{x})][\mathbf{x} - E(\mathbf{x})]^{\mathrm{H}}\}$ where $E(\mathbf{x})$ refers to the statistical mean or expectation of $\mathbf{x}$ and the superscript H refers to conjugate transposition. The received signal $\mathbf{r}(a)$ depends on the transmitted symbol a and may be presented as the $N \times 1$ vector (Kailath, 1961) $\mathbf{r}(a) = \mathbf{h}(a) + \mathbf{n}$. The vectors $\mathbf{h}(a)$ and $\mathbf{n}$ are assumed to be mutually uncorrelated. The received signal $\mathbf{r}$ has the $N \times N$ covariance matrix $\mathbf{R}_{rr}(a) = \mathbf{R}_{hh}(a) + \mathbf{R}_{nn}$ where $\mathbf{R}_{hh}(a)$ is the covariance matrix of $\mathbf{h}(a)$ and $\mathbf{R}_{nn} = N_0\mathbf{I}$ is the covariance matrix of $\mathbf{n}$, $N_0 > 0$ is the noise variance, and $\mathbf{I}$ is a unit matrix.

In the MAP detector, the decision $\mathbf{s}(\hat{a})$ is based on the rule (Proakis, 2001)

$$\mathbf{s}(\hat{a}) = \arg_{\mathbf{s}(\tilde{a})} \max P(\tilde{a}\,|\mathbf{r}) \tag{1}$$

where

$$P(\tilde{a}|\mathbf{r}) = \frac{p(\mathbf{r}|\tilde{a})P(\tilde{a})}{p(\mathbf{r})} \tag{2}$$

is the a posteriori probability that $\mathbf{s}(\tilde{a})$ was transmitted given $\mathbf{r}$, $p(\mathbf{r}|\tilde{a})$ is the a priori probability density function of $\mathbf{r}$ given $\mathbf{s}(\tilde{a})$ was transmitted, $P(\tilde{a})$ denotes the a priori probability for the symbol $\tilde{a}$, and $p(\mathbf{r})$ denotes the probability density function of $\mathbf{r}$ averaged over all a. The symbol $\tilde{a}$ refers to the symbol under test and $\hat{a}$ to the final decision. We

assume that the a priori probabilities $P(\tilde{a})$ are equal, and $p(\mathbf{r})$ does not have any effect on the maximization in (2). An equivalent decision variable is the a priori probability density function or the likelihood function $p(\mathbf{r}|\tilde{a})$. To proceed, we need some knowledge of the statistics of $\mathbf{r}$ to compute $p(\mathbf{r}|\tilde{a})$. By far the simplest case is to assume that for each $\tilde{a}$, $\mathbf{r}$ is Gaussian. The decision variables to be defined can be used also in diversity systems by using simple addition when there is no crosstalk or correlation between the diversity channels, see for example (Turin, 1980).

Coherent receiver: In the coherent receiver, $\mathbf{h}(a)$ is assumed to be known for each a. Since $\mathbf{n}$ is Gaussian, also $\mathbf{r}$ is Gaussian, and (Barrett, 1987; Papoulis, 1991)

$$p(\mathbf{r}|\tilde{a}) = \frac{1}{\pi^N \det[\mathbf{R}_{rr}(\tilde{a})]} \exp\{-[\mathbf{r} - E(\mathbf{r})]^{\mathrm{H}}[\mathbf{R}_{rr}(\tilde{a})]^{-1}[\mathbf{r} - E(\mathbf{r})]\} \tag{3}$$

viewed as a function of $\tilde{a}$. The right-hand side of (3) represents the probability density function of a random vector whose elements are complex Gaussian random variables. Since the noise is assumed to be white with $N_0 > 0$, the matrix $\mathbf{R}_{rr}(\tilde{a})$ is always positive definite (Marple, 1987) and nonsingular. In the coherent receiver the $\mathbf{R}_{rr}(\tilde{a}) = \mathbf{R}_{nn} = N_0\mathbf{I}$. We take the natural logarithm and the MAP criterion leads to the decision variable

$$y(\tilde{a}) = \frac{1}{N_0}\mathrm{Re}[\mathbf{r}^{\mathrm{H}}\mathbf{h}(\tilde{a})] + B(\tilde{a}), B(\tilde{a}) = -\frac{1}{2N_0}\mathbf{h}^{\mathrm{H}}(\tilde{a})\mathbf{h}(\tilde{a}) \tag{4}$$

where $B(\tilde{a})$ is the bias term, which depends on the energy of $\mathbf{h}(\tilde{a})$. The term $\mathrm{Re}[\mathbf{r}^{\mathrm{H}}\mathbf{h}(\tilde{a})]$ corresponds to the correlator which can be implemented also by using a matched filter, which knows the absolute phase of the received signal. In a diversity system the receiver can be generalized to *maximal ratio combining*.

2.4.2 Noncoherent receiver

In a noncoherent receiver $\mathbf{h}(a)$ has the form $\mathbf{h}(a) = \mathbf{v}(a)e^{j\theta}$ where θ is a random variable uniformly distributed in the interval $[0, 2\pi)$ and is $\mathbf{v}(a)$ assumed to be known for each a. Now for a given θ the received signal is Gaussian and

$$p(\mathbf{r}|\tilde{a}, \theta) = \frac{1}{\pi^N \det[\mathbf{R}_{rr}(\tilde{a}, \theta)]} \exp\{-[\mathbf{r} - E(\mathbf{r})]^{\mathrm{H}}[\mathbf{R}_{rr}(\tilde{a}, \theta)]^{-1}[\mathbf{r} - E(\mathbf{r})]\}. \tag{5}$$

The MAP criterion is obtained from $p(\mathbf{r}|\tilde{a}, \theta)$ by removing θ by averaging (Meyr et al., 1998), i.e., $p(\mathbf{r}|\tilde{a}) = \int_0^{2\pi} p(\mathbf{r}|\tilde{a}, \theta)\, p(\theta) d\theta$. The conditional probability density function $p(\mathbf{r}|\tilde{a})$ is not Gaussian although $p(\mathbf{r}|\tilde{a}, \theta)$ is Gaussian and therefore the receiver includes a nonlinearity. When $p(\mathbf{r}|\tilde{a})$ is maximized, the decision variable is

$$y(\tilde{a}) = \ln I_0\left(\frac{1}{N_0}\left|\mathbf{r}\mathbf{v}^{\mathrm{H}}(\tilde{a})\right|\right) + B(\tilde{a}), B(\tilde{a}) = -\frac{1}{2N_0}\mathbf{v}^{\mathrm{H}}(\tilde{a})\mathbf{v}(\tilde{a}) \tag{6}$$

where $I_0(\cdot)$ is the zeroth order modified Bessel function and $B(\tilde{a})$ is the bias term that depends on the energy of $\mathbf{v}(\tilde{a})$. The term $\left|\mathbf{r}\mathbf{v}^{\mathrm{H}}(\tilde{a})\right|$ corresponds to noncoherent correlation and can be implemented with a noncoherent matched filter, which includes a matched filter and a linear envelope detector. The envelope detector is needed because the absolute phase of the received signal is unknown.

For large arguments, an approximation is (Turin, 1980)

$$y(\tilde{a}) \approx \frac{1}{N_0}\left|\mathbf{r}\mathbf{v}^{\mathrm{H}}(\tilde{a})\right| + B(\tilde{a}). \tag{7}$$

In a diversity system the decision variable (6) leads to a nonlinear combining rule and the approximation (7) to a linear combining rule. It can be shown that the performance of the linear envelope detector is almost identical to that of quadratic or square-law envelope detector, but performance analysis is easier for square-law envelope detector although in practical systems the dynamic range requirements are larger (Proakis, 2001, p. 710; Skolnik, 2001, p. 40; McDonough & Whalen, 1995). If the energies of $\mathbf{v}(\tilde{a})$ for all $\tilde{a}$ are identical, no bias terms are needed and the decision variable (6) is simplified to the form $y'(\tilde{a}) = \left|\mathbf{r}\mathbf{v}^{\mathrm{H}}(\tilde{a})\right|$ or, alternatively, to the form $y''(\tilde{a}) = \left|\mathbf{r}\mathbf{v}^{\mathrm{H}}(\tilde{a})\right|^2$. In a diversity system the receiver can be generalized to *square-law combining*. The use of these simplifications is an approximation only since the signals coming from different diversity channels do not in general have identical energies, and ideally the nonlinearity in (6) is needed (Turin, 1980).

2.4.3 Estimator-correlator receiver

Now the signal part $\mathbf{h}(a)$ for a given a is random and complex Gaussian and it has zero mean, i.e., $E[\mathbf{h}(a)] = \mathbf{0}$ where $\mathbf{0}$ is a zero vector. This implies that the channel is a Rayleigh fading multipath channel. As in the noncoherent receiver, the effect of the channel can be removed by averaging (Kailath, 1963). The MAP criterion (2) corresponds to the decision variable (Kailath, 1960)

$$y(\tilde{a}) = -\mathbf{r}^{\mathrm{H}}[\mathbf{R}_{rr}(\tilde{a})]^{-1}\mathbf{r} + B(\tilde{a}), B(\tilde{a}) = -\ln\{\det[\mathbf{R}_{rr}(\tilde{a})]\}. \tag{8}$$

The bias term $B(\tilde{a})$ can be ignored if the determinant of $\mathbf{R}_{rr}(\tilde{a})$ does not depend on $\tilde{a}$. The conditions where the bias terms are identical are considered in (Mämmelä & Taylor, 1998).
The inverse of the covariance matrix can be expressed in the form $[\mathbf{R}_{rr}(\tilde{a})]^{-1} = \mathbf{R}_{nn}^{-1} - \mathbf{R}_{nn}^{-1}\mathbf{G}(\tilde{a})$ where the matrix

$$\mathbf{G}(\tilde{a}) = \mathbf{R}_{hh}(\tilde{a})[\mathbf{R}_{rr}(\tilde{a})]^{-1} = \mathbf{I} - \mathbf{R}_{nn}[\mathbf{R}_{rr}(\tilde{a})]^{-1} \tag{9}$$

is a linear minimum-mean square error (MMSE) estimator of the received signal. The optimal estimator is an MMSE estimator although the whole receiver is a MAP detector (Kailath, 1969). Since the noise covariance matrix in (9) does not depend on the transmitted signal, and the noise is white, the decision variable

$$y'(\tilde{a}) = \frac{1}{N_0}\mathbf{r}^{\mathrm{H}}\mathbf{G}(\tilde{a})\mathbf{r} + B(\tilde{a}) \tag{10}$$

can be maximized where $\mathbf{G}(\tilde{a})$ is a Hermitian matrix since it is a difference of two Hermitian matrices. Thus the decision variables (10) are real. Since the expression $\mathbf{r}^{\mathrm{H}}\mathbf{G}(\tilde{a})\mathbf{r}$ has a Hermitian quadratic form, it is nonnegative and almost always positive.
In (10) the receiver estimates the received signal, and the estimate is $\mathbf{s}(\tilde{a}) = \mathbf{G}(\tilde{a})\mathbf{r}$. However, the estimate is the actual signal estimate only in the receiver branch where $\tilde{a} = a$ (Kailath, 1961). The receiver based on the decision variables (10) is called the *estimator-correlator receiver* (Kailath, 1960) and the *quadratic receiver* (Schwartz et al., 1966; Barrett, 1987), see Fig. 1. It does not use any knowledge of the absolute phase of the received signal. Thus for phase-modulated signals there is a phase ambiguity problem, which can be solved by using known pilot signals. The structure is similar to that of the DPSK detector when two consecutive symbols are observed and only the earlier symbol is used in the estimator. The detector (6) can be also interpreted as an estimator-correlator receiver, but the estimator is nonlinear because $p(\mathbf{r}|\tilde{a})$ is not a Gaussian probability density function (Kailath, 1969). In

fact, any MAP receiver used in a fading channel with AWGN has an estimator-correlator interpretation having an MMSE estimator, possibly nonlinear.

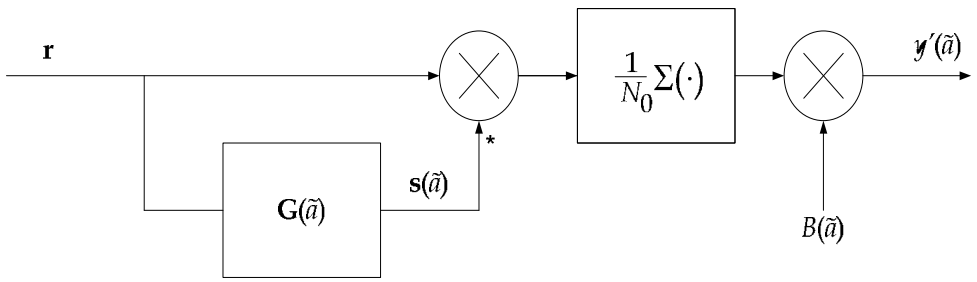

Fig. 1. Estimator-correlator. Asterisk (*) refers to complex conjugation. For each $\tilde{a}$ there is a similar receiver branch and the maximum of the outputs corresponds to the MAP decision.

We now assume that $\mathbf{h}(\tilde{a})$ can be expressed in the form $\mathbf{h}(\tilde{a}) = \mathbf{S}(\tilde{a})\mathbf{c}$ where $\mathbf{S}(\tilde{a})$ is a suitably defined signal matrix (Kailath, 1961) and $\mathbf{c}$ is the channel vector. As shown in (Kailath, 1961), the decision variable can be alternatively expressed in the form

$$y'(\tilde{a}) = \frac{1}{N_0}\mathbf{r}^{\mathrm{H}}\mathbf{S}(\tilde{a})\mathbf{F}(\tilde{a})\mathbf{S}^{\mathrm{H}}(\tilde{a})\mathbf{r} + B(\tilde{a}) \tag{11}$$

where

$$\mathbf{F}(\tilde{a}) = \frac{1}{N_0}(\mathbf{R}_{cc}^{-1} + \frac{1}{N_0}\mathbf{S}^{\mathrm{H}}(\tilde{a})\mathbf{S}(\tilde{a}))^{-1} \tag{12}$$

and the inverses can be shown to exist. We now assume that the channel is flat fading and the variance of the fading gain is $\sigma_c^2 = E(|c(n)|^2)$. The matrix $\mathbf{F}(\tilde{a})$ reduces to the scalar

$$F(\tilde{a}) = \frac{\sigma_h^2}{E(\tilde{a})\sigma_h^2 + N_0} \tag{13}$$

and the signal matrix $\mathbf{S}(\tilde{a})$ reduces to a vector $\mathbf{s}(\tilde{a})$ whose energy is denoted by $E(\tilde{a})$. The decision variable has now the form

$$y'(\tilde{a}) = \frac{F(\tilde{a})}{N_0}\left|\mathbf{s}^{\mathrm{H}}(\tilde{a})\mathbf{r}\right|^2 + B(\tilde{a}). \tag{14}$$

This receiver represents the generalized noncoherent receiver where the amplitude of the received signal is an unknown random variable. The detector includes a square-law envelope detector. In a diversity system the receiver corresponds to *generalized square-law combining*. Compared to the ordinary noncoherent detectors the generalized noncoherent receiver (14) must know the second order statistics of the channel and noise. The instantaneous amplitude is assumed to be unknown.

The effect of weighting with $\mathbf{F}(\tilde{a})$ is discussed in channel estimators in (Li et al., 1998). An important special case is equal gain combining (EGC), which has some loss in performance but the robustness is increased and the complexity is reduced partially because the noise variance and the mean-square strengths of the diversity branches are not needed to estimate. It is important not to include weak paths in EGC combining.

As a positive definite matrix, $\mathbf{G}(\tilde{a})$ can be factored in the form $\mathbf{G}^{(q)} = [\mathbf{G}_{\mathrm{l}}(\tilde{a})]^{\mathrm{H}}\mathbf{G}_{\mathrm{l}}(\tilde{a})$ where $\mathbf{G}_{\mathrm{l}}(\tilde{a})$ is a lower-triangular matrix (Kailath, 1961). Therefore

$$y'(\tilde{a}) = \frac{1}{N_0}[\mathbf{G}_\mathrm{l}(\tilde{a})\mathbf{r}]^\mathrm{H}\mathbf{G}_\mathrm{l}(\tilde{a})\mathbf{r} + B(\tilde{a}). \quad (15)$$

This receiver is called the *filter-squarer-integrator (FSI) receiver* (Van Trees, 1971).
If the knowledge about the received signal is at the minimum, we may assume that $\mathbf{G}_\mathrm{l}(\tilde{a})$ corresponds to an ideal band-pass filter, and the receiver corresponds to the *energy detector* (ED). If the signals share the same frequency band and time interval, the ED can only discriminate signals that have different energies. If the received symbols have similar energies, they must be time disjoint or frequency disjoint.
Joint data and channel estimation. In joint estimation both the data and channel are assumed to be unknown as in the estimator-correlator but they are estimated jointly (Mämmelä et al., 2002). In a Rayleigh fading channel the MAP joint estimator is identical to the estimator-correlator (Meyr et al., 1998). Due to symmetry reasons the MAP estimator for this channel is identical to the MMSE estimator. This is not true in more general channels and joint estimation differs from the optimal MAP detector whose aim is to detect the data with a minimum error probability.

3. Historical development of phase-unaware detection methods

Optimal MAP receivers were first analyzed by Woodward and Davis (1952). They showed that the a posteriori probabilities form a set of sufficient statistics for symbol decisions. Price (1956) and Middleton (1957) derived the estimator-correlator receiver for the time-continuous case. In addition, Middleton presented an equivalent receiver structure that has been later called the FSI receiver (Van Trees, 1971). Kailath (1960) presented the estimator-correlator for the time-discrete case and generalized the results to a multipath channel where the fading is Gaussian. If the channel includes a known deterministic part in addition to the random part, the receiver includes a correlator and the estimator-correlator in parallel (Kailath, 1961). Later Kailath (1962) extended the result to a multi-channel case. Kailath (1969) also showed that the estimator-correlator structure is optimum for arbitrary fading statistics if the noise is additive and Gaussian. If the noise is not white, a noise whitening filter can be used (Kailath, 1960).
According to Turin (1960) the noncoherent matched filter was first defined by Reich and Swerling and Woodward in 1953. Noncoherent receivers were studied by (Peterson et al., 1954; Turin, 1958). Noncoherent diversity systems based on square-law combining were considered in (Price, 1958; Hahn, 1962).
Helström (1955) demonstrated the optimality of orthogonal signals in binary noncoherent systems. Jacobs (1963) and Grettenberg (1968) showed that energy-detected disjointly orthogonal and noncoherent orthogonal M-ary systems approach the Shannon limit and capacity in an AWGN channel. Scholtz and Weber (1966) showed that in M-ary noncoherent systems noncoherently orthogonal signals are at least locally optimal. They could not show the global optimality. Pierce (1966) showed that the performance of a noncoherent M-ary system with L diversity branches approaches the Shannon limit just as that of a coherent system when M and L approach infinity. However, in a binary system ($M = 2$) there is a finite optimal L dependent on the received signal-to-noise ratio (SNR) per bit for which the bit error probability performance is optimized (Pierce, 1961). In this case there is always a certain loss compared to the corresponding binary coherent orthogonal system.
One of the earliest papers on differential phase-shift keying (DPSK) includes (Doelz, 1957). Cahn (1959) analyzed the performance of the DPSK detector. DPSK was extended to multiple

symbols in (Leib & Pasupathy, 1988; Divsalar & Simon, 1990; Leib & Pasupathy, 1991). An extension to differential quadrature amplitude modulation (QAM) is described in a voiceband modem standard (Koukourlis, 1997). The estimator-correlator principle was used in a DPSK system in (Dam & Taylor, 1994).

EDs are sometimes called radiometers. Postdetection or noncoherent integration similar to energy detection has been originally considered in radar systems by North in 1943 (North, 1963) and Marcum in 1947 (Marcum, 1960). The authors analyze the noncoherent combining loss. Peterson et al. (1954) showed the optimality of energy detection when the signal is unknown. A general analysis of EDs was presented in (Urkowitz, 1967; Urkowitz, 1969).

Energy detection was studied for digital communications in (Helström, 1955; Middleton, 1957; Harris, 1962; Glenn, 1963). Dillard (1967) presented an ED for pulse-position modulation (PPM), and Hauptschein & Knapp (1979) for *M*-ary orthogonal signals. A general result from these studies was the fact that the performance of the system is decreased when the time-bandwidth product is increased.

4. Recent trends in designing phase-unaware detectors

In this section, a more detailed view on selected signal design and data estimation methods, suitable for PUDs is given. Specifically, we first focus on basic signal design principles, followed by a discussion on the data estimation and generation of the decision variable for the subsequent symbol decision approaches at the receiver. Advanced signal processing approaches, which represent more recent trends, are considered next. Finally, we discuss specific analysis problems arising with the PUD. With a PUD system, any information on the absolute signal phase is not recovered, thus demodulation methods based on absolute phase information are useless unless pilot symbols are used.

4.1 Basic signal design principles

We start from a transmission model for single-input single-output (SISO) time-division-multiplexed (TDM) signals given as

$$s(t) = \sum_{k=-\infty}^{\infty} a_k g_k (t - kT - \tau_k) \tag{16}$$

where T is the symbol interval, a_k is the kth amplitude selected from the symbol set with OOK, $g_k(t)$ is the kth pulse shape selected the symbol set for binary frequency-shift keying (BFSK), and τ_k is the kth delay selected the symbol set for binary pulse position modulation (BPPM). In general, the overall pulse modulation method for the selected PUD method can be based on one of these approaches or a combination of them.

Alternatively, we can use the frequency domain to multiplex signals by using appropriate frequency-division-multiplexed (FDM) signals. In this case, (16) becomes

$$s(t) = \sum_{k=-\infty}^{\infty} \sum_{j=1}^{N} a_{k,j} g_{k,j} (t - kT - \tau_{k,j}) \tag{17}$$

where now $a_{k,j}$ and $\tau_{k,j}$ are, respectively, the amplitude and delay at kth time and jth (j = 1, 2,…, N) frequency. Typically, in PUD-based systems, the pulses $g_{k,j}(t)$ are nonoverlapping in frequency. An example of nonoverlapping FDM with OOK is given for UWB systems in (Paquelet, 2004). Overlapping FDM signals were analyzed in (Al-Dweik, 2003) using the PUD approach. Nonoverlapping FDM is also called as a multiband modulation system (Anttonen & Mämmelä, 2009).

Some PUD structures may require additional reference, pilot, or training signals in order to be able to recover the transmitted information. For instance, an unmodulated reference symbol and modulated information symbol are required to be sent in pairs or a known training signal is needed to acquire some knowledge of the instantaneous state of the channel. This former system is sometimes called as a transmitted-reference system (Franz & Mitra, 2006). It is also possible to use the previous symbol as a local reference template given rise to differential modulation approach. In this case, variants of DPSK become possible (Ma et al., 2005).
The comparison of different modulation methods depends on the target system specification and selected receiver structure but some general conclusions can be drawn (cf. Proakis, 2001; Guvenc, 2003; Simon & Alouini, 2005). For instance, the OOK can be preferred for its simple transceiver structure. Orthogonal BFSK and BPPM result in improved energy efficiency per information bit at the cost of occupying larger bandwidth.

4.2 Symbol-by-symbol data estimation without interference

As described in the previous section, data estimation is in general based on the estimator-correlator structure. In the optimal receiver the aim is to develop a symbol detector which is somehow matched to the transmitted signal and the channel. On the other hand, in a suboptimal symbol detection approach, the aim is to match the combination of the channel and receiver front-end to a simpler detector by using suitable signal pre-processing. Several important pre-processing tasks include an out-of-band noise filtering, solving the phase ambiguity problem, and a multipath energy combiner. In case of a PUD system, these pre-processing tasks have some special features and will be discussed in more detail.
Figure 2 illustrates some important pre-processing parts for the given received signal $r(t)$. We have excluded parts such as amplifiers and down-converters which may be needed in some PUD systems. The order of the blocks is naturally not fixed and can be changed resulting in different trade-offs. As an example, the sampling operation can take place at any stage after limiting the bandwidth of the noise. If the signal bandwidth is very high, as it is typical for UWB systems, it is desired to locate the sampling unit as late as possible to avoid the use of extremely high sampling rates. In an ideal case, the noise filtering can follow two principal approaches, namely sinc filtering and matched filtering. In the former case, the frequency response is a rectangular function in frequency domain for removing all frequency components outside a given two-sided bandwidth B. On the other hand, in the latter case the aim is to match the impulse response of the receiver filter to the transmitted pulse $g(t)$. In practice, some approximations of these approaches are usually used. After the noise filtering, the phase ambiguity between resolvable multipaths must be removed by an appropriate co-phasing scheme in order to combine the energy from different multipaths

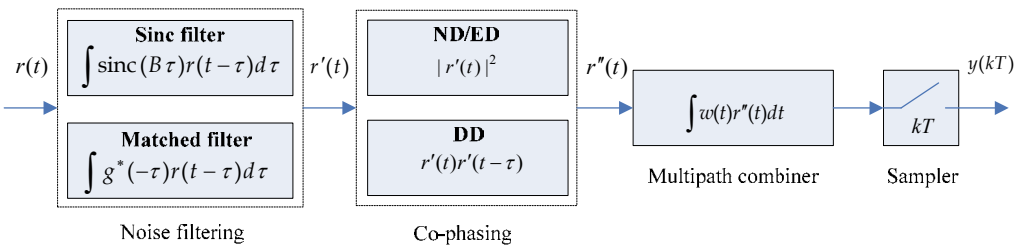

Fig. 2. Pre-processing of received signal for different PUD systems (linear modulation assumed).

constructively. The difference between DD and ED is clear, i.e., for ED the correlation delay is zero whereas for the DD it is nonzero. The DD method is sometimes called as an autocorrelation detector (Franz & Mitra, 2006).

The main consequence is that the noise characteristics become different at the output of the correlator. However, the difference between the ED and ND is often not so clear when used together with a multipath combiner. In fact, with certain approximate assumptions they become equivalent. The main differences lie in the assumptions on noise filtering and time-variability. Typically, ND is defined as a pulse matched filter structure followed by a quadratic envelope detector. Thus, ND must assume that the channel phase is constant over at least the symbol interval. On the other hand, such assumptions are not, by definition, made with ED indicating that ED is a more robust concept.

In a PUD-based system, the multipath combiner can be based on similar approaches as with the systems which have an access to the phase information. The integration interval determines the amount of multipath and noise energy accumulation. The aim is to collect the energy optimally from different resolvable multipaths separated by a delay so that the SNR at the output of the combiner is maximized. The most convenient approach is to use an EGC where the weighting signal $w(t)$ is one. The EGC approach with different PUD systems has been analysed in (Proakis, 2001; Simon & Alouini, 2005, Anttonen et al., 2011a). A more complicated approach is to use a weighted gain combiner where $w(t)$ is now changing in time based on a selected criterion (Romme & Witrisal, 2006; Wang et al., 2011). If weighting is done with sampled signals, the weighting signal can be presented as a weight vector $\mathbf{w}$. Typically, weight optimization based on the minimization of symbol error probability of a PUD system is difficult for non-Gaussian statistics and other criteria such as minimum mean square error or maximum SNR are used. Weighting changes also the distribution of the decision variable and this needs to be taken into account in symbol detection (cf. Kotz, 1967). Consequently, the maximum available gain from the weighting of the diversity paths with respect to the EGC depends especially on the fading statistics. Using the results form (Kotz, 1967) for a weighted chi-square distribution, the effect of different normalized weighting vectors $\mathbf{w} / \overline{w}$, where $\overline{w}$ is the average of the elements of $\mathbf{w}$, is illustrated in Fig. 3.

After the pre-processing blocks, a discrete decision variable $y(kT)$ is provided for the subsequent symbol detector. The PUD systems can be also classified based on the used symbol decision approach. Typically the symbols are equally probable and ML criterion is used in all cases. However, the ML criterion may or may not need instantaneous channel energy information depending on the used modulation method and the corresponding decision variable. In case of uncoded nonconstant envelope OOK signals, the receiver must know the noise level and the instantaneous SNR in order to recover the transmitted information. However, with constant envelope BPPM and BFSK, the transmitted information is detected by comparing the decision variables at each candidate time-frequency intervals. If the channel does not change relatively within these intervals, the symbols can be detected without instantaneous channel information.

4.3 Advanced signal processing approaches

In this section, we overview some recent trends to improve the performance of the basic PUD-based systems described in the previous section. The selected techniques we tend to highlight include multilevel modulation, multiantenna modulation, multiple-symbol sequence detection, multiuser communication techniques, and ISI avoidance methods.

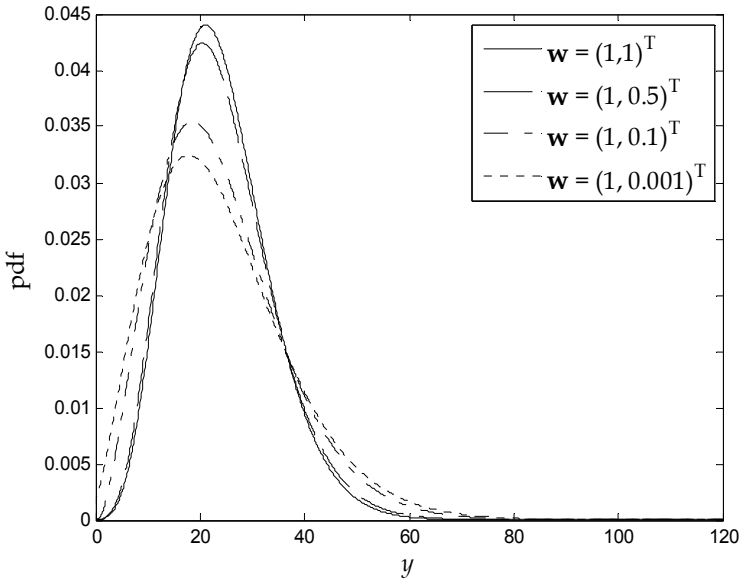

Fig. 3. Illustration of the effect of weighting on the pdf of the decision variable y.

4.3.1 Multilevel modulation and demodulation

Multilevel modulation is a powerful way to increase the spectral efficiency or the energy efficiency to transmit the information bits. The binary modulation methods are extended to *M*-PAM, *M*-PPM, or *M*-FSK with *M*-ary constellations. Each of the methods has its own specific advantages and challenges. For instance, the optimum delay parameter of *M*-PPM depends on the selected pulse shape and receiver structure (Jayaweera, 2005). In case of *M*-PAM signals, it is often necessary to use nonnegative symbol constellations when applied with a PUD system as shown in (Anttonen et al., 2009; Anttonen et al., 2011a). When combining nonnegative *M*-PAM signals with ED, the receiver must know the noise level and the instantaneous SNR to calculate *M*-1 symbol decision thresholds. However, it has been shown recently that the decision thresholds can be found blindly without using a known training signal (Anttonen et al., 2010; Anttonen et al., 2011b). The main advantages of the *M*-PAM approach are that the complexity of the generation of the decision variable for the symbol detector is independent of the number of modulation levels M, and the bandwidth is decreased when M is increased for a given bit rate. On the other hand, *M*-PPM and *M*-FSK result in an improved bit error probability with M as, unlike with *M*-PAM, the symbol distances do not change for a given average signal energy. Naturally, various hybrids of the modulation methods presented above are possible. Combinations of *M*-PAM and *M*-PPM schemes can be applied to provide compromises between the spectral and energy efficiency. It is also possible to use multilevel differential phase shift keying and combine it with amplitude modulation, resulting in a differential QAM approach (Koukourlis, 1997) without a need to know the absolute phase information of the received signal.

4.3.2 Multiantenna modulation and demodulation

Using multiple-input-multiple-output (MIMO) methods with coherent systems have become a standard approach to improve the performance of the system. The use of MIMO methods with

PUD systems lags behind but has become more popular recently. Spatial diversity methods have been most popular with ND and DD. The capacity of multiple antenna systems without having access to the instantaneous channel state was studied in (Hochwald & Marzetta, 2000). Under the AWGN and Rayleigh channel assumptions, it has been shown that at a high SNR, or when the coherence time in symbols intervals is much larger than the number of transmitter antennas, the capacity can be achieved by using constellations of unitary matrices as codebooks. Differential space-time encoding and decoding principles are developed in (Hughes, 2000) and analysed for UWB short-range systems in (Zhang & Ng, 2008). Beamforming with an ND-based PUD receiver is studied in (Naguib & Paulraj, 1996). While MIMO-extended PUD systems typically rely on orthogonal space-time matrices, some techniques have been proposed that allow the transmission of independent space-time signals (Song et al., 2007). This kind of differential spatial multiplexing approach can achieve maximum bandwidth efficiency without the need of any channel state information.

4.3.3 Multiple symbol sequence detection

So far we have assumed that the symbol decision is made using a symbol-by-symbol detector. In order to improve the performance, an increasing trend for PUD systems is to use a sequence of symbols at each time instant and apply a ML estimator for the used symbol sequence (Leib & Pasupathy, 1988; Divsalar & Simon, 1990; Lodge & Moher, 1990; Leib & Pasupathy, 1991; Leib & Pasupathy, 1992; Colavolpe & Raheli, 1999; Guo & Qiu, 2006; Tian & Yang, 2008). The performance of noncoherent sequence detectors, which have no access to the absolute signal phase information, has been shown to approach that of the corresponding coherent sequence detectors if the phase ambiguity problem is solved but at the cost of increasing the decoder complexity (Raphaeli, 1996).

4.3.4 ISI avoidance by signal design

In systems using a PUD approach, the receiver often includes some nonlinear operation which makes it difficult to post-equalize the ISI. Furthermore, phase information is required to completely remove the ISI. Consequently, it would be more reasonable to aim at avoiding the interference using appropriate signal design methods. In principle, the avoidance is possible via pre-distortion or pre-equalization of the transmitted signal according to the instantaneous ISI (Harashima & Miyakawa, 1972), spread-spectrum signalling with interference-rejecting autocorrelation characteristics of the pseudo-noise codes (Peterson et al., 1995), increasing the symbol interval for a given bit rate by using M-ary modulation, or frequency or spatial multiplexing, using gaps longer than the delay spread of the channel between symbols (Proakis, 2001), delay spread reduction of the channel with signal beamforming (Hansen & Loughlin, 1981), or commutating the signal, e.g., with frequency-hopping code according to the delay spread of the channel (Turin, 1984). A rough comparison of these fundamental approaches is presented in Table 1.

4.3.5 Multiuser communications

Multiuser detection involves the study of methods for the demodulation of simultaneously transmitted information from different user terminals. In general, the user information can be detected in a serial or parallel fashion. Multiuser and multiantenna detection methods pose similar type of problems but from different viewpoints, and the techniques that are used for data recovery have many commonalities. There has been a considerable research on

Avoidance scheme	Required channel information	Main Challenge
Pre-equalization	Impulse response	Channel estimation
Pseudo-noise coding	None	Mitigating severe ISI
Length of symbol interval	Delay spread	Complexity
Gaps	Delay spread	Bandwidth waste
Delay spread reduction	Terminal direction	Tracking of terminal
Frequency-hopping	Delay spread	Complexity

Table 1. Comparison of ISI avoidance methods.

the coherent multiuser detection problem in the past, see a good summary in (Verdu, 1998). A pioneering work in studying multiuser detection techniques for DD-based PUD systems in found from (Varanasi, 1993). Other recent work on studying and analysing multiuser techniques with DD can be found from (Dang & van der Veen, 2007). Although multiuser DD schemes have been a more popular research topic, recently multiuser approaches have also been applied to ED (Xu & Brandt-Pearce, 2006). The most significant challenge in designing PUD transceivers with multiple users is to compensate the nonlinear interference generated by the nonlinear operations at the receiver front-end. Another challenge is naturally the evaluation of the analytical error probability of these systems.

5. On analysis of phase-unaware detectors

In this section, we outline some important analysis challenges and available solutions to evaluate the error probability of PUD-based systems. Our purpose is not to explicitly compare the error probability performance of different PUD approaches as this has been done in many contributions, see good overviews from (Proakis, 2001; Simon & Alouini, 2005). We discuss selected approximation approaches which significantly ease the analysis of PUD systems.

5.1 Idealization of the receiver filter

The receiver filter reduces the noise by convolving the received signal with a selected impulse response which is sometimes matched to the pulse shape of the transmitted signal. The receiver filter can be a bandpass or lowpass filter depending on the location of the filter with respect to the possible down-converter. The consequences of the nonideal filtering are that the received signal is distorted and the output noise samples become correlated. Typically, these effects are difficult to include in the performance analysis of PUD systems. To avoid such a situation, the filter bandwidth should be larger than the bandwidth of the received signal without noise (Choi & Stark, 2002). In the bandpass case, this kind of filter is called as ideal bandpass zonal filter in (Quek & Win, 2005). At the output of the idealized filter with a sufficiently large bandwidth B, no ISI is introduced and the noise samples, which are separated by $1/B$, can be approximated to be statistically independent.

5.2 Integration model and the sampling theorem

In order to come up with a proper probability density function for the decision variable of a PUD system, we need to approximate the continuous integration operation involved with the multipath combiner in Fig. 2. A natural approximation is obtained from the sampling

theorem as follows (cf. Urkowitz, 1967). In a general case, with an appropriate choice of time origin, we may express a real signal $r(t)$ in the form

$$r(t) = \sum_{k=-\infty}^{\infty} r_k \mathrm{sinc}\,(Bt - k) \approx \sum_{k=1}^{K} r_k \mathrm{sinc}\,(Bt - k) \tag{18}$$

where $r_k = r(k/B)$ is a sampled version of $r(t)$, K is the finite number of signal components, and B is the bandwidth of the receiver filter. It is obvious that the approximation improves as K increases. It is shown in (Urkowitz, 1967) that for a given integration interval T, it is sufficient to select $K = BT$ discrete terms to obtain

$$\int_0^T r(t)dt \approx y = \frac{1}{B}\sum_{k=1}^{BT} r_k. \tag{19}$$

An example to use the result is presented as follows by applying the ED principle. If $r(t) = [s(t) + n(t)]^2$, where $s(t)$ is the information signal with nonzero energy and $n(t)$ is the zero mean Gaussian random variable, y can readily be shown to follow the noncentral chi-square distribution with $2BT$ degrees of freedom since each complex sample includes two real samples.

5.3 Gaussian quadratures

Important approaches to solve analytical problems of PUD systems arise from the application of Gaussian quadratures. Gaussian quadratures approximate the integrals of the form (Abramowitz & Stegun, 1972)

$$\int_a^b \omega(x) f(x) dx \approx \sum_{i=1}^{G} \omega_i f(x_i) \tag{20}$$

where a and b set the integration interval, $\omega(x)$ is a positive weight function, $f(x)$ is an arbitrary function, ω_i and x_i are, respectively, the weighting factors and abscissas of the

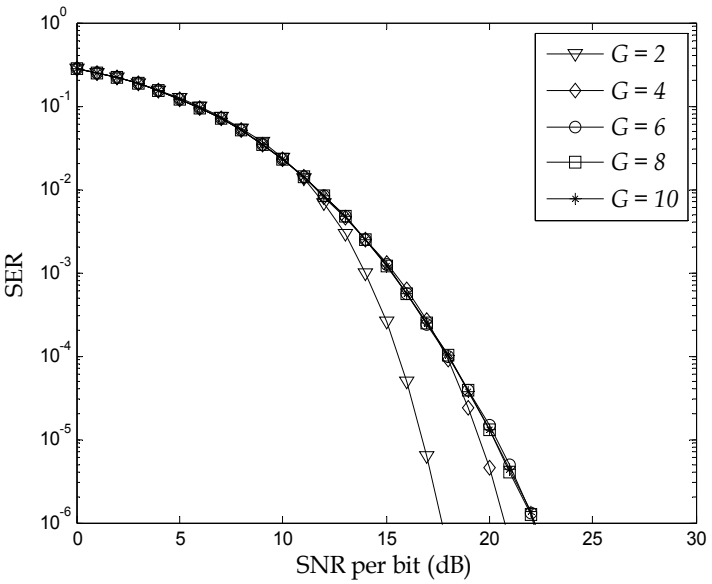

Fig. 4. SER approximation of binary ED-PAM system with different orders of Gaussian quadratures.

selected Gth order Gaussian quadrature. The selection of the quadrature depends on the form of $f(x)$. An important example arises from the analysis of ED-based PAM systems (Anttonen et al., 2011a). The optimal ML symbol decision thresholds of ED-PAM systems cannot be represented in a closed form. Consequently, the evaluation of the analytical error probability in multipath fading channels becomes difficult, if not impossible. Following the results of (Anttonen et al., 2011a), the symbol error rate is given as Gaussian quadratures enable a convenient framework to select only few discrete points in which the continuous time integral is evaluated, and the threshold values are calculated. Figure 4 illustrates the effect of the order of the Gauss quadrature for the symbol error rate (SER) of the ED-PAM system with $M = 2$ in a flat lognormal fading channel, see further details of the analysis in (Anttonen et al., 2011a). It is seen that already when $G \geq 6$, the approximation accuracy is not significantly improved anymore. In addition to the Gaussian guadratures, other types of guadratures exist as well if a suitable weighting factor is not available for the function $f(x)$ at hand or the function involves multiple random variables, see an excellent summary from (Cools, 2002).

5.4 Probability density function of the decision variable

Essential information for ML symbol detection is to know the probability density function (pdf) of the decision variable after sufficient pre-processing has been performed to allow the maximum possible signal-to-noise ratio for the decision variable and a simple symbol-by-symbol detector structure. The noncentral chi-square distribution, which was inferred from the sampling theorem in the previous subsection, is used extensively to model the distribution of the decision variable of PUD-based systems (Quek & Stark, 2005; Anttonen et al., 2011a). In case of a weighted PUD system, we must use a weighted chi-square distribution which has alternate series forms as shown in (Kotz et al., 1967).

Since the chi-square distribution (both weighted and nonweighted) involves complicated functions with series forms, Gaussian approximation approach can be used to approximate the pdf of the decision variable, provided that the number of degrees of freedom is large enough. This is justified by the Berry-Esseen theorem given in (Feller, 1972). The Gaussian approximation approach enables also a nice framework to compare the noise statistics which has a major role in determining the error probability of the system. Let $N(\mu,\sigma)$ denote the Gaussian or normal distribution where μ and σ are, respectively, the mean and standard deviation of the of the decision variable y. Following the work from (Guvenc et al., 2006; Wang et al., 2011), the noise statistics of y with nonzero signal energy for different PUD systems are approximated as

$$y \sim \begin{cases} N(E_s, BT\sigma^4 + 2E_s\sigma^2) & \text{for DD} \\ N(2BT\sigma^2 + E_s, 4BT\sigma^4 + 4E_s\sigma^2) & \text{for ED} \\ N(2BT\sigma^2\mathbf{w}^{\mathrm{T}}\mathbf{1} + \mathbf{w}^{\mathrm{T}}\mathbf{z}, 4BT\sigma^4\mathbf{w}^{\mathrm{T}}\mathbf{w} + 4\sigma^2\mathbf{w}^{\mathrm{T}}\mathbf{Z}\mathbf{w}) & \text{for WED} \end{cases} \quad (21)$$

where E_s is the signal energy, $\mathbf{w}$ is the weighting column vector of the weighted energy detection (WED), $\mathbf{1}$ is the column vector of ones, $\mathbf{z}$ is the column vector including the energies from different diversity paths, $\boldsymbol{Z}$ = diag($\mathbf{z}$), and diag($\mathbf{a}$) is the diagonal matrix where vector $\mathbf{a}$ is on the diagonal.

5.5 Nonlinear filtering models for analysis and equalization of interference

PUD systems introduce inherent nonlinearity in the signal processing in the process of co-phasing the signal. Consequently, the compensation of various types of interferences becomes

difficult with linear filters. In case the interference cannot be avoided by signal design, optimal receiver principles, nonlinear filtering models including linearization represent systematic procedures for reducing the interference or distortion caused by a nonlinear device. Linearization techniques have been traditionally used to ease the design of power amplifiers which are typically nonlinear (Katz, 2001). Linearization techniques as well as simplified nonlinear models are also very useful with the design and analysis of nonlinear PUD systems in the presence of interference. A nice framework is proposed in (Witrisal et al., 2005) for DD-type PUD systems. A second-order Volterra model (cf. Sicuranza, 1992) is proposed to describe the data dependency in the presence of ISI, whereby the nonlinearity is caused by the multiplication in the pulse-pair correlators. This Volterra model divides the problem into the linear and nonlinear counterparts to find more efficient ways to equalize the interference. Consequently, nonlinear structures can be more effectively handled. Furthermore, if the interference is not severe, the nonlinear parts may be found to have an insignificant effect on the performance. The approach can readily be extended to other type of PUD systems as well.

6. Concluding remarks

In this chapter, we have presented an overview of low complexity PUD systems which do not need carrier phase recovery at the receiver. This is an important advantage for the systems using a very high bandwidth or centre frequency. We started from the optimal MAP receiver which lead to the estimator-correlator concept. We then provided a selected snapshot of historical landmark papers of PUD systems. Furthermore, some recent trends in designing advanced PUD systems were discussed. Finally, we provided some insight for the approximation approaches to ease the analysis of PUD systems using some specific examples.
The design and analysis of advanced PUD systems lags behind the corresponding coherent receivers and there is a clear need for better understanding of these systems, especially in more complicated environments. To help to achieve this goal we emphasize the importance of the estimator-correlator concept which nicely connects the approaches under the same theoretical framework. The main motivation of using the PUD systems is to lower the complexity of the transceivers not being able to recover the carrier phase information inexpensively. However, in more complicated environments with significant ISI or multiuser interference, the nonlinear operations involved with the PUD receivers may also increase the complexity of some parts of the symbol detection with respect to the coherent detection. To this end, we also emphasize the significance of interference avoidance with PUD systems by signal design. It is obvious that the PUD systems inherently tend to amplify the noise energy at the receiver. Consequently, a remaining open question is to reveal the overall trade-offs including the required transmitter signal energy, signal processing energy, and the related hardware complexity. The PUD systems have traditionally been used with low data rate applications. Due to the recent advances in both algorithm and implementation designs, the PUD systems have created much attention among academic and industrial research communities to apply PUD-based transceivers also for high data rate applications. This is true especially in case of UWB wireless short-range systems operating at 3-10 GHz as well as 60 GHz frequency ranges.

7. Acknowledgment

The authors would like to acknowledge the FP7/EUWB and ITSE projects. The former project is partly funded by the European Union and the latter one by VTT.

8. References

Abramowitz M. & Stegun I. (1972). *Handbook of Mathematical Functions with Formulas, Graphs, and Mathematical Tables*, (10th ed.), Dover Publications, Inc., ISBN: 978-0-486-61272-0, New York.

Al-Dweik A. & Xiong F. (2003). Frequency-hopped multiple-access communications with noncoherent *M*-ary OFDM-ASK. *IEEE Trans. Commun.*, Vol. 51, No. 1, pp. 33–36.

Anttonen A. & Mämmelä A. (2009). Multiband modulation in UWB systems; In: *Short Range Wireless Communications: Emerging Technologies and Applications*, R. Craemer and M. Katz, Eds., John Wiley & Sons, ISBN: 978-0-470-69995-9, New York.

Anttonen A., Kotelba A. & Mämmelä A. (2009). Energy detection of multilevel PAM signals with systematic threshold mismatch, *Research Letters in Commun.*, Vol. 2009, 4 pages.

Anttonen A., Kotelba A. & Mämmelä A. (2010). Nondata-aided hypothesis testing of PAM signals with energy detection, *IEEE Commun. Letters*, Vol. 14, No. 10, pp. 957–959.

Anttonen A., Kotelba A. & Mämmelä A. (2011a). Error performance of PAM systems using energy detection with optimal and suboptimal decision thresholds. *Physical Commun.*, to be published.

Anttonen A., Kotelba A. & Mämmelä A. (2011b). Blind decision-directed parameter estimation for energy detection of PAM signals. *Proceedings of IEEE Int. Conf. Commun.*, Kioto, Japan.

Barrett M. J. (1987). Error probability for optimal and suboptimal quadratic receivers in rapid Rayleigh fading channels, *IEEE J. Sel. Areas Commun.*, Vol. SAC-5, No. 2, pp. 302–304.

Bello P. A. (1963). Characterization of randomly time-variant linear channels, *IEEE Trans. Commun. Syst.*, Vol. CS-11, No. 4, pp. 360–393.

Cahn C. (1959). Performance of digital phase-modulation communication systems, *IRE Trans. Commun. Syst.*, Vol. 7, No. 1, pp. 3–6.

Choi J. & Stark W. (2002). Performance of ultra-wideband communications with suboptimal receivers in multipath channels. *IEEE J. Sel. Areas Commun.*, Vol. 20, No. 9, pp. 1754–1766.

Colavolpe G. & Raheli R. (1999). Noncoherent sequence detection. *IEEE Trans. Commun.*, Vol. 47, No. 9, pp. 1376–1358.

Cools R. (2002). Advances in multidimensional integration. *Journal of Computational and Applied Mathematics*, Vol. 149, No. 1, pp. 1–12.

Dam W. C. & Taylor D. P. (1994). An adaptive maximum likelihood receiver for correlated Rayleigh-fading channels, *IEEE Trans. Commun.*, Vol. 42, No. 9, pp. 2684–2692.

Dang Q. & van der Veen A.-J. (2007). A decorrelating multiuser receiver for transmit-reference UWB systems. *IEEE J. Sel. Areas Commun.*, Vol. 1, No. 3, pp. 431–442.

Dillard G. M. (1973). Pulse-position modulation based on energy detection, *IEEE Trans. Aerospace Elect. Syst.*, Vol. AES-9, No. 4, pp. 499–503.

Divsalar D. & Simon M. (1990). Multiple-symbol differential detection of MPSK. *IEEE Trans. Commun.*, Vol. 38, No. 3, pp. 300–308.

Doelz M. L., Heald E. T. & Martin D. L. (1957). Binary data transmission techniques for linear systems, *Proc. IRE*, Vol. 45, No. 5, pp. 656–661.

Feller W. (1972). *An Introduction to Probability Theory and Its Applications*, John Wiley & Sons, ISBN: 0-471-25709-5, New York.

Franks L. E. (1969). *Signal Theory*, Prentice-Hall, ISBN: 0-13-810077-2, Englewood Cliffs, NJ.

Franz S. & Mitra U. (2006). Generalized UWB transmitted reference systems. *IEEE J. Select. Areas Commun*., Vol. 24, No. 4, pp. 780–786.

Garth L. M. & Poor H. V. (1994) Detection of non-Gaussian signals: a paradigm for modern statistical signal processing, *Proc. IEEE*, Vol. 82, No. 7, pp. 1061–1095.

Glenn A. & Lieberman G. (1963). Performance of digital communications systems in an arbitrary fading rate and jamming environments, *IEEE Trans. Commun. Syst.*, Vol. 11, No. 1, pp. 57–68.

Grettenberg T. (1968). Exponential error bounds for incoherent orthogonal signals, *IEEE Trans. Inf. Theory*, Vol. 14, No. 1, pp. 163–164.

Guo N. & Qiu R. (2006). Improved autocorrelation demodulation receivers based on multiple-symbol detection for UWB communications. *IEEE Trans. Wireless Commun*., Vol. 5, No. 8, pp. 2026–2031.

Guvenç I., Sahinoglu Z. & Arslan H. (2006). TOA estimation for IR-UWB systems with different transceiver types. *IEEE Trans. Microw. Theory Tech*., Vol. 54, No. 4, pp. 1876–1886.

Hahn P. M. (1962). Theoretical diversity improvement in multiple frequency shift keying, *IEEE Trans. Commun. Syst*., Vol. 10, No. 2, pp. 177–184.

Hansen P. & Loughlin J. (1981). Adaptive array for elimination of multipath interference at HF. *IEEE Trans. Antennas and Prop*., Vol. 29, No. 6, pp. 836–841.

Harashima H. & Miyakawa H. (1972). Matched-transmission technique for channels with intersymbol interference. *IEEE Trans. Commun*. Vol. 20, No. 4, pp. 774–780.

Harris, D. (1962). Techniques for incoherent scatter communication. *IRE Transactions on Communications Systems*, Vol. 10, No. 2, pp. 154–160.

Hauptschein A. & Knapp T. (1979). Maximum likelihood energy detection of *M*-ary orthogonal signals, *IEEE Trans. Aerospace Elect. Syst.*, Vol. AES-15, No. 2, pp. 292–299.

Helstrom C. W. (1955). The resolution of signals in white, Gaussian noise, *Proc. IRE*, Vol. 43, No. 9, pp. 1111–1118.

Hirt W. & Pasupathy S. (1981). Continuous phase chirp (CPC) signals for binary data communication - Part 2: Noncoherent detection. *IEEE Trans. Commun*., Vol. 29, No. 6, pp. 848–858.

Hochwald B. & Marzetta T. (2000). Unitary space-time modulation for multiple-antenna communication in Rayleigh flat-fading, *IEEE Trans. Inf. Theory*, Vol. 46, No. 2, pp. 543–564.

Hughes B. (2000). Differential space-time modulation. *IEEE Trans. Inf. Theory*, Vol. 46, No. 7, pp. 2567–2578.

Jacobs, I. (1963). The asymptotic behavior of incoherent *M*-ary communication systems. *Proc. IEEE*, Vol. 51, No. 1, pp. 251–252.

Jayaweera S. (2005). Signal design for noncoherent PPM modulation with applications to UWB communications. *IEEE Commun Lett*., Vol. 9, No. 5, pp. 411–413.

Kailath T. (1960). Correlation detection of signals perturbed by a random channel, *IRE Trans. Inf. Theory*, Vol. IT-6, No. 3, pp. 361–366.

Kailath T. (1961). Optimum receivers for randomly varying channels, *Proceedings of the Fourth London Symposium on Information Theory*, Butterworth Scientific Press, London, pp. 109–122.

Kailath T. (1962). On multilink and multidimensional channels, *IRE Trans. Inf. Theory*, Vol. IT-8, No. 3, pp. 260–262.

Kailath T. (1963). Adaptive matched filters; In: *Mathematical Optimization Techniques*, R. Bellman, Ed., University of California Press, Berkeley, CA, pp. 109 - 140.

Kailath T. (1969). A general likelihood-ratio formula for random signals in Gaussian noise, *IEEE Trans. Inf. Theory*, Vol. IT-15, No. 3, pp. 350–361.

Katz A. (2001). Linearization: Reducing distortion in power amplifiers. *IEEE Microw. Mag.*, Vol. 2, No. 4, pp. 37–49.

Kay S. M. (1993). *Fundamentals of Statistical Signal Processing, Vol. I: Estimation Theory*, Prentice-Hall, ISBN: 0-13-345711-7, Englewood Cliffs, NJ.

Kay S. M. (1998). *Fundamentals of Statistical Signal Processing, Vol. II: Detection Theory*, Prentice-Hall, ISBN: 0-13-504135-X, Englewood Cliffs, NJ.

Kotz B., Johnson N. & Boyd D. (1967). Series representations of distributions of quadratic forms in normal variables II. Non-central case. *Annals of Mathematical Statistics*, Vol. 38, No. 1, pp. 838–848.

Koukourlis C. S. (1997). Hardware implementation of a differential QAM modem, *IEEE Trans. Broadcast.*, Vol. 43, No. 3, pp. 281 – 287.

Leib H. & Pasupathy S. (1988). The phase of a vector perturbed by Gaussian noise and differentially coherent receivers, IEEE Trans. Inf. Theory, Vol. 34, No. 6, pp. 1491-1501.

Leib H. & Pasupathy S. (1991). Optimal noncoherent block demodulation of differential phase shift keying (DPSK), AEU, Vol. 45, No. 5, pp. 299-305.

Leib H. & Pasupathy S. (1992). Noncoherent block demodulation of MSK with inherent and enhanced encoding. *IEEE Trans. Commun.* Vol. 40, No. 9, pp. 1430–1441.

Li Y., Cimini L. J. & Sollenberg N. (1998). Robust channel estimation for OFDM systems with rapid dispersive fading channels, *IEEE Trans. Commun.*, Vol. 46, No. 7, pp. 902–915.

Lodge J. H. & Moher M. L. (1990). Maximum likelihood sequence estimation of CPM signals transmitted over Rayleigh flat-fading channels, *IEEE Trans. Commun.*, Vol. 38, No. 6, pp. 787–794.

Ma Y., Zhang Q., Schober R. & Pasupathy S. (2005). Diversity reception of DAPSK over generalized fading channels. *IEEE Trans. Wireless Commun.*, Vol. 4, No. 4, pp. 1834–1846.

Madhow U. (2008). *Fundamentals of Digital Communication*, Cambridge University Press, ISBN: 978-0521874144, Cambridge, UK.

Mämmelä A. and Taylor D. P. (1998). Bias terms in the optimal quadratic receiver, *IEEE Communications Letters*, Vol. 2, No. 1, pp. 57–58.

Mämmelä A., Polydoros A., and Järvensivu P. (2002). Data and channel estimators: A systematic classification (invited paper), in *Proceedings of the X National Symposium of Radio Science*, pp. 13-25, Poznan, Poland, March.

Marcum J. (1960). A statistical theory of target detection by pulsed radar, *IRE Trans. Inf. Theory*, Vol. 6, No. 2, pp. 59–267.

Marple S. L., Jr. (1987). *Digital Spectral Analysis*, Prentice-Hall, ISBN: 978-0132141499, Englewood Cliffs, NJ.

McDonough R. N. & Whalen A. D. (1995). *Detection of Signals in Noise*, (2nd ed.), Academic Press, ISBN: 0-12-744852-7, San Diego, CA.

Mengali U. and D'Andrea A. N. (1997). *Synchronization Techniques for Digital Receivers*. Plenum Press, ISBN: 0-306-45725-3, New York.

Meyr H., Moeneclaey M. & Fechtel S. A. (1998). *Digital Communication Receivers: Sychronization, Channel Estimation, and Signal Processing*, John Wiley & Sons, ISBN: 978-0471502753, New York.

Middleton D. (1957), On the detection of stochastic signals in additive normal noise I, *IRE Trans. Inf. Theory*, Vol. 3, No. 2, pp. 86–121.

Naguib A. & Paulraj A. (1996). Performance of Wireless CDMA with *M*-ary orthogonal modulation and cell cite antenna arrays. *IEEE J. Sel. Areas Commun.* Vol. 14, No. 9, pp. 1770–1783.

North D. O. (1963). An analysis of the factors which determine signal/noise discrimination in pulse-carrier systems. *Proc. IEEE*, Vol. 51, No. 7, pp. 1016–1027.

Pandey R., Leib H. & Pasupathy S. (1992). Noncoherently orthogonal digital phase modulation. *IEEE Trans. Commun.*, Vol. 40, No. 6, pp. 992–995.

Papoulis A. (2002). *Probability, Random Variables, and Stochastic Processes*, McGraw-Hill, ISBN: 978-0071226615, New York.

Paquelet S., Aubert L.-M. & Uquen B. (2004). An impulse radio asynchronous transceiver for high data rates. *Proceedings of Int. Workshop Ultra Wideband Syst.*, Kyoto, Japan.

Pasupathy S. (1979). Minimum shift keying: A spectrally efficient modulation, *IEEE Commun. Mag.*, Vol. 17, No. 4, pp. 14–22.

Peterson R., Ziemer R. & Borth D. (1995). *Introduction to Spread-Spectrum Systems*, Prentice Hall, ISBN: 0024316237, Inglewood Cliffs, NJ.

Peterson W., Birdsall T. & Fox W. (1954). The theory of signal detectability, *IRE Professional Group on Information Theory*, Vol. 4, No. 4, pp. 171–212.

Pierce J. (1961). Theoretical limitations on frequency and time diversity for fading binary transmissions, *IRE Trans. Commun. Syst.*, Vol. 9, No. 2, pp. 186–187.

Pierce J. N. (1958). Theoretical diversity improvement in frequency-shift keying, *Proc. IRE*, Vol. 46, No. 5, pp. 903–910.

Pierce, J. N. (1966). Ultimate performance of *M*-ary transmissions on fading channels. *IEEE Trans. Inf. Theory*, Vol. 12, No. 1, pp. 2–5.

Price R. (1956). Optimum detection of random signals in noise, with application to scatter-multipath communication. *IRE Trans. Inf. Theory*, Vol. IT-2, No. 4, pp. 125–135.

Proakis J. (2001). *Digital Communications*, (4th ed.), McGraw-Hill, ISBN: 0-07-232111-3, New York.

Quek T. & Win M. (2005). Analysis of UWB transmitted-reference communication systems in dense multipath channels. *IEEE J. Sel. Areas Commun.*, Vol. 23, No. 9, pp. 1863–1874.

Raphaeli D. (1996). Noncoherent coded modulation. *IEEE Trans. Commun.*, Vol. 44, No. 2, pp. 172–183.

Romme J. & Witrisal K. (2006). Transmitted-reference UWB systems using weighted autocorrelation receivers. *IEEE Trans. Microw. Theory Tech.*, Vol. 54, No. 4, pp. 1754–1761.

Scholtz R. & Weber C. (1966). Signal design for phase-incoherent communications, *IEEE Trans. Inf. Theory*, Vol. 12, No. 4, pp. 456–463.

Schwartz M., Bennett W. R. & Stein S. (1966). *Communication Systems and Techniques*, McGraw-Hill, ISBN: 0-7803-4715-3, New York.

Shaft P. D. (1963). Error rate of PCM-FM using discriminator detection, *IEEE Trans. Space Electron. and Telemetry*, Vol. 9, No. 4, pp. 131-137.

Sicuranza G. (1992). Quadratic filters for signal processing. *Proc. IEEE*, Vol. 80, No. 8, pp. 1263–1285.

Simon M. & Alouini M.-S. (2005). *Digital Communication over Fading Channels: A Unified Approach to Performance Analysis*, (2nd ed.), John Wiley & Sons, ISBN: 0-471-64953-8, New York.

Skolnik M. I. (2001). *Introduction to Radar Systems*, (3rd ed.), McGraw-Hill, ISBN: 0072881380, New York.

Song L.-Y., Burr A. & Lamarre R. (2007). Differential Bell-Labs layered space time architectures. *Proceedings of IEEE Int. Conf. Commun.*, Glasgow, UK.

Tian Y. & Yang C. (2008). Noncoherent multiple-symbol detection in coded ultra-wideband communications. *IEEE Trans. Wireless Commun.*, Vol. 7, No. 6, pp. 2202–2211.

Turin G. L. (1958). Error probabilities for binary symmetric ideal reception through nonselective slow fading and noise. *Proc. IRE*, Vol. 46, No. 9, pp. 1603–1619.

Turin G. L. (1960). An introduction to matched filters, *IRE Trans. Inf. Theory*, Vol. 6, No. 3, pp. 311–329.

Turin G. L. (1980). Introduction to spread-spectrum antimultipath techniques and their application to urban digital radio, *Proc. IEEE*, Vol. 68, No. 3, pp. 328–353.

Turin G. L. (1984). Commutation signaling – An antimultipath technique. *IEEE Trans. Veh. Tech.*, Vol. 33, No. 3, pp. 164–178.

Urkowitz H. (1967). Energy detection of unknown deterministic signals, *Proc. IEEE*, Vol. 55, No. 4, pp. 523–531.

Urkowitz H. (1969). Energy detection of a random process in colored Gaussian noise, *IEEE Trans. Aerospace Elect. Syst.*, Vol. AES-5, No. 2, pp. 156–162.

Van Etten W. (1976). Maximum likelihood receiver for multiple channel transmission systems, *IEEE Trans. Commun.*, Vol. 24, No. 2, pp. 276 - 283

Van Trees H. L. (1968). *Detection, Estimation, and Modulation Theory, Part I: Detection, Estimation, and Linear Modulation Theory*, John Wiley & Sons, ISBN: 978-0471095170, New York.

Van Trees H. L. (1971). *Detection, Estimation, and Modulation Theory, Part III: Radar-Sonar Signal Processing and Gaussian Signals in Noise*, John Wiley & Sons, ISBN: 978-0471094135, New York.

Varanasi M. (1993). Noncoherent detection in asynchronous multiuser channels. *IEEE Trans. Inf. Theory*, Vol. 39, No. 1, pp. 157–176.

Verdu S. (1998). *Multiuser Detection*, Cambridge University Press, ISBN: 0-521-59373-5, Cambridge, UK.

Wang F., Tian Z. & Sadler B. (2011). Weighted energy detection for noncoherent ultra-wideband receiver design. *IEEE Trans. Wireless Commun*., Vol. 10, No. 2, pp. 710–720.

Witrisal K., Leus G., Janssen G., Pausini M., Troesch F., Zasowski T. & Romme J. (2009). Noncoherent ultra-wideband systems. *IEEE Sig. Process. Mag*., Vol. 26, No. 4, pp. 48–66.

Witrisal K., Leus G., Pausini M. & Krall C. (2005). Equivalent system model and equalization of differential impulse radio UWB systems. *IEEE J. Sel. Areas Commun*., Vol. 23, No. 9, pp. 1851–1862.

Woodward, P. M. & Davies, I. L. (1952). Information theory and inverse probability in telecommunication, *Proc. IEE - Part III: Radio and Communication Engineering*, Vol. 99, No. 58, pp. 37–44.

Xu B. & Brandt-Pearce M. (2006). Multiuser square-law detection with applications to fiber optic communications. *IEEE Trans. Commun*., Vol. 54, No. 7, pp. 1289–1298.

Xu Z. & Sadler B. (2006). Multiuser transmitted reference ultra-wideband communication systems, *IEEE J. Select. Areas Commun*., Vol. 24, No. 4, pp. 766–772.

Yilmaz Ö. & Richard S. (2004). Blind separation of speech mixtures via time-frequency masking, *IEEE Trans. Signal Process.*, Vol. 52, No. 7, pp. 1830–1847.

Zhang Q. & Ng C. (2008). DSTBC Impulse radios with autocorrelation receiver in ISI-free UWB channels. *IEEE Trans. Wireless Commun*., Vol. 7, No. 3, pp. 806–811.

Ziemer R. E. & Tranter W. H. (2002). *Principles of Communications*, (4th ed.), John Wiley & Sons, ISBN: 978-0471392538, Hoboken, NJ.

Part 2

Hardware Architecture and Implementation

6

Ultra-Wideband RF Transceiver Design in CMOS Technology

Lingli Xia[1,2], Changhui Hu[1], Yumei Huang[2],
Zhiliang Hong[2] and Patrick. Y. Chiang[1]
[1]*Oregon State University, Corvallis, Oregon*
[2]*Fudan University, Shanghai*
[1]*USA*
[2]*China*

1. Introduction

UWB (Ultra-Wideband) is one of the WPAN (Wireless Personal Area Network) Technologies; its main applications include imaging systems, vehicular radar systems and communications and measurement systems. Ever since the FCC released unlicensed spectrum of 3.1-10.6 GHz for UWB application in 2002, UWB has received significant interest from both industry and academia.

Comparing with traditional narrowband WPANs, (e.g. Bluetooth, Zigbee, etc.), the most significant characteristics of UWB are ultra-wide bandwidth (7.5 GHz) and low emitted spectrum density (-41.3 dBm/MHz). According to Shannon-Hartley theorem (Wikipedia, 2010), through an AWGN (Additive White Gaussian Noise) channel, the maximum rate of clean (or arbitrarily low bit error rate) data is limited to

$$C = BW \cdot \log_2\left(1 + \frac{P_S}{N_0 \cdot BW}\right) = BW \cdot \log_2\left(1 + SNR\right) \tag{1}$$

where, C is the channel capacity, BW is the channel bandwidth, P_s is the average power of the received signal, N_0 is the noise spectral density. As can be seen from (1), Channel capacity increases linearly with bandwidth but only logarithmically with SNR. With a wide bandwidth, high data rate can be achieved with a low transmitted power.

Mutli-Band OFDM (MB-OFDM) and Direct-Sequence UWB (DS-UWB) are two main proposals for UWB systems; each gained multiple supports from industry. Due to incompatible of these two proposals, UWB technology faces huge difficulties in commercialization. On the other hand, Impulse Radio UWB (IR-UWB) has been a hot research area in academia because of its low complexity and low power.

In the following, we first introduce previous works on different kinds of UWB RF transceiver architectures, including MB-OFDM UWB, DS-UWB and IR-UWB transceivers. Both advantages and disadvantages of these architectures are thoroughly discussed in section 2. Section 3 presents a monolithic 3-5 GHz carrier-less IR-UWB transceiver system. The transmitter integrates both amplitude and spectrum tunability, thereby providing adaptable spectral characteristics for different data rate transmission. The noncoherent

receiver employs a simplified, low power merged-correlator, eliminating the need for a conventional sample-and-hold circuit. After self-correlation, the demodulated data is digitally synchronized with the baseband clock. Section 4 shows the measurement results and section 5 draws a conclusion.

2. Previous works on UWB RF transceivers

Both MB-OFDM (Ranjan & Larson, 2006; Zheng, H. et al., 2007; Bergervoet et al., 2007; Beek et al., 2008) and DS-UWB (Zheng, Y. et al., 2007, 2008) are carrier-modulated systems, where a mixer is used to up/down convert the baseband (BB)/radio frequency (RF) signal, therefore requiring local oscillator (LO) synthesis. The main difference between these two systems is that MB-OFDM systems are dealing with continuous ultra-wideband modulated signals while DS-UWB systems are transmitting discrete short pulses which also occupy ultra-wide bandwidth. On the other hand, IR-UWB is a carrier-less pulse-based system, therefore, the fast hopping LO synthesis can be eliminated, thus reducing the complexity and power consumption of the entire radio. Furthermore, since the signal of a pulse-based UWB system is duty-cycled, the circuits can be shut down between pulses intervals which would lead to an even lower power design.

2.1 MB-OFDM UWB

The main architectures of MB-OFDM UWB transceivers can be categorized into superheterodyne transceivers (Ranjan & Larson, 2006; Zheng, H. et al., 2007) and direct-conversion transceivers (Bergervoet et al., 2007; Beek et al., 2008), which are quite similar as those traditional narrow-band RF transceivers.

2.1.1 Superheterodyne transceivers

In a superheterodyne transceiver, the frequency translation from BB to RF in the transmitter or from RF to BB in the receiver is performed twice. A superheterodyne receiver for MB-OFDM UWB is shown in Fig. 1, after being received by the antenna and filtered by an off-chip SAW (Surface Acoustic Wave) filter (which is not shown in this figure), the UWB RF signal is down-converted to intermediate frequency (IF) signal first, and then further down-converted to BB signal by a quadrature mixer. Superheterodyne transceiver is a very popular architecture used in communication systems because of its good performance.

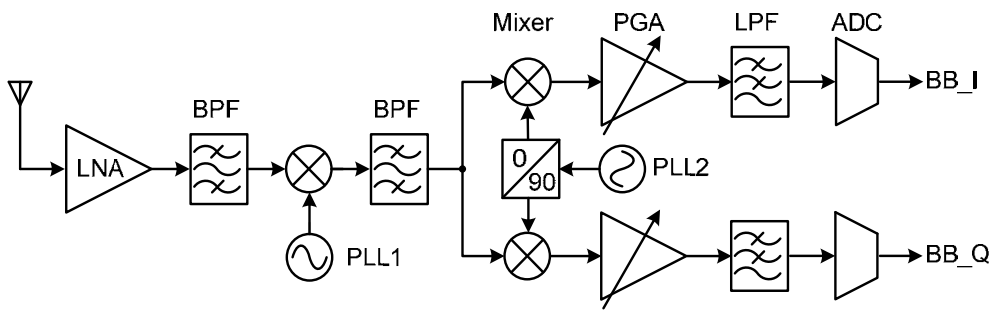

Fig. 1. Superheterodyne Receiver

Because of the two-step frequency translation, LO leakage does not have a significant impact on the receiver. Furthermore, multiple filters are employed to get rid of unwanted image and interference signals, which increase the dynamic range, sensitivity and selectivity of the receiver. However, superheterodyne receivers also exhibit significant disadvantages. Firstly, those bandpass filters need high Q to effectively filter out unwanted image and interference signals, which makes these filters difficult to be integrated in CMOS technology and thus off-chip components are employed which increase the cost. Secondly, two-step frequency translation architecture makes superheterodyne receivers less attractive in power consumption and chip area.

2.1.2 Direct-conversion transceivers

Another more commonly used architecture for MB-OFDM UWB is direct-conversion, as shown in Fig. 2. The RF signal is directly down-converted to a BB signal or vice versa without any intermediate frequency (Gu, 2005), thus expensive IF passive filter can be eliminated, and then the cost and size of the overall transceiver are reduced. And because only one-step frequency translation is needed, the power consumption of a direct-conversion transceiver is much lower than a superheterodyn transceiver. The main problems that limit the application of a direct-conversion transceiver are flicker noise and DC offset. Flicker noise depends on the technology. A PMOS transistor exhibits less flicker noise than a NMOS transistor. DC offset is caused by LO or interference self-mixing, and mismatch in layout. DC offset can be solved by AC coupling or high-pass filtering with a SNR (Signal-to-Noise Ratio) loss. Fortunately, this SNR loss will not be a big issue in a MB-OFDM UWB system since the BB signal bandwidth is as high as 264 MHz.

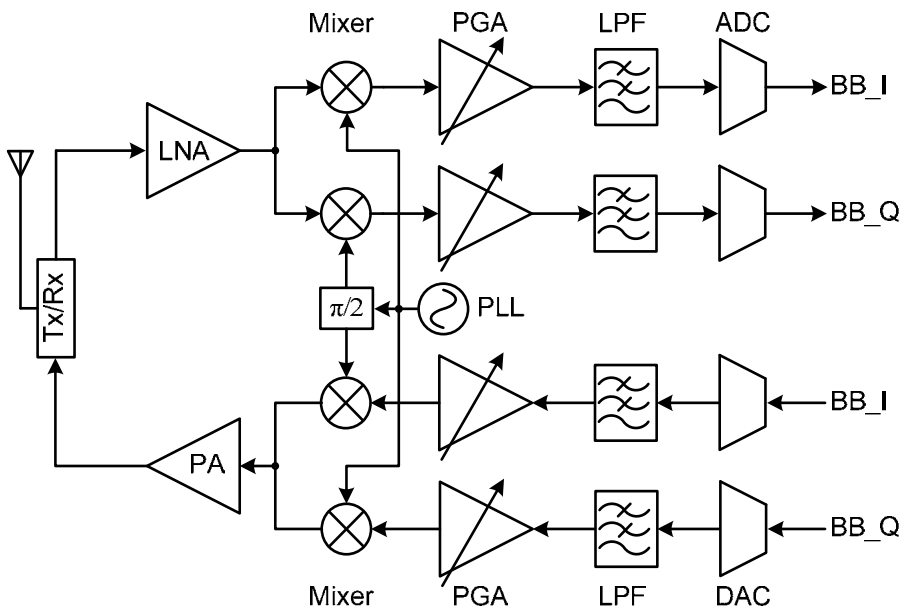

Fig. 2. Direct-conversion Transceiver

2.2 Pulse-based UWB

Unlike MB-OFDM UWB systems, pulse-based UWB systems are dealing with discrete pulses. There are many types of pulse modulation, such as OOK (On Off Keying), BPSK (Binary Phase Shift Keying) and PPM (Pulse Position Modulation), etc. As shown in Fig. 3, OOK modulation is performed by generating transmitted pulses only while transmitting '1' symbols. BPSK modulation generates 180° phase-shifted pulses while transmitting baseband symbols '1' and '0'. PPM modulation is performed by generating pulses at different phase delays. Therefore, BPSK has an advantage over other modulation types due to an inherent 3 dB increase in separation between constellation points (Wentzloff & Chandrakasan, 2006); however, BPSK modulation is not suitable for some receiver architectures, e.g., noncoherent receivers.

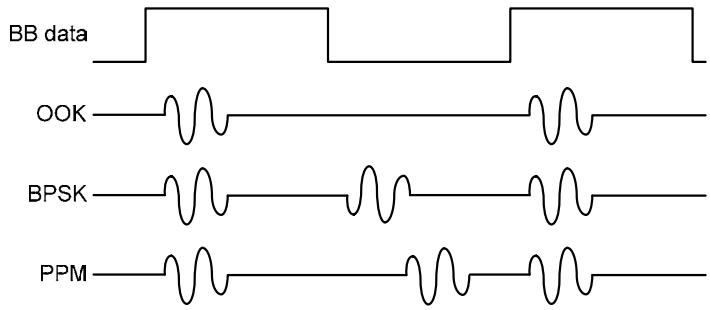

Fig. 3. Three commonly used pulse modulation

Pulse width is the duty cycle of a pulse in time domain, which is inversely proportional to the pulse bandwidth in frequency domain. The pulse width of a Gaussian pulse is defined as the pulse's temporal width at half of the maximum amplitude. As shown in Fig. 4, Gaussian pulse width is proportional to variance σ, the larger the σ is, the larger the pulse width and the smaller the signal bandwidth. For higher order Gaussian pulses, the pulse width is defined as the temporal width from the first to the last zero-crossing point.
Pulse repetition rate (PRR) is another important characteristic of the transmitted pulse,

$$f_p = n \cdot f_d \tag{2}$$

Where f_p is the pulse repetition rate, f_d is the baseband data rate, and n represents how many pulses are generated for each bit of information. If the PRR is doubled by increasing n or f_d, the transmitted power is elevated by 3 dB. Therefore, the IR-UWB transmitter needs gain control ability in order to satisfy the FCC spectral mask while transmitting at different pulse repetition rate. On the other hand, system throughput is limited by a high n. Therefore, high n is usually employed for low data rate systems where the goal is increased communication distance and improved BER.
Pulse UWB can be categorized into carrier-based DS-UWB (Zheng, Y. et al., 2007, 2008) and carrier-less IR-UWB (Lee, H. et al., 2005; Zheng, Y. et al., 2006; Xie et al., 2006; Phan et al., 2007; Stoica et al., 2005; Mercier et al., 2008). In a carrier-based pulse UWB system, the baseband pulse is up-converted to RF pulse by a mixer at the transmitter side, and vice verse at the receiver side, therefore a power consuming local oscillator is needed. In a carrier-less UWB system, no local oscillator is needed, the transmitted signal is up-converted

to RF band by performing differentiation on a Gaussian pulse; at the receiver side, the received pulse can be demodulated by down-sampling (Lee, H. et al., 2005), coherent (Zheng, Y. et al., 2006; Xie et al., 2006) or noncoherent (Phan et al., 2007; Stoica et al., 2005; Mercier et al., 2008) architectures.

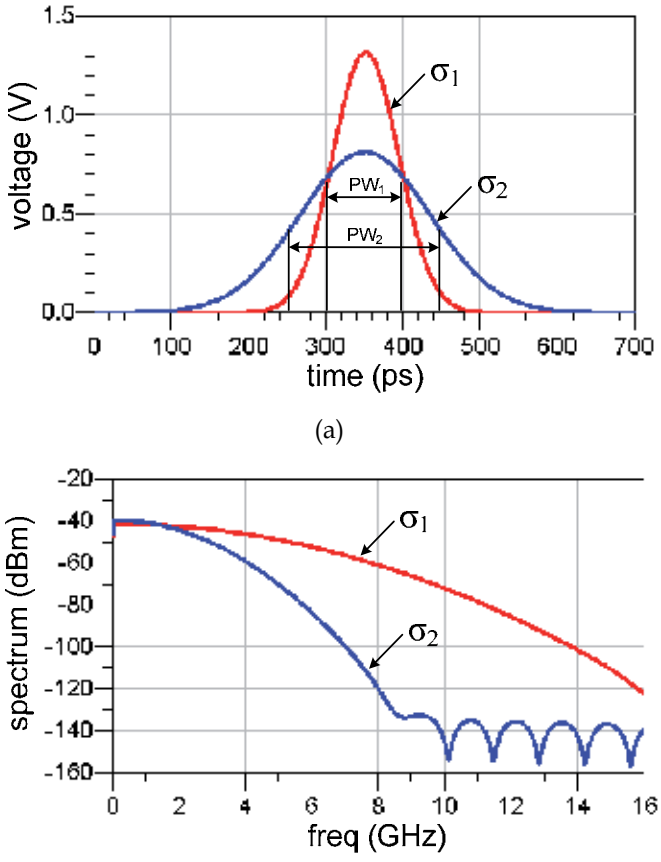

Fig. 4. Pulse width vs. bandwidth as $\sigma_1<\sigma_2$ (a) pulse width in time domain (b) signal bandwidth in frequency domain

2.2.1 Carrier-based pulse UWB transceivers

Both carrier-based pulse UWB and MB-OFDM UWB need local oscillators to perform frequency translation. As seen in Fig. 5, although these two systems are dealing with different kinds of signals, the receiver side consists of the same blocks as those in Fig. 2. The difference lies in the transmitter side, a pulse UWB transmitter needs no DAC, the digital baseband directly drives a pulse generator to generate a Gaussian pulse, and then the BB pulse is up-converted to RF band and transmitted through a UWB antenna after pulse shaping. Since the transmitted power spectral density is extremely low, power amplifier is optional in UWB systems. Although carrier-based pulse UWB still consumes significant power in LO signal generation, it has advantage in controlling the exact output spectrum.

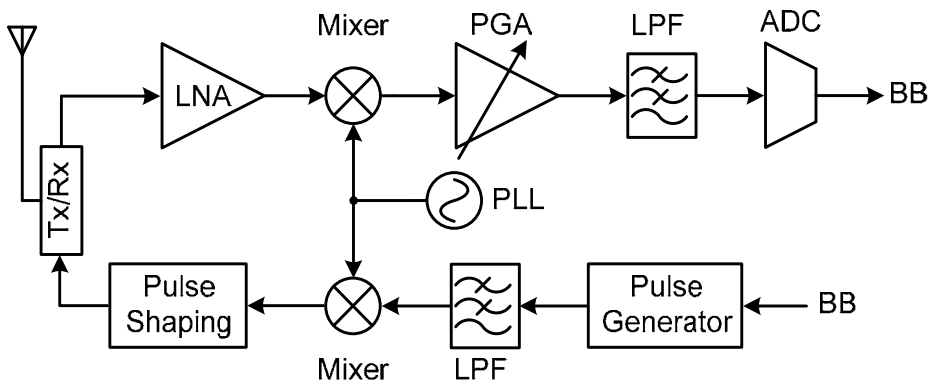

Fig. 5. Carrier-based pulse UWB

2.2.2 Carrier-less pulse UWB transceivers

Gaussian pulse is the most commonly used pulse shape in IR-UWB systems because of its good performance in frequency domain. The expressions for Gaussian pulse and its first order and second order differentiation are:

$$x(t) = \frac{A}{\sqrt{2\pi}\sigma}\exp(-\frac{t^2}{2\sigma^2}) \tag{3}$$

$$x'(t) = -\frac{At}{\sqrt{2\pi}\sigma^3}\exp(-\frac{t^2}{2\sigma^2}) \tag{4}$$

$$x''(t) = (\frac{At^2}{\sqrt{2\pi}\sigma^5} - \frac{A}{\sqrt{2\pi}\sigma^3})\exp(-\frac{t^2}{2\sigma^2}) \tag{5}$$

In time domain, the zero-crossing number increases as the differentiation order increases; while in frequency domain, the higher the differentiation order, the higher the center frequency with no significant change on the signal bandwidth, as shown in Fig. 6. Therefore, in an IR-UWB transmitter, frequency conversion is performed by differentiation of a Gaussian pulse, as show in Fig. 7, the transmitter consists of only a high order pulse generator and an optional power amplifier. An IR-UWB transmitter has the advantage of low complexity and low power; however, it also exhibits a big disadvantage of difficulty in controlling the exact output spectrum. Therefore, how to design a transmitter with tunable output spectrum is the main concern in IR-UWB systems.

IR-UWB receivers can be categorized into coherent receivers, noncoherent receivers, and down-sampling receivers. A down-sampling receiver resembles a soft-defined radio receiver. After being amplified by a low noise amplifier, the received signal is directly sampled by an ADC. In a coherent receiver, the received pulse correlates with a local pulse first to down-convert the RF pulse to BB, and then sampled by an ADC while in a noncoherent receiver the received pulse correlates with itself. These three architectures have different field of applications, and they will be discussed in detail in the following.

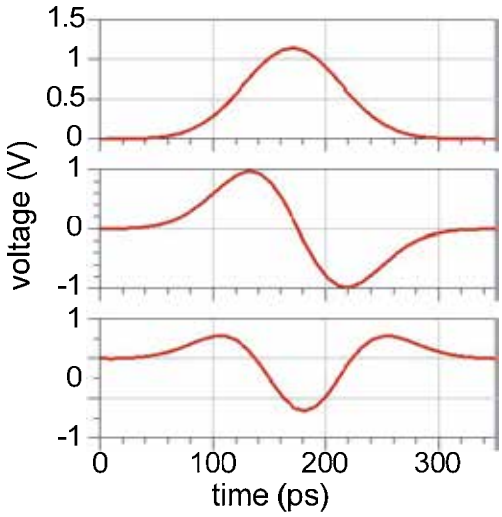

(a)

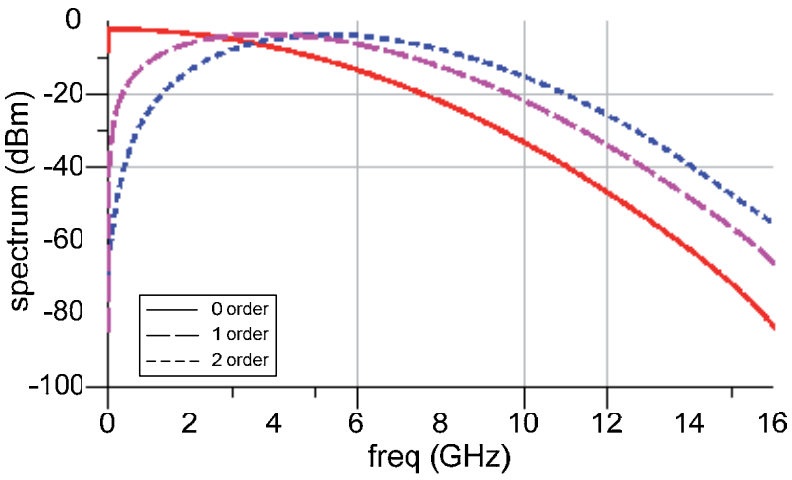

(b)

Fig. 6. Gaussian pulse and its differentiation (a) time domain (b) frequency domain

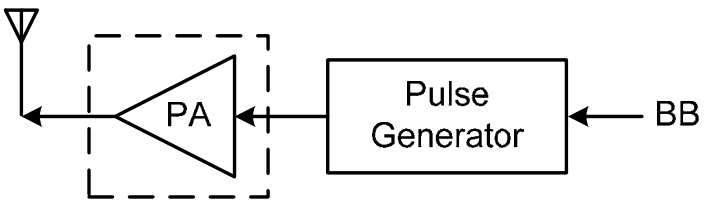

Fig. 7. IR-UWB transmitter

1. Down-sampling receivers

Fig. 8 is a down-sampling receiver (Lee, H. et al., 2005), although at first glance this architecture seems simple, it is seldom used in the 3-10.6 GHz frequency band for several reasons:

- It is very difficult to implement a high gain, ultra-wide bandwidth RF amplifier (at least 60 dB for 10 m transmission range), as it may easily oscillate and also consumes significant power;
- A high Q RF bandpass filter is not trivial. As mentioned earlier in 2.1.1, the requirement of a high Q off-chip BPF increases the cost. This problem also exists in a down-sampling IR-UWB receiver. As can be seen in Fig. 8, the ADC needs a high Q BPF to filter out the out of band interferences and noise to improve the dynamic range and linearity of the receiver and also to relax the stringent requirement on the ADC performance. Furthermore, the ultra-wideband impedance matching of the PGA output and the ADC input is also a big issue if an off-chip BPF is employed.
- A multi-gigahertz sampling rate ADC is very power consuming. According to Shannon theorem, for a signal bandwidth of 2 GHz (3-5 GHz frequency band), at least 4 GHz sampling rate is needed for down-sampling. Although 1 bit resolution may be sufficient (Yang et al., 2005), this ADC consumes significant power in the clock distribution of the high data rate communications.

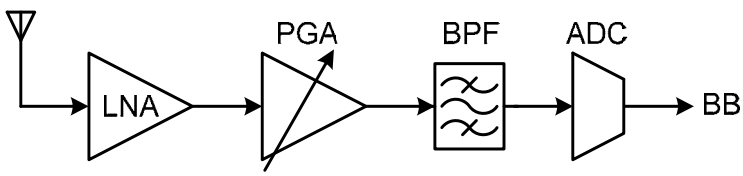

Fig. 8. Down-sampling IR-UWB receiver

2. Coherent and noncoherent receivers

Both coherent and noncoherent receivers correlate the received pulse first, such that the center frequency is down-converted to baseband. The difference is that in a coherent receiver, the received pulse correlates with a local template pulse; in a noncoherent receiver, the received pulse correlates with itself. Therefore, a noncoherent technique exhibits the disadvantage that the noise, as well as signal, is both amplified at the receiver (Stoica et al., 2005). Fig. 9 shows an ADS simulation comparison of the BER performance between a BPSK modulated coherent receiver and an OOK modulated noncoherent receiver within a non-multipath environment. As observed, a noncoherent receiver requires higher SNR than a coherent receiver for a fixed BER. However, the advantage of a noncoherent receiver is that it avoids the generation of a local pulse as well as the synchronization between the local and received pulses. As shown in Fig. 10, in order to obtain large enough down-converted signals for quantization, the local and received pulses must be synchronized within at least 100 ps in 3-5 GHz frequency band, which would be even tougher in 6-10 GHz frequency band. This precise timing synchronization can be achieved with a DLL or PLL which is very power consuming (Zheng, Y. et al., 2006; Sasaki et al., 2009). However, in a noncoherent receiver, only symbol level synchronization between the baseband clock and received data is needed with a resolution of ns.

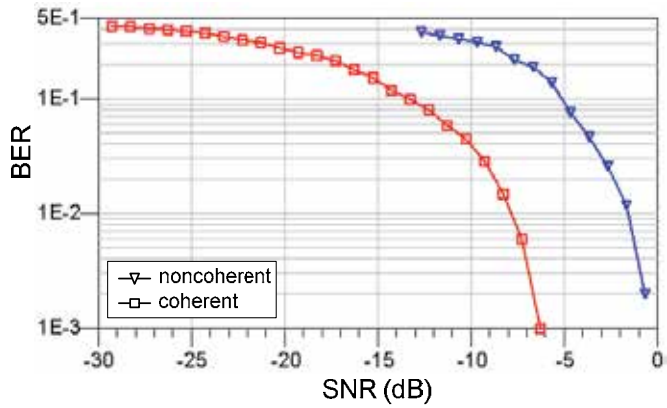

Fig. 9. Performance of a coherent receiver and a noncoherent receiver

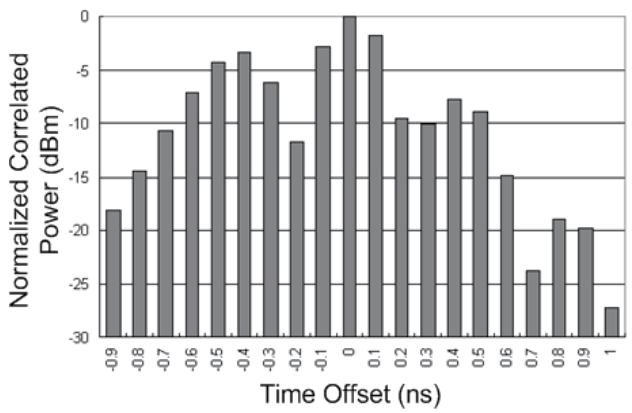

(a)

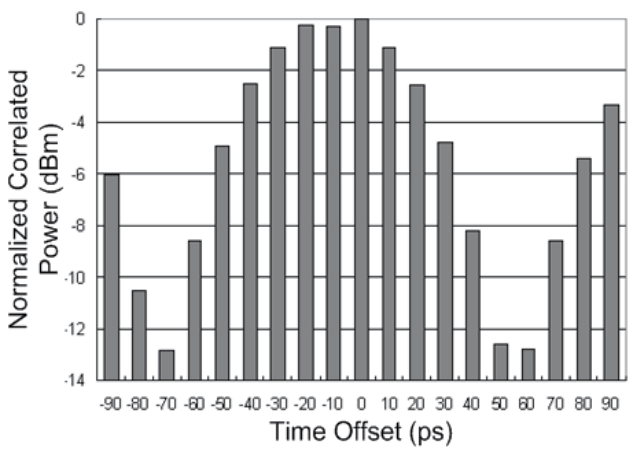

(b)

Fig. 10. Correlated power vs. time offset (between the received and local pulses) in a 3-5 GHz coherent receiver (a) every 100 ps (b) every 10 ps

3. Proposed RF transceiver for IR-UWB systems

Considering those advantages and disadvantages discussed above, a 3-5 GHz fully integrated IR-UWB transceiver is presented as shown in Fig. 11 (Xia et al., 2011). The transmitter integrates both amplitude and spectrum tunability, thereby providing adaptable spectral characteristics for different data rate transmission. The receiver employs noncoherent architecture because of its low complexity and low power.

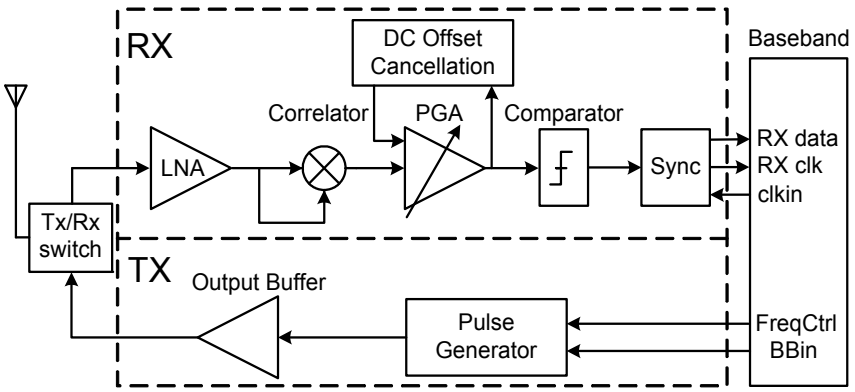

Fig. 11. The proposed IR-UWB transceiver system architecture with OOK modulation

3.1 Transmitter

Since a noncoherent receiver detects only the energy of the received pulses rather than the phase of the pulses, BPSK modulation is not suitable for the noncoherent receiver. Hence, the types of possible modulation are limited to OOK and PPM. In this design, OOK modulation is chosen, with BPSK modulation implemented for future coherent receiver design. The detailed transmitter implementation includes a pulse generator, output buffer, mode selection and power control blocks, as shown in Fig. 12.

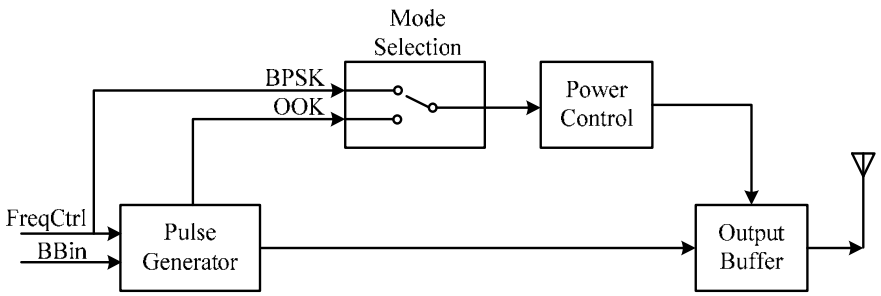

Fig. 12. The proposed IR-UWB transmitter

3.1.1 Pulse generator

Basically, there are two categories of pulse generators, the analog pulse generator and the digital pulse generator. In (Zheng, Y. et al., 2006), an analog pulse generator is designed employing the square and exponential functions of transistors biased in saturation and weak

inversion region, respectively. The main disadvantage of this method is that the amplitude of the output pulse is very small; an ultra-wideband amplifier is thus needed. The basic concept of a digital pulse generator is to combine the edges of a digital signal and its inverted signal to form a very short duration pulse, and then a differential circuit is used to up-convert the signal. Except using a differential circuit, (Kim & Joo, 2005) presents another way to up-convert the signal. Four pulses are combined successively to form a fifth derivative Gaussian pulse. This method eliminates the inductor used in the differential circuit which consumes the majority portion of chip area. Unfortunately, this method severely suffers from the process variations. All these previous pulse generators have difficulty in controlling the exact pulse shape and its spectrum. In this design, an amplitude and spectrum tunable pulse generator is introduced to solve this problem (Xia et al., 2008).

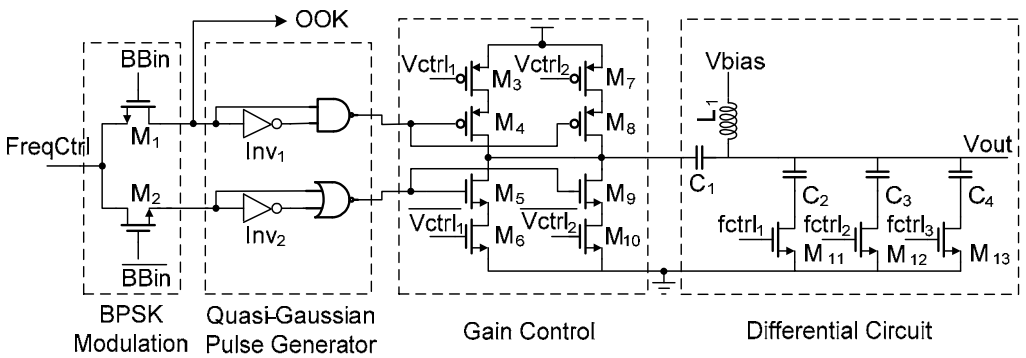

Fig. 13. The proposed pulse generator

As can be seen in Fig. 13, BBin is the baseband input signal and FreqCtrl is a square-wave signal that determines the PRR of the transmitted pulses. M_1 and M_2 realize the BPSK modulation as selecting the upper path when BBin is high and selecting the lower path when BBin is low. When OOK modulation is chosen, only those pulses generate by the upper path is sent to the antenna by the power-controlled output buffer. M_3-M_{10} are employed to implement 3-step amplitude control of the pulses, thereby enabling adaptable output spectral density in order to meet the FCC spectral mask at different data rate. 4-step spectrum control is also realized by control signals $fctrl_{1\text{-}3}$ showing a measured frequency tuning range of 3.2-4.1 GHz.

3.1.2 Power-controlled output buffer

Since the transmitted power spectral density of UWB is extremely low, the power amplifier is optional in the transmitter. In this design, an output buffer is implemented to drive the antenna. As shown in Fig. 14(a), the cascode structure is employed to improve the input-output isolation. R2 is the 50 ohms impedance of a UWB antenna. Since the signal of pulse UWB is inherently duty-cycled, the output buffer can be disabled during the pulses intervals to save power. M16 is a large scale PMOS switch with a gate control signal rst generated by the power control block. C6 is a large capacitor to suppress the unwanted pulse generated by switching on/off. The power control block is shown in Fig. 14(b). M5 and M8 are used to control the charging and discharging current, thus controlling the delay time of the inverter. The biasing circuit is also shown in the figure. When BPSK is slected, the power control

block turns the output buffer on before the rising edge of the signal FreqCtrl and lasts for about 2 ns, regardless of whether BBin is high or low, as observed in Fig. 14(c); otherwise, when OOK is selected, the output buffer is enabled only when BBin is high. Therefore, the introduction of the power control block means that the transmitter power consumption is proportional to the data rate.

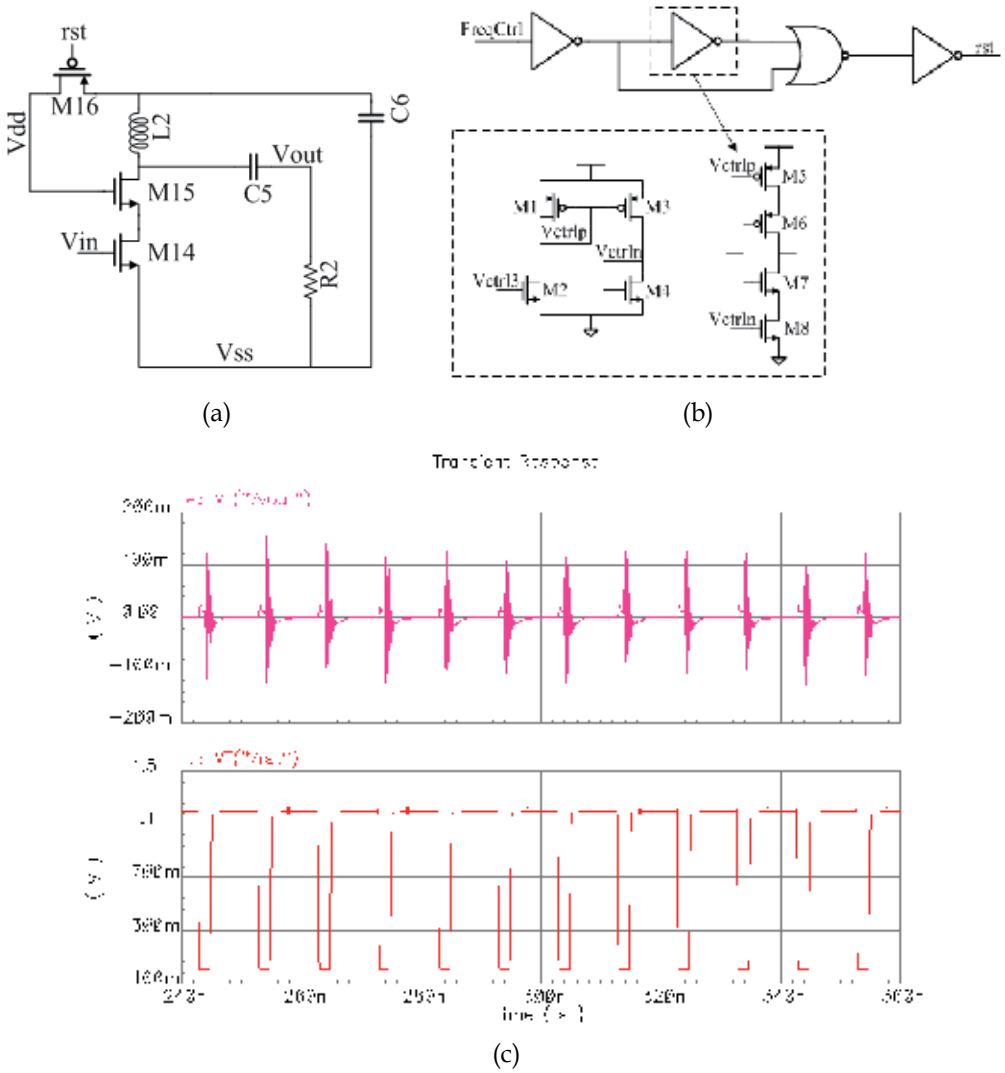

Fig. 14. Power-controlled output buffer (a) output buffer (b) power control block (c) transient simulation results

3.2 Receiver

The proposed IR-UWB receiver employs the noncoherent receiver architecture as shown in Fig. 11. After first being amplified by the low noise amplifier (LNA), the received pulse is then self-correlated by a correlator, amplified by a programmable gain amplifier (PGA), and

then sent to a comparator for digital quantization. Finally the received data is synchronized with the baseband clock.

3.2.1 Low noise amplifier

A UWB low noise amplifier needs to provide reasonable noise figure (NF) and impedance matching as well as a very large bandwidth. Hence, the design of a UWB LNA is more challenging than a traditional narrow-band LNA. Furthermore, wideband receivers typically incorporate single-ended inputs (Mastantuono & Manstretta, 2009) that remove the loss of the passive balun but also deteriorate the second-order distortion. In order to compromise these limitations, a single-ended LNA with a following active balun is implemented. As shown in Fig. 15(a), the single-ended LNA employs both current-reuse and staggered tuning techniques - using a common-source stage stacked on top of a common-gate input stage with different resonance frequencies (Weng & Lin, 2007). Inductor L_1 resonates out the parasitic capacitances at the drain of transistor M_1 at 3 GHz while also isolating the source of M_2 from the drain of M_1. Inductor load L_d of the common-source stage resonates at 5 GHz such that the output of the LNA covers the frequency range of 3-5 GHz. As shown in Fig. 15(b), the output load of M_1 can be approximated to

$$Z_1 = sL_1 \,||\, \frac{1}{sC_c} \tag{6}$$

where, $C_c = C_2 C_{gs2} / (C_2 + C_{gs2})$, and the resonance frequency of the common-gate and common-source stages are

$$f_L = \frac{1}{2\pi}\sqrt{\frac{1}{L_1 C_c}} \tag{7}$$

$$f_H = \frac{1}{2\pi}\sqrt{\frac{1}{L_d C_x}} \tag{8}$$

where, $C_x = C_{gd2} + C_{gd3} + C_{gs4}$.

Transistor M_3, which is parallel with M_2, provides gain control tunability. If M_3 is switched on, the bias current for M_1 increases, thereby increasing g_{m1}. The measured gain variation of the high gain and low gain mode is 7.5 dB.

A two-cascode stage active balun is used to convert the single-ended output of the LNA to differential signals. The output of M_4 connects to M_6 and the input of the second cascode. Since v_{gs5}=-v_{gs6}, two balanced differential outputs can be achieved if g_{m5}=g_{m6}. The maximum gain and phase mismatch of the balanced outputs in 3-5 GHz are 0.3 dB and 2.8°, respectively, as observed from post-extracted layout simulation.

3.2.2 Correlator

The output of the LNA must be correlated - multiplied and then integrated in order to detect the energy of the received signal. Previous correlators used in both coherent receivers (Zheng, Y.et al., 2006, Liu et al., 2009) and noncoherent receivers (Lee, F.S. et al., 2007) needs

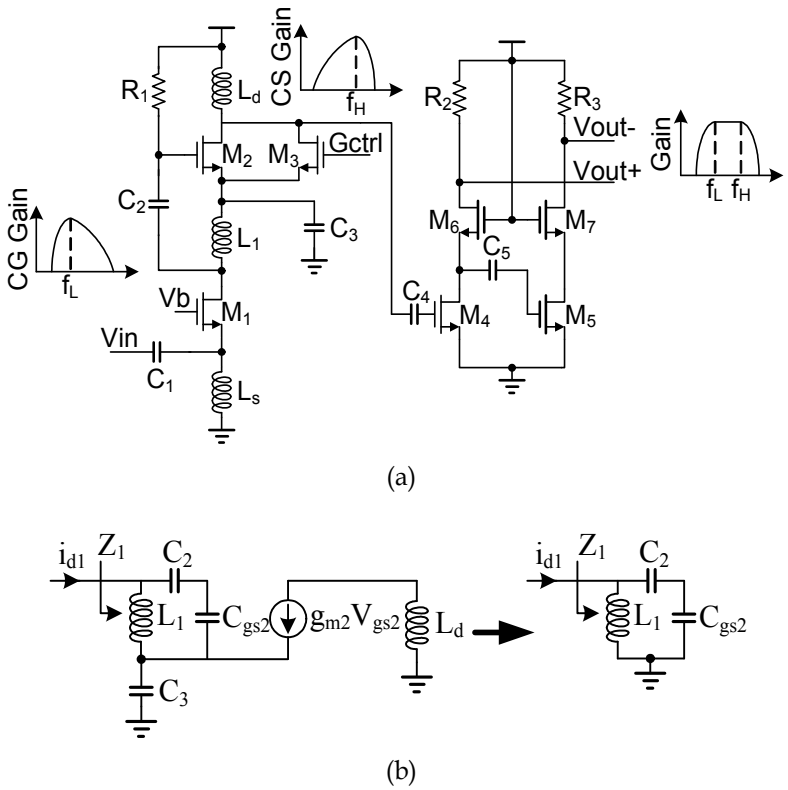

Fig. 15. Low noise amplifier and active balun (a) circuit implementation (b) small signal model of Z_1

to synchronize the received pulse with local controlling signals first. This synchronization process is analogous to the RF front-end synchronization in a coherent receiver requiring a strict timing resolution. In this design, the duty-cycled characteristic of the IR-UWB system is used to remove the timing synchronization. Fig. 16(a) presents the proposed multiplier and integrator-merged correlator. The multiplier employs a Gilbert topology, while the integrator is realized by capacitors C_1 and C_2. As shown in Fig. 16(b), after the pulse is multiplied with itself, the integrator begins to integrate, and between the pulses intervals, the integrator starts to discharge and ready for the next integration. C_1 and C_2 should be large enough to hold the integrated voltage for the comparator and yet small enough to discharge between pulses intervals in order to be ready for the next integration. The main limitation of the proposed correlator is that in order to get quantized signal with enough duty cycle, the reference voltage level of the comparator must be set to a lower level than that for a conventional correlator, inevitably sacrificing SNR of the receiver. As shown in Fig. 17, Vref and Vmax represent the reference voltage of the comparator and the maximum output voltage of the correlator, respectively. The SNR reduces by 2.64 dB as Vref is set to half of the Vmax. However, implementation complexity and power consumption are greatly reduced with the proposed technique and the noise introduced by sampling can be eliminated. Furthermore, this SNR reduction can be relaxed by introducing a proceeding programmable gain amplifier.

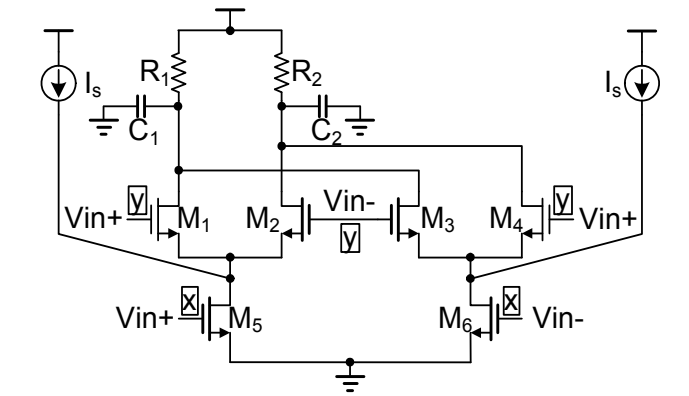

(a)

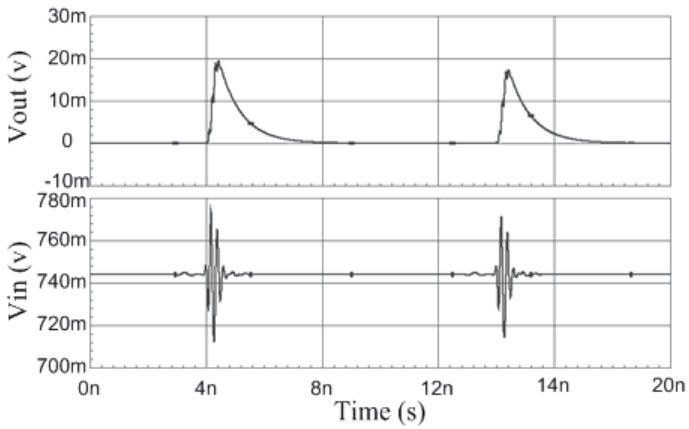

(b)

Fig. 16. Correlator (a) circuit implementation (b) simulation result

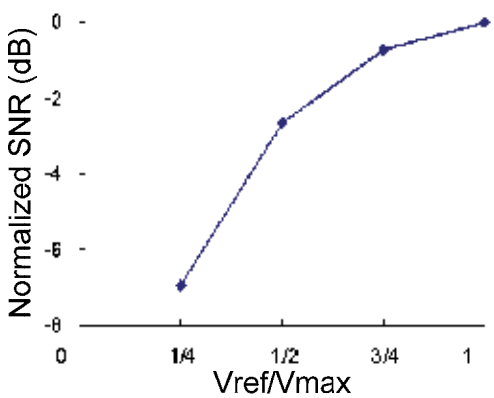

Fig. 17. SNR reduction due to the proposed correlator

3.2.3 Programmable gain amplifier

The PGA is critical in the receiver in order to increase the dynamic range of the system and also complement the SNR reduction in the proposed correlator. The proposed PGA consists of a fixed gain stage, an 8-step gain stage and a DC-offset cancellation circuit. Fig. 18 shows the 8-step wideband source degeneration programmable gain stage. The transconductance of the first stage is $1/(Rs_1+Rs)$, in which Rs_1 is the resistance looking into the source of M_1. By varying the value of Rs, a variable gain is realized. The linearity of this amplifier is determined by Rs_1, where a smaller Rs_1 results in better linearity performance. In Fig. 18, a negative feedback through M_3 is employed (Helleputte et al. 2009), allowing Rs_1 to be reduced to $g_{o1}/(g_{m1}g_{m3})$, greatly improving the linearity. The degeneration resistance Rs is controlled by 3-bit digital words to realize the 8-step gain control, with a minimum step size of 3 dB.

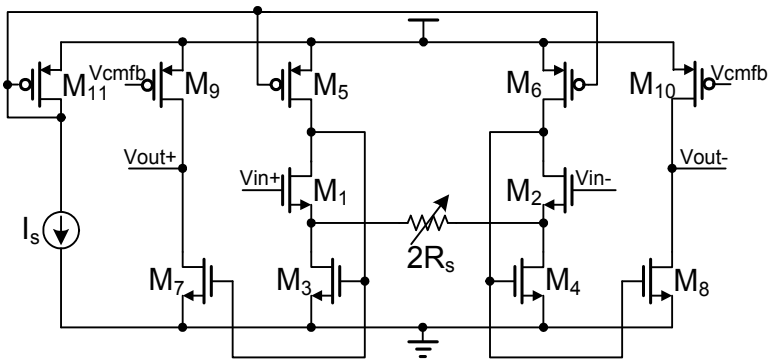

Fig. 18. 8-step programmable gain amplifier

3.2.4 Comparison and synchronization

After the received signal is squared and integrated by the correlator, a comparator compares it with a reference voltage and performs digital quantization. However the comparator output is a return-to-zero (RZ) signal which needs to be converted to a non-return-to-zero (NRZ) signal that can synchronize with the baseband clock. In a coherent receiver, a DLL/PLL is usually introduced to perform synchronization between the received pulse and the local pulse, needing precision on the order of several tens of picoseconds. However, in a noncoherent receiver, the RZ signal quantized by the comparator exhibits a duty cycle on the order of ns. Therefore, a low jitter DLL/PLL is no longer necessary and a sliding correlator is employed. The digital synchronization circuit is shown in Fig. 19, where clkin, comp_out, RX clk and RX data are the baseband clock, the comparator output, the recovered baseband clock and the recovered data, respectively. With a reset signal, the delay line control signal dctrl is set to 0, such that there is no delay between the RX clk and clkin. Then the Sync block starts operation, and RX clk samples comp_out. If the RX clk is not synchronized with comp_out, the decision block enables the counter that increases the value of dctrl -- thus elongating the latency of the delay line until RX clk and comp_out are synchronized. The inevitable frequency offset between the baseband clock of the transmitter and receiver can be compensated by the digital baseband circuit, which is out of the discussion of this paper. During the measurement, the same clock source is used to get rid of the frequency offset.

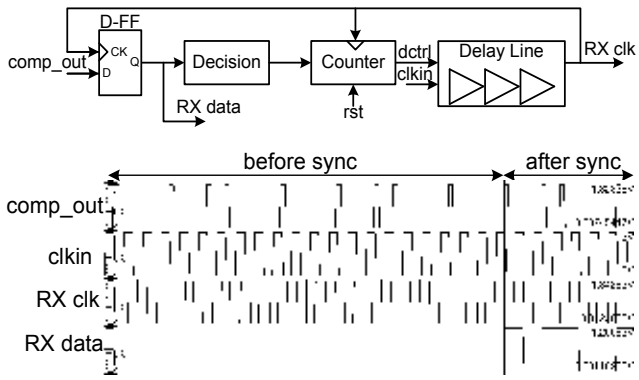

Fig. 19. Clock and data synchronization

4. Measurement results

The proposed IR-UWB transceiver is implemented in a 0.13 μm 1P8M CMOS technology. The transceiver die microphotograph is shown in Fig. 20. The die area is 2 mm×2 mm. The chip is bonded to the 4-layer FR-4 PCB with chip-on-board (COB) assembly. With a supply voltage of 1.2 V, the power consumption of the transmitter is only 1.2 mW and 2.2 mW when transmitting 50 Mb/s and 100 Mb/s baseband signals, respectively; the power consumption of the receiver is 13.2 mW.

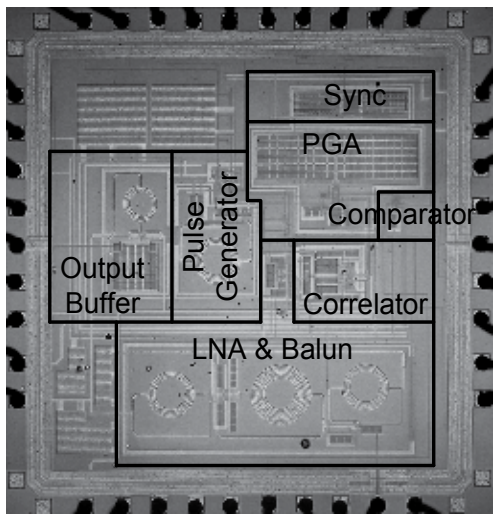

Fig. 20. Microphotograph of IR-UWB transceiver

Fig. 21 shows OOK and BPSK modulated pulses. Baseband data (BBin) and clock (FreqCtrl) are generated by FPGA, and the output of the transmitter is measured with high sampling rate oscilloscope. As can be seen, with OOK modulation, pulses are generated only when transmitting symbols '1'; and with BPSK modulation, pulses are generated every clock cycle with polarity shift depending on the transmitting symbols. The amplitude and spectrum tunable transmitter has output pulses with peak-to-peak voltage of 240 mV, 170 mV and 115

mV and the frequency center of the spectrum has a tuning range of 3.2-4.1 GHz. Fig. 22 shows the transmitted spectrum with pulse amplitude of 240 mV at data rate of 50 Mb/s and 100 Mb/s, respectively. As can be seen, the transmitted power increases by approximately 3 dB while the data rate is doubled. Hence, the amplitude of the transmitted pulses should be optimized in order to meet the FCC spectral density. The transmitted power at low frequency range is introduced by the switch in output buffer, and it can be filtered by off-chip filter and UWB antenna.

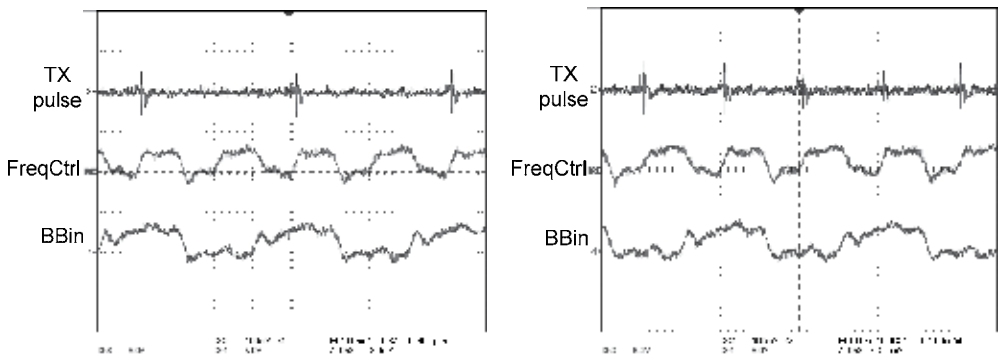

(a) (b)

Fig. 21. OOK/BPSK transmitter (a) OOK modulation (b) BPSK modulation

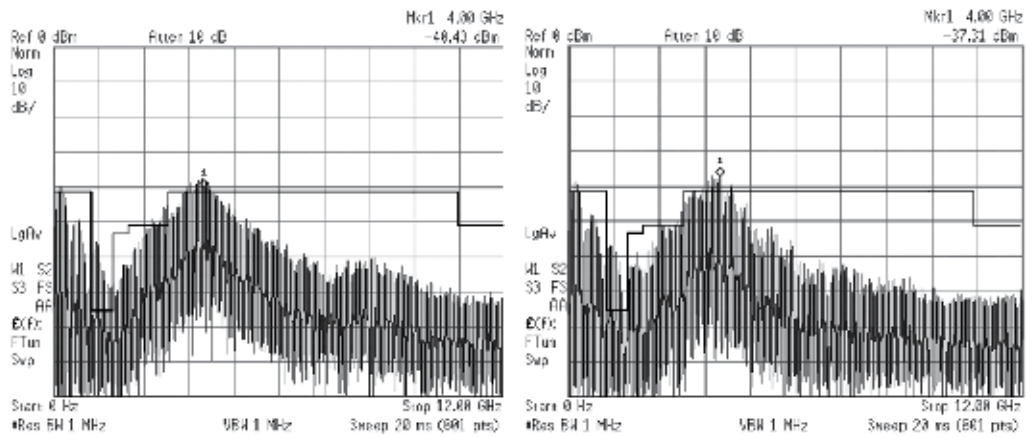

(a) (b)

Fig. 22. Transmitted Spectrum with maximum pulse amplitude at data rate of (a) 50 Mb/s (b) 100 Mb/s

The receiver provides a total gain ranging 43-70 dB, in which the LNA exhibits a gain variation of 7.5 dB in high/low gain mode; the PGA incorporates an 8-step, 3-dB gain control with an rms error of 0.7 dB. The receiver shows a minimum noise figure of 8.6/13.3 dB while operating in high/low gain mode, with a noise figure variation less than 2 dB in the 3-5GHz frequency band, as shown in Fig. 23. The 1-dB compression point of the receiver is -28/-22 dBm in high/low gain mode.

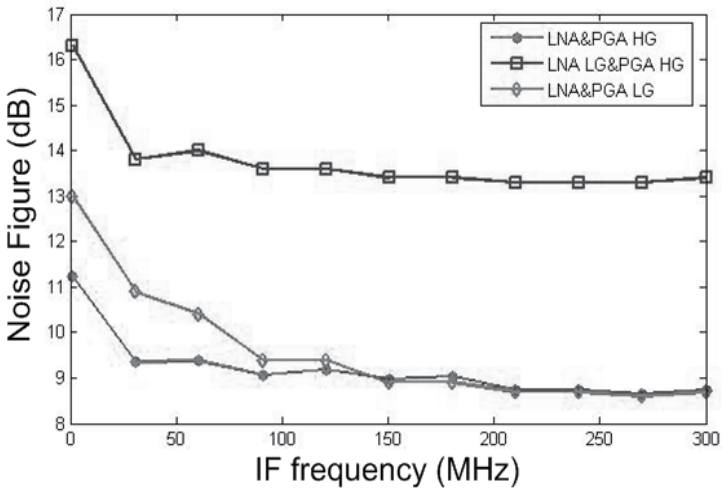

Fig. 23. Noise figure of the receiver

BER performance of the receiver with n of 1 is measured by transmitting 50 Mb/s random data from FPGA. The employed antennas are 3-5 GHz monopole omnidirectional antennas, manufactured by Fractus Corporation. As can be seen in Fig. 24, with transmitted amplitude of 115 mV, the received pulses are attenuated to only 20.4 mV (-50 dBm) and 6.4 mV (-61 dBm) when the distance between the antennas is 1 cm and 10 cm, respectively. The receiver achieves a BER of 10^{-3} when the distance between the antennas is set to 1 cm (-50 dBm). While the distance extends to 10 cm (-61 dBm), the BER performance is greatly deteriorated to over 10^{-2}. As shown in Fig. 25, the TX pulse is OOK modulated, every pulse represents bit 1 at baseband. The received pulses are correlated and then amplified by the PGA, where PGA out is the buffered output of the PGA. A bit error occurred in the synchronized RX data as the received pulses are distorted by the antennas and the transmission channel.

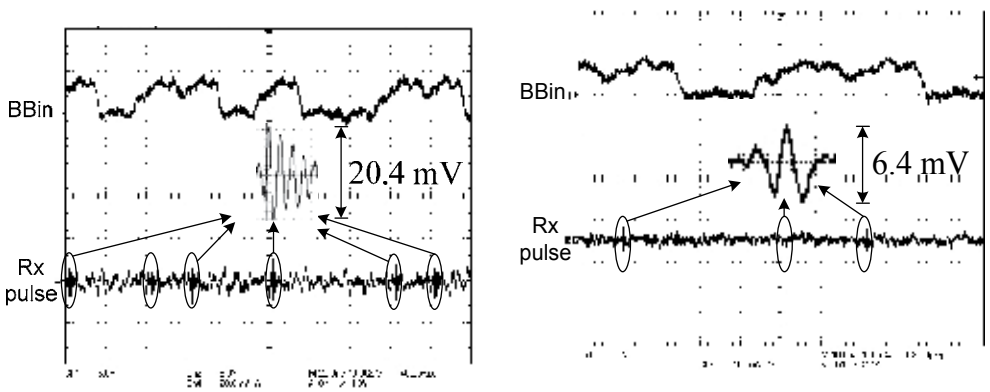

(a) (b)

Fig. 24. Received pulses (a) 1 cm (b) 10 cm

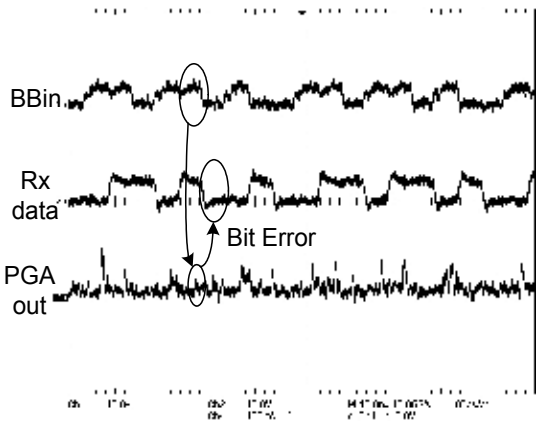

Fig. 25. BER performance of the receiver when the distance between the antennas is 10 cm

A summary of the measured results and a comparison with previously published papers is shown in Table 1.

Paper	Zheng, Y. et al. 2006	Mercier et al. 2009 Lee, F.S. et al. 2007	Crepaldi, M. et al. 2010	This work
Band	3-5 GHz	3-5 GHz	3.6-4.3 GHz	3-5 GHz
Data rate	400 Mb/s	16.7 Mb/s	1 Mb/s	100 Mb/s
Modulation	PPM	PPM	S-OOK	OOK
TX pulse amp.	195 mVpp	370 mVpp	610 mVpp	240 mVpp
TX pulsewidth	1.5 ns	/	2.0 ns	1.0 ns
RX Arch.	coherent	noncoherent	noncoherent	noncoherent
RX NF	7.7-8.1 dB	8.5-9.5 dB	/	8.6 dB
RX Gain	83.5 dB	40 dB	/	70 dB
$IP_{1\text{-}dB}$	-22 dBm	-45 dBm	/	-28 dBm
Sensitivity	-80~-72 dBm	-99 dBm @10^{-3}	-60~-66 dBm@10^{-3}	-50 dBm @10^{-3} -61 dBm @10^{-2}
Power Consumption	0.19nJ/pulse(TX) 0.2nJ/pulse(RX)	43pJ/pulse(TX) 2.5nJ/pulse(RX)	65pJ/pulse+184 μW(TX) 134.5pJ/pulse(RX)	22pJ/pulse(TX) 0.13nJ/pulse(RX)
Chip Area	2.6 mm×1.7 mm	0.2mm×0.4mm(TX) 1 mm×2.2 mm(RX)	0.6 mm^2 (TX) 1 mm^2 (RX)	2 mm×2 mm
Process	0.18 μm CMOS	90 nm CMOS	90 nm CMOS	0.13 μm CMOS

Table 1. Summary of the transceiver performance and comparison

5. Conclusion

A low power 3-5 GHz IR-UWB transceiver system with maximum data rate of 100 Mb/s is presented in this paper. The power consumption of the transmitter and receiver is 22 pJ/pulse and 0.13 nJ/pulse, respectively. The transmitter implementation is based on a

former design and can realize OOK/BPSK modulation, where both the amplitude and spectrum of the output pulses are tunable. The introducing of a power control block in transmitter improves the power efficiency of the output buffer. In the receiver, a noncoherent technique is adopted for its low power and low complexity. A single to differential LNA with active balun is designed to eliminate off-chip balun. The correlator eliminates the sample-and-hold circuit to greatly simplify the circuit implementation. At baseband front-end, a synchronization circuit is implemented to have the data and clock synchronized at the output of the receiver. However, the duty-cycled characteristic of IR-UWB system is not utilized in the receiver to further reduce the power consumption. And lacking of low pass filter in the receiver could also deteriorate the performance. These should be improved in the future research.

6. Acknowledgment

This work was supported by 863 project of China under Grant SQ2008AA01Z4473469.

7. References

Beek, R.; Bergervoet J.; Kundur, H. et al. (2008). A 0.6-to-10GHz receiver front-end in 45nm CMOS, *IEEE International Solid-State Circuits Conference*, 2008, pp. 128-129

Bergervoet, J.R.; Harish, K.S.; Lee, S. et al. (2007). A WiMedia-compliant UWB transceiver in 65nm CMOS, *IEEE International Solid-State Circuits Conference*, 2007, pp. 112-113

Crepaldi, M. et al. (2010). An Ultra-low-power interference-robust IR-UWB transceiver chipset using self-synchronizing OOK modulation", *IEEE International Solid-State Circuits Conference*, 2010, pp. 226-227

Gu Q. (2005). *RF system design on transceivers for wireless communications*, Springer, ISBN 0-387-24161-2, United States of America

Helleputte, N.V. & Gielen G. (2009). A 70 pJ/pulse analog front-end in 130 nm CMOS for UWB Impulse Radio Receivers, *IEEE Journal of Solid-State Circuits*, Vol. 44, No. 7, July 2009, pp. 1862-1871

Kim, H.; Joo, Y. (2005). Fifth-derivative Gaussian pulse generator for UWB system, *IEEE Radio Frequency Integrated Circuits Symposium*, 2005, pp.671-674

Lee, F.S. & Chandrakasan, A.P. (2007). A 2.5 nJ/b 0.65V 3-to-5GHz subbanded UWB receiver in 90nm CMOS, *IEEE Journal of Solid-State Circuits*, 2007, pp. 116-117

Lee, H.; Lin, C.; Wu, C. et al. (2005). A 15mW 69dB 2Gsample/s CMOS analog front-end for low-band UWB applications, *IEEE International Symposium on Circuits and Systems*, 2005, pp. 368-371

Liu, L.; Sakurai, T. & Takamiya M. (2009), A 1.28mW 100Mb/s impulse UWB receiver with charge-domain correlator and emedded sliding scheme for data synchronization, *Symposium on VLSI Circuits*, 2009, pp. 146-147

Mastantuono, D. & Manstretta D. (2009). A Low-noise active balun with IM2 cancellation for multiband portable DVB-H receivers, *International Solid-State Circuits Conference*, 2009, pp. 216-217

Mercier P.P.; Daly, D.C.; Bhardwaj, M. et al. (2008). Ultra-low-power UWB for sensor network applications, *IEEE International Symposium on Circuits and Systems*, 2008, pp. 2562-2565

Phan, T.; Krizhanovskii, V. & Lee, S.G. (2007). Low-power CMOS energy detection transceiver for UWB impulse radio system, *IEEE Custom Integrated Circuits Conference*, 2007, pp. 675-678

Ranjan, M. & Larson, L. (2006). A sub-1mm2 dynamically tuned CMOS MB-OFDM 3-to-8GHz UWB receiver front-end, *IEEE International Solid-State Circuits Conference*, 2006, pp. 128-129

Sasaki, N.; Kimoto, K.; Moriyama, W. et al. (2009). A single-chip ultra-wideband receiver with silicon integrated antennas for inter-chip wireless interconnection, *IEEE Journal of Solid-State Circuits*, Vol. 44, No. 2, February 2009, pp. 382-392

Stoica, L.; Rabbachin, A.; Repo, H.O. et al. (2005). An ultrawideband system architecture for tag based wireless sensor networks, *IEEE Transactions on Vehicular Technology*, Vol. 54, No. 5, September 2005, pp. 1632-1645

Weng, R. & Lin P. (2007). A 1.5-V low-power common-gate low noise amplifier for ultrawideband receivers, *International Symposium on Circuits and Systems*, 2007, pp. 2618-2621

Wentzloff, D.D. & Chandrakasan, A.P. (2006). Gaussian pulse generators for subbanded ultra-wideband transmitters, *IEEE Transactions on Microwave Theory and Techniques*, Vol. 54, No. 4, April 2006, pp. 1647-1655

Wikipedia. (2010). Shannon-Hartley theorem, http://en.wikipedia.org/wiki/Ultra-wideband

Xia, L; Huang, Y. & Hong, Z. (2008). Low power amplitude and spectrum tunable IR-UWB transmitter, *Electronics Letter*, Vol. 44, No. 20, September 2008, pp. 1200-1201

Xia, L.; Shao, K.; Chen, H. et al. (2010). 0.15-nJ/b 3-5-GHz IR-UWB system with spectrum tunable transmitter and merged-correlator noncoherent receiver, *IEEE Transactions on Microwave Theory and Techniques,* Vol. 59, No. 4, April 2011, pp. 1147-1156

Xie, H.L.; Fan, S.Q.; Wang, X. et al. (2006). An ultra-low power pulse-based UWB transceiver SoC with on-chip ADC, *IEEE International Midwest Symposium on Circuits and Systems*, 2006, pp. 669-673

Yang, C.; Chen, K. & Chiueh, T. (2005). A 1.2V 6.7mW impulse-radio UWB baseband transceiver, *International Solid-State Circuits Conference*, 2005, pp. 442-443

Zheng, H.; Lou, S.; Lu, D. et al. (2007). A 3.1-8.0GHz MB-OFDM UWB transceiver in 0.18μm CMOS, *IEEE Custom Integrated Circuits Conference*, 2007, pp. 651-654

Zheng, Y.; Tong, Y.; Ang, C.W. et al. (2006). A CMOS carrier-less UWB transceiver for WPAN applications, *IEEE International Solid-State Circuits Conference*, 2006, pp. 116-117

Zheng, Y.; Wong, K.W.; Asaru, M.A. et al. (2007). A 0.18μm CMOS dual-band UWB transceiver, *IEEE International Solid-State Circuits Conference*, 2007, pp. 114-115

Zheng, Y.; Arasu, M.A; Wong, K.W. et al. (2008). A 0.18μm CMOS 802.15.4a UWB transceiver for communication and localization, *IEEE International Solid-State Circuits Conference*, 2008, pp. 118-119

7

Ultra Wideband Impulse Radio Superregenerative Reception

F. Xavier Moncunill-Geniz, Pere Palà-Schönwälder, Jordi Bonet-Dalmau,
Francisco del Águila-López and Rosa Giralt-Mas
Universitat Politècnica de Catalunya
Spain

1. Introduction

Since the superregenerative (SR) receiver was invented by E. H. Armstrong in 1922 (Armstrong, 1922), it has been used in myriad applications. In the 1930s, it came into widespread use by radio amateurs as an economical communications receiver. Various *walkie-talkie* communications devices were developed based on SR receivers, exploiting their light weight and low cost. With the advent of World War II, the circuit was mass-produced as a pulse responder for radar identification of ships and aircraft (Identification, Friend or Foe (I.F.F.)) (Whitehead, 1950). As the transistor replaced the vacuum tube, the superheterodyne receiver, characterized by improved selectivity, relegated SR receivers to very specific applications, such as altitude and Doppler radar (Levanon *et al*., 1974; Milner & Shell, 1968), and solar-powered devices (McCoy, 1992). Superregenerative receivers have also harnessed for optical communications (España & Puerta, 1999).

Currently, SR receivers are chiefly used in short-distance radiofrequency (RF) links, which demand low cost and low power consumption. These include remote control systems (*e.g.* garage-door openers, robotics, and radio-controlled toys), short distance telemetry, and wireless security (Hickman, 2002; Telecontrolli, 2011). These receivers are typically used as narrowband AM receivers and, occasionally, as FM receivers. Superregenerative receivers have recently garnered renewed attention for their integration into CMOS, which, when combined with modern digital techniques in mixed-signal designs, improves performance implementations (Favre *et al*., 1998; Chen *et al*., 2007). Thus, SR receivers are a promising alternative to other architectures in emerging applications such as wireless sensor networks and medical devices (Ayers *et al*., 2010, Bohorquez *et al*., 2009; Otis *et al*., 2005). Recent proposals for their use include: reception of spread spectrum, phase and frequency modulations (Ayers *et al.* 2010, Moncunill *et al*., 2005b; Palà *et al*., 2009); use of stable frequency references such as bulk-acoustic-wave (BAW) resonators (Otis *et al*., 2005); implementation of digital self-calibrating techniques (Chen *et al*., 2007); and, very recently, reception of ultra wideband impulse radio (UWB IR) modulations (Anis *et al*., 2008; Moncunill *et al*., 2007b; Moncunill *et al*., 2009; Pelissier *et al*., 2009; Thoppay, 2010).

In this chapter, we analyze the suitability of SR receivers for UWB IR communications. In Section 2, we provide basic concepts on the principle of superregeneration. In Section 3, we present several SR architectures and assess their amenability to UWB IR signal detection. In Section 4, we characterize the superregenerative oscillator as a pulse filter and amplifier with characteristic parameters and functions. In Section 5, we outline the features that

superregenerative oscillators require for use as a UWB IR receiver. In Section 6, we assess the expected performance from these types of receivers, and finally, in Section 7, we present the main conclusions from this chapter.

2. The principle of superregeneration

The block diagram of a typical SR receiver is shown in Fig. 1 (a). The input and output variables of each block are represented by voltages, although depending on the particular circuit, some of these variables may be physical currents. The core of the receiver is a superregenerative oscillator (SRO), an RF oscillator that can be modeled as a frequency selective network or resonant circuit fed back through a variable-gain amplifier (Moncunill *et al.*, 2005a). The gain of the amplifier is controlled by a low-frequency quench generator or quench oscillator, which causes the circuit to become alternatively unstable and stable, with the RF oscillations rising and falling repeatedly. As shown in Fig. 1 (b), the signal generated in the SRO (v_o) comprises a series of RF pulses separated by the quench period T_q, in which the periodic build-up of the oscillations is controlled by the input signal (v). In the linear mode of operation, the oscillations are damped before reaching their limiting equilibrium amplitude, and their peak amplitude is proportional to that of the injected signal. In the logarithmic mode, the amplitude of the oscillations is allowed to reach its limiting equilibrium value, which is determined by the non-linearity of the active devices. In this mode, the amplitude of the RF pulses remains constant, but the incremental area under the envelope is proportional to the logarithm of the amplitude of the input signal. The data carried by the input signal, usually an on-off keying (OOK) amplitude modulation, can be retrieved by detecting the amplitude or the width of the envelope of the RF pulses, depending on the operation mode. The low-noise amplifier (LNA) improves signal reception and minimizes SRO re-radiation through the antenna. Fig. 2 shows the characteristic signals in a classical SR receiver operating in the linear mode, in which the modulating signal is retrieved by simply averaging the envelope of the RF pulses provided by the envelope detector, thus removing the quench components and preserving those of the modulating signal.

An important issue regarding operation of SR receivers is that they become sensitive to the input signal for relatively short periods of time, called *sensitivity periods*. These periods occur when the output oscillation begins to rise ($t = 0$ in Fig. 1 (b)). The RF reception bandwidth of the receiver is inversely proportional to the duration of the sensitivity periods.

The primary advantages provided by SR receivers are:

- Simplicity: tuning capability and high gain can be obtained from very few active devices. At RF frequencies, a reduction in the number of RF stages usually implies a reduction in power consumption, and also a small integration area, which reduces cost. Thus, SR receivers are in a privileged position compared to other architectures, which tend to be more complicated.
- Low power consumption. This stems from both the small number of active stages and the pulsating nature of the receivers (*i.e.* they operate with low duty cycles). Additionally, they tolerate low supply voltages (Chen *et al*., 2007; Otis *et al*., 2005), and therefore are excellent candidates for battery-operated systems.
- In the logarithmic mode, the receivers exhibit low-level variations of the demodulated output for large variations in the incoming signal level, which constitutes a built-in automatic gain control mechanism.
- They offer both AM and FM (although limited) demodulation.

- Lastly, and paramount to this chapter, SR receivers are very well suited to UWB IR communications, due to the low duty cycle of the received signals.

Traditionally, SR receivers have had three major drawbacks:

- Excessive reception bandwidth when applied to narrowband communications. Because of their relatively short sensitivity periods, their RF bandwidth is much wider than the signal modulation bandwidth, making them more sensitive to noise and interference compared to other systems.
- Frequency instability in tank (LC) implementations due to temperature changes, mechanical shock, etc. This problem, which is not exclusive of SR receivers, can be overcome via stable frequency references, such as coaxial ceramic resonators or acoustic wave devices (*e.g.*, SAW, BAW and FBAR).
- Re-radiation: part of the RF energy generated in SR oscillators tends to be radiated by the receiver antenna, becoming a source of interference. However, this effect can be minimized through a well-designed low-noise isolation amplifier.

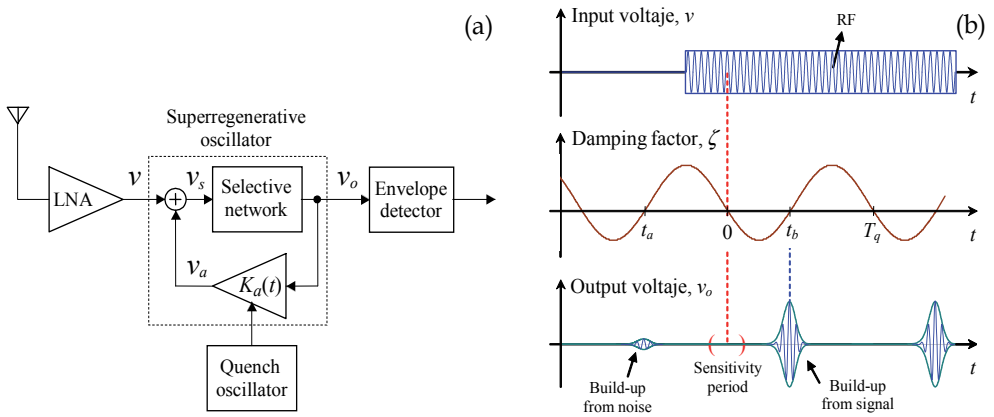

Fig. 1. (a) Block diagram of an SR receiver; and (b) input signal, instantaneous damping factor generated by the quench oscillator, and output voltage in the linear mode of operation.

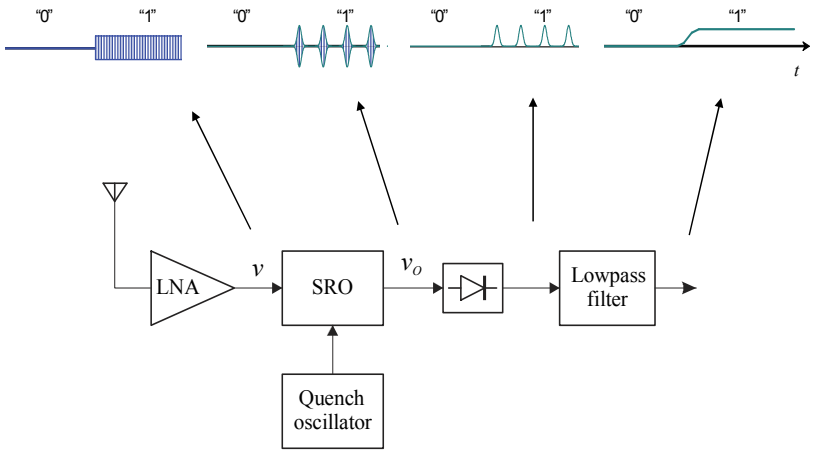

Fig. 2. Characteristic signals in a classical SR receiver operating in the linear mode.

3. Superregenerative architectures for narrowband, wideband and UWB signal reception

Although SR receivers have traditionally been used in short-range narrowband communications, new modes for their operation have been proposed and evaluated over the past few years. In this section, we describe and compare these operation modes and their corresponding receiver architectures to evaluate their suitability for UWB IR signal reception. Here we consider the simplest case of OOK modulation.

3.1 Classical superregenerative receiver

Fig. 3 shows the block diagram of a classical SR receiver. In this architecture, the quench oscillator runs asynchronously with respect to the received data. The quench frequency is considerably higher than the data rate, such that several quench cycles are generated during reception of a bit. Each quench cycle provides a sample of the input bit pulse. Several samples are envelope-detected and averaged by a lowpass filter, and the bit value is retrieved by a comparator. In practice, five to ten samples are typically required to retrieve a single bit.

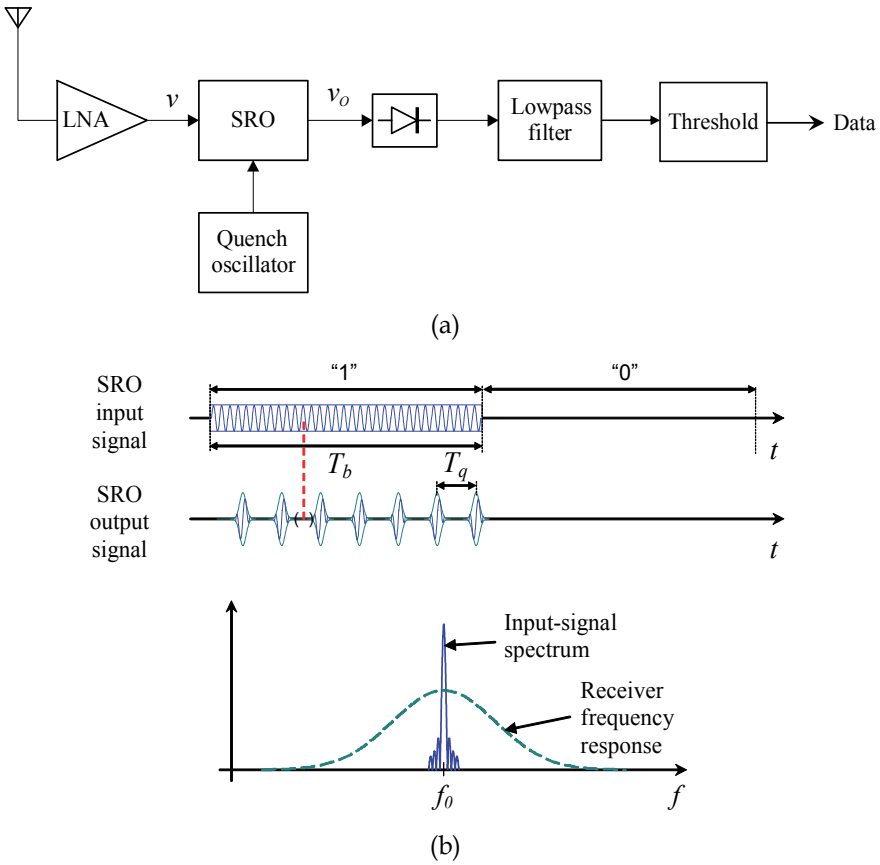

Fig. 3. (a) Block diagram of a classical SR receiver, and (b) corresponding time and frequency domain signals.

This architecture, characterized by a minimal number of constituting blocks, offers the following advantages:

- Simplicity and low cost;
- Low power consumption.

However, it has several disadvantages:

- Poor frequency selectivity: since the quench frequency is considerably higher than the bit frequency, the sensitivity periods are much shorter than the bit periods (T_b); consequently, the RF bandwidth of the receiver is much larger than the modulation bandwidth.
- Poor sensitivity: the noise bandwidth is much greater than the signal bandwidth.
- Not suitable for UWB IR communications: taking several samples of a UWB pulse is not feasible, as it would require an excessively high quench frequency.

3.2 Synchronous superregenerative receiver

In this architecture, shown in Fig. 4, the input signal is sampled synchronously at a rate of one sample per bit (Moncunill *et al.*, 2007a). Thus, the required quench frequency is much lower than in a classical receiver, and therefore, the selectivity is significantly higher. Furthermore, since the quench frequency is equal to the bit rate, the RF bandwidth is closer to the signal bandwidth than in a classical receiver. Moreover, synchronous operation enables optimization of the transmitted bit pulse shape, as shown in Fig. 4 (c), which is done to concentrate the bit energy in the sensitivity periods of the receiver. Consequently, synchronous SR receivers can make more efficient use of the incoming signal than classical SR receivers, exhibiting greater sensitivity and requiring lower levels of transmitted power.

Synchronous operation requires a synchronization phase-locked loop (PLL) that controls the quench voltage-controlled oscillator (VCO) to keep the quench cycles in phase with the received data. A proper error signal can be generated via early/late sampling of the received pulses, as shown in Fig. 5. In this case, the lowpass filter used by classical receivers to remove the quench components is not required, since each output pulse corresponds to a single bit.

On one hand, synchronous SR receivers are amenable to narrowband communications, namely, to overcome the problems of classical receivers. On the other hand, provided that the SRO is designed to exhibit short sensitivity periods, this architecture is also very well suited for reception of UWB IR signals, as they comprise bursts of short RF pulses. This architecture offers the following advantages:

- Simplicity and low cost;
- Low power consumption;
- High frequency selectivity, with RF bandwidth close or equal to the signal bandwidth.
- High sensitivity: up to 10 dB better than that of a classical receiver, with values similar to those offered by superheterodyne and zero-IF schemes.
- Fast data rates: for a given quench frequency, this architecture maximizes the data rate.
- Suitability for UWB IR communications, including OOK and pulse-position modulations.

It has one major disadvantage:

- It requires a PLL, which must be carefully designed to achieve effective acquisition and tracking of the received signal. This point is especially relevant in UWB IR applications, which demand high-precision synchronization.

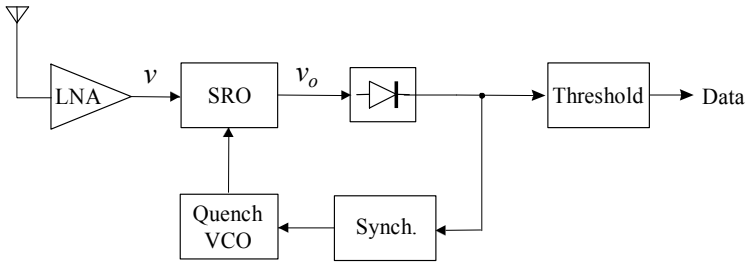

(a)

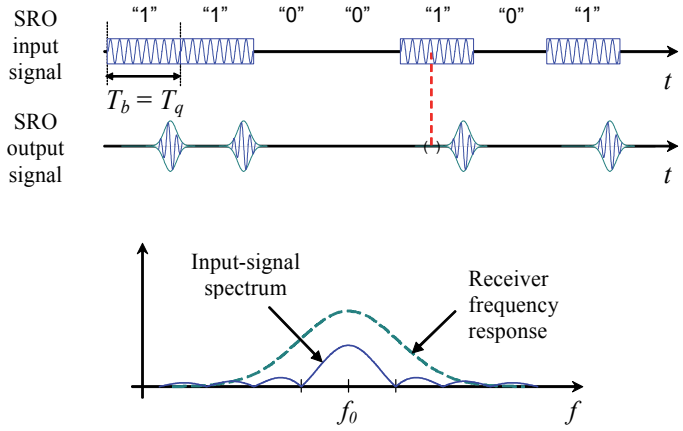

(b)

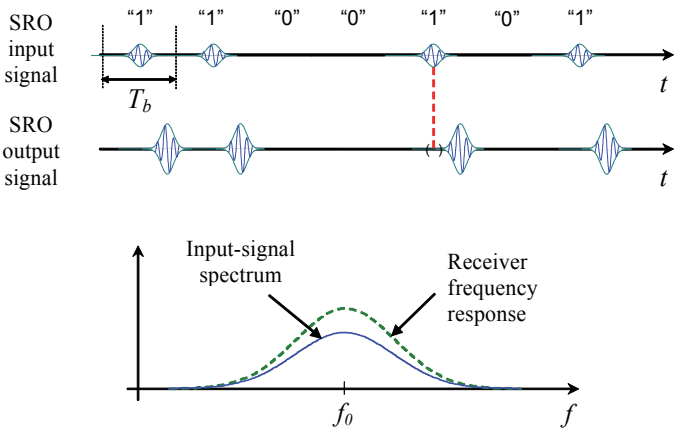

(c)

Fig. 4. (a) Block diagram of a synchronous SR receiver. Time and frequency domain signals (b) with a constant bit envelope and (c) with an envelope matched to the sensitivity periods of the receiver.

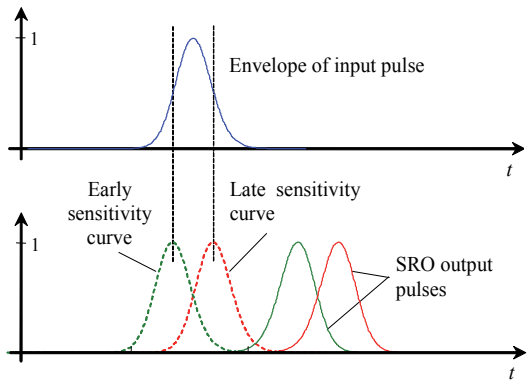

Fig. 5. Early and late sampling of the input pulse, achieved by periodically alternating between an advanced quench and a delayed quench (in this example the input pulse has a Gaussian envelope).

3.3 Direct-sequence spread-spectrum superregenerative receiver

This architecture, shown in Fig. 6, is basically a modified version of the synchronous architecture (Moncunill *et al*., 2005b, 2005c). The input signal is a direct-sequence spread-spectrum (DSSS) OOK modulation, in which a burst of chip pulses is transmitted for each bit according to a known pseudonoise (PN) spreading sequence. This enables lower levels of energy per transmitted pulse, and therefore, leads to minimal interference caused to other systems. The received signal is synchronously sampled by the receiver at a rate of one sample per chip period (T_c). The receiver includes a PN-code generator clocked by the quench VCO, a PN-code multiplier, and an integrate-and-dump filter with sample and hold (ISH). These blocks correlate the received signal to the locally-generated PN code, thereby enabling both retrieval of the desired data and rejection of noise and interference. Synchronous operation requires a synchronization loop that controls the quench VCO in order to keep the quench cycles in phase with the received data. Early and late sampling of the input chip pulses, similar to that shown in Fig. 5 can be used. Due to the synchronous operation, the signal bandwidth and the receiver RF bandwidth are similar. Also, in this case, the chip pulses can be optimally shaped in order to increase the sensitivity of the receiver.

In addition to having the main advantages of the synchronous SR receiver, the DSSS SR architecture also offers the following benefits:

- The specific features of spread-spectrum communications, including better data privacy (owing to the PN-coded signal), stronger interference rejection, less interference caused to other systems, and code-division multiple-access (CDMA) capability.
- Suitability for UWB IR communications (DSSS techniques and UWB IR communications are compatible).

Among the main inconveniences of the DSSS SR receiver are:

- Greater complexity than narrowband or synchronous architectures, as it requires PN-code generation and correlation of this code to the received signal.
- A PLL is required to maintain receiver synchronization. Additionally, PN-code acquisition and tracking techniques must be implemented.

The SR architectures described above are compared in Table 1.

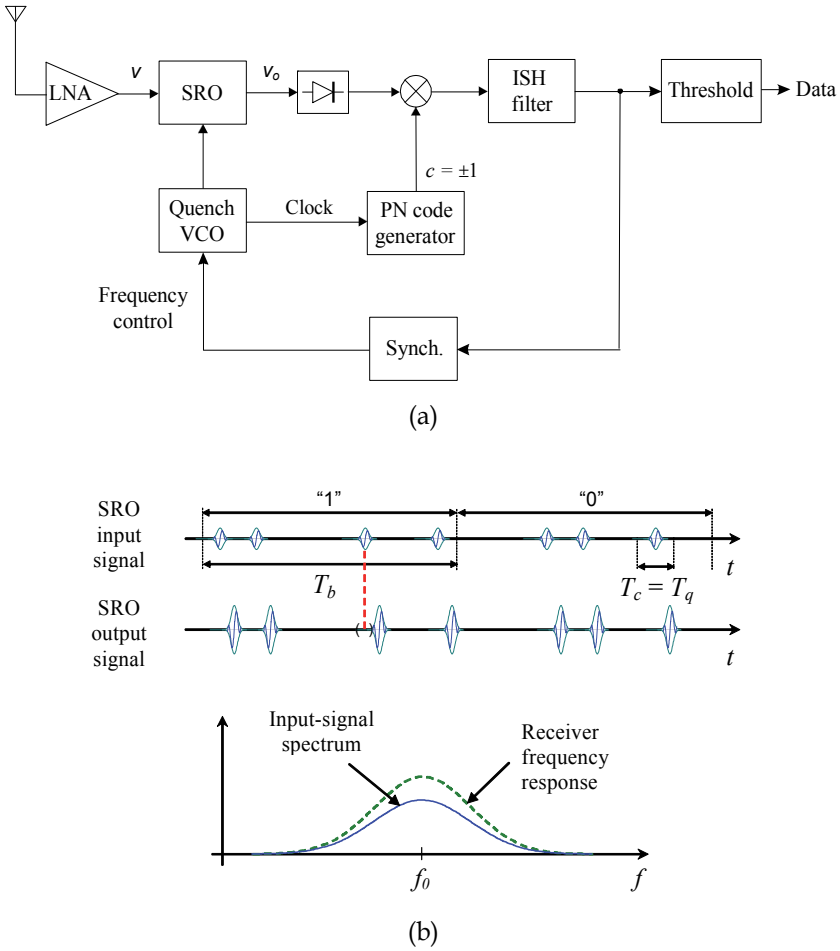

Fig. 6. (a) Block diagram of a DSSS SR receiver, and (b) corresponding time and frequency domain signals.

Feature	*Classical*	*Synchronous*	*DSSS*
Architecture simplicity	High	High	Medium
Power consumption in the RF stages	Low	Very low	Low
Frequency selectivity	Low	Medium	Low
Signal sensitivity	Low	High	High
Available data rates	Low	High	Medium
Interference rejection, coexistence ability	Low	Medium	Medium-high
Suitable for UWB IR communications	No	Yes	Yes

Table 1. Comparison of the three SR architectures.

4. The superregenerative oscillator as a pulse filter and amplifier

4.1 Model of an SRO

An SRO can be modeled as a selective network or resonant circuit fed back through an amplifier (Fig. 1 (a)) (Moncunill *et al*., 2005a). The amplifier has a variable gain $K_a(t)$ controlled by the quench signal, which has a frequency $f_q = 1/T_q$, making the system alternatively stable and unstable. The selective network has two dominant poles that provide a bandpass response centered on $\omega_0 = 2\pi f_0$, characterized by the transfer function

$$G(s) = K_0 \frac{2\zeta_0 \omega_0 s}{s^2 + 2\zeta_0 \omega_0 s + \omega_0^2}, \tag{1}$$

or, equivalently, by the differential equation

$$\ddot{v}_o(t) + 2\zeta_0 \omega_0 \dot{v}_o(t) + \omega_0^2 v_o(t) = K_0 2\zeta_0 \omega_0 \dot{v}_s(t), \tag{2}$$

where ζ_0 is the quiescent damping factor and K_0 is the maximum amplification. The corresponding quiescent quality factor represents the loaded Q of the resonant circuit

$$Q_0 = \frac{1}{2\zeta_0}. \tag{3}$$

The feedback loop establishes the relationship $v_s(t) = v(t) + K_a(t)v_o(t)$, which, assuming that $K_a(t)$ is a slow-variation function, enables formulation of the general form of the differential equation for the SR receiver (Moncunill *et al*., 2005a),

$$\ddot{v}_o(t) + 2\zeta(t)\omega_0 \dot{v}_o(t) + \omega_0^2 v_o(t) = K_0 2\zeta_0 \omega_0 \dot{v}(t), \tag{4}$$

where $\zeta(t)$ is the instantaneous damping factor (or damping function) of the closed-loop system, Eq. 5 must have a single dot at the end instead of two.

$$\zeta(t) = \zeta_0 (1 - K_0 K_a(t)) .. \tag{5}$$

This function is very important, as it controls the overall performance of the receiver. By identifying the coefficients in the corresponding differential equations, one can obtain the equivalence between the parameters of the block diagram in Fig. 1 and those of a particular circuit. For example, Fig. 7 shows the equivalence for a parallel RLC circuit, a commonly used topology. In this case, the net conductance of the circuit is

$$G(t) = G_0 - G_a(t), \tag{6}$$

and the resulting damping function becomes

$$\zeta(t) = \frac{G(t)}{2C\omega_0} = \frac{1}{2C\omega_0}(G_0 - G_a(t)). \tag{7}$$

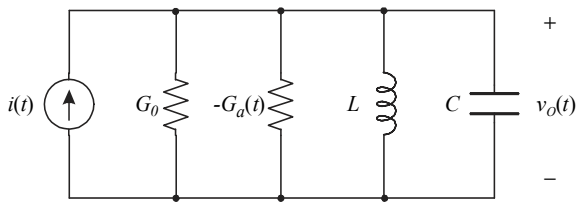

(a)

Block diagram	v	v_o	K_0	ζ_0	ω_0	$K_a(t)$
Circuit	i	v_o	$\frac{1}{G_0}$	$\frac{G_0}{2C\omega_0}$	$\frac{1}{\sqrt{LC}}$	$G_a(t)$

(b)

Fig. 7. (a) Parallel RLC circuit with variable conductance, and (b) equivalence between the block diagram of an SRO and the RLC circuit parameters. G_0 includes both source resistance and tank losses.

4.2 The quench cycle and the damping function

The quench oscillator generates a periodic damping function, $\zeta(t)$ (Fig. 8), which comprises successive quench cycles. A new quench cycle starts when the damping function becomes positive ($t = t_a$), which extinguishes any oscillation present in the oscillator. When $\zeta(t)$ returns to negative ($t = 0$), the oscillation builds up from the injected signal $v(t)$, and when $\zeta(t)$ becomes positive again ($t = t_b$), it achieves its maximum amplitude. Mathematical analysis and experimental results have revealed that the receiver is especially sensitive to the input signal in a given environment at the instant $t = 0$.

The behavior of the receiver is mainly determined by the characteristics of the damping function (*i.e.* its shape, repetition frequency, and mean value). Since $\zeta(t)$ gives global information on the system performance, it is a better descriptor than is the feedback gain, $K_a(t)$. In practice, $K_a(t)$ is adjusted to obtain the desired $\zeta(t)$. In the case of a non-inverting feedback amplifier, the minimum value of $K_a(t)$ is zero, and, consequently, the maximum value of $\zeta(t)$ is limited by ζ_0.

4.3 SRO response to a narrow RF pulse

The operation of SROs can be described from their response to an RF pulse applied within the limits of a single quench cycle (*i.e.*, the interval (t_a, t_b); see Fig. 8 (b)). The input RF pulse can be expressed as

$$v(t) = V p_c(t) \cos(\omega t + \varphi) , \tag{8}$$

where $p_c(t)$ is the normalized pulse envelope, and V, its peak amplitude. $p_c(t)$ is assumed to be zero beyond the cycle limits defined by t_a and t_b. Although in some practical cases (*e.g.* classical receivers operating with narrowband modulation) $p_c(t)$ can be assumed to be

constant and to represent a fraction of the input signal, in others (*e.g.* a UWB IR receiver), it may be a narrow pulse of relatively slow variation. The response of the SRO to the aforementioned input RF pulse is another RF pulse, described by

$$v_o(t) = VK\left|H(\omega)\right| p(t)\cos(\omega_0 t + \varphi + \angle H(\omega)), \tag{9}$$

where K is a peak amplification factor, $H(\omega)$ is a bandpass function centered on the resonance frequency ω_0, and $p(t)$ is the unity-normalized envelope of the output oscillation. The expressions for the characteristic parameters and functions, and the restrictions for their validity, are summarized in Table 2 and defined below.

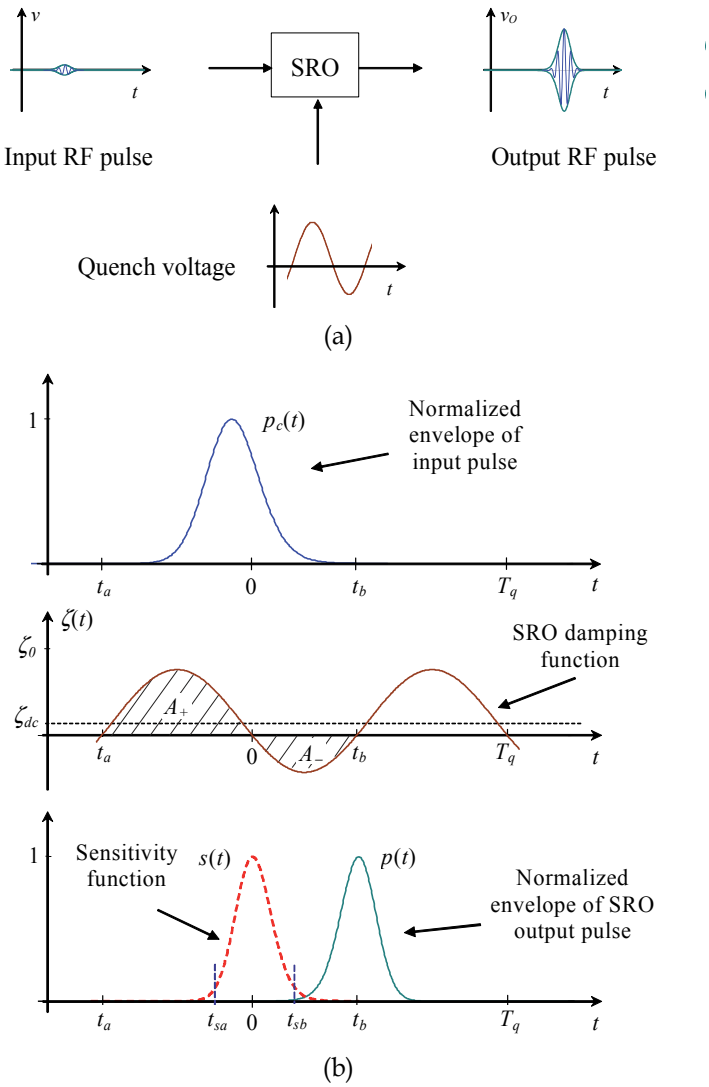

Fig. 8. (a) Input signal, quench voltage and output signal in an SRO; (b) characteristic functions of an SRO.

Circuit Parameters

Selective network

$$G(s) = K_0 \frac{2\zeta_0 \omega_0 s}{s^2 + 2\zeta_0 \omega_0 s + \omega_0^2}$$

Periodic feedback gain

$$K_a(t)$$

$\Rightarrow$ Periodic closed-loop damping factor

$$\zeta(t) = \zeta_0 (1 - K_0 K_a(t))$$

Input pulse

$$v(t) = V p_c(t) \cos(\omega t + \varphi), \qquad t_a < t < t_b$$

Restrictions: $\zeta^2(t) << 1$, $\left|\dot{\zeta}(t)\right| << \omega_0$, $|\dot{p}_c(t)| << p_c(t)\omega$, $\omega \geq 0$

Output pulse

$$v_o(t) = V K \left|H(\omega)\right| p(t) \cos(\omega_0 t + \varphi + \angle H(\omega)), \qquad t > t_{sb},$$

Peak gain → $K = K_0 K_r K_s$

Regenerative gain → $K_r = \zeta_0 \omega_0 \int_{t_a}^{t_b} p_c(\tau) s(\tau)\, d\tau$, $s(t) = e^{\omega_0 \int_0^t \zeta(\lambda) d\lambda}$

Superregenerative gain → $K_s = e^{-\omega_0 \int_0^{t_b} \zeta(\lambda) d\lambda}$

Frequency response → $H(\omega) = \frac{\omega}{\omega_0} \frac{\psi(\omega - \omega_0)}{\psi(0)}$, $\psi(\omega) = F^* \{p_c(t) s(t)\}$

Normalized oscillation envelope → $p(t) = e^{-\omega_0 \int_{t_b}^{t} \zeta(\lambda) d\lambda}$

Table 2. Summary of the characteristic parameters and functions of SROs (when operating in linear mode). The operator F^* in the frequency response calculation refers to a conjugate Fourier transform.

4.4 Characteristic parameters of SROs

The parameters and functions shown in Table 2 are defined below:

- Feedforward gain, (K_0): is the gain that is provided by the selective network at the resonance frequency, which equals the receiver gain when the feedback amplifier is inactive (open-loop situation).
- Sensitivity function ($s(t)$): a normalized function that describes the sampling process performed by the SRO. Its maximum value is one. Because this function is exponentially time-dependent, its value becomes quite small relatively close to the origin ($t = 0$). The shape of $s(t)$ is determined mainly by the environment of the zero-crossing of $\zeta(t)$. A slow transition provides a wide curve, whereas a fast one yields a narrow curve. Both the regenerative gain and the frequency response depend on the product $p_c(t)s(t)$. Thus, the sensitivity curve acts as a function that weighs the incoming envelope $p_c(t)$: the values of $p_c(t)$ near $t = 0$ are considered, whereas those close to either t_a or t_b are irrelevant. Therefore, $t = 0$ represents the instant of maximum sensitivity.
- Regenerative gain (K_r): this gain depends on the product $p_c(t)s(t)$. If either $p_c(t)$ or $s(t)$ is narrow, then K_r will be small; however, if both $p_c(t)$ and $s(t)$ are wide, then K_r will be large.
- Superregenerative gain (K_s): this gain, associated with the exponential growth of the oscillation, is usually the most significant amplification factor. It is determined by the area enclosed by the negative portion of the damping function (Fig. 8 (b)).
- Frequency response ($H(\omega)$): a bandpass function centered on ω_0 that is related to the complex conjugate of the Fourier transform of $p_c(t)s(t)$. If both $p_c(t)$ and $s(t)$ are wide, then the reception bandwidth of the receiver will be small; however, if either $p_c(t)$ or $s(t)$ is narrow, then this bandwidth will be large.
- Normalized oscillation envelope ($p(t)$): determined mainly by the evolution of the damping function close to $t = t_b$. The same conclusions obtained for $s(t)$ apply to $p(t)$ in the environment of t_b.

4.5 Noise performance

Expressions for calculating the noise performance of an SRO can be obtained from those in Table 2 (Moncunill *et al.*, 2005a). The signal-to-noise ratio (SNR) at the SRO output can be expressed as

$$SNR_o = \frac{E_c}{\eta} \frac{\left[\int_{t_a}^{t_b} p_c(\tau)s(\tau)\,d\tau\right]^2}{\int_{t_a}^{t_b} p_c^2(\tau)d\tau \int_{t_a}^{t_b} s^2(\tau)d\tau}, \tag{10}$$

where E_c is the average input-pulse energy, and η is the one-sided noise power spectral density at the input. To maximize the SNR at the SRO output, one can use Schwarz's inequality, which states that the maximum value of (10) is achieved when $p_c(t)$ and $s(t)$ are proportional. In this case, since both functions are unity-normalized, proportionality implies equality,

$$p_c(t) = s(t)\,. \tag{11}$$

Thus, the optimum SNR is

$$SNR_{o,opt} = \frac{E_c}{\eta}, \tag{12}$$

which is that of a matched filter. This result is highly important, because the condition of a matched filter can be achieved in UWB IR SR receivers, but not in narrowband SR receivers. The optimum pulse envelope typically equals a Gaussian curve.

4.6 Hangover

Under normal receiver operation, the output oscillation in a given quench cycle is generated mainly from the incoming signal, and not from the remnant of the previous cycle. This implies that sufficient damping must be applied at the beginning of the cycle to extinguish said remnant; otherwise, the output pulse would extend beyond a single quench cycle to overlap with other pulses. In this case, the output in a given cycle significantly depends on that of the preceding cycles, and the receiver is said to operate with appreciable *hangover* (Moncunill *et al.*, 2005a). This effect is generally undesirable, as it produces a sort of intersymbol interference. For the receiver to operate with negligible hangover, the mean value of the damping function ζ_{dc} must satisfy the following condition (Moncunill *et al.*, 2005a):

$$\zeta_{dc} > \frac{f_q}{2\pi f_0} \ln\frac{1}{h}, \tag{13}$$

where h is the hangover coefficient, for which a value much smaller than one (*e.g.* 0.01) should be assigned. Eq. (13) becomes more restrictive at high quench frequencies.

5. Ultra wideband impulse radio superregenerative reception

According to the currently prevailing definition, a signal can be classified as UWB if the signal bandwidth exceeds either 20% of the center frequency or 500 MHz (Opperman *et al.*, 2004). Impulse radio is a type of UWB signaling in which baseband pulses of extremely short duration (typically, 0.1 to 1.5 ns) are transmitted. The pulsating nature of SR receivers, and the fact that they are sensitive to the input signal in a small fraction of the quench period—and therefore, exhibit large reception bandwidths—makes them ideal for UWB IR signal reception. Furthermore, Gaussian pulses are not only optimum signals for SR receivers operated in the slope-controlled state (Moncunill *et al.*, 2007a), but they, and their derivatives (*e.g.* Gaussian monopulse; first derivative of Gaussian; Mexican hat, second derivative of Gaussian; and Gaussian doublet) are among the most widely used signals for UWB IR (Ghavami *et al.*, 2004; Opperman *et al.*, 2004).

Superregenerative oscillators targeting the FCC/ECC UWB spectrum mask must oscillate at a frequency higher than that of SROs operating at lower frequency bands (*e.g.* 2.4-GHz ISM band), and consequently, will inherently exhibit larger reception bandwidths. However, to efficiently filter and amplify UWB IR pulses, additional requirements must be met. In this section, we present these requirements, considering the restrictions on the resonator Q and on the quench parameters.

Fig. 9 shows a preferred damping function for UWB IR SR receivers. Due to the low duty cycle of UWB IR signals, the quench must be active during a small portion of the pulse repetition period. Therefore, the damping must remain at the quiescent positive value ζ_+ most of the time, and only switch to the negative value during reception and amplification of the short pulse. The transition between these two states is assumed to be linear and is characterized by the fall time (t_f) and the rise time (t_r). This type of quench waveform belongs to the category in which an SRO is said to operate in the slope-controlled state,

because the characteristics of the SRO (*e.g.* sensitivity function and frequency response) are determined by the slope of the quench transition around $t = 0$.

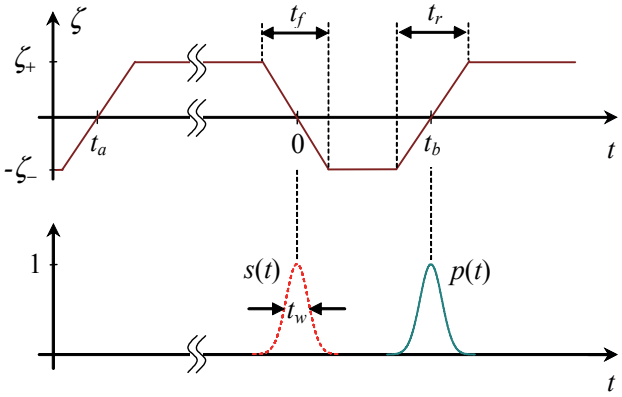

Fig. 9. Trapezoidal quench waveform, $s(t)$ and $p(t)$ for a UWB IR SRO.

Table 3 summarizes the main parameters and functions in the slope-controlled state. For the sake of simplicity and symmetry, we have assumed that $\zeta_+ = \zeta_- = \zeta_0$ and that $t_f = t_r$. The table also includes the information on the step-controlled state, characterized by an abrupt damping transition at $t = 0$. The step-controlled state can be understood as a particular case of the damping shown in Fig. 9 in which $t_f = t_r = 0$. In practice, generating transition times that are negligible compared with the duration of the UWB IR pulses is not trivial, and therefore, the step-controlled state is only of minor interest.

In the slope-controlled state, under the circumstances assumed above, and when truncation effects due to the finite quench period length are ignored, the sensitivity function can be approximated by the Gaussian expression

$$s(t) = e^{-\frac{1}{2}\left(\frac{t}{\sigma_s}\right)^2}, \quad \sigma_s = \sqrt{\frac{t_f}{2\zeta_0\omega_0}}. \tag{14}$$

For simplicity, we have defined the function width at 60.7% of the maximum

$$t_w = 2\sigma_s = \sqrt{\frac{2t_f}{\zeta_0\omega_0}}, \tag{15}$$

which is a measure of the time resolution of the SRO. For the fixed oscillation frequency ω_0, t_w is controlled by the ratio between the fall time and the quiescent damping, t_f / ζ_0. The fall time must satisfy the following condition (Moncunill *et al.*, 2009)

$$t_f > 4\sigma_s = 2t_w, \tag{16}$$

to avoid significant distortion of the Gaussian shape due to saturation of the damping function outside of the transition period. Considering (15), condition (16) can be rewritten as

$$t_f\zeta_0 > \frac{8}{\omega_0}, \tag{17}$$

which shows a tradeoff between t_f and ζ_0 to obtain a near-Gaussian sensitivity function. The frequency response of the receiver to a continuous wave (CW) can be obtained from the Fourier transform of $s(t)$, according to Table 2, using $p_c(t) = 1$. The resulting function also includes a Gaussian term,

$$H(2\pi f) = \frac{f}{f_0} e^{-\frac{1}{2}\left(\frac{f-f_0}{\sigma_f}\right)^2}, \quad \sigma_f = \frac{1}{\pi}\sqrt{\frac{\zeta_0 \omega_0}{2t_f}}, \tag{18}$$

and the -3-dB bandwidth, assuming that the value of the quotient f/f_0 is close to 1 within the pass band, can be approximated by

$$\Delta f_{-3dB} \approx 2\sqrt{\ln 2}\,\sigma_f = \frac{1}{\pi}\sqrt{\frac{2\zeta_0 \omega_0 \ln 2}{t_f}}. \tag{19}$$

For a matched input-pulse envelope, the bandwidth in (19) must be increased by a factor of $\sqrt{2}$. Note that $s(t)$ provides information on the SRO sensitivity as well as on the optimum envelope of the received pulse. $H(2\pi f)$ provides the frequency response of the receiver and is related to the spectrum of the optimum received pulse. As expected, the product of t_w and Δf_{-3dB} is constant (*i.e.* the RF reception bandwidth and the temporal duration of the sensitivity are inversely proportional), as shown below

$$t_w\, \Delta f_{-3\mathrm{dB}} = \frac{2\sqrt{\ln 2}}{\pi} \approx 0.53 \ . \tag{20}$$

To meet the requirements for reception of very short pulses, a narrow sensitivity function is necessary. From the above results, one can conclude that a sensitivity function can be narrowed by:

a. Increasing the oscillation frequency ω_0;
b. Increasing the quiescent damping (ζ_0) (*i.e.* reducing Q_0), which entails a wider dynamic range for the damping function.
c. Reducing the fall time of the damping function (t_f).

Table 4 shows the calculated widths of the sensitivity function at the frequency $f_0 = 7$ GHz, considering different values of Q_0 and t_f, and provides the corresponding -3-dB reception bandwidths. As a reference, $Q_0 = 5$ with $t_f = 2$ ns yields a 1-ns time resolution with a bandwidth that exceeds 500 MHz. Similar results are obtained with higher transition times, provided that the Q is decreased accordingly; for larger values of Q_0, t_f must be decreased, although in this case, the Gaussian functions become distorted. By combining very low Q_0 values with short transition times, the pulse width can be decreased to less than 500 ps and the bandwidth can be made greater than 1 GHz. In conclusion, for SROs to operate correctly with UWB IR signals, they must be designed with a Q of less of 10, and must be controlled by quench signals that switch quickly, with transition times shorter than 5 ns. Unlike in narrowband SR receivers, the sensitivity function width and the reception bandwidth of a UWB IR SR receiver are determined by the quench transition time, rather than by the quench frequency.

		Slope-controlled ($t_r = t_f$, $t_f > 2t_w$)	*Step-controlled* ($t_r = t_f = 0$)
$s(t)$ ($t_a < t < t_b$)		$e^{-\zeta_0\omega_0\frac{t^2}{t_f}}$	$e^{-\zeta_0\omega_0\lvert t\rvert}$
$p(t)$ ($0 < t < T_q$)		$e^{-\zeta_0\omega_0\frac{(t-t_b)^2}{t_f}}$	$e^{-\zeta_0\omega_0\lvert t-t_b\rvert}$
$H(2\pi f)$ (CW)		$\frac{f}{f_0}e^{-\pi^2\frac{t_f}{\zeta_0\omega_0}(f-f_0)^2}$	$\frac{f}{f_0}\frac{1}{1+\frac{1}{\zeta_0^2}\left(1-\frac{f}{f_0}\right)^2}$
t_w (60.7 %)		$\sqrt{\frac{2t_f}{\zeta_0\omega_0}}$	$\frac{1}{\zeta_0\omega_0}$
$\Delta f_{\text{-3dB}}$		$\frac{1}{\pi}\sqrt{\frac{2\zeta_0\omega_0\ln 2}{t_f}}$	$\frac{\zeta_0\omega_0}{\pi}\sqrt{\sqrt{2}-1}$
K_r	Matched pulse	$\sqrt{\frac{\pi\zeta_0\omega_0 t_f}{2}}$	1
	Constant envelope pulse	$\sqrt{\pi\zeta_0\omega_0 t_f}$	2
K_s		$e^{\zeta_0\omega_0(t_b-\frac{t_f}{2})}$	$e^{\zeta_0\omega_0 t_b}$

Table 3. Characteristic parameters and functions of an SRO with trapezoidal quench and $\zeta_+ = \zeta_- = \zeta_o$.

Q_0	ζ_0	t_f = 5 ns		t_f = 2 ns		t_f = 1 ns	
		t_w (ns)	$\Delta f_{\text{-3dB}}$ (MHz)	t_w (ns)	$\Delta f_{\text{-3dB}}$ (MHz)	t_w (ns)	$\Delta f_{\text{-3dB}}$ (MHz)
10	0.05	2.13	249	1.35 *	393 *	0.95 *	556 *
5	0.1	1.51	352	0.95	556	0.67 *	785 *
2.5	0.2	1.07	~ 500	0.67	785	0.48	1110

(*) These values may only be approximate, since the requirement $t_f > 2t_w$ is not met in these cases.

Table 4. Sensitivity function width t_w (= optimum received-pulse width) and -3-dB reception bandwidth $\Delta f_{\text{-3dB}}$ (= optimum received-pulse bandwidth) at a frequency of 7 GHz for different values of Q_0 and t_f.

6. Performance analysis and experimental results

6.1 Performance analysis of selected examples

To gain additional information on the behavior expected from UWB IR SR receivers, we have closely analyzed the cases of $Q_0 = 5$ and $t_f = 2$ ns, and $Q_0 = 2.5$ and $t_f = 1$ ns. Table 5 summarizes the SRO parameters for a total peak gain of 50 dB. The results were calculated numerically from the exact expressions shown in Table 2, rather than from the approximate ones shown in Table 3.

Parameter	*Symbol*	$Q_0 = 5$, $t_f = 2$ ns	$Q_0 = 2.5$, $t_f = 1$ ns
Oscillation frequency	f_0	7 GHz	
Duration of instability period	t_b	2 ns	1 ns
Selective-network damping factor	ζ_0	0.1	0.2
Selective-network gain	K_0	0 dB	
Regenerative gain (matched pulse)	K_r	11.4 dB	
Superregenerative gain	K_s	38.6 dB	
Total peak gain	K	50 dB	
Sensitivity function width at 60.7%	t_w	0.95 ns	0.48 ns
Sensitivity full width at half maximum	FWHM	1.12 ns	0.56 ns
-3-dB reception bandwidth (CW)	$\Delta f_{\text{-3dB}}$	534 MHz	1072 MHz
-10-dB reception bandwidth (CW)	$\Delta f_{\text{-10dB}}$	1010 MHz	2016 MHz

Table 5. Main parameter values for the considered UWB IR SROs.

The gain of the SRO (in dB) is proportional to the duration of the instability period (t_b). Therefore, extremely large gains can be achieved by adequately increasing t_b. However, excessive gain will cause the SRO to operate in the logarithmic mode. Eventually, the gain may be reduced by decreasing ζ_- relative to ζ_+ (Fig. 9). Since UWB IR pulses exhibit larger amplitudes than do narrowband signals (due to the energy compression in the time domain), UWB SR receivers generally require lower gain than do other types of SR receivers.

Fig. 10 (a) shows the damping function, the sensitivity function and the generated pulse for a UWB SR receiver at $Q_0 = 2.5$ and $t_f = 1$ ns. A characteristic of these types of receivers is that the generated pulse contains a small number of carrier cycles. Since in this example $t_r = t_f$, the envelope of the generated pulse has the same shape as the sensitivity function, and therefore, provides the pattern for the optimum pulse during reception. Figs. 10 (b) and 10 (c) show the selectivity of the SRO in the time and frequency domains. The curves differ from exact parabolas (as expected from exact Gaussian functions), mainly due to damping saturation and to end effects associated to the finite quench cycle. The poor frequency selectivity (*i.e.* the curves decrease progressively over several GHz) is compensated by high selectivity in the time domain, which would enable use of this receiver in high resolution ranging systems. Fig. 11 shows the plot of the maximum pulse repetition frequency (PRF), which represents also the maximum quench frequency and the maximum data rate if a single pulse per bit is transmitted. The curve in Fig. 11 was constructed considering

hangover limitations (Eq. (13)) and reveals that data rates faster than 200 Mbps are available for low-Q-resonator SR receivers.

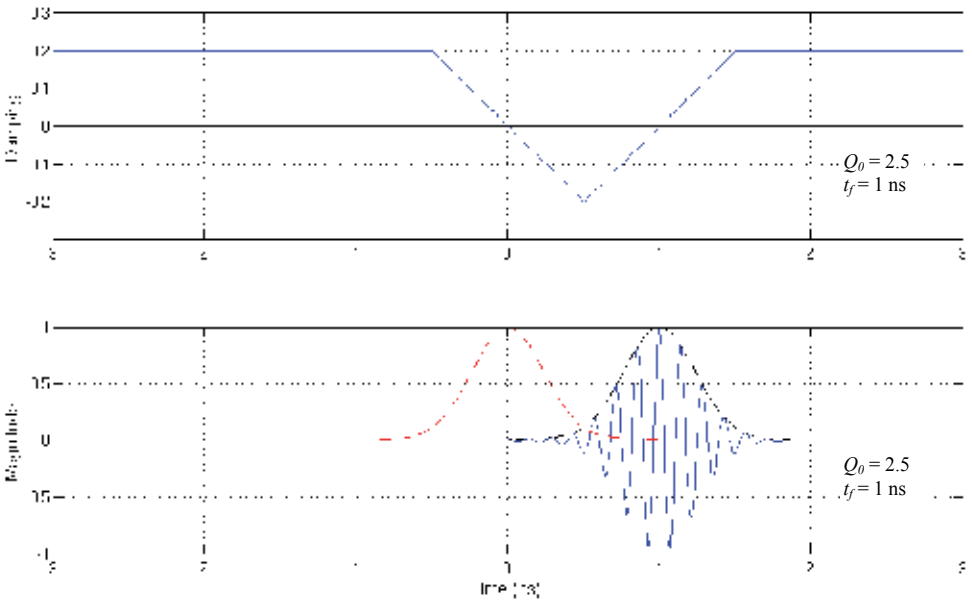

(a)

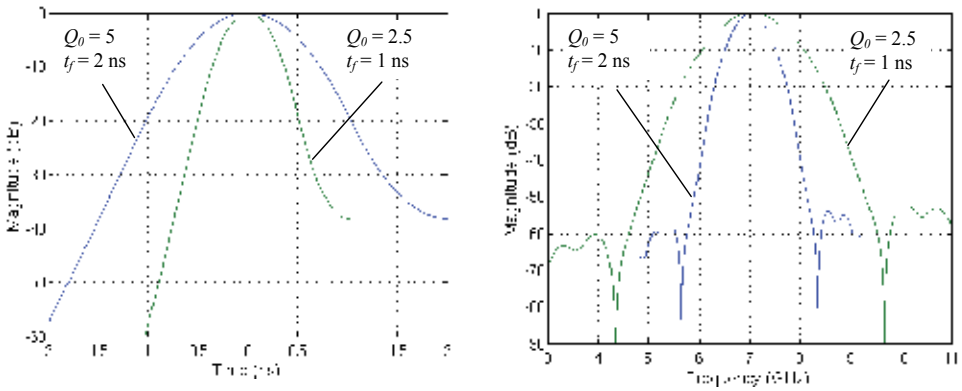

(b) (c)

Fig. 10. (a) Damping function, sensitivity function and normalized output pulse at f_0 = 7 GHz. Selectivity curves (b) in the time domain and (c) in the frequency domain.

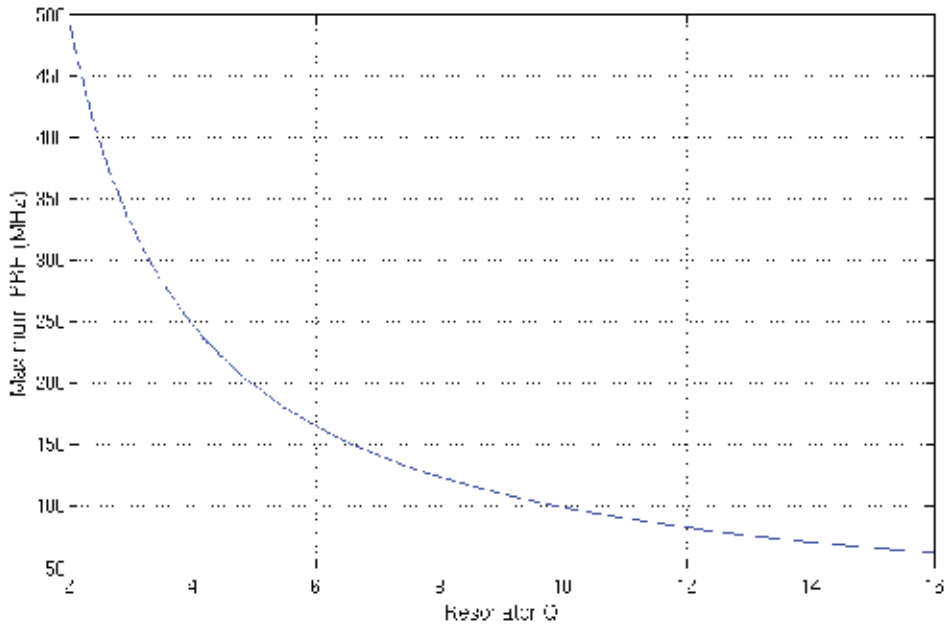

Fig. 11. Maximum pulse repetition frequency (= maximum quench frequency) as a function of Q_0. Note that at one bit per pulse, the maximum PRF is also the maximum data rate.

6.2 Experimental UWB SRO

We implemented a test SRO according to the schematic in Fig. 12 (a). The SRO, which is connected to a symmetric bow-tie UWB antenna, operates at a frequency of 7 GHz with a shorted λ/4 microstrip resonator as selective network. The bow-tie antenna is suspended on a small portion of the circuit board to minimize substrate parasitic effects. Low-power and low-parasitic-capacitance transistors in a cross-coupled differential configuration were selected as the active devices to compensate the overall circuit losses. The lower transistor acts as a current source controlled by the quench signal. It controls the instantaneous bias current of the pair, and consequently, the degree of regeneration, in the form of negative resistance, generated in the SRO. A relatively low value of $R_0 = 1/G_0 = 39+39\ \Omega$ was included to significantly reduce the loaded Q. As shown in Fig. 12 (c), this circuit can generate pulses of approximately 500-ps (FWHM) when a quench transition time of 1.8 ns is applied. The SRO may yield amplified pulses of more than 200-mV peak from input pulses of about 2-mV amplitude, thus exhibiting a gain in excess of 40 dB. The SRO consumes 150 μA at 10-MHz quench frequency and at a supply voltage of 1.5 V.

6.3 Comparison with other receiver architectures

Several implementations of UWB IR SR receivers integrated in CMOS technology have recently been described in the literature. Table 6 summarizes the performance of several SR implementations and compares them with those of other UWB receiver architectures. As indicated by the table, SR receivers are characterized by lower power consumption and better energy-per-bit ratios. Compared to narrowband SR receivers, UWB IR SR receivers also offer faster data rates with better energy-per-bit efficiencies.

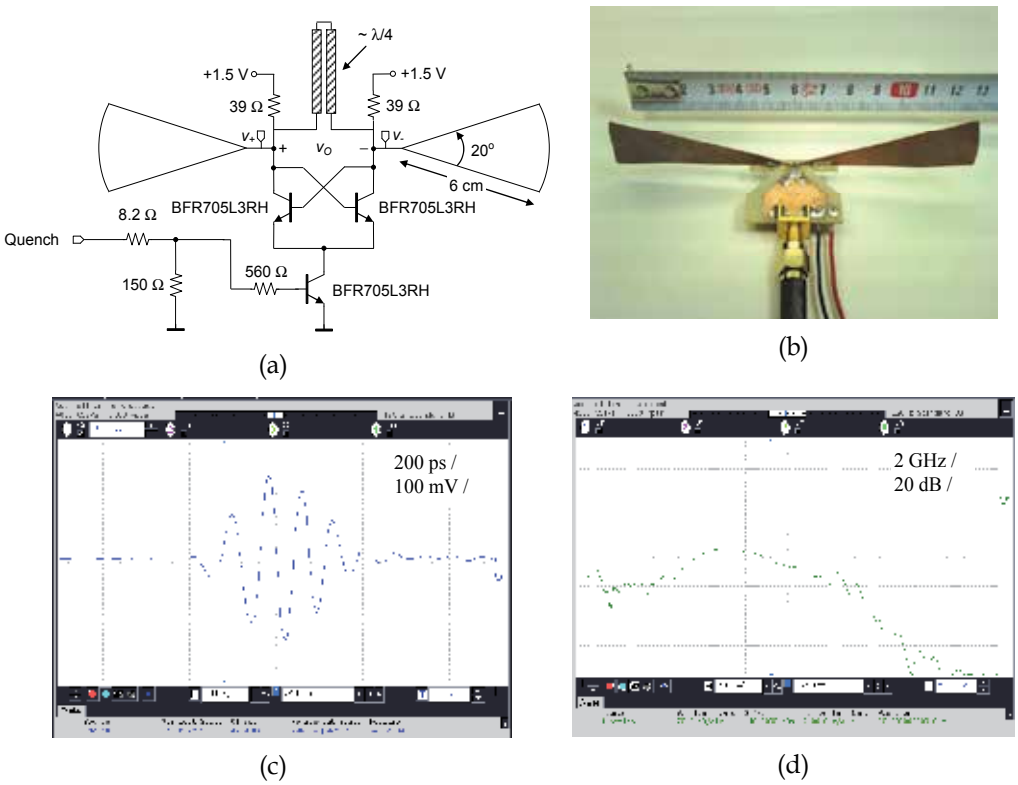

(a) (b) (c) (d)

Fig. 12. (a) Schematic and (b) photograph of an experimental UWB IR SRO. (c) Pulse generated in the SRO, and (d) corresponding spectrum.

	Zheng *et al.*, 2008	Lee *et al.*, 2007	Daly *et al.*, 2010	Chen *et al.*, 2007	Pellissier *et al.*, 2009	Thoppay, 2010
Architecture	Coherent	Non-coherent	Non-coherent	SR *	SR	SR
Technology	180 nm CMOS	90 nm CMOS	90 nm CMOS	130 nm CMOS	130 nm CMOS	180 nm CMOS
Operating frequency (GHz)	5.6 to 9	4.4	3 to 5	2.4	3.5	3.5 to 4
Data rate (Mbps)	15.6	0.1	16	0.5	10	10
Receiver sensitivity (dBm)	-75	-99	-76	-90	-99	-66
Power consumption (mW)	102	35.8 **	22.5	2.8	11.2 **	10.8 **
Energy per bit (nJ/bit)	6.5	2.5	1.4	5.6	1.1	0.24

* Narrowband SR receiver

** The power consumption may be reduced by decreasing the receiver duty cycle

Table 6. Comparison of UWB IR receiver architectures.

7. Conclusions

In this chapter, we have demonstrated that SR receivers are a promising, low-power and low-cost alternative for UWB IR communications. The relatively short sensitivity periods of SROs makes them ideal for reception of short RF pulses in general, and of UWB IR in particular. Proper pulse reception requires implementation of a quench synchronization mechanism. Although synchronous operation generally leads to more complex receivers, it offers myriad advantages. For example, the receiver may operate as a matched filter, achieving improved noise and interference rejection; faster data rates become accessible; and energy efficiency can be improved. We have shown that to achieve efficient filtering and amplification of UWB IR signals, low-Q (< 10) superregenerative oscillators must be designed, and that quench signals with short switching times (< 5 ns) must be applied. Theoretical and experimental results show that an optimized design can efficiently process sub-500-ps pulses, achieving peak gains in excess of 40 dB and reception bandwidths at -3-dB above 1 GHz. Furthermore, in a UWB IR SR receiver, the data transfer rate may be maximized by generating a single quench period per received bit. This implies that the quench generator must operate with a quench frequency equal to the data rate. Taking into account hangover effects, which set an upper bound for the quench frequency, we have predicted data transfer rates faster than 200 Mbps for very low-Q SROs. The power consumption of implemented UWB IR SR receivers are among the lowest ever reported, with efficiencies less than 500 pJ/bit at data rates of roughly 10 Mbps.

8. References

Anis, M.; Tielert, R. & Wehn, N. (2008). Super-regenerative UWB impulse detector with synchronized quenching mechanism, *Proceedings of ESSCIRC 2008 34th European Solid-State Circuits Conference*, pp. 390-393, ISSN 1930-8833, Edinburgh, Scotland, UK, September 15-19, 2008

Armstrong, E. H. (1922). Some recent developments of regenerative circuits. *Proc. IRE*, Vol. 10, (August 1922), pp. 244-260, ISSN 0731-5996

Ayers, J.; Mayaram, K. & Fiez, T. S. (2010). An ultra low-power receiver for wireless sensor networks. *IEEE Journal of Solid-State Circuits*, Vol. 45 , No. 9 (August 2010). pp. 1759 – 1769, ISSN 0018-9200

Bohorquez, J. L.; Chandrakasan, A.P. & Dawson, J. L. (2009). A 350μW CMOS MSK Transmitter and 400μW OOK Super-Regenerative Receiver for Medical Implant Communications. *IEEE Journal of Solid-State Circuits*, Vol. 44 , No. 4, (March 2009), pp. 1248 – 1259, ISSN 0018-9200

Chen, J. Y.; Flynn, M. P. & Hayes, J. P. (2007). A fully integrated auto-calibrated super-regenerative receiver in 0.13-μm CMOS; *IEEE Journal of Solid-State Circuits*, Vol. 42 , No. 9, (September 2007), pp. 1976 – 1985, ISSN 0018-9200

Daly, D. C.; Mercier, P. P.; Bhardwaj, M.; Stone, A. L.; Aldworth, Z. N.; Daniel, T. L.; Voldman, J.; Hildebrand, J. G. & Chandrakasan, A. P. (2010). A Pulsed UWB Receiver SoC for Insect Motion Control. *IEEE Journal of Solid-State Circuits*, Vol. 45, No. 1, (January 2010), pp. 153 – 166, ISSN 0018-9200

España-Boquera, M. C. & A. Puerta-Notario, A. (1999). Bit-error rate and frequency response in superregenerative semiconductor laser receivers. *Optics Letters*, Vol. 24, No. 3, (February 1999), pp. 157-159, ISSN 0146-9592

Favre, P.; Joehl, N.; Vouilloz, A.; Deval, P.; Dehollain, C. & Declercq, M. J. (1998). A 2-V 600-μA 1-GHz BiCMOS super-regenerative receiver for ISM applications. *IEEE Jour. of Solid-State Circ.*, Vol. 33 , No. 12, (December 2008), pp. 2186 – 2196, ISSN 0018-9200

Ghavami, M.; Michael, L. B. & Kohno, R. (2004). *Ultra Wideband Signals and Systems in Comm. Engineering*, John Wiley & Sons, ISBN 0-470-86751-5, West Sussex, England

Hickman, I. (2002). *Practical RF Handbook* (3rd ed.). Newnes, ISBN 0 7506 5369 8, Oxford

Lee, F.S. & Chandrakasan, A.P. (2007). A 2.5 nJ/bit 0.65 V pulsed UWB receiver in 90 nm CMOS. *IEEE Journal of Solid-State Circuits*, Vol. 42, No. 12, (November 2007), pp. 2851 – 2859, ISSN : 0018-9200

Levanon, N.; Stremler, F. G. & Suomi, V.E. (1974). A new approach to lightweight radar altimeters. *Proceedings of the IEEE*, Vol. 62 , No. 6, (June 1974), pp. 784 – 792, ISSN 0018-9219

McCoy, W.G. (1992). Design of a superregenerative receiver for solar powered applications. *IEEE Transactions on Consumer Electronics*, Vol. 38, No. 4, (November 1992), pp. 869-873, ISSN 0098-3063

Milner C. J. & Shell, G. S. (1968). A super-regenerative microwave Doppler moving-target indicator. *IEEE Transactions on Vehicular Technology*, Vol. vt-17, No. 1, (October 1968), pp. 13-23, ISSN 0018-9545

Moncunill-Geniz, F. X.; Palà-Schönwälder, P. & Mas-Casals, O. (2005a). A generic approach to the theory of superregenerative reception. *IEEE Transactions on Circuits and Systems I: Regular Papers*, Vol. 52 , No. 1, (January 2005), pp. 54 – 70, ISSN 1549-8328

Moncunill-Geniz, F. X.; Palà-Schönwälder, P. & del Aguila-Lopez, F. (2005b). New superregenerative architectures for direct-sequence spread-spectrum communications. *IEEE Transactions on Circuits and Systems II: Express Briefs*, Vol. 52, No. 7, (July 2005), pp. 415 – 419, ISSN 1549-7747

Moncunill-Geniz, F. X.; Palà-Schönwälder, P.; Dehollain, C.; Joehl, N. & Declercq, M. (2005c). A 2.4-GHz DSSS superregenerative receiver with a simple delay-locked loop. *IEEE Microwave and Wireless Components Letters*, Vol. 15 , No. 8, (August 2005), pp. 499 – 501, ISSN 1531-1309

Moncunill-Geniz, F. X.; Palà-Schönwälder, P.; Dehollain, C.; Joehl, N. & Declercq, M. (2007a). An 11-Mb/s 2.1-mW Synchronous Superregenerative Receiver at 2.4 GHz. *IEEE Transactions on Microwave Theory and Techniques*, Vol. 55, No 6, Part 2, (June 2007), pp. 1355 – 1362, ISSN 0018-9480

Moncunill-Geniz, F. X.; Palà-Schönwälder, P.; del Àguila-Lopez, F. & Giralt-Mas, R. (2007b). Application of the superregenerative principle to UWB pulse generation and reception. *Proceedings of the 14th IEEE International Conference on Electronics, Circuits and Systems, 2007*, pp. 935 – 938, ISBN 978-1-4244-1377-5, Marrakech, Morocco, December 11, 2007

Moncunill-Geniz, F. X.; Pala-Schonwalder, P.; Bonet-Dalmau, J.; del Aguila-Lopez, F. & Giralt-Mas, R. (2009). Sub-nanosecond pulse filtering and amplification through first-order controlled circuit instability. *Proc. of the 39th European Microwave Conf., 2009*, pp. 1319 – 1322, ISBN: 978-1-4244-4748-0, Rome, Italy, September 29, 2009

Opperman, I.; Hämäläinen, M. & Ianatti, J. (2004). *UWB Theory and Applications*, John Wiley & Sons, ISBN 0-470-86917-8, West Sussex, England

Otis, B.; Chee, Y. H. & Rabaey, J. (2005). A 400μW-RX, 1.6mW-TX super-regenerative transceiver for wireless sensor networks. *2005 IEEE International Solid-State Circuits*

Conference, 2005, Digest of Technical Papers, Vol. 1, pp. 396 – 606, ISSN 0193-6530, San Francisco, CA, February 10, 2005

Palà-Schönwälder, P.; Moncunill-Geniz, F. X.; Bonet-Dalmau, J.; del-Aguila-Lopez, F. & Giralt-Mas, R. (2009). A BPSK superregenerative receiver. Preliminary results. *Proceedings of the IEEE International Symposium on Circuits and Systems*, pp. 1537 – 1540, ISBN 978-1-4244-3827-3, Taipei, Taiwan, June 26, 2009

Pelissier, M.; Morche, D. & Vincent, P. (2009). Super-regenerative architecture for UWB pulse detection: from theory to RF front-end design. *IEEE Transactions on Circuits and Systems I*, Vol. 56, No. 7, (July 2009), pp. 1500-1512, ISSN 1549-8328

Telecontrolli Srl, 15.03.2011, Available from http://www.telecontrolli.com

Thoppay, P. (2010). *A low power super-regenerative impulse radio ultra-wideband receiver in CMOS technology,* Ph.D. Dissertation, EPFL, Lausanne, Switzerland

Whitehead, J. R. (1950). *Super-Regenerative Receivers*, Cambridge Univ. Press, Cambridge, UK

Zheng, Y.; Annamalai Arasu, M.; Wong, K.-W.; The, Y. J.; Suan, A.-P.-H.; Tran, D.-D.; Yeoh, W.-G. & Kwong, D.-L. (2008). A 0.18μm CMOS 802.15.4a UWB Transceiver for Communication and Localization. *2008 IEEE International Solid-State Circuits Conference, 2008, Digest of Technical Papers*, pp. 118 – 600, ISBN 978-1-4244-2010-0, San Francisco, CA, February 3, 2008

8

Transmitter Multi-Path Equalization and Receiver Pulse-Injection Locking Synchronization for Impulse Radio Ultra-Wideband Communications

Changhui Hu, Lingli Xia and Patrick Chiang
Oregon State University
USA

1. Introduction

Impulse radio systems have received much attention as a possible architecture for UWB transceivers due to the large data bandwidth, low spectral interference with nearby channels, and simplicity of UWB transmitter/receiver architectures using mostly digital implementations. Due to the low emitted power spectral density of -41.3dBm/MHz mandated by the FCC, impulse radio is especially well suited for low-cost, low-power, and short-range wireless communications. This paper presents an IR UWB transceiver for a typical short-range wireless communication application as shown in Fig. 1 within computer

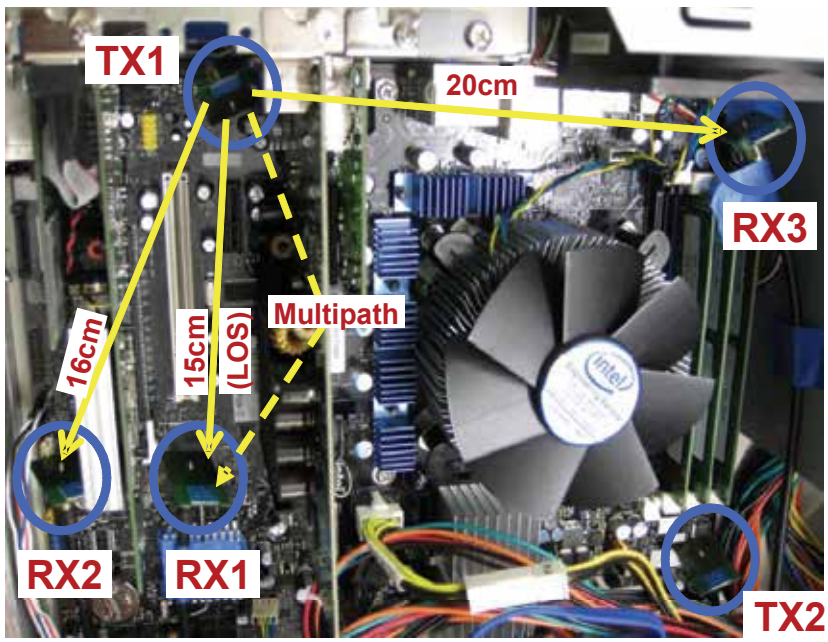

Fig. 1. Inter-chip wireless communication within computer chassis

chassis chip-to-chip wireless interface. However, it is not limited to this; any short-range, high-data-rate wireless communication is applicable.

1.1 Conventional impulse-radio receiver architectures

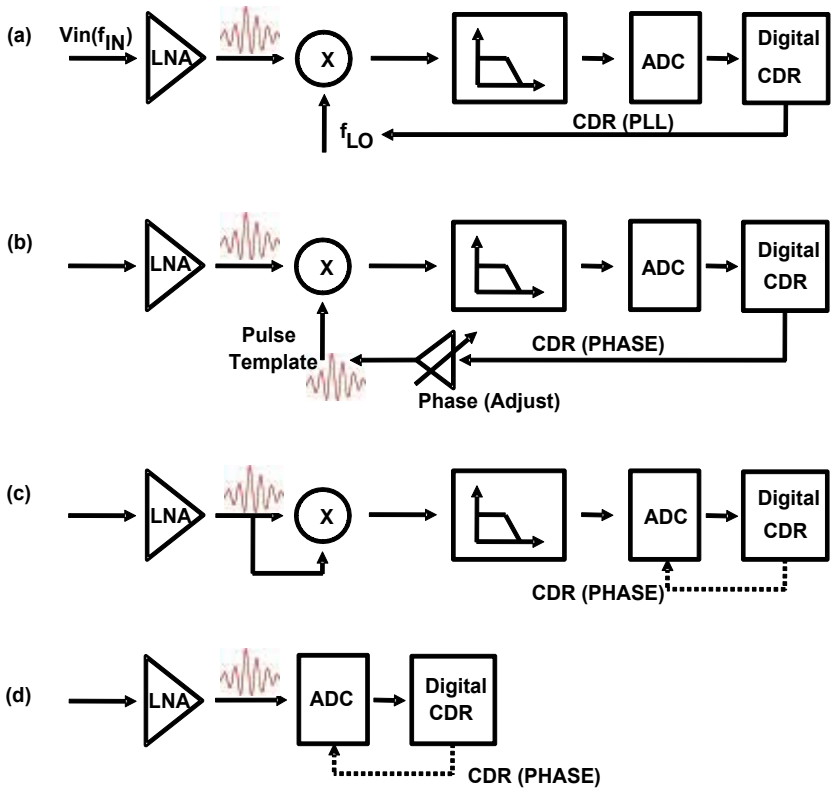

Fig. 2. RX architecture overview

While recent research has demonstrated the energy-efficiency of impulse-based UWB transmitters (Lachartre et al., 2009; Wentzloff & Chandrakasan, 2007), the more critical problem lies within the receiver. Due to the short timing duration of the transmitted impulse, determining the exact arrival of the UWB pulse is extremely difficult, placing most of the system complexity and power burden on to the design of the receiver architecture.
Conventional IR-UWB receiver architectures can be summarized in Fig. 2 above: a) direct-conversion receiver with a local oscillator multiplier/correlator; b) direct-conversion receiver using pulse template multiplier (Zhou et al., 2009); c) non-coherent receiver with self-correlation Lee & Chandrakasan (2007); and d) direct over-sampling analog-digital converter (ADC)O'Donnell & Brodersen (2006). The LO direct-conversion architecture is the most common, and is similar to narrow-band receiver systems. This approach typically consumes the most power due to the clock generation of the high-frequency local oscillator. In addition, due to the large data bandwidth, the low-pass filter is difficult to design, and ADC oversampling is still required to recover the optimal ADC sampling position. In addition, a CDR is still required, as the local receiver clock may be plesiochronous from the transmitter clock. The pulse-template, direct-conversion architecture is commonly used in coherent

IR-UWB RX, but RX phase synchronization is power-consuming and difficult because accurate alignment between TX impulses and RX templates must be achieved. Furthermore, the transmitted impulse from the channel and the antennas may be significantly distorted, increasing the difficulty in generating an accurate pulse template. The non-coherent, self-correlating receiver is an attractive option, as it simplifies the pulse-template generation and synchronization. Unfortunately, bit-error rate will increase as the receiver will not be able to discriminate between noise and transmitted data. In addition, the design of a CDR loop is still required, as the demodulated data needs to be phase-locked with the local receiver clock. The direct over-sampling ADC method is the most straightforward, as the pulse input is directly quantized by the ADC, moving the demodulation and CDR requirements to the digital baseband. Unfortunately, the power overhead for the over-sampling ADC is extremely expensive, as a multi-gigahertz, medium resolution ADC is necessary for the 3.1-10GHz receiver bandwidth.
One overarching constraint of all of these conventional structures is that some mechanism for synchronizing the receiver sampling clock with the incoming transmitted data is required. Because the eventual goal for IR-UWB systems is several hundred Mbps, the design of an over-sampling CDR loop adds both system complexity as well as additional power consumptionZheng et al. (2006).

1.2 Proposed architecture: Receiver pulse injection-locking phase synchronization

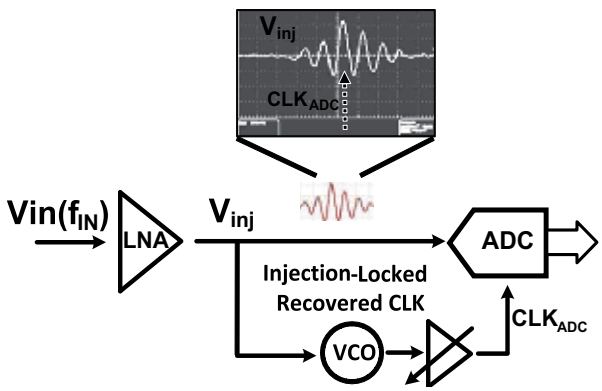

Fig. 3. RX_IL_VCO

In this work, we present a new receiver phase synchronization method using pulse injection-lockingHu et al. (2010), as shown in Fig. 3. This technique provides several advantages over the previously described architectures. First, no CDR is necessary, as the received local oscillator is injection-locked to the incoming pulses and hence is automatically phase-aligned with the transmitted clock. Second, the architecture is inherently a feed-forward system, with no issues with feedback loop stability as seen in phase-locked loops. The proposed system is similar to a "forwarded clock" receiver approach used for high-speed links which have been shown to be extremely energy-efficientHu, Jiang, Wang, O'Mahony & Chiang (2009). The difference here is that the receiver sampling clock is locked to the actual incoming transmitted pulses, eliminating any requirement for a separate clock channel. Third, since the receiver clock is now injection-locked and synchronized with the transmitter, the ADC sampling requirements can be severely relaxed and can now run at the actual data rate. This is a significant advantage for power reduction, as a multi-gigahertz, over-sampling ADC is no longer necessary.

2. System analysis and operation principle

2.1 Transmission power and pulse shaping

For the 3.1-10.6GHz UWB band, the FCC limits the maximum transmitting power spectrum mask to -41.3dBm/MHz. Therefore, the maximum allowable transmitted power within 3-5GHz is -8.3dBm, but no such a pulse can meet the FCC mask in practice, assuming a filling coefficient of k ($0 < k < 1$), or spectral efficiencyWentzloff (2007). The filling coefficient (spectral efficiency) k of a pulse is the loss incurred from incomplete filling of the -10dB channel bandwidth, calculated by:

$$k = \frac{E_{ch}}{P_{EIRP} BW_{-10dB}} \tag{1}$$

where Ech is the pulse energy within the -10dB channel bandwidth, PEIRP is the maximum average power spectral density, and BW-10dB is the -10dB bandwidth.
Due to this filling coefficient, the maximum transmission power will be much smaller. To improve this filling coefficient, many techniques for baseband pulse shaping have been investigated since the release of the UWB FCC mask *First Report and Order* (n.d.). For example, a gaussian pulse is theoretically the ideal pulse shaping technique, but it is difficult to implement Wentzloff & Chandrakasan (2007); Zheng et al. (2006).

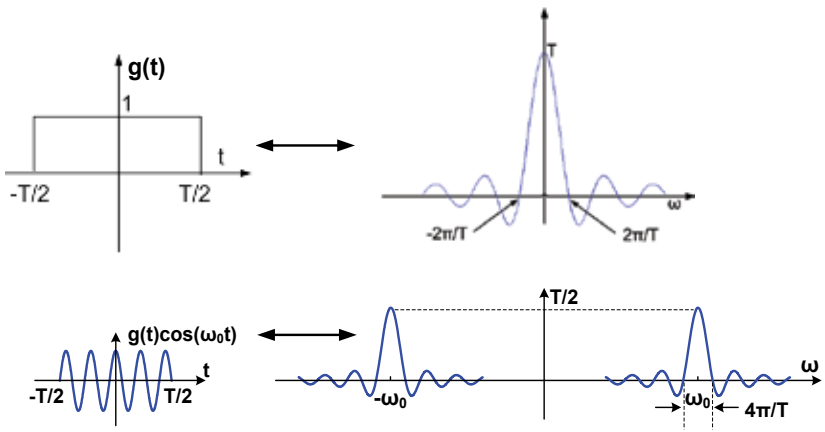

Fig. 4. Rectangular baseband and sine-wave modulated pulses in time and frequency domain

Fig. 4Lathi (n.d.) shows the Fourier transform of a baseband rectangle pulse and a rectangle pulse modulated by a sine wave. Notice that the spectral bandwidth is inversely proportional to the pulse width, where for a rectangle pulse of T(s) pulse width, its frequency bandwidth is 2/T(Hz). For the 3-5GHz UWB band, the maximum bandwidth is 2GHz when the carrier frequency is 4GHz, with a minimum pulse width W_{pulse} of 1ns. Assuming a 1ns pulse width, the pulse amplitude will depend on the pulse repetition frequency (PRF or data rate), limited by the maximum allowed transmission power. For data rates of 500Mbps, 250Mbps, and 125Mbps, with equal probability of "1" and "0" symbols, a filling coefficient of k=0.5, and a 50ohm antenna load, the corresponding pulse amplitudes required will be 172mV, 243mV, and 344mV, as derived from Equation 2:

$$V_p = \sqrt{\frac{2R \cdot P}{0.5 \cdot DR \cdot W_{pulse}}} = \sqrt{\frac{200 \cdot k \cdot P_{max}}{DR \cdot W_{pulse}}} \tag{2}$$

2.2 Modulation scheme

Several modulation schemes have been used for IR-UWB transceivers, such as binary-phase shift keying (BPSK)Zheng et al. (2006), pulse-position modulation (PPM)Wentzloff & Chandrakasan (2007), and on-off keying (OOK)Lachartre et al. (2009). To recover the clock phase information from the data using pulse injection locking, OOK is chosen for this transceiver due to simplicity, although PPM and amplitude modulation (AM) would also work. Note that to maintain a sufficient number of transmitted impulses necessary to insure receiver phase locking, DC balancing and maximum run length limiting are required for the proposed system, such as 8b/10b encoding.

2.3 Path loss

Ideal free space (FS) propagation (no multipath reflections) exhibits a path loss that is proportional to the square (α=2) of the separation distance "d", with λ the wavelength*UWB Channel Modeling Contribution from CEA-LETI and STMicroelectronics* (n.d.):

$$PL_{dB}(d) = \alpha \cdot 10\log_{10}(\frac{4\pi d}{\lambda}) = \alpha \cdot 10\log_{10}(d) + c \tag{3}$$

where α is the path loss exponent and c is a power scaling constant obtained after channel calibration. $Frris's$ formula suggests that for a propagation distance of 1m, the path loss equals to 44.5 dB at a 4GHz center frequency; a 25cm distance exhibits a path loss of 32.5dB, assuming antenna gains of 0dBi for both the transmitter and receiver.

2.4 Link budget

For a targeted bit error rate(BER) of 10^{-3}, coherent OOK modulation requires E_b/N_0 of 9dB.

$$SNR = \log_{10}(E_b/N_0 \cdot DR/B) \tag{4}$$

where DR is the data rate, and B is the signal bandwidth.
For a 500Mbps data rate, after converting E_b/N_0 to SNR using Equation(4), 9dB E_b/N_0 is equivalent to an SNR of 3dB, and 0dB SNR is required for 250Mbps.
Assuming a 3-5GHz UWB spectral mask filling coefficient of k=0.5 or -3dB, 44.5dB line-of-sight (LOS) loss at 4GHz, and data rate 500Mbps, the link budget is estimated as follows:

$$SNR = P_{TX} - PL - N_{channel} - NF - I \tag{5}$$

$$N_{channel} = -174dBm/Hz + \log_{10}(B) = -81dBm \tag{6}$$

$$\begin{aligned} NF + I &= -11.3dBm - 44.5dB + 81dBm - 3dB \\ &= 17.2dB \end{aligned} \tag{7}$$

Therefore, a 17.2dB noise figure NF(including implementation loss I) is sufficient for a communication data rate of 500Mbps, assuming a raw BER of 10^{-3} through a distance of 1mVan Helleputte & Gielen (2009). Note that the calculation above is an estimation, as many other factors, such as receiver clock jitter, are not considered.

2.5 Synchronization

RX phase synchronization with the incoming TX impulses is a critical issue in conventional coherent transceiversVan Helleputte & Gielen (2009). Initially, the receiver has no information

about when the transmitted pulses are arriving. Therefore, for the receiver to synchronize with the incoming impulses, conventional systems undergo two modes of operation: data acquisition and data reception. During data acquisition, a known header is transmitted. The receiver synchronizer scans all the possible window positions for this header and measures the received signal energy in each window. These correlation algorithms run in the digital back-end, which control the analog-front-end (AFE). Once the proper window is found, the receiver is locked to the transmitter and is then switched to data reception mode.
Unfortunately, practical conventional IR-UWB transceivers exhibit a frequency offset drift between transmitter and receiver. This small offset will result in a slow but gradually increasing phase difference between the received pulse and receiver pulse template window. As a result, the received impulse will move out of the receiver pulse template window, such that receiver must switch to data acquisition mode again, consequently reducing the data rate and increasing BER. One possible solution is implementing a matched filter receiver within a control loop that locks to the peak value of the correlated received signal, but in practice, this is extremely difficult due to the small received input signal.
In this work, the receiver clock is extracted from the received impulses using pulse injection-locking. Hence, the receiver clock is automatically phase aligned with the received pulse, exhibiting neither clock offset nor phase drift. Additionally, the phase difference between the received impulse and the receiver clock can be statically adjusted by a programmable phase shifter in the receiver clocking path, aligning the receiver sampling point with the optimal SNR position of the incoming impulses . Hence, the proposed clock synchronization technique solves the conventional synchronization issue without requiring a CDR.

3. IR-UWB transceiver implementation

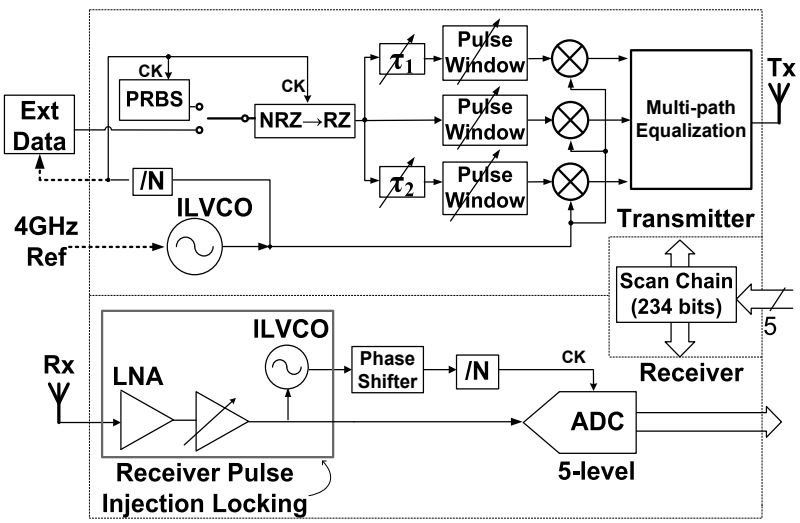

Fig. 5. IR-UWB transceiver architecture

The proposed IR-UWB transceiver is shown in Fig. 5, consisting of a UWB transmitter with multi-path equalization, a pulse-injection-locking receiver with an integrated ADC, an on-chip PRBS TX-generator and RX-checker, and a 234-bit scan chain for controlling low-frequency calibration of DC calibration bits such as current sources and resonant tank tuning. In the transmitter, OOK modulation is generated from a passive modulator, using

a $2^{15} - 1$ bit pseudo-random bit sequence (PRBS) selectable during testing operation. An on-die, 3-5GHz LC-VCO is clock-gated that generates the transmitted pulses, followed by a pulse-shaping control block that enables tunable pulse widths between 0.4-10ns.
In the receiver, the received pulse is amplified by a two-stage LNA before being directly injected into both a five-level flash ADC and a 3.4-4.5GHz, injection-locked VCO (IL-VCO). After the receiver VCO is injection-locked and phase-synchronized with the transmitted pulses, it is phase-shifted and divided down to provide the baseband ADC sampling clock. After the ADC sampling clock is divided down to the same frequency as the incoming data rate, the sampling clock is phase locked and aligned to the peak of the received input pulse, eliminating any requirements for baseband clock/data recovery. Setting the optimal phase position of the ADC sampling clock can be achieved by measuring the BER and building a bath-tub curve, sweeping through all possible phase positions. The five-level flash ADC is designed using dynamic sense amplifiers with offset-adjustable, current-steering DACs. The phase-shifter, which enables programmable, tunable phase delay of the ADC sampling clock, uses a Gilbert-cell, current-summing DAC that achieves a minimum step size of 0.5ps.

3.1 Multi-path equalization

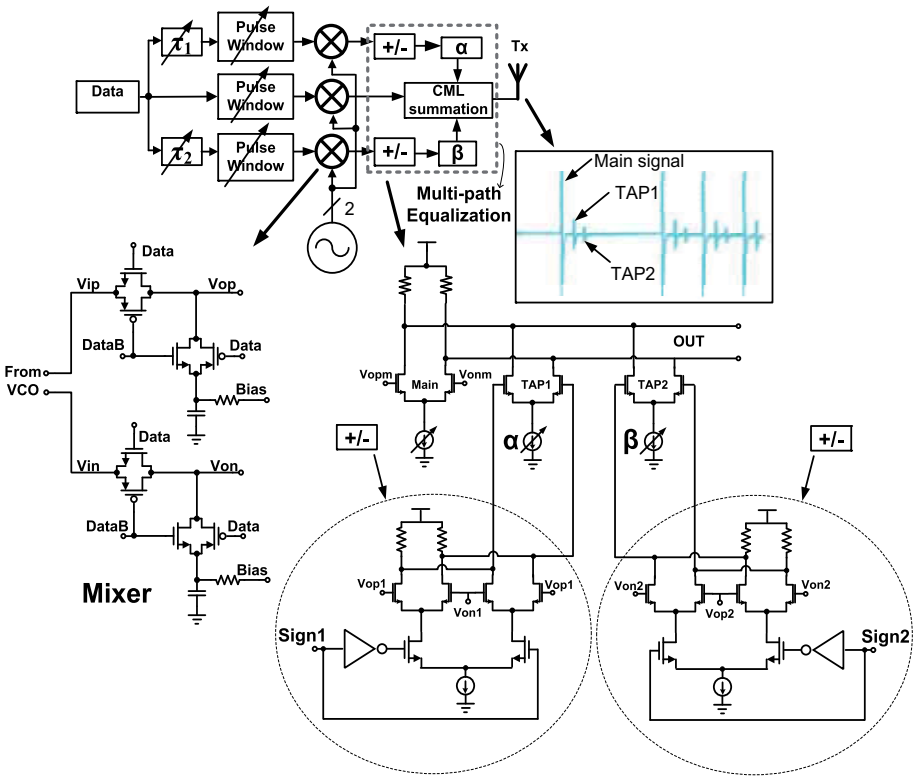

Fig. 6. Transmitter equalization

Some UWB environments exhibit severe multi-path interference, such as within a computer chassis Chiang et al. (2010), severely degrade the receiver BER, especially at high data rates. To reduce the interference from nearby reflections, a multi-path transmitter equalizer is designed that can reduce the two most severe multi-path reflections Hu, Redfield, Liu, Khanna, Nejedlo & Chiang (2009). Tap1 and Tap2 are delayed versions of

the main signal, with sign and coefficient control, depending on the actual multi-path channel environment Hu, Redfield, Liu, Khanna, Nejedlo & Chiang (2009).
Fig. 6 shows the transmitter block diagram and schematic of the pulse gating mixer and equalizer. The pulse windowing circuit controls the baseband pulse width and consequently the modulated pulse width, enabling control of the spectral bandwidh. The delay control circuits τ_1 and τ_2 control the Tap1 and Tap2 signal delay for the equalization implementation.

3.2 Receiver pulse injection-locking

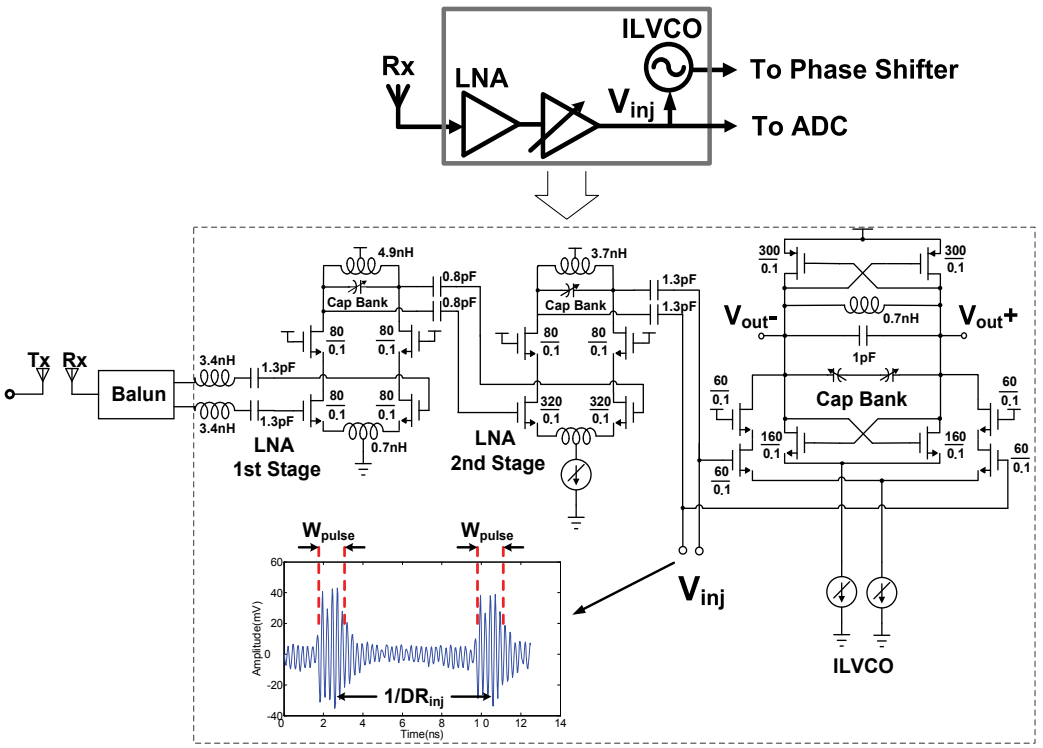

Fig. 7. Receiver injection locking

Receiver clock phase synchronization and acquisition with the received UWB pulses is critical for achieving low power consumption, as discussed in the introduction. Fig. 7 shows the injection-locking block diagram, consisting of a two-stage LNA and an IL-LCVCO.
The first stage of the LNA is source-degenerated with on-chip input matching to 50 Ohms. The LNA second stage is a source-degenerated, cascaded gain stage, with its input conjugate matched to the output of the first stage. Low Q differential inductors are used to achieve wideband frequency response. For example, staggered center frequencies of f_1=3.5GHz(first stage) and f_2=4.5GHz(second stage) are designed to achieve a broad frequency response from 3.1GHz to 5GHz. Additionally, digitally tuned capacitor banks at the outputs of both the first and second stage help to compensate for any process variations or model inaccuracies. Digital calibration loops for determining the correct capacitor values have been previously proposed in Jayaraman et al. (2010).
Due to the limited bandwidth within the LNA, the LNA output exhibits inductive tank oscillations that will elongate the received pulses width to more than 1ns. These may cause

inter-symbol-interference (ISI), limiting the highest achievable data rate to approximately 500Mbps.
In the injection-locked VCO (ILVCO), a 4-bit cap bank is used to tune the VCO free-running frequency, so that the input pulse carrier frequency is close to the ILVCO free-running frequency and injection locking will happen. The smaller the frequency difference, the smaller is the jitter of recovered clock.

3.2.1 Phase noise

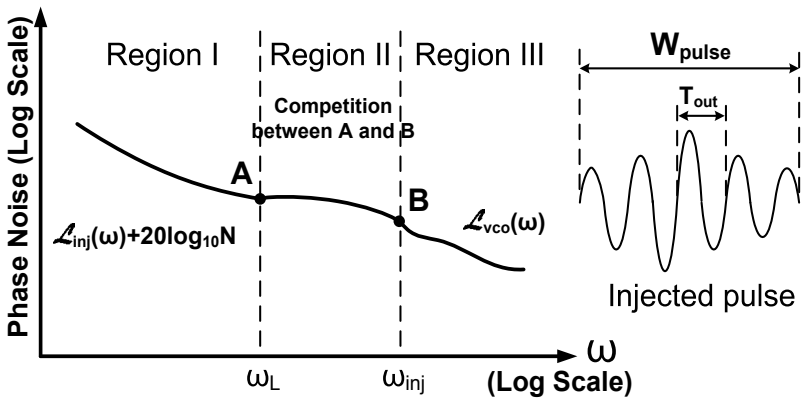

Fig. 8. Phase noise model of injection-locked VCOsLee et al. (2009)

The proposed receiver clock recovery uses pulse injection-locking from the transmitted pulses, similar to sub-harmonic injection-locking proposed in Lee et al. (2009),Lee & Wang (2009). As shown in Fig. 8, Region I denotes the region where the offset frequency is smaller than the locking range of the injection-locked VCO, where the VCO noise is suppressed by the injected signal. Region II is the competition region, where the VCO phase noise is the result of the competition between the injected signal and the VCO free-running signal. In Region III, beyond the injected signal frequency, the VCO phase noise is dominated by the VCO free running phase noise. Similar to a sub-harmonic-injection-locked PLLLee & Wang (2009), for this pulse-injection-locked VCO, the effective division ratio N can be expressed as:

$$N = \frac{f_{out}}{\alpha \cdot \beta \cdot DR_{inj} \cdot n} = \frac{f_{out}}{\alpha \cdot \beta \cdot DR_{inj} \cdot (W_{pulse}/T_{out})} = \frac{1}{\alpha \cdot \beta \cdot DR_{inj} \cdot W_{pulse}} \tag{8}$$

where α is the probability that data is "1"; β is the roll-off coefficient due to pulse-shaping at the Tx output compared with an uniformly-gated, sine-wave pulse; DR_{inj} is the data rate; f_{out} and T_{out} are the the ILVCO output signal frequency and period; and W_{pulse} is the pulse width, as shown in Fig. 7. Similar to Lee et al. (2009), the phase noise degrades as $20logN$ dB, compared with the injected signal. From Equation8, we can see that an increase in the injection pulse rate or pulse width reduces the phase noise of ILVCO output, because more external clean energy is injected into the noisy oscillator.

3.2.2 Locking range

An injection-locked VCO suppresses the noise within the locking range, similar to a first-order PLL, where the bandwidth ω_{BW} is equal to the locking range ω_L. Similar to the sub-harmonic injection-locked PLL, the locking range ω_L degrades as N increases. The locking range of a sine-wave-injected VCO is described in Razavi (2004), Adler (1973):

$$\omega_L = \frac{\omega_{out}}{2Q} \cdot \frac{I_{inj}}{I_{osc}} \cdot \frac{1}{\sqrt{1 - \frac{I_{inj}^2}{I_{osc}^2}}} \tag{9}$$

where Q represents the quality factor of the tank, and I_{inj} and I_{osc} represent the injected and oscillation currents of the LC-tank VCO, respectively. With pulse injection-locked VCOs, the effective injection current is $I_{inj,eff} = I_{inj}/N$, because less current is injected when compared with full sine-wave injection. Consequently, the locking range of a pulse-injection-locked VCO is modified as:

$$\omega_L = \frac{\omega_{out}}{2Q} \cdot \frac{I_{inj}}{I_{osc}} \cdot \frac{1}{N} \cdot \frac{1}{\sqrt{1 - \frac{I_{inj}^2}{I_{osc}^2 \cdot N^2}}} \approx \frac{\omega_{out}}{2Q} \cdot \frac{I_{inj}}{I_{osc}} \cdot \frac{1}{N} \tag{10}$$

3.3 Phase shifter

The phase shifter uses a current-steering DAC that supplies tail current to the two differential pairs while sharing the same resistive loadingBulzacchelli et al. (2006), as shown in Fig. 9. The bottom current-steering pair controls the weight of the current of the input clock phase for the two differential pairs. For example, the input phases of Φ_1, Φ_2, Φ_3, and Φ_4 are 0°, 90°, 180°, and 270° respectively. When the current-steering is changed, the combination of Φ_1 and Φ_2 can be rotated from 0° to 90°. The DAC-controlled current-steering employs 8-bit binary weighted cells with another half that are statically fixed, such that the output phase can be adjusted with a total range of 70ps and a minimum step size of 0.5ps, which is small enough for aligning the ADC clock with the received signal.

3.4 ADC

Fig. 10 shows the five-level flash ADC that incorporates latched sense-amplifiers as the comparatorsSchinkel et al. (2007). Different quantizer offsets/thresholds can be digitally programmed with the current DACLee et al. (2000), allowing for different comparator references. The sampling clock is directly derived from received recovered output from the injection-locked VCO after passing through the phase shifter and divider. The ADC sampling rate is the same as the impulse data rate, resulting in significant power savings over a conventional 2x-Nyquist sampling. The total power consumption for the ADC is about 2mW for a data rate of 500Mbps.

4. Measurement results

Fig. 11 shows the measurement setup. A laptop installed with Labview controls the on-chip scan-chain via a Ni-DAQ interface. Free-space measurements are performed with two 0dBi gain UWB antennas across a 10-20cm distance. Compared to a wired connection measurement (BER $< 10^{-3}$), the interference noise in the air degrades the BER significantly.

The $2mm^2$ IR-UWB transceiver is built in a 90nm-CMOS, 1.2V mixed-signal technology as shown in Fig. 12. The chip is mounted on a PCB using chip-on-board (COB) assembly with an off-chip, low-speed scan interface implemented through a NIDAQ/Labview module.

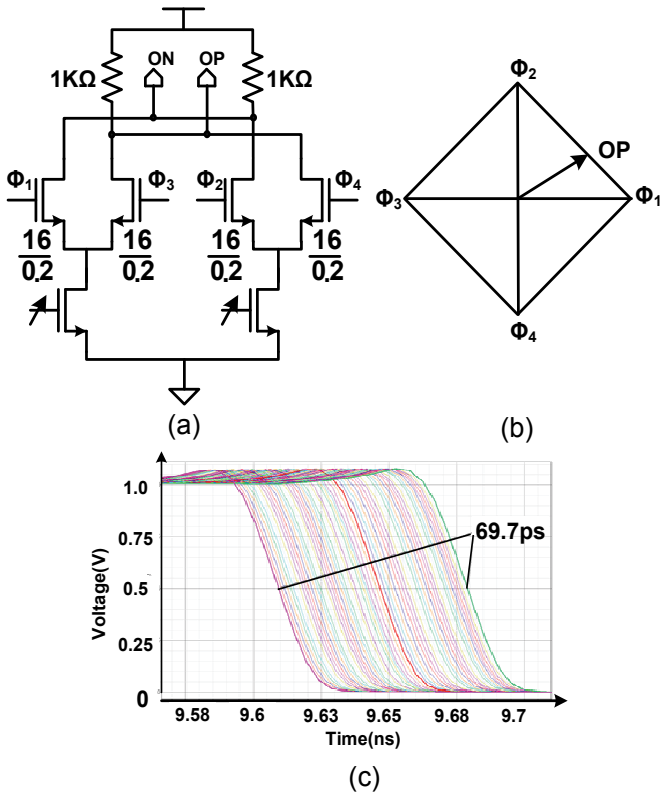

Fig. 9. Phase shifter: (a) Simplified schematic: (b) Phase shifter operation; (c) Phase shifter simulation results.

4.1 Free-space measurement

The measured transmitted signal and its spectrum are shown in Fig. 13. The amplitude of the pulse is 160mVpp, with a nominal pulse width of 1ns. The frequency spectrum fulfills the FCC UWB spectral mask except for the GPS band, which can be easily improved by incorporating more design attention to spectral shaping in the transmitter output Zheng et al. (2006). The maximum transmission data rate is 500Mbps.

Fig. 14 shows the S11/S21 simulation results of 2-stage LNA as well as S11 measurement of the receiver input. The measured S11 is centered at 4GHz, < -10dB is achieved for frequencies between 3.1-5GHz. Digital capacitor banks in LNA1 and LNA2 can adjust the inter-stage matching.

Fig. 15 shows the recovered IL-VCO clock locked to the LNA output, after phase/data alignment of the pulse zero crossing is achieved with the ADC sampling clock. With a 1ns pulse width, data rate of 250Mbps, the recovered clock jitter is 7.6ps-RMS. For the same pulse width, data rates of 125Mbps and 500Mbps are also measured, with RMS jitter of 8.0ps, and 23ps. Due to the limited bandwidth of LNA, the ISI (inter-symbol-interference) seems worse at the high data rate of 500Mbps, increasing the clock jitter.

Fig. 16(a) shows the measured injection-locking range versus varying pulse width and pulse repetition rate. As can be seen, wider pulse width and higher data rate will improve the locking range, as more transmitted pulse energy synchronizes the receiver IL-VCO. Fig. 16(b) shows the measured close-in phase noise, from free-running without injection, to pulse

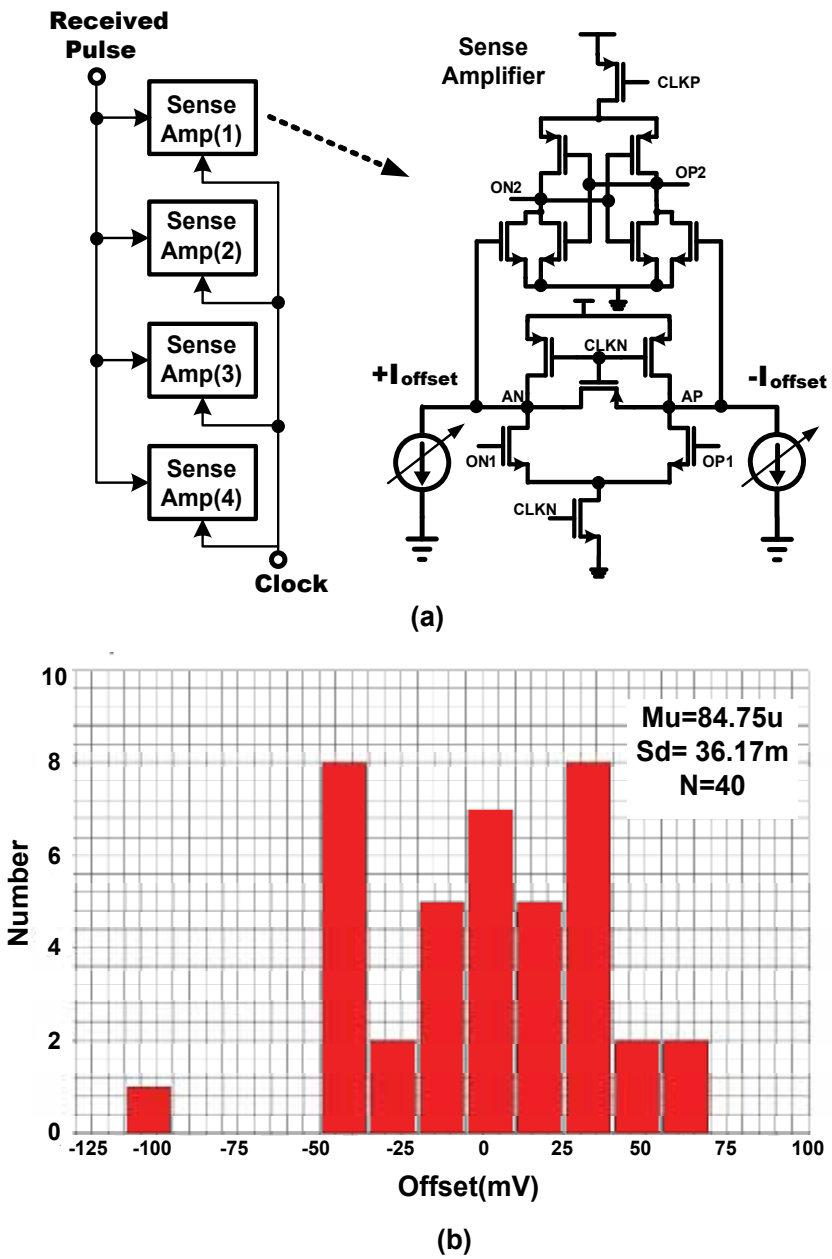

Fig. 10. Flash ADC: (a) flash ADC block diagram and comparator; (b) Monte Carlo histogram simulation results of the comparator offset with process variation and mismatch

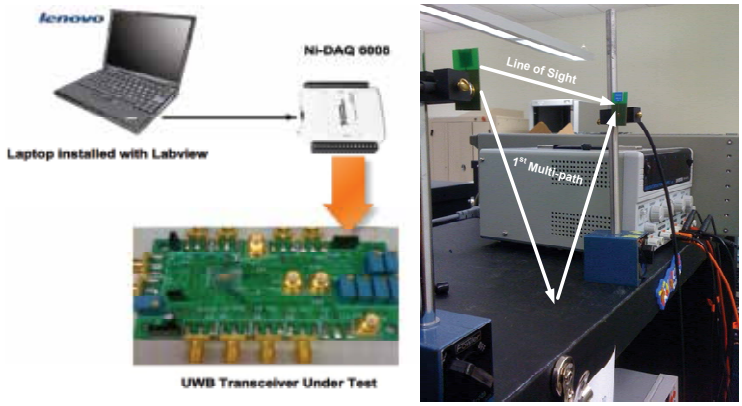

Fig. 11. Measurement setup

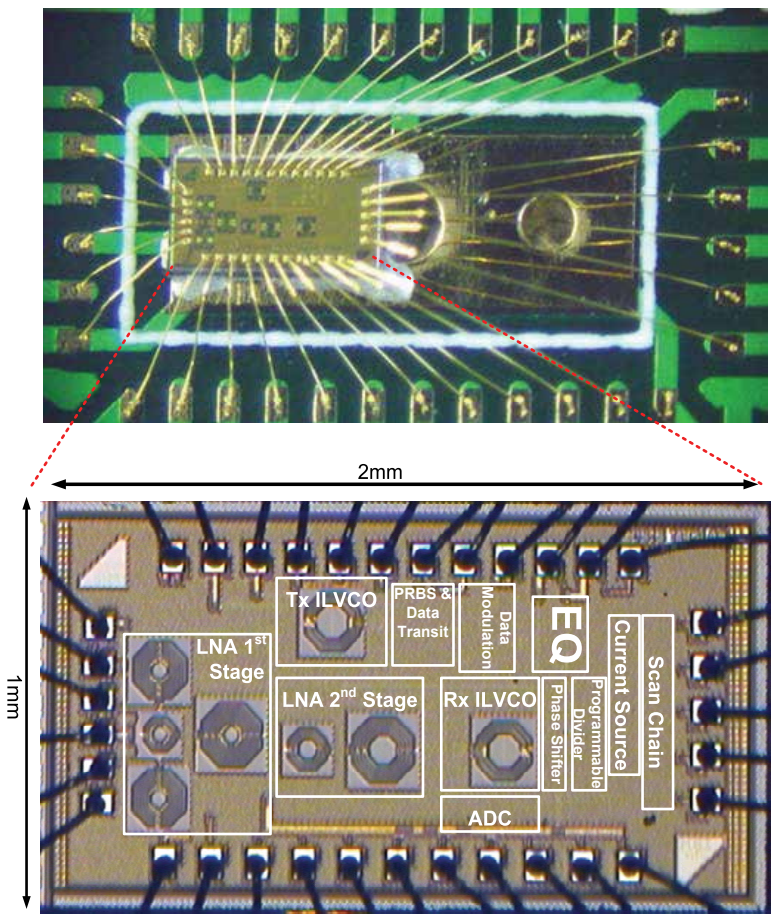

Fig. 12. COB and die photo

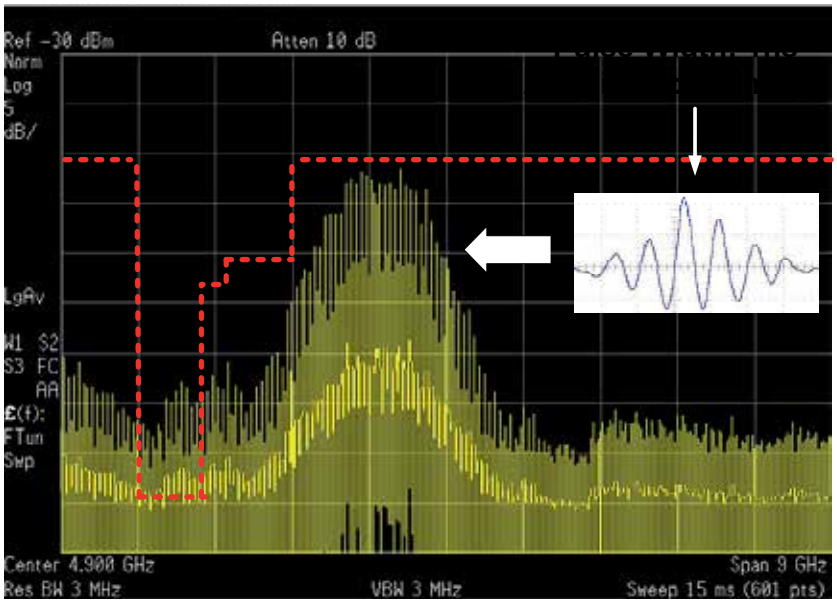

Fig. 13. Transmitted signal and power spectrum

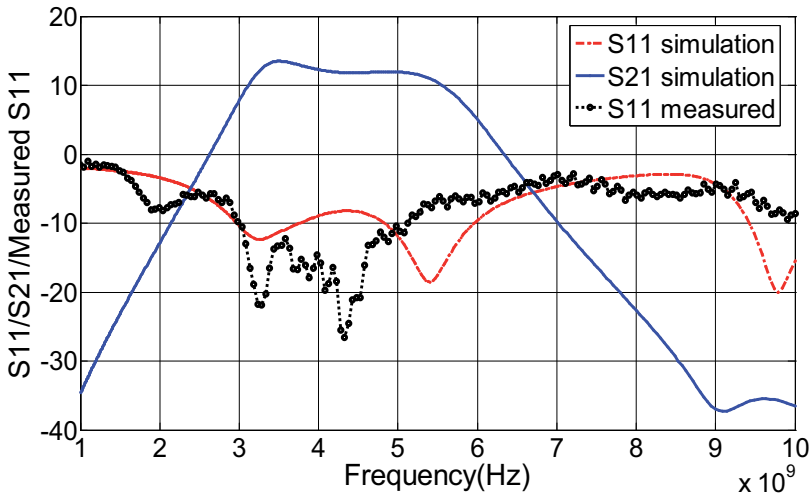

Fig. 14. S11/S21 simulations results of 2-stage LNA and S11 measurement of receiver input

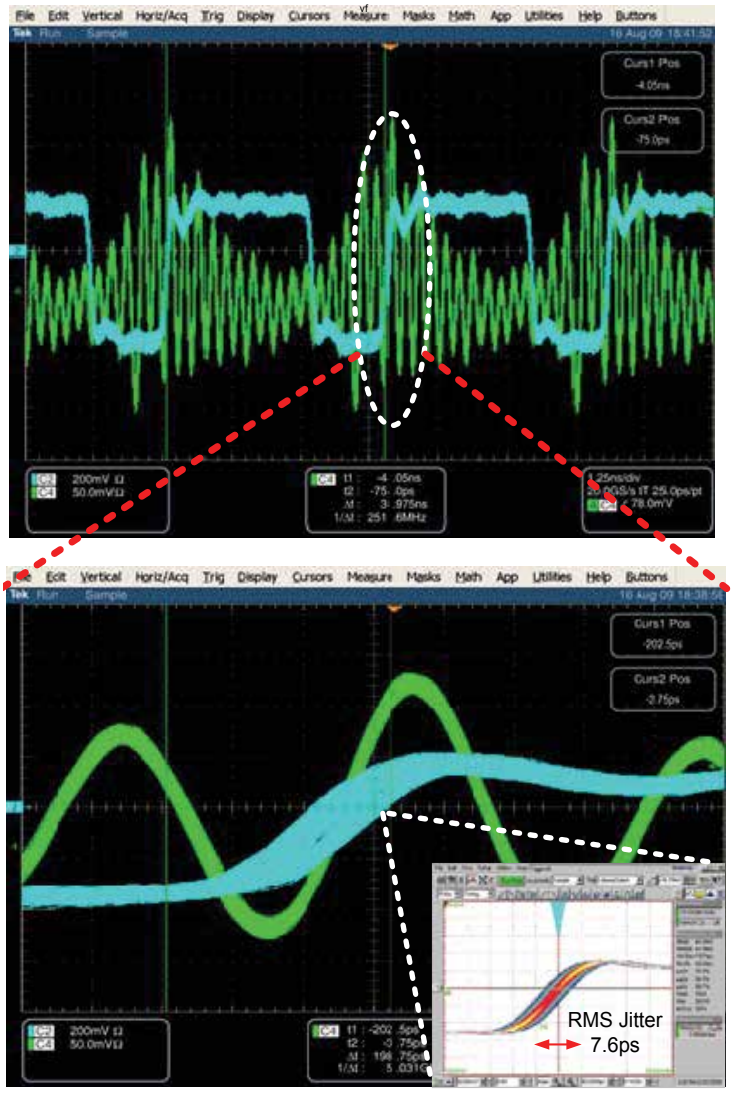

Fig. 15. ADC clock and received signal alignment measurement

repetition frequencies of (DR_{inj}) 125Mbps and 500Mbps, and finally sine-wave injection. Lower phase noise is exhibited at higher injection rates, as the phase updates occur at a higher frequency, similar to the dynamics in a first-order phase-locked loop (PLL). The results also verify Equation 8, showing approximately a 12dB phase noise difference between 125Mbps and 500Mbps pulse injection rates. Without pulse injection, the free running VCO shows very large phase noise at a low-frequency offset.

While a long string of empty data transitions would result in loss of phase synchronization, conventional DC-balanced codes such as 8b/10b can limit maximum run length. Transmission using the on-chip PRBS-15 modulator, exhibiting a maximum string length of fourteen zeros, showed no loss in receiver phase synchronization.

The free-space measurement setup uses two UWB antennas that are placed 10cm away. Fig. 17(a) and (b) show the transmitted digital data, received pulses after LNA gain, the

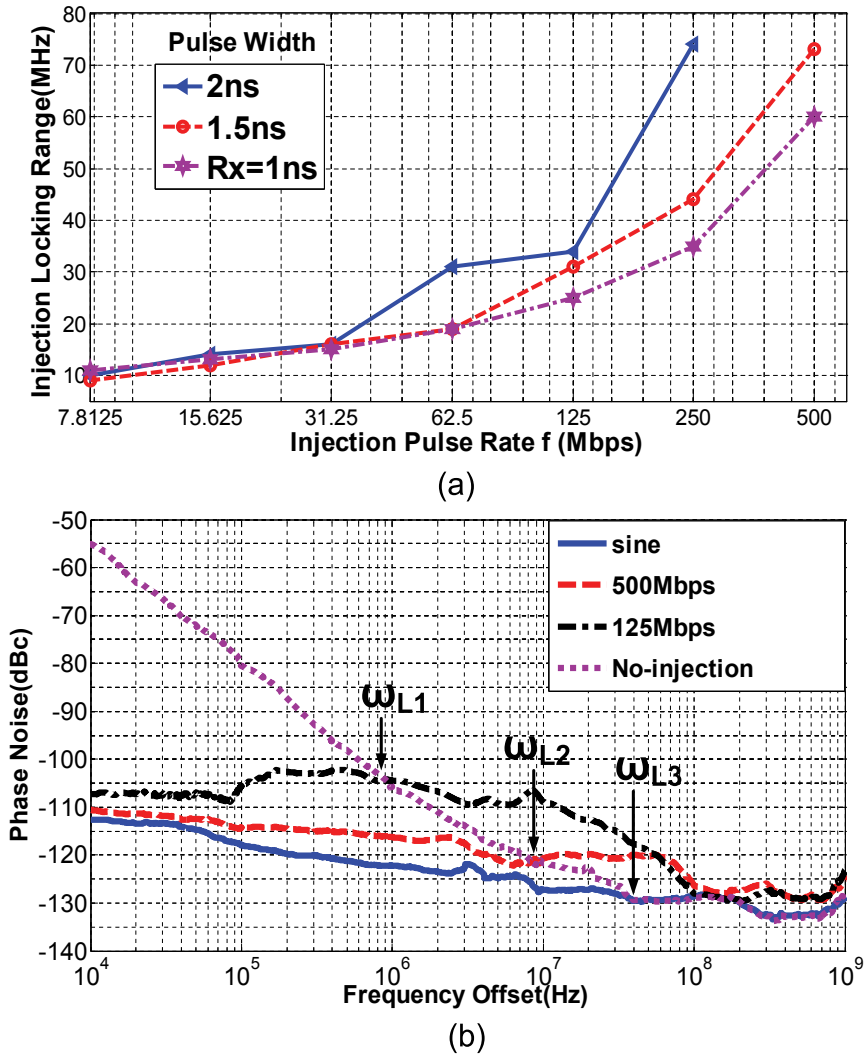

Fig. 16. Injection-locking measurement: (a) Pulse injection lock range vs. pulse width and pulse rate, (b) Pulse-injection-locked VCO phase noise vs. pulse rate. (ω_{L1}, ω_{L2} and ω_{L3} are the estimated locking range when injection data rate are 125Mbps, 500Mbps, and full sine-wave injection.)

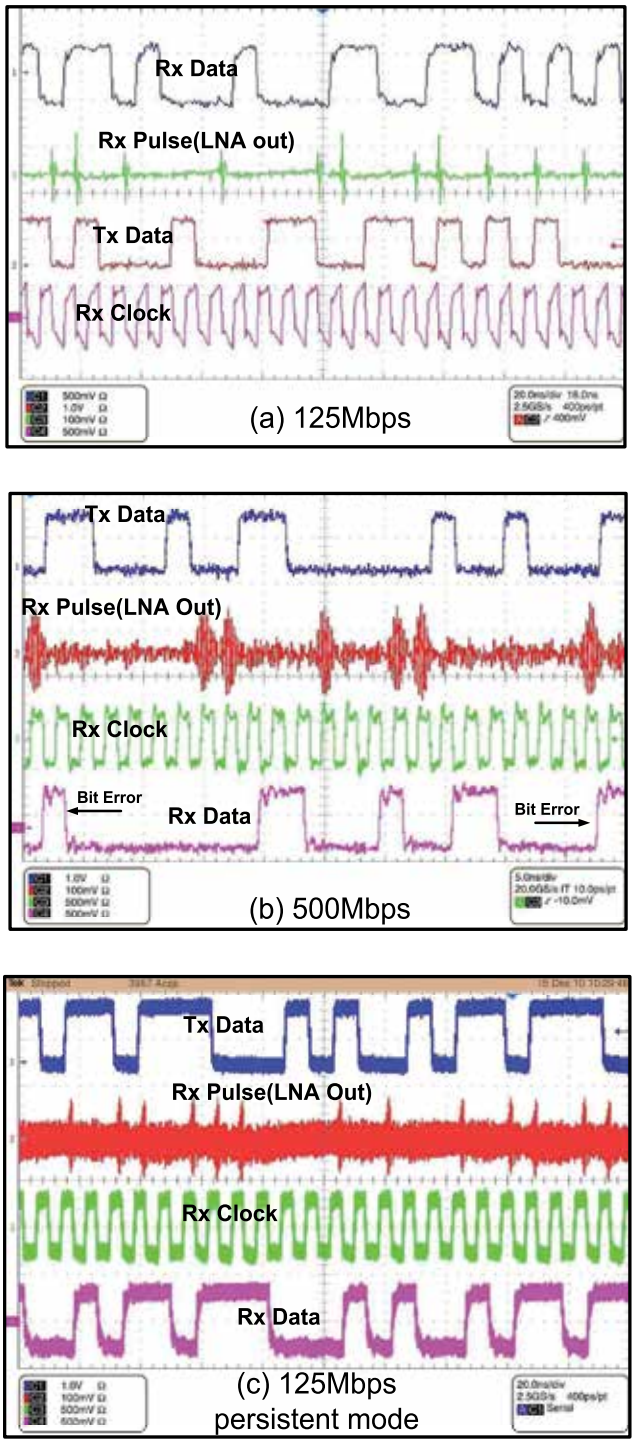

Fig. 17. Measured Tx data, Rx clock, received pulse and recovered data (125Mbps, 500Mbps) through 10cm: (a) 125Mbps, (b)500Mbps, (c) 125Mbps in infinite persistent mode.

recovered Rx clock, and finally the received demodulated data at 125Mpbs and 500Mbps. In addition to the above, at 125Mbps, 8cm distance with less multi-path reflection environment, infinite persistent mode is measured with a data pattern as in Fig. 17(c).

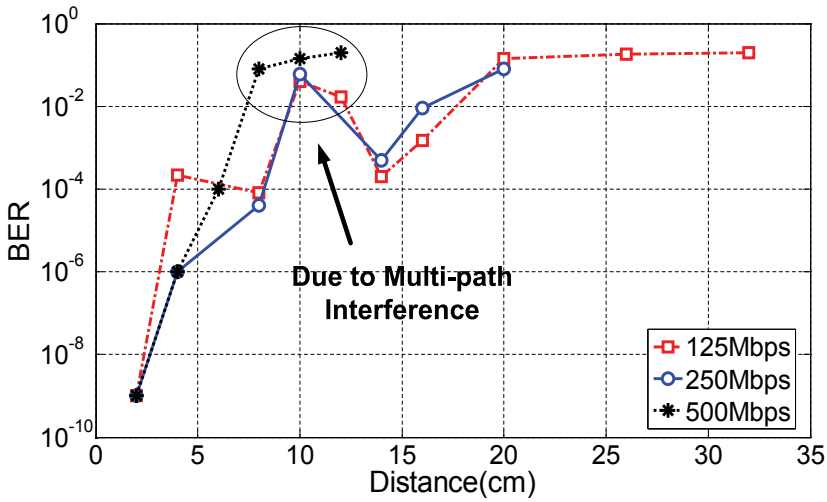

Fig. 18. Measured receiver BER versus distance @125Mbps, 250Mbps and 500Mbps with 110mVpp 1ns wide pulse

Free-space BER measurement is done with different distances for data rates of 125Mbps, 250Mbps, and 500Mbps, as shown in Fig. 18, while the transmitting pulse amplitudes are set to 110mVpp. Due to multi-path interference, it can be seen that at around 10cm, the BER is worse than that at 14cm distance because the multi-path reflections happen to be out of phase with the direction path signal at 10cm distance.
Because this receiver is injection-locked, interferer will increase the recovered clock jitter and increase the BER, so it is important to measure interference performance. By putting a single tone interferer through a UWB antenna close to the receiver antenna, characterizing the received interference power at receiver input, and increasing the interference power until the BER reaches 10^{-3}, we get the maximum tolerable power at receiver input. With a communication distance of 14cm, 125Mpbs 110mVpp 1ns wide pulses are transmitted for the interferer test. The measurement interference performance is shown in Fig. 19 for both in-band and out-band. The maximum tolerable interferer power is -50dBm at 4GHz and -25dBm at 2.4GHz.
Eight PCB evaluation boards are measured, showing consistently good measurement results. Measured performances are summarized in Table 1. Table 2 compares the performance with prior state-of-the-art, energy-efficient IR-UWB transceivers.

4.2 Multi-path equalization measurement

Multi-path reflections affect the signal differently in short-distance channels and long-distance channels (relative to the data rate): 1) For short channels, multi-path reflections are close to the main signal (direct path), causing intra-symbol interference; (while OOK modulation is somewhat enhanced by this additive energy from multi-path reflections, BPSK modulation would be severely limited due the sign change inversion.) 2) For long channels, multi-path reflections show longer delay from the main signal and may fall in the next symbol. Both intraference and interference can degrade the BER.

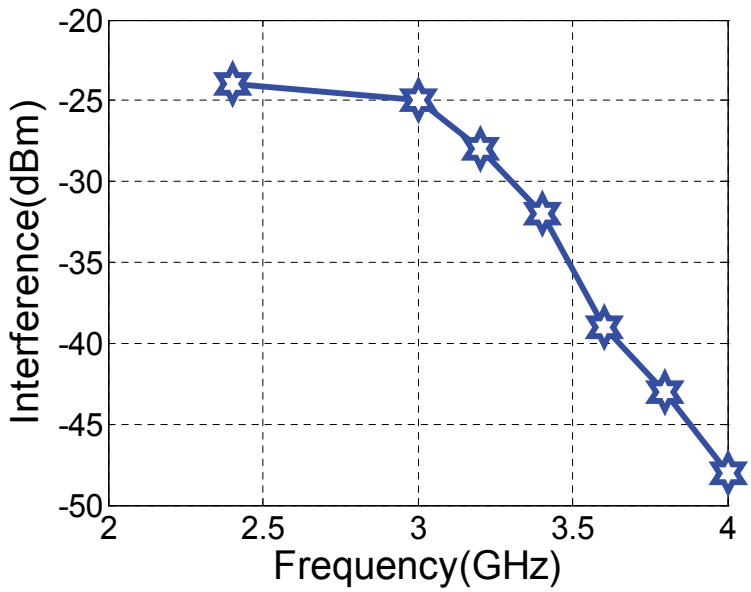

Fig. 19. Measured maximum tolerable interference power to maintain 10^{-3} BER at 125Mbps and 14cm distance when transmitting 110mVpp 1ns wide pulse.

The multi-path equalizer can cancel multi-path reflections in both short-distance and long distance channels for this OOK IR-UWB transceiver. For short channels, intra-symbol interference helps to increase the symbol energy but degrade the clock jitter, while the equalizer can help to remove intraference to reduce recovered clock jitter, consequently improving BER. For long channels, the equalizer can cancel inter-symbol interference, reduce recovered clock jitter, and improve the BER.

Measurements of the UWB transceiver were obtained for short-range, high data-rate communications inside a computer chassisChiang et al. (2010). A pre-distorting equalizer in the IR-UWB transmitter was activated in order to reduce ISI (intra-symbol-interference/inter-symbol-interference) caused by the existence of multi-path reflections from nearby metallic reflections. Fig. 20 (a) shows the simulated multi-path intra-symbol-interference of the main symbol (or baseband pulse) and the two most dominant multi-path interferer. Note that the combined energy of all three pulses sums to a symbol amplitude that exceeds the direct-path symbol. For short-distance channels, these multi-path reflections typically are a result of the main symbol generating post-cursors off of nearby reflections. For example, a time-of-flight of 1ns is equivalent to a 30cm propagation distance. For higher data rates, proceeding symbols may additively combine with current symbols, causing multi-path interference that affects the maximum data rate.

In the equalization measurement setup, all antennas are stationary, resulting in a fixed amplitude and time delay for the multi-path signal that arrive at each receiver. Hence, the two-tap coefficient delay, amplitude, and sign of the equalizer were calibrated at reset time, and adjusted differently for each of the multi-path propagations.

Fig. 20 (b) shows the pulse response (after squaring and low-pass filtering) before and after equalization is applied, for one of the receivers on the motherboard. On the left, a single pulse response is observed with several multi-path pulse interferer causing a long pulse tail. On the right, a single pulse is observed where the first tap equalization is activated, significantly reducing the multi-path reflections. At a data rate of 250Mbps, the recovered ADC clock jitter

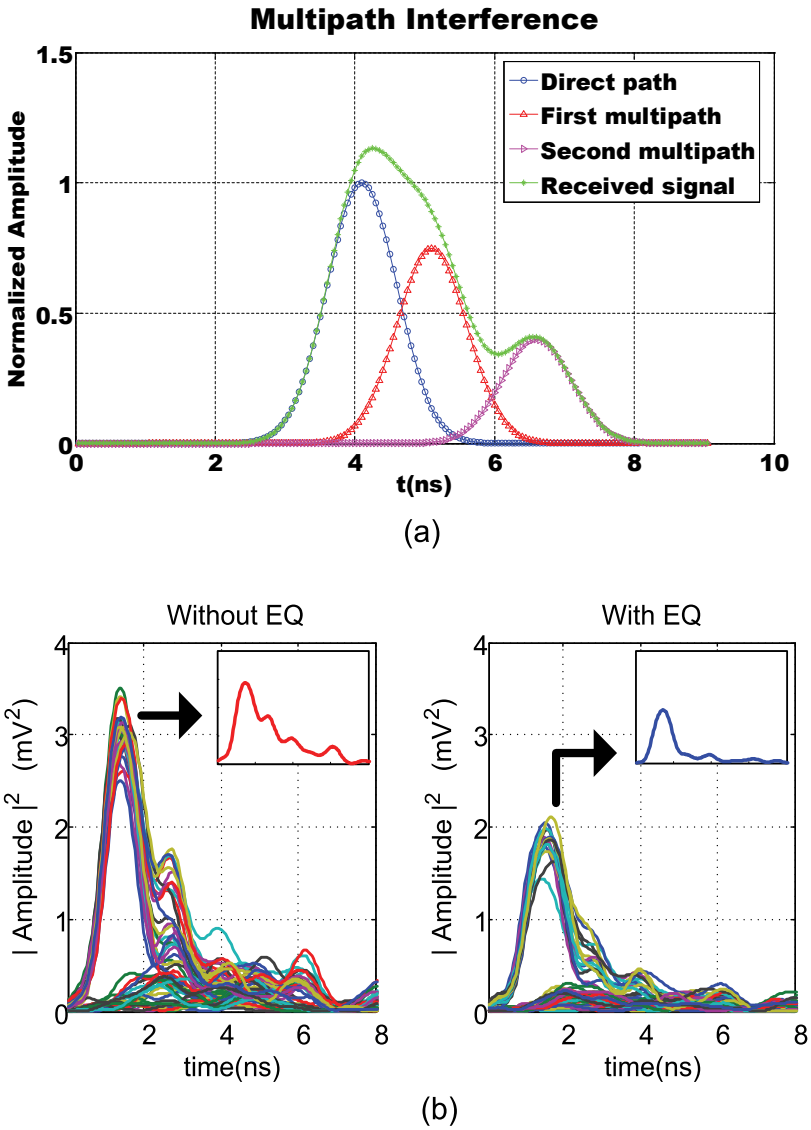

Fig. 20. Multi-path interference: (a) Simulated multi-path interference, (b) Measured received signal with and without multi-path equalization inside computer chassis

was improved significantly after applying the equalizer, reducing RMS clock jitter by 27.4% at RX1 in Fig. 1 while the motherboard was operational. Within an enclosed chassis that exhibits significant multi-path interference, at 250Mbps BER is improved from 0.0158 to 0.0067 without/with first-tap equalization enabled respectively. While the proposed equalization can help cancel the multi-path reflections, it is difficult in practice to eliminate them completely.

5. Conclusion

A fully integrated, single-chip IR-UWB transceiver with ADC in 90nm CMOS is presented. A novel pulse-injection-locking method is used for receiver clock synchronization in the receiver demodulation, leading to significant power reduction by eliminating the high-power oversampling ADC and mixer. The complete transceiver achieves a maximum data rate of 500Mbps, through a 10cm distance, consuming 0.18nJ/bit. Measured BER achieves 10^{-3} at 125Mbps through 10cm of free space. Due to the FCC transmitted power limitation, the pulse amplitude for higher data rates will be smaller, limiting the communication distance to up to half a meter. Further improvements include increasing the communication distance and reducing the BER by adding gain to the RF front-end, investigating pulse spectral shaping, and incorporating receiver pulse integration and low-pass filtering.

Technology	90nm CMOS
Die Size	1mmx2mm
Modulation	OOK
Data Rate	7.8125-500Mbps
VCO Range	3.7-4.5GHz
Power Dissipation	70mA@1.3V
Transmitted Pulse Width	0.5-10ns
Rx Sensitivity(Free space)	-64dBm@125Mbps, BER $< 10^{-3}$
Rx Sensitivity(Free sapce)	-60dBm@500Mbps, BER $< 10^{-1}$
BER(within chasis, w/o EQ)	1.7×10^{-3}@15cm
BER(within chasis, w/ EQ)	3.3×10^{-4}@15cm
Energy Efficiency(W/ADC)	Tx: 90pJ/b; Rx:90pJ/b

Table 1. Chip performance summary

paper	CMOS (nm)	Frequency (GHz)	Energy(pJ/b) Tx	Rx	Modulation	ADC	Data Rate (Mbps)	Size (mm^2)
Zheng et al. (2008)	180	3.1-9	740	6500	BPSK	No	1000	4.5
Verhelst et al. (2009)	130	0-0.96	-	110	BPSK	No	40	4.52
Lachartre et al. (2009)	130	3.1-5	1100		OOK/PPM/BPSK	No	31	8
Wentzloff & Chandrakasan (2007)	90	3.1-5	47	-	PPM w/ DB-BPSK	N/A	16.7	0.08(w/o pads)
Lee & Chandrakasan (2007)	90	3.1-5	-	2500	PPM	No	16.7	2.2
Crepaldi et al. (2010)	90	3.6-4.3	249	1450	OOK	No	1	0.6(Tx),1(Rx)
Joo et al. (2010)	130	3.1-5	3300		BPM-BPSK	YES	0.85	3x2.5(RF)
(Zheng et al., 2010)	180	3.5-4.5	920	5300	OOK/BPSK	YES	1	17.22mm^2
This work	90	3.1-5	90	90	OOK	Yes	500	1mmx2mm

Table 2. Comparison with previous published work

6. References

Adler, R. (1973). A study of locking phenomena in oscillators, *Proceedings of the IEEE* 61(10): 1380 – 1385.

Bulzacchelli, J., Meghelli, M., Rylov, S., Rhee, W., Rylyakov, A., Ainspan, H., Parker, B., Beakes, M., Chung, A., Beukema, T., Pepeljugoski, P., Shan, L., Kwark, Y., Gowda, S. & Friedman, D. (2006). A 10-gb/s 5-tap dfe/4-tap ffe transceiver in 90-nm cmos technology, *IEEE J. Solid-State Circuits* 41(12): 2885 –2900.

Chiang, P., Woracheewan, S., Hu, C., Guo, L., Khanna, R., Nejedlo, J. & Liu, H. (2010). Short-range, wireless interconnect within a computing chassis: Design challenges, *Design Test of Computers, IEEE* 27(4): 32 –43.

Crepaldi, M., Li, C., Dronson, K., Fernandes, J. & Kinget, P. (2010). An ultra-low-power interference-robust ir-uwb transceiver chipset using self-synchronizing ook modulation, *IEEE Int. Solid-State Circuits Conf. (ISSCC) Dig. Tech. Papers*, pp. 226 –227.

First Report and Order (n.d.). FCC, 2002.

Hu, C., Chiang, P., Hu, K., Liu, H., Khanna, R. & Nejedlo, J. (2010). A 90nm-cmos, 500mbps, fully-integrated ir-uwb transceiver using pulse injection-locking for receiver phase synchronization, *IEEE Radio Frequency Integrated Circuits (RFIC) Symposium*, pp. 201 –204.

Hu, C., Redfield, S., Liu, H., Khanna, R., Nejedlo, J. & Chiang, P. (2009). Transmitter equalization for multipath interference cancellation in impulse radio ultra-wideband(ir-uwb) transceivers, *VLSI Design, Automation and Test, 2009. VLSI-DAT '09. International Symposium on*, pp. 307 –310.

Hu, K., Jiang, T., Wang, J., O'Mahony, F. & Chiang, P. Y. (2009). A 0.6mw/gbps, 6.4 -8.0gbps serial link receiver using local injection-locked ring oscillators in 90nm cmos, *Symp. VLSI Circuits Dig. Tech. Papers*, pp. 46 –47.

Jayaraman, K., Khan, Q., Chi, B., Beattie, W., Wang, Z. & Chiang, P. (2010). A self-healing 2.4ghz lna with on-chip s11/s21 measurement/calibration for in-situ pvt compensation, *Radio Frequency Integrated Circuits Symposium (RFIC), 2010 IEEE*, pp. 311 –314.

Joo, S., Chen, W.-H., Choi, T.-Y., Oh, M.-K., Park, J.-H., Kim, J.-Y. & Jung, B. (2010). A fully integrated 802.15.4a ir-uwb transceiver in 0.13μm cmos with digital rrc synthesis, *IEEE Int. Solid-State Circuits Conf. (ISSCC) Dig. Tech. Papers*, pp. 228 –229.

Lachartre, D., Denis, B., Morche, D., Ouvry, L., Pezzin, M., Piaget, B., Prouvee, J. & Vincent, P. (2009). A 1.1nj/b 802.15.4a-compliant fully integrated uwb transceiver in 0.13μm cmos, *IEEE Int. Solid-State Circuits Conf. (ISSCC) Dig. Tech. Papers*, pp. 312 –313,313a.

Lathi, B. (n.d.). *Modern Digital and Analog Communication Systems*, Oxford University Press, 3rd edition, New York.

Lee, F. & Chandrakasan, A. (2007). A 2.5nj/b 0.65v 3-to-5ghz subbanded uwb receiver in 90nm cmos, *IEEE Int. Solid-State Circuits Conf. (ISSCC) Dig. Tech. Papers*, pp. 116 –590.

Lee, J. & Wang, H. (2009). Study of subharmonically injection-locked plls, *Solid-State Circuits, IEEE Journal of* 44(5): 1539 –1553.

Lee, J., Wang, H., Chen, W.-T. & Lee, Y.-P. (2009). Subharmonically injection-locked plls for ultra-low-noise clock generation, *IEEE Int. Solid-State Circuits Conf. (ISSCC) Dig. Tech. Papers*, pp. 92 –93,93a.

Lee, M.-J., Dally, W. & Chiang, P. (2000). A 90 mw 4 gb/s equalized i/o circuit with input offset cancellation, *IEEE Int. Solid-State Circuits Conf. (ISSCC) Dig. Tech. Papers*, pp. 252 –253, 463.

O'Donnell, I. & Brodersen, R. (2006). A 2.3mw baseband impulse-uwb transceiver front-end in cmos, *VLSI Circuits, 2006. Digest of Technical Papers. 2006 Symposium on*, pp. 200–201.

Razavi, B. (2004). A study of injection locking and pulling in oscillators, *Solid-State Circuits, IEEE Journal of* 39(9): 1415 – 1424.

Schinkel, D., Mensink, E., Kiumperink, E., van Tuijl, E. & Nauta, B. (2007). A double-tail latch-type voltage sense amplifier with 18ps setup+hold time, *IEEE Int. Solid-State Circuits Conf. (ISSCC) Dig. Tech. Papers*, pp. 314 –605.

UWB Channel Modeling Contribution from CEA-LETI and STMicroelectronics (n.d.). J. Keignart, N. Daniele, and J.B. Pierrot, Nov 2002 [Online].

Van Helleputte, N. & Gielen, G. (2009). A 70 pj/pulse analog front-end in 130 nm cmos for uwb impulse radio receivers, *IEEE J. Solid-State Circuits* 44(7): 1862 –1871.

Verhelst, M., Van Helleputte, N., Gielen, G. & Dehaene, W. (2009). A reconfigurable, 0.13μm cmos 110pj/pulse, fully integrated ir-uwb receiver for communication and sub-cm ranging, *IEEE Int. Solid-State Circuits Conf. (ISSCC) Dig. Tech. Papers*, pp. 250 –251,251a.

Wentzloff, D. (2007). *Pulse-Based Ultra-Wideband Transmitters for Digital Communication*, PhD thesis, MIT.

Wentzloff, D. & Chandrakasan, A. (2007). A 47pj/pulse 3.1-to-5ghz all-digital uwb transmitter in 90nm cmos, *IEEE Int. Solid-State Circuits Conf. (ISSCC) Dig. Tech. Papers*, pp. 118 –591.

Zheng, Y., Annamalai Arasu, M., Wong, K.-W., The, Y. J., Suan, A., Tran, D. D., Yeoh, W. G. & Kwong, D.-L. (2008). A 0.18μm cmos 802.15.4a uwb transceiver for communication and localization, *IEEE Int. Solid-State Circuits Conf. (ISSCC) Dig. Tech. Papers*, pp. 118 –600.

Zheng, Y., Diao, S.-X., Ang, C.-W., Gao, Y., Choong, F.-C., Chen, Z., Liu, X., Wang, Y.-S., Yuan, X.-J. & Heng, C. (2010). A 0.92/5.3nj/b uwb impulse radio soc for communication and localization, *IEEE Int. Solid-State Circuits Conf. (ISSCC) Dig. Tech. Papers*, pp. 230 –231.

Zheng, Y., Zhang, Y. & Tong, Y. (2006). A novel wireless interconnect technology using impulse radio for interchip communications, *Microwave Theory and Techniques, IEEE Transactions on* 54(4): 1912 – 1920.

Zhou, L., Chen, Z., Wang, C.-C., Tzeng, F., Jain, V. & Heydari, P. (2009). A 2gbps rf-correlation-based impulse-radio uwb transceiver front-end in 130nm cmos, *IEEE Radio Frequency Integrated Circuits (RFIC) Symposium*, pp. 65 –68.

9

Synchronization Technique for OFDM-Based UWB System

Wen Fan and Chiu-Sing Choy
The Chinese University of Hong Kong
Hong Kong

1. Introduction

Synchronization issue is inevitable in all wireless communication receiver systems and it plays the key role to the system performance. Synchronization technique includes timing synchronization and frequency synchronization. Timing synchronization is to detect valid packet and the accurate start position of fast Fourier transform (FFT) window from noise. Frequency synchronization is to correct the phase error caused by the mismatch of local oscillator (LO) between transmitter and receiver.

Synchronization technique has been extensively studied for years. Although UWB system can leverage on successful experiences of orthogonal frequency division multiplexing (OFDM), it cannot use the traditional synchronization technology directly due to the distinct features. In IEEE 802.15.3a standard, the specified emission power spectral density is only -41 dBm/MHz, which is extremely small compared with other wireless systems. It indicates that timing synchronization for UWB system should be robust in high noise environment. In addition, to satisfy 528 Msps throughput, the UWB baseband receiver system should be designed in parallel architecture. The inherent high complexity, the requirements of high performance, high speed, low cost and low power consumption make the design of synchronization blocks for UWB quite a challenge work.

This chapter will be divided into three parts: timing synchronization, coarse frequency synchronization and fine frequency synchronization. The traditional algorithms and innovative methods with low complexity and good performance will be introduced. Architecture design of each part is also provided.

2. Timing synchronization

As soon as the receiver starts up, it searches for the presence of OFDM-based UWB packet in the received signals. Usually, packet detection can only acquire the rough timing information by exploiting the repetition in the received signal. The accurate timing information, such as the symbol boundary or the start position of FFT window, is necessary, which relies on matching the received waveform with the preamble waveform by a matched filter.

2.1 Effects of timing offset

Assume the channel maximum delay is shorter than the guard interval; the position of FFT window can have several situations, as shown in Fig. 1. The exact start position of FFT

window is at the boundary of region B and C. If the start position is in region B, the signals in FFT window will not be contaminated by the previous symbol and thus no inter-symbol interference (ISI) occurs. The only effect is introducing phase shift. After demodulation, the received signal with timing offset in region B is expressed in (1).

$$R_{k,l} = S_{k,l} H_{k,l} e^{-j2\pi\Delta n/N} + W_{k,l} \tag{1}$$

where $S_{k,l}$, $H_{k,l}$ and $W_{k,l}$ are the transmitted signal, channel impulse response (CIR) and the noise signal respectively at the k-th subcarrier and the l-th symbol in frequency domain. Δn is defined as the delayed samples to the correct FFT window position.

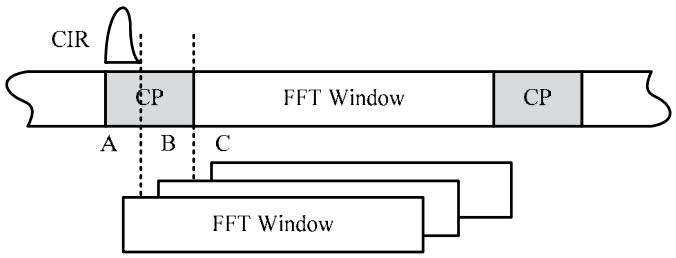

Fig. 1. The scenario of timing offset

When the FFT window leads or lags by a large degree, such as in region A or C, ISI will be introduced and both the magnitude and the phase of the received signal will be distorted, as shown in (2).

$$R_{k,l} = S_{k,l} H_{k,l} e^{-j2\pi\Delta n/N} \frac{N-\Delta n}{N} + W_{k,l} + W_{ISI} \tag{2}$$

where W_{ISI} is the introduced ISI noise. Due to the introduced ISI and the phase rotation, there is slight magnitude attenuation in the signal.

2.2 Timing synchronization algorithms

Timing synchronization can be divided into two categories: coarse timing synchronization and fine timing synchronization. Coarse timing synchronization is usually based on auto-correlation (AC), while fine timing synchronization is based on cross-correlation (CC). The traditional algorithms of AC, maximum likelihood (ML), minimum mean square error (MMSE) and CC will be introduced.

Auto-correlation

The AC algorithm (Schmidl & Cox, 1997) for coarse timing synchronization is quite straightforward. It searches for the repetition in the received signal with a correlator and a maximum searcher. Let the repetition interval length be denoted as L. r_n is the received signal in time domain. The timing metric can be defined as

$$M(n) = \frac{|\sum_{k=0}^{L-1} r_{n+k}^{*} r_{n+k+L}|^2}{(\sum_{k=0}^{L-1} |r_{n+k+L}|^2)^2} \tag{3}$$

where * is the conjugated operation. The estimated time index of the maximum $M(n)$ can be expressed as

$$\hat{n} = \arg\max_{n} M(n) \tag{4}$$

If the maximum $M(n)$ is over the threshold, the packet is presented and the estimated timing index is the symbol boundary. The drawback of this scheme is when the correlation window moves away from the repeated period, the power of timing metric $M(n)$ may not fall off as expected, especially in low signal-to-noise ratio (SNR). In this case, there may be a large error in the detected symbol boundary.

Maximum likelihood

ML algorithm (Van de Beek et al., 1997; Coulson, 2001) improves the performance of AC. ML function can be expressed as

$$M(n) = 2\left|\sum_{k=0}^{L-1} r_{n+k}^{*} r_{n+k+L}\right| - \rho\sum_{k=0}^{L-1}\left(|r_{n+k}|^2 + |r_{n+k+L}|^2\right) \tag{5}$$

$$\rho \triangleq \left|\frac{E\{r_{n+k}^{*} r_{n+k+L}\}}{\sqrt{E\{|r_{n+k}|^2\}E\{|r_{n+k+L}|^2\}}}\right| = \frac{\sigma_s^2}{\sigma_s^2 + \sigma_n^2} = \frac{SNR}{SNR+1} \tag{6}$$

$\sigma_s^2/\ \sigma_n^2$ is SNR. The estimated symbol boundary is derived by searching the maximum output of ML function. The complexity of ML is quite high because the estimation of SNR is difficult and the errors in SNR estimation will make the system less reliable.

Minimum mean square error

MMSE metric (Minn et al., 2003) is equivalent to a special case of the ML metric with $\rho = 1$. It shows almost the same timing estimation performance as ML. The principle is to search the minimum output of the metric, as shown in (7).

$$M(n) = \sum_{k=0}^{L-1}|r_{n+k}|^2 + \sum_{k=0}^{L-1}|r_{n+k+L}|^2 - 2\left|\sum_{k=0}^{L-1} r_{n+k}^{*} r_{n+k+L}\right| \tag{7}$$

For AC, ML and MMSE algorithms, when the preamble has more than two identical segments, there will be a plateau or a wide basin in the correlator output waveforms. Theoretically, the plateau or basin indicates the ISI-free region for FFT window. However, noise in the received signal may cause the max/min to drift away from the optimal point. So AC, ML and MMSE are the methods to detect packet coarsely and the detection of accurate symbol boundary or FFT window needs fine timing synchronization, such as CC.

Cross-correlation

CC is the mechanism for fine timing synchronization. Instead of correlating the noisy received waveform with its delayed version, CC is defined as correlating the received signal with preamble waveform (Fort et al., 2003). It can fit into the low SNR situation and can be expressed as

$$M(n) = \sum_{k=0}^{Q-1} r_{n+k} c_k^{*} \tag{8}$$

where c_k is the preamble coefficients and Q is the length of preamble.

Dual-threshold detection

Dual-threshold (DT) detection scheme is based on the idea in (Fan et al., 2009) for OFDM-based UWB system. Fig. 2 shows the block diagram of the DT detection scheme. The signal detection process is divided into two steps. The first step is based on CC algorithm. Express the peak CC energy of each symbol as

$$T_1 = \max_n |A_n|^2 = \max_n |\sum_{k=0}^{N-1} r[n+k]c^*[k]|^2 \tag{9}$$

$$\sum_{k=0}^{N-1} c^2[k] = N \tag{10}$$

where A_n is the moving sum of CC value; $c[k]$ is the preamble coefficients; $r[k]$ is the received signal and N is the FFT size. If the peak CC energy T_1 is over the first threshold, the estimated sample index of symbol boundary and the moving sum will be stored in FIFO for further use by the following auto-correlator. Otherwise, the peak CC energy of the next symbol will be calculated.

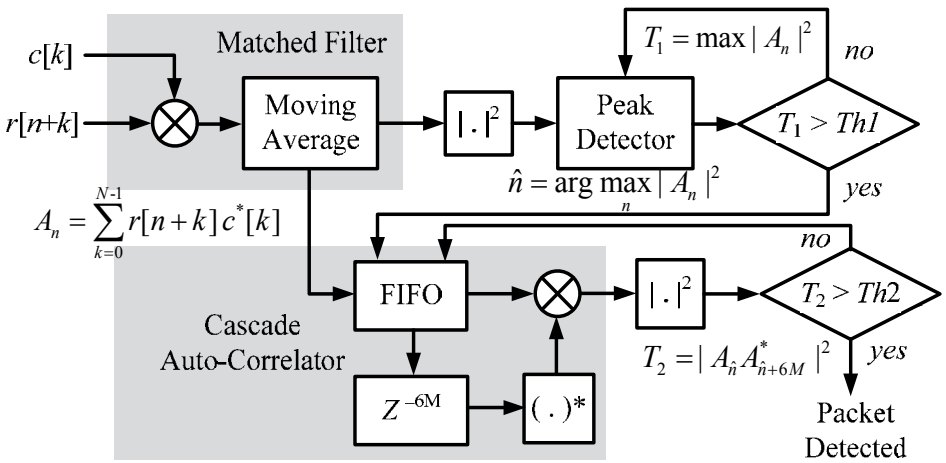

Fig. 2. Block diagram of DT detection scheme

The second step is to read the moving sum from FIFO and auto-correlating with its delayed version. The energy of the cascaded auto-correlator can be derived as

$$T_2 = |A_{\hat{n}} A^*_{\hat{n}+6M}|^2 \tag{11}$$

where M is the repeated preamble interval length of UWB system. The delay interval of the auto-correlator is decided by the period of time frequency code (TFC). In order to ensure the moving sum and its delayed version are in the same band no matter what kind of TFC mode is adopted, the delay interval is set to six-symbol length. If the output energy of cascaded auto-correlator T_2 is over the second threshold, the packet is detected. Otherwise, fetch the next value in FIFO and calculate T_2 again.

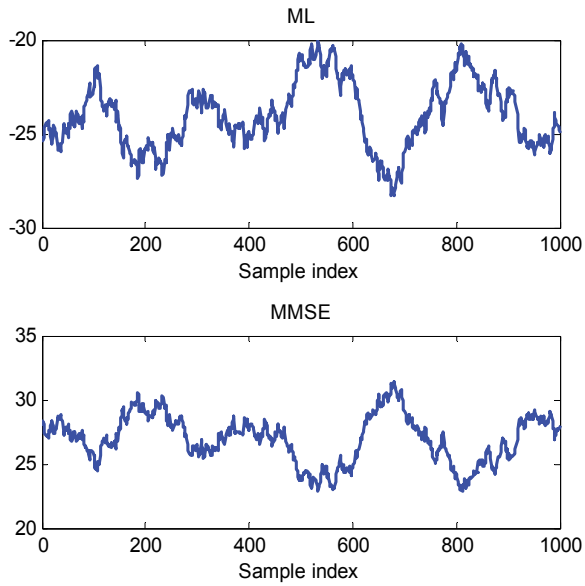

Fig. 3. Output waveforms of ML and MMSE algorithms at 10 dB SNR

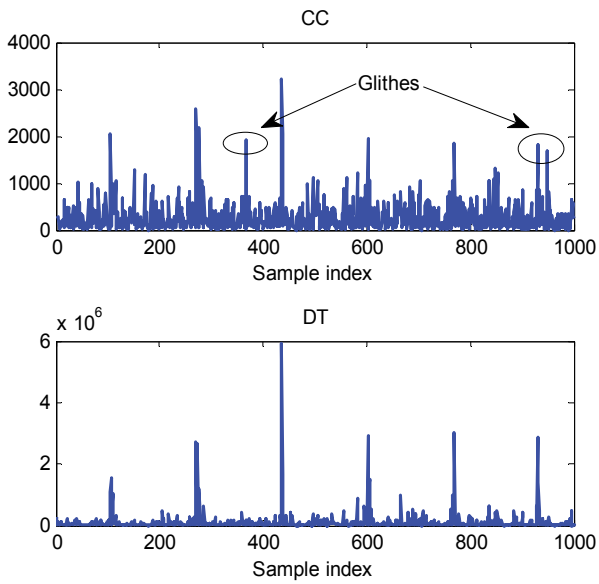

Fig. 4. Output waveforms of CC and DT algorithms at 10 dB SNR

Fig. 3 depicts the output waveforms of ML and MMSE algorithms at 10 dB SNR. There are plateaus and basins in the output waveforms of ML and MMSE, which make the peak energy ambiguous. It is much easier to find accurate timing information in the output waveform of CC in Fig. 4. However, there are glitches in CC output waveform, which will corrupt the detection of symbol boundary and increase the false alarm probability. The waveform of DT has much lower noise floor compared with CC and there is not any glitch.

2.3 Architecture of the matched filter

Matched filter is the basic component in timing synchronization for detecting a known piece of signal in noise. The architecture of mated filter determines the complexity and the power consumption of the timing synchronizer. An optimum architecture of the matched filter for OFDM-based UWB is provided, as shown in Fig. 5. To satisfy 528 Msps throughput, the baseband receiver system of UWB is designed at 132 MHz clock frequency with four parallel paths and twelve-level pipelines. For low complexity, both the received signal and the preamble coefficients are truncated to sign-bit. In this case, five-bit multipliers can be replaced with NXOR gates. In addition, the 128 sign-bits of preamble coefficients are generated by spreading a 16 sign-bit sequence with an 8 sign-bits sequence as follows

$$\begin{aligned} &sgn(c_{16(j-1)+i}) = a_i \times b_j \\ &i = 1,2,...,16 \quad j = 1,2,...,8 \end{aligned} \tag{12}$$

where a_i and b_j are 1 or -1. According to (12), the 128 taps matched filter can be decomposed to 16 taps cascaded with 8 taps, as shown in Fig. 5. With the decomposition, the processing period of the matched filter can be reduced to 19% and the length of the circle shift register can be reduced to 20. In CC operation, if the shift register is full, shift the data from address of [5:20] to [1:16] and save the coming four sign-bits to the address of [17:20]. The data with the addresses of [1:16], [2:17], [3:18] and [4:19] are distributed to four parallel data paths and cross-correlated with the coefficients a_i. This optimum architecture of the matched filter not only guarantees the high speed, but also reduces the cost of the hardware.

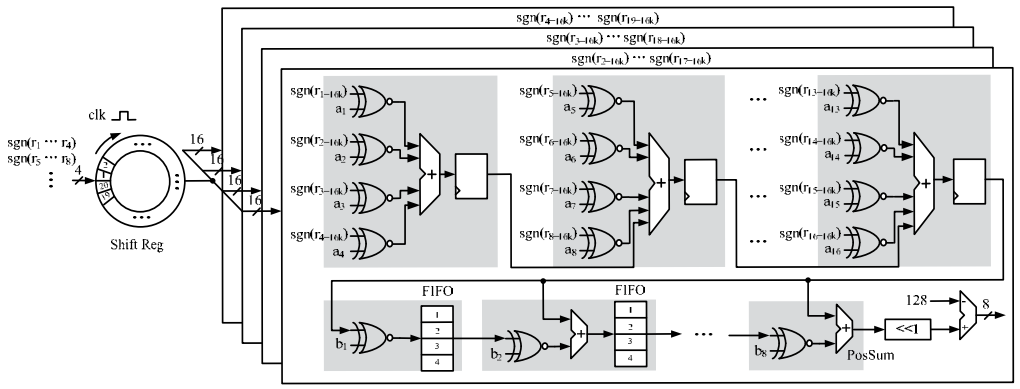

Fig. 5. Architecture of the matched filter for UWB

3. Coarse frequency synchronization

OFDM-based UWB system is sensitive and vulnerable to carrier frequency offset (CFO), which can be estimated and compensated by coarse frequency synchronization in time domain. Due to the Doppler Effect, even very small CFO will lead to very serious accumulated phase shift after a certain period.

3.1 Effects of carrier frequency offset

Define the normalized CFO, $\varepsilon_f = \Delta f / f_s$, as the ratio of CFO to subcarrier frequency spacing. The received signal with CFO in frequency domain can be expressed as (Moose, 1994)

$$R_{k,l} = S_{k,l} H_{k,l} \frac{\sin(\pi\varepsilon_f)}{N\sin(\pi\varepsilon_f / N)} e^{-j2\pi\varepsilon_f (N-1)/N} + W_{k,l} + W_{ICI} \tag{13}$$

where $S_{k,l}$, $H_{k,l}$ and $W_{k,l}$ stand for the transmitted signal, channel impulse response and noise respectively at k-th subcarrier and l-th symbol. W_{ICI} is the noise contributed by inter-carrier interference (ICI). ICI will not only destroy the orthogonality of the subcarriers in OFDM-based UWB system, but also degrade SNR. The SNR degradation can be approximated as (Pollet et al., 1995)

$$D_{SNR} \approx \frac{10}{3\ln 10} (\pi\varepsilon_f)^2 \frac{E_s}{N_o} \tag{14}$$

where E_s/N_o is the ratio of symbol energy to noise power spectral density.

3.2 Frequency synchronization algorithm

The most straightforward frequency synchronization algorithm is based on AC functions. CFO can be estimated by the phase difference between two symbols. For traditional OFDM system, the CFO can be estimated as

$$\hat{\varepsilon}_f = \frac{N}{2\pi M} tan^{-1} \left(\sum_{k=0}^{N-1} r^*_{n+k} r_{n+k+M} \right) \tag{15}$$

where N is the FFT size and M is the interval of two symbols. If apply traditional AC algorithm in UWB system, the sliding window length (SWL) is 128. The four-parallel architecture with 128 SWL will be in high complexity. Shortening the SWL can reduce the complexity with degradation of the estimation performance. To improve the performance with low complexity, an optimized AC algorithm is provided by shortening the SWL to 64 and making a sum average over three symbols located at three different subbands, as expressed in (16).

$$\begin{aligned} \hat{\varepsilon}_f = \frac{N}{2\pi G_1 M} tan^{-1} \Big(& \sum_{k=1}^{L} r[\frac{N}{L}k + G_1 M] r^*[\frac{N}{L}k] + \sum_{k=1}^{L} r[\frac{N}{L}k + (G_1 + G_2)M] r^*[\frac{N}{L}k + G_2 M] \\ & + \sum_{k=1}^{L} r[\frac{N}{L}k + (G_1 + 2G_2)M] r^*[\frac{N}{L}k + 2G_2 M] \Big) \end{aligned} \tag{16}$$

where L denotes the SWL of each symbol. The values of G_i (i = 1,2) depend on TFC. If TFC is {1 2 3 1 2 3} or {1 3 2 1 3 2}, $G_1 = 3$, $G_2 = 1$; if TFC is {1 1 2 2 3 3} or {1 1 3 3 2 2}, $G_1 = 1$, $G_2 = 2$.
Although the SWL can be further reduced for lower complexity, the performance degradation requires a much longer period sum average to compensate. Tradeoff in complexity, performance and the processing period, $L = 64$ is the best choice. Fig. 6 shows the MSE performance comparison with different SWL. The normalized CFO is set to 0.01. Due to the sum average over three subbands, the optimized AC algorithm with SWL 64 has better performance than the traditional AC algorithm with SWL 128. The optimized AC algorithm with SWL 32 cannot perform as good as traditional AC algorithm with SWL 128. It needs longer period for sum average to compensate the performance degradation.
For UWB, the CFO compensation algorithm can be optimized as well. The basic idea is to take the CFO values on four-parallel paths as the same if the differences of the four CFO

values are very small (Fan & Choy, 2010a). In the specification of UWB, the center frequency is about 4 GHz and the maximum impairment at clock synthesizer is ±20 ppm (parts per million). Therefore, the normalized CFO should be less than 0.04. And the maximum CFO difference between any two parallel samples should be less than 2.5×10^{-4}, which is small enough and can be ignored. The optimized CFO compensation scheme can be expressed as

$$\begin{aligned} &\tilde{r}[4(m-1)+q] = r[4(m-1)+q]\,exp(-j2\pi 4m\hat{\varepsilon}_f / M) \\ &m = 1,2,...,\lceil M/4 \rceil, \quad q = 1,2,3,4 \end{aligned} \tag{17}$$

where $4(m\text{-}1)+q$ is the sample index. The optimum CFO compensation strategy not only reduces the four-parallel digital synthesizer to one, but also alleviates the workload of the phase accumulator.

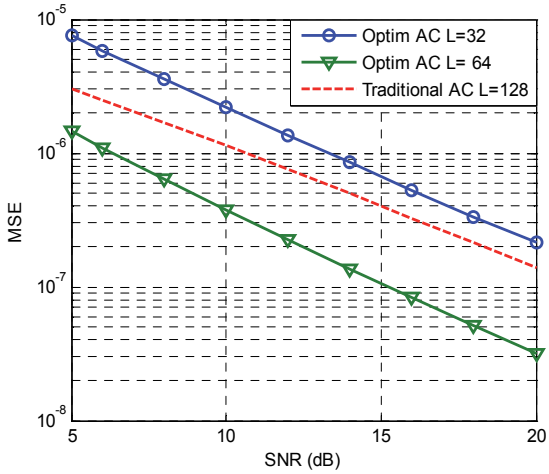

Fig. 6. MSE performance comparison with different SWL

3.3 Implementation of frequency synchronizer

The design of frequency synchronizer is divided into two parts. The first part is to estimate the phase difference between two preambles by AC and arctangent calculation. The second part is to compensate the signals by multiplying a complex rotation vector. In this part, the phase accumulator and sin/cos generator are involved.

Fig. 7 shows the architecture of CFO compensation block. The phase accumulator produces a digital weep with a slope proportional to the input phase. The phase offset is scaled from [0, 2π] to [0, 8] by multiplying a factor 4/π, so that just the three most significant bits (MSBs) can be used to control the phase offset regions. During CFO compensation, the sine and cosine values of the phase offset in the range of [0, π/4] are necessary to be calculated. If the phase offset is in other ranges, input complement, output complement or output swap are operated correspondingly.

In the design of frequency synchronizer, implementation of arctangent, sine and cosine functions is the most critical work since it decides the complexity of the synchronizer and the performance of the UWB receiver system. The traditional OFDM-based or CDMA-based

systems usually employed classic coordinate rotation digital computer (CORDIC) algorithm for function evaluation (Tsai & Chiueh, 2007; Troya et al., 2008). Actually, there are other techniques for function evaluation, such as polynomial hyperfolding technique (PHT) (Caro et al., 2004), piecewise-polynomial approximation (PPA) technique (Caro & Steollo, 2005), hybrid CORDIC algorithm (Caro et al., 2009) and multipartite table method (MTM) (Caro et al., 2008).

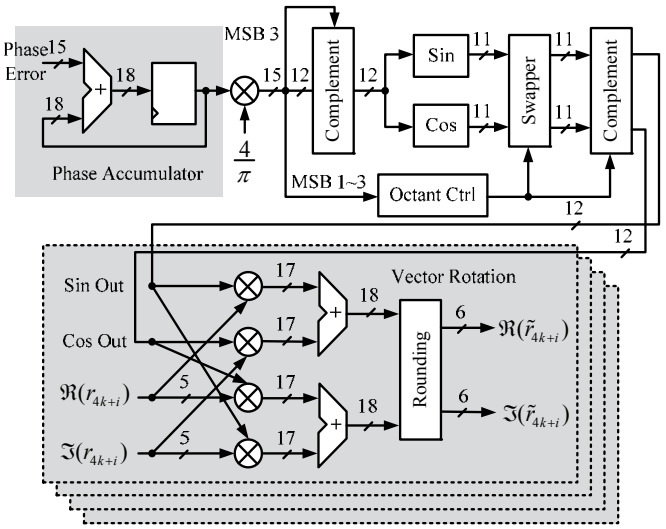

Fig. 7. Architecture of the CFO compensation block

Polynomial hyperfolding technique

PHT calculates sine and cosine functions using an optimized polynomial expression with constant coefficients. The sine and cosine functions can be expressed by polynomial expressions of degree *K*.

$$\begin{aligned} S(x) &= sin(\frac{\pi}{4}x + \frac{LSB}{2}) \cong a_K x^K + a_{K-1}x^{K-1} + \cdots + a_0 \\ C(x) &= cos(\frac{\pi}{4}x + \frac{LSB}{2}) \cong b_K x^K + b_{K-1}x^{K-1} + \cdots + b_0 \end{aligned} \tag{18}$$

where $0 \le x < 1$ is the scaled input of sine and cosine functions. Optimization is conducted on two-order ($K = 2$) and three-order ($K = 3$) approximated polynomials, expressed as (19) and (20) respectively (Caro et al., 2004). The two-order PHT can achieve about 60 dBc spurious free dynamic range (SFDR) while the three-order PHT can achieve 80 dBc SFDR.

$$\begin{aligned} S(x) &\cong -0.004713 + 0.838015x - 2^{-3}x^2 \\ C(x) &\cong 0.9995593 - 0.011408x + (-2^{-2} - 2^{-5})x^2 \end{aligned} \tag{19}$$

$$\begin{aligned} S(x) &\cong 0.00015005 + 0.77436217x - 0.00530040x^2 + (-2^{-2} + 2^{-5})x^3 \;/\; 3 \\ C(x) &\cong 0.98423596 + 0.00452969x - 0.32417224x^2 + (2^{-3} - 2^{-5})x^3 \;/\; 3 \end{aligned} \tag{20}$$

Piecewise polynomial approximation

The technique of PPA is based on the idea of subdividing the interval in shorter subintervals. Polynomials of a given degree are used in each subinterval to approximate the trigonometric functions. The signal x represents the input phase scaled to a binary fraction in the interval of [0, 1], which is subdivided in s subintervals, with $s = 2^u$. The u MSBs of x encode the segment starting point x_k and are used as an address to the small lookup tables that store polynomial coefficients. The remaining bits of x represent the offset $x - x_k$. The quadratic PPA of sine and cosine functions can be expressed as (Caro & Steollo, 2005)

$$\begin{aligned} f_s(x) &= y_{sk} + m_{sk}(x - x_k) - p_{sk}(x - x_k)^2 \\ f_c(x) &= y_{ck} - m_{ck}(x - x_k) - p_{ck}(x - x_k)^2 \\ x_k &\le x \le x_{k+1};\ k = 1,2,...,s;\ x_1 = 0;\ x_{s+1} = 1 \end{aligned} \tag{21}$$

Fig. 9 shows the architecture of sine and cosine blocks with PPA. Use r bits and t bits for the first-order and the second-order coefficients quantization respectively. The constant coefficients are (Q – 1) bits. The input and output of the sine and cosine functions are represented by P bits and Q bits. The constant, linear and quadratic coefficients are read from ROMs to conduct polynomial calculation. The partial products are generated by the *PPGen* block to compute linear terms. And the carry-save addition tree adds the partial products together after aligning all the bits according to their weights.

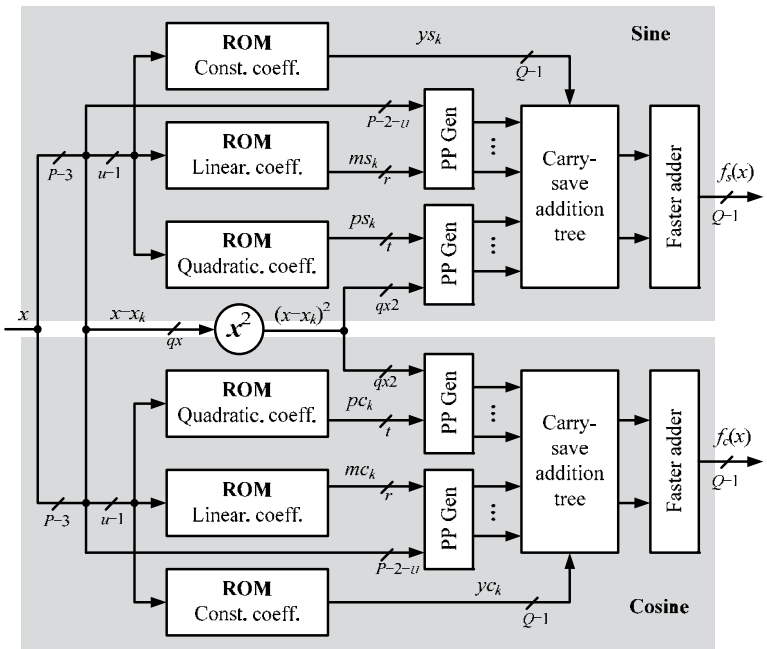

Fig. 9. Architecture of sine and cosine blocks with PPA (Caro & Steollo, 2005)

Hybrid coordinate rotation digital computer

This approach splits the phase rotation in three steps. The first two steps are CORDIC-based with computing the rotation directions in parallel. The final step is multiplier-based (Caro et al., 2009).

Suppose the word length of input vector [X_{in}, Y_{in}] and output vector [X_{out}, Y_{out}] are 12 and 13 bits respectively. Represent the rotation phase $\varphi \in [0, \pi/4]$ with a binary fractional value in [0, 1] as

$$\frac{4}{\pi}\varphi = f_1 2^{-1} + f_2 2^{-2} + \cdots + f_{13} 2^{-13} \tag{22}$$

The least significant bit (LSB) of φ has a weight that will be indicated in the following as $\varphi_{LSB} = (\pi/4)2^{-13}$. In the first step, the phase is divided in two subwords $\varphi = \alpha + \beta$, where

$$\begin{aligned} \alpha &= (f_1 \cdot 2^{-1} + \ldots + f_3 \cdot 2^{-3} + 2^{-4})\frac{\pi}{4} \\ \beta &= (-\overline{f_4} \cdot 2^{-4} + f_5 \cdot 2^{-5} + \ldots + f_{13} \cdot 2^{-13})\frac{\pi}{4} \end{aligned} \tag{23}$$

The goal of the first stage is to perform a rotation by an angle close to $\alpha + \varphi_{LSB}/2$. To that purpose, the first rotation uses CORDIC algorithm can be described by the following equations.

$$\begin{cases} X_{i+1} = X_i - \sigma_i \cdot 2^{-i} \cdot Y_i \\ Y_{i+1} = Y_i + \sigma_i \cdot 2^{-i} \cdot X_i \\ Z_{i+1} = Z_i - \sigma_i \cdot tan^{-1} 2^{-i} \end{cases} \qquad i = 1, \ldots, 4 \tag{24}$$

where σ_i is equal to the sign of Z_i. The algorithm starts with $X_1 = X_{in}$, $Y_1 = Y_{in}$ and $Z_1 = \alpha + \varphi_{LSB}/2$.

The second and third stages rotate the output vector of the first stage by a phase $\gamma = Z_{residual} + \beta$, which is represented with 11 bits. γ is then split as the sum of two subwords $\gamma_1 + \gamma_2$, where

$$\begin{aligned} \gamma_1 &= 2^{-3}(-g_0 + g_1 \cdot 2^{-1} + g_2 \cdot 2^{-2} + 2^{-3}) \\ \gamma_2 &= 2^{-3}(-\overline{g_3} \cdot 2^{-3} + g_4 \cdot 2^{-4} + \ldots + g_{10} \cdot 2^{-10}) \end{aligned} \tag{25}$$

The second rotation is aimed to perform the rotation by the phase γ_1. The rotation directions are obtained by the bits of γ_1 as follows.

$$\tau_0 = 2 \cdot \overline{g_0} - 1 \qquad \tau_i = 2 \cdot g_i - 1 \qquad i = 1, 2 \tag{26}$$

The corresponding CORDIC equations are

$$\begin{cases} X'_{i+1} = X'_i - \tau_i \cdot 2^{-(i+4)} \cdot Y'_i \\ Y'_{i+1} = Y'_i + \tau_i \cdot 2^{-(i+4)} \cdot X'_i \end{cases} \qquad i = 0, 1, 2 \tag{27}$$

And the operation to be performed in the final rotation block can be written as

$$\begin{cases} X_{out} = X_{T2} \cos\gamma_2 - Y_{T2} \sin\gamma_2 \\ Y_{out} = X_{T2} \sin\gamma_2 + Y_{T2} \cos\gamma_2 \end{cases} \tag{28}$$

where $[X_{T2}, Y_{T2}]$ is the output vector of the second rotation. The absolute value of γ_2 is smaller than 2^{-6}. Therefore, sine and cosine functions can be approximated as $sin\ \gamma_2 \approx \gamma_2$ and $cos\ \gamma_2 \approx 1$.

The architecture of hybrid CORDIC rotator is shown in Fig. 10. The elementary stage is composed with adders and shifters. The two final vector merging adders (VMAs) convert the results to two's complement representation.

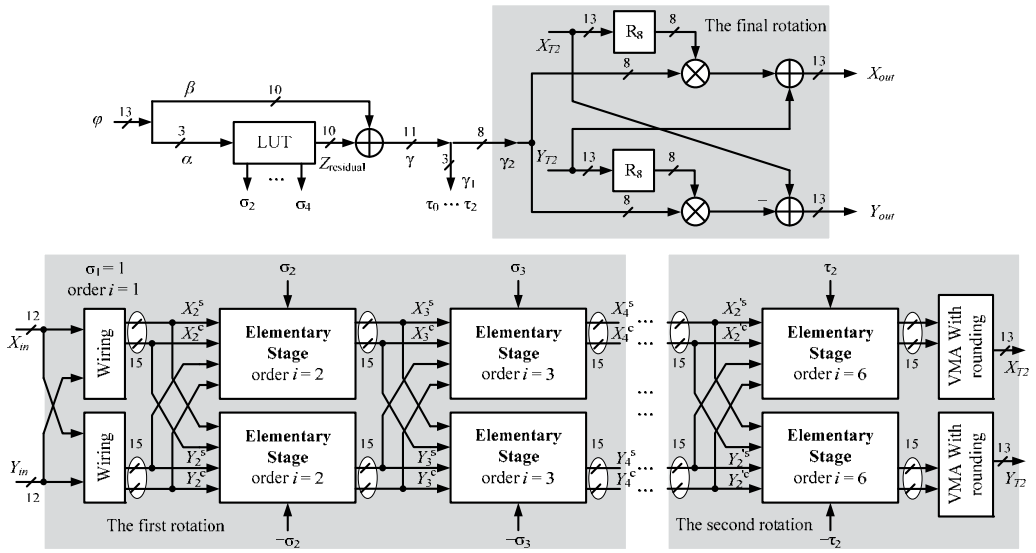

Fig. 10. Architecture of hybrid CORDIC technique (Caro et al., 2009)

Multipartite table method

MTM is a very effective lookup table compression technique for function evaluation. It has been found ideally suited for high performance synthesizer, requiring both very small ROM size and simple arithmetic circuitry (Caro et al., 2008). The principle of MTM is to decompose Q-bit input signal x in $K + 1$ non-overlapping sub-words: x_0, x_1, …, x_K with lengths of q_0, q_1, …, q_K respectively, where $x = x_0 + x_1 + \ldots + x_K$ and $Q = q_0 + q_1 + \ldots + q_K$. The angle $[0, \pi/4]$ is scaled to a binary fraction in [0, 1]. A piecewise linear approximation of $f(x)$ can be expressed as

$$\begin{aligned} f(x) &= f(x_0 + x_1 + \ldots + x_K) \simeq A(x_0) + B(x_0)(x_1 + \ldots + x_K) \\ &= A(x_0) + B(x_0)x_1 + \ldots + B(x_0)x_K \\ &\simeq A(x_0) + B_1(\alpha_1)x_1 + \ldots + B_K(\alpha_K)x_K \end{aligned} \tag{29}$$

The interval of x has been divided in 2^{q0} subintervals. x_0 represents the starting point of each subinterval and $x_1 + \ldots + x_K$ is the offset in each interval between x and x_0. α_1 is a sub-word of x_0 including its $p_1 \le q_0$ MSBs. Likewise, α_i ($i = 2 \ldots K$) is a sub-word of x_0 including its $p_i \le p_i - 1$. The term $A(x_0)$ can be realized with a ROM, which is named as table of initial values (TIV), with 2^{q0} entries. And the terms $B(\alpha_i)\ x_i$ ($i = 1 \ldots K$) can be implemented with K ROMs, which is named as table of offsets (TO_i), with 2^{pi+qi} entries each. Making the TOs symmetric, the size of ROMs can be reduced by a factor of two. Then, the equation (29) becomes

$$f(x) \simeq \tilde{A}(x_0) + B_1(\alpha_1)(x_1 - \frac{\delta_1}{2}) + \cdots + B_K(\alpha_K)(x_K - \frac{\delta_K}{2}) \tag{30}$$

where the coefficients can be calculated as follows (Caro et al., 2008).

$$\begin{aligned}
&\tilde{A}(x_0) = \frac{f(x_0) + f(x_0 + \Delta_0)}{2} \\
&B_i(\alpha_i) = \frac{f(\alpha_i + \delta_i) - f(\alpha_i) + f(\alpha_i + \delta_i + \sigma_i) - f(\alpha_i + \sigma_i)}{2\delta_i} \\
&\mathrm{TO}_i(\alpha_i, x_i) = B_i(\alpha_i)(x_i + 2^{-si-1}) \\
&\delta_i = (2^{qi} - 1)2^{-si};\ s_i = \sum_{j=0}^{i} q_j;\ \sigma_i = 2^{-pi} - 2^{qi-si};\ \Delta_0 = \sum_{j=1}^{K} \delta_j = 2^{-q0} - 2^{-Q}
\end{aligned} \tag{31}$$

The architecture of MTM with symmetric TOs is shown in Fig. 11. The content of TOs is conditionally added or subtracted from the content stored in TIV. The addition or subtraction of the content in ROMs and complement operation of the inputs are controlled by the MSB of each subword.

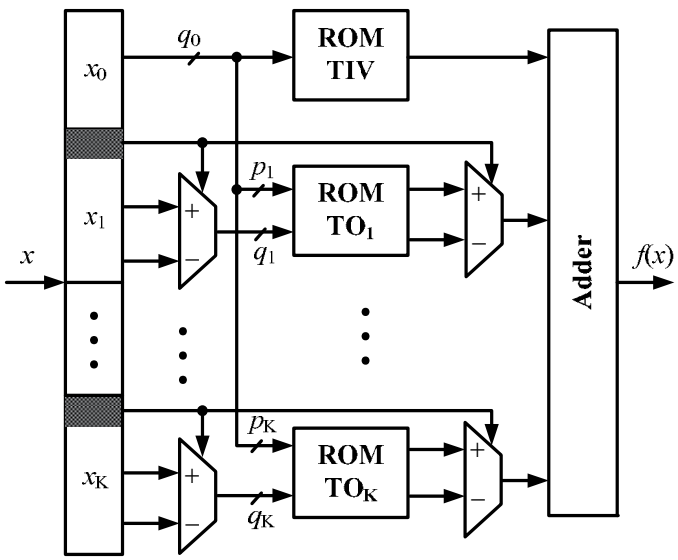

Fig. 11. Architecture of MTM with symmetric TOs

In order to give a fair comparison of the four techniques, they are used to implement CFO compensation block. The parameters of the design are set to make the SFDR of the four techniques nearly the same. The inputs and outputs of the four algorithms are 12 bits. Synthesized with UMC 0.13 μm high speed library at 132 MHz clock frequency, the power, area and latency of the four methods are listed in Table 1. MSE is a statistical value, so it is not easy to set the MSEs of the four approaches exactly the same. But they are very closed. With the smallest MSE, MTM outperforms other algorithms in area, power and latency. Since MTM is proved to be an efficient approach for function evaluation, it can be applied to implement arctangent fucntion in CFO estimation block.

Technique	MTM	PPA	PHT	Hybrid CORDIC
Design parameter	$q_0 = 4$ $q_1 = 2$ $q_2 = 3$ $q_3 = 3$ $p_1 = 3$ $p_2 = 3$ $p_3 = 1$	$s = 64$ $r = 6$ $t = 7$	$K = 3$	(1) 4 rep. (2) 3 rep. (3) $8b \times 8b$
MSE ($\times 10^{-7}$)	2.97	4.91	7.82	5.73
Area (mm^2)	0.018	0.027	0.031	0.146
Power (mW)	0.84	0.88	1.55	13.93
Latency (Clock cycs.)	3	3	4	6

Table 1. Synthesis performance comparison of CFO compensation with four techniques

4. Fine frequency synchronization

Although CFO can be coarsely estimated by frequency synchronizer in time domain, the residual CFO (RCFO), sampling frequency offset (SFO) and common phase error will lead to accumulated phase shift after a certain period and thus degrade the system performance if they are not carefully tracked. In OFDM-based UWB systems, pilot subcarriers can help to solve the residual phase distortion issue in frequency domain, which is also called fine frequency synchronization.

4.1 Effects of sampling frequency offset

The oscillators used to generate the DAC and ADC sampling instants at the transmitter and receiver will never have exactly the same period. Thus, the sampling instants slowly shift relative to each other. The SFO has two main effects: a slow shift of the symbol timing, which rotates subcarriers; and a loss of SNR due to the ICI generated by the slightly incorrect sampling instants, which causes loss of the orthogonality of the subcarriers.

Define the normalized sampling error as $\Delta t = (T' - T)/T$, where T' and T are the receiver and transmitter sampling periods respectively. Then the overall effect on the received signal in frequency domain is expressed as

$$R_{k,l} = S_{k,l} H_{k,l} e^{j2\pi k \Delta t l T_S / T_u} sinc(\pi k \Delta t) + W_{k,l} + N_{\Delta t}(k,l) \tag{32}$$

where T_s and T_u are the duration of the total symbol and the useful data respectively. $W_{k,l}$ is additive white Gaussian noise (AWGN) and the last term $N_{\Delta t}(k, l)$ is the additional interference due to the SFO. The power of the last term is approximated by

$$P_{\Delta t} \approx \frac{\pi^2}{3}(k\Delta t)^2 \tag{33}$$

Hence the degradation grows as the square of the produce of the offset Δt and the subcarrier index k. This means that the outermost subcarriers are most severely affected. The degradation can also be expressed directly by SNR loss as (Pollet et al., 1995)

$$D_n \approx 10log_{10}(1+\frac{\pi^2}{3}\frac{E_s}{N_0}(k\Delta t)^2)\ (dB) \tag{34}$$

The OFDM-base UWB system does not have a large number of subcarriers and the value of Δt is quite small. So $k\Delta t << 1$, and the interference caused by SFO can usually be ignored. However, the term showing the amount of rotation angle experienced by the different subcarriers will lead to serious problem. Since the rotated angle depends on both the subcarrier index and symbol index, the angle is the largest for the outermost subcarrier and increases with the consecutive symbols. Although Δt is very small, with the increasing of the symbol index, the phase shift will eventually corrupt the demodulation. In this case, tracking SFO is necessary.

4.2 Phase tracking algorithms

Conventionally, SFO can be estimated by computing a slope from the plot of pilot subcarrier differences versus pilot subcarrier indices (Speth et al., 2001). Recently, joint estimation of CFO and SFO has also been studied extensively, such as the linear least squares (LLS) algorithm (Liu & Chong, 2002) and joint weighted least squares (WLS) algorithm (Tsai et al., 2005).

Auto-correlation

The reveived signal with residual phase distortion in frequency domain after removing the channel noise can be modeled as

$$Z_{k,l} = S_{k,l}P_{k,l} = S_{k,l}\ exp(j\Phi_{k,l}) = S_{k,l}\ exp(j(\alpha k + \beta_l)) \tag{35}$$

where $P_{k,l}$ is the phase distortion vector and $\Phi_{k,l}$ is the residual phase error. The relationship of α, β_l and $\Phi_{k,l}$ is shown in Fig. 12. α is the slope of the phase distortion and is contributed by SFO. β_l is the intercept of phase distortion and is caused by RCFO of symbol l.
The basic idea of AC is to get the phase differences of pilot subcarriers between two symbols.

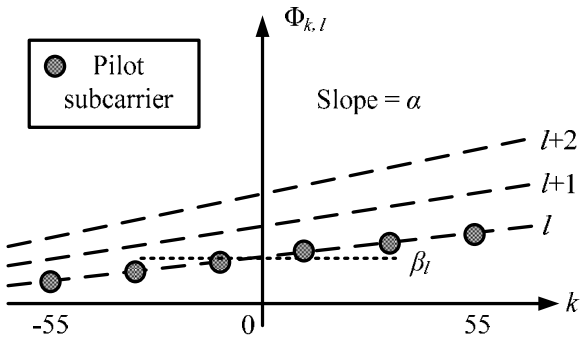

Fig. 12. The relationship of phase distortion and subcarriers

The pilot subcarriers are divided into two parts, C_1 and C_2. C_1 is on the left of the spectrum, and C_2 is on the right of the spectrum. Then the estimated intercept phase β_l and the slope α are written as (Speth et al., 2001)

$$\hat{\beta}_l = \frac{1}{2}(\Phi^-_{k,l} + \Phi^+_{k,l}) \qquad \hat{\alpha} = \frac{\Phi^+_{k,l} - \Phi^-_{k,l}}{\sum_{k\in C2} k - \sum_{k\in C1} k} \tag{36}$$

where

$$\Phi^-_{k,l} = tan^{-1} \sum_{k\in C1} Z_{k,l-1} Z^*_{k,l} \qquad \Phi^+_{k,l} = tan^{-1} \sum_{k\in C2} Z_{k,l} Z^*_{k,l-1} \tag{37}$$

Linear least squares

Applying LLS estimation to (37) with K pilots in one symbol, each pilot is located at the subcarrier of k_i. The RCFO and SFO estimation yield (Liu & Chong, 2002)

$$\Delta\hat{\theta}_f = \frac{\sum_{i=1}^{K} \Phi_{k_i,l}}{2\pi \frac{MK}{N}} \qquad \hat{\delta} = \frac{\sum_{i=1}^{K} \Phi_{k_i,l} k_i}{2\pi \frac{MK}{N} \sum_{i=1}^{K} k_i^2} \tag{38}$$

where

$$\Phi_{k_i,l} = tan^{-1} \sum_{i=1}^{K} Z_{k_i,l} Z^*_{k_i,l-1} \tag{39}$$

Such an estimation algorithm that is based on the phase differences between two symbols can remove the common channel fading terms in slow-fade scenarios. Consequently, this estimation scheme can be applied before channel estimation and equalization.

Weighted least squares

Though the joint LLS estimation algorithm provides accurate estimation results in the AWGN channel, diverse channel responses on the pilot subcarriers can render its estimation useless. For instance, phase of several deeply faded pilot subcarriers, when employ the estimation of the joint LLS, can lead to a large error in the estimation results. On the other hand, the phases of those subcarriers with little fading are naturally more reliable. Therefore, weighting the subcarrier data is advantageous, and data of serious faded subcarriers should be assigned smaller weights to minimize their adverse effect on estimation accuracy. The WLS algorithm for joint estimation of RCFO and SFO can be expressed as (Tsai et al., 2005)

$$\Delta\hat{\theta}_f = \frac{\sum_{i=0}^{K} \omega_i k_i^2 \sum_{i=0}^{K} \omega_i \Phi_{k_i,l} - \sum_{i=0}^{K} \omega_i k_i \sum_{i=0}^{K} \omega_i \Phi_{k_i,l} k_i}{2\pi \frac{MK}{N} \left[\sum_{i=0}^{K} \omega_i \sum_{i=0}^{K} \omega_i k_i^2 - \left(\sum_{i=0}^{K} \omega_i k_i \right)^2 \right]} \tag{40}$$

$$\hat{\delta} = \frac{\sum_{i=0}^{K} \omega_i \sum_{i=0}^{K} \omega_i \Phi_{k_i,l} k_i - \sum_{i=0}^{K} \omega_i k_i \sum_{i=0}^{K} \omega_i \Phi_{k_i,l}}{2\pi \frac{MK}{N} \left[\sum_{i=0}^{K} \omega_i \sum_{i=0}^{K} \omega_i k_i^2 - \left(\sum_{i=0}^{K} \omega_i k_i \right)^2 \right]} \tag{41}$$

The weight ω_i should be inversely proportional to the variance of phase error, which depends on noise, ICI and the complex channel gain. Usually, the residual synchronization error is so small that the ICI term can be neglected and ω_i only depends on the channel gain of the pilot subcarriers. The disadvantage is this algorithm is very complicated, especially the computation of the parameter of ω_i. Without estimating the ω_i accurately, there will be large error in phase tracking.

Novel approach for UWB

In traditional phase tracking solutions, arctangent, sine and cosine functions are necessary, which are quite complicated in hardware implementation. The algorithm presented in (Troya et al., 2007) simplifies the hardware cost significantly compared with the traditional approaches. However, it sacrifies system performance slightly. In (Fan & Choy, 2010b), a novel phase tracking method for UWB is proposed. It not only has low complexity, but also improves the performance.

Considering the condition $|\alpha k| << 1$ is satisfied with $k \in [-55, 55]$, the first order approximation can be made as $cos(\alpha k) \approx 1$ and $sin(\alpha k) \approx \alpha k$. Then the phase distortion in (35) can be rewritten as

$$P_{k,l} = cos\beta_l - \alpha k \cdot sin\beta_l + j(sin\beta_l + \alpha k \cdot cos\beta_l) \tag{42}$$

In (42), four parameters are of interests: $sin\beta_l$, $cos\beta_l$, $\alpha \cdot sin\beta_l$ and $\alpha \cdot cos\beta_l$. The former two can be easily obtained by

$$\begin{cases} cos\beta_l = \dfrac{1}{8} \displaystyle\sum_{k=\pm 25,\pm 35,\pm 45,\pm 55} \Re\{P_{k,l}\} \\ sin\beta_l = \dfrac{1}{8} \displaystyle\sum_{k=\pm 25,\pm 35,\pm 45,\pm 55} \Im\{P_{k,l}\} \end{cases} \tag{43}$$

where $\Re(\cdot)$ and $\Im(\cdot)$ denote the real and imaginary part respectively. There are 12 pilots in each symbol of OFDM-based UWB system. Since 1/8 is much easier to implement than 1/12 and the pilots near DC subcarrier suffer more channel noise than the ones far away from DC subcarrier, the pilots outermost should be used as many as possible.

Approximating the scaling factor 1/260 to 1/256, which can be easily implemented by 8-bit right-shifting, the parameters of $\alpha \cdot sin\beta_l$ and $\alpha \cdot cos\beta_l$ are given by

$$\begin{cases} \alpha \cdot sin\beta_l \approx \dfrac{1}{256}\left(\displaystyle\sum_{k=-55,-35,-25,-15} \Re\{P_{k,l}\} - \sum_{k=15,25,35,55} \Re\{P_{k,l}\} \right) \\ \alpha \cdot cos\beta_l \approx \dfrac{1}{256}\left(\displaystyle\sum_{k=55,35,25,15} \Im\{P_{k,l}\} - \sum_{k=-15,-25,-35,-55} \Im\{P_{k,l}\} \right) \end{cases} \tag{44}$$

In the traditional algorithms, although LLS and WLS algorithms have better phase tracking performance than AC, they have very high complexity for practical application. For hardware implementation, AC is in low complexity and moderate phase correction performance. Therefore, the MSE performance of the novel approach for UWB and AC are compared in different phase dostrotion conditions, as shown in Fig. 13. Obviously, the novel phase tracking method for UWB has much better proformance than the traditional AC

algorithm. In addition, with the increasing of phase error, the traditional AC algorithm degrades seriously, which is not associated with the novel method.

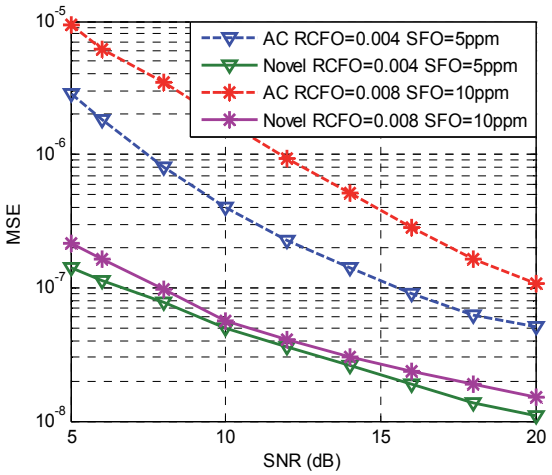

Fig. 13. MSE performance comparison between traditional AC algorithm and the novel approach for UWB

4.3 Architecture of the phase tracking block

The architecture of phase tracking block with the novel approach for UWB is shown in Fig. 14. The signals after channel equalization are stored in pilots buffer and data buffer separately. Considering that the transmitted pilots are known and have the modulus of one, the phase error vector of the pilots can be derived by multiplying the conjugation of transmitted pilots. As shown in Fig. 14, no arctangent, sine or cosine function appeared, they are replaced by eight complex adders and two complex shifters.

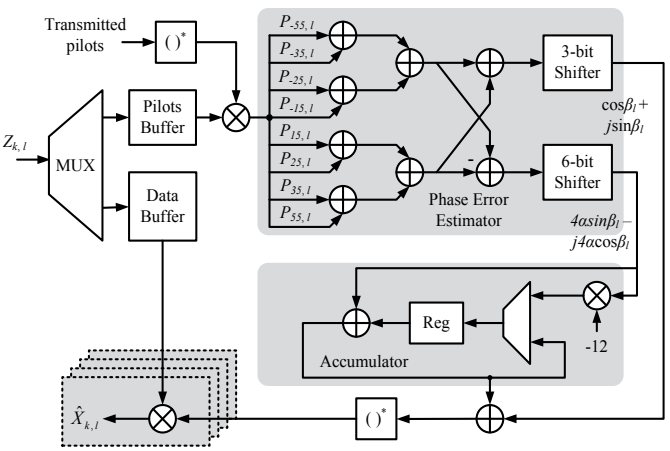

Fig. 14. Highly simplified architecture of the phase tracking block

The values of parameters $\alpha \cdot sin\beta_l$ and $\alpha \cdot cos\beta_l$ are very small, so the phase errors contributed by SFO of four parallel data can be approximately thought the same, rewritten as $\alpha\lfloor k/4 \rfloor sin\beta_l$

and $\alpha[k/4]cos\beta_l$ ($[k/4] \in [-12, 12]$). Calculating the parameters of $4\alpha \cdot sin\beta_l$ and $4\alpha \cdot cos\beta_l$ instead of $\alpha \cdot sin\beta_l$ and $\alpha \cdot cos\beta_l$ further simplifies the architecture of phase tracking block.

5. Conclusion

This chapter provides a compreshensive review of the algorithms and architectures for timing and frequency synchronization. Although there are many literatures on UWB synchronization techniques, most of them do not take the real application or implementation into account. This chapter introduces three parts of the synchronizaiton progress.

In timing synchroniztion, DT detection scheme improves the detection performance significantly due to the cascaded auto-correlator. Although it meanwhile increases the hardware cost slightly, the optimum architecture of the matched filter with low complexity can save the hardware. In coarse frequency synchronization, the CFO estimation approach can be simplified by shortening the SWL and the sum average over three subbands will compensate the SNR degradation. MTM is proved to be a low cost, low power and high speed approach to implement arctangent, sine and cosine functions compared with other function evaluation techniques. In fine frequency synchronization, a novel phase tracking approach for UWB is proposed for good performance. Additionaly, there is not any arctangent, sine or cosine intensive computation unit appeared and they are replaced by adders and shifters, which indicates that the implementation complexity of the novel phase tracking method is low.

The low compxity and power efficent synchronization techniques provide possibilities of developing the robust, low cost, low power and high speed OFDM-based UWB receiver.

6. References

Caro, D. D., Napoli, E., & Steollo, A. G. M. (2004). Direct digital frequency synthesizer with polynomial hyperfolding technique. *IEEE Transactions on Circuits and Systems II, Express Briefs*, Vol. 51, No. 7, Jul. 2004, pp. 337-344, ISSN 1549-7747

Caro, D. D, & Steollo, A. G. M. (2005). High-performance direct digital frequency synthesizer using piecewise-polynomial approximation. *IEEE Transactions on Circuits and Systems I, Regular Papers*, Vol. 52, No. 2, Feb. 2005, pp. 324-337, ISSN 1549-8328

Caro, D. D, Petra, N., & Steollo, A. G. M. (2008). Reducing lookup-table size in direct digital frequency synthesizers using optimized multipartite table method. *IEEE Transactions on Circuits and Systems I, Regular Papers*, Vol. 55, No. 7, Aug. 2008, pp. 2116-2127, ISSN 1549-8328

Caro, D. D, Petra, N., & Steollo, A. G. M. (2009). Digital synthesizer/mixer with hybrid CORDIC-multiplier architecture : error analysis and optimization. *IEEE Transactions on Circuits and Systems I, Regular Papers*, Vol. 56, No. 2, Feb. 2009, pp. 364-373, ISSN 1549-8328

Coulson, A. J. (2001). Maximum likelihood synchronization for OFDM using a pilot symbol : algorithms. *IEEE Journal on Selected Areas in Communications*, Vol. 19, No. 12, Dec. 2001, pp. 2486-2494, ISSN 0733-8716

Fan, W., Choy, C-S., & Leung K-N. (2009). Robust and low complexity packet detector design for MB-OFDM UWB. *Proceedings of IEEE Int. Symposium on Circuits and Systems*, pp. 693-696

Fan, W., & Choy, C-S. (2010a). Power efficient and high speed frequency synchronizer design for MB-OFDM UWB. *Proceedings of IEEE Int. Conference on UWB*, pp. 669-673

Fan, W., & Choy, C-S. (2010b). Efficient and low complexity phase tracking method for MB-OFDM UWB receiver. *Proceedings of IEEE Midwest Symposium on Circuits and Systems*, pp. 221-224

Fort, A., Weijers, J. W., & Derudder, V. et al. (2003). A performance and complexity comparison of auto-correlation and cross-correlation for OFDM burst synchronization. *Proceedings of IEEE Int. Conference on Acoustics, Speech, and Signal Processing*, pp. 341-344

Liu, S. Y., & Chong, J. W. (2002). A study of joint tracking algorithms of carriers frequency offset and sampling clock offset for OFDM-based WLANs. *Proceedings of IEEE Int. Conference on Communications, Circuits and Systems and West Sino Expositions*, pp. 109-133.

Minn, H., Bhargava, V. K., & Letaief, K. B. (2003). A robust timing and frequency synchronization for OFDM systems. *IEEE Transactions on Wireless Communications*, Vol. 2, No. 4, Jul. 2003, pp. 822-839, ISSN 1536-1276

Moose, P. H. (1994). A technique for orthogonal frequency division multiplexing frequency offset correction. *IEEE Transactions on Communications*, Vol. 42, No. 10, Oct. 1994, pp. 2908-2914, ISSN 0090-6778

Pollet, T., Van Bladel, M., & Moeneclaey, M. (1995). BER sensitivity of OFDM systems to carrier frequency offset and Wiener phase noise. *IEEE Transactions on Communications,* Vol. 43, No. 2, Mar. ~ Apr. 1995, pp. 191-193, ISSN 0090-6778

Schmidl, T. M., & Cox. D. C. (1997). Robust frequency and timing synchronization for OFDM. *IEEE Transactions on Communications,* Vol. 45, No. 12, Dec. 1997, pp. 1613-1621, ISSN 0090-6778

Speth, M., Fechtel, S., & Fock, G. et al. (2001). Optimum receiver design for OFDM-based broadband transmission-part II: a case study. *IEEE Transactions on Communications,* Vol. 49, No. 4, Apr. 2001, pp. 571-578, ISSN 0090-6778

Troya, A., Maharatna, K., & Krstic, M. et al. (2007). Efficient inner receiver design for OFDM-based WLAN systems: algorithm and architecture. *IEEE Transactions on Wireless Communications,* Vol. 6, No. 4, Apr. 2007, pp. 1374-1385, ISSN 1536-1276

Troya, A., Maharatna, K., & Krstic, M. (2008). Low-power VLSI implementation of the inner receiver for OFDM-based WLAN systems. *IEEE Transactions on Circuits and Systems I, Regular Papers*, Vol. 55, No. 2, Mar. 2008, pp. 672-686, ISSN 1549-8328

Tsai, P-Y., Kang, H-Y., & Chiueh, T-D. (2005). Joint weighted least squares estimation of carrier frequency offset and timing offset for OFDM systems over multipath fading channel. *IEEE Transactions on Vehicular Technology*, Vol. 54, No. 1, Jan. 2005, pp. 211-224, ISSN 0018 9545

Tsai, P-Y., & Chiueh, T-D. (2007). A low-power multicarrier-CDMA downlink baseband receiver for future cellular communication systems. *IEEE Transactions on Circuits and Systems I, Regular Papers*, Vol. 54, No. 10, Oct. 2007, pp. 2229-2239, ISSN 1549-8328

Van de Beek, J. J., Sandell, M., & Borjesson, P. O. (1997). ML estimation of time and frequency offset in OFDM systems. *IEEE Transactions on Signal Processing*, Vol. 45, No. 7, Jul. 1997, pp. 1800-1805, ISSN 1053-587X

10

Frequency Synthesizer Architectures for UWB MB-OFDM Alliance Application

Owen Casha and Ivan Grech
Department of Micro and Nanoelectronics - University of Malta
Malta

1. Introduction

Ultra Wideband (UWB) is an emerging wireless technology supporting data rates as high as 480 Mb/s. As proposed by the MB-OFDM Alliance, the current frequency spectrum for an UWB communication system ranges from 3.1-to-10.6 GHz divided into 14 bands each with a 528 MHz bandwidth, and are categorised into 5 groups with a strict regulation in emission power of less than -41 dBm as set by the Federal Communications Commission (FCC). The US allows the deployment of UWB systems in the whole frequency band, while Japan, Europe, China and Korea have restricted the use of UWB to a subset of the available frequencies in the US (Batra et al., 2004a). The current frequency plan of the MBOA-UWB system is shown in Fig. 1(a) where the highlighted bands are those deployed in Japan, Europe, China and Korea. An alternative frequency plan is shown in Fig. 1(b) (Mishra et al., 2005).

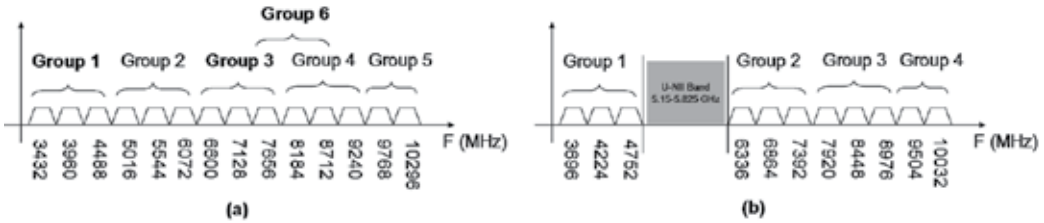

Fig. 1. (a) Current Frequency Plan and (b) Alternative Frequency Plan of the MBOA-UWB System (Batra et al., 2004a; Mishra et al., 2005)

Designing frequency synthesizers for UWB MB-OFDM alliance applications faces particularly stringent challenges and performance criteria. Amongst these one may list the wide range of frequencies to be synthesized, the in-group frequency hopping time (less than 9.5 ns), the reduction of the silicon area and the power consumption in the implementation and the limitation of the integrated spurious tone level in the different bands (less than -32 dBc in a 528 MHz bandwidth). Such challenges cannot be catered for by simply employing standard frequency synthesizer techniques such as a stand alone phase locked loop (Casha et al., 2009a). One of the main objectives of this chapter is to study and compare the current state of the art in frequency synthesis for UWB MBOA applications. On one hand several frequency synthesizers based on single side band frequency mixing will be discussed. These generally require multiple phase-locked loops (PLL), complex dividers and mixers to provide adequate sub-harmonics for the full-band frequency synthesis (Batra et al., 2004b; Mishra et al., 2005).

Such architectures are hungry in both silicon area and power consumption. On the other hand, other novel frequency synthesis architectures being investigated as a low silicon area alternative will be included in the discussion. These are either based on delay locked loops (DLL) (Lee & Hsiao, 2005; 2006) or based on phase interpolation direct digital synthesis (DDS) (Casha et al., 2009a).

The chapter then discusses a study on such frequency synthesizer architectures with special reference to the investigation of the spurious tone levels at their output. The discussion is aided by means of mathematically derived analysis tools implemented using Matlab. These analytic tools provide an adequate system level simulation with low computational complexity, from which particular design considerations are drawn and are then verified by means of the design and the simulation of actual circuit building blocks using a particular integrated circuit technology. The design considerations focus on the reduction of the spurious tone levels by means of applying different techniques including non-linearity compensation and dynamic element matching techniques. In addition, based on the observations obtained from both the analytic tools and the circuit level simulation, the discussion compares the DLL versus the DDS approach in designing a frequency synthesizer whilst highlighting the advantages and the disadvantages and commenting on the feasibility of the two architectures.

2. The state of the art - PLL and sideband (SSB) mixer approach

2.1 Architectures

By far, the most common frequency synthesis approach for UWB OFDM frequency synthesis has been based on dividers and single-sideband (SSB) mixers as proposed in (Batra et al., 2004b) and depicted in the block diagram shown in Fig. 2. The advantage of this topology is that it uses just one PLL and allows fast switching between the 3 bands in Group 1. The first mixer outputs the upper sideband of the 264 and 528 MHz input signals, resulting in the generation of the 792 MHz signal. A multiplexer is used to select one of the 264 or 792 MHz signals and input the selected signal into the second mixer. Bands 1 and 2 centre frequencies are synthesized from the lower sidebands derived by mixing the 4224 MHz signal with 264 or 792 MHz. Band 3 centre frequency is generated by configuring the second mixer for upper sideband generation and using the 4224 MHz and 264 MHz signal frequencies.

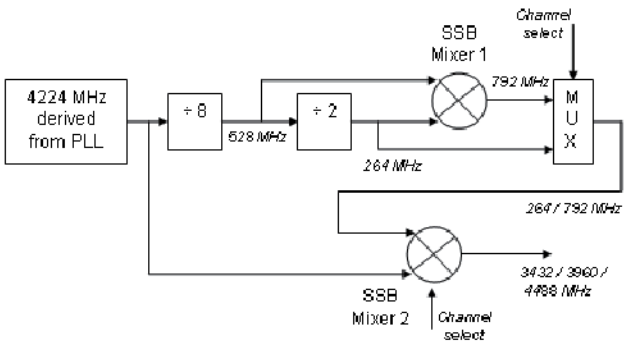

Fig. 2. Synthesis of Group 1 frequency bands using a single PLL, dividers and SSB mixers (Batra et al., 2004b)

The phase noise from a UWB frequency synthesizer is crucial since interchannel interference can result if the phase noise performance is poor. In mixer-based synthesizers, the output

phase noise from a mixer stage can be computed, by assuming that the phase noise in the inputs of the mixer are uncorrelated and therefore, the output phase noise is given by the rms sum of the input noise contributions (Mishra et al., 2005). This assumption holds, even though the signals are derived from the same source, since the delays from the PLL to each mixer input are significantly different. Typically, the phase noise contribution of the mixer itself is negligible, since the signal swings involved are orders of magnitude higher than the mixer thermal noise. Hence the output phase noise L_{mixer} at an offset frequency Δf, of a mixer stage can be computed from the phase noise levels of the inputs L_1 and L_2, using Equation 1, where all noise levels are in dB/Hz relative to the carrier.

$$L_{mixer}(\Delta f) = 10\log_{10}(10^{\frac{L_1(\Delta f)}{10}} + 10^{\frac{L_2(\Delta f)}{10}}) \quad (1)$$

The worst case output phase noise of a mixer-based frequency synthesizer can therefore be computed by taking into account the synthesis path involving the largest number of frequency translations. Thus, in the scenario depicted in Fig. 2, the output phase noise L_{output} exhibits a degradation of 0.75 dB relative the PLL phase noise L_{PLL} as can be verified from the following computation:

$$L_{output}(\Delta f) = 10\log_{10}(10^{\frac{L_{PLL}(\Delta f)}{10}} + \frac{10^{\frac{L_{PLL}(\Delta f)}{10}}}{8} + \frac{10^{\frac{L_{PLL}(\Delta f)}{10}}}{16}) = 10\log_{10}(\frac{19}{16} \bullet 10^{\frac{L_{PLL}(\Delta f)}{10}}) \quad (2)$$

Mixer-based architectures are investigated to some extent in (Mishra et al., 2005), where several topologies are discussed, capable of generating all the UWB bands in Groups 1, 3, 4 and 5. Such frequency synthesizer topologies have been adapted and used in complete OFDM UWB receivers as in (Tanaka et al. (2006), Valdes-Garcia et al. (2006)). In such topologies, some of the frequency divider stages form path of the feedback path of the PLL itself. It should be noted, that in order to preserve signal purity, bandpass filters typically have to be employed at the outputs of the mixers. If frequency selection is carried out before a mixer stage (as in Fig. 2), then these filters have to be configurable or switchable, making the system more complex and costly. For this reason, topologies which involve no frequency selection preceding the mixer stages, tend to be preferred. One such topology is depicted in Fig. 3 and is capable of generating all bands in groups 1, 2, 3 and 4 (Mishra et al., 2005) of the MB-OFDM alternate plan. The main advantage of this topology is that the output frequency from the mixers is fixed and any subsequent filters need not be configurable. Another receiver design for MB-OFDM application, based on a similar architecture can be found in (Valdes-Garcia et al., 2007). Other approaches avoid the problems associated with SSB mixing completely, by having a separate PLL for each band as in (Razavi et al., 2005), where three PLLs are used to generate the required signals for bands 1 to 3.

Alternative architectures (Roovers et al. (2005), Leenaerts (2005), Lee & Chiu (2005), Liang et al. (2006), Lee (2006), Leenaerts (2006), Pufeng et al. (2010)) can be found in literature using a number of PLLs working in parallel. The architecture proposed in (Roovers et al., 2005) and (Leenaerts, 2005) uses 2 PLLs: one PLL generates a quadrature 3960 MHz signal while the other PLL generates a quadrature 528 MHz signal. In this way, output quadrature signals of frequencies 3432, 3960 and 4488 MHz, corresponding to bands 1 to 3 of the MBOA spectrum are generated. The PLLs have a fixed output frequency and therefore the switching time of the synthesizer does not depend on the loop bandwidth of the PLLs. In (Lee & Hsiao, 2005), two parallel PLLs are again employed. The first PLL generates a selectable 6864 or 3432 MHz output signal while the second PLL generates a selectable 2112 or 1056 MHz signal. Both PLLs

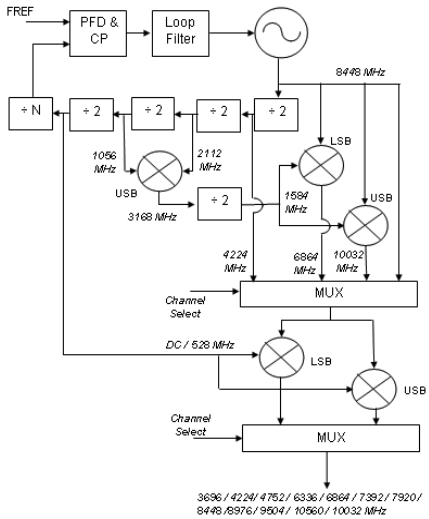

Fig. 3. Generation of MB-OFDM alternate plan bands 1, 3, 4, 5 (Mishra et al., 2005)

use a 264 MHz reference clock. The output of the second PLL drives a tri-mode divide-by-2 buffer circuit which is capable of generating either a swappable quadrature signal or else a DC signal. These signals are fed to an SSB mixer which can thus generate output frequencies: 6864, 6864 ± 1056, 6864 ± 528, 3432, 3432 ± 1056 and 3432 ± 528 MHz. These frequencies correspond to bands 1 to 3 and 4 to 7 of the MBOA spectrum, as well as some unused signal frequencies.

2.2 SSB mixers

SSB mixers can be designed around two Gilbert multiplier cells with the second multiplier driven by the corresponding quadrature signals as shown in Fig. 4 (Ismail & Abidi, 2005a;b). The matrix in Equation 3 shows that quadrature outputs can also be generated.

$$\begin{pmatrix} \cos(\omega_1-\omega_2)t \\ \cos(\omega_1+\omega_2)t \\ \sin(\omega_1+\omega_2)t \\ \sin(\omega_1-\omega_2)t \end{pmatrix} = \begin{pmatrix} \cos(\omega_1 t) & \sin(\omega_1 t) \\ \cos(\omega_1 t) & -\sin(\omega_1 t) \\ \sin(\omega_1 t) & \cos(\omega_1 t) \\ \sin(\omega_1 t) & -\cos(\omega_1 t) \end{pmatrix} \times \begin{pmatrix} \cos(\omega_2 t) \\ \sin(\omega_2 t) \end{pmatrix} \tag{3}$$

The upper or the lower SSB signal is selected, by reversing the polarity of the outputs of the second multiplier. Spurious signals can occur if the two mixers are not adequately matched. Furthermore, emitter-resistor degeneration may be employed in order to improve linearity of the mixer (Roovers et al., 2005). It is in fact essential that at least one port of the mixer is linear in order to prevent mixing with harmonics of that input. It is also important that the inputs themselves exhibit a low distortion level. Furthermore, different delay paths will also lead to the generation of spurs, while a DC offset on one port will cause leakage of the other input signal to the output. The linearity requirements often lead to a mixer design with low conversion gain and low signal swing, often requiring power (and area) hungry buffers. These problems are particularly troublesome in CMOS technology (Razavi et al., 2005). For multiple-band output operation, selection of the tank circuit resonant frequency is essential. In (Zheng & Luong, 2007), this is achieved by having switchable LC sections, controlled by MOS switches: in this way high Q-factor LC sections can still be used for multiple frequency

operation. The use of RC polyphase filters for harmonic suppression, as well as phase and amplitude adjustment has also been investigated (Jiang et al., 2010).

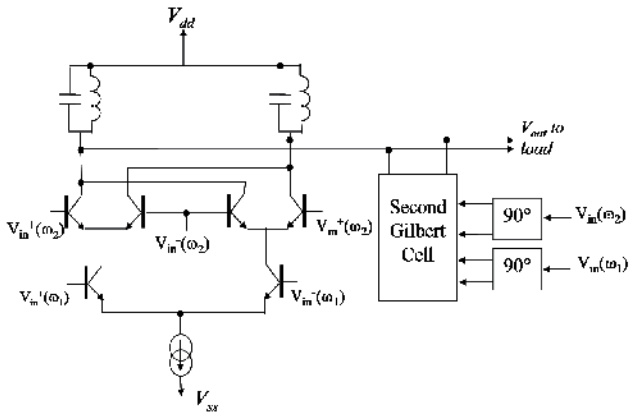

Fig. 4. SSB mixer based on two Gilbert Multiplier Cells

Gain and phase mismatches can also arise when the signals travel through different paths. In order to compensate for this non-ideality, the use of a vector-calibrated clock buffer (Lu & Chen, 2005) has been investigated. This buffer essentially adds one of the two quadrature signals in a controlled manner. In order to achieve this, the tail current of one of the differential pairs is controlled digitally via a 4-bit DAC. The use of sub-harmonic mixing has also been investigated in literature (Lin & Wang, 2005a), where eight phases of a 2.244 GHz signal are generated via the use of a 4-stage ring oscillator. These phases are mixed with 2.112 and 1.056 GHz signals in order to generate the 3.432, 3.960 and 4.488 GHz carriers via sub-harmonic mixer, based on Gilbert cells with switchable differential pairs. When generating the 4.488 GHz carrier, the sub-harmonic mixer actually functions as an edge-combiner.

2.3 Signal select multiplexers

Signal multiplexers are typically implemented as a number of differential pairs driving the same load. At any point in time, only one differential pair is enabled by activating its tail current source. One such topology, reported in (Ismail & Abidi, 2005a;b), is shown in Fig. 5.

2.4 Frequency dividers

2.4.1 Divide-by-2 circuits

High speed divide-by-2 circuits can be implemented using pairs of D-FFs, based on latched differential pairs, cascaded in master-slave configuration. These master-slave D-FFs are configured as T-FFs by feeding back the complimentary outputs. The concept is shown in Fig. 6 as documented in (Ismail & Abidi, 2005b). It should be noted that quadrature signals are available after at the first (master) stage outputs. Differential-pair buffers are often used to couple the outputs of the divider circuits to subsequent dividers or mixers (Leenaerts, 2005).

2.4.2 Tri-mode divider

The concept of the tri-mode divider (Lee, 2006) is essentially an extension of the divide-by-2 circuit which incorporates inherent multiplexing such that it permits swappable quadrature outputs (clockwise and anticlockwise variations) as well as the generation of a DC output.

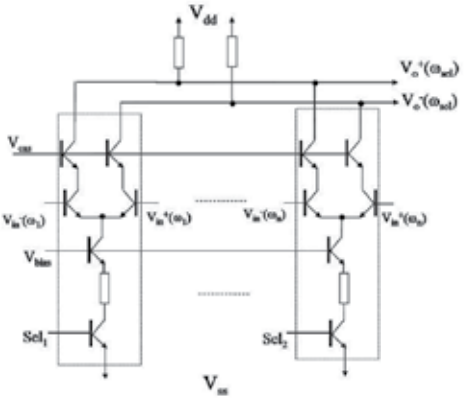

Fig. 5. Signal Select Multiplexer implemented using switched differential pairs (Ismail & Abidi, 2005b)

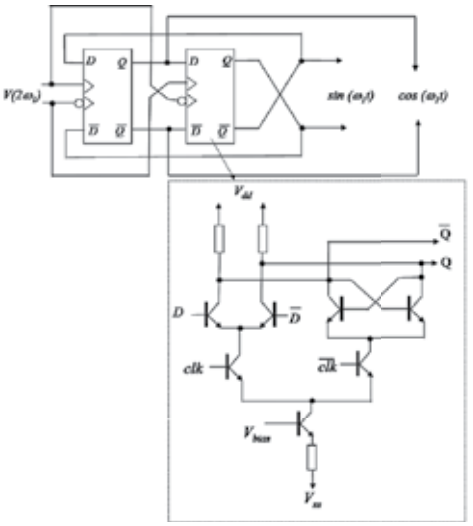

Fig. 6. Divide-by-2 circuit based on Master-Slave D-FFs

This is achieved by introducing switches in the input stages of the dividers which essentially select a differential pair which is connected either to the input clock signal, or its complement, or else to a DC signal. In this way, this type of divider can be used to select between three different bands as depicted in Fig. 7.

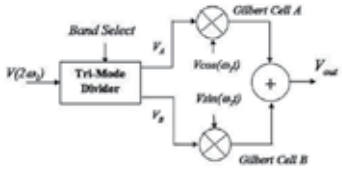

V_A	V_B	V_{out}
sin (ω_1t)	cos (ω_1t)	sin(ω_1+ω_2)t
cos (ω_1t)	sin (ω_1t)	cos(ω_1-ω_2)t
+DC	0	cos(ω_2t)

Fig. 7. Tri-Mode Divider Concept for Band-Selection (Lee, 2006)

A block diagram of the final tri-mode divider is shown in Fig. 7 (Lee, 2006). A practical CMOS implementation is shown in Fig. 8. The circuit allows for clockwise (CW) and counter-clockwise (CCW) quadrature signal generation, by flipping the corresponding quadrature signal in relation to the input clocking signal clk($2\omega_1$). In addition, the divider also allows for DC signal generation. The operation mode is selected by enabling the CW Select, CCW-Select or DC-Select signals respectively, which effectively steer the tail current source to the required section to be used.

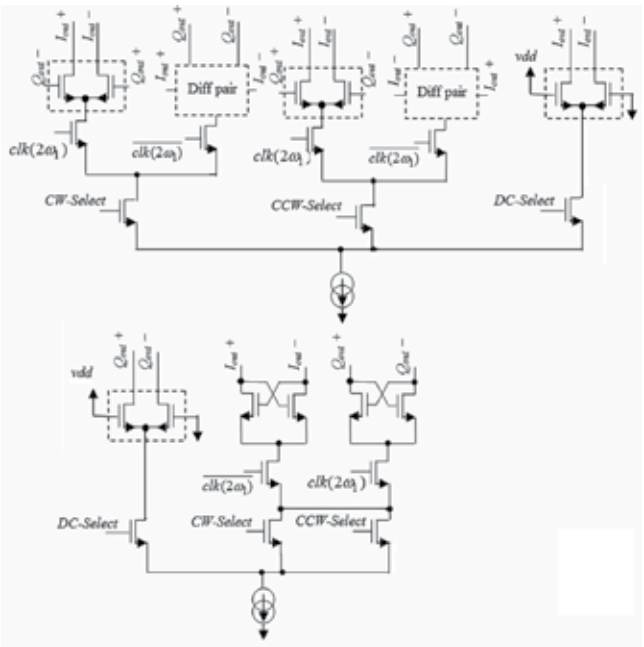

Fig. 8. CMOS implementation or the trimod divider/buffer

2.4.3 Regenerative (Miller) divider

A Miller divider is based on a feedback loop around a filter with a mixer driven by the input and feedback signals. This topology has been used in some designs intended for UWB application (Lin & Wang (2005b),Lee & Huang (2006)). In (Lee & Huang, 2006), the three different Miller-based dividers, depicted in Fig. 9 are discussed.

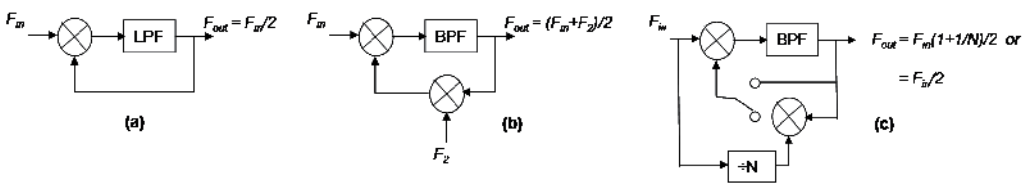

Fig. 9. (a) Miller Divider, (b) Modified Miller Divider and (c) Combined Miller/modified Miller divider (Lee & Huang, 2006)

It can be shown that for the topologies shown in Fig. 9, the following relationships do hold:

$$
\begin{gathered}
\textit{Miller Divider} : F_{out} = F_{in} - F_{out} \Rightarrow F_{out} = F_{in}/2 \\
\textit{Modified Miller Divider} : F_{out} = F_{in} - F_{out} \pm F_2 \Rightarrow F_{out} = (F_{in} \pm F_2)/2 \\
\textit{Combined Miller Divider/Modified Miller Divider} : \\
F_{out} = F_{in} - F_{out} \pm F_{in}/N \Rightarrow F_{out} = F_{in}(1 \pm N)/2 \textit{ or } F_{out} = F_{in}/2
\end{gathered}
\tag{4}
$$

In the latter two cases, two frequencies are theoretically possible, but the actual frequency which is sustained by the loop is selected by the centre frequency of the BPF. The design proposed in (Lee & Huang, 2006) makes use of a gyrator-based tuned circuit for the BPF, where the effective inductance of the gyrator circuit is controlled by tuning the transconductance: in this way tuning of the operating frequency is possible. In this case, the input signal F_{in} is generated by a PLL operating at 7.92 GHz, while N is set to 7.5. In this way the 3432, 3960 and 4488 MHz UWB bands can be generated.

2.4.4 Non-integer (Half-cycle) dividers

Some architectures (Lee & Huang (2006), Van de Beek et al. (2006)) entail the use of non-integer dividers. Specifically a divide-by-7.5 circuit is used in (Lee & Huang, 2006) while a divide-by-1.5 circuit is used in (Van de Beek et al., 2006). In (Lee & Huang, 2006), a specific D-flipflop design is used with selectable positive or negative edge-triggering mode. The edge-triggering mode is selected via feedback signal as shown in Fig. 10.

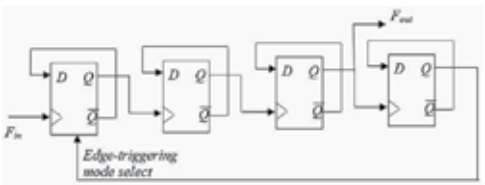

Fig. 10. Divide-by-7.5 circuit based on selectable edge-triggering mode (Lee & Huang, 2006)

The approach in (Van de Beek et al., 2006), depicted in Fig. 11 uses multiplexors for the selection of the appropriate signal used to clock the D-flipflops in the divider.

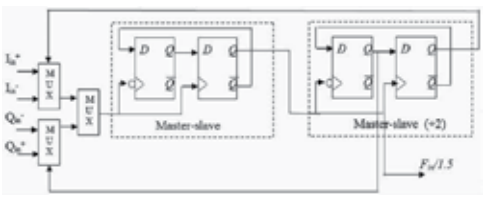

Fig. 11. Divide-by-1.5 circuit based on multiplexors with quadrature input signals (Van de Beek et al., 2006)

2.4.5 ROM-based dividers

Dividers based on ROM lookup tables (LUTs) have been proposed for UWB application (Sandner et al., 2005). In this case the UWB generation circuit is driven by a single PLL running at 8.448 GHz, which is subsequently divided by two. The resulting 4.224 GHz signal is used for addressing ROM LUTs storing values of quadrature generation of $\pm$264 or 792 MHz

signals, depending on a hop-control signal. The output of the LUTs drive 4 bit current steering DACs. Via SSB mixers, it is then possible to generate 3960, 4488 and 3432 MHz quadrature signals.

2.4.6 Injection locked frequency divider (ILFD)

The use of injection locked frequency dividers (ILFDs) for MB-OFDM application can also be found in literature (Kim et al. (2007), Chang et al. (2009)). In both cases, a divide-by-5 ring oscillator-based ILFD is implemented. In (Kim et al., 2007), the divider consists of five cascaded CMOS inverters connected in ring oscillator configuration. The supply source and sink currents are controlled via two switches controlled by the input signal. ILFDs can also be constructed using LC-based oscillators, resulting in better phase noise performance compared to ring oscillator-based ILFDs, at the expense of a higher power consumption. In (Chang et al., 2009), the ILFD consists of two ring oscillators, whose supply is clocked by the input signal. In this case, the two ring oscillators are coupled together via inverters in order to improve the quadrature phase accuracy.

3. DLL-based frequency multiplier for UWB MBOA

3.1 Delay locked loops

PLL-based frequency synthesis has been widely employed until recent times. Another approach drawing attention in this field is DLL-based frequency synthesis. DLL-based frequency synthesizers outperform their counterparts in terms of phase noise since they derive the output signal directly from a clean crystal reference with limited noise accumulation (Chien & Gray, 2000). Additionally, the DLLs can be designed as a first-order system to allow wider loop bandwidth and settling times in the order of nanoseconds, especially important in applications where fast band-hopping is required such as in MBOA-UWB (Lee & Hsiao, 2005; 2006). The main challenge in designing DLL-based frequency synthesizers is limiting the fixed pattern jitter that result in spurious tones around the desired output frequency.

There exist mainly two types of DLL-based frequency synthesizers or multipliers: the edge-combining type (Chien & Gray, 2000) and the recirculating type (Gierkink, 2008). Static phase offsets in the loop cause pattern jitter in both topologies, whilst the edge combining type is also prone to pattern jitter resulting from mismatches between the delay stages in the delay line. The design of an edge-combining type is generally less complex than the recirculating one since the latter requires extra components such as a divider and extra control logic. This work focuses on edge combining DLL-based frequency synthesizers.

3.2 Concept of edge combining DLL-based frequency multipliers

Fig. 12(a) shows the block diagram of a typical edge combining DLL-based frequency multiplier. The DLL consists of a voltage-controlled delay line (VCDL), a charge pump based phase comparator, a loop filter and an edge combiner. The phase difference between the input and the output of the VCDL is smoothed by the loop filter to generate a control voltage which is then fed back to the VCDL to adjust its delay.

When the VCDL delay is locked to one period of the reference signal, F_{in}, an output signal whose frequency is a multiple of the input frequency is obtained by combining the delay stage outputs of the VCDL by means of an edge combiner, as shown in Fig. 12(c). Each delay stage outputs a pulse P_n having a width of half its delay time (see Fig. 12(b)). These pulses are sent to a pulse combiner that generates the output signal. Via this architecture, only the

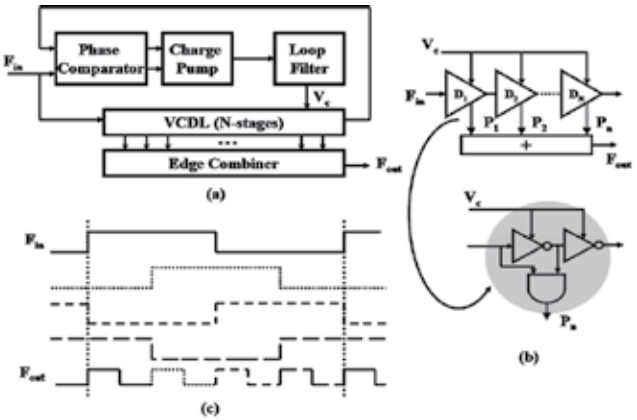

Fig. 12. (a) Edge combining DLL-based frequency multiplier (b) VCDL with edge combiner: each delay stage DN consists of two inverting variable delay cells (c) Concept of a multiply-by-4 DLL-based frequency synthesizer

rising edges of the reference signal are used resulting in a frequency synthesizer output which is immune to any duty-cycle asymmetry in the reference signal. Ideally if all the delay stages provide the same delay and their sum is exactly one period of the reference signal, a spur free output signal is generated, whose frequency is N times the reference frequency, where N is the number of delay stages. In practice the above conditions cannot be satisfied exactly and so some spurious tones show up in the frequency synthesizer output spectrum. This implies that there are two main sources by which spurs can result in the output spectrum: the in-lock error of the DLL and the delay-stage mismatch.

3.3 Analysis of spurious tones

This work provides a complete analysis of the spur characteristics of edge combining DLL-based frequency multipliers (Casha et al., 2009b). An analysis concerning the spur characteristics of such frequency synthesizers was presented in (Zhuang et al. (2004), Lee & Hsiao (2006)), but the theoretical treatment was mainly limited to the effect of the phase static offsets on the spurious tones. In this work, the effect of the delay-stage mismatch is also included. As a matter of fact in this section an analytic tool is presented, via which it is possible to estimate the effect of both the DLL in-lock error and the delay-stage mismatch on the spurious level of the frequency multiplier shown in Fig. 12.

The analysis presented here considers a DLL operating at lock state. Even though there could be delay stage mismatches, the VCDL at lock state will have a delay which is formed by unequal contributions, whose value is such that the total loop delay is equal to T_{in}, where T_{in} is the periodic time of the reference signal. But in an edge combining DLL frequency synthesizer although the DLL can lock exactly to T_{in}, the pulses generated by the edge combiner may not be equally spaced, such that spurious tones are generated. It is assumed that the delay of the inverter delay cells, T_{dcell}, making up the delay stages of the VCDL (see Fig. 12(b)) follows a standard normal distribution with a variance σ^2_{Tdcell}, which models the mismatch between the delay cells and a mean μ_{Tdcell} given by Equation 5:

$$\mu_{Tdcell} = \frac{T_{in} + \Delta T}{2N} \tag{5}$$

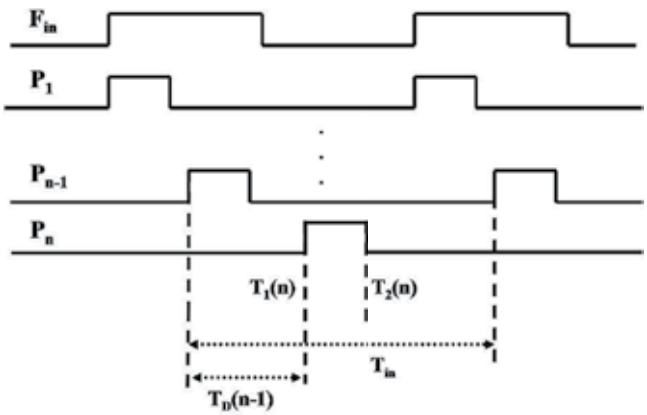

Fig. 13. Decomposition of the frequency multiplier output into N shifted pulse signals generated by the VCDL.

where ΔT is the DLL in-lock error which is ideally zero. The output signal of the frequency multiplier can be decomposed into N shifted pulse signals which have a periodicity of T_{in}, as shown in Fig. 13. Since P_n is periodic it is possible to calculate its Fourier series coefficients A_k using:

$$A_k = \frac{1}{T_{in}} \int_0^{T_{in}} x(t) e^{-jk\omega_{in}t} dt = \frac{1}{T_{in}} \int_{T_1(n)}^{T_2(n)} B e^{-jk\omega_{in}t} dt = B \frac{\sin\phi_2 - \sin\phi_1}{2\pi k} + jB \frac{\cos\phi_2 - \cos\phi_1}{2\pi k} \tag{6}$$

where ω_{in} is the angular frequency of the reference signal, k is the harmonic number, B is the amplitude of the pulse and $\phi_1 = kT_1(n)\omega_{in}$ and $\phi_2 = kT_2(n)\omega_{in}$. For $2N$ different values of T_{dcell}, the time characteristics of P_n can be defined as:

$$\begin{aligned} T_D(n) &= T_{dcell}(2n-1) + T_{dcell}(2n) \quad 1 \le n \le N \\ T_n &= \begin{cases} 0 & n = 1 \\ T_D(n-1) + T_1(n-1) & 2 \le n \le N \end{cases} \\ T_2(n) &= T_{dcell}(2n-1) + T_1(n) \qquad 1 \le n \le N \end{aligned} \tag{7}$$

Using the linearity property of the Fourier Transform the output frequency spectrum of the frequency synthesizer, X_{out} can be obtained by summing the Fourier Transform of each respective pulse P_n:

$$X_{out}(kf_{in}) = \sum_{n=1}^{N} X_{p(n)}(kf_{in}) \;\; where \; X_{p(n)}(kf_{in}) = \sum_{n=-\infty}^{\infty} 2\pi A_k \delta(\omega - k\omega_{in}) \tag{8}$$

where δ is the Dirac Impulse Function. In an ideal situation, if all the delay stages provide the same delay and their sum is exactly equal to T_{in}, i.e. ΔT and σ^2_{Tdcell} are zero, it can be shown using Equation 8 that X_{out} will have a non-zero value only at values of k which are multiples of N, meaning that the output frequency will be equal to N times f_{in} and no spurious tones

are present in the output of the frequency multiplier. In reality, there is always some finite in-lock error in the DLL and mismatch in the VCDL such that the output spectrum is not zero when k is not equal to a multiple of N, such that spurs are generated. The relative integrated spurious level can be determined using the output spectrum of the frequency synthesizer and is defined as the ratio of the sum of all the spurious power in the considered bandwidth to the carrier power at Nf_{in}, as indicated by Equation 9. The spurs nearest to the carrier frequency are considered in the calculation since they are the major contributors to the total integrated spurious power, i.e. at k = N-1 and k = N+1.

$$R_{spur}(dB) = 10\log_{10}\frac{\sum_{k\neq N}|X_{out}(kf_{in})|^2}{|X_{out}(Nf_{in})|^2} \tag{9}$$

Assuming a delay cell variance of zero, i.e. no delay-stage mismatch, a plot of the integrated spurious level due to the normalized in-lock error for different values of N was obtained using Equation 9 and is shown in Fig. 14(a). These set of curves indicate the importance of reducing the in-lock error to reduce the output spur level of the DLL based frequency multiplier. Note also that for the same normalized in-lock error the spurious level increases with an increase in the N value. The generality of the analysis presented above, permits also to estimate the mean spurious level due to the possible mismatches in the VCDL. Fig. 14(b) shows a plot of the mean estimated R_{spur} against the normalized delay cell variation for different values of N, assuming ΔT is equal to zero. As expected the higher the mismatch in the VCDL the higher the spurious level the output of the frequency multiplier, indicating that the reduction of this mismatch is equally important as the reduction of the DLL in-lock error.

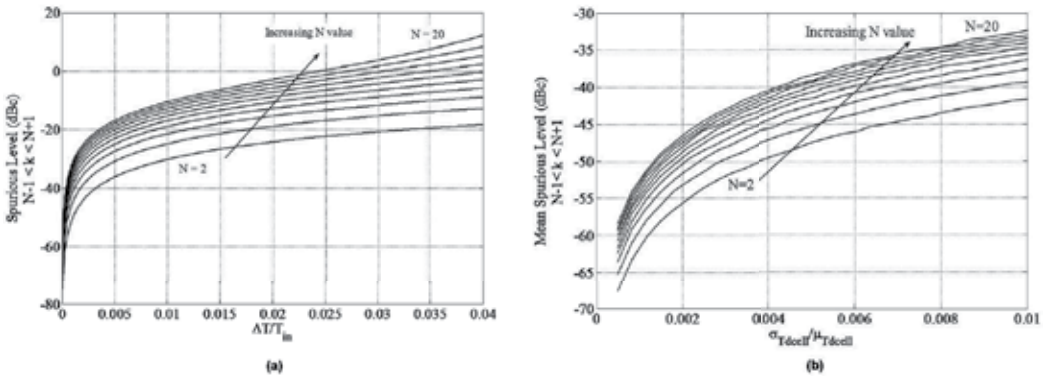

Fig. 14. (a) Plot of the estimated integrated spurious level (N-1<k<N+1) against normalized in-lock error for different values of N (b) Plot of the mean estimated integrated spurious level against normalized delay cell variation for different values of N

3.4 DLL-based frequency synthesizer

The concept of using DLL-based frequency synthesizer architecture for UWB MBOA was introduced in (Lee & Hsiao, 2006) and is shown in Fig. 15. Although the implementation results showed that the architecture exhibits a sideband magnitude of -35.4 dBc (which is within the specification), it considered only the generation of signals in the band group 1 (N = 13, 15, 17).

As discussed in Section 3.3, for the same normalised in-lock error and delay cell mismatch the spurious level increases with an increase in the N value. Considering the generation of the

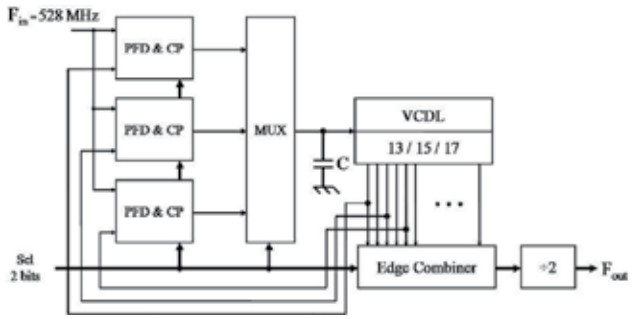

Fig. 15. Proposed UWB MBOA Frequency Synthesizer Architecture in (Lee & Hsiao, 2006)

8.712 GHz signal which is the highest frequency in band group 6 one would require a value of N = 33. Using the analysis presented in Section 3.3 it is possible to estimate the maximum in-lock error and the maximum delay mismatch such that integrated spur level at the output of the DLL frequency multiplier is less than -32 dBc. Note that one must keep in mind that the ÷2 frequency divider at the output of the DLL improves the spur level at the output of the DLL by 6.02 dB, such that R_{spur} < -26 dBc. Assuming there is no mismatch in the delay stages, the in-lock error ΔT needs to be less than (0.001073 ÷ 528 MHz) = 2 ps for an input frequency F_{in} of 528 MHz as shown in Fig. 16. Since the in-lock error is generally determined by the PFD and the CP, it is definitely not easy to design such circuits operating at 528 MHz. In fact the in-lock error in the DLL frequency multiplier proposed in (Lee & Hsiao, 2006) is around 3.3 ps which is definitely larger than the required value.

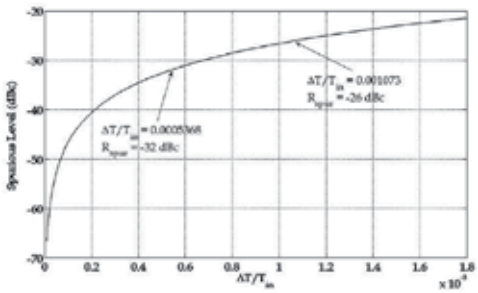

Fig. 16. Plot of the estimated spurious level against normalized in-lock error for N = 33

Reducing the value of F_{in} can ease the design of the PFD and the CP. This comes at the cost of reducing the loop bandwidth of the DLL which is directed constrained by F_{in} and so increasing its settling time. An alternative architecture to the one proposed in (Lee & Hsiao, 2006) would be the one shown in Fig. 17 in which the three signals in each band group are generated concurrently and fast switching between the signals in group is performed via the multiplexer which can guarantee a switching time of less than 9.5 ns even if F_{in} is not equal to 528 MHz.

Note that in this case F_{in} is equal to 264 MHz such that a ÷2 frequency divider at the output is not required. Note that in this case the in-lock error is still 2 ps as can be extracted from Fig. 16 but is definitely much easier to attain with a PFD and a CP operating at 264 MHz rather than 528 MHz. Further reduction of F_{in}, to for instance 132 MHz would require a utilisation of N = 66 thus degrading the spurious level such that the required in-lock error would still need to be less than 2 ps.

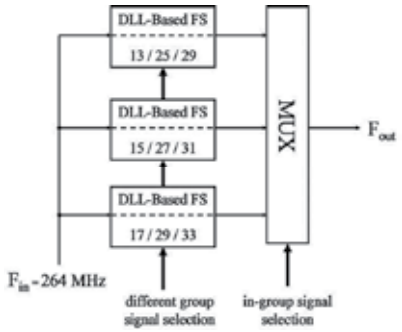

Fig. 17. Proposed DLL-based Frequency Synthesizer for BG 1, BG 3 and BG 6 signals

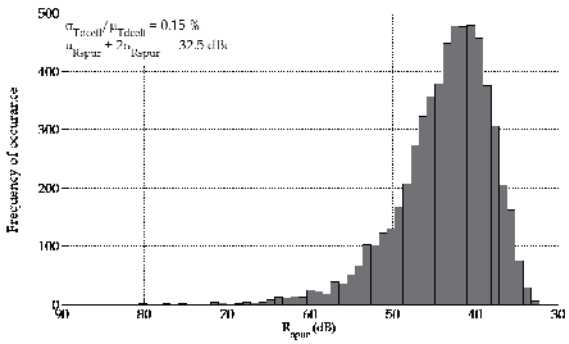

Fig. 18. Plot of the probability density of R_{spur} for an output of 8.712 GHz from a DLL-based FS with N = 33, F_{in} = 264 MHz and $\sigma_{Tdcell} / \mu_{Tdcell}$ = 0.15%

In addition to the in-lock error, in an edge-combining DLL-based frequency synthesizer the delay mismatch also degrades the spur level: assuming a perfectly locked DLL the variation of the delay cell T_{dcell} must be less than 90 fs for F_{in} = 264 MHz (0.15%) to guarantee that $\mu_{Rspur} + 2\sigma_{Rspur}$ < -32 dBc as estimated using the analytic tool described in Section 3.3 (refer to Fig. 18), where μ_{Rspur} is the mean and σ_{Rspur} is the standard deviation of R_{spur}. Reduction of the delay cell variation via transistor sizing as presented in (Casha et al., 2009b) is generally limited to about 0.85% due to area considerations. Making use of a recirculating DLL surely will complicate the design of the DLL due to the additional circuitry required (Gierkink, 2008). Based on these considerations, a study on an UWB MBOA frequency synthesizer based on a direct digital synthesizer was made due to the short comings of the DLL approach especially for generating the high frequencies in the UWB MBOA spectrum.

4. CMOS Direct Digital Synthesizer for UWB MBOA

4.1 Concept of the Direct Digital Synthesizer (DDS)

Direct digital synthesis (DDS) provides a lot of interesting features for frequency synthesis. It provides a fine frequency resolution suitable for state of the art digital communication systems. Moreover, a digital architecture makes the DDS highly configurable and allows fast settling time and fast frequency hopping performance. A conventional DDS consists of a clocked phase accumulator, a phase to amplitude ROM, and a digital to analogue converter (DAC) (Vankka, 2005). Depending on the slope of the phase accumulator, an output signal of a

particular frequency is generated via the look-up table stored in the ROM and the DAC. DDS generates spurious tones due to a phase to amplitude truncation. Increasing the resolution of the ROM and the phase accumulator decreases the spurious level while on the other hand increases the power dissipation and the ROM access time. Solutions have been proposed to compress ROM capacity (Vankka (2005),Nicholas & Samueli (1991)).

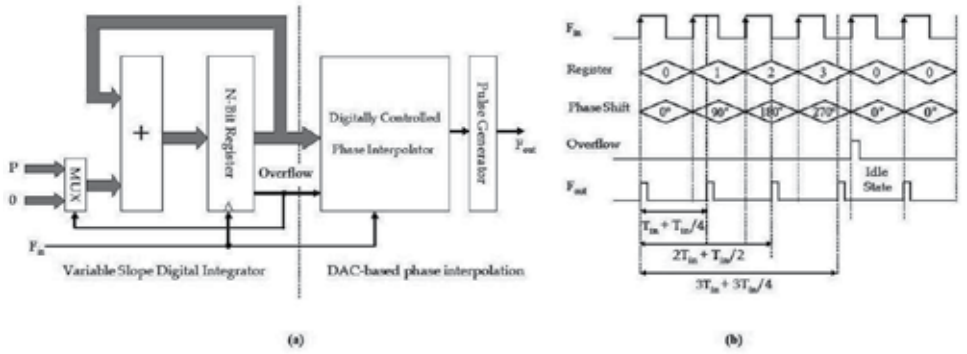

Fig. 19. (a) Block diagram of a DDS (b) Concept of a 2-bit DDS with P = 1

The DDS considered here is known as a phase-interpolation DDS (Badets & Belot (2003), Nosaka et al. (2001), Chen & Chiang (2004)) which consists of an N-bit variable slope digital integrator (adder and register), a 2-to-1 multiplexer (MUX), a digitally controlled phase interpolator (PI) and a pulse generator. In this type of DDS no ROM is used. Its block diagram representation is shown in Fig. 19(a) whilst the concept of a 2-bit DDS is depicted in Fig. 19(b) to facilitate the explanation of the fundamental principle. On the arrival of every rising edge from the input signal F_{in}, the output of N-bit digital integrator increments according to the assigned input control word P, such to control the digitally controlled phase interpolator to generate a pulse via the pulse generator. Ideally this pulse lags the rising edge of F_{in} by an angle of $2\pi\frac{R}{2^N}$ radians, where N is the resolution of the digital integrator and R is the instantaneous value of the register. Whenever an overflow occurs in the digital integrator, the process is stopped for one cycle of the input signal, by changing the input control word value from P to 0 and no pulse is generated.

$$F_{out} = \frac{2^N}{2^N + P} F_{in} \quad where\, 1 \leq P \leq 2^N - 1 \tag{10}$$

Through such mechanism, an output signal F_{out} with a frequency given by Equation 10 is generated. Equation 10 can be intuitively proven by noting that the process of the DDS is repeated every $2^N + P$ input clock cycles, during which 2^N pulses are generated at the output. In Section 4.2 a formal proof of Equation 10 is presented. Such a concept can be used to generate various sub frequencies from a main source without requiring the use of multiple PLLs or analogue mixers. In practice, non-idealities in the phase interpolator cause the generation of spurious tones at the output of the DDS: in Section 4.4.2 these non-idealities are identified and ways how to reduce them are presented.

4.2 Transfer function of the DDS

Similarly to the case of the DLL, the transfer function of the DDS given by Equation 10 can be derived by applying a Fourier analysis on its output. The DDS has a periodicity given by:

$$T_{DDS} = T_{in}(2^N + P) \tag{11}$$

where T_{in} is the periodic time of the input signal, N is the resolution of the DDS and P is the control word. Assuming there is some mechanism in the DDS to generate pulses of a fixed duration and required phase shift from the input signal, it can be shown that the Fourier content of the output is given by:

$$X_{out}(k\omega_{DDS}) = X_p(k\omega_{DDS}) \sum_{n=0}^{2^N-1} e^{jk\omega_{DDS}T_d(n)} \tag{12}$$

where X_p is the Fourier transform of the pulse generated with no offset from the input signal, i.e., the pulse generated when the digital accumulator value is equal to zero, T_d is the delay of the generated pulse and ω_{DDS} is the angular frequency of the DDS. Ideally the phase interpolator has a linear transfer function such that:

$$T_d(n) = (T_{in} + \frac{P}{2^N}T_{in})n = n\frac{T_{DDS}}{2^N} \tag{13}$$

So the Fourier content of the DDS output signal can be written as:

$$X_{out}(k\omega_{DDS}) = X_p(k\omega_{DDS}) \sum_{n=0}^{2^N-1} e^{j\frac{2\pi nk}{2^N}} \tag{14}$$

$$X_{out}(k\omega_{DDS}) = \begin{cases} 2^N X_p(k\omega_{DDS}) & for\ k = 2^N \\ 0 & for\ k \neq 2^N \end{cases} \tag{15}$$

meaning that the output signal will have a frequency which is 2^N times the periodic frequency of the DDS, F_{DDS}:

$$F_{out} = 2^N F_{DDS} = \frac{2^N}{(2^N + P)T_{in}} = \frac{2^N}{(2^N + P)}F_{in} \tag{16}$$

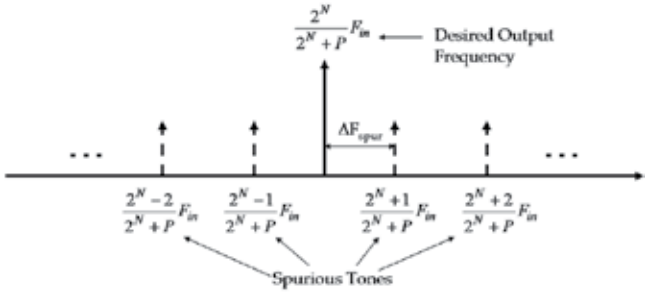

Fig. 20. Position of spurs with respect to the desired output frequency in a practical DDS

In practice the transfer function of the phase interpolator is non-linear such that energy exists in X_{out} even for $k \neq 2N$. This means that the output spectrum will include spurious tones at $k \neq 2N$ separated from each other by Equation 17 as shown in Fig. 20.

$$\Delta F_{spur} = \frac{F_{in}}{2^N + P} \tag{17}$$

4.3 Cascaded DDS

When a high resolution DDS is required, it is often possible to obtain the same function by employing two cascaded low resolution DDS. A cascaded DDS topology, has the advantage of facilitating the design at high frequency operation due to the need of low resolution circuit blocks whilst the compensation of the phase interpolator non-ideality is more feasible. In this case, the positioning of the spurious tones at the output of the cascaded DDS cannot be easily derived as in the previous case. To simplify matters, two cascaded DDS can be represented by the second DDS in the chain being fed by a jittery signal whose frequency and jitter are defined by the first DDS in the cascaded chain. This is represented in Fig. 21(a).

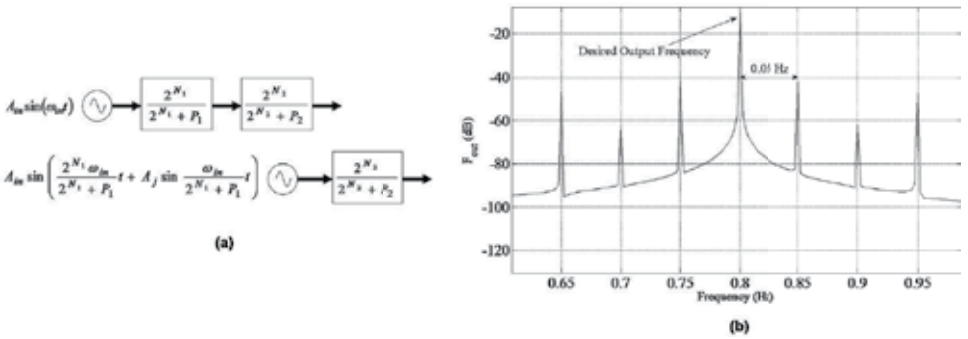

Fig. 21. (a) Alternative representation of a cascaded DDS (b) Demonstration of the positioning of the spurs of a DDS being fed by a jittery signal

If a DDS is injected by a jittery input signal y_{in} represented by:

$$y_{in} = A_i \sin(\omega_i t + A_j \sin \omega_j t) \tag{18}$$

where ω_i is the input frequency and ω_j is the jitter frequency then the output will have spurious tones separated from each other by the inverse of the least common multiple of $1/f_j$ and the periodicity of the DDS, i.e., $(2^N + P)T_i$. A high level model of a DDS being fed by a jittery signal was implemented in MATLAB to verify this result. Consider an example with T_i = 1 s, $\frac{\omega_j}{2\pi}$ = 0.25 Hz, N = 2, P = 1 and A_j = 0.2 rad. The least common multiple of 4 s and $(2^2 + 1)$ is 20 s such that the expected spurious tones are separated by 0.05 Hz. The simulation results confirm this as shown in Fig. 21(b). Now applying the above theory to the cascaded DDS topology presented in Fig. 21(a) one can derive an expression describing the positioning of the spurious tones in a cascaded DDS. In this case $T_i = (2^{N_1} + P_1)T_{in}/2^{N_1}$, $\omega_j = \omega_{in}/(2^{N_1} + P_1)$, $N = N_2$ and $P = P_2$, such that the output will have spurious tones separated from each other by the inverse of the least common multiple of $(2^{N_1} + P_1)T_{in}$ and the periodicity of the second stage $(2^{N_2} + P_2)(2^{N_1} + P_1)T_{in}/2^{N_1}$. Since the latter is the least common integer multiple of both terms then, for a cascaded DDS topology the spurious tones at the output are located at:

$$F_{spur} = \frac{kF_{in}2^{N_1}}{(2^{N_1} + P_1)(2^{N_2} + P_2)} + F_c \tag{19}$$

where F_c is the expected cascaded DDS output frequency and k is an integer number.

4.4 DDS-based frequency synthesizer

4.4.1 Architecture

The proposed architecture for the DDS-based frequency synthesizer is presented in Fig. 22. As a proof of concept, the generation of the carrier signals in the sixth band group (BG 6) of the UWB MBOA spectrum is considered. Since the frequency of the UWB MBOA signals is a multiple of half the bandwidth (264 MHz) it is possible to generate the signals from a reference[1] based on such frequency. For instance, the output signals in BG 6 are related to the crystal frequency by:

44 MHz x 6 x **29** = 264 MHz x **29** = 7.656 GHz
44 MHz x 6 x **31** = 264 MHz x **31** = 8.184 GHz
44 MHz x 6 x **33** = 264 MHz x **33** = 8.712 GHz

Let us consider the synthesis of the 7.656 GHz signal and see how the architecture in Fig. 22 can generate it:

$$44MHz \times \frac{6 \times 29 \times 31 \times 33}{8 \times 128} \times \frac{1}{4} \times \frac{2^5}{2^5+1} \times \frac{2^4}{2^4+15} \times 8 = 7.656GHz \tag{20}$$

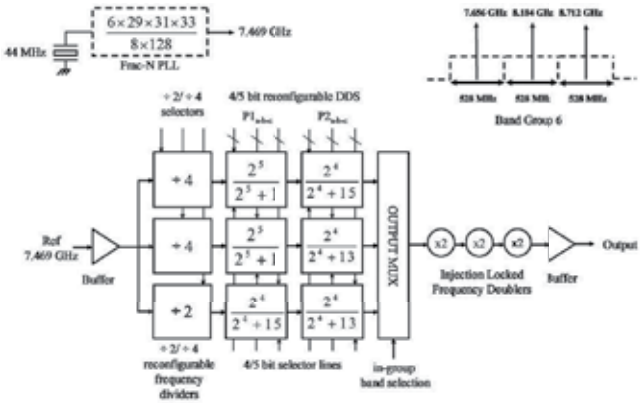

Fig. 22. Architecture of the DDS-based frequency synthesizer: a particular configuration of the architecture which generates the required signals in BG6 of the UWB MBOA spectrum is shown

The concept is to generate a reference frequency which is a multiple of 29x31x33 by means of a PLL and then the 31x33 factor is effectively divided using the DDS structure in order to generate the 7.656 GHz frequency. The other BG 6 frequencies are generated in a similar way and concurrently with this one, without having to switch the frequency of the PLL or requiring multiple PLLs. Note that a 128 divisor in the PLL feedback ratio together with the fixed frequency dividers are required to cancel the frequency multiplication effect of the DDS transfer function (refer to Equation 20).

A cascaded DDS topology rather than a single one is chosen, because as explained in Section 4.3, the design of low resolution circuit blocks is easier considering the operation in the gigahertz range and in addition the non ideality compensation is facilitated. Since in this feed forward architecture, the three group signals are generated concurrently, it is possible to hop from one frequency to another via multiplexing in an extremely short time (Alioto & Palumbo,

[1] Implementation of high frequency Fractional-N PLLs is possible in submicron technologies such as 90nm and 65nm CMOS as demonstrated in (Ravi et al., 2004).

2005). In addition, this architecture does not violate the phase coherency property, which is a requirement of UWB MBOA frequency synthesizer (Batra et al., 2004a)[2]. The use of injection locked frequency doublers (ILFD) permits the reduction of the DDS input frequency at the cost of increasing the phase noise and spurious level gain in the synthesis path. This implies that a careful design of the stages preceding the ILFD is fundamental, in order to limit their phase noise and spurious level. A possible implementation of the ILFD is via injection-locked ring oscillators which do not make use of integrated inductors thus limiting the utilised silicon area (Badets et al., 2008).
Note that the signals in the other band groups can be generated by reconfiguring the resolution of the DDS blocks and changing their P input, selecting between divide by-2 and divide-by-4 frequency dividers in each path whilst changing the multiplication ratio of the PLL accordingly. Note that the frequency hopping time from one band group to another is not very demanding as in the case of the in-group frequency hoping (it is in the order of milliseconds) making such an implementation a practical solution.

4.4.2 Spurious tones

The main sources of spurious tones in this architecture are the fractional-N reference PLL and the DDS stages. It is imperative to reduce the spurs from the fractional-N PLL because they will be increased and synthesized by passing through the chains of non-linear sub-blocks in the system such as the cascaded DDS. Since this issue is already well discussed in literature (Ravi et al. (2004), Kozak & Kale (2003)), this work focuses on the mechanisms in the DDS stages leading to spurious tone generation and ways how to reduce them. The major spur contributor in a DDS stage is the PI (Seong, 2006). A typically used PI, based on the Gilbert's multiplier cell is shown in Fig. 23.

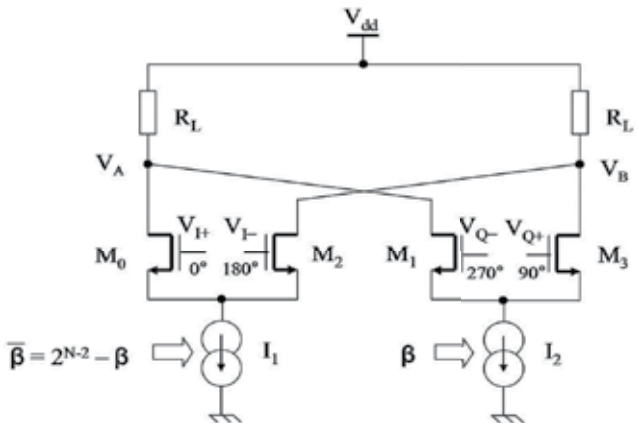

Fig. 23. PI based on a Gilbert's cell multiplier topology. Two such PI can be combined together to cover the four phase quadrants ($0° < \Theta < 360°$)

It consists of two complementary variable current bias circuits, implemented as DACs I_1 and I_2 which are controlled by a thermometer coded control word β, two differential pairs driven by quadrature input signals, and two loads for each output node. Assuming perfectly

[2] When the output in an UWB MBOA FS is hopping between the three possible frequencies in a particular band group, it should always continue from the phase as if that frequency signal was never stopped.

matched differential pairs it can be shown that the signal at the output node V_B lags the V_{I+} input by:

$$\Theta = -\arctan(\frac{I_2}{I_1})^{\frac{1}{\eta}} \tag{21}$$

where $I = I_1 + I_2$ is twice the constant current flowing through the load R_L and $\eta = 1$ for large signal operation and $1 \leq \eta \leq 2$ for small signal operation. As shown in Section 4.2, for the DDS output to be free of spurious tones it is important that the phase transfer function of the phase interpolator is linear. The transfer function of the phase interpolator can be linearised by introducing systematic non-linearity in the current steering DACs. Considering DAC I_2, the amount of non linearity required to linearise the phase transfer function is given by:

$$\frac{I_m}{I_2} = (\frac{A^\eta}{1+A^\eta} \times \frac{2^{N-2}}{\beta} - 1) \times 100\% \quad where\ A = tan(\frac{\beta\pi}{2^{N-1}}) \tag{22}$$

where N is the DDS resolution, β is the DAC control word and I_m / I_2 is the percentage change required in I_2 for a particular β value. Note that for β = 0, 2^{N-3} and 2^{N-2}, no compensation is required. A similar process is applied to DAC I_1, in this case a change opposite in sign to that applied to I_2. In practice since the non-linearity in the DACs is usually implemented via the sizing of the transistors (Seong, 2006), it is not possible to exactly linearise the transfer function as implied by Equation 22. In fact as a good layout practice, which is important to limit the spurious tone energy due to DAC transistor mismatches, the transistors need to be based on unit size transistor cells. Due to this discretisation in the transistor sizing, the non-linear compensation as defined by Equation 22 cannot be exactly applied. Note also that a quadrature error in the input signals or a mismatch in input transistors increases the non-linearity in the phase transfer function which degrades the spurious level and makes compensation more difficult too. In this architecture since the quadrature signals are derived from the divide-by-2 or divide-by-4 frequency dividers, the signal quadrature error can be kept quite low.

4.4.3 System level simulation

A system level model of the frequency synthesizer architecture was implemented using MATLAB, to estimate its integrated spurious level, R_{spur}, over a particular band (528 MHz). A block diagram representation is shown in Fig. 24. This model assumes that the reference frequency generated by the fractional-N PLL is free of spurious tones and that the architecture consists of two cascaded DDS stages and a spurious tone gain stage of around 18 dB which models the spurious level degradation due to the frequency multiplication effect of the ILFD. The PI is modelled by the equations shown in Fig. 24. Since the PI of Fig. 23 can deliver phase shifts in only one quadrant $[0^\circ, 90^\circ]$, the other quadrants are generated by having multiple PIs. This is modelled by parameter λ, assuming that the PIs are identical. Both the non-linearity of the phase transfer function and the variation of the current states (I_1 or I_2) in the biasing DACs due to transistor mismatches are considered. Note that each current state variation is modelled by a standard normal distribution, X, with a mean zero and a standard deviation σ, whose value is dependent on the current state[3]. Note that the pulse generator provides a pulse of fixed duration on every rising edge of the PI signal. Using this model an estimate for spur magnitude R_{spur} for the signals in BG 6 was obtained for both an uncompensated PI (UPI)

[3] The standard deviation of the current states $\sigma = \sqrt{\beta} \times \sigma_{LSB}$, where σ_{LSB} is the standard deviation of the least significant bit value.

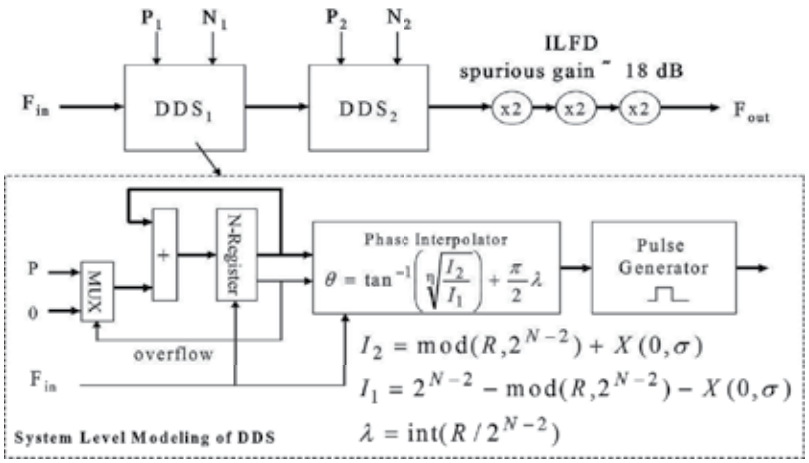

Fig. 24. System level model of the cascaded DDS topology implemented using MATLAB to estimate the spurious tone energy at the output of the proposed frequency synthesizer, where R is the value of N-bit register and λ is the quadrant number

and a compensated PI (CPI). The simulation results are given in Table 1. Note that, in this case, no variation in the possible DAC current values was assumed ($\sigma = 0$). These estimations show that by adequate non-linearity compensation the proposed architecture can generate outputs which meet the spurious level specifications of UWB MBOA. Table 1 presents also the separation of the spurious tones and the number of them captured in a given band confirming the prediction given by Equation 19.

F_{out} (GHz)	F_{in} (GHz)	R_{spur} (dBc) UPI	R_{spur} (dBc) CPI	Spur Separation MHz	No. of in-band spurs
7.656	1.91225	-25	-47	60	8
8.184	1.91225	-19	-44	64	8
8.712	3.82450	-42	-62	68	6

Table 1. Integrated R_{spur} over a 528 MHz band for BG 6 signals

The compensation values for the two cascaded DDS were estimated using Equation 22 with η = 1.35. These values were slightly rounded off to permit physical implementation via transistor sizing as follows:

4-bit DDS: β=1: I_{LBS}(1-0.065) β=3: I_{LBS}(3+0.065)

5-bit DDS: β=1: I_{LBS}(1-0.16) β=2: I_{LBS}(2-0.16)
β=3: I_{LBS}(3-0.08) β=5: I_{LBS}(5+0.08)
β=6: I_{LBS}(6+0.16) β=7: I_{LBS}(7+0.16)

Fig. 25 shows a plot of the frequency content at the input of the three ILFD for both the uncompensated (red plot) and the compensated case (black plot) of the 8.712 GHz signal generation path. This plot shows substantial reduction of the magnitude of the spurious tones in both the 528 MHz band of interest (blue plot) and the adjacent bands.

Another simulation was done this time considering a mismatch in the current states of the DACs in a CPI. Table 2 presents the results of this Montecarlo simulation for the three signals

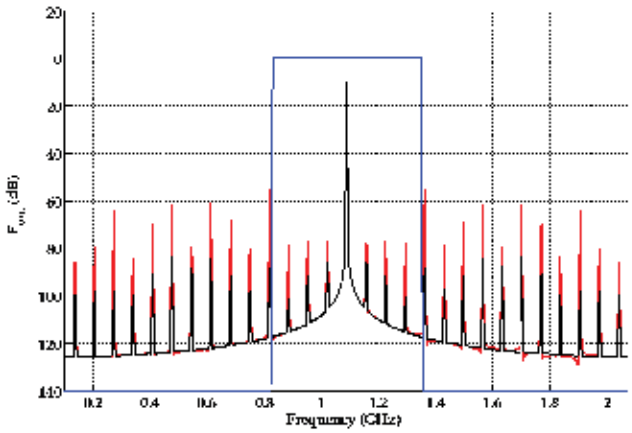

Fig. 25. Frequency spectrum of the output of the cascaded DDS for the 8.712 GHz signal generation path: (a) UPI in red (b) CPI in black (c) Band of interest in blue

in BG 6 over a sample of 300 DDS with σ_{LSB} = 1% in the current steering DACs. This is the maximum permissible DAC variation such that $\mu_{Rspur} + 2\sigma_{Rspur} < -32$ dBc for the three signal generation paths, where μ_{Rspur} is the mean and σ_{Rspur} is the standard deviation of R_{spur}. Note that in the three cases μ_{Rspur} is higher than that given in Table 1 due to mismatch in the current states of the DACs. Mismatch compensation of the DACs can be performed to achieve mismatch levels as low as 1% as proposed in (Gagnon & MacEachern, 2008). Dynamic element matching techniques can also be applied in the DAC design to reduce the effects of mismatch (Henrik, 1998). Fig. 26 presents the results of the simulation for F_{out} = 7.656 GHz and σ_{LSB} = 1%.

F_{out} (GHz)	μ_{Rspur} (dBc)	σ_{Rspur} (dBc)	*Maximum* R_{spur} (dBc)	*Minimum* R_{spur} (dBc)	$\mu_{Rspur}+2\sigma_{Rspur}$ (dBc)
7.656	-42.58	5.58	-32.03	-59.35	-32.04
8.184	-37.81	1.73	-32.16	-43.24	-34.36
8.712	-57.28	3.31	-47.52	-62.79	-50.68

Table 2. Statistical simulation data of the variation of R_{spur} for a DAC variation of 1% over a sample of 300 cascaded DDS-based frequency synthesizers

These simulations indicate the importance of both linearising the phase transfer function of the PI and reducing the variations of the DACs due to mismatches by good layout techniques and adequate compensation (Gagnon & MacEachern, 2008). Note also that if it would be possible to design a DDS which can be driven at higher frequencies than those proposed here, the number of ILFD can be limited thus resulting in further reduction of the spurious level at the output. In addition a higher F_{in} implies also a larger separation between the spurs as predicted by Equation 19, such that less spurs are captured in a given band although these may still act as interferes to devices using the UWB MBOA on an adjacent band.

4.5 Design and simulation of circuit blocks

The critical blocks of this DDS, namely the digital accumulator, phase interpolator and the pulse generator were designed in a 1.2 V 65-nm CMOS process. For the generation of BG 6

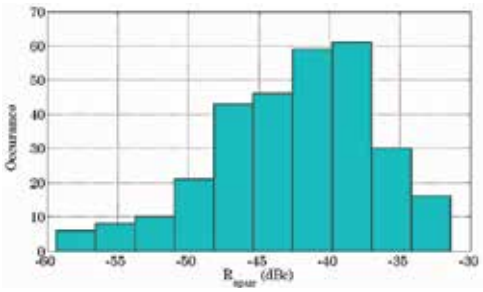

Fig. 26. Plot of the probability density of R_{spur} for an output of 7.656 GHz from a DDS-based FS with compensated phase interpolator having current steering DACs with σ_{LSB} = 1%

signals, as shown in Fig. 22 the DDS stage being driven by the divide-by-2 frequency divider is operating at the highest input frequency (around 4 GHz). Therefore the functionality of the designed DDS building blocks as well as their impact on the FS performance was verified via simulation at this frequency of operation.

4.5.1 Digital accumulator

The pipelined digital integrator considered in this study is shown in Fig. 27(a). The digital integrator has the special feature to stop the integration process for one cycle after the occurrence of an overflow. Due to the pipelining nature, this feature could not be implemented by simply setting the P control word to zero, as shown in Fig. 19.

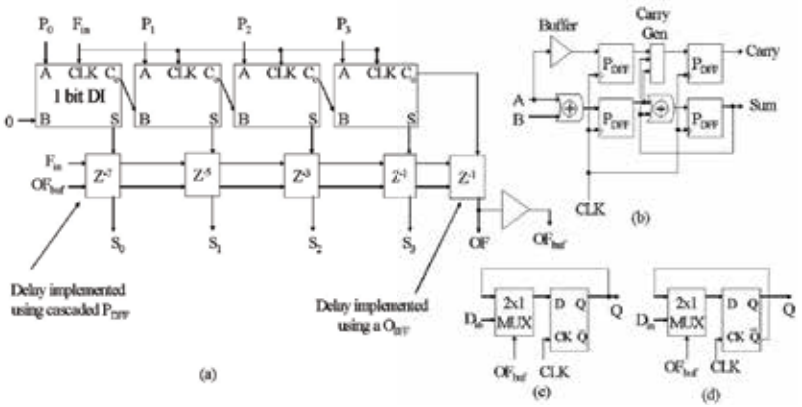

Fig. 27. (a) Block diagram of the 4-bit pipelined digital integrator (b) 1 bit integrator (DI) (c) Pipeline DFF (P_{DFF}) (d) Overflow DFF (O_{DFF})

In fact this could be only done by retaining the same state of the D-flip flops (DFFs) for one cycle. This requires the implementation of a special type of DFF shown in Fig. 27(c) which includes a 2-to-1 multiplexer (MUX) at its input being controlled by the integrator overflow signal: on the arrival of a clock transition this DFF can either store the value of D_{in} or hold the previously stored value. In order to enable the integration after one idle cycle, a slightly different DFF implementation is required for the overflow signal and is shown in Fig. 27(d): in this case on the arrival of a clock transition, the DFF can either store the value of D_{in} or store the compliment of the previously stored value. Note that the overflow signal drives the DFFs via a buffer. The DFFs were implemented using true-single phase clocking logic which allows

high operating frequencies with lower power consumption than other techniques (Yuan & Svensson, 1989). Fig. 28 shows a transient plot of the output (S_{3-0}) and overflow (OF) signals of the digital integrator with P = 15, being fed by a 4 GHz input frequency. The current demand at typical process parameter corners, a temperature of 27 $^{\circ}C$ and a 1.2 V supply voltage is 1.43 mA. The digital integrator can be operated at a maximum frequency of 4.5 GHz under a slow corner condition at 105 $^{\circ}C$ with a supply voltage of 1.08 V.

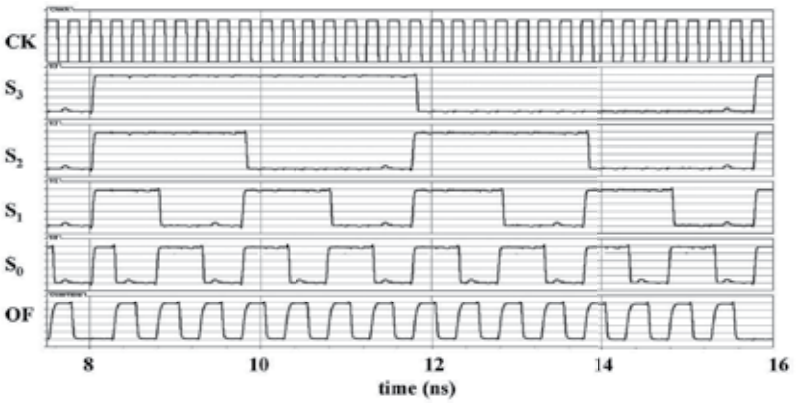

Fig. 28. Transient plot of the 4-bit digital integrator for P=15 at an input frequency of 4 GHz

4.5.2 DDS controller

Fig. 29 shows the block diagram of a practical 4-bit DDS implementation. Since the differential Gilbert cell based phase shifter is able to provide a phase shift in the range [0°, 90°] and [180°, 270°] two such phase shifters are used in conjunction with a 4-to-1 current mode logic (CML) multiplexer (Alioto & Palumbo, 2005) in order cover the four phase quadrants.

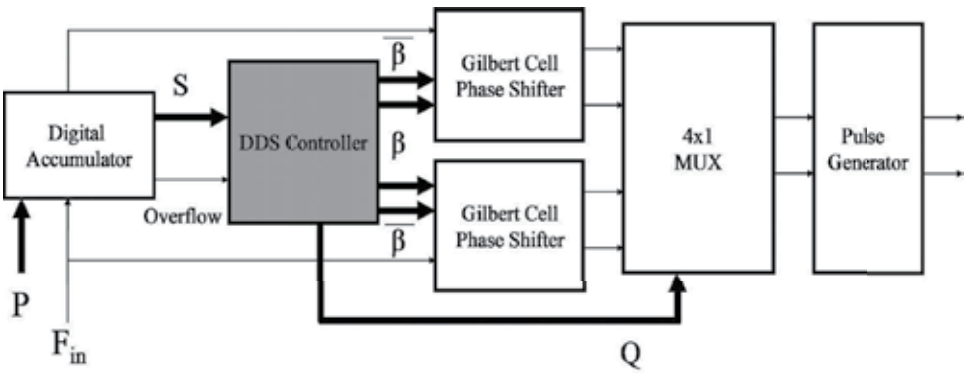

Fig. 29. Block diagram of a practical 4-bit DDS

The DDS controller has thus a two-fold task: according to the input word generated by the digital accumulator S, the DDS controller must issue a control word Q, to select the required phase quadrant via the 4-to-1 multiplexer and another two complementary control words β and $\bar{\beta}$ to generate the required phase shift via the Gilbert cell based phase shifters. Note that since the implemented phase shifter is based on thermometer coded DACs (see Section 4.5.3), the DDS controller includes an encoder to translate the control words in the required format.

4.5.3 Phase interpolator

As explained above, the phase interpolator was implemented using two phase shifters shown in Fig. 23 together with a 4-to-1 CML multiplexer (Alioto & Palumbo, 2005) to cover the four phase quadrants (Fig. 29). In order to minimise the level spurious tones, the critical section of the phase interpolator is the non-linear compensation of the current steering DACs I_1 and I_2.

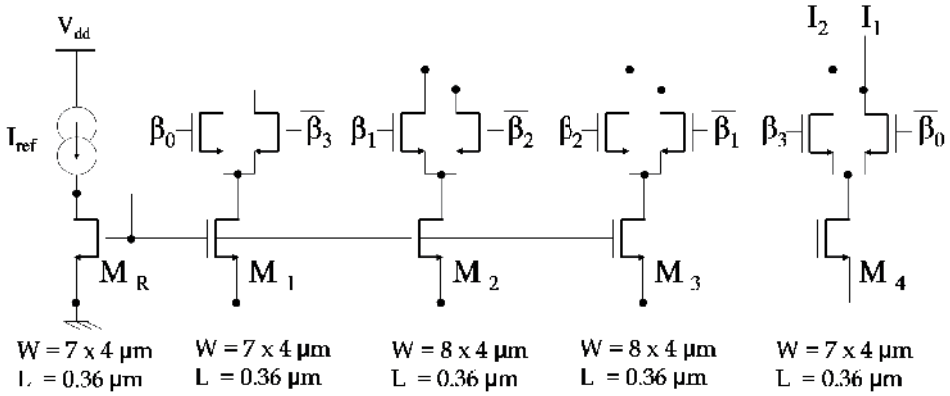

Fig. 30. Differential thermometer decoded DAC with non-linear compensated transistors

The current steering in the PI cell is achieved via 5-state differential thermometer coded DACs, shown in Fig. 30. This DAC design permits the operation at high frequencies since the current sources are never switched off and in addition two complementary DACs are implemented in a single one, thus reducing silicon area. Due to the thermometer nature, the required non-linearity in the DACs is easily introduced by non-uniform sizing of the transistors (M_{1-4}). Table 3 shows how non-uniform sizing of the M_{1-4} can be applied. It can be easily seen that this is the compensation discussed in Section 4.4.2 for a four bit DDS.

	M1	*M2*	*M3*	*M4*
Uncompensated W/L	X	X	X	X
Compensated W/L	X - ΔX	X + ΔX	X + ΔX	X - ΔX

Table 3. Non-uniform sizing of transistors in current steering DACs

Using Equation 22 the compensation required for a four bit DDS was estimated to be $\Delta = 0.065$. It is important to note that the aspect ratio of all transistors must be composed of an integer number of common unit cells to permit interdigitation in the layout. This is essential to limit mismatch between the transistors and thus limiting mismatch in the DACs which also incur degradation in the spurious tones at the output of the DDS. This implies that $\Delta = \frac{n_1}{n_2}$ must be a rational fractional with n_1 and n_2 being either both odd integers or both even integers. In this case the closest integers to 0.065 are $n_1 = 1$ and $n_2 = 15$ such that $\Delta = 0.067$. Taking the uncompensated transistor gate channel width to be 30 μm, the sizes of the DAC transistors shown in Fig. 30 were determined, with 4 μm being the gate width of the common unit cell. Table 4 shows the difference between the theoretical (given by Equation 21) and the practical compensated phase shift response of the PI cell of Fig. 30 for the 5 current state positions. At an input frequency of 4 GHz a constant 25° phase shift is noted due to the finite bandwidth of the PI cell. This does not affect the functionality of the DDS since it is almost uniform at each current state position. As regards the power consumption, post layout simulations

$\beta_3\beta_2\beta_1\beta_0$	$I_1(mA)$	$I_2(mA)$	*Theoretical Phase*(°)	*Actual Phase* 1 GHz(°)	*Actual Phase* 4 GHz(°)
1111	1.69e-5	2.71	-89.99	-89.95	-114.95
0111	0.641	2.14	-67.76	-67.23	-92.23
0011	1.41	1.41	-45.00	-44.87	-69.87
0001	2.14	0.641	-22.24	-21.39	-46.39
0000	2.72	8.20e-5	-0.03	-4.46e-2	-25.05

Table 4. Theoretical and practical compensated phase shift response of the PI cell

indicate that the PI cell demands 2.78 mA whilst the 4-to-1 MUX demands 2.86 mA at 27°C. Fig. 31 shows a plot of the relative spur content of the compensated phase interpolator output for both the transistor level simulations and the MATLAB high level model simulations for different values of P in which an input frequency of 4 GHz was considered.

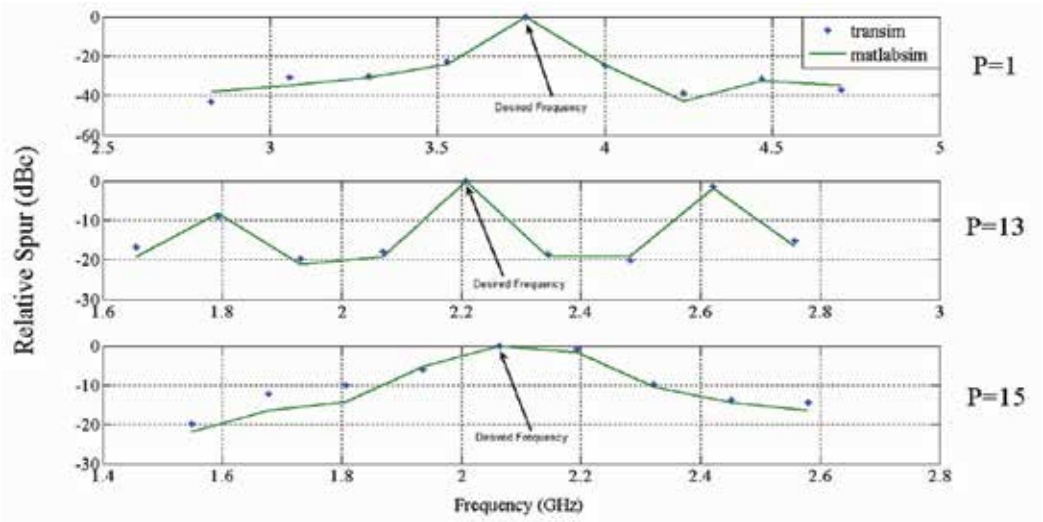

Fig. 31. Relative spur levels at the output of phase interpolator

As can be noted from Fig. 31, the simulation results match the predicted results. In addition one can note that the relative spur levels at the output of the PI are high for the given application. In fact this is caused due to the number of discontinuities in the output waveform which "hide" the phase shift information. The important information in the output signal of the phase interpolator is the phase shift from the input signal. This can be extracted via a technique in which a square wave pulse signal is generated (see Fig. 32(a)). The rising edges of this square wave signal are used to trigger pulses of fixed duration via a one-shot multivibrator discussed in Section 4.5.4. For clarity, Fig. 32(b) shows the principle of this technique for a 2-bit DDS. Note that the discontinuities in the output of the PI are highlighted. Fig. 33 shows a comparison between the frequency spectrum of the output of the phase interpolator and the output of the pulse generator of a 4-bit DDS with P = 15 obtained via MATLAB simulations. It shows the effectiveness of the algorithm to eliminate spurs due to discontinuities in the output of the phase interpolator. Note that the PI is compensated accordingly to have a linear transfer function.

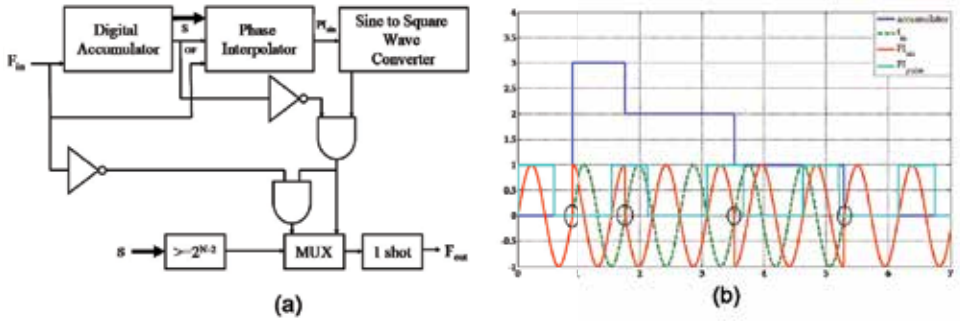

Fig. 32. (a) Block diagram of the technique to extract phase information (b) Concept of the technique for a 2-bit DDS with P=3

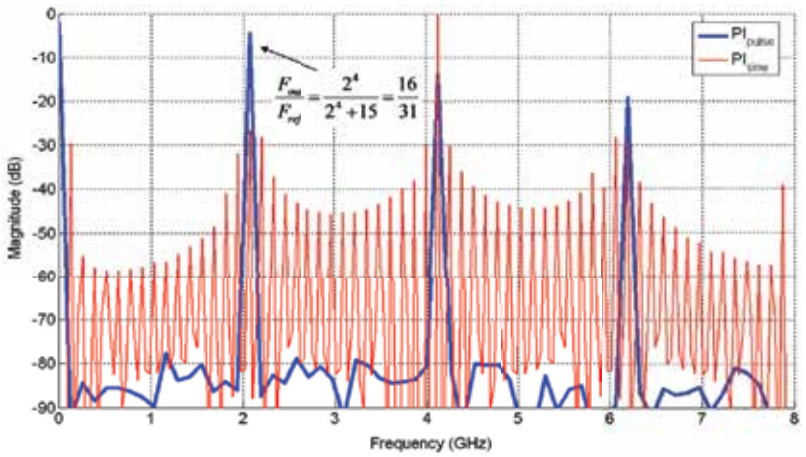

Fig. 33. Comparison between the frequency spectrum of PI and the Pulse Generator

4.5.4 Pulse generator

Fig. 34(a) shows the circuit diagram of the pulse generator used to generate a pulse signal of constant pulse-width at every rising edge of the signal generated by the wave shaping circuit. It is based on the one-shot multivibrator circuit proposed in (Lockwoodm, 1976) with the difference that it is based on CMOS inverters rather than NMOS inverters to limit the power consumption and includes buffering at both the input and the output stages. To permit reliable operation of the one-shot multivibrator at high frequencies, the implementation does not include any regenerative feedback mechanisms. This was possible since the pulse width required can be made to be smaller than the pulse width of the incoming signal.

Fig. 34(b) presents the transient response of the pulse generator for an applied pulse signal of around 2 GHz generating a pulse of 70 ps whilst demanding an average current of 273 μA. When the input signal V_{in} increases, node voltage V_a follows it, since it is a buffered version of V_{in}. As a consequence since the voltage on capacitor C cannot change instantaneously, node voltage V_b increases too making the output go high. The capacitor starts charging up via transistors M_4 and M_3, where the latter acts as a current source. Since V_a is fixed at around 1.2 V, V_b starts going down to permit the capacitor to charge up. When V_b goes below the

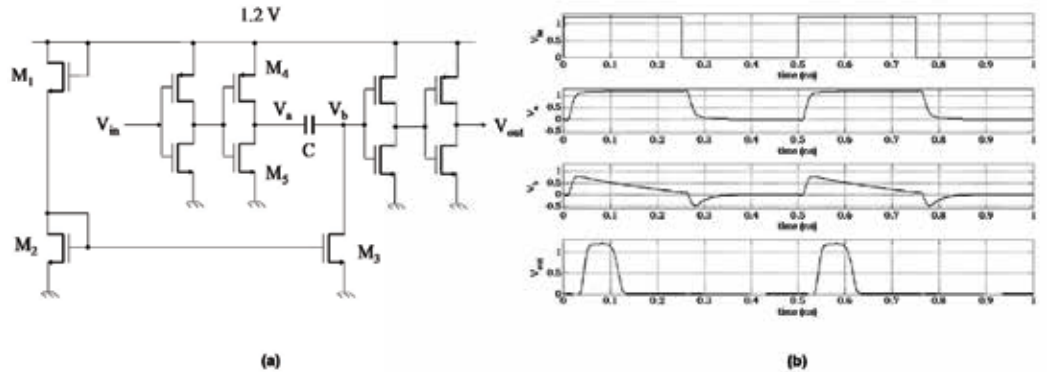

Fig. 34. (a) Feed forward CMOS one-shot multivibrator (b) Transient response of the pulse generator for an input frequency of 2 GHz

threshold of the output buffer the output goes low again. The pulse duration thus depends on the size of the capacitor and the current mirrored in M_3.

4.5.5 Performance summary

The sections above presented the design and simulation of the main circuit blocks used in a DDS to be driven by an input frequency of around 4 GHz. Table 5 presents a summary of the current demand of these circuit blocks. Note that the DDS used to generate the 8.712 GHz signal in BG 6 was chosen to study the maximum current demand in the frequency synthesizer architecture. The other DDS in the frequency synthesizer architecture presented in Fig. 22 can be designed with a lower current demand whilst achieving the same transient performance since they are driven at a lower input frequency.

Block Description	*Current Demand*
4-bit digital accumulator	1.43 mA
Gilbert Cell Based Phase Shifters	2.78 mA (x2)
4x1 CML Multiplexer	2.86 mA
Pulse Generator	273 μA

Table 5. Summary of the current demand of the main DDS circuit blocks

Simulation results show that a 4-bit DDS designed around the presented digital integrator (at P = 15) and the 4-quadrant PI, has an integrated output spurious level of approximately of -60 dBc over a 528 MHz band. The frequency content of the PI output and the pulse generator output of the DDS are shown in Fig. 35.

Since the ILFD degrades the spurious level by 18 dB, assuming the second cascaded DDS has similar characteristics as the first DDS stage, an integrated spurious level of approximately -42 dBc can be estimated at the output for the 8.712 GHz signal. The difference between the practical simulations shown in Fig. 35 and the system level simulations comes from the jitter limitations in the practical phase extraction technique, the one shot pulse generator (Lockwoodm, 1976) and from second order effects such as the channel length modulation of the DAC transistors which introduce additional and unaccounted-for non-linearities in the phase interpolator transfer function. The estimated spur level is still within the specifications of the UWB MBOA.

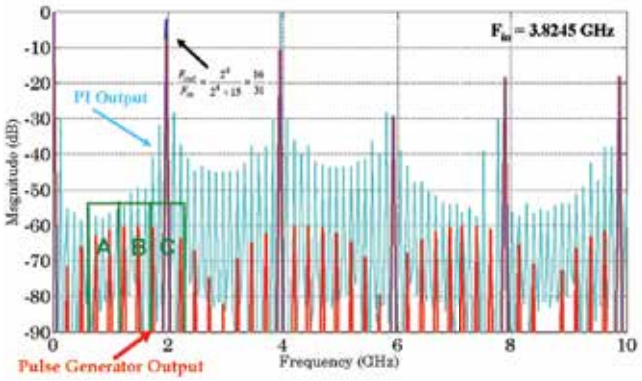

Fig. 35. Frequency content of the PI output and the pulse generator output of the DDS

5. Conclusion

The first part of this chapter discussed and compared the current state of the art in frequency synthesis for UWB MBOA applications; in particular frequency synthesizers based on single side band frequency mixing were tackled. In the second part, the chapter presented a study on novel frequency synthesis architectures proposed as low silicon area alternatives to state of the art solutions: one is based on DLLs whilst the other is based on the phase-interpolation DDS. In particular, an investigation of the spurious tones in such architectures was presented and ways how to reduce them are discussed. These architectures can enable the reduction of the required silicon area by limiting the number of required PLLs and the removal of analogue mixers from the architectures.

Based on this study, conclusions can be drawn indicating the advantages and disadvantages of each architecture. The main advantage of the DDS-based FS is that being a feed-forward architecture, the design does not have to take care of stability issues in the three respective signal generation paths, as in the case of the DLL based FS. This is an important issue especially during reconfiguration of the system to generate signals of different frequencies in the various bands. The DDS architecture can be seen as a more modular architecture since the main synthesizing block is the same in the three respective signal generation paths. The DLL-based FS requires an input reference which is much lower than that of the other architecture, thus facilitating its generation. In addition, the DLL-based FS does not make use of ILFD as in the DDS-based FS, which degrade both the phase noise and spurious tone level at the output of the synthesizer. The number of utilised ILFD can be reduced if the DDS can be operated at a high input frequency.

Although the DDS architecture generates more spurs in a given band than the DLL architecture, they are small in magnitude especially those in the vicinity of the desired output frequency. In the DLL architecture the spurs adjacent to the required output signal contain the highest amount of energy and are therefore more prone to have a degrading effect on the integrated spurious level in the chosen band of operation as well as adjacent bands. The analyses have shown that spur compensation in the DLL via in-lock error and delay stage mismatch minimisation are generally much more difficult than spur compensation in the DDS architecture. This is particular true when the DLL is used to generate high frequency signals such as those in BG 6 which require a loop in lock error of less than 2 ps and a mismatch in the delay cell of less than 80 fs for an input frequency of 264 MHz. To eliminate the

problems associated with delay mismatches one needs to use a recirculating type DLL at the expense of a more complex feedback loop design. Spurious tones minimisation via non-linear phase interpolator compensation and mismatch compensation in the DACs is facilitated in the DDS architecture since low resolution cascaded DDS are used. In light of spurious tone minimisation, the layout of the main synthesizing blocks can prove to be easier for the DDS than for the DLL.

6. References

Alioto M. & Palumbo G. (2005). *Model and design of Bipolar and MOS current-mode logic: CML, ECL and SCL digital circuits*, Kluwer Academic Publishers - Springer, ISBN: 1402028784.

Badets, F. & Belot D. (2003). A 100 MHz DDS with synchronous oscillator-based phase interpolator, *International Solid-State Circuits Conference (ISSCC)*, pp. 410-503, February 2003.

Badets, F. et al. (2008). Injection Locked CMOS Buffer Dedicated to NanoMagnetic Based Voltage Controlled Oscillator, *Proceedings of the ICECS 2008*, pp. 190-193, Malta, August 2008, St. Julian's.

Batra, A. et al. (2004a). *Multi-Band OFDM Physical Layer Proposal for IEEE 802.15 Task Group 3a*, Multi-Band OFDM Alliance SIG.

Batra, A. et al. (2004b). Design of a multiband OFDM system for realistic UWB channel environments, *IEEE Transactions on Microwave Theory and Technology*, Vol., 52, September 2004, pp. 2123-2138, ISSN: 0018-9480.

Casha, O.; Grech, I. & Badets, F. (2009a). CMOS Phase-Interpolation DDS for an UWB MB-OFDM Alliance Application, *Proceedings of the 5th PRIME Conference*, pp. 200-203, Ireland, July 2009, Cork.

Casha, O. et al. (2009b). Analysis of the Spur Characteristics of Edge Combining DLL-based Frequency Multipliers, *IEEE Transactions on Circuits and Systems-II: Express Briefs*, Vol., 56, February 2009, pp. 132-136, ISSN: 1549-7747.

Chang, J. et al. (2009). A Single-PLL UWB Frequency Synthesizer Using Multiphase Coupled Ring Oscillator and Current-Reused Multiplier, *IEEE Transactions on Circuits and Systems II: Express Briefs*, Vol., 56, February 2009, pp. 107-111, ISSN: 1549-7747.

Chen, H.C. & Chiang, J.S. (2004). A Low-Jitter Phase-Interpolation DDS Using Dual-Slope Integration, *IEICE Electronics Express*, Vol., 1, September 2004, pp. 333-338, ISSN: 1349-2543.

Chien, G. & Gray, P.R. (2000). A 900-MHz Local oscillator using a DLL-based Frequency Multiplier Technique for PCS Applications, *IEEE Journal of Solid-State Circuits*, Vol., 35, December 2000, pp. 1996-1999, ISSN: 0018-9200.

Gagnon, G. & MacEachern, L. (2008). Digital compensation of DAC mismatches in multibit delta-sigma ADCs, *Electronics Letters*, Vol., 44, June 2008, pp. 721-722, ISSN: 0013-5194.

Gierkink, S. (2008). An 800 MHz -122dBc/Hz-at-200kHz clock multiplier based on a combination of PLL and recirculating DLL, *Proc. 2008 IEEE International Solid-State Circuits Conference*, pp. 454-455, ISSN: 0193-6530.

Henrik, T.J. (1998). A Low-Complexity Dynamic Element Matching DAC for Direct Digital Synthesis, *IEEE Transactions on Circuits and Systems-II: Analog and Digital Signal Processing*, Vol., 45, January 1998, pp. 13-27, ISSN: 1057-7130.

Ismail, A. & Abidi, A. (2005a). A 3.1 to 8.2 GHz direct conversion receiver for MB-OFDM UWB communications, *Proceedings of the IEEE International Solid-State Circuits Conference Digest of Technical Papers*, pp. 208-209, ISSN: 0193-6530.

Ismail, A. & Abidi, A. (2005b). A 3.1- to 8.2-GHz zero-IF receiver and direct frequency synthesizer in 0.18- μm SiGe BiCMOS for mode-2 MB-OFDM UWB communication, *IEEE Journal of Solid-State Circuits*, Vol., 40, December 2005, pp. 2573-2582, ISSN: 0018-9200.

Jiang, X. et al. (2010). A single-PLL dual-PPF synthesizer for Mode-1 MB-OFDM UWB communication, *Journal of Analog Integrated Circuits and Signal Processing*, Vol., 62, 2010, pp. 291-299.

Kim, C. et al. (2007). A CMOS Frequency Synthesizer Block for MB-OFDM UWB Systems, *ETRI Journal*, Vol., 29, April 2007, pp. 437-444, ISSN: 1225-6463.

Kozak, M. & Kale, I. (2003). *Oversampled Delta-Sigma Modulators*, Kluwer Academic Publishers, Springer, ISBN: 1402074204, Boston.

Lee, J. & Chiu, D.W. (2005). A 7-band 3-8 GHz frequency synthesizer with 1 ns band-switching time in 0.18μm CMOS technology, *Proceedings of the IEEE International Solid-State Circuits Conference Dig. Technical Papers*, pp. 204-205, 2005, ISSN: 0193-6530.

Lee, T.C. & Hsiao, K.J. (2005). A DLL-based Frequency Multiplier for MBOA-UWB System, *Proceedings of 2005 Symposium on VLSI Circuits Digest of Technical Papers*, pp. 42-45, July 2005.

Lee, T.C. & Hsiao, K.J. (2006). The Design and Analysis of a DLL-Based Frequency Synthesizer for UWB Application, *IEEE Journal of Solid-State Circuits*, Vol., 41, June 2006, pp. 1996-1999, ISSN: 0018-9200.

Lee, T.C. & Huang, Y.C. (2006). The design and analysis of a Miller-divider-based clock generator for MBOA-UWB application, *IEEE Journal of Solid-State Circuits*, Vol., 41, June 2006, pp. 1253-1261, ISSN: 0018-9200.

Lee, J. (2006). A 3-to-8-GHz fast-hopping frequency synthesizer in 0.18-μm CMOS technology, *IEEE Journal of Solid-State Circuits*, Vol., 41, March 2006, pp. 566-573, ISSN: 0018-9200.

Leenaerts, D.M.W. (2005). A SiGe BiCMOS 1 ns fast hopping frequency synthesizer for UWB radio, *Proceedings of the IEEE International Solid-State Circuits Conference Digest of Technical Papers*, pp. 202-203, 2005, ISSN: 0193-6530.

Leenaerts, D. M. W. (2006). Transceiver design for multiband OFDM UWB, *EURASIP Journal of Wireless Communication Networks*, 2006, pp. 1-8.

Liang, C.F. et al. (2006). A 14-band frequency synthesizer for MB-OFDM UWB application, *Proceedings of the IEEE Solid-State Circuits Conference*, pp. 428-437, 2006, ISSN: 0193-6530.

Lin, C.C. & Wang, C.K. (2005a). Subharmonic direct frequency synthesizer or mode-1 MB-OFDM UWB system, *Proceedings of the Symposium on VLSI Circuits Digest of Technical Papers*, pp. 38-41, 2005, ISBN: 4-900784-01-X.

Lin, C.C. & Wang, C.K. (2005b). A regenerative semi-dynamic frequency divider for mode-1 MB-OFDM UWB hopping carrier generation, *Proceedings of the IEEE International Solid-State Circuits Conference Digest of. Technical Papers*, pp. 206-207, 2005, ISSN: 0193-6530.

Lockwoodm, G.C. (1976). *One Shot Multivibrator Circuit*, US Patent 3996482, December 1976.

Lu, T.Y. & Chen, W.Z. (2008). A 3-to-10 GHz 14-band CMOS frequency synthesizer with spurs reduction for MB OFDM UWB system, *Proceedings of the IEEE Solid-State Circuits Conference*, pp. 126-601, 2005, ISSN: 0193-6530.

Mishra, C. et al. (2005). Frequency planning and synthesizer architectures for multiband OFDM UWB radios, *IEEE Transactions on Microwave Theory and Technology*, Vol., 53, December 2005, pp. 3744-3756, ISSN: 0018-9480.

Nicholas, H.T. & Samueli, H. (2005). A 150-MHz Direct Digital Frequency Synthesizer in 1.25-μm CMOS with -90-dBc Spurious Performance, *International Journal of Solid-State Circuits*, Vol., 26, December 1991, pp. 1959-1969, ISSN: 0018-9200.

Nosaka, H. et al. (2001). A Low-Power Direct Digital Synthesizer Using a Self-Adjusting Phase-Interpolation Technique, *International Journal of Solid-State Circuits*, Vol., 36, August 2001, pp. 1281-1285, ISSN: 0018-9200.

Pufeng, C. et al. (2010). A 6-9 GHz 5-band CMOS synthesizer for MB-OFDM UWB, *Journal of Semiconductors*, Vol., 31, July 2010, ISSN: 1674-4926.

Ravi, A. et al. (2004). 8 GHz, 20mW, fast locking, fractional-N frequency synthesizer with optimized 3rd order, 3/5 bit IIR and 3rd order 3-bit-FIR noise shapers in 90nm CMOS, *CICC 2004*, pp. 625-628, October 2004.

Razavi, B. et al. (2005). A UWB CMOS Transceiver, *IEEE Journal of Solid-State Circuits*, Vol., 40, December 2005, pp. 2555-2562, ISSN: 0018-9200.

Roovers, R. et al. (2005). An Interference-Robust Receiver for Ultra-Wideband Radio in SiGe BiCMOS Technology, *IEEE Journal of Solid-State Circuits*, Vol., 40, December 2005, pp. 2563-2572, ISSN: 0018-9200.

Sandner, C. et al. (2006). A WiMedia/MBOA-Compliant CMOS RF Transceiver for UWB, *IEEE Journal of Solid-State Circuits*, Vol., 41, December 2006, pp. 2787-2794, ISSN: 0018-9200.

Seong, C.K. (2006). *A 1.25 Gb/s digitally-controlled dual loop clock and data recovery circuit with enhanced phase resolution*, M.Sc. Thesis, Graduate School of Yonsei University.

Tanaka, A. et al. (2006). A 1.1V 3.1-9.5 GHz MB-OFDM UWB transceiver in 90 nm CMOS, *Proceedings of the IEEE International Solid-State Circuits Conference Digest of. Technical Papers*, pp. 120-121, 2006, ISSN: 0193-6530.

Valdes-Garcia, A. et al. (2006). An 11-Band 3.4 to 10.3 GHz MB-OFDM UWB receiver in 0.25 μm SiGe BiCMOS, *Proceedings of the Symposium on VLSI Circuits Technical Digest Papers*, pp. 254-255, 2006, ISBN: 1-4244-0006-6.

Valdes-Garcia, A. et al. (2007). An 11-Band 3-10 GHz Receiver in SiGe BiCMOS for Multiband OFDM UWB Communication, *IEEE Journal of Solid-State Circuits*, Vol., 42, April 2007, pp. 935-948, ISSN: 0018-9200.

Van de Beek, R.C.H. et al. (2006). A Fast-Hopping Single-PLL 3-Band MB-OFDM UWB Synthesizer, *IEEE Journal of Solid-State Circuits*, Vol., 41, July 2006, pp. 1522-1529, ISSN: 0018-9200.

Vankka, J. (2005). *Digital Synthesizers and Transmitters for Software Radio*, Springer, ISBN: 1402031947, Netherlands.

Yuan, L. & Svensson, C. (1989). A 1.5 V 3.1 GHz-8 GHz CMOS Synthesizer for 9-Band MB-OFDM UWB Transceivers, *IEEE Journal of Solid-State Circuits*, Vol., 24, January 1989, pp. 62-70, ISSN: 0018-9200.

Zheng, H. & Luong, H.C. (2007). A 1.5 V 3.1 GHz-8 GHz CMOS Synthesizer for 9-Band MB-OFDM UWB Transceivers, *IEEE Journal of Solid-State Circuits*, Vol., 42, June 2007, pp. 1250-1260, ISSN: 0018-9200.

Zhuang, J. et al. (2004). Noise, Spur Characteristics and in-lock error reduction of DLL-based frequency Synthesizers, *Proc. International Conference on Communications, Circuits and Systems*, pp. 1443-1446, 2004.

11

Ultra-Wideband GaN Power Amplifiers - From Innovative Technology to Standard Products

Andrey Kistchinsky
Microwave Systems JSC
Russia

1. Introduction

A number of the modern electronic systems applications require generation, processing, amplification, and emission of signals that have a continuous broadband spectrum or modulated signals with a relatively narrow spectrum whose frequency may change in broad ranges. The first group of applications may include UWB systems of short distance data transmission, radar systems with UWB signals of different kinds (pulse, multi-frequency, or quasi-noise), RFID-systems, and a number of others. The second group includes electronic warfare (EW) systems, EMC-testing systems, as well as universal measuring and testing equipment.

Usually, signals with fractional bandwidth over 20% of band center or more than 500 MHz of absolute bandwidth are referred to UWB signals. As applied to the signal-processing devices, in particular, to amplifiers, the interpretation of the term UWB is somewhat different. Depending on the relative bandwidth the amplifiers are usually divided into the following kinds: narrowband (frequency coverage - relation of the upper working frequency to the lower working frequency (W) is less than 1.2:1); wideband (W from 1.2:1 to 2:1), and ultra-wideband ones (W greater than 2:1). In the present article we shall speak about technologies of microwave ultra-wideband power amplifiers.

The main parameters determining the possibility of using an power amplifier in a definite electronic system are as follows: a working frequency bandwidth (ΔF), the output power with the given criteria of distortion (Po), and the efficiency of transformation DC source power into the output power (DE). With the increase of the frequency coverage W the achieved DE is significantly lowered. Some typical dependence of DE on W, built for typical microwave transistor power amplifiers, is shown in Fig.1.

The highest DE values (up to 70-80%) are realized due to different special circuits, named Harmonic Reaction Amplifiers (Colantonio et al., 2009). In these circuits a special combination of transistor source and load impedances and special biasing allows to achieve the forms of drain current and voltage close to the switching form which results in minimal losses of DC source energy. However, the frequency coverage W, in which these combinations may be realized, is usually limited by 1.1:1 to 1.2:1 values. Amplifiers with the frequency coverage up to 1.5:1 may be built by classical A/AB biasing schemes with multi-contour reactive input and output matching circuits. The forms of currents and voltages in such schemes are close to sinusoidal ones while the DE is limited by the values of 40-50%.

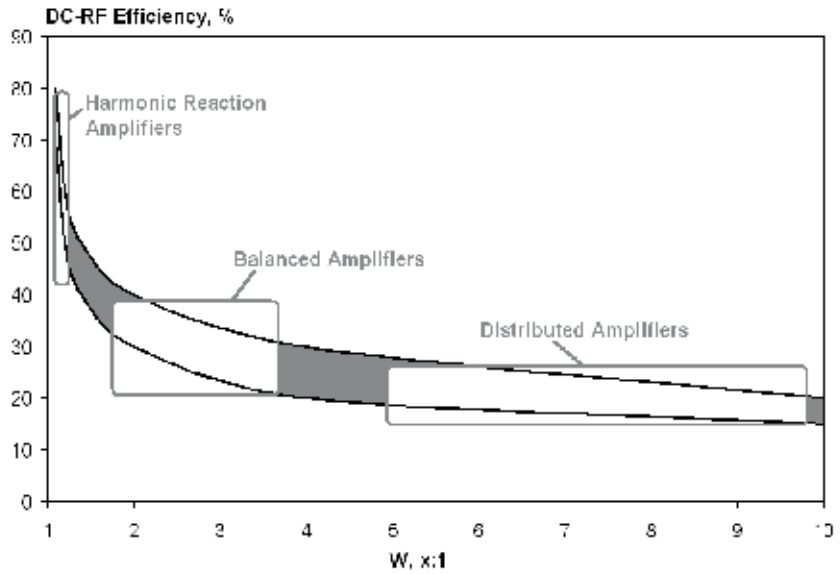

Fig. 1. Typical DC-RF efficiency for power amplifiers with a various bandwidth

For amplifier with W greater than 1.5:1 a high quality input matching and cascading of active elements becomes problematic; here a balance circuit is widely used, in which two identical active elements are connected with the help of 3-dB quadrature directional couplers while the input reflections are fully absorbed by the ballast loads and a close to ideal input and output matching is achieved (Sechi & Bujatti, 2009). In practice the balance amplifiers are used for frequency coverage from 1.4:1 to 4:1 and have efficiency up to 25-45%.

To realize the frequency coverage over 4:1, most often a scheme of a distributed amplifier (DA) is used, in which gates and drains of several transistors are united in artificial transmission lines with a characteristic impendence close to 50 Ohm (Wong, 1993). The lower working frequency of DA is limited only by DC-blocking circuits while the upper frequency is determined by the upper frequencies of the input and output artificial lines and depends on the transistor's own capacitances. The DC-RF efficiency of DA is still lower because of the difference of loads referred to individual transistors and redundancy of the number of transistors used in the circuit. In practice W from 4:1 to over 1000:1 and efficiency of 15-25% are achieved.

The qualitative ratios described above are applicable to amplifiers built on any types of transistors (HBT, MESFET, MOSFET, HEMT). However, we shall go on considering amplifiers on GaN HEMT transistors whose technology is rapidly developing and is taking the first place by the combination of W-Po-DE among the modern semiconductor microwave frequency devices.

2. GaN transistors and MMIC technology

2.1 A short history

The history of invention and development of the GaN microwave transistors and MMICs is rather short – a little less than 20 years from the moment of the first GaN-transistor demonstration to the beginning of industrial devices implementation in electronic

systems. Of this period the first 10 to 15 years were devoted to the search for the best transistor constructions and the ways for making them reliable and stable, while during the next five years numerous efforts were directed to the industrial adoption of the technology (Fig.2).

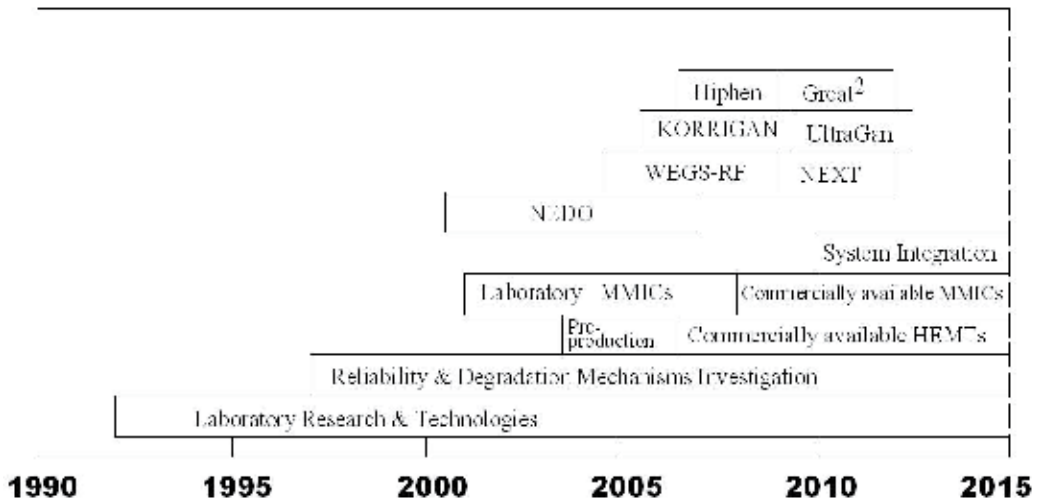

Fig. 2. The steps of GaN technology development history

This later stage was greatly promoted by a number of research programs financed by military, governmental and corporate bodies of the USA, Japan and Europe. Among the one should mention the Japanese program NEDO (Nanishi et al., 2006), the American DARPA programs, called WBGS-RF and NEXT (Rosker et al., 2010), as well as the European programs KORRIGAN, UltraGan, Hyphen, Great2 (Quay & Mikulla, 2010).

Early in the 2000s practically all the leading world electronic companies somewhat connected with the production of GaAs-components begin making their own investments in the GaN technology. These investments have given results and in the years 2006 and 2007 one watches announcing and then real appearance in the market of the first commercial GaN-products: universal wideband transistors in the range of frequencies up to 2-4 ГГц with the output CW power from 5 to 50 Watt (and somewhat later from 120 to 180 Watt). The following companies have become the pioneers of the commercial market: Eudyna (now Sumitomo Electric Devices Innovation, SEDI), Nitronex, Cree, and RFHIC. A little later Toshiba, RF Microdevices (RFMD), TriQuint Semiconductor (TQ), and a number of other companies have joined this first team.

In 2009 TriQuint began producing ultra-wideband MMIC amplifiers with the band of 2 to 17 GHz. By the end of 2010 GaN-based transistors and MMICs were already present in catalogs of more than 15 companies – producers of semiconductor components from the USA, Europe, Japan, South Korea, China and Russia.

2.2 Advantages

The interest of developers in GaN-transistors (or to be more precise in transistors on the basis of heterostructures AlGaN/GaN) was due to combination of a number of important material properties (Table 1).

Properties	Si	AlGaAs /InGaAs	SiC	AlGaN /GaN
Bandgap (E_g), eV	1.1	1.4	3.2	3.4
Electron mobility (μ_n), $cm^2 V^{-1}s^{-1}$	1350	8500	700	1200-2000
Saturation field electron velocity (υ_{sat}), $*10^7$ cm/s	1.0	2.0	2.0	2.5
2D sheet electron density (n_s), cm^{-2}	--	$3 * 10^{12}$	--	$(1\text{-}2) * 10^{13}$
Critical breakdown field (E_c), MV/cm	0.3	0.4	2.0	3.3
Thermal conductivity (K), $Wcm^{-1}K^{-1}$	1.5	0.5	4.5	1.3

Table 1. Basic properties of semiconductor materials for microwave power transistors

The maximum band-gap is determines the possibility of a transistor's work at high levels of activating influences (temperature and radiation). Very high electron density in the area of two-dimentional electronic gas and a high saturation field electron velocity make possible high channel current density and high transistor's gain. The maximum critical breakdown field allows realizing breakdown voltages of 100 to 300 V and increasing the working DC voltage up to 50-100 V, which together with a high current density provides for power density of industrial GaN transistors 4 to 8 W/mm (and up to 30 Watt/mm in laboratory samples), which is ten times greater than the output power density of GaAs transistors. The quality relations given in Fig.3 (Okumura, 2006) illustrate well the connection of the material physical properties with the possible device output power density.

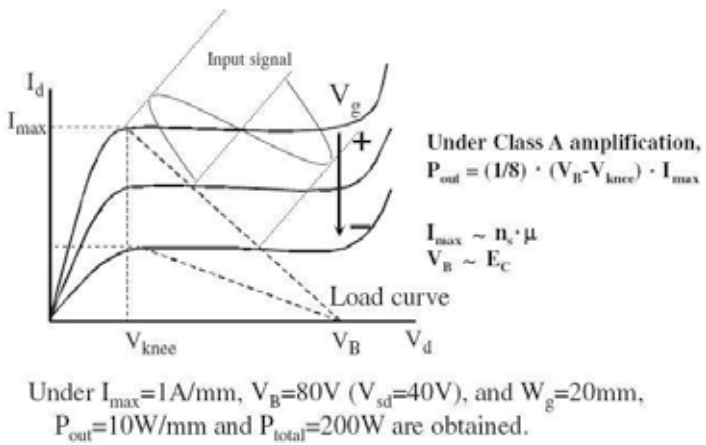

Fig. 3. Relations between the material physical properties and transistor power density (Okumura, 2006)

The main power microwave transistors and MMIC technology well developed in the mass production – the GaAs pseudomorphic HEMT technology (pHEMT) – is the main competitor of the rapidly developing GaN technology. That is why further on we shall compare parameters of transistors and MMICs having in mind these two technologies. For estimating and comparing the application possibilities of GaN and GaAs transistors in the wideband power amplifiers, as well as possible „migration" of technical solutions from one material to the other, let us make a simple analysis of their specific (i.e.related to 1 mm of the

gate width) parameters. Here was shall use the known (Cripps, 1999) estimations for the A class amplifier with maximum output power P_{max} and optimal (for reaching such power) transistor's load resistance R_{opt} :

$$P_{max} = V_{ds} * I_{max} / 8 \quad (1)$$

$$R_{opt} = 2 * V_{ds} / I_{max} \quad (2)$$

where V_{ds} is DC drain supply voltage, I_{max} is maximum open channel current.
From the presented expressions one can easily receive a formula for a new parameter – specific optimal load resistance (R_x):

$$R_x = V_{ds}{}^2 / (4 * P_x) \quad (3)$$

where P_x is a transistor's output power density, which is the parameter that is widely used in literature. The typical specific parameters of GaN HEMT and GaAs pHEMT transistors received from the analysis of their linear equvivalent circuits given in literature and in datasheets, as well as the above parameter R_x are presented in Table 2.

Parameters	**GaAs** pHEMT		**GaN** HEMT	
	typical	TQ **TGF2022-12** (1.2 mm)	typical	TQ **TGF2023-01** (1.25 mm)
Specific gate-source capacitance (C_{gsx}), pF/mm	1.8 - 3	2.77	1.1 - 2	1.43
Specific transconductance (G_{mx}), mS/mm	200-400	313	150-300	216
Specific drain-source capacitance (C_{dsx}), pF/mm	0.15-0.3	0.19	0.2-0.4	0.246
Output power dencity (P_x), W/mm	0.7	1.0	5	4.5
Drain-source DC voltage (V_{ds}), V	9	10	28	28
Specific optimal load (R_x), Ohm*mm	29	25	39	43.5
Power gain @ 10 GHz, dB	--	12.9	--	10.4
PAE @ 10 GHz, %	--	52.4	--	52
Output CW power @ 10 GHz, Watt	--	1.2	--	5.5

Table 2. Absolute and specific transistor parameters comparison for GaAs and GaN technologies

For comparison in this Table to as correct as possible we give specific parameters of two industrial transistors produced by same company (TriQuint Semiconductor) and having similar topologies, gate width and the equal gate length (0,25 μm).
The following conclusions can be drawn from the analysis of presented data:

- specific gate-surce capacitance and transconductance of GaN transistors (simultaneously) are from 1.5 to 2 times as low as in GaAs transistors, which is more likely the advantage of the former from the point of view of wideband input matching, because it requires smaller transformation coefficients in matching circuits. The achieved gain with the same gate-length may be considered to be sufficiently close.
- specific drain-source capacitance, that is shunting the optimal load of transistor and making difficult the building of wideband output matching circuit at frequences that are higher some cutt-off frequency, is in both classes of transistors almost the same.
- specific optimal loads of transistor (R_x) also turn out to be close (somewhat higher for GaN-transistors).

2.3 "Technical solution migration"

The above considerations allow making a subtantiated assumption that many projects and technical solutions as matching circuits or topology, worked out for GaAs-transistors and MMICs, may with minimal changes be applied for GaN-transistors with the same or from 20% to 50% greater gate width. And if the gate length of booth types of active structures are close, one can receive the same bandwidth, gain, and size of circuit, but with a several times greater output power.

In the work (Fanning et al., 2005) there is description of rather a successful experiment on „migration" of standard GaAs pHEMT wideband power MMIC amplifier project (TGA9083 MMIC amplifier that have been manufactured for over 10 years by TriQuint Semiconductor) to the GaN-on-Si technology, worked out by Nitronex Company. Frequency characteristics of the saturated CW output power of two MMIC samples (GaAs pHEMT and GaN-on-Si HEMT), assembled in a test circuit are shown in Fig.4, while the comparison of their parameters is made in Table 3.

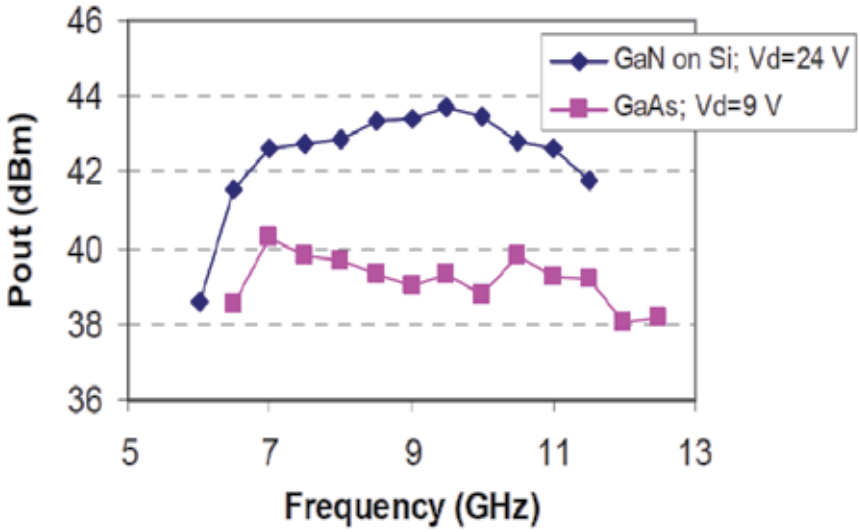

Fig. 4. Saturated output power of two MMIC amplifiers, manufactured according same topology project on GaAs and on GaN-on-Si (Fanning et al., 2005)

Parameters	TGA9083 (GaAs pHEMT)	New (GaN-on-Si HEMT)	Comments
Frequency range, GHz	6.5 - 11	7 – 10.5	=
Linear gain, dB (typ.)	19	20.9	=
Output CW power @ 3-dB gain compression, W	8	20	x 2.5
PAE, %	35	27	=
Vd, V	9	24	x 2.7
Chip size, мм^2	4.5 x 3		=

Table 3. Comparison of parameters of two MMIC amplifiers, manufactured according same topology project on GaAs and on GaN-on-Si (Fanning et al., 2005)

As one can see from the presented data a simple transfer of the complicated wideband MMIC amplifier project onto a new technology gives considerable increase of the device output power while the rest of the parameters remain preserved. A modification of this project with a correct GaN transistor's nonlinear model should further improve PAE and output power of amplifier.

2.4 The ways for further improvement

The further improvement of the GaN transistor constructions is done in several directions. First, it is the increase of the power density by raising break-down voltage, improving heat removal, and increasing of efficiency. Second, is the frequency range extending into the millimeter-wave frequencies with preservation of the power density and efficiency. Third, is the lowering of production cost.

The increase of the transistor's power density depends on the following:

- by increasing the breakdown voltage (V_B);
- by lowering of transistor's heat resistance by improvement thermal conductivity of the substrate and optimization of transistor's construction;
- by increasing the maximum channel current (I_{max});

FP (Field Plate) electrode has become an effective way for increasing the breakdown voltage that is successfully used in manufactured GaN transistors. This term is applied to a number of transistor constructions. An additional electrode is located along the gate and it is connected either with gate, or with source, or it is not connected with transistor electrodes at all. This electrode allows changing the distribution of electric field in the channel, "moving away" the peak of the field from the gate's edge and "smoothing" it. This lows down the gate leakage and increases the drain-source voltage when an avalanche ionization begins. The constructions of FP electrodes used in GaN transistors are quite diverse. Two most widespread ones are shown in Fig.5.

It is evident that the presence of an additional electrode, besides the increase of breakdown voltage and output power density, causes other changes in the transistor characteristics as well. In particular, there are significant changes in the cut-off frequencies F_t и F_{max}, and parasitic capacitances of the active structure. Fig.6 shows relative changes of parameters of GaN transistors with a FP electrode depending on the length of FP electrode L_f. investigated in the works (Kumar et al., 2006) and (Wu et al., 2004).

(a) (b)

Fig. 5. Field-plated AlGaN/GaN HEMTs: (a) integrated field plate; (b) separated field plate (Mishra, 2005)

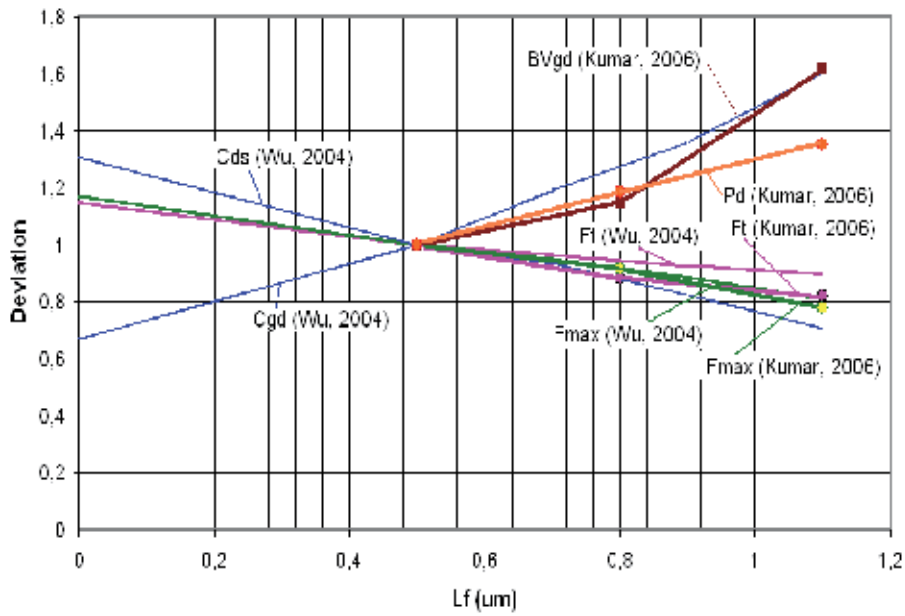

Fig. 6. Deviations of basic transistor parameters with FP-electrode length (L_f) variation

Inserting of the gate-connected FP electrode with L_f = 1,1 um allowed increasing the breakdown voltage from 68 to 110 volt and raising the output power density by 35%, from 5,4 to 7,3 Watt/mm. At the same time the current gain cut-off frequency decreased by 18% to 20% (Kumar et al., 2006). This is probably conditioned by a considerable (two times) increase of the parasitic capacitance Cgd (Wu et al., 2004). Transconductance and gate-source capacitance of transistor after FP inserting have practically no any changes. The use of a field electrode connected with the source of transistor, on the contrary, cuts down the parasitic capacity Cgd and somewhat increases the cut-off frequencies and maximum available (or stable) gain of transistor. The construction of such FP electrode is shown in Fig.7 (Therrien et al., 2005).

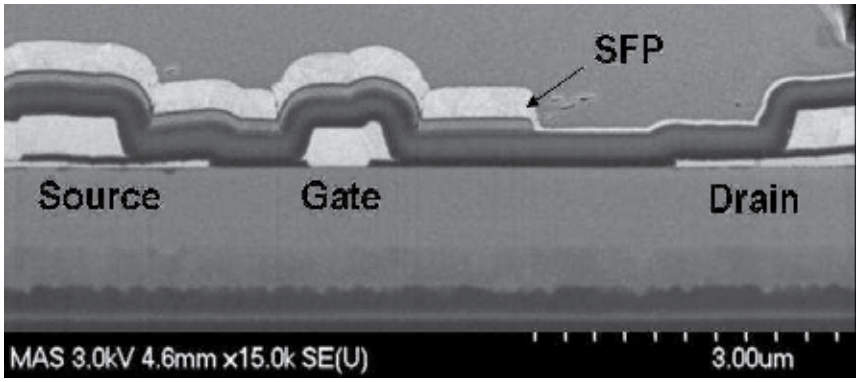

Fig. 7. Cross section of AlGaN/GaN HEMT with source field plate (Therrien et al., 2005)

When such electrode was inserted (Therrien et al., 2005) transistor's Cgd was decreased by 30%, while maximum stable gain (MSG) increased by 1,5 dB. Breakdown voltage also increased significantly and there was also 1,5 times growth of output pulse power density at Vd = 48 V. In the same way the insertion of a field electrode, connected with the source, affected the parameters of transistor produced with the use of other technologies. In particular, in GaAs MESFET transistor (Balzan et al., 2008) the capacity Cgd decreased by 43%, while the F_t increased by 16%. In the SiC MESFET (Sriram et al., 2009) Cgd decreased by 45% and MSG increased by 2, 7 dB.

The growth of output power density also leads to an increase of the heat dissipation on the unit of the area of transistor's active structure. If additional effortes are not taken, the growth of channel temperature will limit the growth of transistor's parameters and will lead to the lowering of reliability. In modern GaN transistors the following materials and composites are used (Table 4) as substrates on which the epitaxial layer of GaN is formed.

Substrate	Thermal conductivity, W/ cm * K
Mono-crystalline SiC	4,9
High Resistive Si $_{(111)}$	1,5
Silicon on poly-crystalline SiC (SopSiC)	3
Silicon on Diamond (SoD)	10-18

Table 4. Substrates for power GaN transistors

The mono-crystalline SiC substrate is the most often used material for industrial growing epitaxial structures for GaN transistors. It is used by TriQuint Semicionductor, RFMD, Toshiba, SEDI, Cree and a number of others. The production on substrates up to 100 mm diameter was developed (Palmour et al., 2010). The technology using inexpensive substrates of high-resistance silicon with intermediate buffer layers (GaN-on-Si) was developed by Nitronex. TriQuint Semiconductor also plans to use this technology in future. Substrates of SopSiC type, manufactured by method of transfer of the thin layer of high-resistance silicon onto the poly-crystalline SiC substrate, are proposed for approbation by PicoGiga (PicoGiga

International, 2011). In commercial production of transistors they are not used yet. Such substrate must be cost-effective as compared to those from mono-crystalline SiC although they are close to them in heat conductivity. A considerable progress in heat conductivity may be expected from the use of composite substrates on the basis of poly-crystalline CVD diamond developed by sp^3 Diamond Technologies (Zimmer & Chandler, 2007). The proposed GaN transistor on SOD substrate cross-section is shown on Fig.8.

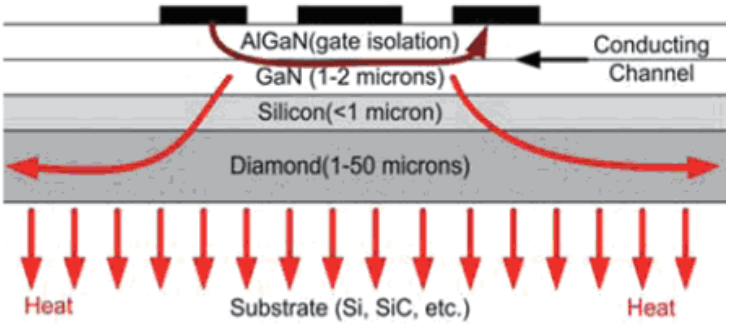

Fig. 8. Proposed GaN on SOD technology (Zimmer & Chandler, 2007)

Authors estimate that this technology will allow increasing the dissipated power of GaN transistor by 50% as related to the mono-crystalline SiC.

The improvement of GaN transistor's gain and extending of working frequencies into the area of millimeter-waves are related with a search for new effective heterostructures that would allow increasing electrons mobility, 2D sheet electron density, and, as a consequence, increasing device's transconductance, maximal open channel current, and cut-off frequencies. These efforts are carried out in different fields. The achieved parameters of some types of heterostructures (Wang et al., 2010, Sun et al., 2010, Jardel et al., 2010) in comparison with the standard AlGaN/GaN structure are given in Table 5.

If the development of the above technologies are successful in industrial production, parameters of GaN transistors and MMICs may be greatly improved already in the current decade and will be characterized by the following figures (Table 6).

Parameters	Heterostructures	
	Industry standard: AlGaN/GaN	Innovative: AlGaN/AlN/GaN, AlInN/GaN, InAlN/GaN …
Electron mobility ($cm^2 V^{-1}s^{-1}$)	1000 - 1200	1400 - 2000
2D sheet electron density (cm^{-2})	$1 * 10^{13}$	$(1.4 – 2.0) * 10^{13}$
Idss (mA/mm)	500 - 1000	1300 - 2300
Gm (mS/mm)	150 - 300	400 - 550

Table 5. Available GaN heterostructures parameters

Parameters	Industry standard 2010	Industry standard 2015 - 2020
Power density (W/mm)	4 - 8	8 - 15
Gate length (um)	0.25 – 0.5	0.05 – 0.5
Frequency Range (GHz)	0 - 20	0 - 100
Output power (W/die)	5 - 100	5 - 200

Table 6. Available vs. today industry standard GaN transistors parameters

3. Manufacturing status

3.1 GaN discrete transistors

Discrete GaN transistors with the working frequencies up to S-band were historically first in the microwave semiconductor market. Today they are produced with output CW power from 5 to 200 Watt in different package types or in die form. The main parameters of the commercially available devices is given in Table 7. There are data on three groups of devices that are of interest as active elements for building UWB power amplifiers. The first group («Low End») includes transistors with the output power of 5 to 12 Watt (this is the minimal power level of the transistors produced today). They are supplied in die form or in miniature SMD packages. On the basis of these transistors on can realize UWB amplifiers with frequency coverage W from 3:1 to more than 100:1, because the maximum output power is provided for with load impedance close to 50 Ohm (see Table 2) and the possibilities for optimal output matching are limited in fact only by the construction of the

Parameters	«Low End» (5W)	"High End Die" (100W)	"High End Flange" (200W)
Output CW Power (W)	5 - 12	100-120	180 - 220
Usable Upper Frequency (GHz)	6 - 20	3-10	1.5 – 2.5
Available UWB ranges (GHz)	0.1 - 3 1 – 6 3 – 10.5 4 - 12	0.8 – 2.5 1 – 3 2 - 4	0.5 – 1 1.0 – 1.5
Linear gain @ UF (dB)	12 - 15		
Power gain @ UF (dB)	8 - 10		
Drain Efficiency (%)	55-65		
Packages	SMD (4x4), Die	Die	Dual Flange
Some models	TQ TGF2023-01 TQ T1G6000528Q3 Cree CGH40006P Cree CGH60008D RFMD RF3930D	TQ TGF2023-20 Cree CGH60120D RFMD RF3934D	Cree CGH40180PP Nitronex NPT1007 SEDI EGNB180M1A

Table 7. Discrete GaN HEMT main parameters

drain DC bias circuit, which can be performed as a very wideband one. The maximum working frequency for the amplifier based on discrete transistor with W greater than 3:1 may be estimated by the value of 12 GHz.

The maximum amplifier's bandwidth may be realized by using transistors in die form that have minimal parasitic gate and drain inductances. In our days there are GaN transistors in die form with the gate width up to 28 mm and output CW power up to 120 Watt ("High End Die"). On the basis of these devices one can realize UWB amplifiers with frequency coverage more than 3:1 on frequencies up to 4 GHz. Here the bandwidth is limited by the difficulties of high-ratio impedance transformers realization to providing for an optimal load at 3 or 4 Ohm with the parallel parasitic capacitance Cds being about 7 to 10 pF. The most powerful CW transistors ("High End Flange") are produced in a double flange ceramic packages, in which two separate transistors are located. They are used in the amplifier either in accordance with the push-pull circuits, or in balanced chains. The first one has an advantage that allows a 4 times increase of impedance of the input and output matching circuits and provides for matching in a larger bandwidth. The second circuits allows providing low input and output reflection coefficients and a good matching with the driver and load. The most powerful industrial transistors of this class have output CW power of up to 220 W. Because of significant package parasitic reactances of such transistors the upper frequency of the wideband amplifier is seldom greater than 1.5 – 2 GHz.

3.2 UWB MMIC GaN amplifiers

Product mix of GaN MMIC power amplifiers is not yet great, but it is growing rapidly. UWB microwave MMIC amplifiers are built in accordance with two main principals which we have already mentioned above. This is a two- or three-stage circuit with reactive/dissipative matching (RMA) and a distributed amplifier (DA). The balance circuits in GaN MMIC devices is not widespread since the SiC substrate is cost-expensive, so using of quadrature couplers on MMIC chip is not considered rational.

3.2.1 Distributed MMIC amplifiers

The greatest frequency coverage is provided for by the amplifier built on the principle of distributed amplification, which is also called traveling-wave amplifier. The principle of distributed amplification (Wong, 1993) has been used in electronics since the middle of the last century and the epoch of vacuum-tube amplifiers. GaAs MMIC DA's are manufactured by dozens of companies. However, the output power and PAE of such devices have already reached their full capacity. The appearance of GaN MMIC technology has allowed making a considerable jump in the parameters of DA amplifiers. In Table 8 we give parameters of the most powerful MMIC DA, realized by GaAs and GaN technologies in the 2-18 GHz frequency range which is standard for such amplifiers (and widely used for EW systems). Image of 2-18 GHz GaN MMIC DA with the output CW power greater than 11 W, developed by specialists of TriQuint Semiconductor (Reese et al., 2010) in the framework of stage III of WBGS-RF program is shown in Fig.9. As compared to the most powerful commercially available GaAs DA this amplifier has 10 times as great output power, higher efficiency and 3,4 times greater die size. As a commercially available only one type of GaN MMIC is so far known (TriQuint TGA2570) with 8 W output power and 15-25% PAE. Improvement of parameters of heterostructure

and development of diamond-based substrates will allow increasing the 2-18 GHz MMIC DA's output power to the level of 20 to 30 W.

Parameters	MMIC DA 2 – 18 GHz	
	GaAs	GaN
Output CW Power (W)	1.0 – 1.2	11.0
PAE (%)	20	28
Linear gain (dB)	14	12
Vd (V)	10	35
Die size (mm^2)	2.89 x 1.55	5.54 x 2.71
Model	Hittite Microwave HMC797	(Reese et al., 2010)

Table 8. GaN vs. GaAs MMIC distributed amplifier's main parameters

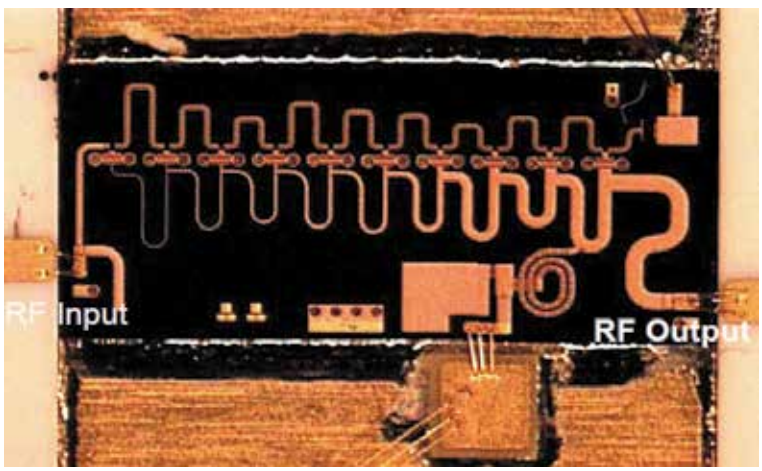

Fig. 9. Photograph of the 2-18 GHz 11 Watt MMIC amplifier (Reese et al., 2010)

3.2.2 Reactive matched multistage MMIC amplifiers

The second solution that is often used for building MMIC amplifiers with frequency coverage from 1.4:1 to 3:1 is a two- or three-stage circuit with a corporate reactive output matching circuit and reactive/dissipative inter-stage and input matching circuits (RMA). Today the majority of GaAs MMIC power amplifiers with the output power of over 1 or 2 W have been built in accordance with this principle. This scheme has a better efficiency, however it does not provide for a good input and inter-stage matching and, as a rule, it has large gain ripple. And here also the appearance of GaN MMIC technology has allowed making a considerable jump in parameters. In Table 9 we give main parameters of RMA-amplifiers realized on GaAs and GaN technologies in the frequency ranges of 2-6 GHz and 6-18 GHz having frequency coverage of 3:1.

Parameters	MMIC RMA 2-6 GHz		MMIC RMA 6 - 18 GHz	
	GaAs	GaN	GaAs	GaN
Output CW Power (W)	10-12	22 - 35	2.5 - 3	6 - 10
PAE (%)	25 - 32	42 - 44	18 - 30	15 - 20
Linear gain (dB)	16 - 21	21 - 28	23 - 27	18 - 20
Vd (V)	10	28	8	25
Die size (mm^2)	5.0 x 6.34	3.6 x 3.6	4.3 x 2.9	6.43 x 3.08
Model	M/A Com MAAPGM 0078-Die	Cree CMPA20600 25D	TriQuint TGA2501	(Mouginot et al., 2010)

Table 9. GaN vs. GaAs MMIC reactively matched amplifier's main parameters

On frequencies up to 6 GHz the advantages of GaN MMICs are considerably in all parameters: the output power is 2.5-3 times higher, the efficiency is 1.5 times higher, and the die size is 2.5 times smaller. In the range from 6 to 18 GHz GaN MMIC has the output power 3 times as great, but in the PAE and dimensions it is still inferior to GaAs amplifier. It should be noted that GaN amplifier is one of the first models in the given class of MMIC, while the GaAs amplifier has already been manufactured for 10 years. With improvement of technology, nonlinear models of GaN transistors, and design methods GaN MMICs in this range will show advantages in the efficiency as well. Image of the 2,5-6 GHz 30 W GaN MMIC amplifiers, developed by the specialists of TriQuint Semiconductor (TGA2576) is shown in Fig.10.

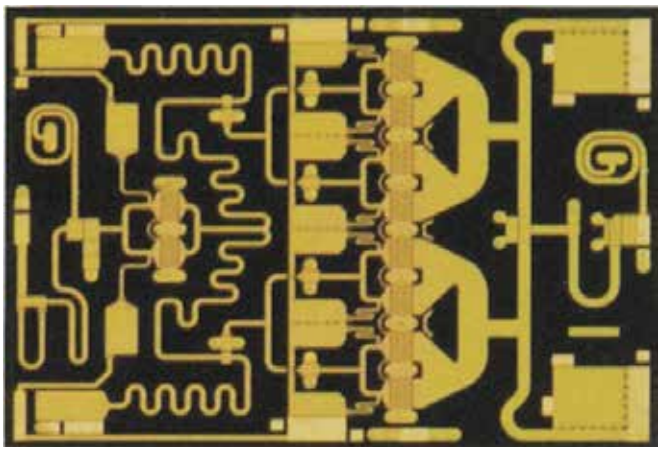

Fig. 10. Photograph of the 2.5-6 GHz 30 Watt MMIC amplifier (www.triquint.com)

Improvement of hetero-structures parameters and mastering of diamond-based substrates will allow increasing further the output power of MMIC RMA in the range from 2 to 6 GHz up to the level of 50 to 60 W.

3.3 Commercially available GaN MMIC amplifiers

Parameters of some types of UWB MMIC amplifiers produced nowadays are given in Table 10. These MMICs cover the range of frequencies from 20 MHz to 17 GHz with the output

saturated power from 2 to 25-30 W. Among the manufactured MMICs only two types are DA amplifiers, while in all the others the principle of reactive/dissipative matching is used. All the UWB ranges with the output CW power from 10 to 30 Watt and DC-RF efficiency from 20% to 50% are being overlapped by GaN MMIC amplifiers already in the third year of manufacturing. Promotion of these devices in the market in future will depend on the successes in the increase of production yield and lowering of prices as well as on the "second jump" of the power density from 4-8 Watt/mm to 10-15 Watt/mm due to the implementation of diamond-based substrates and improvement of transistor heterostructures. The laboratory results of recent years (Micovic, 2008), that have demonstrated the possibility of realizing MMIC amplifiers in the ranges up to 95 GHz with the output power up to 0.5 Watt, will also be realized in commercially available MMICs.

Model	**Manu-facturer**	**ΔF, GHz**	**P_{-3dB}, W**	**G_{ss}, dB**	**ΔG, ±dB**	**PAE, %**	**RL_{in}, dB**	**RL_{out}, dB**
RFHA1000	RFMD	0,03-1,0	12-20	15 - 18	±1.5	60	-13	-5
RF3833	RFMD	0,03-2,1	25	10-13	±1.5	40-50	-9	-5
RF3826	RFMD	0,02-2,5	9	13	±1.0	35-45	-10	--
TGA2540-FL	TQ	0,03-3	9	19	--	40	--	--
CMPA0060002D	Cree	0,02 – 6,0	2-4	17	±1.0	28-43	-9	-11
CMPA0060025F	Cree	0,02 – 6,0	25	16 - 21	±3.0	26-40	-4	-7
CMPA2060025D	Cree	2.0-6.0	25	21 - 28	±3.5	42-44	-7	-7
CMPA2560025F	Cree	2.5-6.0	25-37	22 - 28	±3.0	> 30	-6	-5
TGA2576	TQ	2.5-6.0	35-45	20 - 23	±1.5	> 35	-15	-6
CMPA801B025D	Cree	8 - 11	32-47	27-30	±1.5	37-44	-5	-12
TGA2570	TQ	2 - 17	8-12	10-12	±2.0	20	-10	-10

Table 10. Some GaN power MMIC amplifiers parameters

4. High power GaN amplifier modules

Successes in the industrial development of GaN transistors and MMIC have immediately found response in the efforts and results of the work of the developers of high power UWB amplifier modules and systems. In 2009 through 2011 new devices appeared in the catalogues of the majority of companies producing power amplifiers, which in their overall mass parameters and the levels of CW output power surpass the earlier amplifiers on GaAs components. The attraction of the discrete GaN transistors is conditioned by the following considerations.

First. The scheme of the amplifier's output stage, which provides for the main energy consumption and dimensions, has been greatly simplified. To receive the required output power one needs from 4 to 10 times less of the discrete or MMIC devices, power combiners, and passive components. This cuts down the cost of the module construction and allows making it much smaller in size. To illustrate the above we present in Fig.11 in the same scale photographs of output stages of MIC broadband amplifiers with the output power of 10-15 Watt and the frequency range 4-11 GHz manufactured by Microwave Systems JSC on the

basis of GaAs p-HEMT transistors (by combining the power of four balance quasi-monolithic MIC amplifying chains) and on the basis of GaN HEMT transistors (one balance MIC chain). The width of a module with GaN-based output stage has decreased three times as compared with the variant on GaAs transistors with the same level of the output power.

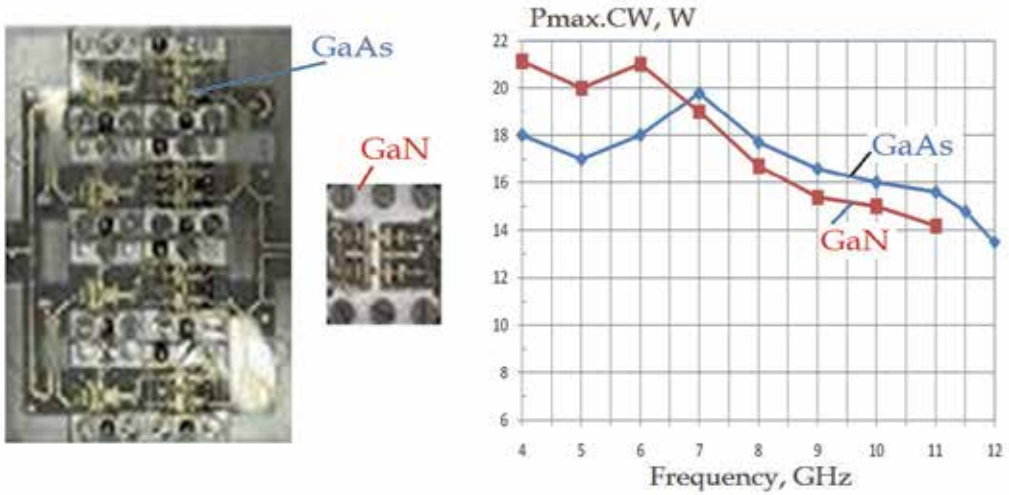

Fig. 11. Output stages of 4-11 GHz 15 Watt MIC amplifiers based on GaAs and GaN commercially available transistors – sizes and output CW power (Microwave Systems JSC)

The advantage in the size of the GaN modules may be estimated looking at Fig.12, where photographs of two amplifiers produced by Empower RF Systems (www.empowerrf.com) are given in the same scale. Both pictured models have the 50 W saturated output power in the 1 to 3 GHz frequency range. GaAs-based model (BBM4A6AH5) have the volume of 71.8 $inch^3$ and weight of 5 lb, while the volume and the weight of the GaN-based model (BBM4A6AHM) are correspondingly 23.9 $inch^3$ and 1.5 lb (the ratio here is 3:1).

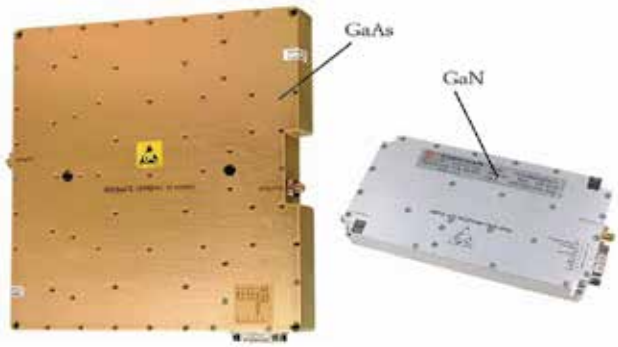

Fig. 12. Comparison of sizes of 1-3 GHz 50W GaAs vs. GaN amplifier modules (Empower RF Systems).

Second. With the appearance of GaN transistors the design methodology of the broadband power amplifiers has been considerably simplified. High supply voltage and high

impedance of the optimal transistor load necessary for obtaining the maximum output power and power-added efficiency make much simpler the construction of the output matching circuits and improve the quality of matching in a much wider band of frequencies.

Third. The use of GaN transistors allows increasing DC-RF efficiency of amplifiers. The drain efficiency of GaN transistor itself biased in class AB without the use of special circuits with harmonic reflections comprises from 60% to 65%, while in GaAs p-HEMT transistors it is rarely over 55%. Due to this, as well as because here is a considerable decrease of losses in the output combiners, DC-RF efficiency of GaN-amplifiers is as a rule from 1.2 to 1.8 times greater than that in GaAs-amplifiers with the same power.

At the same time GaN amplifiers have specific features affecting their application in the some systems. Primarily these are specificities of the dynamic characteristic having a lengthy part of a monotonous gain compression with the growth of the input power, which is not typical for GaAs amplifiers. The maximum output power and DE in GaN amplifiers is realized with the gain compression from 3 to 7 or 8 dB and more, while in most GaAs amplifiers the value of compression is not greater than 1 or 2 dB. Different characters have also dependences of the harmonic level and intermodulation distortions from the input power. Fig.13 gives dependences of the 2-tone output power and third order combination components for two models of amplifiers having the same frequency range (from 2 to 4 GHz), the same maximum output CW power (25 W), and the same linear gain (43 dB), but built on different types of transistors.

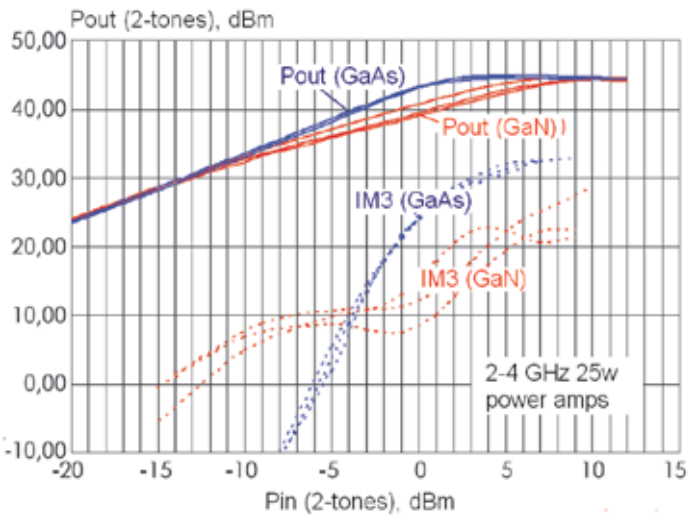

Fig. 13. Dynamic transfer characteristics and third-order intermodulation products of GaN vs. GaAs 2-4 GHz 25W power amplifiers (Microwave Systems JSC)

The active introduction of GaN transistors and MMICs in the industry and the advantages described above have led to the situation that during three years (from 2008 through 2010) tens of UWB high power GaN amplifier modules have been put out into the market, while a considerable part of the earlier GaAs amplifiers up to 3 GHz disappeared from the catalogs of manufacturers due to harsh competition. The main characteristics of the most powerful UWB GaN amplifiers that are being produced in 2011 are described in Table 11.

Model	Manufacturer	ΔF, GHz	P_{sat}, W	G_{ss}, dB	ΔG, ±dB	PAE, %	Vdc, V
BME2719-150	Comtech PST	0,02-1,0	150-200	70	-	35	18-36
BBM3T6AMQ	Empower RF	0,96-3,0	160	56	±2	30	28
BME19258-150	Comtech PST	1,0-2,5	250	70	--	25	18-36
SSPA-1,5-3,0-200	Aethercomm	1,5-3,0	200	67	±2,5	25	36
BME25869-150	Comtech PST	2,5-6,0	150-200	65	--	18	18-36
BBM5A8CGM	Empower RF	2,0-6,0	40	55	±1,5	15	28
PA020180-3932	Aeroflex	2,0-16,0	8	22	±3,5	24	28

Table 11. UWB high power amplifiers parameters.

Thus, the area of radio frequencies from 20MHz to 6 GHz is occupied by module UWB amplifiers on GaN transistors and MMICs with drain efficiency from 20% to 35% and the output CW power up to 200 Watt. On the frequencies of over 6 GHz the level of the output power of GaN amplifiers has so far been somewhat more modest; however there is no doubt that in the nearest future in these ranges up to millimeter waves the models on GaAs will partially be forced out from the market by devices on GaN.

5. Conclusion

This Chapter is devoted to consideration of the development process in the technology of GaN microwave power transistors and MMICs and to demonstration of the prospects for the development of this technology as an industrial standard in the nearest future. Electric and exploitation parameters of GaAs and GaN technologies were compared with the consideration of possible migration of power amplifier technical solutions from one to the other. Considered and analyzed were also parameters and specific features of commercially available GaN discrete transistors and MMICs, features of their application in constructions of high power UWB amplifiers, and the parameters of industrial models of such amplifiers.

6. References

Colantonio P.; Giannini F. & Limiti E. (2009). *High efficiency RF and microwave solid state power amplifiers*, John Wiley & Sons, 2009, ISBN: 978-0-470-51300-2

Sechi F. & Bujatti M. (2009). *Solid-State Microwave High-Power Amplifiers,* Artech House, 2009, ISBN: 978-1-59693-319-4

Wong T.T.Y. (1993). *Fundamentals of Distributed Amplifications*, Artech House, 1993, ISBN: 0-89006-615-9

Nanishi Y.; Miyamoto H; Suzuki A.; Okumura H. & Shibata M. (2006). Development of AlGaN/GaN High Power and High Frequency HFETs under NEDO's Japanese National Project, *CS MANTECH Conference*, 2006, p.p. 45-48

Rosker M.J.; Albrecht J.D.; Cohen E.; Hodiak J. & Chang T-H. (2010). DARPA's GaN Technology Thrust, *2010 IEEE MTT Symposium Digest*, 2010, p.p. 1214-1217, ISSN: 978-1-4244-7732-6

Quay R. & Mikulla M. (2010). Gallium Nitride RF-Devices: An Overview on the Development Activities in Europe, *2010 IEEE MTT Symposium Digest*, 2010, p.p. 1234-1237, ISSN: 978-1-4244-7732-6

Okumura H. (2006). Present Status and Future Prospect of Widegap Semiconductor High-Power Devices, *Japanese Journal of Applied Physics*, Vol. 45, No. 10A, 2006, pp. 7565–7586

Cripps S.C. (1999). *RF Power Amplifiers for Wireless Communications*, Artech House, 1999, ISBN: 0-89006-989-1

Fanning D.M.; Witkowski L.C.; Lee C.; Dumka D.C.; Tserng H.Q.; Saunier P.; Gaiewski W.; Piner E.L.; Linthicum K.J. & Johnson J.W. (2005). 25 W X-band GaN on Si MMIC, *GaAs Mantech Conference Proceedings*, 2005

Mishra U.K. (2005). Status of AlGaN/GaN HEMT Technology-A UCSB perspective, *13th Gallium Arsenide and other Compound Semiconductors Application Symposium*, 2005, p.p. 21-28

Kumar V.; Chen G.; Guo S. & Adesida I. (2006). Field-Plated 0.25-μm Gate-Length AlGaN/GaN HEMTs With Varying Field-Plate Length, *IEEE Transactions on ED*, vol. 53, N 6, 2006, p.p. 1477-1480, ISSN: 0018-9383

Wu Y.-F.; Saxler A.; Moore M.; Wisleder T.; Chavarkar P.M. & Parikh P. (2004). Noise Characteristics of Field-plated GaN HEMTs, *2004 Proceedings on IEEE Lester Eastman Conference on High Performance Devices*, p.p. 192-194, ISBN: 981-256-196

Therrien R.; Singhal S.; Johnson J.W.; Nagy W.; Borges R.; Chaudhari A.; Hanson A.W.; Edwards A.; Marquart J.; Rajagopal P.; Park C.; Kizilyalli I.C. & Linthicum K.J. (2005). A 36mm GaN-on-Si HFET Producing 368W at 60V with 70% Drain Efficiency, *2005 IEEE International Electron Devices Meeting (IEDM)*, p.p. 568-571, ISBN: 0-7803-9268

Balzan M.L.; Drinkwine M.J. & Winslow T.A. (2008). GaAs MESFET with Source-Connected Field Plate for High Voltage MMICs, *GaAs Mantech Conference Proceedings*, 2008

Sriram S.; Hagleitner H.; Namishia D.; Alcorn T.; Smith T. & Pulz B. (2009). High-Gain SiC MESFETs Using Source-Connected Field Plates, *IEEE Electron Device Letters*, vol.30, 2009, N 9, p.p. 952-953

Palmour J.W.; Hallin C.; Burk A.; Radulescu F.; Namishia D.; Hagleitner H.; Duc J.; Pribble B.; Sheppard S.T,; Barner J.B. & Milligan J. (2010). 100 mm GaN-on-SiC RF MMIC Technology, *2010 IEEE MTT Symposium Digest*, 2010, p.p. 1226-1229, ISSN: 978-1-4244-6057-1

PicoGiga International. (2011). GaN Thin Epiwafers for discrete power devices, RF & microwave components, 16.03.2011, Available from http://www.soitec.com/pdf/picogiga-gan-thin-epiwafers.pdf

Zimmer J. & Chandler G. (2007). GaN on SOD Substrates – The Next Step in Thermal Control, *CS MANTECH Conference*, 2007, p.p. 129 – 132

Wang*H.; Chung J.W.; Gao X.; Guo S. & Palacios T. (2010). High Performance InAlN/GaN HEMTs on SiC Substrate *CS MANTECH Conference*, 2010, p.p. 185-188

Sun H.; Alt A.R.; Benedickter H.; Feltin E.; Carlin J.-F.; Gonschorek M.; Grandjean N.R. & Bolognesi C.R. (2010). 205-GHz (Al,In)N/GaN HEMTs, *IEEE Electron Device Letters*, vol.31, 2010, N 9, p.p. 957-959

Reese E.; Allen D.; Lee C. & Nguyen T. (2010). Wideband Power Amplifier MMICs Utilizing GaN on SiC, *2010 IEEE MTT Symposium Digest*, 2010, p.p. 1230-1233, ISSN: 978-1-4244-7732-6

Jardel O.; Callet G.; Dufraisse J.; Sarazin N.; Chartier E.; Reveyrand T.; Oualli M.; Lancereau D.; Di Forte Poisson M.A.; Piotrowicz S.; Morvan E.; & Delage S.L. (2010).

Performances of AlInN/GaN HEMTs for Power Applications at Microwave Frequencies, *Proceedings of the 5th European Microwave Integrated Circuits Conference*, 2010, p.p. 49-52, ISSN: 978-2-87487-017-0

Micovic M.; Kurdoghlian A.; Moyer H.P.; Hashimoto P.; Hu M.: Antcliffe M.; Willadsen P.J.; Wong W.S.; Bowen R.; Milosavljevic I.; Yoon Y.; Schmitz A.; Wetzel M.; McGuire C.; HughesB. & Chow D.H. (2008). GaN MMIC PAs for E-Band (71 GHz – 95 GHz) Radio, *30 th IEEE Compound Semiconductor IC (CSIC) Symposium*, 2008

12

A Method for Improving Out-Of-Band Characteristics of a Wideband Bandpass Filter in an LTCC Substrate

Shinpei Oshima[1], Koji Wada[2], Ryuji Murata[1] and Yukihiro Shimakata[1]
[1]*TAIYO YUDEN CO., LTD*
[2]*The University of Electro-communications*
Japan

1. Introduction

Recently, compact wireless modules using low temperature co-fired ceramic (LTCC) technology are widely used for the wireless systems such as mobile phones, Bluetooth, and wireless local-area networks(Lin et al.,2004; Wang et al.,2005). Fig.1 shows the general structure of the compact wireless modules using the LTCC technology. The modules consist of an LTCC substrate, integrated circuits, chip components, a shield, and passive components embedded in the LTCC substrate (e.g., the bandpass filter, coupler and balun). The embedded components in the LTCC substrate are fabricated by using the multilayer structures based on thin ceramic sheets and conductor patterns. It becomes possible to produce very compact modules compared to those with a general printed circuit board substrate, because a number of passive components can be embedded in the substrate. To adapt this technology for ultra wideband (UWB) wireless systems, a wideband bandpass filter in the LTCC substrate is one of the most important technology because it decreases the influences from other wireless systems. Various wideband bandpass filters have already been presented(Ishida & Araki, 2004; Saitou et al.,2005; Li et al., 2005; Zhu et al.,2005; Horii

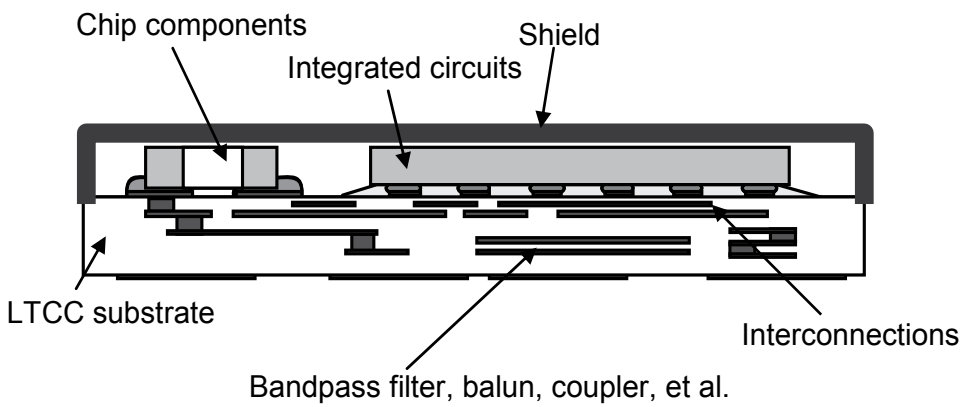

Fig. 1. A general structure of the compact wireless module using the LTCC technology.

et al.,2006; Yamamoto et al.,2007; Shaman & Hong,2007; Tanii et al., 2008 ; Sun & Zhu, 2009). However, these approaches cannot be easily applied for the embedded components in the LTCC substrate. Therefore we have studied the compact wideband bandpass filters based on the LTCC technology(Oshima et al.,2008; Oshima et al.,2010).

In this study, we propose a method for improving out-of-band characteristics of a wideband bandpass filter. It is suitable for the compact UWB wireless modules using the LTCC technology. The UWB systems assume the band group 1 (3.168-4.752GHz) of the multiband orthogonal frequency-division multiplexing systems (Ghorashi et al., 2004).

Section 2 describes a wideband filter using the LTCC technology. We also point out that the filter is desired to improve the attenuation characteristics. Section 3 explains a method for improving out-of-band characteristics. In Section 4 and Section 5, we indicate the LTCC structure of the presented filter, the simulated results, and the experimental results. Finally, the conclusion of this study is summarized in Section 6.

2. Bandpass filter for UWB systems using the low-frequency band

Fig.2 shows the schematic of the wideband bandpass filter for UWB systems using the low-frequency band (Oshima et al., 2010). Resonator 2 is the resonator which has a wide passband and creates attenuation poles near the passband. Resonator 1 and Resonator 3 are tap-feed resonators. The capacitors of C_2 and C_3 are coupling capacitors between the resonators. The capacitors of C_4 and C_5 are used for the impedance matching and they also improve out-of-band characteristics in the high-frequency region. The capacitor C_6 is used to shorten the length of the strip line. In this study, the length of Resonator 3 differs from that of Resonator 1 in order to create two attenuation poles at the high-frequency region. The attenuation pole created by Resonator 1 is given by

$$\frac{jZ_AZ_B}{Z_A \cot \theta_B - Z_B \tan \theta_A} = 0. \tag{1}$$

The attenuation pole created by Resonator 3 is also given by

$$\frac{jZ_EZ_F}{Z_E \cot \theta_F - Z_F \tan \theta_E} = 0. \tag{2}$$

The attenuation poles created by Resonator 2 are given by

$$\frac{Y_0(Y_1 - Y_2)}{(Y_0 + Y_1)(Y_0 + Y_2)} = 0 \tag{3}$$

where,

$$Y_0 = 0.02 \tag{4}$$

$$Y_1 = \frac{1 - 2\omega C_1 Z_D \tan\theta_D}{jZ_D \tan\theta_D} \tag{5}$$

$$Y_2 = \frac{j\tan\theta_D + Y_3 Z_D}{Z_D + jY_3 Z_D^2 \tan\theta_D} \tag{6}$$

$$Y_3 = \frac{j(\omega C_6 Z_C + \tan\theta_C)}{2Z_C(1-\omega C_6 Z_C \tan\theta_C)}. \quad (7)$$

The circuit parameters of the bandpass filter are decided by means of adjusting the parameters in consideration of the conditions for the attenuation poles. This adjustment is carried out by a commercial circuit simulator (ADS, Agilent Technologies, Inc.). Table 1 shows the parameters of the filter. Here, the reference frequency for the electrical length is 4.0 GHz. In this study, we use the physical strip line model in the circuit simulation because this model can simulate the losses of the conductor and the LTCC substrate. Fig.3 shows the physical strip line model. The relative permittivity of the LTCC substrate and the dielectric loss tangent of the substrate are 7.1 and 0.005, respectively. The conductor in the substrate is silver. Fig.4 indicates the results of the circuit simulation. The filter produces good attenuation performances near the passband due to attenuation poles (f_1 and f_2) which are created by Resonator 2. The filter achieves good spurious suppression up to 10 GHz due to the attenuation poles (f_3 and f_4). They are created by Resonator 1 and Resonator 3. The input impedance of the filter is also 50 ohm in the wide passband. However this filter is desired to improve the attenuation characteristics because the filter cannot create a number of attenuation poles at the frequency region lower than the passband and has the spurious responses at the frequency band higher than 10 GHz .

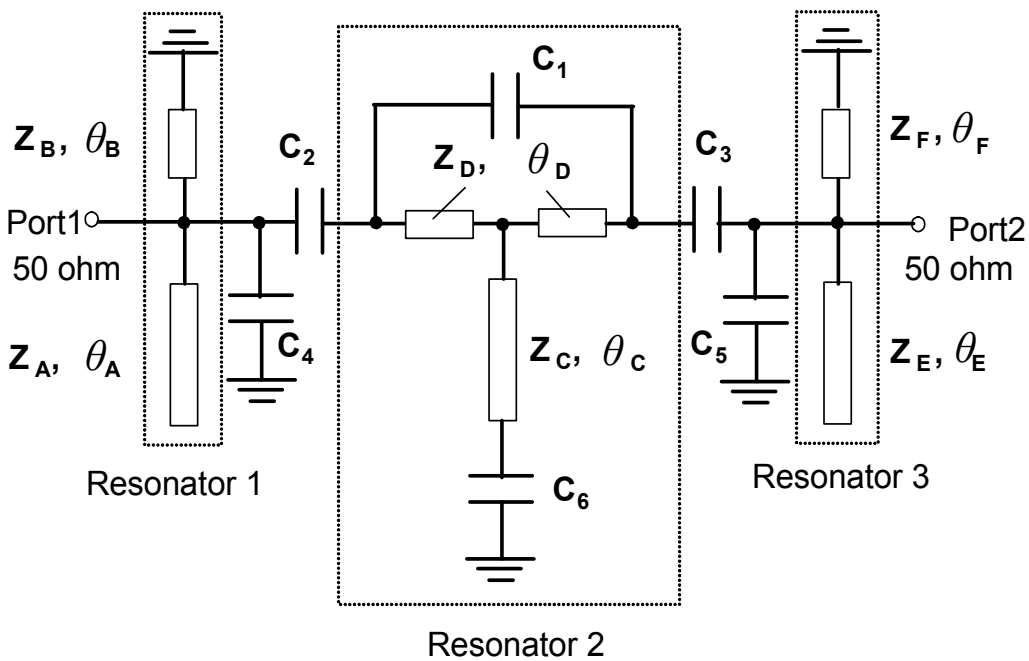

Fig. 2. Schematic of the UWB bandpass filter for the low-frequency band.

C_1	1.0pF	Z_A	46.3 ohm	θ_A	43.9deg.
C_2	0.75pF	Z_B	46.3 ohm	θ_B	26.9deg.
C_3	0.75pF	Z_C	46.3 ohm	θ_C	50.9 deg.
C_4	0.5pF	Z_D	38.6 ohm	θ_D	15.7deg.
C_5	0.5pF	Z_E	46.3 ohm	θ_E	38.4 deg.
C_6	2.7pF	Z_F	46.3 ohm	θ_F	26.9 deg.

Table 1. Parameters for the schematic shown in Fig.2.

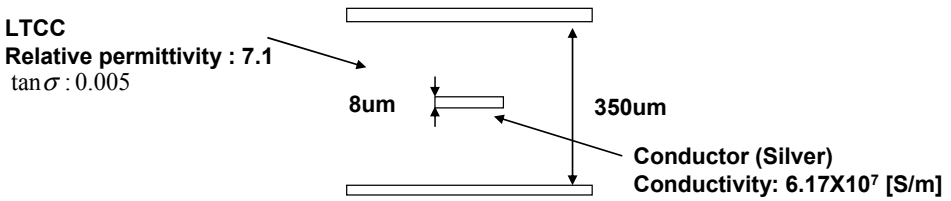

Fig. 3. Physical model for a stripline.

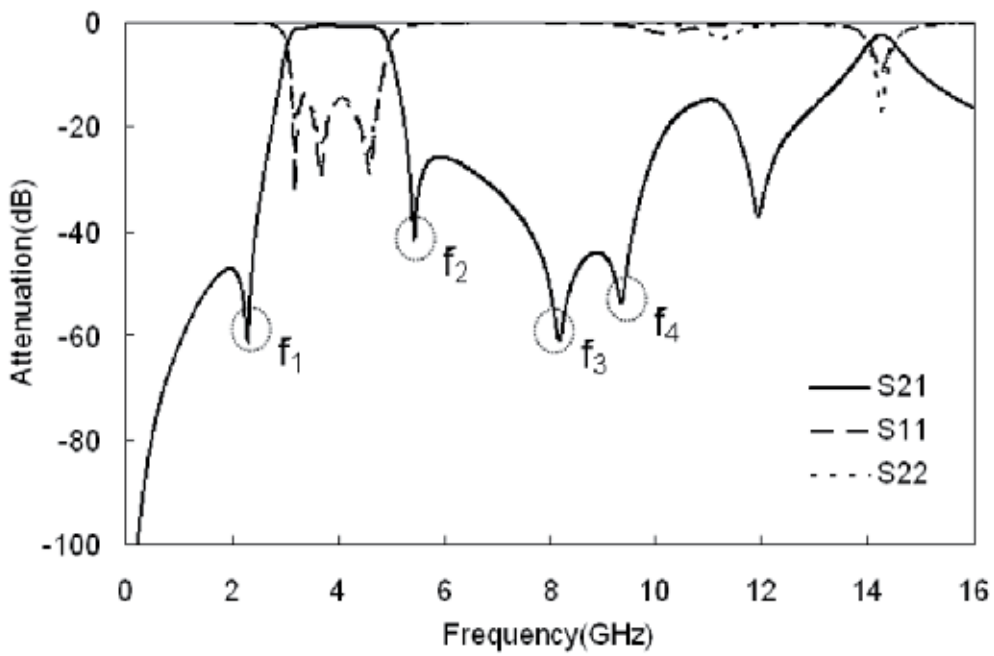

Fig. 4. Simulated results of the filter shown in Fig.2.

3. A method for improving out-of-band characteristics

In order to improve the spurious responses, the lowpass filter is very useful (Kurita & Li, 2007.). Fig.5 shows the schematic of the lowpass filter. This filter consists of a stripline and a capacitor, which is suitable for the embedded components in the LTCC substrate (Ohwada et al., 2002.). Fig.6 indicates the simulated results of the lowpass filter by the circuit simulator. Where, Z_S and θ_S are 46.3ohm and 33 deg.(@4GHz), respectively. In Case A, the capacitor C_a is 0.27 pF. In Case B, the capacitor is 0.34 pF. This lowpass filter can attenuate the frequency region which is higher than 10 GHz. The attenuation characteristics of the filter can be controlled by the value of the capacitor C_a. However, the lowpass filter can not attenuate the low-frequency band.

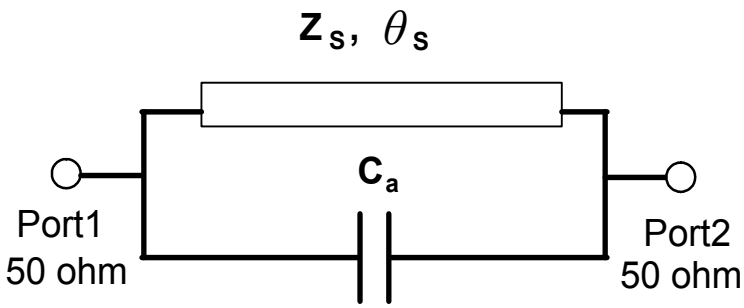

Fig. 5. Schematic of the lowpass filter.

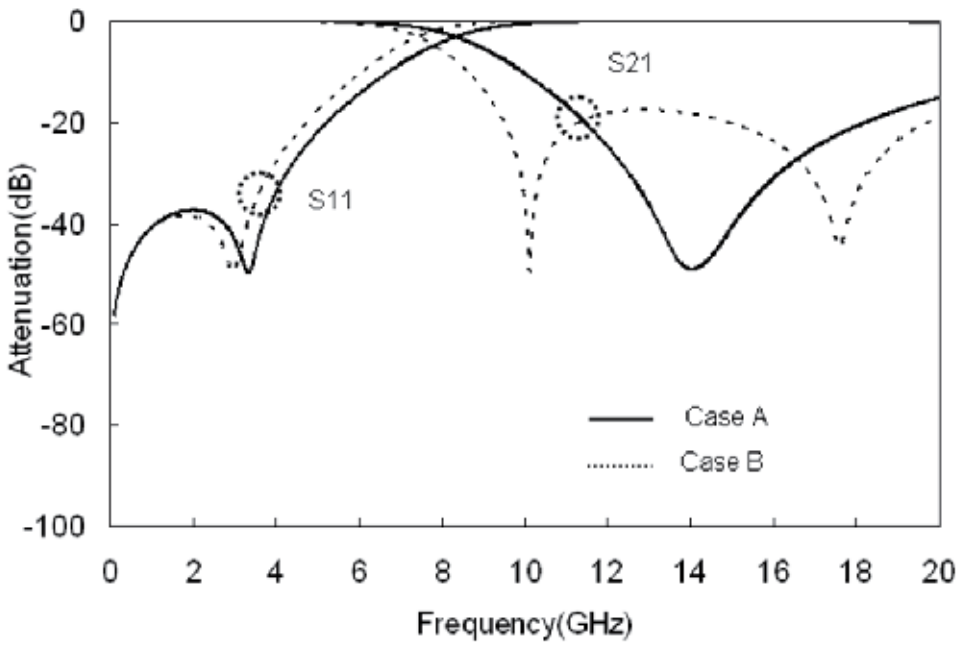

Fig. 6. Simulated results of the lowpass filter shown in Fig.5.

The input/output coupled filter can create attenuation poles (Shaman & Hong. 2007). It is useful for improving the attenuation performances near the passband. However this filter requires the quarter-wavelength coupled line and has the third harmonic.

For improving the out-of-band characteristics of the filter, we propose a method using lowpass filters which consist of the coupling structure. Fig.7 shows the schematic of the filter using the presented method. This circuit adds the lowpass filters at the input/output ports of the filter shown in Fig.2. And a part of the stripline of the lowpass filters is the coupling structure. Table 2 shows the parameters of the lowpass filters shown in Fig.7. In Table 2, the reference frequency for the electrical length is 4.0 GHz. Z_{So} and Z_{Se} are odd- and even-mode characteristic impedances. Fig.8 indicates the simulated results of the filter. We can confirm that the filter has an additional attenuation pole (f_5) at the low-frequency band and suppresses the second and third harmonics. Fig.9 shows the characteristics of the filter, when the coupling condition of the stripline is varied. It is confirmed that the attenuation pole (f_5) is controlled by the coupling stripline. This method uses the weak coupling condition. Therefore it has little effect on the passband and the attenuation poles near the passband. The filter keeps a high attenuation level in the high-frequency region. Note that the locations of attenuation poles especially in the high-frequency region are varied by the coupling condition.

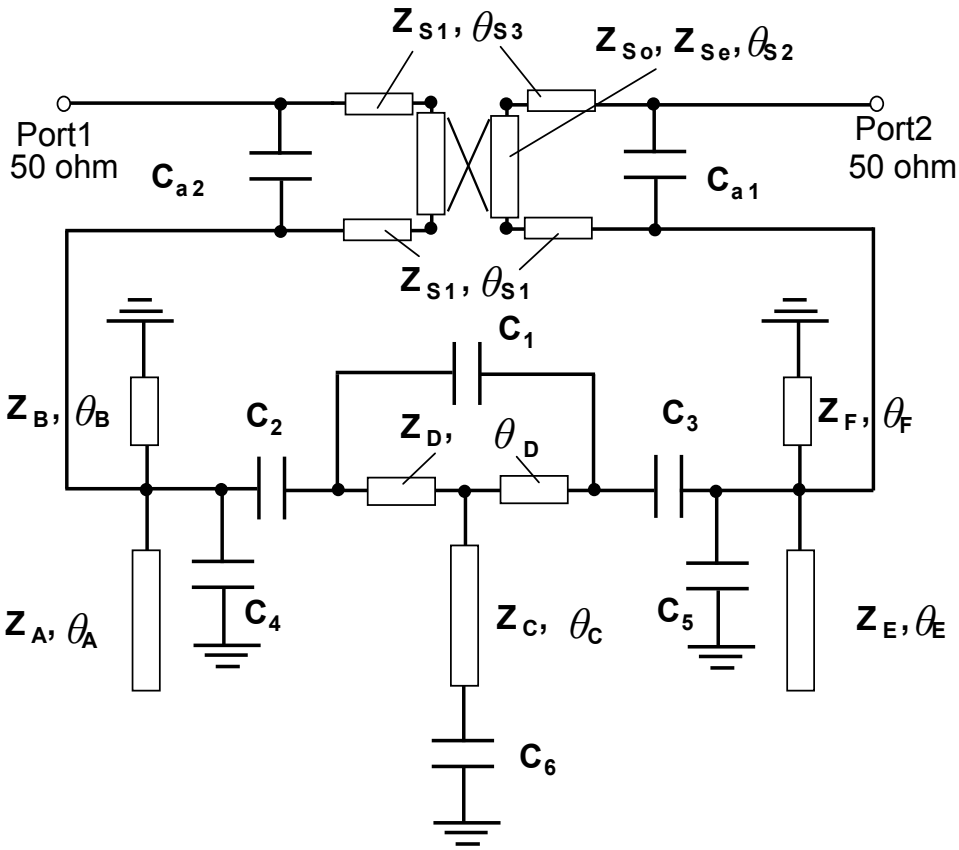

Fig. 7. Schematic of the bandpass filter.

C_{a1}	0.27pF	Z_{S1}	46.3 ohm	Z_{So}	45.7 ohm	θ_{S2}	10 deg.
C_{a2}	0.25pF	Z_{Se}	45.9 ohm	θ_{S1}	18 deg.	θ_{S3}	5 deg.

Table 2. Parameters of the lowpass filters shown in Fig.7.

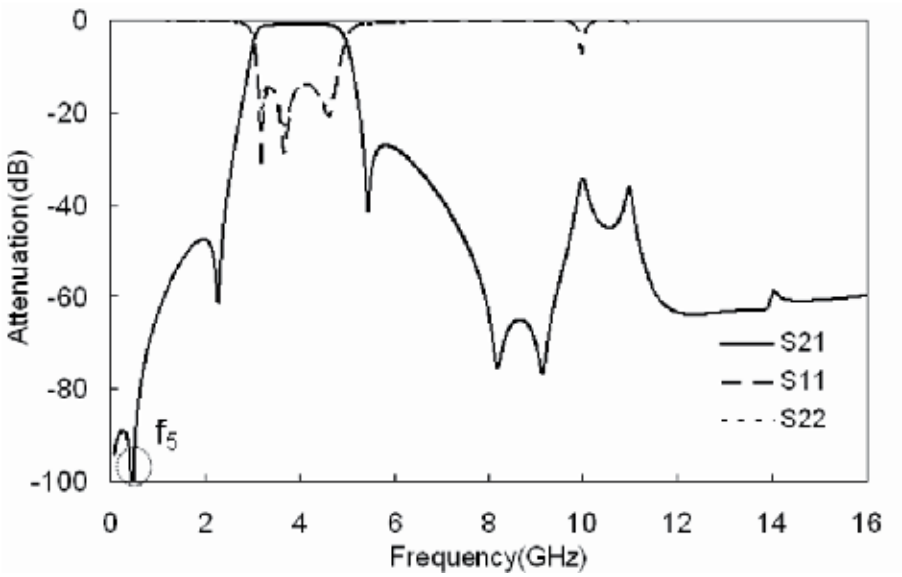

Fig. 8. Simulated results of the filter shown in Fig.7.

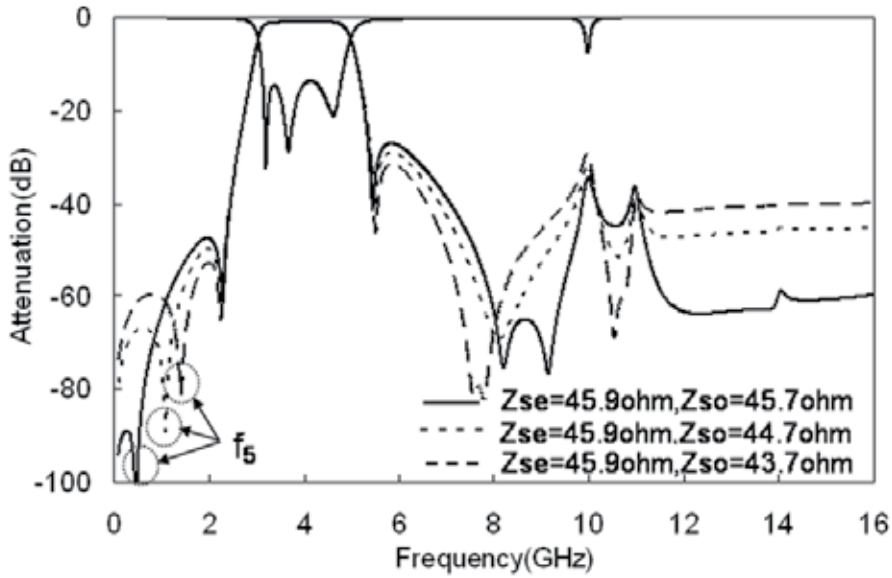

Fig. 9. Simulated results of the filter shown in Fig.7, when the coupling condition of the stripline is varied.

4. LTCC structure

Fig.10, Fig.11 and Fig.12 indicate the LTCC structure of the filter. The filter is obtained by means of modifying the structure based on the basic circuit shown in Fig.7, taking into consideration the various parasitic effects caused by the three-dimensional LTCC structure. The filter consists of the three conductor layers inserted into the middle portion of the LTCC substrate, with the ground planes on the top and bottom layers. The conductor thickness is 8 um. The diameter of via holes is 0.1 mm. The ground planes are connected by the via holes. The via hole between the coupled line adjusts the coupling condition. The dimensions of the bandpass filter are 6.2 x 2.7 x 0.366 mm^3, and this size could be fabricated into the LTCC substrate for wireless modules. Fig.13 shows the simulated results using a commercial electromagnetic simulator (HFSS Ansys Inc.). The filter has the wide passband and suppresses second and third harmonics. The filter also has an additional attenuation pole at the low-frequency region.

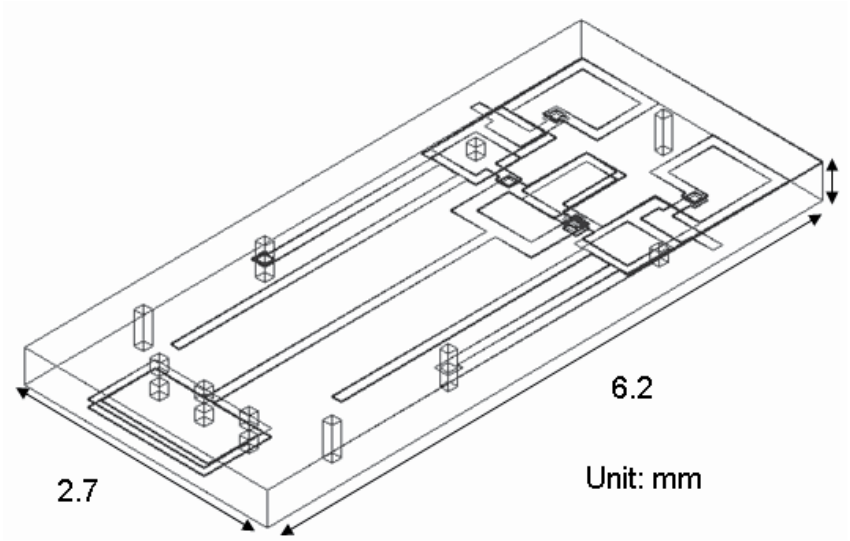

Fig. 10. Three-dimensional structure of the filter.

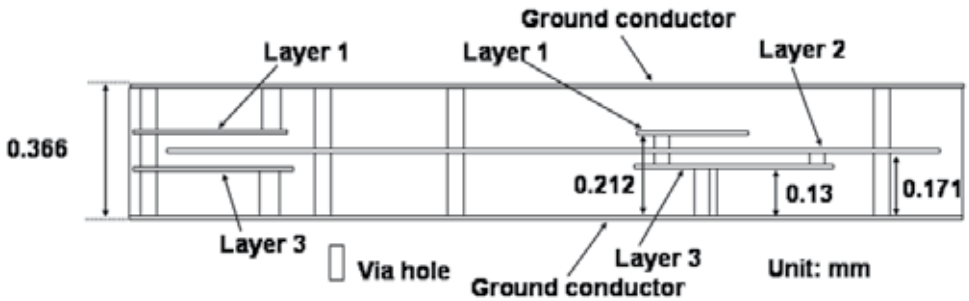

Fig. 11. Cross sectional structure of the filter.

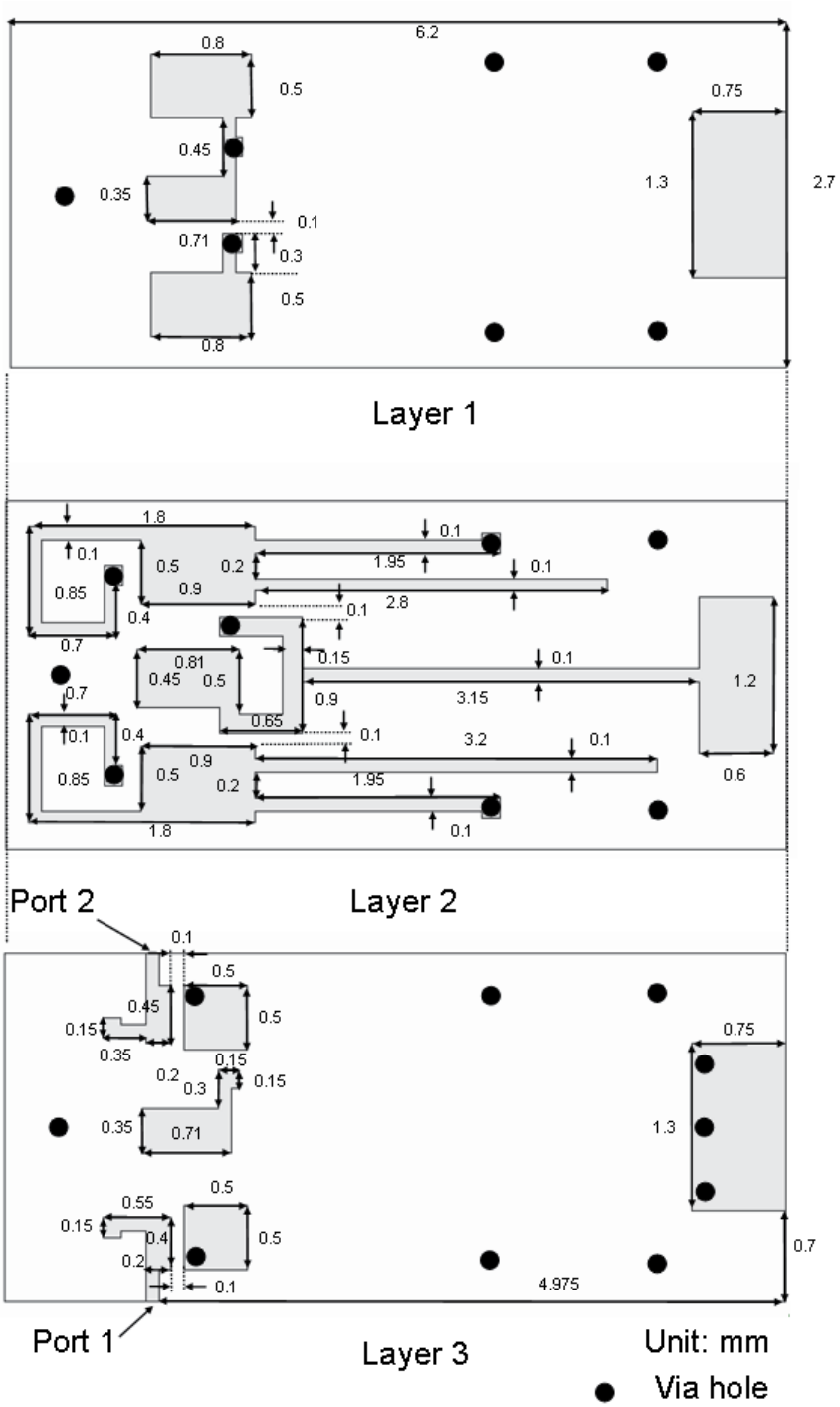

Fig. 12. Top view of the filter.

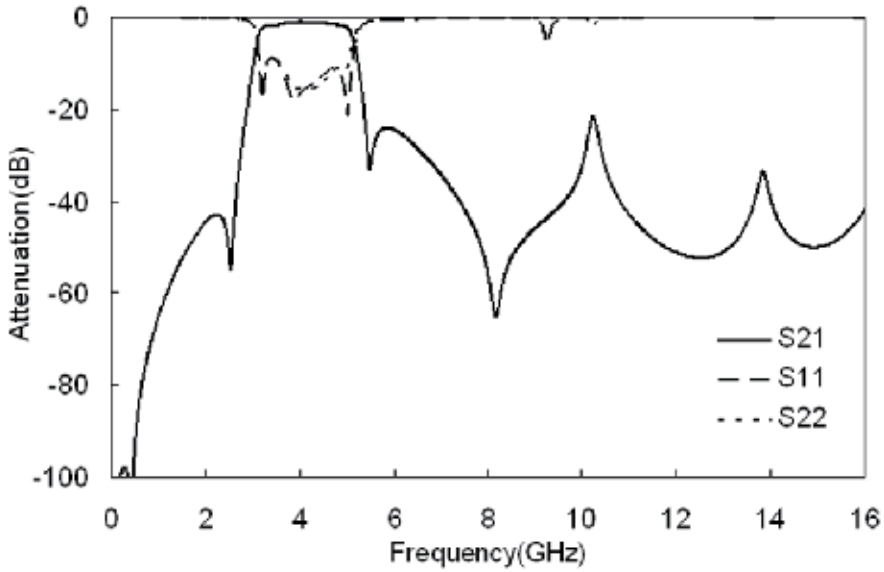

Fig. 13. Simulated results by the electromagnetic simulator.

5. Experiments

We verify the effectiveness of the presented method by experiments. Fig. 14 indicates the LTCC structure for the evaluation of the embedded filter. The dimensions of the LTCC

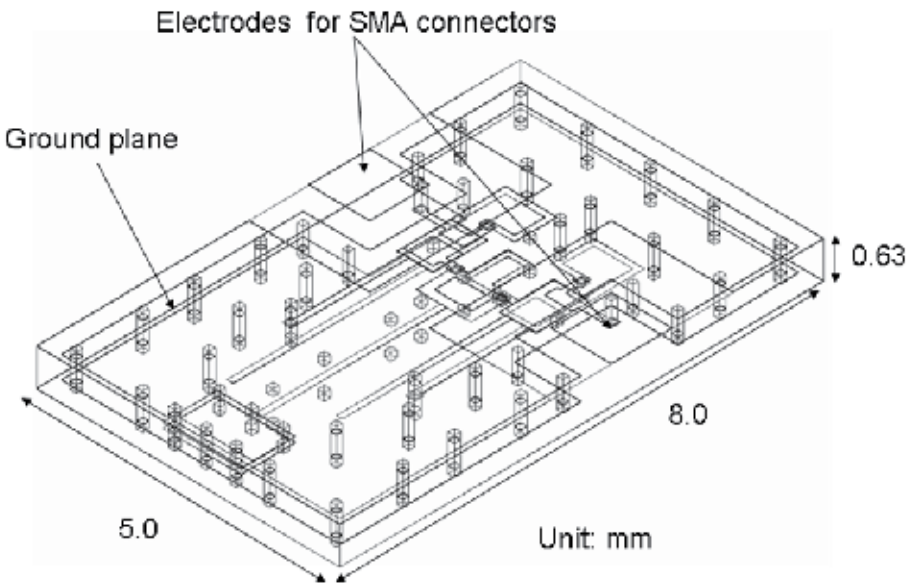

Fig. 14. Structure of the LTCC substrate for evaluation.

substrate are 8.0 x 5.0 x 0.63 mm^3. The presented filter (6.2 x 2.7 x 0.366 mm^3) is fabricated in the substrate. In order to connect the SMA connectors for the evaluation, the top layer of the LTCC substrate has the electrodes for RF signals and a ground plane. The feed lines between the filter and the input/output ports consist of a via hole, a stripline, and the electrode of the top layer. These feed lines are designed 50 ohm. Fig. 15 shows a photograph of the LTCC substrate. The prototype which is connected to the SMA connectors is measured by a vector network analyzer (N5230A PNA-L, Agilent Technologies Inc). Fig.16 and Fig.17 indicate the measured results. It is confirmed that the filter suppresses the spurious responses less than 20 dB up to 16 GHz and has an additional attenuation pole in the low-frequency region. In addition, the insertion loss is less than 3.0dB and the group delay is within 1 ns in the wide passband.

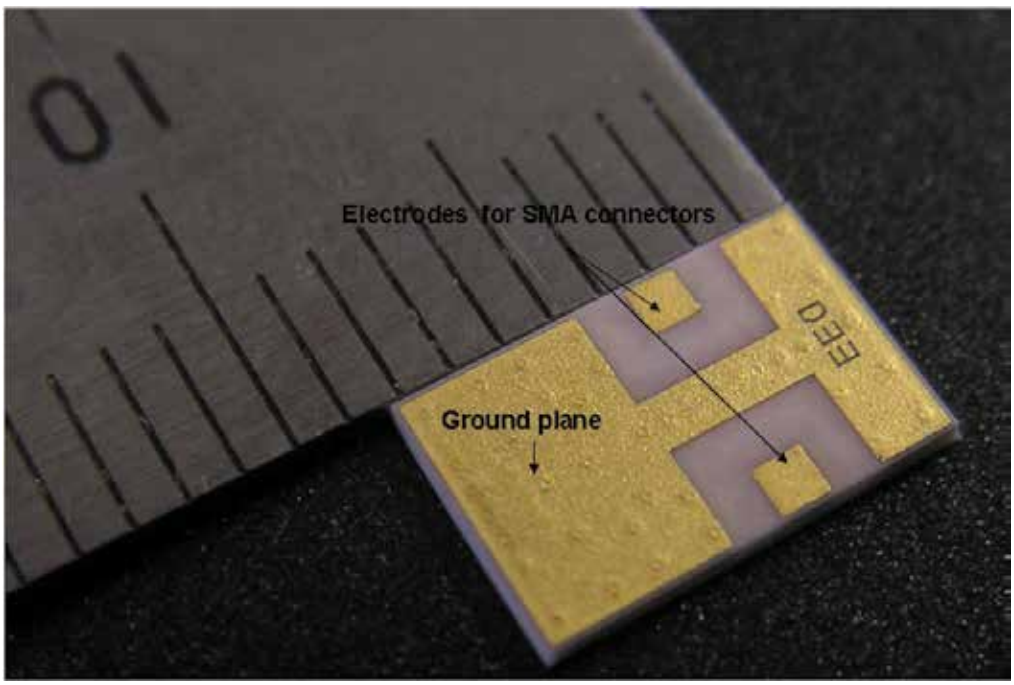

Fig. 15. Photograph of the prototype.

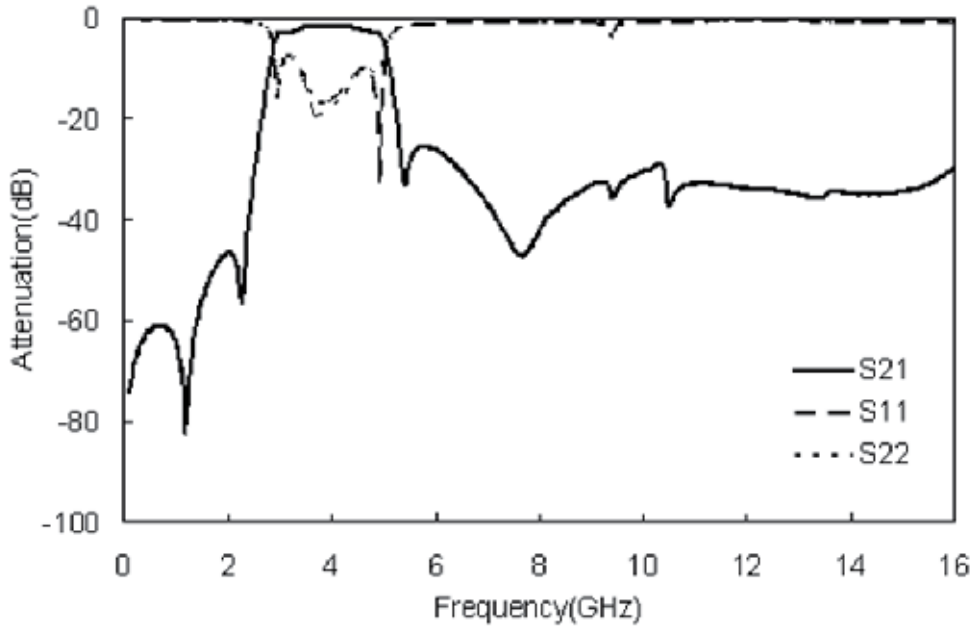

Fig. 16. Measured results of the filter shown in Fig.15.

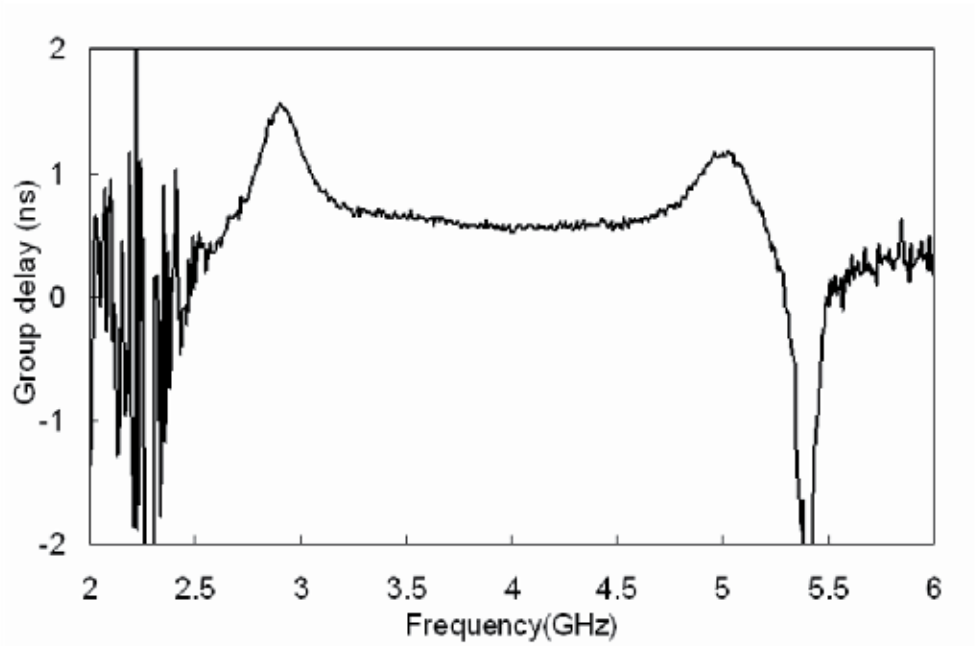

Fig. 17. Measured group delay of the filter shown in Fig.15.

6. Conclusion

In this study, we propose a method for improving out-of-band characteristics for the wideband filter in the LTCC substrate. This method uses the lowpass filters with the coupling structure, which are set at input and output ports of the bandpass filter. This method is very useful for the compact wireless modules because additional compact circuits can suppress spurious responses and can add an attenuation pole in the low-frequency band. The fabricated UWB bandpass filter for the low-frequency band achieves the insertion loss less than 3.0 dB and the group delay within 1 ns in the wide passband. The filter also suppresses spurious responses up to 16 GHz and has the good attenuation performances in the low-frequency region.

7. References

Lin, Y.-S., Liu, C.-C., Li,K.-M., & Chen, C.H. (2004). Design of an LTCC tri-band transceiver module for GPRS mobile applications. *IEEE Transactions on Microwave Theory and Techniques*, Vol. 52, No. 12, pp. 2718-2724.

Wang, G., Van, M., Barlow, F. & Elshabini, A. (2005). An interdigital bandpass filter embedded in LTCC for 5- GHz wireless LAN applications. *IEEE Microwave and Wireless Components Letters,*Vol. 15, No. 5, pp. 357-359.

Ishida, H. & Araki, K. (2004). Design and analysis of UWB bandpass filter with ring filter. *IEEE MTT-S International Microwave Symposium,* pp. 1307-1310.

Saitou, A., Aoki, H. , Satomi, N., Honjo, K., Sato, K., Koyama, T. & Watanabe, K.(2005). Ultra-wideband differential mode bandpass filters embeded in self-complementary antennas. *IEEE MTT-S International Microwave Symposium,* pp. 717-720.

Li, K., Kurita, D. & Matsui, T. (2005).An ultra-wideband bandpass filter using broadside-coupled microstrip-coplanar waveguide structure. *IEEE MTT-S International Microwave Symposium.*, pp. 675-678.

Zhu, L., Sun, S. & Menzel, W.(2005). Ultra-wideband (UWB) bandpass filters using multiple-mode resonator. *IEEE Microwave and Wireless Components Letters,* Vol. 15, No. 11, pp. 796-798.

Horii, Y. , Tanaka, A., Hayashi, T., & Iida, Y.(2006). A compact multi-layered wideband bandpass filter exhibiting left-handed and right-handed behaviors. *IEICE Transactions on Electronics*, Vol. E89-C, No. 9, pp. 1348-1350.

Yamamoto, Y., Li, K. & Hashimoto, O.(2007). Ultra-wideband (UWB) bandpass filter using shunt stub with lumped capacitor. *IEICE Electronics Express*, Vol. 4, No.7, pp. 227-231.

Shaman, H. & Hong, J.-S.(2007). Input and output cross-coupled wideband bandpass filter. *IEEE Transactions on Microwave Theory and Techniques,* Vol. 55, No. 12, pp. 2562-2568.

Tanii, K., Shimizu, Y., Nishimura, F., Sasabe, K., Ueno, Y., Wada, K. & Iwasaki,T.(2008) A study of various wide-band BPFs with attenuation poles using distributed tap-coupling microstrip-line resonators. *IEICE Transactions on Electronics (Japanese Edition)*, Vol.J91-C , No.6 , pp.332-340.

Sun, S. & Zhu, L.(2009). ``Multimode-resonator-based bandpass filters. *IEEE Microwave magazine,* Vol. 10, No. 2, pp. 88-98.

Oshima, S., Wada, K., Murata, R., & Shimakata, Y. (2008). A study of a compact multilayer wideband bandpass filter in LTCC substrate using distributed resonator with

attenuation poles consisted of a capacitor and λ/2 open-ended stub," *IEICE Transactions on Electronics (Japanese Edition)*, Vol.J91-C, No.8, pp.409-417.

Oshima, S., Wada, K., Murata, R., & Shimakata, Y.(2010) . Multilayer dual-band bandpass filter in low temperature co-fired ceramic substrate for ultra-wideband applications. *IEEE Transactions on Microwave Theory and Techniques*, Vol.58, No.3, pp.614-623.

Ghorashi, S.A., Allen,B., Ghavami, M., & Aghvami, A.H. (2004). An overview of MB-UWB OFDM, *IEE Seminar on Ultra Wideband Communications Technologies and System Design, 2004.* , pp.107- 110.

Kurita,D.& Li, K. (2007). Super UWB lowpass filter using open-circuited radial stubs. *IEICE Electronics Express*, Vol.4, No.7, pp.211-215.

Ohwada, T., Ikematu, H., Oh-hashi, H., Takagi, T. & Ishida, O.,(2002). A Ku-band low-loss stripline low-pass filter for LTCC modules with low-impedance lines to obtain plural transmission zeros. *IEEE MTT-S International Microwave Symposium*, pp. 1617-1620.

13

Calibration Techniques for the Elimination of Non-Monotonic Errors and the Linearity Improvement of A/D Converters

Nikos Petrellis[1] and Michael Birbas[2]
[1]*Technological Educational Institute of Larisa,*
[2]*Analogies SA*
Greece

1. Introduction

The Analogue/Digital Converters (ADCs) play a very important role in several wideband applications like wired and wireless high speed telecommunication systems (e.g., 802.11g) or communication over powerlines (IEEE P.1901). High definition TV or high precision real time image processing are also examples of applications that require a conversion rate of several hundreds MSamples/sec or even multi-GSsamples/sec.
While the ADCs may operate in an optimal way when they are initially designed and verified using DC simulation, a transient simulation can designate several problems that appear during the high speed operation. Additional linearity errors are posed by process variations and component mismatches after the chip fabrication. Finally, operating conditions like voltage supply levels and temperature variations can also affect the linearity of an ADC. Several foreground and background calibration techniques have been proposed in the literature. Most of them are developed for specific ADCs and cannot be applied to different ADC architectures.
The most important error sources and the most popular calibration methods for Pipelined, Segmentation/Reassembly and Sigma Delta ADCs as well as a number of generic error compensation methods based on the processing of the ADC output are presented in (Balestrieri et al, 2005). A popular error correction technique used in pipelined ADCs exploits the least significant bit of a "coarse" ADC stage for the error detection and correction. For example, in (Colleran & Abidi, 1993) a 10-bit ADC is constructed by a 4-bit "coarse" and a 7-bit "fine" ADC. The least significant bit of the coarse ADC should match the most significant bit of the fine ADC. Similarly, a 10-bit pipeline ADC consists of a coarse 6-bit and a fine 5-bit ADC in (Sone et al, 1993). Two more recent approaches that are described in (Kurose et al, 2006) and in (Ahmed & Johns, 2005)(Ahmed & Johns, 2008) use 8 stages of 1.5-bit and a 2-bit Flash ADC stage in a 10-bit (or 11-bit in (Ahmed & Johns, 2008)) pipelined ADC architecture. Moreover, in (Ahmed & Johns, 2008), the DAC linearity errors are also taken into consideration. The use of a redundant signed digit also appears at an Analogue-to-Quaternary pipelined converter in (Chan et al, 2006).
The ADC architectures that are based on high precision capacitors suffer from the effects of the mismatch. In (Wit et al, 1993), an additional array of capacitors is used for real time

trimming that is performed by an algorithm implemented on-chip in order to handle component ageing. Trimming arrays are also used in (Ohara et al, 1987). A digital calibration of the capacitor mismatch, the comparator offsets and the charge injection offsets in a pipelined ADC is performed in (Karanicolas et al, 1993) for the improvement of DNL errors.

The biasing of the operational amplifiers used in a pipelined ADC according to the power supply, the temperature and the sampling speed is determined by calibration in (Iizuka et al, 2006). The offset of the residue amplifiers is calibrated in the background in (Ploeg et al, 2005) (Van De Vel, 2009). Background calibration is also performed in (McNeill et al, 2005) where two identical algorithmic ADCs operate in parallel, their output is averaged and any difference in their results steers the calibration procedure. In (Wang et al, 2009), a nested digital calibration method is described for a pipeline ADC that does not require an input Sample/Hold Amplifier. A digital background calibration technique is proposed in (Hung & Lee, 2009) to correct gain errors in pipelined ADCs. This calibration technique performs the error estimation and the adaptive error correction based on the concept of split ADCs. In (Sun et al, 2008), a technique called Commutated Feedback Capacitor Switching is used to extract information about the mismatches of the capacitors used and then this information is exploited by a digital background calibration method.

Post processing techniques offer a different approach to the linearity error reduction of the ADCs. While all the aforementioned techniques target to the correction of the error sources, the post processing methods operate on the ADC output. The Differential or Integral Non-Linearity (DNL/INL) errors can be measured in order to estimate correction factors for each output code. These correction factors are stored in large lookup tables and are added to or subtracted from the corresponding output codes at real time. These lookup tables are also subject to real time calibration as described in (De Vito et al, 2007). The estimation of the correction factors can be performed in the simplest case by applying successive DC levels at the ADC input and measuring the DNL of the generated ADC output codes (Provost & Sanchez-Sinencio, 2004). More sophisticated techniques apply a sinusoidal signal to the ADC input and construct a Histogram using the resulting ADC output in order to estimate the DNL errors and consequently the correction factors (Correa-Alegria & Cruz-Sera, 2009).

In this chapter, some representative calibration approaches presented in the literature are described emphasising on the more general ones in the sense that they can be applied to different ADC architectures. Moreover, the calibration schemes proposed by the authors in a current mode implementation of a 12-bit ADC with a novel binary tree structure (Petrellis et al, 2010a) as well as in a voltage mode subrange ADC (Petrellis et al, 2010b, 2010c) are also presented since they can also be used in different target applications.

2. Resistor and capacitor trimming

The highest speed ADCs are based on the Flash or Parallel architecture where the input signal is concurrently compared to 2^n reference levels generated by a resistor ladder consisting of identical resistors R. The Flash ADCs cannot offer a high resolution (it is practically lower than 8-bits) since the required area and power is increased in an exponential manner. Linearity is essential in these ADCs in order to prevent the already low dynamic resolution from a further reduction.

A significant linearity error source in these ADCs is the component mismatches in the resistor ladders. If the tolerance in these resistors is expressed as $\pm k\Delta R$, then it can be reduced to $\pm\Delta R$ as shown in Fig. 1a where each resistor R has been replaced with a resistor $R\text{-}k\Delta R$ connected in series with $2k$ trimming ΔR resistors that can be bypassed by the calibration algorithm or at a final stage of the fabrication process.

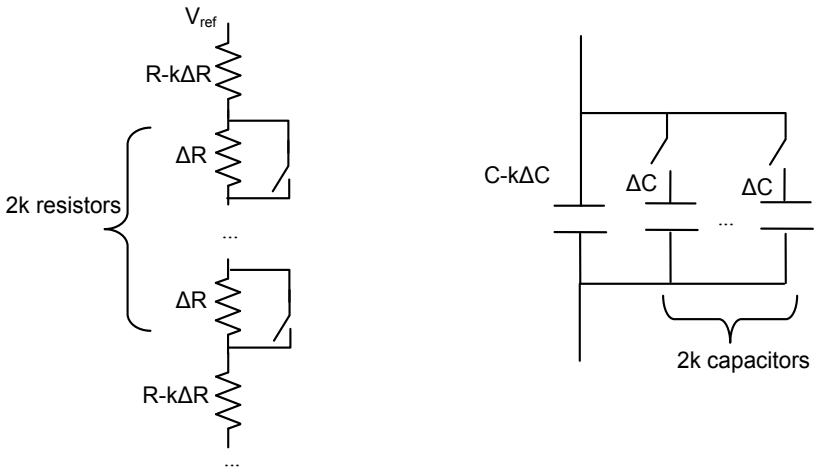

Fig. 1. Resistor (a) and Capacitor (b) trimming

High precision capacitors are used in several ADC architectures that are based on charge redistribution, integrators, Sigma-Delta ADCs etc (Quiquempoix et al, 2006). Capacitor trimming can be performed in a similar way to the resistors whenever high precision capacitors have to be used (Wit et al, 1993). A simple way to perform such a capacitor trimming is shown in Fig. 1b. If the tolerance of a capacitor C is $\pm k\Delta C$ then, by using a fundamental $C\text{-}k\Delta C$ capacitance and $2k$ trimming capacitors ΔC that can be potentially connected in parallel, the tolerance can be reduced to $\pm\Delta C$.

3. Redundant bits in pipeline ADCs

Pipeline, Subfolder and Subrange ADCs can achieve a descent resolution higher than 8-bit with a conversion speed that is comparable to that of the Flash ADCs. This is achieved by using a number of Flash ADC stages with lower resolution. For example in a two stage Pipeline ADC with $m+n$ bits resolution, the analogue input is connected to a "coarse" m-bit ADC that generates the m most significant bits. These bits are used as input to a DAC in order to reconstruct an analogue signal that is subtracted by the original input and a residue is generated that serves as input to the second "fine" ADC stage that has an n-bit resolution. If the "coarse" ADC generates $m+1$ instead of m bits but the least significant bit is not input to the DAC as shown in Fig. 2, then this least significant bit should match the most significant bit of the n-bit "fine" ADC, otherwise the subtraction or the DAC operation has not been performed accurately enough (Iizuka et al, 2005)(Van De Vel et al, 2009). In this case, the offset of the subtraction operational amplifier or a resistor/capacitance trimming at the side of the DAC may be necessary.

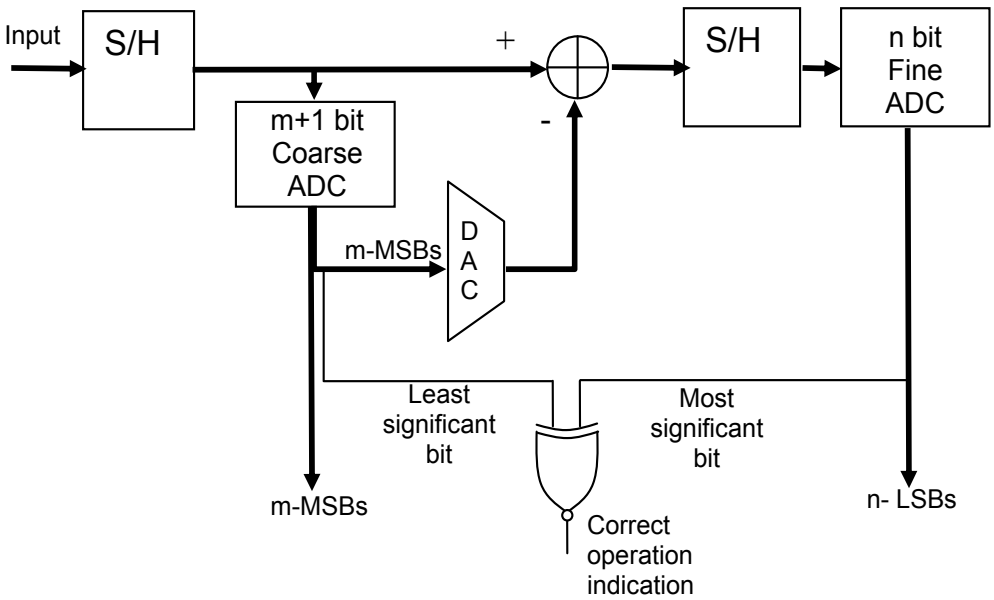

Fig. 2. Two stage pipeline ADC with a redundant bit correction

4. Bias adjustment

The biasing of the operational and differential amplifiers used in several ADC architectures like pipeline or Sigma Delta ADCs often requires an accurate real time calibration around a typical value. An ordinary DAC cannot offer a high resolution adjustment since its dynamic range spans from 0 volts to its maximum range and is not focused around the typical bias

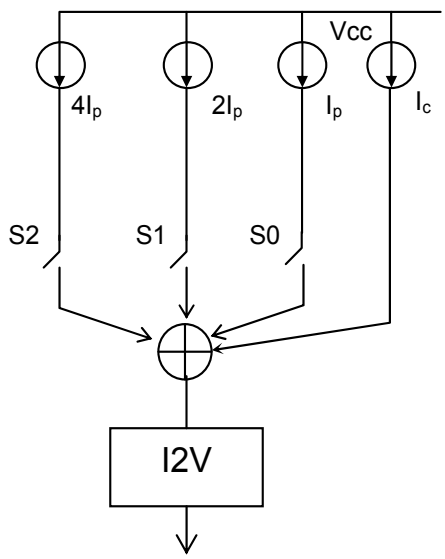

Fig. 3. A 3-bit DAC with offset

value that is required. For example, if an accurate adjustment has to be performed around 500mV in a range of ±16mV in steps of 1mV, then an ordinary 10-bit DAC would be required with reference voltage of 1024mV. Such an ADC is capable of providing any of the voltages between 0 and 1023mV in steps of 1mV, but most of these output levels would be unused in the specific bias requirement.
A much lower area/power 5-bit DAC would be sufficient if it could provide an offset of 484mV and a dynamic range of 32mV above the 484mV level. This can be achieved e.g., with a weighted current source DAC with offset like the one presented in (Petrellis et al, 2010a). An example of such a 3-bit DAC is shown in Fig. 3. The output current range of such a DAC is $[I_c..I_c+7I_p]$ according to the switch configuration. Of course, this current range can be mapped to a voltage one through the current to voltage converter I2V that can be simply a resistor R. In this case the voltage range is $[RI_c..R(I_c+7I_p)]$

5. Averaging the output of a pair of identical ADCs

Another method for the detection and the correction of errors at an ADC output is based on the generation of a duplicated output by a pair of identical ADCs (McNeil et al, 2005). For example, if two ADCs accept the same input they should generate the same digital output. Nevertheless, their outputs may differ slightly due to component mismatches and process variations. The averaging of these outputs can lead to an error reduction. Assuming that the ADC digital outputs are $D+\varepsilon 1$ and $D+\varepsilon 2$ respectively, where D is the ideal output and $\varepsilon 1$, $\varepsilon 2$ are the signed errors of each ADC output, the averaged output is

$$D' = D + \frac{\varepsilon 1 + \varepsilon 2}{2} \tag{1}$$

If $\varepsilon 1<0$ and $\varepsilon 2>0$ the averaged output has lower error than any of the two separate ADC outputs. Moreover, there is a great possibility that $\varepsilon 1=-\varepsilon 2$ and in this case the error is totally eliminated. In the worst case where $\varepsilon 1$ and $\varepsilon 2$ have the same sign, the averaged output has smaller error than the higher $\varepsilon 1$ or $\varepsilon 2$ error. More specifically if $|\varepsilon 1|<|\varepsilon 2|$ then

$$|\varepsilon 1| < \left|\frac{\varepsilon 1 + \varepsilon 2}{2}\right| < |\varepsilon 2| \tag{2}$$

The main drawback of this approach is the required die area and power duplication. A difference in the ADC outputs may trigger a more sophisticated calibration algorithm that corrects the error at its source instead of simply using the average of these outputs.

6. Lookup tables with DNL error correction factors

Another error correction technique that is based on the processing of the ADC output, estimates the DNL error of each output code and a corresponding correction factor. All of these correction factors are stored in a lookup table and are accessed at real time in order to determine how the current output code should be altered to improve linearity.
The DNL error is defined using the ADC transfer function shown in Fig. 4. In the ideal case, any output code should have the same width as the Least Significant Bit (LSB):

$$LSB = \frac{V_{ref}}{2^n} \tag{3}$$

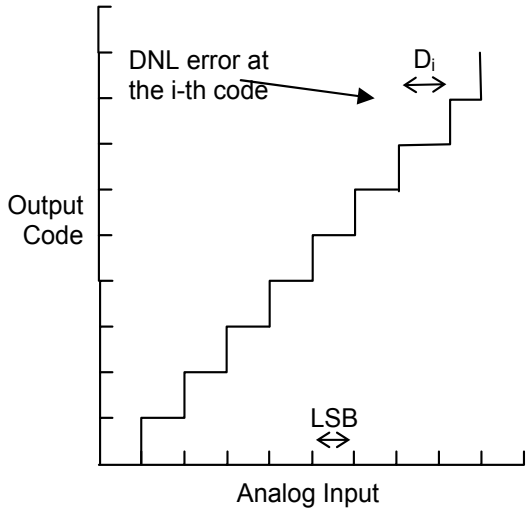

Fig. 4. DNL error

The parameter V_{ref} is the maximum input voltage of the ADC and n is its resolution. The DNL error represents the relative difference of the actual code width from the LSB:

$$DNL_i = \frac{D_i - LSB}{LSB} \tag{4}$$

If the D_i code is corrected by a factor f_i that is defined as:

$$f_i = LSB - D_i \tag{5}$$

the corresponding DNL_i error would be eliminated. Nevertheless, it is easier to estimate the initial DNL_i error of a code instead of its width D_i using for example the Histogram method (Correa-Alegria & Cruz-Sera, 2009). The correction factor can be estimated in this case as:

$$f_i = LSB - LSB(DNL_i + 1) = -LSB \cdot DNL_i \tag{6}$$

The lookup tables with the correction factors may also require real time calibration as described in (De Vito et al, 2007).

7. Current mode circuit calibration

In current mode implementations of ADCs, the current mirrors play a very important role. For example, in current mode Flash ADCs, the input current is compared to a number of current levels that are generated from a single reference level using appropriately scaled mirrors. The input (I_{in}) and the output current (I_{out}) of a simple current mirror consisting of transistors with the same length and width W_{in} and W_{out} respectively, that operate in saturation mode can be approximately expressed as:

$$\frac{I_{out}}{I_{in}} = \frac{W_{out}}{W_{in}} \tag{7}$$

Nevertheless, this scaling is not as accurate as indicated by equation (7) due to component mismatches, while it is also affected by temperature. Cascode current mirrors offer a higher accuracy and temperature stability than simple current mirrors due to higher output resistance but their usage leads to slower implementations.
In (Petrellis et al, 2010a) two versions of an ADC that is based on a current mode integer division are presented. Higher speed can be achieved by using simple current mirrors instead of cascode ones for the generation of reference currents and the implementation of operations like subtraction and multiplication/division by a constant. Since simple current mirrors are faster but more sensitive to component mismatches and temperature variations than cascode ones, replacing some critical simple current mirrors with gain-boosted ones in such an ADC can reassure its correct operation without sacrificing speed. The biasing of these gain-boosted mirrors is controlled by an appropriate calibration algorithm.
The novel ADC architecture presented in (Petrellis et al, 2010a) is based on the integer division of an input current I_{in} by the reference current I_{ref} and is defined using the following relation (q represents the integer quotient):

$$qI_{ref} \le I_{in} < (q+1)I_{ref} \tag{8}$$

The current mode integer division can be implemented by the circuit shown in Fig. 5. If the relation (8) holds, then q current comparators are active connecting the same number of I_{ref} current sources at the output. Thus, the quotient q is expressed as a multiple of the reference

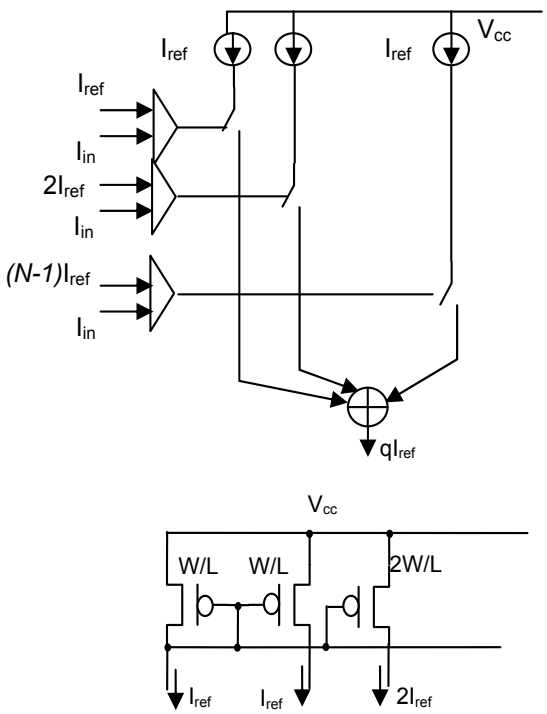

Fig. 5. A current mode integer divider

current I_{ref}. All the I_{ref} current sources are implemented using current mirrors with equally sized transistors, while the $2I_{ref}$, $3I_{ref}$, etc, levels are generated by current mirrors with output transistors that have twice, or three times respectively the width of the input transistor as shown at the bottom of Fig. 5.

A novel ADC architecture based on integer division was presented in (Petrellis et al, 2010a) and is shown in Fig. 6. A binary tree structure is used and each node of the tree implements an integer division by a number of the form: 2^{2^L}, where L is the level of the tree (leaves are assigned to level $L=0$). The quotient and the residue of such a division are the outputs of each node and are connected to subtrees that correspond to ADCs with lower resolution. The residue can be estimated by subtracting the quotient from the original input of the integer divider. For example, if a copy of the input signal is available at the output of a PMOS current mirror and a quotient copy is available at the output of a NMOS current mirror, the subtraction can be carried out by simply connecting these two outputs and driving the residue to the input of a second NMOS current mirror.

Simple current mirrors with small transistors can be used to implement time critical operations of the ADC architecture that is shown in Fig. 6. At such critical nodes like the ones at the root of the binary tree of Fig. 6, gain-boosted current mirrors can be used like (M5, M6, IC0) and (M7, M8, IC1) that are shown in Fig. 7.

Fig. 7 also shows how the amplitude and offset of a current signal like the residue of the integer division can be adjusted by an equation like (9).

$$I_r = a_g(I_{in} - I_q) - a_{off} I_{off} \tag{9}$$

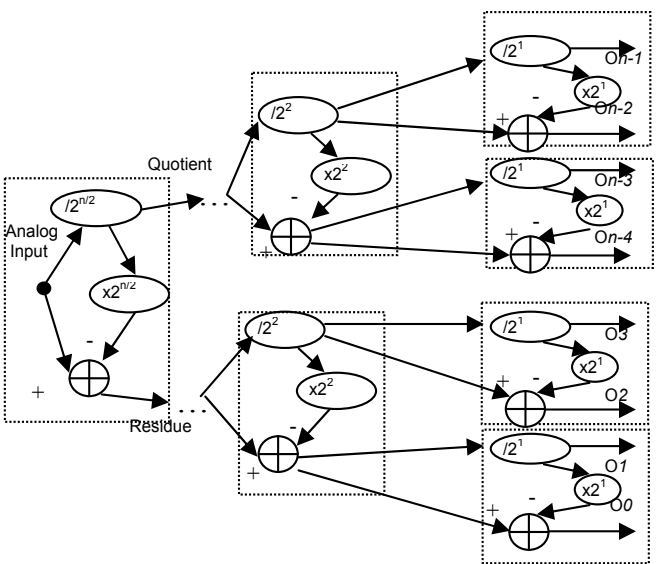

Fig. 6. An ADC with a binary tree structure

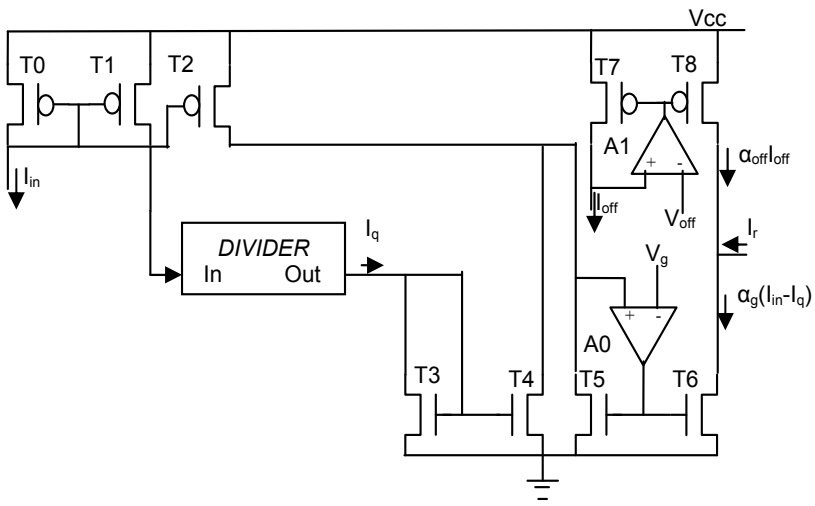

Fig. 7. Gain boosted current mirrors used in the residue adjustment of the integer divider

The a_g and a_{off} gain factors of the corresponding *A0* and *A1* operational amplifiers are determined by the voltages V_g and V_{off} respectively, through an appropriate calibration method that detects whether the residue signal has been shifted up e.g., due to high temperature or if its amplitude is different than the one expected. This conclusion can be extracted by the digital codes at the output of the ADC (e.g., missing codes). If the calibration method detects through missing output codes that the residue signal has been shifted up, it can remove higher offset $a_{off}I_{off}$ current by increasing a_{off} through V_{off}. Similarly, if the residue amplitude is detected to be smaller than the one expected, it can be increased through the appropriate adjustment of a_g.

The gain-boosted current mirrors can also be used in different ADC architectures like current mode pipeline ADCs. The adjustment of the subtraction outcome between the DAC output of a pipeline stage from its input in order to generate the residue can be carried out by a gain boosted current mirror arrangement like the one presented in Fig. 7.

8. Non-monotonic error elimination

Non-monotonic errors are a significant issue at several architectures but fortunately in most cases they do not appear at random transitions. For example, in two-stage pipeline ADCs such monotonic errors may appear during the transition of the residue signal between two peak values. For example, the sawtooth signal shown in Fig. 8 may represent two periods of a pipeline ADC residue. As can be seen in this figure the linearity of this residue is not very good since this signal does not start to rise immediately. Moreover, non-monotonic errors appear during the falling edge of each tooth since it does not fall immediately from its peak value to its minimum.

In ADCs like the ones presented in (Petrellis et al, 2010a) the severe non-monotonic errors appear whenever the bit No. 4 changes. Generally we assume that non-monotonic errors appear when the bit B_i of an ADC changes. These non-monotonic errors are caused by slow falling edges like the one shown in Fig. 8 at the residue of the root ADC divider of Fig. 6.

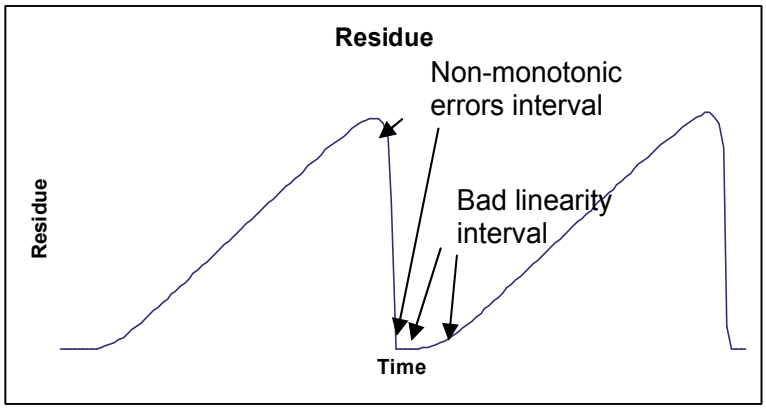

Fig. 8. Residue imperfections

A simple way to handle this kind of problem is to detect the changes in the bit No. 4 and keep the previous ADC output stable for an interval equal to the falling edge of the residue. Although, this technique does not lead to a linear solution, it eliminates most of the non-monotonic errors that are more important than the ones of the linearity. A simple analogue circuit capable of performing this non-monotonic error elimination is shown in Fig. 9.
When the input of each XOR gate in Fig. 9 rises from 0 to 1 the connected capacitor is charged almost immediately but when the input changes from 1 to 0, the capacitor is discharged through the resistor connected in parallel with the capacitor. During the time that it takes the capacitor to discharge the inputs of the corresponding XOR gate are different and its output is 1 generating a pulse with a duration that is determined by the *RC* constant. A pair of *RC* components are driven by the *Q* and the *Q*~ output of the D-flip flop that is used at the input of this circuit in order to generate a pulse at the *BUSY* signal both at the rising and the falling edge of the observed bit B_i of the ADC output. The *BUSY* signal indicates to the system that reads the ADC output, should not take into consideration this output as long as the *BUSY* signal is active.

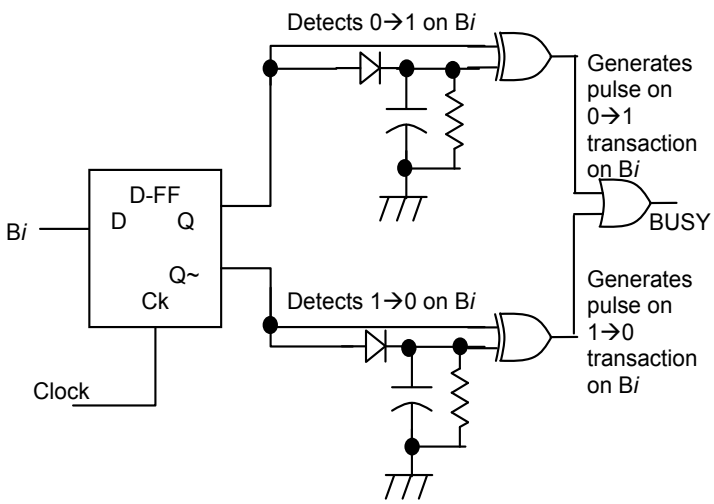

Fig. 9. BSY signal generation based on RC time interval

The BUSY signal duration cannot be determined very accurately in the way described above because it depends on the *RC* constant. A higher precision digital *BUSY* signal generator is shown in Fig. 10. The XOR gate of Fig. 10 compares two successive values of the observed ADC output bit B_i. If they are different, a timer is enabled activating the *BUSY* signal for a specific time period that is determined from simulation results. The effect of the *BUSY* signal use is shown in Fig. 11 where the ADC output is reconstructed by an ideal DAC at the top of this figure and the non-monotonic error reduction that occurs when the *BUSY* signal is taken into consideration is shown at the bottom of this figure.

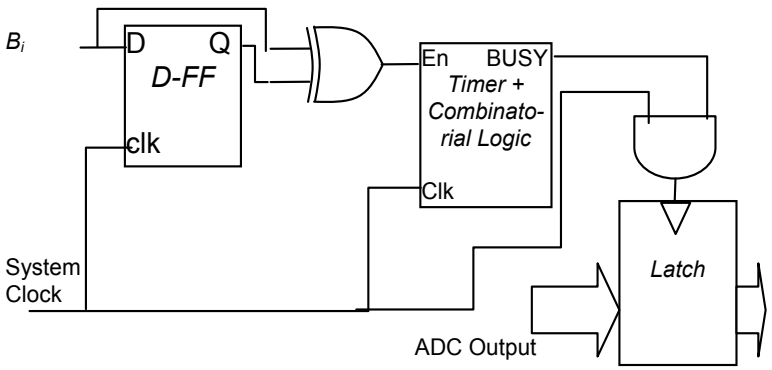

Fig. 10. BUSY signal generation based on digital circuit

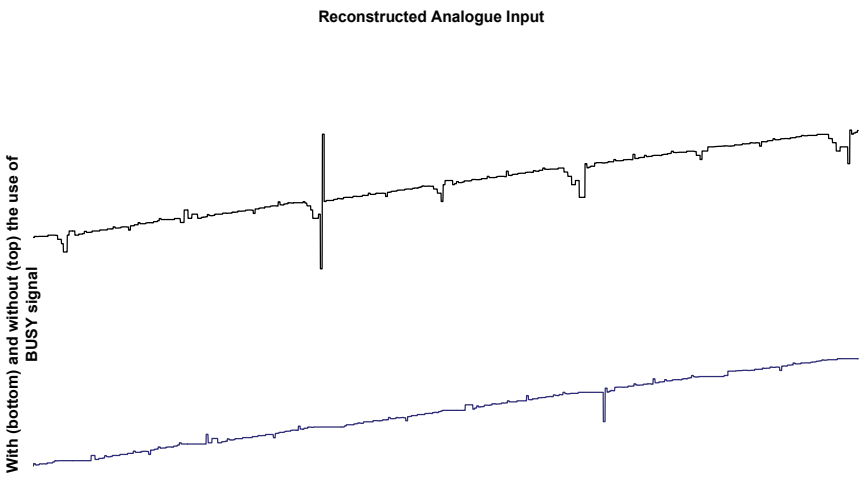

Fig. 11. Non-monotonic error reduction with the use of the BUSY signal

9. Correction of differential signals in voltage mode ADCs

High speed conversion is achieved by ADCs that operate on differential signals. The differential amplifiers are faster because the stage that converts the differential signal to a

single-ended one is omitted. Moreover, differential signals are more immune to noise interference.

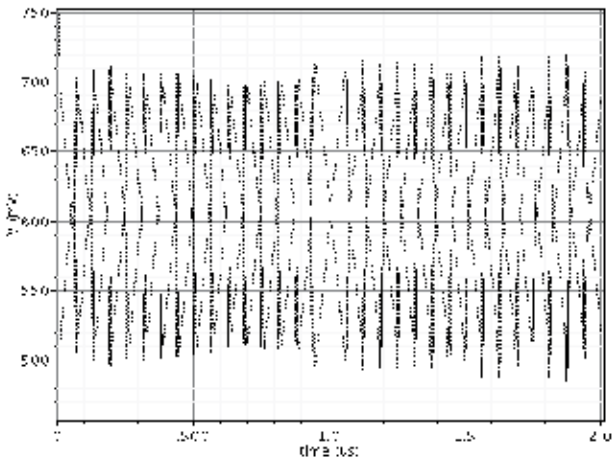

Fig. 12. Expected differential residue

In voltage mode ADCs like the one presented in (Petrellis et al, 2010b, 2010c), the differential amplifiers that are used to perform addition or subtraction are also sensitive to component mismatches that can lead to the drifting of the output differential signals, away from their predefined levels as well as the modification of their amplitude. The authors propose a calibration method that continuously observes such differential signals and shifts them appropriately to their correct positions. Auxiliary components like draft frequency detectors and digital to analogue converters that generate fine voltage levels around an offset, are also required in such ADC architectures and are described in this paragraph.

A monitoring circuit can be used to decide whether two differential signals overlap or not. For example, if Fig. 12 shows the optimal differential residue signals form, then a voltage comparator that accepts as input these differential signals can decide whether they overlap or not.

The circuit shown in Fig. 13a monitors two differential signals (V^+, V^-) and can control the level shifter logic of Fig. 13b. The circuit shown in Fig. 13b can insert delay and shift appropriately the inputs (V_i^+, V_{i^-}) of a differential amplifier stage. Delaying and shifting just one of the differential amplifier inputs (V_i^+ in the case of Fig. 13b) is adequate in order to set the amplifier outputs at the correct level. More specifically, the offset of the signals V_i^+ and V_i^+ can be determined by the bias voltages V_{b1} and V_{b2} respectively. The bias voltage V_{b2} can be connected to a constant source while V_{b1} can be controlled by the Digital to Analogue Converter (DAC) of the circuit presented in Fig. 13a.

When the calibration starts, the counter of Fig. 13a is cleared, shifting away the signals V_i^+ and V_{i^-}. Consequently, the outputs V^+ and V^- of the following differential amplifier stage are also shifted away. The comparator output at the input stage of the differential signal monitor shown in Fig. 13a is low, enabling the counting operation. The increasing counter output values force the differential amplifier input and output signals to get closer. When these signals start overlapping, the D-flip flop output will be set, disabling a further level shifting and after this time point, the differential amplifier output will have the desirable form of Fig. 12.

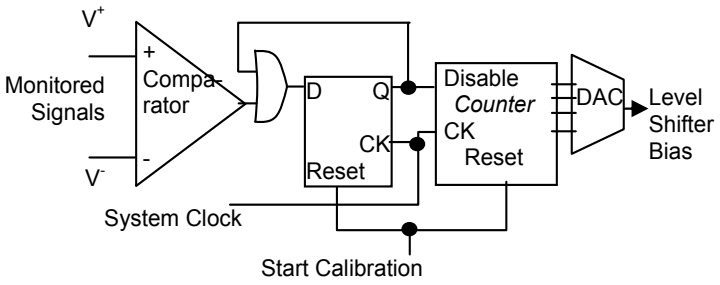

(a)

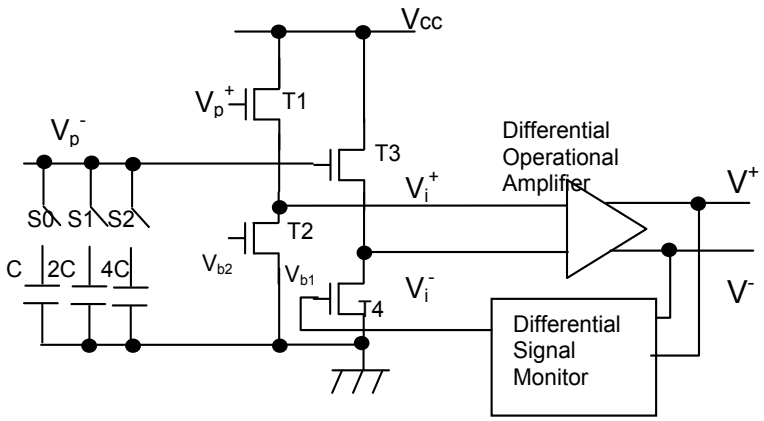

(b)

Fig. 13. Differential Signal Monitor (a) and Delay Insertion/Level Shifting circuit (b)

A higher resolution can be achieved at the output of the DAC in the range that we are interested in, if a DAC with offset is used like the one presented in paragraph 4. An undesirable phase difference in the signals V_p^+ and V_p^- can be corrected by connecting a combination of capacitors (0..7C) in parallel as shown in Fig. 13b.

The undesirable phase shift of the signals V_p^+ and V_p^- is usually dependent on the frequency of these signals. Consequently, a module that detects the draft frequency range of such signals could be employed to decide the appropriate capacitance combination through the switches *S0-S2* of Fig. 13b and such a circuit is shown in Fig. 14.

The comparator of Fig. 14 and the 2nd Counter are used to enumerate how many times a monitored differential signal like V_p^+ crosses a reference voltage V_{cmp} in a time interval specified by the 1st Counter of Fig. 14. The Combinatorial Logic circuit disables both counters after the specified time interval. The output of the 2nd Counter can directly give an indication of the draft frequency range that was detected if this time interval has an appropriate duration. The switches *S0-S2* of Fig. 13b can be directly connected to the output of the 2nd Counter.

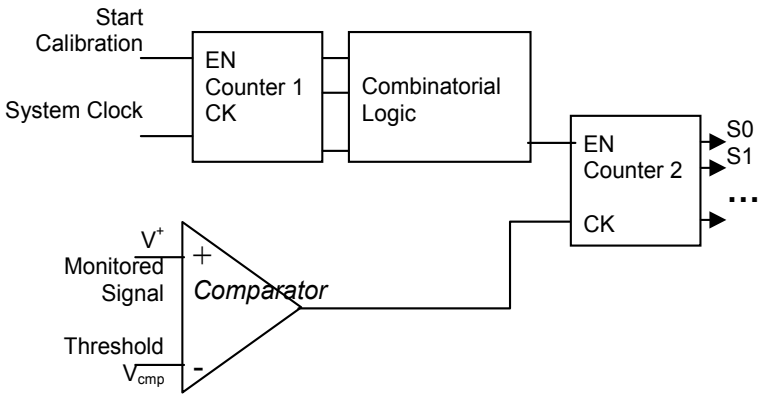

Fig. 14. Frequency Range Detector

The 2nd Counter output of the draft range detector of Fig. 14 can also control the bias of an ADC pipeline stage that accepts as input the signals V^+ and V^-. More specifically, if this stage is implemented as a Flash ADC, the resistor ladders that generate the Flash comparator reference voltage levels may require different bias for different signal frequencies. This is due to the fact that the amplitude of this Flash ADC input signal is usually reduced at high frequencies because the previous pipeline stages may not be fast enough to reach their maximum amplitude as the frequency increases. Instead of attempting to adjust the same signal amplitude in all frequency ranges, the resistor ladder bias can be adapted to the input signal amplitude at a specific frequency. The output *S0-S2* of the frequency detector shown in Fig. 14 can adjust this bias by connecting different voltage dividers or active DC voltage level generators.

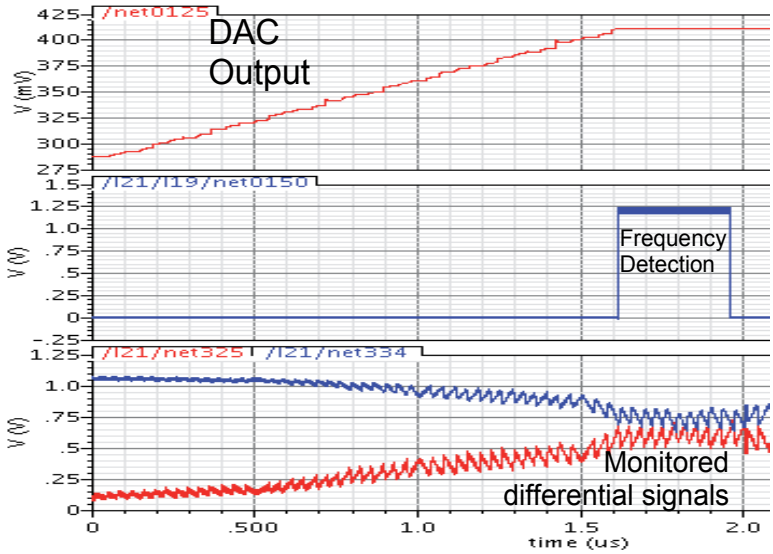

Fig. 15. Simulation Results that demonstrate the use of the circuits presented in Fig. 13 and Fig. 14

The use of the Differential Signal Monitor and the Delay Insertion/Level Shifting circuit of Fig. 13 as well as the draft Frequency Range Detector of Fig. 14 are demonstrated in Fig. 15. The differential sawtooth curves at the bottom of that figure represent the monitored residue signals (V^+ and V^-) that are initially shifted away when the V_{b1} bias voltage of Fig. 13b that is driven by the DAC output of Fig. 13a, has its lowest value. The DAC output is the curve that appears at the top of Fig. 15 and is increased forcing the V^+ and V^- distance to be reduced. When these differential signals start to overlap, the DAC output level is stabilised since the counter operation of Fig. 13a is disabled. The frequency range detector of Fig. 14 estimates then the frequency of the residue signals for the period indicated by the signal in the middle of Fig. 15.

10. Post processing techniques for linearity improvement

The use of the correcting factors stored in lookup tables that were presented in paragraph 6 is a type of post processing technique. The authors are currently developing different post processing techniques that are general enough to be used for the linearity improvement of several ADC architectures. These techniques are based on the fact that often the high DNL errors have a periodic form and appear at output codes with a specific format. For example, in a two stage pipeline ADC the residue that serves as input to the "fine" ADC stage may not consist of identical teeth in the sense that some teeth may have different amplitude or offset as shown in Fig. 16.

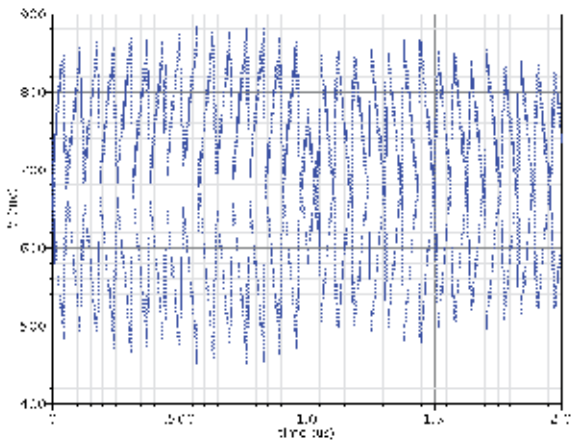

Fig. 16. Differential residue with non-identical teeth

If the differential signals of Fig. 16 are input to a 4-bit "fine" Flash ADC, then the two resistor ladders that generate the voltage levels of each differential comparator at the input stage of this ADC have to be biased appropriately. Consider for example the differential signal at the top of Fig. 16. If the input range of this signal is assumed to be 680mV..880mV in order to cover the minimum/maximum peaks of all teeth, then some codes will be missing at the ADC output since some teeth do not span at the whole range (they have a lower than 200mV amplitude). In order to avoid missing codes, a smaller range can be assumed for this specific differential signal e.g., 700mV..840mV. A similar biasing approach may be chosen for the differential signal at the bottom of Fig. 16 to avoid missing codes.

Nevertheless, in this case the codes of the binary form x0000 and x1111 will have a significantly higher DNL error than the others due to the teeth clipping. In fact, the DNL of these output codes will probably be higher than 1 LSB.
A post processing technique is under development by the authors that corrects such a high DNL error by detecting the erroneous codes at the ADC output and replacing them with successive codes of 1-bit higher resolution. The rest of the codes are simply shifted appropriately and their resolution is also extended by 1-bit. In order to decide the duration of the inserted codes an averaging of the ADC output code duration is continuously performed by a digital circuit. Simulation results show that the SNDR of the 8-bit ADC described in (Petrellis et al, 2010c) can be increased in this way by up to 6dB.
In a more general approach, the average duration of the ADC output codes can be continuously estimated, and a correction of the successive codes' duration can be carried out. For example, if a code appears in average 5 consequent times while the codes X and X+1 appear 7 and 3 times respectively, then the last 2 appearances of X can be replaced with X+1.

11. Conclusion

The appropriate calibration techniques allow the ADCs to operate at the extremely high conversion rates required by the nowadays applications. Although many ADC architectures require customised solutions it was attempted to select and present the most popular and general ones. A number of calibration and post processing techniques that have been developed by the authors have also been presented. These techniques include current mode calibration based on the use of gain boosted mirrors as well as voltage mode calibration methods that perform differential signal monitoring, level shifting, delay insertion, frequency range detection and bias adjustment.

12. Acknowledgement

Part of this work has been supported by Analogies SA and is patent pending. (Application No. PCT/GB2009/051101).

13. References

Ahmed, I. & Johns, D. (2005). A 50MS/s (35mW) to 1kS/s(15uW) Power Scalable 10-bit Pipelined ADC Using Rapid Power-On Opamps and Minimal Bias Current Variation. *IEEE Journal of Solid State Circuits*. Vol. 40, No.12, pp. 2446-2455

Ahmed, I. & Johns, D. (2008). An 11-Bit 45 MS/s Pipelined ADC With Rapid Calibration of DAC Errors in a Multibit Pipeline Stage. *IEEE Journal of Solid-State Circuit*, Vol. 43, No. 7, pp.1626-1637

Balestrieri, E.; Daponte, P. & Rapuano, S. (2005). A State of the Art on ADC Error Compensation Methods. *IEEE Transactions on Instrumentation and Measurement*, Vol.54, No.4, pp. 1388–1394

Chan, C. H.; Chan, C. F.; Choy, C. S. & Pun, K. P. (2006). A 6-digit CMOS Current-Mode Analog-to-Quaternary Converter with RSD Error Correction Algorithm. *Proceedings of the IEEE ISCAS*, pp. 4771-4774

Colleran, W. & Abidi, A. (1993). A 10-b 75MHz Two-Stage Pipelined Bipolar A/D Converter. *IEEE Journal of Solid State Circuits*, Vol. 28, No. 12, pp. 1187-1119

Correa-Alegria, F. & Cruz-Sera, A. (2009). Precision of Independently Based Gain and Offset Error of an ADC Using the Histogram Method. *IEEE Transactions on Instrumentation and Measurement,* Vol.58, No.3, pp. 512-521

Deguchi, K.; Suwa, N.; Ito, M.; Kumamoto, T. & Miki, T. (2008). A 6-bit 3.5GS/s 0.9-V 98-mW Flash ADC in 90-nm CMOS. *IEEE Journal of Solid-State Circuits*, Vol. 43, No. 10, pp. 2303-2310

De Vito, L.; Lundin, H. and Rapuano, S. (2007). Bayesian Calibration of a Lookup Table for ADC Error Correction. *IEEE Transactions on Instrumentation and Measurement*, Vol.56, No.3, pp. 873–878

Hung, L. H. & Lee, T. C. (2009). A Split-Based Digital Background Calibration Technique in Pipelined ADCs. *IEEE Transactions on Circuits and Systems II, Express Briefs*, Vol.56, No.11, pp. 855–859

Iizuka, K.; Matsui, H.; Ueda, M. & Daito, M. (2006). A 14-bit Digitally Self-Calibrated Pipelined ADC with Adaptive Bias Optimization for Arbitrary Speeds Up to 40MS/s. *IEEE Journal of Solid State Circuits*, Vol. 41, No. 4, pp.883-890

Karanicolas, A.; Lee, H.S., Bacrania, K. (1993). A 15-b 1MS/s Digitally Calibrated Pipeline ADC. *IEEE Journal of Solid State Circuits*, Vol. 28, No. 12, pp. 1207-1215

Kurose, D.; Ito, T.; Ueno, T.; Yamaji, T. & Itakura, T. (2006). 55mW 200MS/s 10-b Pipeline ADCs for Wireless Receivers. *IEEE Journal of Solid State Circuits*. Vol. 41, No. 7, pp. 1589-1595

McNeill, J.; Coln, M. & Larivee, B. (2005). Split ADC' Architecture for Deterministic Digital Background Calibration of a 16-bit 1-MS/s ADC. *IEEE Journal of Solid State Circuits*, Vol. 40, No. 12, pp. 2437-2445

Ohara, H.; Ngo, H.X.; Armstrong, M. J.; Rahim, C. F. & Gray, P.R. (1987). A CMOS Programmable Self-Calibrating 13-bit Eight-Channel Data Acquisition Peripheral. *IEEE Journal of Solid-State Circuits*, pp. 930–938

Petrellis, N.; Birbas, M.; Kikidis, J. & Birbas, A. (2010). An Ultra Low Area Asynchronous Combo 4/8/12-bit/Quaternary A/D Converter Based on Integer Division. *Elsevier Microelectronics Journal*, Vol.41, pp. 291-307

Petrellis, N.; Birbas, M.; Kikidis, J. & Birbas, A. (2010). Techniques for Calibrating Differential Signals in Measurement Instruments. *Proceedings of the 2010 IEEE International Conference on Imaging Systems and Techniques*, pp. 171-175, Thessaloniki, Greee, July 2-1, 2010

Petrellis, N.; Birbas, M.; Kikidis, J. & Birbas, A. (2010). Selecting Appropriate Calibration Points for an Ultra Low Area 8-bit Subrange ADC. *Proceedings of the 8th IEEE International Workshop on Intelligent Solutions in Embedded Systems (WISES 2010)*, pp. 73-78, Heraklion, Greece, July 8-9, 2010

Ploeg, H.; Vertregt, M. & Lammers, M. (2005). A 15-bit 30-MS/s 145mW 3-Step ADC for Imaging Applications. *IEEE Journal of Solid State Circuits*, Vol. 41, No. 7, pp. 1572-1577

Provost, B. & Sánchez-Sinencio, E. (2004). A Practical Self-Calibration Scheme Implementation for Pipeline ADC. *IEEE Transactions on Instrumentation and Measurement*. Vol.53, No.2, pp. 448–456

Quiquempoix, V.; Deval, P.; Barreto, A.; Bellini, G.; Márkus, J.; Silva, J. & Temes, G. (2006). A Low-Power 22-bit Incremental ADC. IEEE Journal of Solid State Circuits, Vol.41, No.7, pp. 1562-1571

Sone, K.; Nishida, Y. & Nakadai, N. (1993). A 10-b 100MS/s Pipelined Subranging BiCMOS ADC. *IEEE Journal of Solid State Circuits*. Vol. 28, No.12, pp. 1180-1186

Sun, N.; Lee, H. S. & Ham, D. (2008). Digital Background Calibration in Pipelined ADCs Using Commutated Feedback Capacitor Switching. *IEEE Transactons on Circuits and Systems II, Express Briefs*, Vol.55, No.9, pp. 877–881

Van de Vel, H.; Buter, B.; Van der Ploeg, H.; Vertregt, M.; Geelen, G. & Paulus, E. (2009). A 1.2-V 250-mW 14-b 100-MS/s Digitally Calibrated Pipeline ADC in 90-nm CMOS. *IEEE Journal of Solid-State Circuit*, Vol. 44., No. 4, pp. 1047-1056

Wang, H.; Wang, X.; Hurst, P. & Lewis, S. (2009). Nested Digital Background Calibration of a 12-bit Pipelined ADC Without an Input SHA. *IEEE Journal of Solid State Circuits*, Vol.44, No.10, pp. 2780-2789

Wit, M.; Tan, K. S. & Hester, R. (1993). A Low Power 12-b ADC with On Chip Precision Trimming. *IEEE Journal of Solid State Circuits*, Vol. 28, No. 4, pp. 455-461

Part 3

Cross Layer Design

14

Cross-Layer Resource Allocation for MB-OFDM UWB Systems

Ayman Khalil, Matthieu Crussière and Jean-François Hélard
European University of Brittany (UEB)
Institute of Electronics and Telecommunications of Rennes (IETR)
France

1. Introduction

The demand of wireless services is increasing and new generations of mobile radio systems are promising to provide higher data rates and a large variety of applications to mobile users. Besides, one of the major challenging problems in future wireless communication systems is how to offer the ability to transport multimedia services at different channel conditions and bandwidth capacities with various quality of service (QoS) requirements. However, this goal must be achieved under the constraint of limited available frequency spectrum because numerous licensed services and applications already exploit the spectral resource up to several gigahertz. Thereby, the multiple access and the coexistence are challenging matters for the next generation wireless communication systems.
Two exciting solutions have recently risen to circumvent the limited frequency spectrum problem. The first solution is based on spectrum sensing and dynamic spectrum access (DSA) techniques to find available spectrum which can be used by a cognitive radio user without causing any harmful interference to licensed users. The other solution is to set up underlay communications that would allow so-called secondary users to judiciously exploit some frequency resource already allocated to licensed primary users such that the former does not impact on the quality of the communications of the latter significantly. The latter solution can namely be achieved by imposing tough radiation restrictions to the secondary users.
In that context, ultra-wideband (UWB) has recently been attracting great interest as a suitable technology for unlicensed short range communications. With the data rate of several hundred Mbps, and the restricted power transmission, UWB demonstrates great potential in the coexistence issue and the support of multimedia services such as high-definition television (HDTV), videos and music sharing, console gaming, etc., in home networks known as the wireless personal area network (WPAN).
Given the power constraint and the extremely wide bandwidth of UWB, a fundamental problem arises is how to manage the multiple-user access to efficiently utilize the bandwidth, support the QoS requirements of multimedia applications and provide fairness among the existing users. Moreover, to this date, research works on resource allocation for UWB communications are still limited. Based on the WiMedia Alliance, solution proposed for the UWB communications, the objective of this chapter is to define a new approach for the spectrum sharing and multiple access problems in the scope of the resource allocation in UWB systems while taking into account the various system constraints. Thus, to deal with

the channel quality, and the QoS constraints, which are viewed as heterogeneous constraints, we follow a cross-layer approach based on a cooperation between the two lowest layers of the Open Systems Interconnection (OSI) model, namely the physical (PHY) and the medium access control (MAC) layers.
This chapter is divided into two main parts: In the first part, we describe the multiband orthogonal frequency-division multiplexing (MB-OFDM) approach, solution proposed for the high-rate UWB systems. Next, we present the physical specifications of the WiMedia solution, which is based on the MB-OFDM approach. The indoor channel model that will be used in our simulations is then presented. Afterwards, we present the resource management principles in OFDM and MB-OFDM systems. We then discuss the resource allocation strategies proposed for OFDM systems while stressing on the need of the QoS support in a multiuser context to respond to the different users demands. Finally, we define our cross-layer strategy for a distributed multiuser resource allocation scheme under QoS requirements in MB-OFDM systems.
Based on the cross-layer approach defined in the first part, we analytically study in the second part of the chapter the multiuser resource allocation problem for MB-OFDM systems by deriving a constrained optimization problem. The cross-layer approach is exploited by defining a PHY-MAC interplay mechanism that is able to provide new functionalities of the physical and the medium access control layers. The PHY layer is responsible for providing the physical channel conditions through the exploitation of the channel state information (CSI), while the MAC layer is in charge of differentiating and classifying the existing users using a priority-based approach that guarantees a high level of QoS support for real-time and multimedia services. An optimal sub-band and power allocation is then derived from the formulated cross-layer optimization problem. To evaluate the efficiency of the proposed multiuser allocation scheme, we define a cross-layer metric called the satisfaction index (SI). Finally, the new multiuser resource allocation solution is compared to the single-user WiMedia solution in terms of bit error rate (BER).

2. MB-OFDM system

Multiband OFDM (MB-OFDM) is the primary candidate for high data rate UWB applications. It was first proposed by Anuj Batra *et al.* from Texas Instruments for the IEEE 802.15.3a task group (Batra et al., 2003, 2004a, 2004b). This approach is today supported by the WiMedia Alliance and adopted by the ECMA-368 standard (Standard ECMA-368, 2007).

Data rate (Mbps)	Constellation	Coding rate (r)	FDS	TDS	Coded bits / OFDM symbol (NCBPS)
53.3	QPSK	1/3	Yes	Yes	100
80	QPSK	1/2	Yes	Yes	100
110	QPSK	1/3	No	Yes	200
160	QPSK	1/2	No	Yes	200
200	QPSK	5/8	No	Yes	200
320	DCM	1/2	No	No	200
400	DCM	5/8	No	No	200
480	DCM	3/4	No	No	200

Table 1. WiMedia-based MB-OFDM data rates.

The WiMedia Alliance MB-OFDM scheme consists in combining OFDM with a multi-banding technique that divides the available band into 14 sub-bands of 528 MHz each, as illustrated in Fig. 1. An OFDM modulation with 128 subcarriers is applied on each sub-band separately. As evident from the figure, five band groups or channels are defined, each being made from three consecutive sub-bands, except for the fifth one which encompasses only the last two sub-bands. To be exhaustive, a sixth band group is also defined within the spectrum of the first four, consistent with usage within worldwide spectrum regulations. A WiMedia compatible device should actually make use of only one out of these six defined channels. Initially, most of the studies in the literature have been performed on the first band group from 3.1 to 4.8 GHz.

The MB-OFDM system is capable of transmitting information at different data rates varying from 53.3 to 480 Mbps, listed in Table 1. These data rates are obtained through the use of different convolutional coding rates, frequency-domain spreading (FDS) and time-domain spreading (TDS) techniques. FDS consists in transmitting each complex symbol and its conjugate symmetric within the same OFDM symbol. It is used for the modes with data rates of 53.3 and 80 Mbps. With the TDS, the same information is transmitted during two consecutive OFDM symbols using a time-spreading factor of 2. It is applied to the modes with data rates between 53.3 and 200 Mbps.

For data rates lower than 320 Mbps, the constellation applied to the different subcarriers is a quadrature phase-shift keying (QPSK). Nevertheless, for data rates of 320 Mbps and higher, the binary data is mapped onto a multi-dimensional constellation using a dual-carrier modulation (DCM) technique. The DCM modulation consists in mapping four bits onto two 16-point constellations. The resulting mapped tones are then separated by at least 200 MHz of bandwidth. The DCM technique is not applied for low data rates (200 Mbps and below) since the frequency diversity is better exploited through the use of low rate Forward Error Correction (FEC) codes, TDS and FDS techniques. Therefore, the expected DCM diversity gain for these data rates is minimal and the added complexity for DCM is not justified. Note that the first MB-OFDM proposals for IEEE 802.15.3a, including the September 2004 proposal, considered only a QPSK constellation for all the data rates (Batra et al., 2004b).

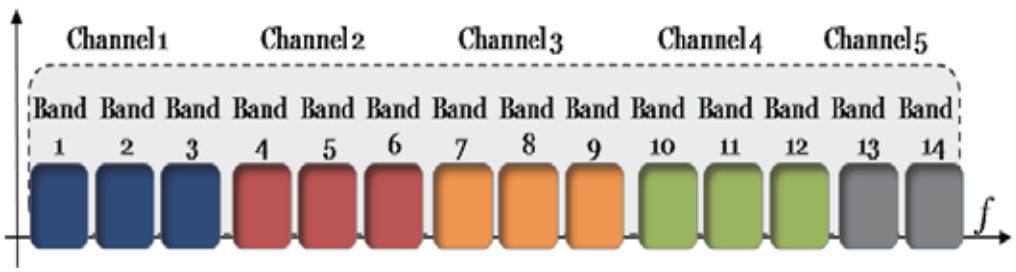

Fig. 1. UWB spectrum bands in the MB-OFDM system.

2.1 UWB indoor channel model

Since UWB channels have some particular propagation process and models which carry a considerable difference with the classical narrowband models, many studies on the propagation and the channel models for UWB signaling have been issued since the late 1990s (Cassioli et al., 2002) (Win & Sholtz, 2002).

In fact, since we are working in an indoor environment and due to the very fine resolution of UWB waveforms, different objects or walls in a room could contribute to different clusters of multipath components. In early 2003, the IEEE 802.15.3a committee adopted a new UWB channel model for the evaluation of UWB physical layer proposals (Foerster, 2003). This model is a modified version of Saleh-Valenzuela (SV) model for indoor channels (Saleh & Valenzuela, 1987), fitting the properties of UWB channels. A log-normal distribution is used for the multipath gain magnitude. In addition, independent fading is assumed for each cluster and each ray within the cluster. The impulse response of the multipath model is given by

$$h_i(t) = G_i \sum_{z=0}^{Z_i} \sum_{p=0}^{P_i} \alpha_i(z,p)\delta\left(t - T_i(z) - \tau_i(z,p)\right) \tag{1}$$

where G_i is the log-normal shadowing of channel realization i, $T_i(z)$ the delay of cluster z, $\alpha_i(z,p)$ and $\tau_i(z,p)$ represent the gain and the delay of multipath p within cluster z, respectively. Independent fading is assumed for each cluster and each ray within the cluster. The cluster and path arrival times can be modeled as Poisson random variables. The path amplitude follows a log-normal distribution, whereas the path phase is a uniform random variable over $[0, 2\pi]$. Four different channel models (CM1 to CM4) are defined for the UWB system modelling, each with arrival rates and decay factors chosen to match different usage scenarios and to fit line-of-sight (LOS) and non-line-of-sight (NLOS) cases. The channel models characteristics are presented in Table 2.

3. Resource allocation in OFDM systems

OFDMA has attracted great interest as a promising approach to provide an efficient modulation and multiple-access technique for future wireless communications (Astely et al., 2006) (Moon et al., 2006). It is based on OFDM modulation, which is characterized by its immunity to intersymbol interference (ISI), its robustness in presence of frequency selective

	CM1	CM2	CM3	CM4
Mean excess delay (ns)	5.05	10.38	14.18	–
Delay spread (ns)	5.28	8.03	14.28	25
Distance (m)	< 4	< 4	4–10	10
LOS/NLOS	LOS	NLOS	NLOS	NLOS

Table 2. Multipath channel characteristics.

fading and narrowband interference and its high spectral efficiency. Besides, the major advantage of OFDMA is its ability to schedule resources in both time and frequency dimensions which gives a good flexibility in any multiple-access scheme. However, the performance of OFDMA depends on the ability to provide an efficient and flexible resource allocation scheme that should adapt to wireless fading channels, as well as improve the spectrum efficiency and satisfy the existing users.

In OFDM, the broadband channel is divided into orthogonal narrowband subcarriers. In a multiuser context, different subcarriers can be allocated to different users. However, the channels on each subcarrier are independent for each user; the subcarriers that experience

deep fading for one user could be in a good condition for another user. Consequently, efficient resource allocation in OFDMA shall be based on dynamic subcarrier allocation that responds to each user channel quality.
In the literature, related studies have addressed the OFDM radio resource allocation problem as an optimization problem where optimal and suboptimal algorithms have been proposed. Two well-known classes of optimization techniques have been proposed for the dynamic multiuser OFDM allocation: margin adaptive (MA) and rate adaptive (RA). The MA concept is to achieve the minimum overall transmit power under a data rate or BER constraint. On the other hand, the RA concept is to maximize the users data rate under a total transmit power constraint (Jang & Lee, 2003) (Shen et al., 2005).

3.1 Resource allocation in MB-OFDM UWB systems

UWB channel response varies slowly in time and could be considered as quasi-static during one frame. Accordingly, the CSI can be sent to the transmitter by a simple feedback that does not increase significantly the complexity of the resource allocation mechanism. However, to this date, research works on resource allocation for UWB communications are still limited.
Several research studies on MB-OFDM UWB systems have been strictly devoted to physical layer issues or have addressed the question of resource allocation yet without taking into consideration the MAC layer constraints. In (Chen et al., 2006) for instance, in order to improve the BER performance, an adaptive carrier selection and power allocation is proposed. An optimal algorithm with Lagrange multiplier method is derived. Based on the CSI information, the carriers and the power are dynamically allocated with the constraint of fixed data rate and fixed total power. In (Wang et al., 2005), the authors propose two power allocation schemes to maximize the total capacity for single-band OFDM UWB transmissions with space-time codes, under the assumption of perfect and partial CSI at the transmitter. The results show that the water-filling scheme provides the smallest outage probability while the scheme with limited CSI feedback has lower feedback overhead and slight performance loss. In (Xu & Liu, 2004), a power allocation scheme is proposed for clustered MB-OFDM. In this study, a cluster which is a group of subcarriers is dynamically assigned a unique power in order to maximize the total system throughput. The results show that the proposed solution, with its low complexity, has a performance close to the one of a standard water-filling scheme.
On the other hand, other studies have been focusing on improved MAC algorithms independently of any information feedback from the PHY layer. In (Cuomo et al., 2002), a joint rate and power assignment algorithm is proposed for multiuser UWB networks. Optimal and suboptimal algorithms are proposed to dynamically assign the rate and the transmitted power of each node. To establish a communication link, the proposed radio resource sharing scheme defines a handshaking stage between a sender and receiver. The proposed allocation scheme relies on two handshakes between the sender and its neighbors to obtain the required information for link rate and power assignments. In (Zhai, 2008), a QoS support mechanism for multimedia services in UWB-based WiMedia mesh networks is proposed. An integer-linear programming model is derived to solve the path available bandwidth problem. Lower and upper bounds are also derived to reduce the computation complexity. In addition, a distributed QoS routing algorithm is defined to find the paths with enough end-to-end available bandwidth. Results show that the proposed algorithms perform very well in predicting the available bandwidth of paths and can admit more traffic flows than existing ones.

Few studies consider both the physical and MAC layers in the resource allocation matter for MB-OFDM UWB systems. In (Siriwongpairat et al., 2007), a novel channel allocation scheme is proposed by efficiently allocating power, data rate and sub-bands among all the users. The sub-band and power assignment problem is formulated as an optimization problem whose goal is to minimize the total power under the condition that all users achieve their requested data rates. A low-complexity fast suboptimal algorithm is also proposed to reduce the complexity of the formulated problem. Results show that the proposed solution can save up to 61% of power consumption compared to the standard multiband scheme. Although this latter study exploits information laying in the physical and MAC layers, some aspects are not ensured in the proposed resource allocation scheme. The QoS support for instance is not fully exploited since no service differentiation scheme is defined. Furthermore, some physical conditions are not taken into consideration in the sub-band assignment such as the number of sub-bands per channel and the number of users that can coexist in the same channel.

3.2 Resource allocation for MB-OFDM-MA: cross-layer approach

While OFDMA is the multiuser OFDM scheme that allows multiple access on the same channel by distributing subcarriers among users, MB-OFDM-MA is the multiuser MB-OFDM scheme that shares the available sub-bands of the same channel among the existing users.
Inevitably, there is a need in any resource allocation scheme to exploit some channel parameters reflecting the channel quality of each user aiming at accessing the network. These physical conditions are provided by the PHY layer. On the other hand, in a multiuser context, we need to determine how much end-users are satisfied and how efficient the available resources are shared among the existing users. Information about QoS requirements and fairness are thus of great importance to be provided by the MAC layer. As a result, the interplay between the two lowest layers of OSI model becomes a crucial need for the resource allocation in the next generation wireless communication systems since independent optimization of the two layers may not lead to an optimal overall system performance. Fig. 2 illustrates the idea of the PHY-MAC interaction model for a cross-layer optimization resource allocation scheme.

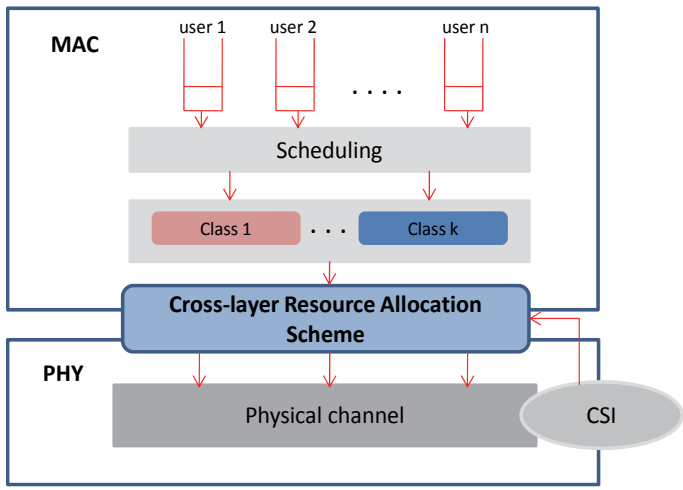

Fig. 2. PHY-MAC interaction for a cross-layer resource allocation scheme.

3.2 Cross-layer performance optimization

The management of the available resources is of major importance in a multiuser system when we want to optimize its performance. In our proposed cross-layer system that takes into consideration two different layers aspects, we should ensure an efficient exploitation of the available optimization features.

From the physical perspective, metrics such as spectrum efficiency and minimum BER are the most important constraints to be considered. On the other hand, from a user perspective, QoS as well as fairness among the competing users are the main metrics because they determine how much end-users are satisfied and how efficient the available resources are shared among the existing users. The optimization of the joint consideration of the PHY and MAC layers through the proposed cross-layer mechanism is thus performed by adopting two strategies:

Optimization problem formulation

The proposed cross-layer resource allocation problem is first studied analytically by deriving a constrained optimization problem to find the optimal allocation solution. Indeed, different parameters from the PHY and MAC layers are collected to define the objective function and the different constraints of the optimization problem.

Layer abstraction

To reduce the overall processing and the complexity of the layer-independent performance evaluation, an abstraction of one layer processing is carried out in the other layer. More precisely, all the proposed MAC processes will be abstracted at the PHY level for the sake of a simplified system performance evaluation.

4. Multiuser resource allocation optimization for MB-OFDM UWB

The proposed multiuser allocation scheme counts on the collection of information located at two different levels, more precisely the PHY and the MAC levels. In this section, we present the new functionalities of these two layers that should contribute to the optimization problem formulation.

4.1 PHY layer information

As mentioned before, the main functionality of the PHY layer is to provide the users channel gains of each sub-band in order to achieve efficient spectrum utilization and a sub-band allocation that respects the competing users PHY conditions. Therefore, the CSI is needed at the transmitter side.

In an OFDM system, by assuming a normalized emission power, we can derive the instantaneous signal to interference and noise ratio (SINR) for each subcarrier given by

$$SINR_i = \frac{|h_i|^2}{\sigma^2} \tag{2}$$

where h_i is the channel response of subcarrier i, $|h_i|^2$ and σ^2 are the subcarrier power and the noise and interference power respectively.

On the other hand, in a multiuser environment, it is desirable to evaluate the system level performance in terms of BER, considered as the physical QoS parameter. This can be motivated by the need of such parameter for accurate and realistic evaluation of the system

level performance but also for suitable development of adaptive resource allocation and packet scheduling algorithms. However, the heavy computation cost of any simulator assessing the system performance in terms of BER would result in long simulation times.
Therefore, separate link and system simulators are needed for the evaluation of the network performance. For this purpose, link to system (L2S) methods have been proposed in recent 3GPP standardizations, which can be effectively be used in OFDM systems by using effective SNR concept (3GPP, 2003a, 2003b).
The basic idea of the effective SINR method is to find a compression function that maps the sequence of varying SINRs to a single value that is correlated with the BER. This can be stated as

$$SINR_{eff} = I^{-1}\left(\frac{1}{N}\sum_{i=1}^{N} I(SINR_i)\right) \tag{3}$$

where *I(x)* is called the information measure function and N the number of subcarriers in a sub-band. An approach used for the effective SINR mapping method is called the Exponential Effective SINR Mapping (EESM) (3GPP, 2004a, 2004b).EESM uses the following information measure

$$I(x) = \exp(-\frac{x}{\lambda}) \tag{4}$$

The inverse function of I(x) is

$$I^{-1}(x) = -\lambda \ln(x) \tag{5}$$

Eventually, the effective SINR writes

$$SINR_{eff} = -\lambda \ln\left[\frac{1}{N}\sum_{i=1}^{N}\exp(-\frac{SINR_i}{\lambda})\right] \tag{6}$$

where λ is a scaling factor that is used to adjust the compression function in a way that compensates the difference between the actual BER and the predicted BER. λ depends only on the selected modulation and coding scheme (MCS).
In order to apply the effective SINR mapping method to MB-OFDM systems, we evaluate the value of λ for the eight data rate modes of the WiMedia system defined in Table 1. These values are listed in Table 3. In practice, based on the CSI knowledge, each user is capable of computing the effective SINR value in each sub-band by using (6). For instance, in the case of one channel divided into $N = 3$ sub-bands, and with $K = 3$ users, the physical layer information is reduced to the knowledge of only $N \times K = 9$ effective SINR values.

4.2 MAC layer information

In a multiuser context, the MAC layer is responsible for providing medium access mechanisms that should manage the radio access in an efficient way that respects the different users conditions. However, optimizing the use of radio resources is a critical issue when spectrum has to be allocated with respect to end-users needs. Scheduling and queuing are key concepts of medium access mechanisms to ensure fairness among the users aiming at accessing the medium as well as to respond to high-priority users demands.

On the other hand, to achieve an efficient scheduling in a heterogeneous context where users have different level of QoS requirements, a service differentiation scheme is crucial for end-to-end QoS provisioning. In the WiMedia solution, we have seen that none of the proposed medium access mechanisms is based on an efficient service differentiation scheme that ensures prioritization without causing access problems. Therefore, we define in this section a service differentiation model for UWB users based on service classification and weight assignment.

4.2.1 Service differentiation

Since multimedia applications or real-time services are key applications for next generation wireless networks, especially in high-rate UWB networks, it is desirable to assign them a high level of priority in any radio access mechanism. A two-level service classification model is proposed in this chapter to ensure the prioritization principle and to respond to next generation systems QoS requirements. Consequently, we classify the UWB service types into two classes:

1. Hard-QoS class: This class is defined for applications or services that require strong QoS support, more precisely real-time or multimedia applications. Voice and video services for instance are non delay-tolerant applications; they have thus strict QoS requirements and they definitely belong to this class.
2. Soft-QoS class: This class is dedicated to applications that don't have strict QoS requirements, more precisely non real-time or data applications. BE and file transfer services for instance are delay-tolerant applications. Thus, they belong to this class.

Data rate (Mbps)	Constellation	Coding rate (r)	λ
53.3	QPSK	1/3	1.49
80	QPSK	1/2	1.57
110	QPSK	1/3	1.52
160	QPSK	1/2	1.57
200	QPSK	5/8	1.82
320	DCM	1/2	1.85
400	DCM	5/8	1.82
480	DCM	3/4	1.80

Table 3. WiMedia data rates and associated parameter λ.

4.2.2 Weight assignment

The defined service classification scheme offers a two-level priority-based model which affects the scheduling decision. Effectively, we assign a class weight to the different users or applications belonging to the two defined classes. A higher weight is thus to be assigned to the service type with strict QoS requirements.

Our weight assignment model is divided into two parts: fixed class weight assignment and dynamic service weight assignment.

Fixed class weight

According to our two-level service classification model, the priority level of the hard-QoS users is set to be two times greater than the priority level of the soft-QoS users. Weight $q = 2$ is thus attributed to the hard-QoS class and weight $q = 1$ to the soft-QoS class.

Dynamic service weight

Since different services belonging to the same class may have different QoS requirements, we define a dynamic service weight that ensures an additional level of differentiation between users according to their requested data rates. Consequently, a user k is assigned a service weight s_k defined as

$$s_k = 1 + \frac{R_k - R_{\min}}{R_{\max} - R_{\min}} \tag{7}$$

where R_k is the user k requested data rate, $R_{\min}$ and $R_{\max}$ are the lowest and the highest data rates respectively, taken dynamically from WiMedia rate modes as presented in Table 1. Thereby, this service weight gives advantage to users having higher data rate requirements. Note that this dynamic weight assignment which depends on the WiMedia specifications can be applied in any other system by adjusting the values of $R_{\min}$ and $R_{\max}$. This reflects the flexibility and the generality of this weight assignment approach.

Absolute user weight

Provided by the MAC layer, the fixed and dynamic weights definition ensures an adaptive rate differentiation for the end-users according to their requirements and to the system constraints. Accordingly, the absolute user weight W is the combination of the class weight with the service weight defined as

$$W_k = q_k \times s_k \tag{8}$$

where q_k is the user k class weight and s_k its service weight.

4.3 Analytical study for the multiuser optimization problem

In order to address the resource allocation matter in a multiuser context under QoS requirements, we follow an analytical study by deriving a constrained optimization problem. Since UWB communication systems are based on an underlay usage of the spectrum obtained under tough power spectral density limitations, there is no necessity to minimize the total power transmission. MA technique is however of interest for our aimed multiuser allocation scheme since we want to allocate sub-bands to different users having different data rate requirements. As our objective is to ensure fairness among the different users while satisfying high-priority users, we actually define our optimization goal as:

- Optimizing the resource allocation under the power constraint imposed by UWB systems. Note that the power spectral density constraint is transformed into a total power constraint. This is justified by the fact that, in our allocation scheme, we need to differentiate between the heterogeneous users by assigning them different power levels that respect the different QoS requirements.
- Maximizing the total data rate of the soft-QoS users while guaranteeing a certain level of transmission rate for the hard-QoS users.

4.3.1 Problem formulation

We consider a system that consists of K UWB users aiming at accessing the network. The users are classified into two groups; the first K_h users are hard-QoS users and the remaining

$K - K_h$ users are soft-QoS users. We first derive the expression of the rate used for the problem formulation. The rate of a user k in a sub-band b is expressed as

$$r_{k,b} = \log_2(1 + P_{k,b}\mathrm{E}_{k,b}) \tag{9}$$

where $P_{k,b}$ is the allocated power of user k in sub-band b and $\mathrm{E}_{k,b}$ the effective SINR of user k in sub-band b. Actually, the advantage of expressing the rate in terms of the effective SINR is twofold: First, in the sub-band allocation the effective SINR results from mapping the instantaneous subcarrier SINRs to one scalar value by sub-band. This reduces the computation cost of the rate since the effective SINR values are already computed by the new physical layer entity previously defined. Second, considered as a cross-layer metric, the effective SINR acts as a link between the physical data rate and the MAC user requested rate via the exploitation of λ parameter as shown in Table 3.
The optimization problem can thus be formulated as

$$\begin{aligned} \mathrm{P}: \quad & \max_{S_k, P_{k,b}} \quad \sum_{k=K_h+1}^{K} \sum_{b \in S_k} r_{k,b} \\ & \textit{subject to} \quad \sum_{b \in S_k} r_{k,b} \geq R_k, \quad k = 1,...,K_h \\ & \sum_{k=1}^{K} \sum_{b=1}^{B} P_{k,b} \leq P_T \end{aligned} \tag{10}$$

where B is the total number of sub-bands, R_k the hard-QoS user k required data rate, S_k the set of sub-bands assigned to user k. In our case, $S_1, S_2, .., S_k$ are disjoint and each user is assigned one sub-band during one time interval. This problem is a mixed integer linear programming problem since S_k are integer variables. Consequently, the problem is classified as NP-hard. A method that makes the problem solvable is to relax the constraint that each sub-band is assigned to one user only. This approach is used in (Zhang & Letaief, 2004). The idea is to allow the users to time-share each sub-band by defining a new parameter $\omega_{k,b}$, which represents the time-sharing factor for user k in sub-band b. The optimization problem can then be stated as

$$\begin{aligned} \mathrm{P}: \quad & \max_{P_{k,b}, \omega_{k,b}} \quad \sum_{k=K_h+1}^{K} \sum_{b=1}^{B} \omega_{k,b} \log_2\left(1 + \frac{P_{k,b}\mathrm{E}_{k,b}}{\omega_{k,b}}\right) \\ & \textit{subject to} \quad \sum_{b=1}^{B} \omega_{k,b} \log_2\left(1 + \frac{P_{k,b}\mathrm{E}_{k,b}}{\omega_{k,b}}\right) \geq R_k, \quad k = 1,.....K_h \\ & \sum_{k=1}^{K} \omega_{k,b} = 1, \quad \forall b \quad 0 \leq \omega_{k,b} \leq 1 \quad \forall k,b \\ & \sum_{k=1}^{K} \sum_{b=1}^{B} P_{k,b} \leq P_T \end{aligned} \tag{11}$$

The latter optimization problem is a convex optimization problem since it has the following characteristics:

- The objective function of the maximization problem is concave since it is a linear combination of concave functions.

- The first and third constraints (inequality constraints) of the problem are convex.
- The second constraint (equality constraint) is affine.

Consequently, using the properties of a convex optimization problem, we derive the Lagrangian of the problem:

$$L = \sum_{k=K_h+1}^{K}\sum_{b=1}^{B}\omega_{k,b}\log_2(1+\frac{P_{k,b}\mathrm{E}_{k,b}}{\omega_{k,b}}) \;+\; \sum_{k=1}^{K_h}\alpha_k\;(\sum_{b=1}^{B}\omega_{k,b}\log_2(1+\frac{P_{k,b}\mathrm{E}_{k,b}}{\omega_{k,b}})-R_k)+ \\ \sum_{b=1}^{B}\beta_b(1-\sum_{k=1}^{K}\omega_{k,b}\;) \;+\; \gamma(P_T-\sum_{k=1}^{K}\sum_{b=1}^{B}P_{k,b}) \tag{12}$$

where a_k, β_b and γ are the Lagrange multipliers for the different constraints of the optimization problem. Besides, to find the optimal solution of the problem, we need the Karush–Kuhn–Tucker or KKT conditions (Bertsekas, 1999). Let $\omega^*_{k,b}$ and $P^*_{k,b}$ denote the optimal solution. The KKT conditions of the formulated problem are given by

$$\begin{aligned} &1)\ \frac{\partial L}{\partial P^*_{k,b}}\begin{cases}=0, & P^*_{k,b}>0\\ <0, & P^*_{k,b}=0\end{cases}\\ &2)\ \frac{\partial L}{\partial \omega^*_{k,b}}\begin{cases}<0, & \omega^*_{k,b}=0\\ =0, & \omega^*_{k,b}\in\,]0,1[\\ >0, & \omega^*_{k,b}=1\end{cases}\\ &3)\ \alpha_k\;(\sum_{b=1}^{B}\omega_{k,b}\log_2(1+\frac{P_{k,b}\mathrm{E}_{k,b}}{\omega_{k,b}})-R_k)=0\end{aligned} \tag{13}$$

Applying the first KKT condition, we obtain:

$$\begin{aligned} P^*_{k,b} &= \omega_{k,b}(\frac{\alpha_k}{\gamma\ln 2}-\frac{1}{\mathrm{E}_{k,b}}), \qquad \text{for } k=1,..,K_h\\ P^*_{k,b} &= \omega_{k,b}(\frac{1}{\gamma\ln 2}-\frac{1}{\mathrm{E}_{k,b}}), \qquad \text{for } k=K_h+1,..,K\end{aligned} \tag{14}$$

Then, the second KKT condition derives:

$$\begin{aligned} &\alpha_k\left[\log_2(1+\frac{\mathrm{E}_{k,b}P_{k,b}}{\omega_{k,b}})-\frac{1}{\ln 2}(\frac{\mathrm{E}_{k,b}P_{k,b}}{\omega_{k,b}+\mathrm{E}_{k,b}P_{k,b}})\right]-\beta_b=0, \qquad \text{for } k=1,..,K_h\\ &\log_2(1+\frac{\mathrm{E}_{k,b}P_{k,b}}{\omega_{k,b}})-\frac{1}{\ln 2}(\frac{\mathrm{E}_{k,b}P_{k,b}}{\omega_{k,b}+\mathrm{E}_{k,b}P_{k,b}})-\beta_b=0, \qquad \text{for } k=K_h+1,..,K\end{aligned} \tag{15}$$

Substituting (14) into (15) we get:

$$\begin{aligned} &\alpha_k\left[\log_2(\frac{\alpha_k\mathrm{E}_{k,b}}{\gamma\ln 2})-\frac{1}{\ln 2}(1-\frac{\gamma\ln 2}{\alpha_k\mathrm{E}_{k,b}})\right]-\beta_b=0, \qquad \text{for } k=1,..,K_h\\ &\log_2(\frac{\mathrm{E}_{k,b}}{\gamma\ln 2})-\frac{1}{\ln 2}(1-\frac{\gamma\ln 2}{\mathrm{E}_{k,b}})-\beta_b=0, \qquad \text{for } k=K_h+1,..,K\end{aligned} \tag{16}$$

After having used the time-sharing factor to find the optimal solution, we now go backward and enforce that one sub-band is assigned to one user only during one time interval. Therefore, we consider that $\omega_{k,b}$ cannot take values other than 0 or 1. Consequently,

$$\omega^*_{k,b} = \begin{cases} 1, & H_{k,b} > \beta_b \\ 0, & H_{k,b} < \beta_b \end{cases} \tag{17}$$

where $H_{k,b}$ is defined as:

$$\begin{aligned} H_{k,b} &= \alpha_k \left[\log_2\left(\frac{\alpha_k \mathrm{E}_{k,b}}{\gamma \ln 2}\right) - \frac{1}{\ln 2}\left(1 - \frac{\gamma \ln 2}{\alpha_k \mathrm{E}_{k,b}}\right) \right], \qquad \text{for } k = 1,..,K_h \\ H_{k,b} &= \log_2\left(\frac{\mathrm{E}_{k,b}}{\gamma \ln 2}\right) - \frac{1}{\ln 2}\left(1 - \frac{\gamma \ln 2}{\mathrm{E}_{k,b}}\right), \qquad \text{for } k = K_h + 1,..,K \end{aligned} \tag{18}$$

We conclude that, for a selected sub-band b, the user k having the highest Hk,b is assigned the sub-band. In other words, for a sub-band b, if Hk,b are different for all k then

$$\omega^*_{k',b} = 1 \ , \ \omega^*_{k,b} = 0 \qquad \text{for all } k \neq k' \tag{19}$$

Where

$$k' = \arg\max_k H_{k,b} \tag{20}$$

Afterwards, we derive the last KKT condition that characterizes the hard-QoS users rate constraint:

$$r_{k,b} = \sum_{b=1}^{B} \omega_{k,b} \log_2\left(1 + \frac{P_{k,b}\mathrm{E}_{k,b}}{\omega_{k,b}}\right) \geq R_k \tag{21}$$

Substituting (14) into (21) we get:

$$r_{k,b} = \sum_{b=1}^{B} \omega_{k,b} \log_2\left(\frac{\alpha_k \mathrm{E}_{k,b}}{\gamma \ln 2}\right) \geq R_k \tag{22}$$

As a result, to obtain the optimal solution, we have to compute the optimal power allocation function $P_{k,b}$ and the optimal sub-band allocation function $H_{k,b}$. To do so, we need to find the set of a_k such that the hard-QoS users rate constraint given in (22) is satisfied.

4.3.2 Mathematical characteristics of the optimal solution

To solve the formulated optimization problem, we first study the characteristics of the sub-band and power allocation functions given in (14) and (18) respectively. These two functions have the following properties:

- First, they are monotonically increasing with respect to $\mathrm{E}_{k,b}$. This means that, for a selected sub-band, the user having better channel conditions has more chance to be assigned this sub-band with a good power level.
- Second, the two allocation functions are monotonically increasing with respect to a_k. This can be viewed as a result of the service differentiation principle. In other terms, the functions depend on the user priority and thus, the stricter the user requirements, the higher the value of αk and consequently the higher the value of these functions.

- Third, we conclude from the hard-QoS users constraint given in (22) that a_k is monotonically increasing with respect to R_k.

As a result, the power and the sub-band allocation functions depend on the rate constraints of the users, in particular the hard-QoS users which have strict data rate requirements.

4.3.3 Optimal power and sub-band allocation algorithm

Based on the above observations, we propose an iterative algorithm for the search of the optimal sub-band and power allocations. The process consists in incrementing a_k iteratively by a small value δ until reaching the hard-QoS users data rate request while respecting the power constraint.

The algorithm is detailed in Algorithm 1. We first start by initializing the a_k by a value slightly greater than one. Then, we process the sub-band allocation based on the defined a_k value by computing $H_{k,b}$ using (18) and finding $\omega_{k,b}$ and k' using (19) and (20). We test afterwards the rate constraint of the hard-QoS users by using (22). While there are hard-QoS users not satisfying their rate constraints, we increment their corresponding a_k values by δ.

1. Initialization

alpha = 1;

a_k = alpha + δ, for $k = 1,..,k_h$

2. Sub-band allocation

a. **for** sub-band $b = 1,..,B$

compute $H_{k,b}$ using (18) for all k

obtain $\omega_{k,b}$ and k' using (19) and (20)

b. **for** $k = 1,..,k_h$

compute r'_k using (22)

c. **for** $k = 1,..,k_h$

find $\tilde{k}$ with $r'_{\tilde{k}} < R_{\tilde{k}}$ and $r'_{\tilde{k}} - R_{\tilde{k}} \le r'_k - R_k$

d. **while** $r'_{\tilde{k}} < R_{\tilde{k}}$

$\alpha_{\tilde{k}} = \alpha_{\tilde{k}} + \delta$

repeat a., b. and c.

3. Power allocation

a. compute $P_{k,b}$ using (14) for all k

b. compute $P'_T = \sum_{k=1}^{K}\sum_{b=1}^{B} P_{k,b}$

c. **if** $P'_T < P_T$

$\alpha_{\tilde{k}} = \alpha_{\tilde{k}} + \delta / 2$

else

$\alpha_{\tilde{k}} = \alpha_{\tilde{k}} - \delta / 2$

repeat 2. and 3. until $P'_T = P_T$

Algorithm 1. Iterative algorithm for optimal power and sub-band allocation.

Next, based on the obtained a_k values we process the power allocation by using (14). We then check the total power constraint. If we find that the total power exceeds the imposed total power, we decrement the a_k values by half the value of δ; otherwise we increment it by half of the same value.

4.3.4 Performance evaluation

In this section, we present some results of simulations obtained with the MB-OFDM UWB systems described previously. In these simulations, we consider an indoor environment, and we use the channel model adopted by the IEEE 802.15.3a task group, whose characteristics are listed in Table 2. In what follows, simulations are applied on channel model CM1 where a LOS case is considered and the transceiver spacing is less than 4 meters. Frames of 150 OFDM symbols are used, and each frame is transmitted on a different channel realization, from a total of 100 available realizations.

The objective is to study the performance of the allocation of three users in the same WiMedia frequency channel so that they can transmit simultaneously by assigning each user one sub-band according to the optimal allocation solution previously derived. Further, we compare our multiuser solution performance to the single-user WiMedia solution.

Thereby, we define a cross-layer performance metric called the satisfaction index (SI) defined as

$$SI(k) = \frac{\mathrm{E}_{k,b'}}{\max\limits_{b} \mathrm{E}_{k,b}} \tag{23}$$

where $\mathrm{E}_{k,b'}$ is the effective SINR of the user k in its assigned sub-band b'. This metric evaluates the satisfaction level of a user k by using the effective SINR value which is correlated to its BER and its effective data rates via parameter λ as given in Table 2. It will be equal to one if the user is fully satisfied since it is assigned its best sub-band. The SI is consequently a QoS parameter and can be used to evaluate fairness among users.

In Fig. 3, we consider a 'three-users' allocation scheme. Four scenarios with different users rate requirements are studied where the three users are classified according to their highest allocation function value given by (18). We consider that all the users requesting a data rate greater than 200 Mbps are hard-QoS users. As evident from the obtained results, the proposed scheme respects the priority of the users so that the highest priority user is fully satisfied in all the cases since it is first assigned its most favorite sub-band. Consequently, the SI of the highest priority user is always equal to one. On the other hand, the SI of the other users depends on their rate requirements. We observe from the four scenarios that, for the second and third users, the SI is inversely proportional to the data rate requirement. For instance, if we compare the SI of the second user in the first and fourth scenarios, we see that it is more satisfied when its data requirement is lower. This is due to the fact that the satisfaction level is represented in terms of the effective SINR including parameter λ which is correlated to the data rate as shown in Table 2.

Fig. 4 shows the simulation results performed on the band group 1 {3168 - 4752} MHz of the WiMedia solution using a TFC (time-frequency code) sequence of [1 3 2] which provides a frequency hopping between the three bands at the end of each OFDM symbol. The BER is presented as a function of E_b/N_0, where E_b is the average energy per useful bit and N_0 is the AWGN power density. The ideal case of perfect channel estimation is considered. The

performance of the MB-OFDM system is presented for the different MB-OFDM data rates listed in Table 1. Evidently, the MB-OFDM system with a data rate of 53.3 Mbps has the lowest BER, since it uses the lowest coding rate with FDS and TDS techniques. Similarly, the system with the highest data rate of 480 Mbps has the worst performance in terms of BER due to its high coding rate of $r = 3/4$. Besides, if we compare data rates 53.3 and 110 Mbps, as well as data rates 80 and 160 Mbps, we notice that the difference in E_b / N_0 at a BER level of 10^{-4} is less than 0.5 dB. This means that applying the FDS reduces the data rate by half without offering a considerable E_b / N_0 gain. In addition, if we compare systems with data rates of 80 and 110 Mbps, we notice that the system with a data rate of 110 Mbps offers better performance even if it provides higher data rate. This is due to the fact that the FDS applied to the system with a data rate of 80 Mbps is not efficiently exploited.

To compare the performance of our proposed multiuser allocation scheme to that of the single-user WiMedia scheme, we present in Fig. 5 two different scenarios where we evaluate the performance of the hard-QoS users in terms of BER. In both scenarios, we consider two hard-QoS users transmitting at the same data rate of 400 Mbps in the first scenario and 320 Mbps in the second one. The soft-QoS user is transmitting at the same data rate of 53.3 Mbps in both scenarios. The average BER of the two hard-QoS users is computed and the result is compared to the single-user WiMedia transmitting at the same data rate. We can notice from the figure that in both scenarios the hard-QoS users in the multiuser allocation solution outperforms the single-user WiMedia by an average gain of 1.5 dB at a BER level of 10^{-4}. This is justified by the fact that in the proposed allocation solution, the hard-QoS users are given a high level of privilege that affects the quality of their assigned channels and consequently decreases their BER level.

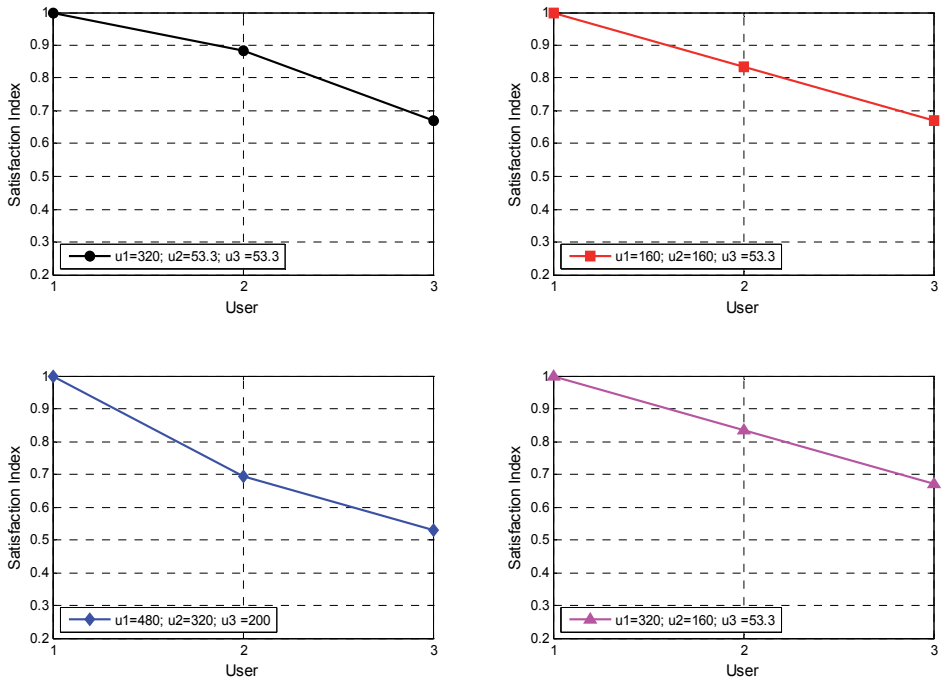

Fig. 3. Satisfaction Index of the 'three users' allocation scheme in different scenarios.

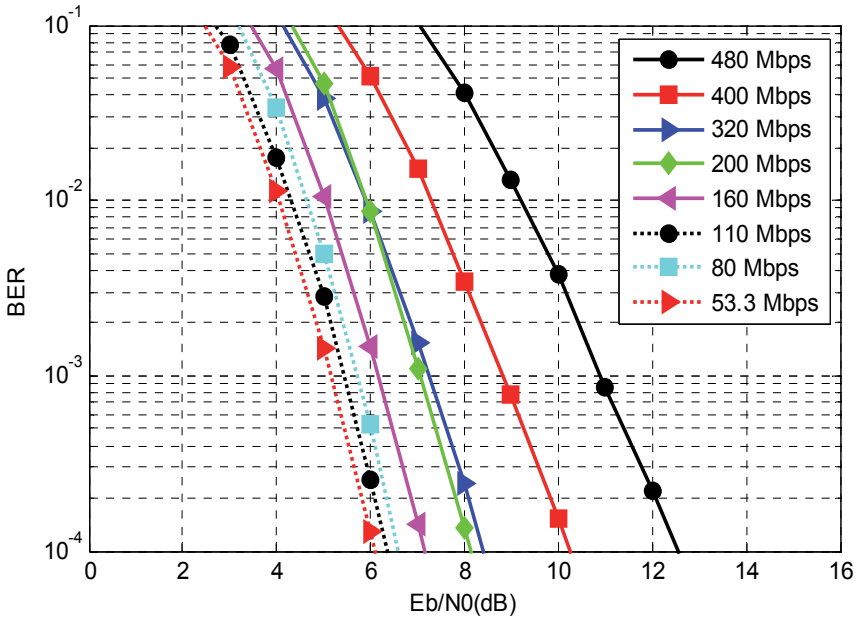

Fig. 4. Single-user WiMedia system performance on bands 1, 2 and 3, using channel model CM1 and considering a TFC frequency hopping between the three bands.

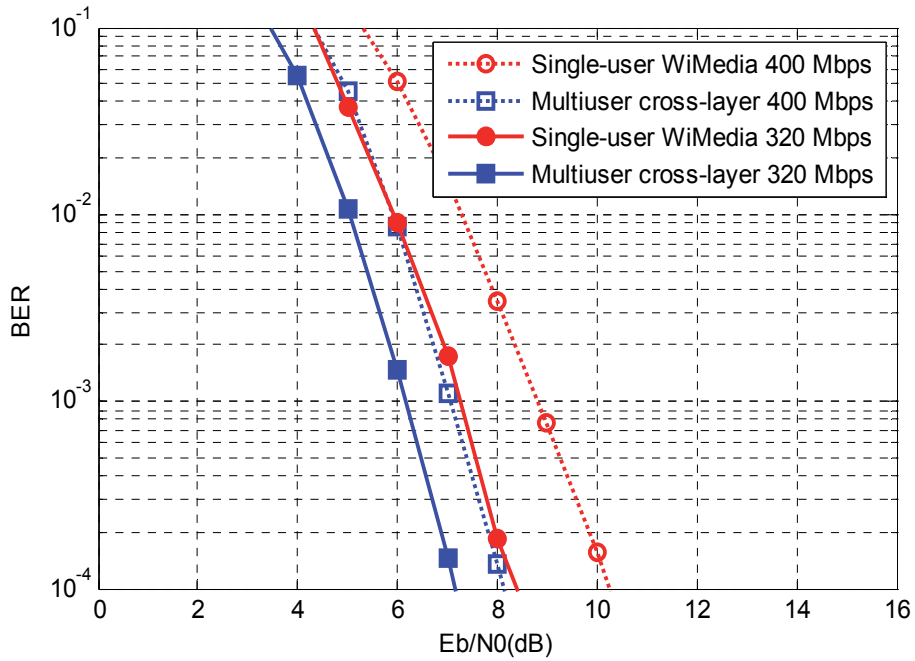

Fig. 5. Hard-QoS performance improvement in the proposed multiuser solution compared to the single-user WiMedia solution.

Fig. 6 shows further comparison between the proposed multiuser cross-layer scheme and the single-user WiMedia solution. To perform an efficient comparison, we consider scenarios where all the users are transmitting at the same data rate but belonging to different service classes. All the scenarios consist of two hard-QoS users and one soft-QoS user. The evaluation is performed for the eight WiMedia data rates, i.e. from 53.3 to 480 Mbps. The plotted curves represent the E_b/N_0 required to reach a BER level of 10^{-4} for each of the data rates. As shown in the figure, the highest priority user has a considerable gain compared to the lowest priority user. For instance, at a data rate equal to 480 Mbps, the highest priority user outperforms the lowest priority user with a 2.8 dB gain. On the other hand, the lowest priority user performance is slightly degraded compared to the WiMedia solution. This performance degradation of the low priority users can be viewed as a sacrifice for the sake of the high priority users to ensure their strict QoS requirements

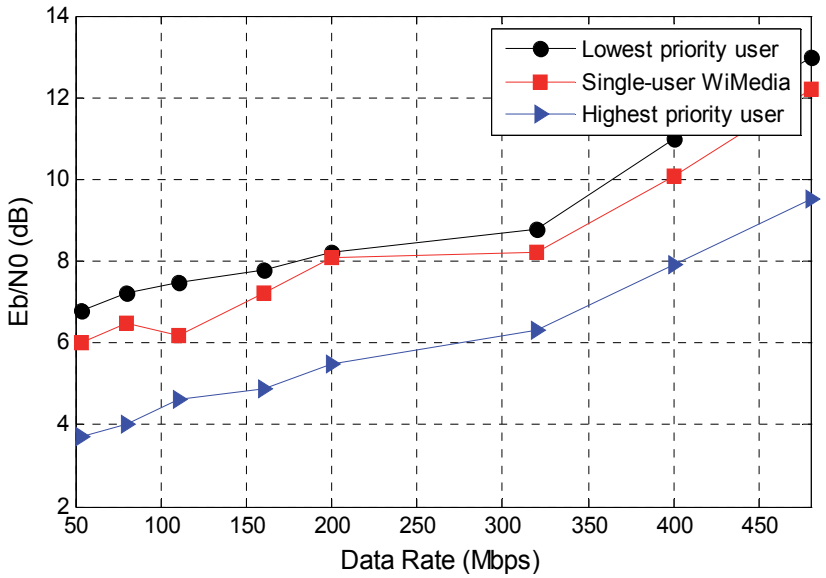

Fig. 6. Performance comparison of the highest and lowest priority users with the single-user WiMedia solution for the eight data rate modes.

5. Conclusion

In this chapter, we have investigated the sub-band and power allocation for MB-OFDM UWB systems in a multiuser context taking into account the users QoS requirements. For this purpose, we have defined new PHY-MAC metrics that are at the core of the cross-layer allocation scheme, so that new functionalities are added in the PHY and MAC layer respectively. While the PHY layer task is achieved through the use of the effective SINR method, the MAC layer is responsible for differentiating and classifying the users by assigning them different QoS weights.

We have then studied the multiuser allocation problem analytically by formulating a constrained multiuser optimization problem. An optimal solution for the sub-band and the power allocation has been thus carried out. To evaluate the performance of the different users, we have defined a satisfaction index parameter considered as a cross-layer metric to

assess the QoS level of the different users. Simulation results have shown that the new multiuser allocation scheme can guarantee a good level of QoS for users having strict QoS requirements by adopting a strict priority-based approach in any 'three-users' allocation scenario. This priority-based approach gives advantage to the highest priority user that is totally satisfied while the other users satisfaction depends on their constraints and requirements. Compared to the single-user WiMedia solution, the proposed multiuser scheme is advantageous for hard-QoS users and slightly inconvenient for soft-QoS users. However, the performance degradation of the soft-QoS is tolerable since these users QoS requirements are less restrictive.

6. References

Batra, A.; Balakrishnan J.; Aiello R.; Foerster J. R. & Dabak A. (March 2003). TI Physical layer proposal for IEEE 802.15 task group 3a, IEEE P802.15-03/142r2-TG3a.

Batra, A.; Balakrishnan J.; Aiello R.; Foerster J. R. & Dabak A. (September 2004) Design of multiband OFDM system for realistic UWB channel environments, IEEE Transactions on Microwave and Techniques, Vol. 52, pp. 2123-2138.

Batra, A.; Balakrishnan J.; Aiello R.; Foerster J. R. & Dabak A. (September 2004). Multiband OFDM physical layer proposal for IEEE 802.15 task group 3a, IEEE P802.15-04/0493r1-TG3a.

Standard ECMA-368. (2007). High rate ultra wideband PHY and MAC standard.

Cassioli D.; Win M. Z. & Molisch A. F. (August 2002). The ultra-wide bandwidth indoor channel: from statistical model to simulations, IEEE Journal on Selected Areas in Communications, Vol. 20, pp. 1247-1257.

Win M. Z. & Sholtz R. A. (December 2002). Characterization of ulra-wide bandwidth wireless indoor channels: a communication theoretic view, IEEE Journal on Selected Areas in Communications, Vol. 20, pp. 1613-1327.

Foerster J. R. (February 2003). Channel modeling sub-committee report final, IEEE P802.15 Working Group for Wireless Personal Area Networks (WPANs).

Saleh A. & Valenzuela R. (February 1987). A statistical model for indoor multipath propagation, IEEE Journal on Selected Areas in Communications, Vol. 5, pp. 128-137.

Astely D.; Dahlman E.; Ludwig R.; Meyer M.; Parkvall S.; Skillermark P. I. & Wiberg N. (March 2006). A future radio-access framework, IEEE Journal on Selected Areas in Communications, Vol. 24, pp. 693-706.

Moon J.; Ko J. Y. & Lee Y. H. (March 2006). A framework design for the next generation radio access system. IEEE Journal on Selected Areas in Communications, Vol. 24, pp. 554-564.

Jang J. & Lee K. B. (February 2003). Transmit power adaptation for multiuser OFDM systems, IEEE Journal on Selected Areas in Communications, Vol. 21, pp. 171-178.

Shen Z.; Andrews J. G. & Evans B. L. (November 2005). Adaptive resource allocation in multiuser OFDM systems with proportional fairness, IEEE Transactions on Wireless Communications, Vol. 4, pp. 2726- 2737.

Chen Z.; Wang D. & Ding G. (September 2006). An OFDM-UWB scheme for adaptive carrier selection and power allocation. IEEE International Conference on Wireless Communications (WiCOM'06), pp. 1-4.

Wang J.; Zhu G. & Jin J. (September 2005). Optimal power allocation for space-time coded OFDM UWB systems, International Conference on Wireless Communications, Networking and Mobile Computing (WCNM'05), Vol. 1, pp. 189-192.

Xu Z. & Liu L. (September 2004). Power allocation for multi-band OFDM UWB communication networks, IEEE Vehicular Technology Conference (VTC'04-fall), Vol. 1, pp. 368-372.

Cuomo F.; Martello C.; Baiocchi A. & Capriotti F. (December 2002). Radio resource sharing for ad hoc networking with UWB, IEEE Journal on Selected Areas in Communiactions, Vol. 20, pp. 1722-1732.

Zhai H. (April 2008). QoS support over UWB mesh networks, IEEE Wireless Communications and Networking Conference (WCNC'08), pp. 2283-2288.

Siriwongpairat W. P.; Han Z. & Ray Liu K. J. (February 2007). Power controlled channel allocation for multiuser multiband UWB. IEEE Trans. on Wireless Communications, Vol. 6, pp. 583-592.

3GPP. (2003). Considerations on the system-performance evaluation of HSDP using OFDM modulations (R1-030999). TSG-RAN-1 # 34.

3GPP. (2003). System level evaluation of OFDM further considerations (R1-031303). 3GPP TSG-RAN-1 # 35.

3GPP. (2004). OFDM-HSPDA system level simulator calibration (R1-040500). TSG-RAN-1 # 37.

3GPP. (2004). System level performance evaluation for OFDM and WCDMA in UTRAN (R1-04-0090). TSG-RAN-1 # 4.

Zhang Y. J. & Letaief K. B. (September 2004). Multiuser adaptive subcarrier and bit allocation with adaptive cell selection for OFDM systems, IEEE Transactions on Wireless Communications, Vol. 3, pp. 1566- 1575.

Bertsekas D. P. (1999). Nonlinear Programming 2nd Edition, Athena Scientific.

Part 4

UWB Applications

15

Throughput Efficiency of Hybrid ARQ Error-Controlling Scheme for UWB Body Area Network

Haruka Suzuki and Ryuji Kohno
Division of Physics, Electrical & Computer Engineering
Graduate School of Engineering, Yokohama National University
Japan

1. Introduction

Recently, semiconductor and circuits have been developed to make many high technologies of processing be easier to be introduced. By using this technology, there has been considerable amount of research effort directed towards applied information and communications technology (ICT) to medical services [1, 2]. Body area networks (BANs) have emerged as an important subject in personal wireless communications. The standardization task group IEEE 802.15.6 determines the standardization of PHY and MAC layers for BANs. WBAN are networks composed of in vivo and in vitro wireless communication. Communication between devices located outside of a human body is named wearable WBAN, and similarly, Communication between devices located inside of a human body is called implanted WBAN.

Wearable WBAN is expected to have numerous applications [3]. For example, each sensor device, which consists of wearable WBAN, can continuously measure and transmit vital parameters data via wearable WBAN. Based on the information sent by a wearable WBAN worn by a particular patient, the hypo-thetical Healthcare Central System of the hospital can be continuously aware of the patient vital functions and is able to take the appropriate countermeasures in case of medical alert. And wearable WBAN is also taken non-medical use (entertainment: video game, music, etc) into consideration. The potential mass market includes medical and non-medical applications. In wearable WBAN, devices treat vital signs of a human body and, therefore, more secure communications are needed. Furthermore, medical ICT has needed data rates of about 10 kbps. Considering practical purposes and non-medical use, however, it is necessary to achieve higher data rates [4, 5]. Most cases of non-medical applications do not require strong error controlling but less complexity and power consumption, and in the special case of video transmission a large throughput and low latency are needed to keep their battery life longer. On the contrary, medical applications require high reliability and relative low data rate transmission as well high data rate transmission. Hence, strong error controlling is expected while relatively larger complexity is allowed. As they require different quality of service (QoS) in terms of reliability and performance, a fixed error controlling mechanism like forward error correction (FEC) is not appropriate.

In order to reconcile medical and non-medical applications requirements, we propose an adaptive error controlling mechanism in the form of hybrid ARQ (H-ARQ). Such error-controlling system adapts to the channel conditions which can optimize the throughput, latency and reliability according to the application specification and channel conditions.

The proposed scheme can be used for both narrowband and wideband PHYs. Although, in the current status of the task group IEEE 802.15.6, non-medical applications are envisioned for the wideband PHY proposal only, i.e., UWB-PHY. On the other hand, medical applications use the narrowband and wideband PHYs. Therefore, we focus on the UWB-PHY for designing and showing the coexistence of medical and non-medical applications for BANs through the proposed H-ARQ.

UWB systems have emerged as a potential candidate for on-body communications in BANs. Indeed, UWB radios allow [1]:

- Low implementation complexity, which is critical for low power consumption.
- The signal power levels are in the order of those used in the MICS band. That is, UWB provides safe power levels for the human body, besides low interference to other devices.
- Finally, impulse radio based UWB systems allows bit rate scalability.

In this section, we propose a simple and practical binary pulse position modulation (2PPM) scheme with energy detection at the receiver. This makes it feasible to implement and analogue front-end at the receiver (with low power consumption) in the high band of UWB, where UWB-BANs are proposed to operate, globally.

In this research, it is assumed that there are interference among coexisting piconets BANs, because a coordinator in each piconet BAN of IEEE802.15.6 can control the whole device access within its coordinating piconet so as to avoid contention among accesses of all the devices although interference among coexisting piconet BANs due to asynchronous access among the coexisting piconets. Since high band of UWB regulation such as 7.25-10.25GHz has suppressed interference enough low for coexistence with other radio communication systems. However, non-coherent transceivers have poorer performance than coherent architectures. Therefore, it is necessary to introduce an error controlling mechanism that can guarantee QoS and performance depending on the application and channel condition, while relying on a simple UWB-PHY.

We show that the good performance in UWB-BAN channels can be achieved. Therefore, a robust scheme is possible for the medical applications of BANs. The advantage of this scheme is its less complex and consequently less power consumption plus it achieves higher throughput compared to using the FEC alone, which are important for BAN applications. Furthermore, from comparing the performance of without our proposed scheme, the proposed schemes obtain up to 2dB of gain at the uncorrected erroneous packet rate and its throughput efficiency improves at a maximum 40 percent while the bit rate for non-medical communications is not changed. Moreover, this error-controlling scheme is proposed at IEEE 802.15.6 committee and that standardization makes agreement to oblige employing this scheme for UWB based medical applications.

2. System model and the definition of WBAN

In this section, we briefly describe the definition of wireless body area network (WBAN) [1, 2], and the description of ultra wideband (UWB) signal and transmission system [4, 5].

2.1 Aim of WBAN

WBAN is for short range, wireless communication in the vicinity of, or inside, a human body (but not limited to humans). It uses existing ISM bands as well as frequency bands approved by national medical and/or regulatory authorities such as UWB(Ultra Wide Band). Quality of service (QoS), extremely low power, and data rates up to 10 Mbps are required while satisfying a strict non-interference guideline. IEEE 802.15.6 standardization considers effects on portable antennas due to the presence of a person (varying with male, female, skinny, heavy, etc.), radiation pattern shaping to minimize Specific Absorption Rate(SAR) into the body, and changes in characteristics as a result of the user motions.
The purpose of WBAN is to provide an international standard for a short range (ie about human body range), low power and highly reliable wireless communication for use in close proximity to, or inside, a human body. Data rates can be offered to satisfy an evolutionary set of entertainment and healthcare services. Current Personal area networks (PANs) do not meet the medical (proximity to human tissue) and relevant communication regulations for some application environments. They also do not support the combination of reliability, QoS, low power, data rate and non-interference required to broadly address the breadth of body area network applications.

2.2 General framework elements

This section provides the basic framework required for all nodes and hubs. It covers the following fundamental aspects: the network topology used for medium access, the reference model used for functional partitioning, the time base used for access scheduling, the state diagram used for frame exchange, and the security paradigm used for message protection.

2.2.1 Network topology

All nodes and hubs will be organized into logical sets, referred to BANs in this specification, and coordinated by their respective hubs for medium access and power management as illustrated in figure 1. There should be one and only one hub in a BAN. In a one-hop star BAN, frame exchanges may occur directly only between nodes and the hub of the BAN. In a two-hop extended star BAN, the hub and a node may optionally exchange frames via a relay capable node.

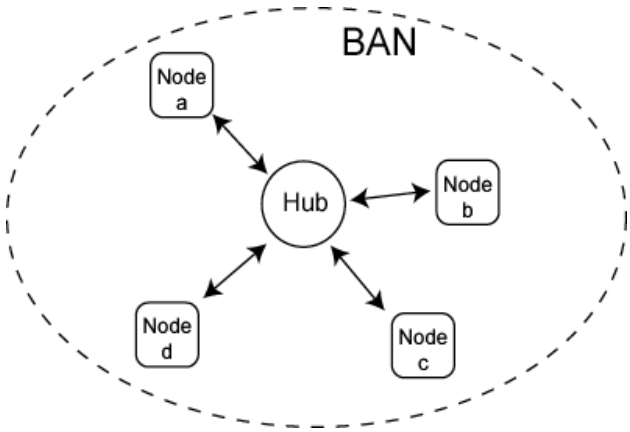

Fig. 1. Network topology

2.2.2 MAC frame formats

All nodes and hubs should establish a time reference base, if their medium access must be scheduled in time, where the time axis is divided into beacon periods (superframes) of equal length and each beacon period is composed of allocation slots of equal length and numbered from 0, 1, ... An allocation interval may be referenced in terms of the numbered allocation slots comprising it, and a point of time may be referenced in terms of the numbered allocation slot preceding or following it as well.

If time reference is needed for access scheduling in its BAN, the hub will choose the boundaries of beacon periods (superframes) and hence the allocation slots therein. In beacon mode operation for which beacons are transmitted, the hub shall communicate such boundaries by transmitting beacons at the start or other specified locations of beacon periods (superframes), and optionally time frames (T-Poll frames) containing their transmit time relative to the start time of current beacon period (superframe). In non-beacon mode operation for which beacons are not transmitted but time reference is needed, the hub will communicate such boundaries by transmitting time frames (T-Poll frames) also containing their transmitted time relative to the start time of current superframe.

A node requiring a time reference in the BAN will derive and recalibrate the boundaries of beacon periods (superframes) and allocation slots from reception of beacons or/and time frames (T-Poll frames). A frame transmission may span more than one allocation slot, starting or ending not necessarily on an allocation slot boundary.

2.3 UWB PHY description

The UWB PHY specification is designed to provide robust performance for BANs. UWB transceivers allow low implementation complexity (critical for low power consumption). Moreover, the signal power levels are in the order of those used in the MICS (Medical Implant Communication Services) band, for example, safety power levels for the human body and low interference to other devices.

2.3.1 Signal model

The paper assumes UWB impulse radio and non-coherent modulation in the form of 2PPM, energy detection. This is the most promising candidate as mandatory mode for the wideband PHY of the IEEE 802.15.6 TG on BANs.

$$x(t) = \sum_{m} w(t - g_m T_{BPM} - m T_{sym}) \tag{1}$$

$$w(t) = \sum_{n=0}^{N_{cpb}-1} d_{m,n} p(t - n T_c) \tag{2}$$

where $g_m \in \{0,1\}$ is the mth component of a given codeword, T_{BPM} is the slot time for 2PPM, and T_{sym} is the symbol time. The basis function $w(t)$ is a burst of short pulses $p(t)$, where $d_{m,n}$ is a scrambling sequence and N_{cpb} is a sequence length. This is only to control data rate and legacy to IEEE 802.15.4a systems.

For the sake of illustration and without loss of generality, it is assumed that $N_{cpb}=1$ and $d_{m,0}=1$,for all m. Moreover, $p(t)$ is a modulated square root raised cosine pulse waveform with duration T_p=2nsec, roll-off factor of 0.5 and truncated to 8 pulse times. The central frequency

f_c is 7.9872 GHz (corresponding to the 9th band of the IEEEE 802.15.4a band plan) and the bandwidth is 499.2 MHz.

3. Proposed error-controlling scheme for WBAN

This section explains our proposed error controlling scheme for WBAN. First, proposed scheme and system model description are described. Next, we derive the theoretical performance of our proposed scheme.

3.1 Error-controlling scheme necessity

Medical and non-medical applications need to coexist in BANs. In particular, the communication link for medical applications requires higher reliability or QoS in contrast to non-medical applications. Most cases of non-medical applications do not require strong error controlling but less complexity and power consumption, and in the special case of video transmission a large throughput and low latency are needed. On the contrary, medical applications require high reliability and relative low data rate transmission. Hence, strong error controlling is expected while relatively larger complexity is allowed. Consequently, the higher QoS BAN needs, the more complexity and higher power consumption are required.

3.1.1 Our idea for error-controlling scheme

As they require different QoS in terms of reliability and performance, a fixed error controlling mechanism like FEC is not appropriate. Thus, in order to reconcile between medical and non-medical applications requirements, we propose an adaptive error controlling mechanism in the form of H-ARQ. Such error system adapts to the channel conditions which can optimize the throughput, latency and reliability according to the application specification and channel conditions.

As H-ARQ combines FEC and retransmission, the main purpose is to design the FEC such that it corrects the error patterns that appear frequently in the channel. The FEC is maintained with low complexity as much as possible. On the other hand, when error patterns appear less frequently like time-varying behaviour and/or deep fades, a retransmission is requested. Hence, a fine balance between throughput and error correction is achieved, which makes the system much more reliable.

3.1.2 H-ARQ scheme of our proposed system

The compliant UWB PHY in cases of medical and non-medical should support a mandatory FEC [1] : (63, 51) BCH codes. Since it is not our research, we refer the draft of IEEE 802.15.6 WBAN standard. In order to harmonize medical a non-medical applications, the first transmission packet should be encoded by (63, 51) BCH code. H-ARQ is only required for high QoS medical applications. Thus, we propose that non-medical devices employ only (63, 51) BCH code and medical devices are H-ARQ enabled.

As WBAN devices should be as less complex as possible, when the retransmitted packet is received, it would be better to minimize the buffering size of the receiver.

In general, the two main types of H-ARQ are Chase combining (CC) and incremental redundancy (IR) [6, 7, 8]. With CC schemes, the same encoded packet is sent for transmission and retransmission. On retransmission, the packets are combined based on

either the weighted SNR's (signal to noise ratio) of individual bits or soft energy values. Thus, the receiver must utilize soft decision, and buffer soft output. Its buffering size is three times higher than without using H-ARQ; i.e., '111'represents '1'.
With IR schemes, transmission and retransmission differ. However, if a half-rate code is used in this scheme, the buffering size is same or double than without using H-ARQ. In this scheme, retransmission packets consist only of parity bits. The receiver combines additional parity bits from retransmission, and decodes in an efficient manner. The retransmissions are alternate repetitions of the parity bits and first transmission bits.
Thus, we employ the notion of IR scheme. At the first transmission of both medical and non-medical, the transmission packets consist only of (63, 51) BCH codewords. For a retransmission, the transmitter encodes the first transmission packets based on a half-rate systematic codes and obtains retransmission packets of parity bits only. Therefore, the buffering size of our proposed scheme is same or double than without using H-ARQ. Additionally, decoding (63, 51) BCH codes and a half-rate systematic codes makes its performance more effective than the basic IR scheme since double coding and decoding.
This error-controlling scheme is proposed at IEEE 802.15.6 committee by Prof.Kohno in March and May 2009. That standardization makes agreement to oblige employing this scheme for UWB based medical applications.

3.2 Proposed system description

As mentioned above, the proposed system is H-ARQ with IR scheme. In such scheme, only parity bits are sent with some retransmissions. Erroneous packets are not discarded and the decoder can employ the previous received packets. The main requirement for the error controlling scheme are low coding overhead and are suitable for bursty (time-varying) channels.
Figures 2 and 3 show the flowchart and our proposed system model, respectively. Where, $\hat{u}$ and u′ represent demodulated and decoding bits
In our proposed system, both of the medical and non-medical applications use the same modulation and demodulation schemes. But only the medical application has a H-ARQ function. Hence, when the lack of the reliability has detected, the medical devices can request a retransmission.
First transmissions packet (we call data packet) shown in figure 3(a) consists of (n=63, k=51) BCH codewords $\mathbf{c}_0=(\mathbf{m},\mathbf{p}_0)$ where

$$\mathbf{m} = \{m_1, m_2, ..., m_i, ..., m_k\}, m_i \in \{0,1\}, (1 \le i \le k) \tag{3}$$

$$\mathbf{p}_0 = \{p_{01}, p_{02}, ..., p_{0j_0}, ..., p_{0(n-k)}\}, p_{0j_0} \in \{0,1\}, (1 \le j_0 \le n-k) \tag{4}$$

denote information and parity bits respectively.
Date packets occur in both case of medical and non-medical and decoding based on (63, 51) BCH codes is processed. If medical receiver detects erroneous bits by computing its syndrome, the packet consists only of half-rate systematic parity bits $\mathbf{c}_1$ (we call parity packet) is required by sending *NAK*. Figure 3(b) shows the parity packet transmission. Upon receiving the second *NAK*, the transmitter re-sends the data packet or the parity packet alternately. The parity bits $\mathbf{c}_1=(\mathbf{p}_1)$

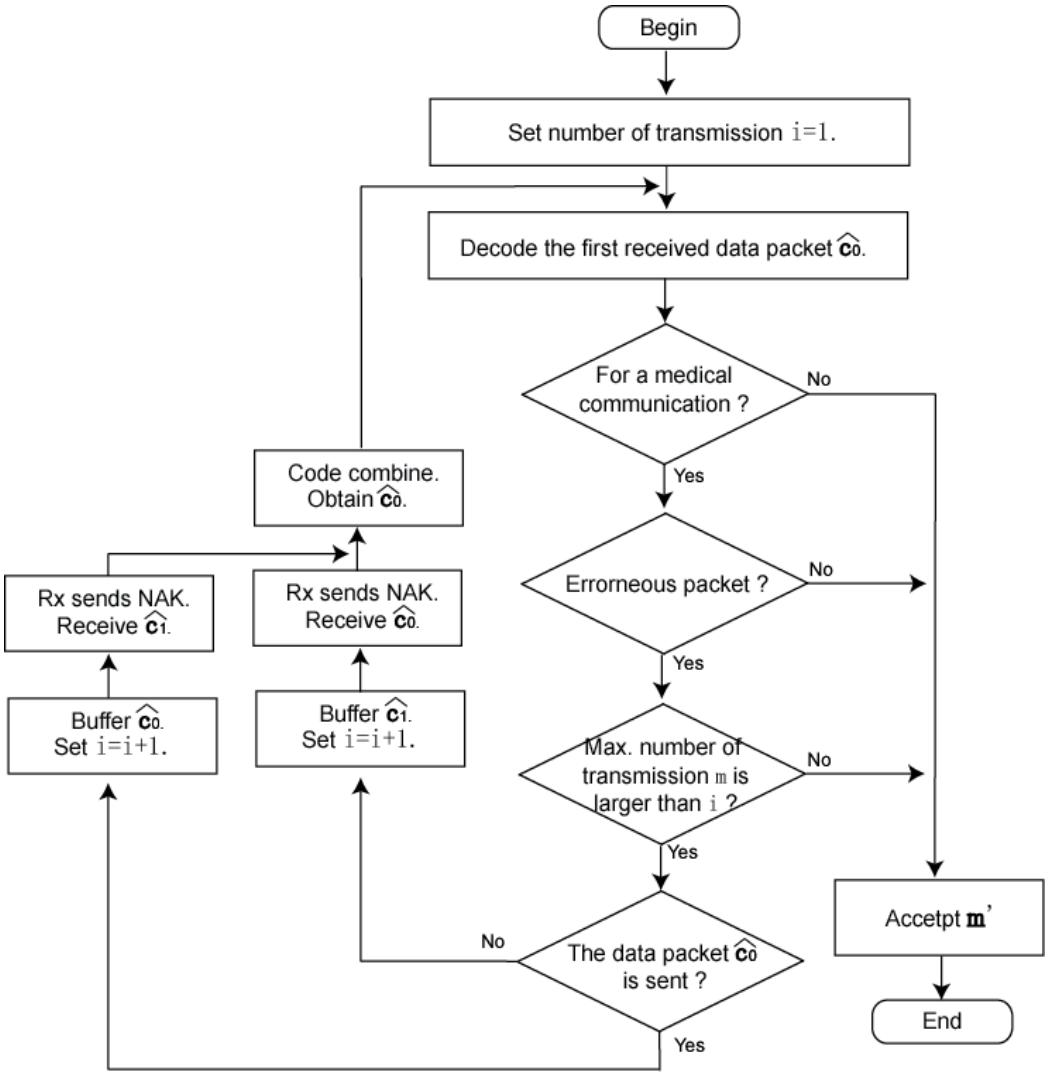

Fig. 2. The flowchart of the proposed system

$$\mathbf{p}_1 = \{p_{11}, p_{12}, ..., p_{1j_1}, ..., p_{1(n_1-k_1)}\}, p_{1j_1} \in \{0,1\}, (1 \le j_1 \le n_1 - k_1) \tag{5}$$

are obtained from encoding the data packet $\mathbf{c}_0$.

After receiving the data (or parity) packet or parity packet, previous data (or parity) packet is discarded and combined with previous parity (or data) packet. And the receivers decode based on (63, 51) BCH codes and a half-rate systematic codes. Thus, the data and parity packet are buffered at the receiver.

The retransmissions continue until the error bits are not detected in information bits $\mathbf{m}'$ or the number of retransmission reaches the limited number.

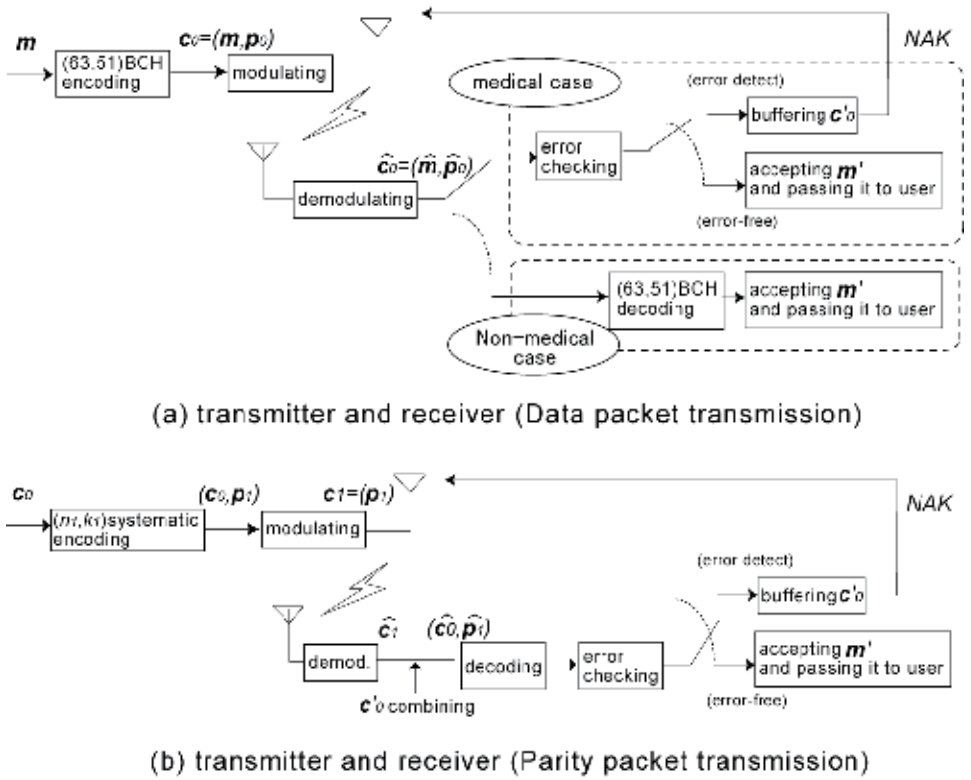

Fig. 3. The proposed system model

3.2.1 Packet construction of our proposed system

From above mentioned, figure 4 shows packet construction of our proposed system.

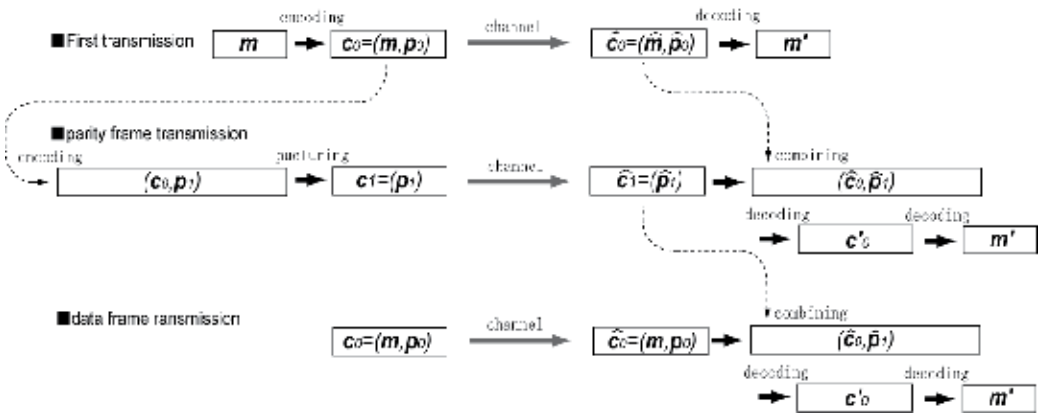

Fig. 4. Packet construction of our proposed system

The data packets $\mathbf{c}_0=(\mathbf{m}, \mathbf{p}_0)$ comprise of (n=63, k=51) BCH codewords. And the parity packets $\mathbf{c}_1=(\mathbf{p}_1)$ consist of only parity bits of a half-rate systematic (n_1, k_1) codewords.

After receiving the parity packets, the receivers combine the data packets $\mathbf{c}_0$ and the parity packets $\mathbf{c}_1$ and obtain a half-rate systematic (n_1, k_1) codewords.
First, the receivers decode based on a half-rate systematic (n_1, k_1) codes, and then decode based on (n=63, k=51) BCH codes.

3.3 Derived theoretical performance

In this section, we derive the theoretical performance of our proposed scheme. For comparison, we also consider the case of ARQ system. In this case, the retransmission is occurred by collision.

3.3.1 Assumed MAC layer configuration

Figure 5 shows the diagram of transmission protocol.
The message is divided into the packets and then transmitted. The length of the packet is less the length of the slot. If the number of retransmission is limited, there is a possibility of accepting the erroneous packet. The quality of the message is deteriorated by accepting the erroneous packet. We evaluate this performance after.
Considering the message of other devices, it is necessary to think about not only PHY but also MAC. Hence, the network coordinator defines the start and end of a superframe by transmitting a periodic beacon. The superframe may consist of both an active and inactive period. The active portion of the superframe is composed of three parts: a beacon, a contention access period (CAP), and a contention free period (CFP). In this research, only CAP or CFP case is assumed. Therefore, we evaluated the proposed scheme in each network algorithm of Slotted ALOHA or Polling.

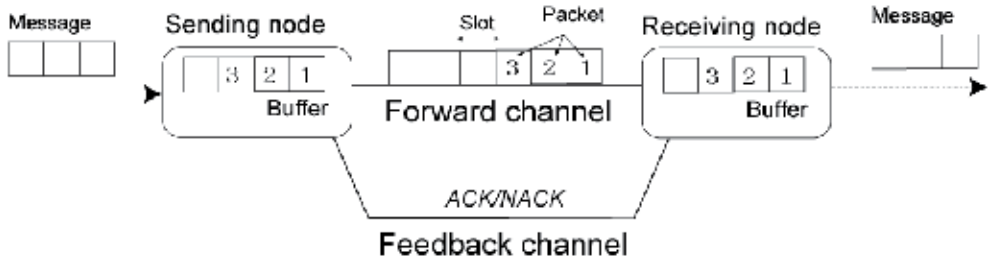

Fig. 5. Transmission protocol

The message transmission delay D is assumed to be a passing number of slots between the message #A arrive at sending node and all N packets that belong to #A are accepted at receiving node. Then we can calculate the throughput efficiency η .

$$\eta = L_m(1-\varepsilon)/D \tag{6}$$

where L_m and ε represent message length and message error rate respectively.

3.3.2 ARQ system

We determine the following variables.
q : The collision probability.
m : The number of transmission per one packet.
N : The total packets belonging to one message.

p_b : Channel bit error rate.
R_c : Passing number of slots until the following transmission (or retransmission) when collision occurred.
We must note that ACK/NAK is sent until the end of slot.
The probability of transmission success P_s and failure P_f with each number of retransmission are followed.

- m=1, P_s=1-q, P_f=q.
- m=2, P_s=q(1-q), P_f=q^2, P_s (when m=1)=1-q.
- m=i, P_s=$q^{(i-1)}$(1-q), P_f=q^i , P_s (when m=1,2,...,i-1)=1-$q^{(i-1)}$.

Thus，when the maximum number of transmission equals M, received bit error rate p_{ARQ} and the message transmission delay D_{ARQ} are calculated by these equations.

$$p_{ARQ} = (1+q^M)p_b + q^M \tag{7}$$

$$D_{ARQ} = R_c\{\sum_{m=1}^{M-1}(m-1)q^{m-1}(1-q)+(M-1)q^{M-1}\}+N \tag{8}$$

3.3.3 Our proposed system

Additionally, we use the following variables.
p_{b1}, p_{b2}, ... , p_{bi}, ... : Channel bit error rate for each number of transmission (i=1,2,...)
p_{f1}, p_{f2}, ... , p_{fi}, ... : Channel packet error rate for each number of transmission (i=1,2,...)
R_e : Passing number of slots until the following transmission (or retransmission) when erroneous packet is detected.

- m=1, P_s=(1-q)(1-p_{f1}), P_f=q+(1-q)p_{f1}.
- m=2, P_s=(1-q)(1-p_{f1})+ (1-q)$^2p_{f1}$(1-p_{f2}) P_f= q^2+2q(1-q)p_{f1}+(1-q)$^2p_{f1}p_{f2}$.
- m=i,

P_s : sum of the following matrix $\mathbf{X}_i\mathbf{Y}_i$'s row.
P_f : sum of the following matrix $\mathbf{X'}_i\mathbf{Y'}_i$'s row

$$\mathbf{X}_i\mathbf{Y}_i = \mathbf{X}_i\begin{bmatrix} q^{i-1}(1-q)^1(1-p_{f1})\prod_{j=0}^{1-1}p_{fj} \\ \vdots \\ q^{i-k}(1-q)^k(1-p_{fk})\prod_{j=0}^{k-1}p_{fj} \\ \vdots \\ q^0(1-q)^m(1-p_{fi})\prod_{j=0}^{i-1}p_{fj} \end{bmatrix}^T \tag{9}$$

$$\mathbf{X}'_i\mathbf{Y}'_i = \mathbf{X}'_i\begin{bmatrix} q^i(1-q)^{1-1}\prod_{j=0}^{1-1}p_{fj} \\ \vdots \\ q^{i-k+1}(1-q)^{k-1}\prod_{j=0}^{k-1}p_{fj} \\ \vdots \\ q^0(1-q)^i(1-p_{fi})\prod_{j=0}^{i-1}p_{fj} \end{bmatrix}^T \tag{10}$$

where,

$$\mathbf{X}_i = \begin{bmatrix} \mathbf{X}_{i-1} \\ 0 \end{bmatrix} + \begin{bmatrix} 0 \\ \mathbf{X}_{i-1} \end{bmatrix}, \mathbf{X}_1 = 1 \tag{11}$$

$$\mathbf{X}'_i = \begin{bmatrix} \mathbf{X}'_{i-1} \\ 0 \end{bmatrix} + \begin{bmatrix} 0 \\ \mathbf{X}'_{i-1} \end{bmatrix}, \mathbf{X}'_1 = \begin{bmatrix} 1 \\ 1 \end{bmatrix} \tag{12}$$

Thus, when the maximum number of transmission equals M, received bit error rate p_{prop} and the message transmission delay D_{prop} are described by the equations below.

$$p_{prop} = \sum_{m=1}^{M} p_{sm} + p_{eM} \tag{13}$$

$$D_{prop} = \sum_{m=1}^{M} d_{sm} + d_{eM} \tag{14}$$

Where,
p_{sm} : sum of the following matrix $\mathbf{X}_{\text{m}}\mathbf{Y}_{\text{m}}\mathbf{P}_{\text{m}}$'s row.
p_{fm} : sum of the following matrix $\mathbf{X'}_{\text{m}}\mathbf{Y'}_{\text{m}}\mathbf{P'}_{\text{m}}$'s row
d_{sm} : sum of the following matrix $\mathbf{X}_{\text{m}}\mathbf{Y}_{\text{m}}\mathbf{R}_{\text{m}}$'s row.
d_{fm} : sum of the following matrix $\mathbf{X'}_{\text{m}}\mathbf{Y'}_{\text{m}}\mathbf{R'}_{\text{m}}$'s row

$$\mathbf{X}_m\mathbf{Y}_m\mathbf{P}_m = \mathbf{X}_m\mathbf{Y}_m \begin{bmatrix} p_{b1} \\ \vdots \\ p_{bk} \\ \vdots \\ p_{bm} \end{bmatrix}^T, \mathbf{X}'_m\mathbf{Y}'_m\mathbf{P}'_m = \mathbf{X}'_m\mathbf{Y}'_m \begin{bmatrix} p_{b0} = 1 \\ \vdots \\ p_{b(k-1)} \\ \vdots \\ p_{bm} \end{bmatrix}^T \tag{15}$$

$$\mathbf{X}_m\mathbf{Y}_m\mathbf{R}_m = \mathbf{X}_m\mathbf{Y}_m \begin{bmatrix} (m-1)R_c + R_e \\ \vdots \\ (m-k)R_c + kR_e \\ \vdots \\ mR_e \end{bmatrix}^T \tag{16}$$

$$\mathbf{X}'_m\mathbf{Y}'_m\mathbf{R}'_m = \mathbf{X}'_m\mathbf{Y}'_m \begin{bmatrix} (m-1)R_c + R_e \\ (m-1)R_c + R_e \\ \vdots \\ (m-(k-1))R_c + (k-1)R_e \\ \vdots \\ mR_e \end{bmatrix}^T \tag{17}$$

4. Code selection for proposed error-controlling scheme

First, we explain the description of a mandatory FEC for WBAN. And the bit error rate performance of our proposed scheme in cases of using other codes is showed. Moreover, we derive the effect of FEC of Hybrid ARQ on the bit error rate performance at each number of retransmission.
Finally, we determine which code employed for proposed scheme. Moreover, since our proposed scheme is employed the IEEE802.15.6 standardization, code selection is important research.

4.1 Requirements for codes of our proposed H-ARQ scheme

In order to ensure interoperability, a mandatory mode is required. A compliant FEC for UWB PHY should support systematic (63, 51) BCH code [1].
From the construction of packet for our proposed system in section 3, candidate codes must have the following features:

- The code is a half-rate and systematic. For decreasing the buffer usage as far as possible, it is desired that the length of candidate codeword is double as long as first transmission codeword.
- The information length of the code is 63 or it is a divisor of 63. Since a compliant FEC for UWB PHY should support systematic (63, 51) BCH code.

If a compliant FEC for UWB PHY is different, requirement of the code is a half-rate and systematic is same.

4.2 Candidate codes for proposed error-controlling scheme

The above mentioned are qualified as a candidate FEC for H-ARQ of our proposed system.
Since it is satisfied the above mentioned requirements for codes of our proposed H-ARQ scheme, we use shortened BCH codes and systematic convolutional codes to make the code rate 1/2. The decoding methods are the bounded distance decoding and the viterbi decoding. For employment viterbi decoding, constraint length must be less of 10 [8].
Parameters and its generator polynomial are noted in table 1 and 2.
Although, (30, 15) BCH code is not satisfied for our proposed H-ARQ scheme, we consider to compare.

(n, k) code	$d_{\min}$
(6, 3) BCH code (shortened (7,4) BCH code)	3
(30, 15) BCH code (shortened (31,16) BCH code)	7
(126, 63) BCH code (shortened (127,64) BCH code)	21

Table 1. Parameters of systematic BCH code with code rate 1/2.

Constraint length K	$d_{\min}$
3	4
7	6
9 (,10)	8

Table 2. Parameters of systematic convolutional code with code rate 1/2.

4.3 Performance evaluation for code selection

In this section, the performances of the above-mentioned candidate codes are evaluated for code selection.

4.3.1 Decoded bit error performance of candidate codes

The decoded bit error performances of the above-mentioned candidate codes are evaluated by the Monte-Carlo simulations.
The simulation parameters are summarized in the table 3 [1, 5, 8].

Channel	IEEE802.15.6 CM3
Pulse shape	Modulated RRC
Bandwidth	500MHz
Bit rate	2Mbps
Coding	Data packet : (63,51) BCH codes Parity packet : above-mentioned
ARQ protocol	Selective Repeat ARQ

Table 3. Simulation Parameters for code selection

In the case of using the candidate BCH codes, the improvement of the data packet retransmission is larger than the parity packet retransmission. This performance declares the block code is affected by erroneous data bits. On the other hand, using convolutional codes, the improvement of each retransmission is same. It denotes that the encoding and decoding processes are influenced previous bits.

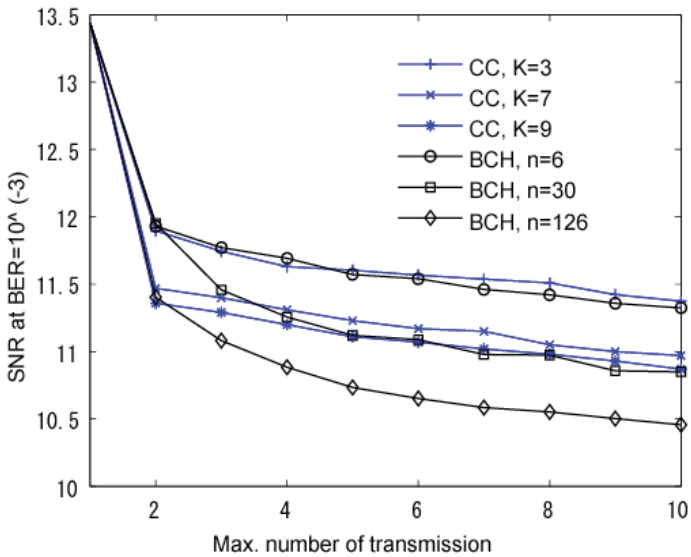

Fig. 6. SNR (signal to ratio) at BER (bit error rate)=10^{-3} with each codes

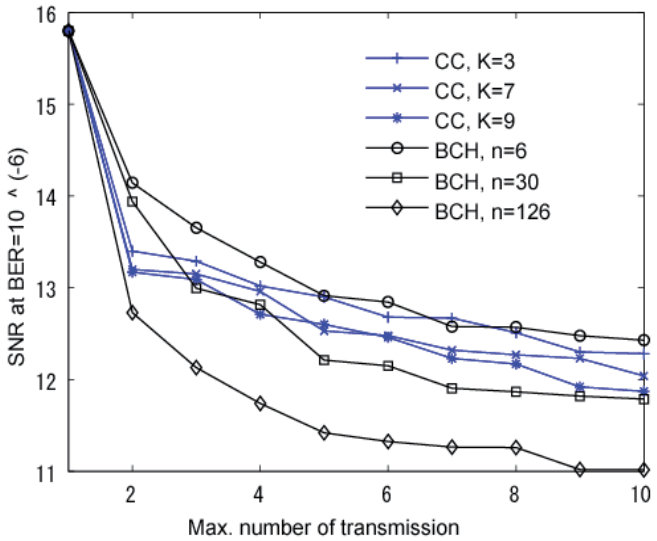

Fig. 7. SNR (signal to ratio) at BER (bit error rate)=10^{-6} with each codes

4.3.2 Decoding complexity of candidate codes

In bounded distance decoding with euclid algorithm, the decoding complexity is $O(t^2)$, where t represents error correcting capability and it is calculated by this equation.

$$t = \left\lfloor \frac{d_{\min} - 1}{2} \right\rfloor \tag{18}$$

(n, k)	(6, 3)	(30, 15)	(126, 63)
$O(t^2)$	$O(1)$	$O(9)$	$O(100)$

Table 4. The decoding complexity $O(t^2)$ of bounded distance decoding

Meanwhile, the complexity of viterbi decoding increases as $O(2^K)$, with the constraint length K.

K	3	7	9
$O(2^K)$	$O(8)$	$O(128)$	$O(512)$

Table 5. The decoding complexity $O(2^K)$ of viterbi decoding

Table 5.4 and 5.5 show $O(t^2)$ and $O(2^K)$ of the candidate codes, respectively.
The complexity of (126, 63) BCH code is smaller than K=7 convolutional code. Also, (126, 63) BCH code has good bit error rate performance. Moreover, lower code rate of block codes makes low undetected erroneous bit. It is good for retransmission to determine.
From these performances, we select (126, 63) BCH code.

5. Performance evaluation

In this section, the above-mentioned proposed system considering PHY and MAC is evaluated by the Monte-Carlo simulations. Then, we evaluate the performance of our

proposed scheme, and we show that our proposed scheme makes low erroneous frame rate. Moreover, message throughput efficiency becomes more efficient than using FEC only.

5.1 Simulation parameters and definitions

The simulation parameters are summarized in the table 6. We refer the standardization of IEEE 802.15.6 [1, 5, 8].

Channel	IEEE802.15.6 CM3
Pulse shape	Modulated RRC
Bandwidth	500MHz
Bit rate	2Mbps
Coding	Data packet : (63,51) BCH codes Parity packet : (126,63) BCH codes
Decoding	Bounded distance decoding
ARQ protocol	Selective Repeat ARQ
R_c	1~5 slot (uniform pseudorandom number)
R_e	1 slot
N	5 [packets]
L_m	1020 [bits]

Table 6. Simulation Parameters

Using Slotted ALOHA algorithm, if the average probability of frame arrival is equal to λ, the probability $P(K)$ that the K frames arrive at the sending node in the interval time τ is

$$P(K) = \frac{(\lambda\tau)^K \exp(-\lambda\tau)}{K!} \tag{19}$$

Then, offered traffic $G = \lambda\ \tau$ is fixed; 0.01, 0.5, 1.00 and the probability of occurring collision are calculated [22]. Besides, using Polling algorithm, the number of users U is fixed; 2, 4, and the performance are derived.

For comparing, we also derive the performance of without using H-ARQ scheme. In this case, the receiver can detect erroneous bits by calculating the syndrome of (63,51) BCH codes. However, an only data packet is retransmitted.

5.2 Numerical results and theoretical value

The maximum number of transmissions M is bounded 1~10.

We show our proposed scheme effectively from evaluating the performances of uncorrected erroneous packet rate and throughput efficiency. And, since the drawback is increasing of buffer usage, also we derive this performance.

5.2.1 Uncorrected erroneous packet rate

Erroneous packet is received when the number of transmission is reached the maximum number of transmission M. Figures 7 shows the performances of uncorrected erroneous packet rate of simulation and theoretical results using S-ALOHA algorithm when G=0.01.

In case of polling algorithm, the performance is not influenced from the number of other users U. We show only the performance of uncorrected erroneous packet rate of simulation and theoretical results using polling algorithm when U =2 at figures 8.
For deriving the performance by Monte-Carlo simulations, the large number of trials requires a lot of time. Thus, at low value of uncorrected erroneous packet rate cannot be shown these figures.

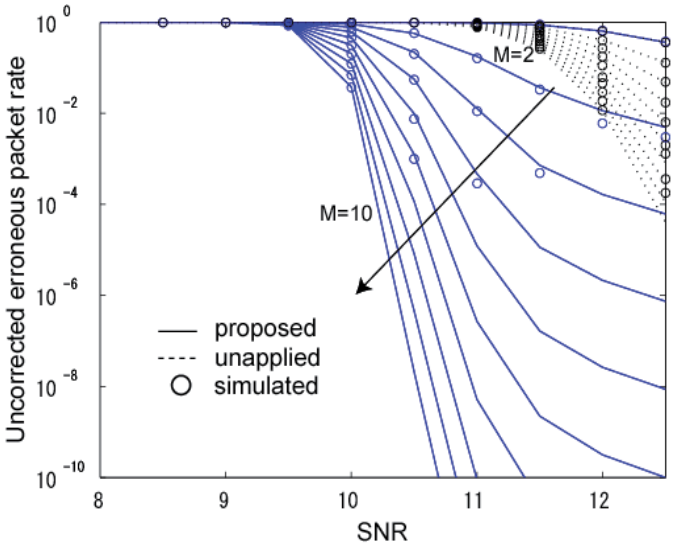

Fig. 8. Uncorrected erroneous packet rate using S-ALOHA algorithm (G=0.01)

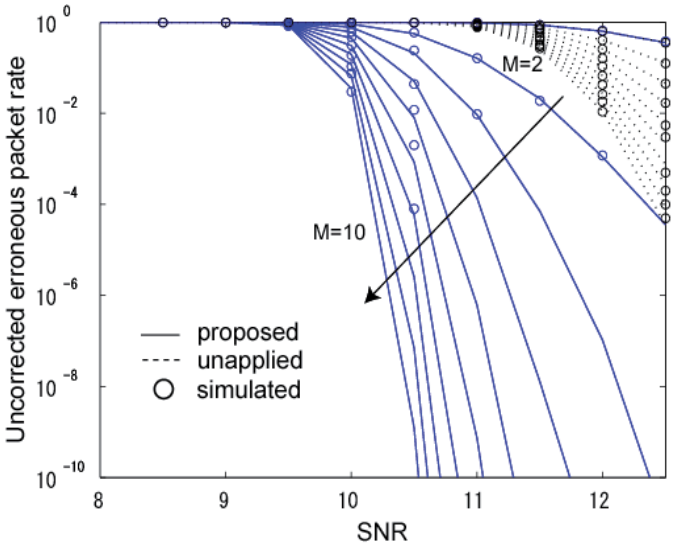

Fig. 9. Uncorrected erroneous packet rate using polling algorithm (U=2)

5.2.2 Buffer usage

Figure 10 shows the average buffering usage [packets] per one message with S-ALOHA and polling algorithms. When the N packets are accepted, they are sent to the user and deleted in buffer.

To compare without using proposed scheme, figure 11 and 12 show the performance of G=1.0 and U=2 respectively.

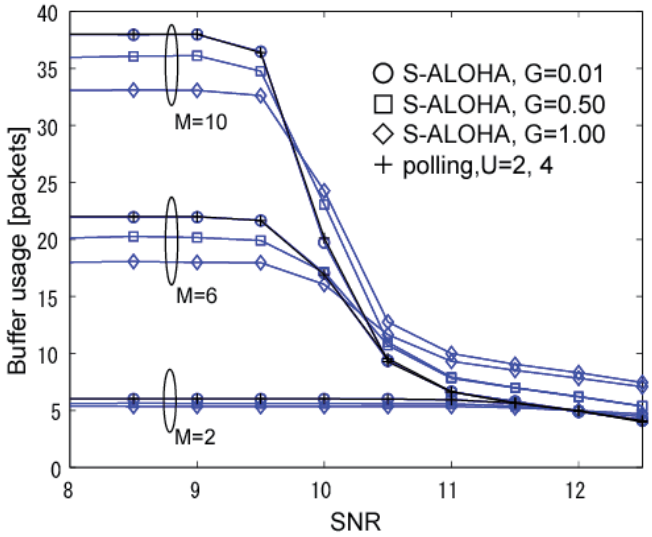

Fig. 10. The average number of buffering packets per one message

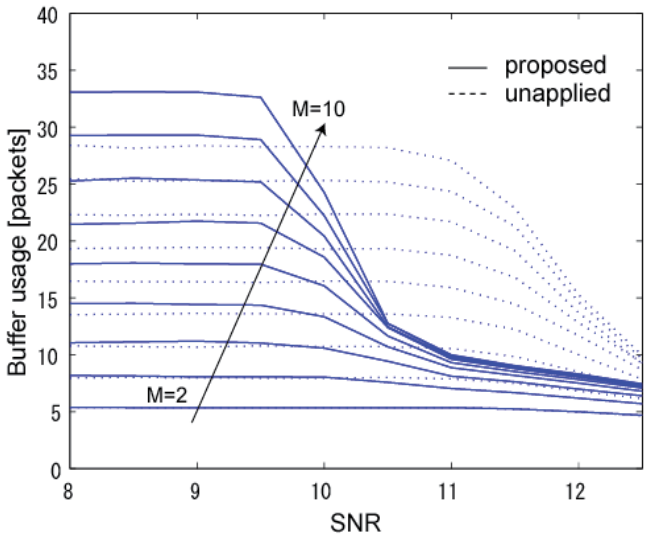

Fig. 11. The average number of buffering packets per one message using S-ALOHA algorithm (G=1.0)

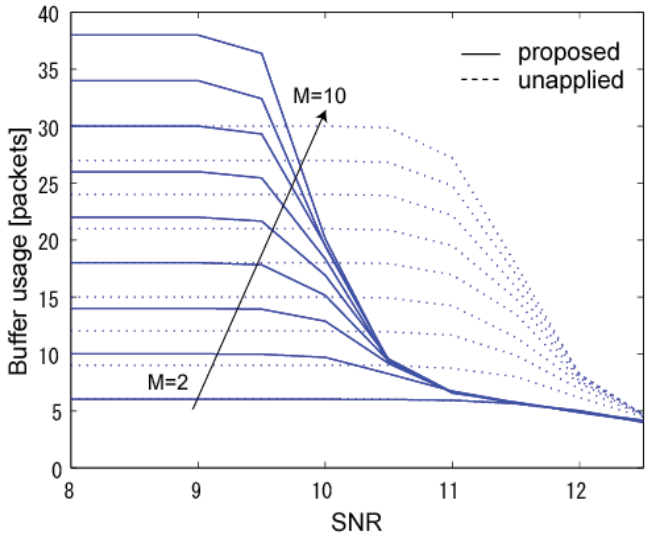

Fig. 12. The average number of buffering packets per one message using Polling algorithm (U=2)

5.2.3 Throughput efficiency

The message throughput efficiency η with S-ALOHA and polling algorithm shows in figures 13 and 14. We want to make the performance more visible, these figures shows at SNR=11.5 and 12.5dB respectively (each marker denotes: ○:S-ALOHA, G=0.01., □:S-ALOHA, G =0.5., ◇:S-ALOHA, G =1., ＋:polling, U=2., ×:polling, U =4.)

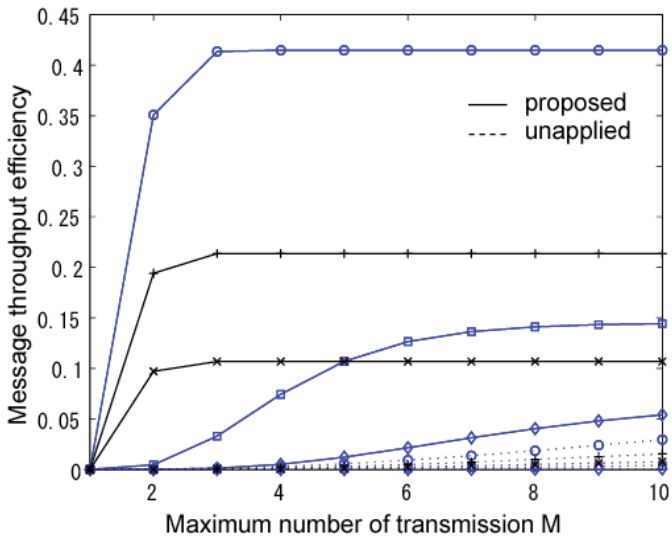

Fig. 13. Message throughput efficiency using S-ALOHA and polling algorithms at SNR=11.5 dB(medical case)

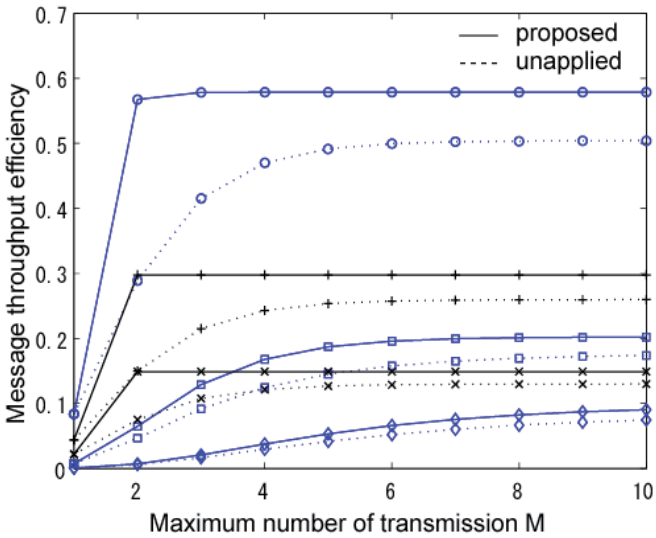

Fig. 14. Message throughput efficiency using S-ALOHA and polling algorithms at SNR=12.5 dB(medical case)

In figure 14, the message throughput efficiency η of without or using our proposed scheme with S-ALOHA algorithm (G=0.01).

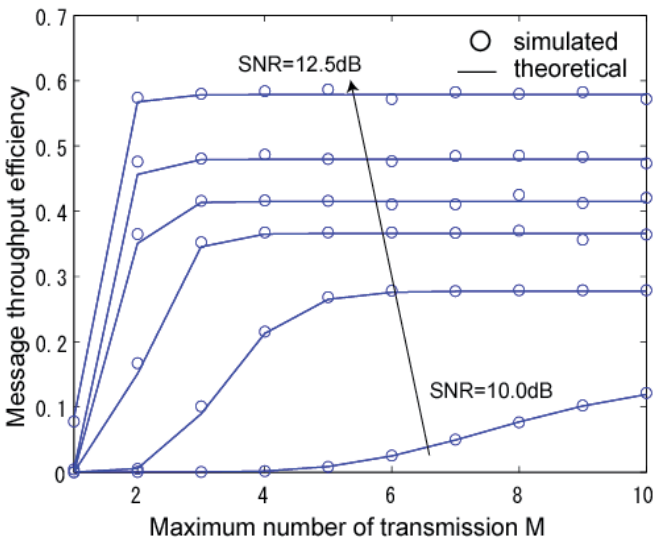

Fig. 15. Message throughput efficiency using S-ALOHA algorithms (medical case)

Furthermore, figures 15 and 16 shows the throughput efficiency of medical and non-medical communication cases. For comparing medical and non-medical usage, the throughput efficiency is redefined the following equations.

$$\eta = L_m(1-\varepsilon')/D \tag{20}$$

Medical cases: ε' denotes received erroneous packet rate.
Non-medical cases: ε' denotes received bit error rate.
In the case of non-medical communications, the receiver does not check the erroneous packet and accepts any packet. On the other hand, in medical cases, the receiver checks. Furthermore, the erroneous packet is discarding.
Since the performances of first transmission of proposed scheme overlap the unapplied one, the first transmission performance of proposed scheme is not shown in figures 15 and 16.

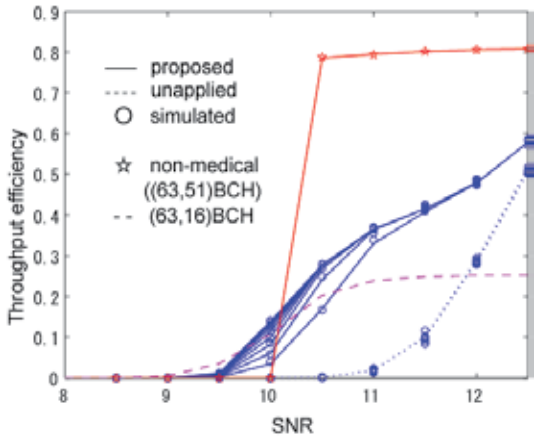

Fig. 16. Throughput efficiency of simulation and theoretical results using S-ALOHA algorithm (medical and non-medical)

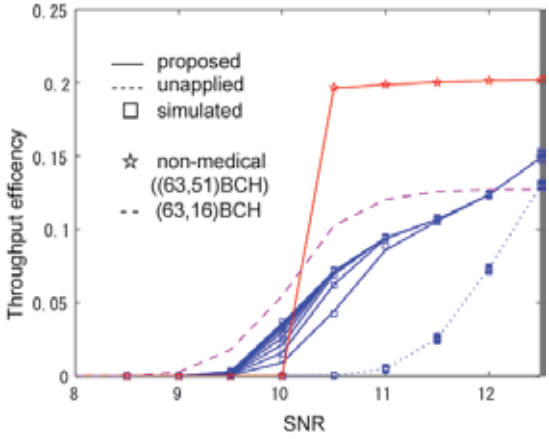

Fig. 17. Throughput efficiency of simulation and theoretical results using polling algorithm (medical and non-medical)

5.3 Performance evaluation

From figure7, since the collision is a lot of occurred and the same data or parity packet are retransmitted, the improvement by H-ARQ is limited. On the other hand, using polling

algorithm, there is no collision. Thus, our proposed scheme performances of each number of transmissions improve as shown figure 8. Both of S-ALOHA and polling algorithm, our proposed schemes achieve up to 2dB of gain from comparing the unapplied proposed scheme. So the proposed scheme provides the high reliability of the medical communications.

Figure 9 shows the average number of buffering packets per one message. If SNR is low, they are not accepted easily. Therefore the buffering usage increases. However, when a lot of the collision makes the number of the transmission reaches M, the receiver accepts the packet and deletes in buffer. So the buffering usage is decreases. Therefore, at SNR < 9.5-11 dB, as G is larger, the buffer usage is lower. Meanwhile, since N packets are accepted successfully by improvement of receiving both of data and parity packets, a lot of deleted packet is arisen. Hence, the buffering usage decreases.

For comparing the unapplied proposed scheme, figures 10 and 11 bring out our proposed scheme drawback. When SNR is low, a lot of data and parity packets are transmitted. Therefore, the proposed scheme is less inferior to the unapplied. However, if the channel condition becomes good, packets are accepted successfully by improvement of H-ARQ and a lot of deleted packet is arisen.

In figures 12 and 13, the performance of our proposed scheme has large efficient at SNR=11.5dB. It shows the effectiveness of H-ARQ on the poor channel conditions. And, the performance of using S-ALOHA algorithm G=0.50 at SNR=11.5dB is larger than using polling U=4 at M > 6. This reason is that the using polling algorithm makes a lot of message delay when the maximum number of retransmission is large. Furthermore, figure 14 shows the adequate number of transmission is determine at each SNR (i.e. at SNR=12.5dB, the adequate number of transmission is 3).

From figures 15 and 16, the throughput performance of non-medical case exceed medical cases at SNR < 10dB. The reason of performance is receivers of non-medical applications do not check erroneous packets. It makes high bit rate for non-medical communications. Also figures show throughput efficiency of proposed scheme improves at a maximum 40 percent. Therefore, the medical communications can satisfy its QoS by using proposed scheme while the bit rate for non-medical communications is not changed. Our proposed scheme achieves to reconcile medical and non-medical applications requirements.

To summarize, using polling algorithm achieves good performance of received erroneous packet rate and buffering usage. However, it is not same for the throughput efficiency. When there are many other communication devices, the performance using polling algorithm is low efficiency as shown figures 12 and 13. Thus, we are going to propose the system which can decide retransmission by consideration of both PHY and MAC.

6. Conclusion

We show using our proposed error-controlling scheme can be achieved robustness for medical applications without ruining efficiency of data rate for non-medical applications in UWB-BAN channels.

This research work explored H-ARQ techniques for BANs. The signalling scheme was IR-UWB in the high band of UWB with 2PPM and energy detection. The investigated H-ARQs were based on IR scheme combined with two linear codes. We employed (126, 63) BCH codes based H-ARQ to achieve both of high data rate of the non-medical application and low bit error rate of the medical one. This error-controlling scheme is proposed at IEEE

802.15.6 committee and that standardization makes agreement to oblige employing this scheme for UWB based medical applications.

Simulations results show that good performance in UWB-BAN channels can be achieved. Hence, a robust scheme is possible for the medical applications of BANs. The advantage of this scheme is less complex and consequently less power consumption plus it achieves higher throughput than when only the FEC was used, which are important for BAN applications. Furthermore, from comparing the performance of without our proposed scheme, the proposed schemes obtain up to 2dB of gain at the uncorrected erroneous packet rat and its throughput efficiency improves at a maximum 40 percent while the bit rate for non-medical communications is not changed. Finally, the proposed schemes showed a practical form of coexistence between the medical and the non-medical applications in BANs.

According to the performance evaluation, it is obvious not only channel condition but also the probability of collision effect the performance. It is considered that if the waiting time for packet transmission exceeds the tolerable quantity or transmission delay D much increases, using more complexity decoding at the receiver makes the number of waiting packet decreases. However, the drawback is the improvement of the error rate cannot exceed when the retransmission is received. In the future, we are going to construct the system which can decide retransmission by consideration of both PHY and MAC.

7. References

IEEE P802.15 Working Group for Wireless Personal Area Networks(WPANs). TG6 Body Area Networks (BAN) draft standard, IEEE P802.15-10-0245-06-0006[Online]

W.ASTRIN, Huan-Bang LI, Ryuji KOHNO. Standardization for Body Area Networks, *IEEE Transactions on Communications,* vol.E92-B, no.2 February 2009

IEEE P802.15 Working Group for Wireless Personal Area Networks(WPANs). Channel Model for Body Area Network (BAN), IEEE P802.15-08-0780-10-0006[Online]

Igor Dotlic, Ryuji Kohno. (2009). NICT Phy Solution:Part1 Chirp Pulse Based IR UWB Physical Layer, IEEE P802.15-09-0166-01-0006[Online]

Marco Hernandez, Ryuji Kohno. (2009) NICT's Wideband PHY Proposal Part2: MB-IR-UWB, IEEE P802.15-09-0613-00-0006[Online]

S. Lin, P. Yu. A Hybrid ARQ with Parity Retransmission for Error Control of Satellite Channels, *IEEE Transactions on Communications,* vol.30, No 7, pp.1701-1719, July 1982.

David Chase. Code Combining--A Maximum-Likelihood Decoding Approach for Combining an Arbitrary Number of Noisy Packets, *IEEE Transactions on Communications,* vol. COM-33, No 5, pp.385-393, May 1985.

S. Lin, D. J. Costello Jr (1983). ErrorControl Coding: Fundamental and Applications, Prentice-Hall, *Englewood Cliffs NJ*

16

UWB-over-Fibre in Next-Generation Access Networks

Roberto Llorente, Marta Beltrán and Maria Morant
Valencia Nanophotonics Technology Center, Universidad Politécnica de Valencia
Spain

1. Introduction

The access network is the part of the telecommunications infrastructure responsible for the connectivity in the last mile, i.e. from the operator's Central Office or Exchange to the customer premises. At the Central Office the access network interfaces with the metropolitan or with the core optical networks, which aggregate and routes the data from a large number of users. At the customer premises, the access network extends the connectivity to the so-called user network. Different user network implementations can be found nowadays: LAN (Local Area Network), PAN (Personal Area Network), HAN (Human Area Network) or even BAN (Body Area Network). A combination of some of these can be present in a given usage scenarios.

Different usage profiles must be accommodated in the access network: a residential user, a small-office, or even a large company - all these exhibit very different connectivity requirements- leading to different technological implementations. Currently deployed access networks are based on copper twisted-pair transmission media and are deployed over legacy telephone networks. This is, by example, the case of ADSL (Asymetric Digital Suscriber Line).

Access networks based on legacy infrastructures are reaching their capacity limits. The conventional access network infrastructures, namely the twisted-pair telephony networks and the coaxial Cable Television (CATV) networks, struggle to support current data traffic demands for high-definition content distribution and real-time applications. Digital Subscriber Line (DSL) techniques and cable modem techniques evolved into higher speeds, but at the cost of a shorter reach. Currently, the unique properties of optical fibres (e.g. low losses and extremely wide bandwidth) have made them the ideal candidate to meet the capacity challenges for now and the foreseeable future (Koonen, 2006). The access network based on optical fibre is called fibre-to-the-home (FTTH). FTTH networks transport baseband data modulated in one or several optical carriers (laser lights) at different wavelengths.

FTTH networks are largely under deployment nowadays (Japan Today, 2008). FTTH access is a flexible, future-proof access technology that enables the provision of Gb/s bitrates per user. FTTH is already being commercially offered in countries like Japan. However, FTTH deployment is a very expensive investment. For example, the Spanish incumbent operator Telefonica has recently announced a €1bn programme to deploy FTTH in Spain. In UK, BT is currently running a £1.5bn programme (recently announced, March 2009) to deploy optical access to 10 million UK homes (40%) by 2012 (Jackson, 2009).

Several studies point out that FTTH will become the key differentiator between competing operators (FTTH Council, 2009; Saorin, 2009). In addition, FTTH is the only technology capable of creating new revenue streams from high-bitrate applications, e.g. high-definition entertainment (HD-video, HD-games, etc). Another advantage to FTTH is that permits better operational efficiencies compared with other access technologies, primarily by reducing maintenance and operating costs. Also, FTTH tends to require smaller central offices, and exhibits lower energy consumption. Next-generation optical access networks (Kazousky et al., 2007) is an step-forward over current FTTH technology. Next-generation optical access must support advanced telecommunications services requiring high bitrate provision to an ever increasing number of users. The access network topology, configuration and functionalities will evolve driven by high-bitrate demanding services like high-definition video, 3-D video, on-line gaming, cloud storage and cloud applications and, of course, Internet browsing of complex webpages. Video or multimedia transmission accounts today for a large percentage of the data transmitted in the access network (Werbach, 2009). Video coding technology is evolving optimising the performance and permitting an effective bitrate reduction in single-digit percentages year-after-year (Etoh et al., 2005). Nevertheless, it is difficult to assure that this coding gain could be sustained in the long term to compensate the data traffic originated in multimedia transmissions (Pyramid Research, 2010). Effectively, the network infrastructure must evolve to accommodate higher bitrates for a larger number of users, i.e. to increase the overall network capacity.

Moreover, in order to satisfy these higher data rates requirements, new techniques for the integrated distribution of wireless communication signal are required. These techniques must facilitate the deployment of an integrated access network at the customer premises, enabling the integration of optical transmission over an optical access network and radio-frequency transmission in the same infrastructure.

In conclusion, three important paradigms should be addressed in next-generation optical access networks:

- Spectral efficiency leads the overall network capacity expansion. The conventional strategy to increase the network capacity relies on deploying more fibre or transmission equipment. Advances in the processing/cost ratio of modern digital signal processors (DSP) and field-programmable gate arrays (FPGA) integrated circuits indicate that a shift from raw transmission equipment to advanced modulations based on very fast data processing is expected. Advanced modulation schemes permit higher spectral efficiency ratios, measured in bit/s/Hz. Updating the programmatic code implemented on these integrated circuits is a less expensive solution compared to the deployment of new transmission equipment on the field.
- Integration of the optical access network and the user radio environment. Optical access becomes the first step to establish the communication with the costumer. The second and last step is the final user radio link. Both optical access and user radio networks must be integrated in order to provide high-performance end-to-end connectivity, from the central office to the user device, including quality of service management.
- Increasing use of commercial off-the-shelf (COTS) electronic equipment. The performance and capabilities of current commercial devices operating wireless technologies make them and interesting option from the operator point of view in order to reduce the deployment cost (CAPEX) and the sustained operational expenses (OPEX).

These three next-generation optical access paradigms can be addressed employing ultra-wideband (UWB) technology. UWB technology is already one of the most promising

techniques for the user wireless networks due tolerance to multi-path fading, low probability of interception and high-bitrate capabilities (Llorente et al., 2008). Nowadays, market applications of UWB aim to high bit-rate wireless communications at picocell range, namely as a replacement of high definition (HD) video/audio cabling (Morant et al., 2009a) among others.

The extension of UWB technology to the optical access network in the so-called radio-over-fibre configuration permits the transmission of UWB signals in their native format through fibre-to-the-home (FTTH) access networks. This approach exhibits several advantages:

i. FTTH networks provide bandwidth enough to distribute a large number of UWB signals, as each one of them can occupy up to 7.5 GHz in current UWB regulation (FCC, 2002).
ii. No trans-modulation is required at user premises. HD audio/video content is transmitted through the fibres in UWB native format.
iii. No frequency up-conversion is required at customer premises. The UWB signals are photo-detected, filtered, amplified and radiated directly to establish the wireless connection.
iv. FTTH networks are transparent to the specific UWB implementation employed. This flexibility is of special interest for operators as UWB regulation is still evolving.

Hence, UWB radio-over-fibre is a rapid and cost-effective solution to deliver HD content in FTTH access networks with further wireless PAN (WPAN) transmission in home. FTTH passive optical network (PON) architectures are cost efficient compared with architectures including amplification and regeneration stages in the field, and are supported by a set of mature international standards (G/E-PON) (Prat, 2008). Current standard PON based on time-division multiple access (TDMA) are expected to evolve toward PON based on wavelength division multiplexing (WDM-PON) to keep up with the requirements of future access networks regarding the aggregated bandwidth.

UWB is a radio technology capable of providing multi-Gbit/s short-range indoor communications. UWB uses regulated spectrum from 3.1 to 10.6 GHz with a minimum signal bandwidth of 500 MHz (or 20% fractional bandwidth) (FCC, 2002). UWB presents the unique characteristic of being designed for coexistence with other licensed or unlicensed services in the same frequency range. This is achieved limiting the equivalent isotropic radiated power (EIRP) density to −41.3 dBm/MHz and introducing detection-and-avoid (DAA) mechanisms (WiMedia, 2009b; ECC, 2008). UWB operation in the 60-GHz band is an open opportunity to provide potential data rates of >3 Gbit/s worldwide (Beltrán & Llorente, 2010a). The EIRP limit constrains UWB radio to WPAN. There is a large market availability of UWB devices addressing wireless peripheral inter-connection and HD audio/video streaming functionalities (Alereon, 2009; Wisair, 2010). These devices are based on the multi-band orthogonal frequency-division multiplexing (OFDM) implementation as defined in the ECMA-368 standard (ECMA, 2008a). Maximum capacity in actual UWB equipment is 480 Mbit/s per band. This gives a maximum overall capacity of 6.72 Gbit/s per user when fourteen bands are combined. This capacity is supported in single-chip UWB solutions (Alereon, 2009). In addition, the impulse-radio UWB implementation is capable of providing simultaneous communications and high-resolution ranging (Dardari et al., 2009).

At this point, multi-service coexistence with other wireless signals is an important factor in optical transmission. With the recent introduction of radio standards such as WiMAX or LTE the coexistence issues appear as a possible issue. From one side, WiMAX is considered as an effective but challenging approach to extend IPTV services in the wireless and

mobility dimension, and from the other, LTE in femtocell applications is expected to become an important part of next-generation cellular networks.
Fig. 1 shows the network architecture integrating the complete optical path (FTTH and in-building distribution network) and also the user radio path for a converged service provision. The network provides triple-play services. HD content is provided by UWB, LAN connectivity is provided by WiMAX, and cellular phone connectivity is provided by LTE. This architecture permits a centralized network management strategy to be used in the LTE, WiMAX, and UWB terminals in a given user area.
In addition, UWB in the 60-GHz band has been reported as a very interesting approach for next-generation integrated PON-radio systems (Beltrán et al., 2011) and for interference-sensitive scenarios like on-board plane equipment (Beltrán & Llorente, 2010a). 60-GHz UWB systems would benefit from the unlicensed worldwide availability of the 60-GHz band together with the maturity and intrinsic coexistence characteristics of UWB technology. 60-GHz radio is about to become easily available for consumer applications and permits secure multi-Gbit/s wireless communications with reach exceeding typical WPAN.

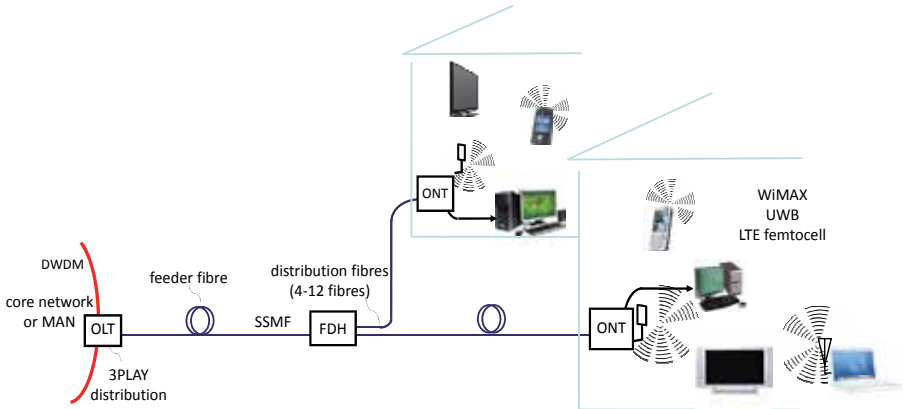

MAN: Metropolitan area network. OLT: Optical line terminal. ONT: Optical network terminal. SSMF: Standard single-mode fibre. FDH: Fibre distribution hub. DWDM: Dense wavelength division multiplexing

Fig. 1. Integrated FTTH and in-building optical and radio transmission of triple-play radio

Optical techniques are critical for future-proof, versatile and high-capacity service provisioning via UWB-over-fibre in optical access networks. Optical techniques can also benefit from the well-known advantages offered by microwave photonics devices, such as light weight, small size, and immunity to electromagnetic interference (Capmany & Novak, 2007).

1.1 Next-generation access networks

FTTH network architectures are the foundation of next-generation optical access. In practice, many access technologies are commonly referred to as FTTx when in fact they are simply combinations of optical fibre and twisted pair or coaxial cable networks. This has created some confusion though as FTTx covers several different architectures and protocols. In fact, some of Digital Subscriber Lines (DSL) and Hybrid Fibre Coax (HFC) networks have been qualified as FTTx networks due to their use of fibre in the access, as a PON does. Hence, it is best when referring to a deep fibre penetration network to specify its actual architecture. The most

common architectures are: Fibre-to-the-Home (FTTH), Fibre-to-the-Building (FTTB), FTTCurb (FTTC) and FTTNode (FTTN) (Kunigonis, 2009).
Fibre-to-the-premises (FTTP) is a term used in several contexts: as a blanket term for both FTTH and FTTB, or in the cases where the fibre network includes both homes and small businesses. Each of these has a different physical architecture as depicted in Fig. 2, and its main characteristics are described below:

- FTTH pushes fibre all the way to individual residential wells. FTTH is completely absent copper in the outside plant and provides at least 30 Mbps service, but due to the inherent characteristics of optical fibre can provide literally infinite bandwidth.
- FTTB typically uses the Point-to-Point (P2P) architecture in the outside plant providing a dedicated fibre to each building or block of buildings. The fibre is terminated at a Remote Terminal (RT) which is an active device requiring powering and security typically located in the basement, communications room or utility closet. Usual FTTB applications have been providing at least 10 Mbps. If twisted pair is installed to provide requirement bandwidth services it can reach up to 50 Mbps.
- FTTC, also called Fibre-to-the-Cabinet (FTTCab), extends fibre to a street-side cabinet or Digital Loop Carrier (DLC). Typically uses ADSL2 technology pushing fibre 150-700 m from the subscriber terminating at a RT.
- FTTN is similar in architecture to FTTC except that the RT is positioned much further from the subscribers up to 1500 m and can serve 3-500 subscribers. Both utilize existing twisted pair outside plant to connect to the customer. In this case, bandwidth is dictated by two factors: DSL technology and copper loop length.

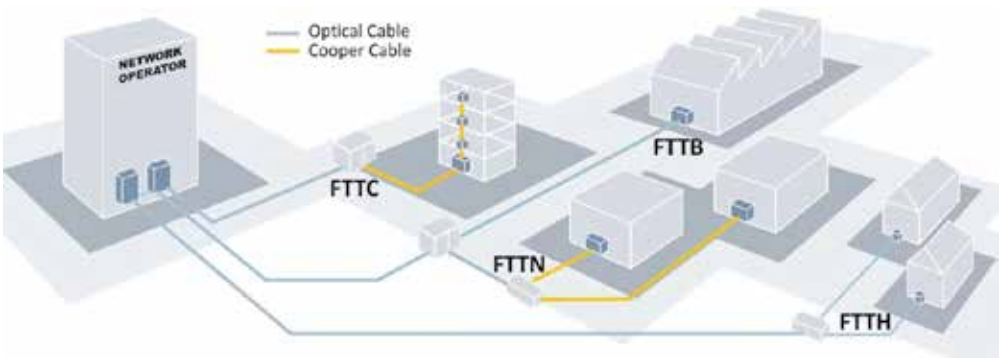

Fig. 2. FTTx Deployment

Signals over copper are significantly degraded over long distances directly affecting the bandwidth capacity. In the most extreme conditions (4-5 km) some customers may not even be able to be served by DSL. In some cases the carrier will use both twisted pairs to boost the bandwidth throughput. Due to shorter copper loop lengths in a FTTC network the operator has improved scalability from a bandwidth perspective.
Fibre penetration directly correlates to the bandwidth throughput of each defined architecture and therefore the service capability for the operator. The bandwidth requirements of each network operator differ but all are growing. Fibre penetration is also an indicator on the CAPEX and OPEX expected. Deep fibre will result in a higher CAPEX for existing neighbourhoods, but is actually near cost parity with all architectures for new builds. Deep fibre will deliver the maximum amount of OPEX savings comparably.

FTTH enables the delivery of savings due to reductions in cost for network, central office and outside plant operations as well as customer service. Network reliability dramatically increases as well with FTTH ensuring a steady stream of revenue and enhanced customer satisfaction (Kunigonis, 2009).

1.2 State-of-the-art of radio-over-fibre systems

Wireless communication has been experiencing phenomenal growth for some time. It is now the fastest growing sector of the telecommunications industry. While voice and low bit-rate data were the main wireless services in the past, the focus of today's wireless networks has clearly shifted towards high bit-rate data services. The proliferation of WiFi hotspots and the introduction of new cellular systems (such as 3G, LTE, and HSPA) and other high-data-rate wireless systems such as WiMAX (IEEE 802.16e) are some examples. With the advent of popular bandwidth services such as HD video or on-line gaming, these and other wireless systems are under pressure to offer higher data speeds in order to enable the delivery of such services to the ever increasing number of wireless users.

Some ways of increasing the data throughput to the wireless users are: using antenna diversity through multiple-input-multiple-output (MIMO) system configurations, greater RF bandwidth or smaller radio cells. As the radio channel is a shared medium, wireless users end up competing for bandwidth in any given radio cell. By reducing the cell size, the number of users sharing bandwidth may be reduced, thereby considerably increasing the share of the average data throughput available to each user in the cell. However, this approach of deploying small radio cells leads to a tremendous increase in the density of the required radio access points. This presents significant challenges in terms of the extensive feeder network required to interconnect the large number of radio access points (antennas) (Sauer et al., 2007). For this reason, the capacity of the wireless system is ultimately dependent on the utilized RF bandwidth. The ISM band frequencies at 2.4 and 5-GHz are severely congested with a multitude of consumer products using those frequencies. Therefore, the most promising path towards high-data rate (Gbit/s) wireless communication is to migrate to higher carrier frequencies, which offer much more bandwidth (Razavi, 2008). For instance the FCC has set aside 7-GHz contiguous bandwidth for wireless data communication in the 60-GHz band (57 – 64-GHz).

Radio-over-fibre technology has long been proposed as an effective way to deal with the demands of small-radio-cell networks (Sauer et al., 2007). This chapter discusses the use of this technology in using UWB-over-fibre techniques in the 3.1-10.6-GHz and in the 60-GHz band.

2. UWB-over-fibre performance in optical access and in-building networks

Radio-over-fibre transport of UWB wireless signals, i.e. radio transmission over a shared optical media fibre, is a rapid and cost-effective solution to extend the UWB radio range to in-home, in-building or even wide area applications. The application scenario in this case is UWB range extension.

Two major UWB implementations are mainstream nowadays: OFDM-based and impulse-radio. The compared performance of the two UWB implementations along different optical access fibre links was demonstrated in the literature (Llorente et al., 2008). The experimental results demonstrate the feasible distribution of 1.25 Gbit/s UWB signals achieving BER operation of 10^{-9} at 50 km with both IR-UWB and OFDM-UWB implementations where impulse-radio UWB is more affected by the frequency response of the electrical devices.

The in-building network distribution performance was evaluated in (Beltrán et al., 2009). Comparing impulse radio and OFDM UWB it is observed that impulse-radio UWB requires less optical launched power than its OFDM-UWB counterpart for successful standard single-mode fibre (SSMF) transmission over a distance of 300 m. In the case of in-building distributions different optical media can be employed, such as multi-mode fibre (Beltrán et al., 2009), plastic optical fibre (POF) (Lethien et al., 2009) or bend-insensitive optical fibre (Beltrán et al., 2011).
The spectral efficiency in these systems can be maximised by the distribution of polarization-multiplexed UWB (PM-UWB) signals is a suitable technique for the provision of wireless connectivity to a large number of users. This approach provides a higher spectral efficiency and the user capacity is doubled compared with UWB on a single wavelength. The maximum transmission reach of the proposed PM-UWB technique has been investigated in (Morant et al., 2009b) demonstrating successful transmission of 1.2 Gbit/s OFDM-UWB signals with 0.76 bit/s/Hz spectral efficiency at PON distances up to 25 km.

3. Multi-service coexistence with UWB

With the recent introduction of radio standards as Mobile WiMAX or LTE the coexistence issues of UWB with other licensed radio signals appear as a possible issue. From one side, WiMAX is considered as an effective but challenging approach to extend IPTV services in the wireless and mobility dimension, and from the other, LTE in femtocell applications is expected to become an important part of next-generation cellular networks. UWB coexistence with WiMAX and LTE is herein addressed.
The most important similarity between UWB, LTE and WiMAX is the OFDM signalling. LTE and WiMAX technologies also employ Viterbi and turbo accelerators for further error correction. From the viewpoint of chip designer view, it is possible to reuse gates if you have to support both schemes in the same chip set. For these reasons, recently it has been proposed to provide triple-play services, mainly data, voice and video using a simultaneous transmission of WiMAX, LTE and UWB standard signals. In particular, this proposal implies the simultaneous radio-over-fibre transmission of the full standard OFDM signals in coexistence in optical access networks as it can be observed in Fig. 3.

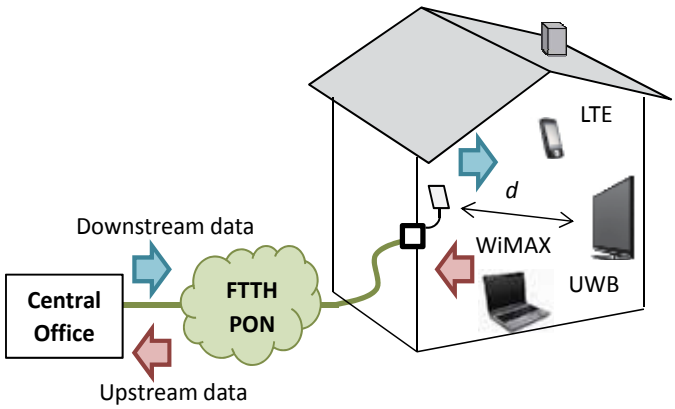

Fig. 3. Application scenario for bi-directional 3PLAY (LTE, WiMAX and UWB) distribution in FTTH access networks and radio propagation at user premises

This provides to the user a higher aggregated capacity and simplifies the overall architecture as it is transparent to the service provided and simplifies the deployment cost at customer premises as no transmodulation or recodification is needed and the different services could be received with standard equipment without additional set-top box.

3.1 Wireless standard overview

3.1.1 WiMAX

WiMAX stands for Worldwide Interoperability for Microwave Access and it is a wireless standard for transmitting data using radio waves. It is a radio technology known as last mile application that allows reception of data by microwave and radio wave transmission. The protocol that characterizes this technology is the IEEE 802.16. One of the main goals of this radio technology is to provide broadband services in areas where the deployment of cable or fibre for the low density of population has a very high cost per user as in rural environments.

WiMAX Forum is the standardization body authorized to certify compliance and interoperability between equipment from different manufacturers, which means that any equipment that does not have this certification, cannot guarantee its interoperability with other products. The profiles of WiMAX equipment that is currently on the market use frequencies of 2.5 GHz and 3.5 GHz.

Currently there are two different mobility profiles contained within the 802.16 standard. One with fixed access (802.16d), which establishes a radio link between base station and user equipment located in the user's home, to the fixed environment. The maximum theoretical speeds that are available are 70 Mbps with a bandwidth of 20 MHz, however, in real environments could achieve speeds of 20 Mbps shared by all the users of the cell with a cell radius of up to 6 km. And a second one with complete mobility 802.16e, which allows the movement of the user in a manner similar to GSM / UMTS.

3.1.2 LTE

LTE (Long Term Evolution) is a 3GPP standard proposed for mobile Internet services like data transmission over 300 meters and high-definition video thanks to OFDM access (OFDMA) technology. The most common frequency band in commercial available devices is 2.6 GHz, but also operates at 800 MHz, 1.5 GHz, 1.8 GHz and 3.5 GHz. The novelty of LTE is that the radio interface based on OFDMA for the downlink (DL) and YSC-FDMA for uplink (UL). The modulation chosen by the 3GPP standard makes the different antenna technologies (such as multiple input multiple output or MIMO) have greater ease of implementation, which improves the performance in even quadrupling the data transmission efficiency.

3.2 Performance evaluation

Following with the radio-over-fibre techniques described in Section 2, polarization multiplexing could be used for the transmission of different radio services in each polarization. This was demonstrated in (Perez et al., 2009) with a simultaneous UWB and WiMAX service provision in two orthogonal polarizations achieving 25 km PON reach with only 2 dB EVM penalty compared with a UWB single-polarization distribution scheme. However the polarization multiplexing technique becomes more complex as the number of services increases, as the orthogonality of the different optical lights is affected. For this reason the coexistence of different radio standards for multiple service provision was further investigated using radio-over-fibre techniques.

In (Morant et al., 2011a) it is proposed and demonstrated the bi-directional radio-over-fibre transmission of triple-format LTE, WiMAX and UWB full-standard OFDM signals in coexistence. Coarse wavelength division multiplexing (CWDM) is employed to map the uplink and downlink optical signals in 1300 nm and 1550 nm respectively. Moreover, the optical-to-radio and radio-to-optical interfaces was investigated in (Morant et al., 2011b) for the triple-play transmission including the wireless transmission at customer premises after the radio-over-fibre distribution through a PON.

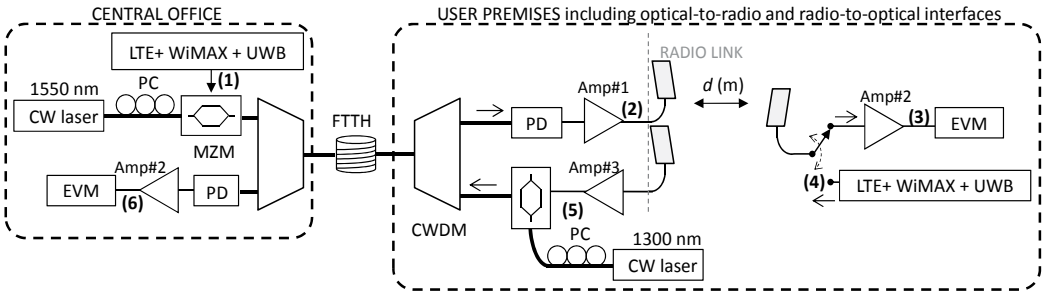

Fig. 4. Block diagram of the experimental setup for the demonstration of triple-play bi-directional UWB-over-fibre transmission

Fig. 4 depicts the experimental setup used for the demonstration of triple-play bi-directional transmission evaluating the optical access performance (connecting point (2) to (3), and (4) to (5)) and the radio performance at customer premises with wireless transmission at different radio distances d(m).

In the optical access evaluation the launch power level of the lasers at both sides of the communication are changed and different lengths of the PON are evaluated in order to emulate a fibre-to-the-home deployment up to 120 km standard single-mode fibre. The triple-play signal comprises: a UWB channel full WiMedia compliant (ECMA-368, 2008a) in center frequency at 3.96 GHz with 528 MHz bandwidth. The LTE and WiMAX signals are generated with two vector signal generators (VSG). The first one generates an advanced LTE signal using frequency division duplex at 2.6-GHz with full-filled 16QAM in 20 MHz bandwidth, and the second one a fixed IEEE 802.16 WiMAX signal at 3.5-GHz using 16QAM in 24 MHz bandwidth. The three standard OFDM signals are combined together and applied to Mach-Zehnder modulators working at quadrature bias point for each 1300 nm and 1550 nm path. Both paths are combined using CWDM splitters and the signal is transmitted through SSMF. Signal detection was accomplished using 10-GHz bandwidth

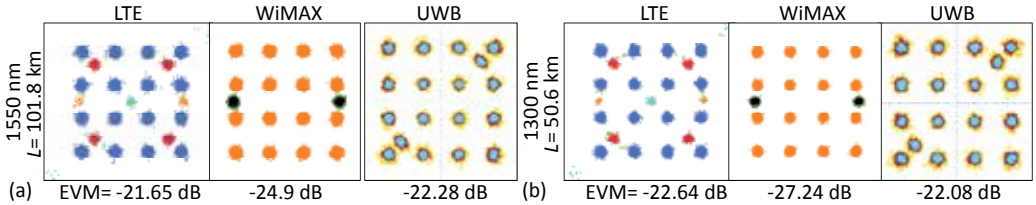

Fig. 5. Received constellations of LTE, WiMAX and UWB at different points of the experimental setup of Fig. 4: (a) after 101.8 km SSMF [Point (2)] for the 1550 nm downstream path, and (b) after 50.6 km SSMF for the 1300 nm upstream path

photodiodes followed by electrical amplification. As it can be observed it is a straight-forward deployment where the signals are only photodetected, amplified and radiated to the final user, without needing any upconversion in frequency or remodulation of the signals. This simplifies the overall scheme and provides transparency to the system, as any other full-standard signal could be transmitted in the same architecture only designing the power levels necessary at the central office.

At both ends of the architecture the error vector magnitude (EVM) of each OFDM standard signal is measured and compared with the maximum EVM limit stated in current regulations: -17 dB for ECMA-368 UWB using dual-carrier modulation (DCM) or -14.5 dB for UWB in QPSK (ECMA-368, 2008a), -24.43 dB for 802.16 WiMAX using 16QAM (IEEE 802.16, 2009a), and -18 dB for GPP LTE using 16QAM (3GPP TS 36.101, 2009).

It is demonstrated that up to 50.6 km SSMF can be reach for successful transmission of the triple play signals in passive optical networks without amplification or regeneration stages. This maximum reach is limited by the performance of the 1300 nm path that has higher losses at the fibre than the 1550 nm path, as it can be observed in Fig. 5 that the 1550 nm can achieve more than 100 km SSMF transmission.

The experimental results show up that signal with less than 14 dB signal-to-noise ratio (SNR) do not fulfil the wireless channel specifications. This can be observed in the received electrical spectrums shown in Fig. 6, where it can be appreciated that when the signals are less than the required limits, the SNR is very similar in both directions: 24.2 dB in the 1550 nm path after 101.8 km, and 23.5 dB in the 1300 nm path after 50.6 km SSMF. This confirms that, for the same PON reach, the 1300 nm path needs more launch power than the 1550 nm path.

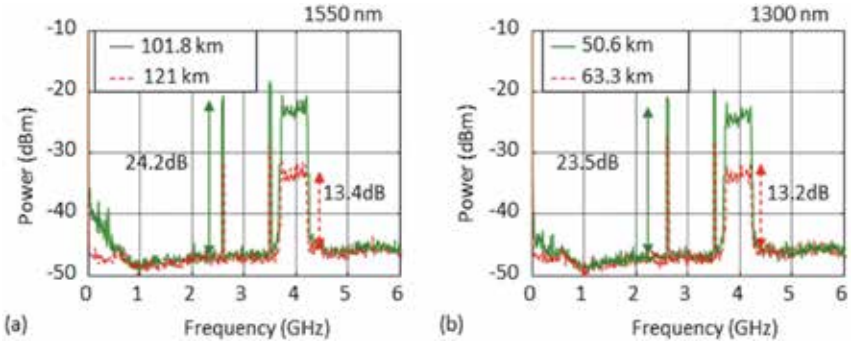

Fig. 6. Electrical spectrum examples and signal-to-noise ratio values working at (a) 1550 nm (after SSMF length of L=101.8 and 121 km) and (b) 1300 nm (L=50.6 and 63.3 km)

In the radio performance evaluation, the wireless path is included as depicted in Fig. 4. Fig. 7 shows the degradation of the received constellations at different points of the system. Clearly defined constellations and the EVM values below the regulation threshold indicate that a reliable opto-electronic link was established after 20.2 km SSMF and 3 m radio transmission in both directions.

4. UWB in the 60-GHz band

UWB technology is capable of providing multi-Gbit/s wireless communications. Maximum capacity in actual UWB devices is 480 Mbit/s per band as of WiMedia specification v1.2 (WiMedia, 2007; ECMA, 2008a). This gives an overall capacity of 6.72 Gbit/s per user when the

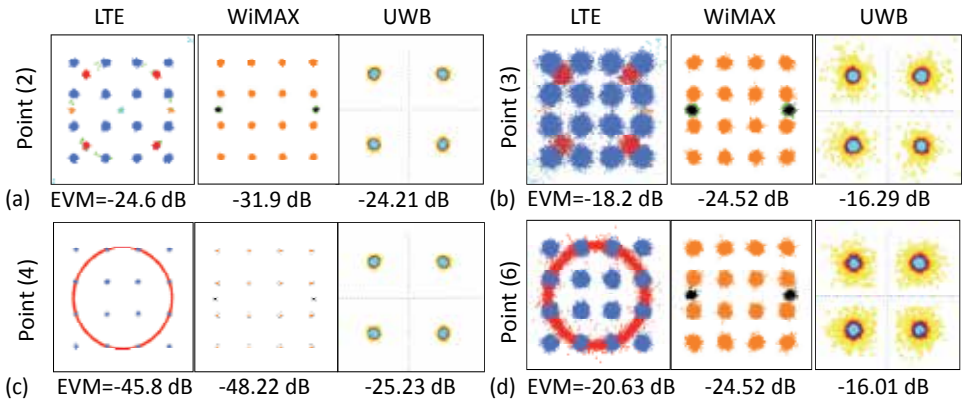

Fig. 7. Received constellations of LTE, WiMAX and UWB at different points of the experimental setup of Fig. 4: (a) input of the MZ [Point (1)] and (b) after 20.2 km SSMF and 3 m radio transmission [Point (3)] for the 1550 nm downstream path, and (c) radiated signal for upstream [Point (4)] and (d) after 20.2 km SSMF and 3 m radio for the 1300 nm upstream path

fourteen OFDM bands are combined. This capacity is supported in commercially-available single-chip UWB implementations (Alereon, 2009). The maximum theoretical UWB capacity would be achieved when the fourteen UWB bands are used bearing 1024 Mbit/s each as of WiMedia specification v1.5 (WiMedia, 2009a) giving 14.336 Gbit/s aggregated bitrate per user. Nevertheless, no commercial equipment to date supports this configuration. UWB capacity is further restricted outside the U.S. by regulation in force in each country due to coexistence issues (WiMedia, 2009b). UWB operation in the 60-GHz band is an open opportunity to provide potential data rates of >3 Gbit/s worldwide (Beltrán & Llorente, 2010a). 60-GHz radio is about to become easily available for consumer applications and permits secure multi-Gbit/s wireless communications with reach exceeding typical WPAN. UWB operation in the 60-GHz band is interesting for several reasons:

1. The unlicensed frequency range regulated for generic 60-GHz radio worldwide (within 57–66 GHz) can allocate very well the UWB bandwidth in current regulation (up to 7.5 GHz).
2. UWB is a mature technology with efficient software and single-chip solutions are also available. This permits UWB to be introduced in devices with specific space and power requirements, like mobile phones.
3. UWB is, in origin, a coexistence technology. Translating UWB technology from the 3.1−10.6-GHz band to the 60-GHz band opens the opportunity of coexistence with other wireless transmissions in the band.
4. UWB operation in the 60-GHz band permits extending the transmission reach by increasing the EIRP spectral density over −41.3 dBm/MHz, as in current UWB regulation worldwide, up to 13 dBm/MHz, as permitted in regulation in force in the band.

60-GHz UWB-over-fibre systems have been considered for two main applications. First, indoor distributed antenna systems (DAS) where 60-GHz UWB signals are distributed over fibre links from a central unit to remote antenna units (RAUs). This application is particularly interesting in interference-sensitive scenarios such as in-aircraft cabins (Beltrán & Llorente, 2010a). The fibre length in indoor DAS application is in the range of a

few hundred meters. In the second application, 60-GHz UWB signals are distributed from a central office through FTTH networks with further 60-GHz UWB wireless transmission in home (Beltrán & Llorente, 2010b; Beltrán et al., 2011). The approach in (Beltrán & Llorente, 2010b) can potentially integrate 60-GHz FTTH networks with 24-GHz and *W*-band optical networks exploiting chromatic dispersion of the fibre links. Cost-effective standard single-mode fibre (SSMF) is widely used in FTTH networks with distances up to approximately 40 km (Hülsermann et al., 2010). Recently-developed bend-insensitive single-mode fibre (BI-SMF) opens up an interesting opportunity for 60-GHz UWB-over-fibre to be deployed at indoor environments including in-home optical distribution as extension of the FTTH network. BI-SMF maintains the transmission properties of SSMF and is backwards compatible with SSMF. BI-SMF presents much lower bending loss than SSMF facilitating installation where tight corners and staples are required, thus reducing installation cost (Li et al., 2010). BI-SMF can also reduce the size of fibre installation and optical cabinets.

4.1 60-GHz radio

Millimetre-wave radio in the 60-GHz band is an open opportunity to support multi-Gbit/s services to multiple televisions and computers distributed throughout a dwelling/office replacing pervasive, HDMI and high-speed Internet cabling. 60-GHz transmission uses up to 9 GHz of frequency range available for unlicensed use over a short range. The increased free space loss in the 60-GHz band limits coverage area compared with links operating at lower frequencies enabling higher frequency reuse per indoor environment and secure communications (Daniels & Heath, 2007). In addition, the increased atmospheric attenuation in the 60-GHz band is the reason that 60-GHz links cannot cover the outdoor distances achieved by other millimetre-wave links without employing very large and very high gain antennas (Wells, 2009).

60-GHz frequency permits to employ directional and high-gain antennas with size much smaller than the lower frequency bands. This facilitates radio coexistence, provides multipath robustness, and makes it possible to have very small radios with multiple antennas solutions, enabling MIMO, beamforming and beam steering, which enhances the channel capacity and also supports non-line-of-sight (NLOS) communications.

International 60-GHz standards have been recently launched, leading to consumer electronics products, which are overviewed in Section 4.1.2.

4.1.1 Worldwide regulatory status

Current regulation in force for unlicensed use of 60-GHz radio worldwide is summarized in Table 1. The frequency range in the 60-GHz band can allocate very well the UWB bandwidth in current regulation (up to 7.5 GHz). Up to 9 GHz bandwidth is permitted in the EU and for indoor use in Australia, 7 GHz bandwidth is allocated in the U.S. and Canada, and 7 GHz in Japan (with 2.5 GHz maximum transmission bandwidths). There is a worldwide overlap in 5 GHz bandwidth in the range from 59 GHz to 64 GHz. In addition, 60-GHz UWB could operate at EIRP spectral density up to 13 dBm/MHz. This allows extending UWB range by increasing EIRP spectral density over −41.3 dBm/MHz provided that the increment in radio path attenuation at 60 GHz is compensated. Relatively high transmitter power employing shorter antennas allow for lower-power shorter-distance communications.

Country	Frequency Range	Usage	Maximum EIRP	Maximum transmitter power	Reference
EU	57 – 66 GHz	Indoor only	13 dBm/MHz 40 dBm	Not Defined	ETSI, 2009
		Indoor and Outdoor	-2 dBm/MHz 25 dBm		
Australia	57 – 66 GHz	Indoor only	43 dBm	13 dBm	ComLaw, 2009
U.S.	57 – 64 GHz	Not Defined	43 dBm peak (= 18 μW/cm²@ 3 m) 40 dBm average (= 9 μW/cm²@ 3 m)	27 dBm	FCC, 2008
Canada	57 – 64 GHz	Not Defined			IC, 2007
Japan	59 – 66 GHz	Not Defined	57 dBm	10 dBm	ARIB, 2005

Table 1. Current regulatory status in the 60-GHz band in major worldwide markets

4.1.2 Standardization status

A number of technologies capable of providing multi-Gbit/s wireless communications in the 60-GHz band targeting different markets have been proposed in the recent years. These technologies are summarized in Table 2. WirelessHD-based chips have been integrated into consumer electronic products such as TVs and wireless adapters. The operation of an ECMA-387-compliant link has also been demonstrated using a single-chip solution (ECMA, 2008b). In addition, the 802.11ad draft standard is expected to seamlessly integrate 60-GHz Wi-Fi into existing 2.4 GHz and 5 GHz Wi-Fi networks thus enabling next-generation tri-band radios.

Standard	Status	Theoretical maximum bitrate	Remarks	Reference
WirelessHD	v1.0 Jan. 2008 v1.1 May 2010	28 Gbit/s	Target WVAN applications: Cable replacement for HDMI, etc. OFDM only up to 10 Gbit/s in current market-available products	WirelessHD, 2010
ECMA-387	Dec. 2008	25.402 Gbit/s	Target WPAN applications single-carrier and OFDM	ECMA, 2008b
IEEE 802.15.3c	Oct. 2009	5 Gbit/s	Target WPAN applications single-carrier and OFDM	IEEE, 2009b
WiGig	July 2010	7 Gbit/s	Based on IEEE 802.11 target WLAN applications single-carrier and OFDM	WiGig, 2010

Table 2. Standards in the 60-GHz band

4.2 Integrated optical access and pico-cell transmission performance

Photonic generation of UWB signals can be a competitive solution supporting A/V streaming in the 60-GHz band due to the inherent coexistence characteristics of UWB, giving the benefit of seamless integration of optical transmission (access network) and radio provision (user pico-cell). Furthermore, optical frequency up-conversion at the central office is an interesting approach to reduce overall complexity and cost by centralized network management and simplified RAUs.

Fig. 8 shows a simple approach for photonic generation and integrated FTTH and radio transmission of 60-GHz UWB signals (Beltrán et al., 2011). At the central office, a 10-Gbit/s 1550-nm vertical-cavity surface-emitting laser (VCSEL) is employed for electro-optical conversion of baseband UWB signals. The optical UWB signal is modulated with a RF signal (local oscillator) in a Mach-Zehnder intensity modulator (MZM) to perform frequency up-conversion. The MZM is biased at the minimum transmission point to generate a double sideband with supressed optical carrier signal. The two sidebands beat in the photodetector located at the RAU, yielding the UWB signal up-converted to the second harmonic of the local oscillator frequency. This up-conversion technique reduces RF power fading induced by chromatic dispersion of the fibre link (Schmuck, 1995) and the frequency requirement of the up-conversion devices at expense of reduced RF power (Ma et al., 2007). The baseband signal is also available after photodetection and it could be radiated meeting current UWB regulation. At the receiver, the received 60-GHz UWB signal is down-converted by electrical mixing with a local oscillator signal and digitized to be processed by digital signal processing (DSP).

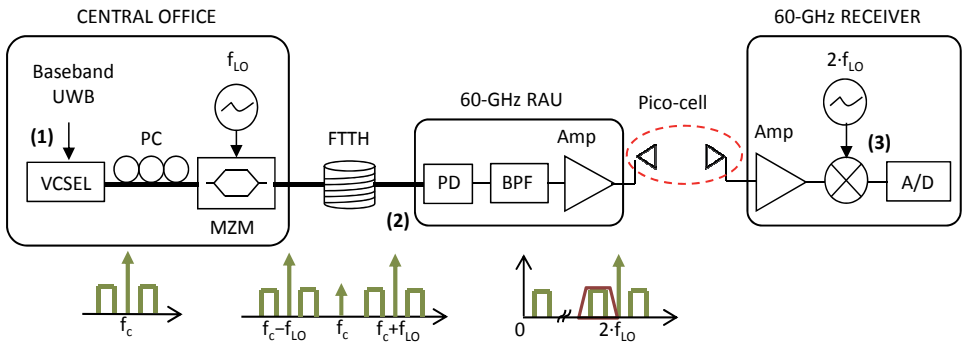

Fig. 8. Photonic generation and integrated FTTH and radio transmission of UWB signals in the 60-GHz band. PC: Polarization controller. LO: Local oscillator. PD: Photodetector. BPF: Band-pass filter. Amp: Amplification. A/D: Analogue-to-digital conversion

Performance of both impulse-radio UWB and standard OFDM UWB signals at 1.44 Gbit/s has been evaluated experimentally employing the scheme in Fig. 8. FTTH PON links employing optical amplification at the central office and 5-m wireless distance (directional antennas, line-of-sight path) is evaluated. Signals at point (3) in Fig. 8 are digitized at 40 GS/s.

4.2.1 OFDM UWB

An OFDM UWB signal fully-compliant with the ECMA-368 standard (ECMA, 2008a) is generated at point (1) in Fig. 8 employing commercially-available dongles. The signal comprises the Band #1, Band #2, and Band #3 employing the time-frequency codes TFC5, TFC6, and TFC7 as specified in the standard. Random data are modulated in each band

employing dual-carrier modulation (DCM) at 480 Mbit/s, thus providing an aggregated bitrate of 1.44 Gbit/s and a spectral efficiency of 0.91 bit/s/Hz.
The OFDM UWB signal is up-converted to 64.5 GHz and filtered at 58.125–61.875 GHz. The down-converted OFDM UWB signal at point (3) in Fig. 8 is demodulated employing commercially-available software. Fig. 9(a) shows performance in terms of EVM as a function of the optical power at point (2) in Fig. 8 for Band #1. Performance is evaluated for each OFDM UWB band and is limited by Band #1. Two optical transmission cases are considered: 40 km of SSMF and a 50-km dispersion-managed link comprising 25 km of SSMF and 25 km of inverse dispersion fibre (IDF) (Mukasa et al., 2006). The optical receiver sensitivity at EVM< −17 dB (ECMA, 2008a) is 1 dBm and −2 dBm for 40 km SSMF and 25-km SSMF+25-km IDF, respectively.
Minimum EVM for optical back-to-back (B2B) is limited by optical SNR. The chromatic dispersion of 40-km SSMF distorts the signal degrading the minimum EVM with respect to B2B. However, this degradation does not translate into penalty on optical receiver sensitivity. This is ascribed to gain in the fibre RF transfer function induced by the interaction of the chirp of the direct-modulated VCSEL with fibre chromatic dispersion (Wedding, 1994). The gain improves SNR limited by electrical noise at low received optical power, thus improving EVM. The gain in the power level as well as signal distortion for 40 km of SSMF with respect to B2B can be verified in Fig. 2(b). In addition, 25 km of IDF compensates for RF power fading induced by 25-km SSMF dispersion. The optical receiver sensitivity improvement for 25-km SSMF+25-km IDF with respect to B2B in Fig. 2(a) is again ascribed to the interplay between VCSEL chirp and residual dispersion of the dispersion-managed link. Fig. 2(c) shows examples of DCM-OFDM constellation diagrams at different EVM values.

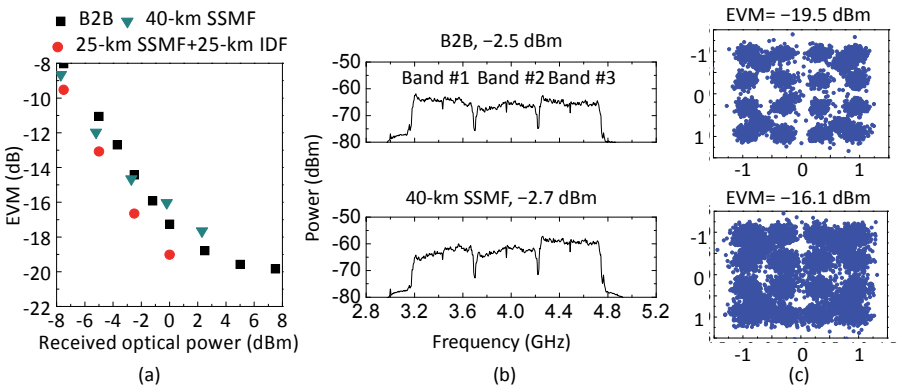

Fig. 9. Performance of the 60-GHz OFDM UWB signal measured at point (3) in Fig. 8 integrating optical and 5-m wireless transmission. (a) EVM for Band #1. (b) RMS spectrum (resolution bandwidth: 5 MHz). (c) Constellation diagrams for Band #1

4.2.2 Impulse-radio UWB

An impulse-radio UWB signal is generated by an arbitrary waveform generator (AWG) at 23.04 GS/s at point (1) in Fig. 8. The UWB pulse is a fifth-order derivative Gaussian shape comprising a single band in good compliance with the UWB EIRP spectral density mask in current regulation (FCC, 2002), as shown in Fig. 10. A pseudo random binary sequence (PRBS) with a word length of 2^{11}–1 is modulated employing bi-phase modulation (binary

phase-shift keying BPSK) at 1.44 Gbit/s. Compared with other modulation formats such as on-off keying (OOK) and pulse position modulation (PPM), BPSK modulation reduces spectral peaks at multiples of the data rate, thus providing better power efficiency under the UWB mask. Power efficiency is critical to extend UWB reach. This system has potential ranging capabilities taking advantage of the excellent accuracy of impulse-radio UWB when short pulses are employed.

The impulse-radio UWB signal is up-converted to 64.66 GHz and filtered at 58.125−61.875 GHz. The down-converted impulse-radio UWB signal at point (3) in Fig. 8 is demodulated employing custom DSP. The DSP comprises re-sampling, low-pass filtering, matched filtering with the original UWB pulse shape, bit synchronization and calculation of the optimum decision threshold. Fig. 10 shows performance in terms of bit error rate (BER) as a function of the optical power at point (2) in Fig. 8. Two optical transmission cases are considered: 25 km of SSMF (5.2-dB loss) and 40 km of SSMF (7.7-dB loss). The optical receiver sensitivity at BER< $2.2 \cdot 10^{-3}$ (BER limit including forward error correction) is −12.5 dBm and −15.6 dBm, respectively. The maximum received optical power in the experiment is 10 dBm so that the optical power budget apart from fibre loss is 17.3 dB and 17.9 dB, respectively. Fig. 10 shows examples of BPSK eye diagrams.

BER is limited by electrical noise. Decreasing the received optical power further increases BER due to the reduction in signal-to-noise ratio (SNR). In addition, BER improves after optical transmission with respect to optical B2B. This is ascribed to gain in the fibre RF transfer function induced by the interaction of the chirp of the directly-modulated VCSEL with fibre chromatic dispersion (Wedding, 1994), like for the OFDM UWB signal.

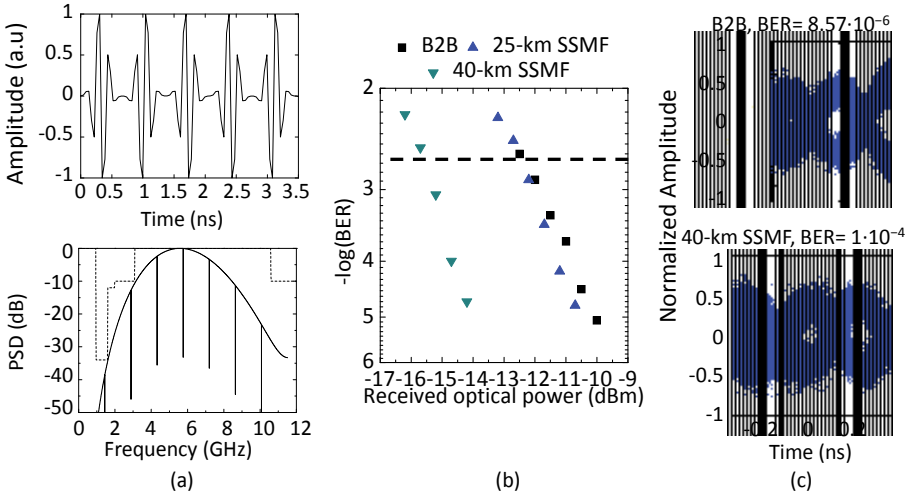

Fig. 10. (a) Impulse-radio UWB signal applied to the AWG. The UWB EIRP spectral density mask in current regulation (FCC, 2002) is shown via a dashed line; Performance of the 60-GHz impulse-radio UWB signal measured at point (3) in Fig. 8 integrating optical and 5-m wireless transmission: (b) BER. The forward error correction limit of $2.2 \cdot 10^{-3}$ is shown via a dashed line. (c) Eye diagrams

5. Conclusion

In this chapter, UWB radio-over-fibre in FTTH access networks with PON architecture is proposed as a next-generation optical access solution. Optical and radio transmission

performance is investigated employing commercially-available UWB transmitters, fully compliant with the ECMA-368 standard. Standard OFDM UWB transmission is reported in FTTH PON access including radio transmission.
The coexistence characteristics of UWB with WiMAX and LTE radio, the most limiting impairment in next-generation optical access, are reported considering bidirectional full-standard triple-play provision. Successful full-duplex provision of triple-play services via UWB in coexistence with standard OFDM-based WiMAX and LTE radio is possible up to 20.2 km of SSMF including 3 m radio propagation.
UWB operation in the 60 GHz radio band has been also proposed as an interesting approach. The 60 GHz UWB systems proposed could operate in a dual 3.1−10.6 GHz/60 GHz configuration if desired. 60-GHz band operation would re-use and extend UWB technology in terms of range and flexibility, and is the focus of this work.
Finally, the performance of the two mainstream UWB implementations -dual-carrier modulation orthogonal frequency division multiplexing (DCM-OFDM) and binary phase-shift keying impulse radio modulation- is also described in this chapter. The results presented permit, from an application point-of-view, to select a given UWB implementation depending on network reach and system complexity desired.

6. References

3GPP, 3GPP TS 36.101 V8. (December 2009). 3rd Generation Partnership Project; Technical Specification Group Radio Access Network; Evolved Universal Terrestrial Radio Access (E-UTRA); User Equipment (UE) radio transmission and reception (Release 8)

Alereon, Inc. (December 2009). AL5301 Chipset, Available from http://www.alereon.com/products/chipsets/al5100al5301-chipset

ARIB, STD-T74 v1.1. (November 2005). Millimeter-Wave Data Transmission Equipment for Specified Low Power Radio Station (Ultra High Speed Wireless LAN System)

Beltrán, M. & Llorente, R. (2010). 60-GHz ultra-wideband radio-over-fibre system using a novel photonic monocycle generation. *IEEE Transactions on Microwave Theory and Techniques*, Vol. 58, No. 6, (June 2010), pp. 1609-1620, ISSN 0018-9480

Beltrán, M. & Llorente, R. (2010). Optical generation with FTTH transmission of 60 GHz impulse-radio ultra-wideband signals, *Proceedings of OSA Access Networks and In-house Communications (ANIC)*, paper AWC7, ISBN 978-1-55752-896-4, Karlsruhe, Germany, June 17-22, 2010

Beltrán, M., Jensen, J. B., Yu, X., Llorente, R., Rodes, R., Ortsiefer, M., Neumeyr, C., & Tafur Monroy, I. (2011). Performance of a 60-GHz DCM-OFDM and BPSK-impulse ultra-wideband system with radio-over-fibre and wireless transmission employing a directly-modulated VCSEL. *IEEE Journal on Selected Areas in Communications, Special Issue on "Distributed Broadband Wireless Communications,"* Vol. 29, No. 6, (June 2011), ISSN 0733-8716

Beltrán, M., Morant, M., Perez, J., & Llorente, R. (2009). Performance Evaluation of OFDM and Impulse-Radio Ultra-Wideband over Fibre Distribution for In-Building Networks, *Proceedings of IEEE International Conference on Ultra-Wideband*, ISBN 9781-4244-2931-8, Vancouver, Canada, September 9-11, 2009

Capmany, J. & Novak, D. (2007). Microwave Photonics combines two worlds. *Nature Photonics*, Vol. 1, (June 2007), pp. 319-330

ComLaw, F2009C00545. (July 2009). Radiocommunications (Low Interference Potential Devices) Class Licence 2000

D. Dardari, D., A. Conti, A., U. Felner, U., A. Giorgetti, A., & and M. Z. Win, M. Z. (2009). Ranging with ultrawide bandwidth signals in multipath environments. *Proceedings of the IEEE*, Vol. 97, No. 2, (February 2009), pp. 404–426, ISSN 0018-9219

Daniels, R. C. & Heath, R. W. (2007). 60 GHz wireless communications: Emerging requirements and design recommendations. *IEEE Vehicular Technology Magazine*, Vol. 2, No. 3, (September 2007), pp. 41-50, ISSN 1556-6072

ECC, Amended ECC/DEC/(06)12. (October 2008). ECC Decision of 1 December 2006 amended 31 October 2008 on supplementary regulatory provisions to Decision ECC/DEC/(06)04 for UWB devices using mitigation techniques

ECMA International, ECMA-368. (December 2008). High rate ultra wideband PHY and MAC standard

ECMA International. (December 2008). ECMA publishes 60 GHz standard, Available from http://www.ecma-international.org/news/PressReleases/PREcma%20publishes%2060%20GHz%20Standard.htm

Etoh, M., Bossen, F., Chu, W., Lashkari, K. (2005). Chapter 8. Multimedia Coding Technologies and Applications. In: *Next Generation Mobile Systems 3G and Beyond*. ISBN 9780470091531, Ed. John Wiley & Sons, June 2005

ETSI, EN 302 567 v1.1.1. (March 2009). Broadband Radio Access Networks (BRAN); 60 GHz Multiple-Gigabit WAS/RLAN Systems; Harmonized EN covering the essential requirements of article 3.2 of the R&TTE Directive

FCC, FCC 02-48. (April 2002). Revision of part 15 of the Commission's rules regarding ultra-wideband transmission systems

FCC, FCC 15.255. (October 2008). Operation within the band 57–64 GHz

FTTH Council (2009). *The Advantages of Optical Access*. The FTTH Council Europe, February 2009.

Hülsermann, R., Breuer, D., & Lange, C. (2010). Impact of network reliability on network costs in next generation access networks, *Proceedings of 12th International Conference on Transparent Optical Networks (ICTON)*, paper Tu.A3.1, ISBN 978-1-4244-7797-5, Munich, Germany, July 2010

IC, RSS-210. (June 2007). Low-power Licence-exempt Radiocommunication Devices (All Frequency Bands): Category I Equipment

IEEE, 802.15.3c-2009. (October 2009). IEEE Standard for Information technology - Telecommunications and information exchange between systems - Local and metropolitan area networks - Specific requirements. Part 15.3: Wireless Medium Access Control (MAC) and Physical Layer (PHY) Specifications for High Rate Wireless Personal Area Networks (WPANs) Amendment 2: Millimeter-wave-based Alternative Physical Layer Extension

IEEE, IEEE 802.16. (2009). Standard for local and metropolitan area networks Part 16: Air Interface for Fixed Broadband Wireless Access Systems

Jackson, M. (2009). *BT shows first fibre-optic broadband rollout plans*. Available at: http://tech.slashdot.org/article.pl?sid=09/03/22/0058237&from=rss, March 2009

Japan Today (2008). *KDDI to launch 1Gbps fibre-optic service in Oct*. Available at: http://www.japantoday.com/category/Technol./view/kddi-to-launch-1gbps-fibre-optic-service-in-oct, September 27, 2008

Koonen, T. (2006). Fibre to the Home/Fibre to the Premises: What, Where, and When?. *Proceedings of the IEEE*, Vol. 94, no. 5, (May 2006), pp. 911-934, ISSN 0018-9219

Kazovsky, L. G., Shaw, W-T, Gutierrez, D., Cheng, N., & Wong, S-W. (2007). Next-Generation Optical Access Networks. *IEEE Journal of Lightwave Technology*, Vol. 25, Issue 11, pp. 3428-3442, (November 2007), ISSN 0733-8724

Kunigonis, M. (2009). FTTH Explained: Delivering efficient customer bandwidth and enhanced services. *Corning Cable Systems*, 2009

Lethien, C., Loyez, C., Vilcot, J-P., Kassi, R., Rolland, N., Sion, C., & Rolland, P-A. (2009). Review of Glass and Polymer Multimode Fibres Used in a Wimedia Ultrawideband MB-OFDM Radio Over Fibre System. *IEEE Journal of Lightwave Technology*, Vol. 27, No. 10, (May 2009), ISSN 0733-8724

Li, M.-J., Tandon, P., Bookbinder, D. C., Bickham, S. R., McDermott, M. A., Desorcie, R. B., Nolan, D. A., Johnson, J. J., Lewis, K. A. & Englebert, J. J. (2010). Ultra-low bending loss single-mode fibre for FTTH, *Proceedings of Optical Fibre Communication Conference (OFC) 2010*, paper PDP10, ISBN 978-1-55752-884-1, San Diego, USA, March 21-25, 2010

Llorente, R., Alves, T., Morant, M., Beltrán, M., Perez, J., Cartaxo, A., & Marti, J. (2008). Ultra-Wideband Radio Signals Distribution in FTTH Networks. *IEEE Photonics Technology Letters*, Vol. 20, No. 11, (June 2008), pp. 945-947, ISSN 1041-1135

Ma, J., Yu, J., Yu, C., Xin, X., Zeng, J., & Chen, L. (2007). Fibre dispersion influence on transmission of the optical millimeter-waves generated using LN-MZM intensity modulation. *IEEE Journal of Lightwave Technology*, Vol. 25, No. 11, (November 2007), pp. 3244-3256, ISSN 0733-8724

Morant, M., Pérez, J., Llorente, R. & Marti, J. (2009). Combined Analysis of OFDM-UWB Transmission in Hybrid Wireless-Optical Access Networks. *IEEE Photonics Technology Letters*, Vol. 21, No. 19, (October 2009), pp. 1378-1380, ISSN 1041-1135

Morant, M., Perez, J. Llorente, R., & Marti, J. (2009). Transmission of 1.2 Gbit/s Polarization-Multiplexed UWB Signals in PON with 0.76 Bit/s/Hz Spectral Efficiency. *Proceedings of Optical Fiber communication/National Fiber Optic Engineers Conference OFC/NFOEC 2009*, paper OTuJ6, Optical Society of America, ISBN 978-1-55752-865-0, San Diego, CA, March 22-26, 2009.

Morant, M., Quinlan, T., Llorente, R., & Walker, S. (2011). Full Standard Triple-Play Bi-Directional and Full-Duplex CWDM Transmission in Passive Optical Networks, *Proceedings of Optical Fibre Communication Conference and Exposition (OFC) and National Fibre Optic Engineers Conference (NFOEC)*, paper OWB3, Optical Society of America, ISBN 978-1-55752-906-0, Los Angeles, USA, March 6-10, 2011.

Morant, M., Quinlan, T., Walker, S., & Llorente, R. (2011). "Real World" FTTH Optical-to-Radio Interface Performance for Bi-directional Multi-Format OFDM Wireless Signal Transmission. *Proceedings of Optical Fibre Communication Conference and Exposition (OFC) and National Fibre Optic Engineers Conference (NFOEC)*, paper NTuB6, Optical Society of America, ISBN 978-1-55752-906-0, Los Angeles, USA, March 6-10, 2011.

Mukasa, K., Imamura, K., Shimotakahara, I., Yagi, T., & Kokura, K. (2006). Dispersion compensating fibre used as a transmission fibre: inverse/reverse dispersion fibre. *Journal of Optical and Fibre Communications Reports*, Vol. 3, No. 5, (2006), pp. 292-339

Perez, J., Morant, M., Cavallin, L., Beltrán, M., Gaudino, R., Llorente, R. (2009). Experimental Analysis of WiMedia-defined UWB and WiMAX 802.16e Coexistence in Personal

Area Networks, *Proceedings of ICT Mobile Summit 2009*, ISBN 978-1-905824-12-0, Santander, Spain, June 10-12, 2009

Prat, J. (Ed.) (2008). *Next-Generation FTTH Passive Optical Networks*, Springer, ISBN 978-1-4020-8469-0

Pyramid Research (2010). Research in Focus: IPTV. 2010 Closes with 46.2m IPTV Subscriptions Worldwide. *IPTV EXCERPT Q4 2010*. Retrieved from http://www.pyramidresearch.com

Razavi, B.(2008). Gadgets gab at 60-GHz. *IEEE Spectrum*, Vol. 45, No. 2, (February 2008), pp. 46-58

Saorin, R. (2009). A Business Model Based on FTTH Infrastructure Neutral Operator to Provide Service to Several Operators. *FTTH Council Europe Conference*, February 2009

Sauer, M., Kobyakov, A., George, J. (2007). Radio over fibre for picocellular network architectures. *IEEE Journal of Lightwave Technology,* Vol. 25, No. 11, (November 2007), pp. 3301-3320, ISSN 0733-8724

Schmuck, H. (1995). Comparison of optically millimeter-wave system concepts with regard to chromatic dispersion. *Electronics Letters*, Vol. 31, No. 21, (October 1995), pp. 1848-1849

Wedding, B. (1994). Analysis of fibre transfer function and determination of receiver frequency response for dispersion supported transmission. *Electronics Letters*, Vol. 30, No. 1, (January 1994), pp. 58-59, ISSN 0013-5194

Wells, J. (2009). Faster than fibre: The future of multi-Gb/s wireless. *IEEE Microwave Magazine,* Vol. 10, No. 3, (May 2009), pp. 104-112, ISSN 1527-3342

Werbach, K. (2009). *Radio Revolution. The Coming Age of Unlicensed Wireless*. Ed. New America Foundation, Washington, DC.

WiMedia Alliance. (August 2009). WiMedia PHY Specification 1.5, Available from http://www.wimedia.org

WiMedia Alliance. (January 2009). Regulatory Status, Available from http://www.wimedia.org

WiMedia Alliance. (May 2007). Spectrum Extension Release (1.2), Available from http://www.wimedia.org

Wireless Gigabit Alliance. (July 2010). Specification whitepaper : Defining the Future of Multi-Gigabit Wireless Communications, Available from http://wirelessgigabitalliance.org

WirelessHD Alliance. (May 2010). WirelessHD Specification version 1.1, Available from http://www.wirelesshd.org

Wisair. (June 20, 2010). Wisair to unveil the WSR602 NEW wireless USB single chip in Computex Taipei. Available from http://www.wisair.com

17

60 GHz Ultra Wideband Multiport Transceivers for Next Generation Wireless Personal Area Networks

Nazih Khaddaj Mallat[1], Emilia Moldovan[2], Serioja O. Tatu[2] and Ke Wu[1]
[1]*Ecole Polytechnique de Montréal / Poly-Grames Research Center*
[2]*Université du Québec / Institut National de la Recherche Scientifique*
Canada

1. Introduction

Ultra wideband (UWB) communications is one of the most promising recent developments in wireless world for high-speed applications as shown in figure 1. In addition, the use of millimeter-waves has allowed in recent years the development of wireless communications: unlicensed short-range (57 – 64 GHz), outdoor semi-unlicensed point to point links (71 - 76 GHz, 81 - 86 GHz, and 92 - 95 GHz), automotive radar (76 - 77 GHz), and imaging sensor (84 – 89 GHz and 94 GHz) systems.

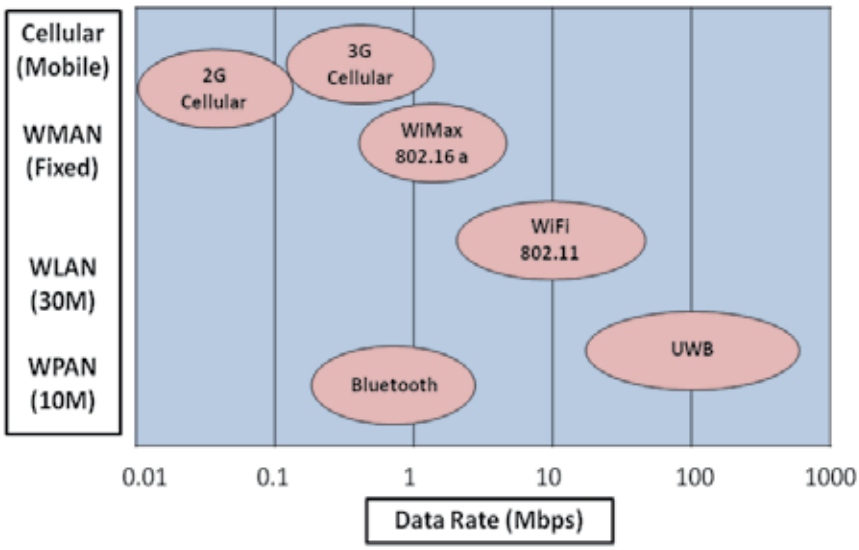

Fig. 1. High-speed wireless applications

The use of microwave frequencies (3.1–10.6 GHz) for UWB systems is actually subject of intensively research. In order to analyze a different very promising approach, this chapter proposes the use of a millimeter-wave carrier for UWB communication systems. Through

the very recent researches, it is known that millimeter-wave technology enables the design of compact and low-cost wireless transceivers which can permit convenient terminal mobility up to Gb/s data-rates.
The chapter is organized as follows:

- Section 2 provides an overview of millimeter-wave technology (60 GHz), compared with other microwave band communications (5 GHz).
- Section 3 states the UWB conventional definition, given by Federal Communications Commission (FCC), and how to use this special technology into millimeter-wave range.
- Section 4 analyses a proposed 60 GHz wireless multiport millimeter-wave system dedicated to high-speed UWB communications.
- Conclusions are summarized at the end of the chapter.

2. Millimeter-wave technology for high-speed communications

Due to the recent dramatic growth of high-bandwidth commercial wireless communications, the microwave communication bands are becoming over crowded. Moreover, the ever increasing high-speed and large-channel capacity digital data rates used in multimedia wireless communications are requiring millimeter-wave bandwidths (frequencies between 30 GHz and 300 GHz). For example, a TV at home will be able to access all sources in the house: a "box" in the lounge, a PlayStation in the bedroom, or a DVD reader in another room through a wireless system focusing on the 60 GHz band.
The 60 GHz band is of much interest since a massive amount of unlicensed spectrum (5 GHz) has been allocated worldwide for dense wireless local communications (Cabric et al, 2006; Park & Rappaport, 2007; Engen, 1977; Yacabe et al, 2001). A couple of multimedia applications calling for wireless transmission over short distances are existing, such as wireless IEEE 1394 (actually this is an international standard digital interface that can run up to 400 Mb/s over a thin cable), wireless high-resolution TV and videoconferences, wireless internet download of lengthy files, wireless direct communication between notebooks and related devices, patient monitoring in hospitals (patients can freely walk within the hospital grounds with devices that transmit ECG (Electro-Cardio-Gram), blood pressure information, etc), remote controls, and wireless embedded systems, etc. This wide range of applications requires low–cost equipment operating at hundred of megabits per second.
In the European Advanced Communication Technology and services (ACTS) program, the 40 and 60 GHz have been addressed by various research projects with target radio bit rates of 150 Mb/s. In Japan, the Multimedia Mobile Access Communication (MMAC) committee is looking into the possibility of Ultra-high speed wireless indoor LANs supporting 156 Mb/s using 40 and 60 GHz. In the United States, the Federal Communications Commission (FCC) sets aside the 59-64 GHz frequency band for general unlicensed applications. This is the largest contiguous block spectrum ever allocated. Thus, a spectral space has been assigned around 60 GHz having a worldwide overlap, as shown in figure 2.
The 60 GHz band can not only achieve very high data rates several Gbit/s but has many other characteristics for applications in millimeter wave range:

- An atmospheric oxygen absorption of 10-15 dB/Km. Indeed, the oxygen have a resonant frequency of 60 GHz. So the transmitted energy is absorbed very quickly by oxygen in the air. (90 % of energy is absorbed by oxygen at 60 GHz).
- 88 dB/Km due to the free space path loss as demonstrated using Friis transmission equation:

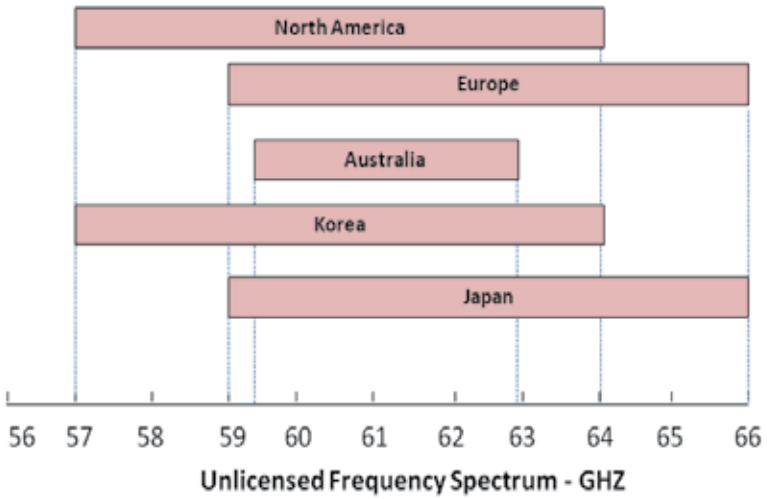

Fig. 2. Unlicensed bandwidth – 60 GHz

$$\frac{P_r}{P_t} = \frac{G_t G_r \lambda^2}{(4\pi R)^2} = G_t G_r A_{fs} \tag{1}$$

P_r and P_t= Power of the received and transmitted signals, respectively
G_r and G_t=Gain of the antennas of receiver and transmitter, respectively
λ = free-space wavelength
R= distance between transmitter and receiver

$$A_{fs} = \frac{\lambda^2}{(4\pi R)^2} \tag{2}$$

$$\lambda = \frac{c}{f} = \frac{3 \cdot 10^8}{60 \cdot 10^9} = 5mm \tag{3}$$

c = speed of the light
f = frequency
The Friis path loss equation shows that, for equal antenna gains, path loss increases with the square of the carrier frequency. Therefore 60 GHz communications must content with an additional 22 dB of path loss when compared to an equivalent 5 GHz system. Then, the free space path loss will be around 88 dB for 10 m and 68 dB for a distance of 1 m, at this very high carrier frequency. The space path loss attenuation for a distance of 10m is calculated for different frequencies, as shown in table 1.

- One of the major limitations of the maximum range for a link at 60 GHz is the attenuation due to rain. In fact, the rainfall of a region is even considered as limiting factor more than the absorption of oxygen. The 60 GHz links shall be constructed in specific way to be able to overcome the rain limitations and will therefore vary according to different regions. The maximum distance increases when the rate of rainfall decreases. In regions with moderate rainfall, attenuation due to rain can be twice higher than oxygen and can be up to three times higher in regions with high rainfall.

Frequency	Wavelength	Free Path Attenuation
2.4 GHz	125 mm	30 dB
5 GHz	60 mm	66 dB
60 GHz	5 mm	88 dB

Table 1. Space attenuation for different frequencies

- The very high attenuation suffered by the 60 GHz links permits the frequency reuse in very close areas. Thus it is possible to deploy multiple devices operating at the same frequency in a high density pattern and without any risk of interference between them.
- The 60 GHz band advantage is to be in the millimeter wave length range. Thus, it is very small, allowing high degree integration for all elements: filters, passive components and antennas. The 60 GHz antennas have a smaller form factor than 5 GHz antennas, as antenna dimensions are inversely proportional to carrier frequency. For example, to obtain an antenna with a gain of 40 dBi and beam width of 1°, the size of the antenna at 60 GHz will be ten times smaller than at 6 GHz. Therefore, at 60 GHz it is possible to produce very compact low-cost antennas with higher directivity. In fact, future high data-rate WLAN will be certainly realized using smart antennas to reduce the power consumption, the link budget and the multipath effects.

This high and severe attenuation makes the 60 GHz band unsuitable for long-range (>2 Km) communications, so it can be entirely dedicated for short-range use (<50 m), where this supplementary attenuation has no significant impact. This makes the 60 GHz band of hugely interesting for many types of short-range wireless applications, as WPANs (Wireless Personal Area Networks) and WLANs (Wireless Local Area Networks). These products are proprietary systems or based on the IEEE 802.11 standards. These products operate in the 2.4 and 5.8 GHz bands and provide a user capacity up to 54 Mb/s. Currently, IEEE 802.15.3c and WirelessHD, the two well-known 60 GHz standards for WLANs and WPANs, are capable to deliver Gb/s streamed video and audio (Daniels & Health, 2010).

In the last decade, intensive researches have been done, especially in terms of designing new millimeter wave components operating over the V-band frequency (50 - 75 GHz). Through those papers and publications, it has been proved that the millimeter-wave frequencies enable the design of compact low-cost wireless millimeter-wave communications front-ends which can permit convenient terminal mobility up to Gb/s data-rates (Smulders et al, 2007; Smulders, 2002; Collonge et al, 2003; Tatu & Moldovan, 2007).

3. UWB in millimeter-wave communications

Before explaining how the UWB characteristics can be reflected in millimeter-wave communications, let's first give a brief description of UWB principles.

The recent development of digital technologies in civil and military fields (radar, instrument for earth observation and space, etc...) associated with the telecommunications (WiFi / WiMAX, WLAN, GPS) demonstrates the great possibility to optimize the use of allocated frequency bands. The FCC defines UWB as "any radio technique that has a bandwidth exceeding 500 MHz or greater than 25% of its center frequency". The UWB technology is

dedicated for transmitting wireless data with a throughput up to several hundreds of Mbit/s. UWB presents itself as an evolution of both Bluetooth and USB wireless. It is a radio technology based on the generation of very short duration pulse over a wide frequency band, hence its name.
In the United States, the FCC has reserved microwave frequency bands between 3.1 and 10.6 GHz for UWB devices. However, in Europe, the frequencies are reduced to the band between 6 and 10 GHz (3 GHz less than in the U.S.). UWB technology is used for radar/sensors, communications, radio astronomy, imaging systems and automotive anti-collision systems. Currently, UWB is already authorized for licensed use in the United Kingdom for the defects detection in runways.
UWB is a good alternative for domestic radio networks (WLAN and WPAN) that is found in the networked home, hotel, conference locations, administrative sites, and all places that do not want the hassle of wiring. Figure 3 gives an idea about the possible applications of UWB, regarding the mobility, costs, speed, and cost, etc.

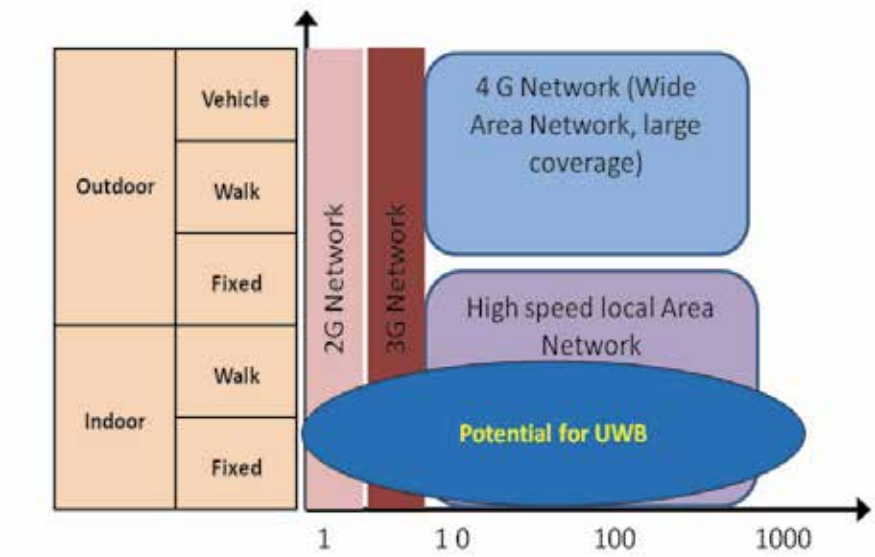

Fig. 3. UWB applications

Although these excellent advantages for microwave UWB, there are some disadvantages at the same time:

- Relatively low frequency carrier
- Low data rate compared to huge ones required in the actual market
- Frequency distortion over wide bandwidth

Compared to conventional microwave UWB technology, 60 GHz millimeter-wave communications will operate in currently unlicensed spectrum (57 – 64 GHz) and will provide high data-rates up to several Gb/s, as detailed in paragraph 2. Hence, the millimeter-wave communications can be largely considered to be used for UWB purposes (WLANs and WPANs). This is the main concern of the following paragraph.

4. UWB at 60 GHz: different approaches

There are many different ways to use the UWB at millimeter-wave frequencies. In this paragraph, two approaches are considered:

- Transposition of conventional impulse radio at millimeter-wave
- Direct use of inherent wide-band into a multi-port interferometer

4.1 Up-conversion of an UWB impulse radio signal (IR-UWB) in the 60 GHz frequency range.

(Deparis et al, 2005) have demonstrated that the impulse radio-UWB used in the 60 GHz band can provide both transceiver simplicity, and high data rate. Their proposed transmitter contains a voltage controlled oscillator (VCO) working at 30 GHz, a double frequency up-converter to reach the 60 GHz frequency, and a pulse generator (1st pulse generator) to generate the pulse position modulation (PPM) pulses in order to modulate the transmitted signal at 60 GHz. This modulation is realized with a switch in ∏-topology, as shown in figure 4. After amplification, Gaussian pulses are transmitted over several GHz bandwidth centered into the 60 GHz band (Tatu el al, 2009).

At the meanwhile, the receiver is composed of a low noise amplifier (LNA), a detector at 60 GHz, and a fast sampling and hold - S/H (Win & Scholtz, 2000; El Aabbaoui et al, 2005; Deparis et al, 2004). A pulse generator (2nd pulse generator) is used to control the S/H circuit. The receiver may contain either a mixer or a detector. If a mixer is implemented, a millimeter-wave oscillator is needed. However, the oscillator is not needed when a topology with detector is chosen, as shown in figure 5.

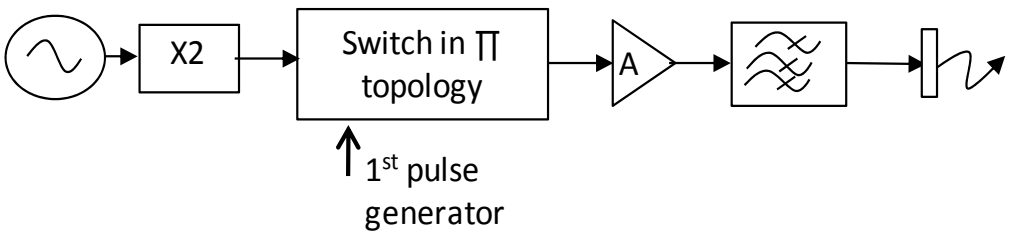

Fig. 4. Transmitter at 60 GHz.

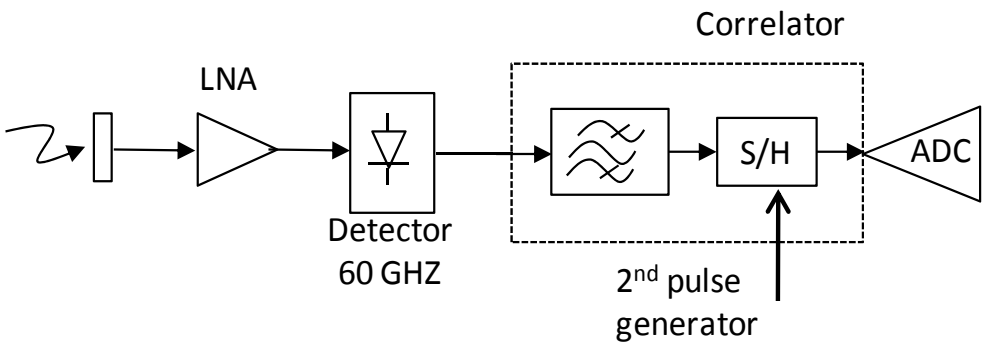

Fig. 5. Receiver at 60 GHz.

The main advantage of this architecture is that no phase information is needed, and thus, no sophisticated coherent stable sources or carrier recovery circuits are involved. This impulse radio-UWB/60 GHz approach can offer transceiver simplicity, high-data rate and is suitable for future low-cost high speed wireless transceivers.

4.2 Proposed 60 GHz transceiver based on six-port circuits

The main objective of this paragraph is to analyze and discuss a 60 GHz transceiver based on six-port circuits. Our target is to provide a transmission bandwidth exceeding 500 MHz, so the proposed architecture can be considered as part of UWB communications systems.

4.2.1 S-parameters and scattering matrix

For high frequencies and since it is very difficult to measure the voltage signal and energy, the scattering parameters [S] are used instead and considered as a convention for describing the RF and microwave waves. In microwave circuits, the required parameters are the amplitude and the phase of the signals. Many electrical properties can be expressed using the S-parameters such as the transmission coefficients, return loss and SWR (standing wave ratio) parameters. S-parameters can be calculated using analytical techniques of network analysis or measured with vector network analyzer equipment. Once identified, these S-parameters can be set in matrix form, called scattering matrix. For example, a two-port network microwave system as shown in figure 6 is represented as follows:

Fig. 6. Quadripole microwave system.

The wave's equations and the S-parameters scattering matrix are:

$$b_1 = S_{11}a_1 + S_{12}a_2 \tag{4}$$

$$b_2 = S_{21}a_1 + S_{22}a_2 \tag{5}$$

$$\begin{pmatrix} b_1 \\ b_2 \end{pmatrix} = \begin{pmatrix} S_{11} & S_{12} \\ S_{21} & S_{22} \end{pmatrix} \times \begin{pmatrix} a_1 \\ a_2 \end{pmatrix} \tag{6}$$

- a_i: Incident wave
- b_i: Reflected wave
- S_{11} : Input reflection coefficient
- S_{12} : transmission coefficient
- S_{21} : transmission coefficient (gain)
- S_{22} : Output reflection coefficient

4.2.2 Six-port modeling versus conventional: architecture equivalence

The six-port circuit is a conventional linear passive component, which consists of several couplers, connected by transmission lines. The idea of using a six-port structure to determine the phase of a microwave signal was first presented in 1964 (Cohn & Weinhouse, 1964). The six-port circuit can be considered as a black box with two inputs, one for the reference signal from local oscillator and one for the RF signal to identify, and four outputs. Using an appropriate algorithm, the amplitude and phase of the RF signal to identify can be determined by measuring the four power signals of the diodes at the outputs of the six-port.

The six port model used in this chapter consists of four 90° hybrid couplers interconnected by transmission lines and four power detectors, as shown in figure 7 (Tatu et al, 2005, 2006). The signals a_5 and a_6 are two normalized waves' inputs and related to local oscillator (LO) and radio-frequency signals, respectively. As known, the hybrid coupler splits

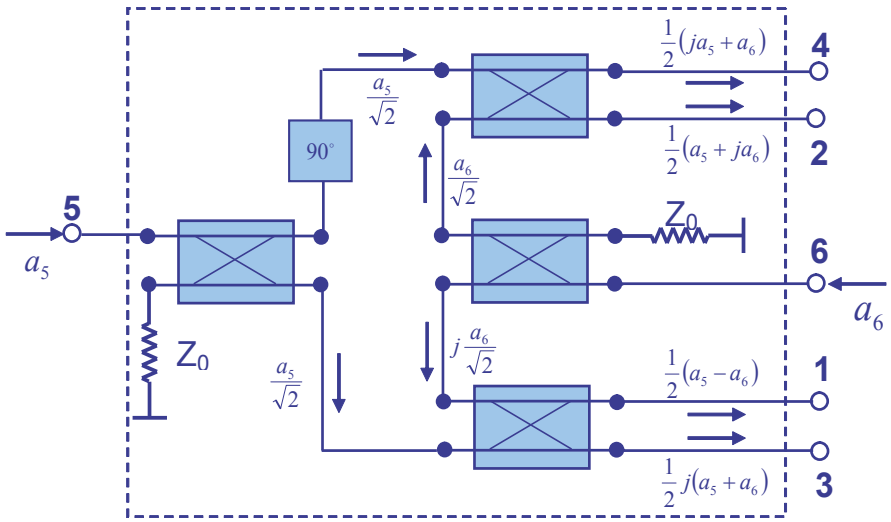

Fig. 7. Six-Port block diagram.

a signal with a 90° phase shift between output ports while maintaining high isolation between the ports. Based on this definition and using the power equations of hybrid couplers, the four outputs wave's equations b_i can be resolved as shown in the following equations:

$$b_1 = -j\frac{a_5}{2} + j\frac{a_6}{2} \tag{7}$$

$$b_2 = \frac{a_5}{2} + j\frac{a_6}{2} \tag{8}$$

$$b_3 = \frac{a_5}{2} + \frac{a_6}{2} \tag{9}$$

$$b_4 = -j\frac{a_5}{2} - \frac{a_6}{2} \tag{10}$$

A popular scheme of the conventional I/Q modulator/demodulator consists of a 90° phase shifter, two mixers and a combiner/divider. The equivalence between the conventional and the six-port demodulator has been demonstrated, as shown in figure 8. (Khaddaj Mallat & Tatu, 2007). The quadrature (I/Q) signals equations are expressed in (11) and (12).

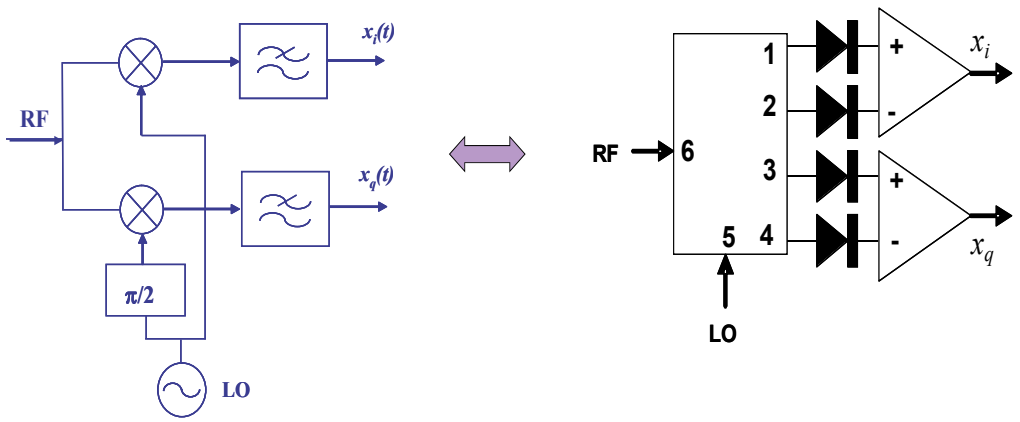

Fig. 8. Conventional and Six-Port Receivers.

$$x_i(t) = V_1(t) - V_2(t) = K \cdot \alpha(t) \cdot |a|^2 \cdot \cos\left[\Delta\varphi(t)\right] \tag{11}$$

$$x_q(t) = V_3(t) - V_4(t) = K \cdot \alpha(t) \cdot |a|^2 \cdot \sin\left[\Delta\varphi(t)\right] \tag{12}$$

In order to obtain the DC output signals, four power detectors are connected to the six-port outputs. The I/Q signals are obtained using a differential approach, as indicated in equations (11) and (12), where K is a constant, I/Q signals (In-phase/Quadrature-phase), V_1 to V_4 are the detectors outputs signal, a is the LO signal power, $\Delta\varphi(t) = \varphi_6(t) - \varphi_5$ is the instantaneous phase difference, and $a(t)$ is the power ratio of RF and LO.

A millimeter-wave receiver system simulation is done by Advanced Design System (ADS) of Agilent Technologies. This receiver system is composed of the proposed six-port, local oscillators, amplifiers, pass-band filters and "Sample_and_Hold" circuits (SHCs). The simulation block diagram is presented in figure 9. The operating frequency is set at 60 GHz and the modulation types discussed are M-PSK/QAM (Phase Shift Keying/Quadrature Amplitude Modulation). In the next paragraph, the simulation of the proposed receiver will be based on the measurements results of a fabricated hybrid coupler and not simulation results.

Figure 10 shows the simulation results of demodulated constellations using the proposed receiver for 16PSK and 16QAM signals respectively. It proves that this receiver is performing the analog demodulator task. For 16 PSK modulations, the constellation points (I/Q) are positioned on a circle and these points are equidistant for the 16QAM modulated signal. During this simulation, a coherent LO is used to generate the six-port reference signal. It is be noted that if the phase of the LO changes in time, the demodulated constellation turns clockwise or anticlockwise depending on the sign of this variation. Figure 11 shows the simulated constellation with additional white noise (a white noise was added in the transmission path), signal to noise ratio is 12 dB for 16PSK and 8 dB for 16QAM. The white noise effect is evident as the constellation point is not clear

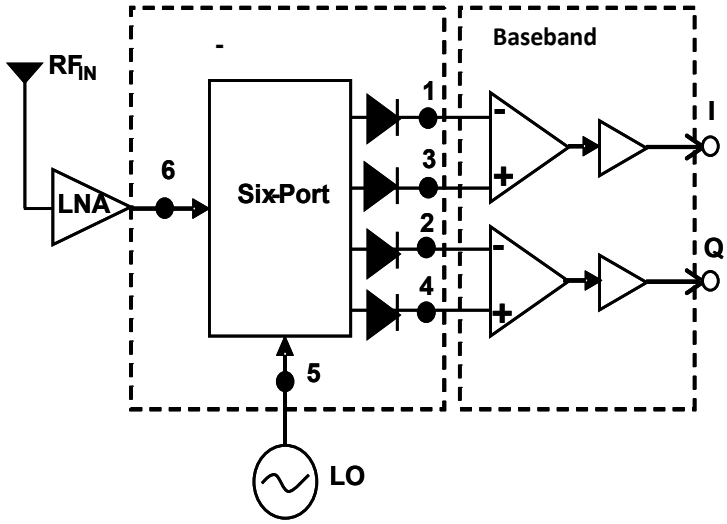

Fig. 9. Conventional and Six-Port Receivers.

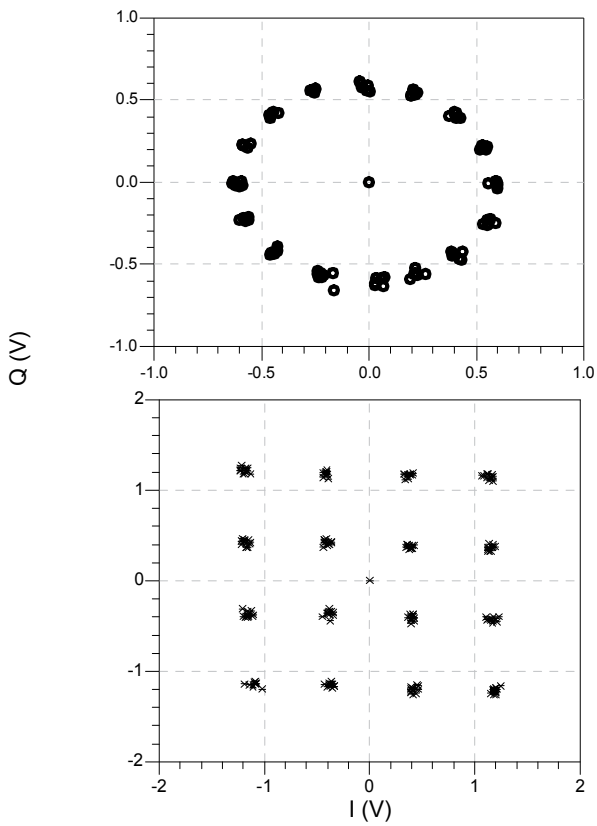

Fig. 10. Demodulated signals: 16PSK/16QAM.

as before. The noise is expressed by the "cloud" covering every point I/Q. As suggested by previous analysis, excellent simulations are obtained as well for another constellation types with reduced number of symbols (BPSK, QPSK, 8PSK). The millimeter-wave frequency conversion and direct quadrature demodulation are obtained using the specific properties of the proposed six-port circuit, avoiding the use of the conventional mixers which require a considerably increased LO power (diode mixers) or active costly devices.

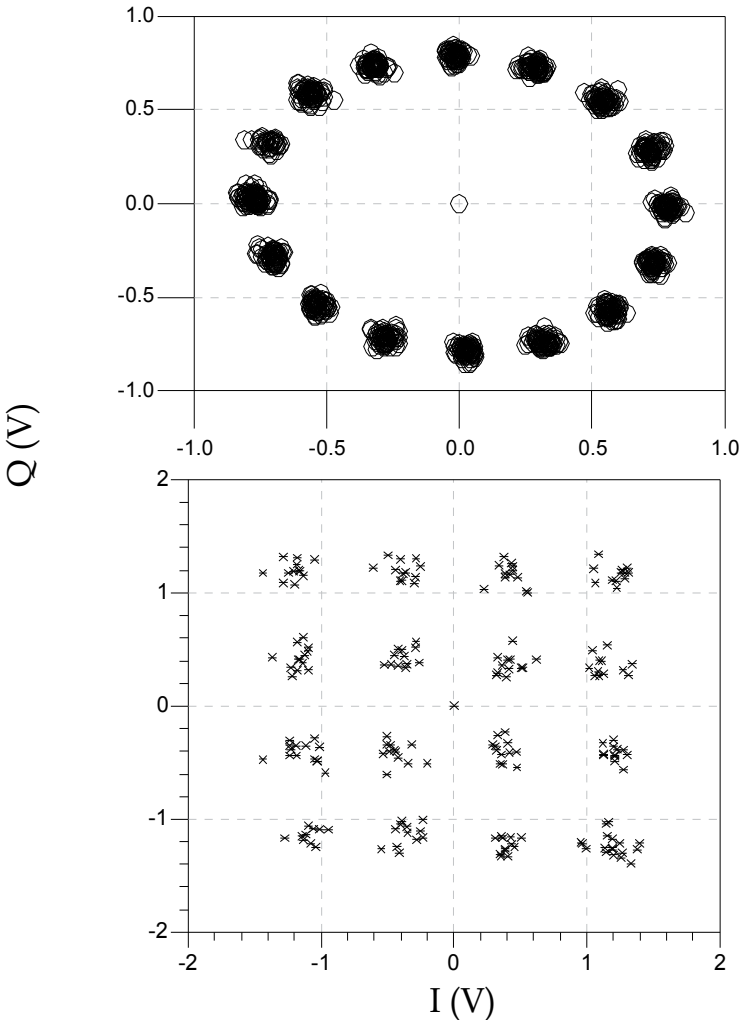

Fig. 11. Demodulated signals with white noise: 16PSK/16QAM.

4.2.2.1 Hybrid coupler characterization

In this paragraph, the four-port 90° hybrid coupler, considered as the core component of the six-port circuit is designed and fabricated to operate in V-band. This circuit is integrated on a 125 µm alumina substrate having a relative permittivity of 9.9, using a Miniature Hybrid

Microwave Integrated Circuit (MHMIC) technology. Figure 12 shows several microphotographs of the MHMIC 90º hybrid coupler. The diameter of the coupler is around 700 μm and the 50 Ω line width is nearly equal to the thickness of the alumina substrate. In order to characterize these circuits, on-wafer measurements are performed using a Microtech probe station connected to an Agilent Technologies millimeter-wave precision network analyzer (PNA) model E8362B.

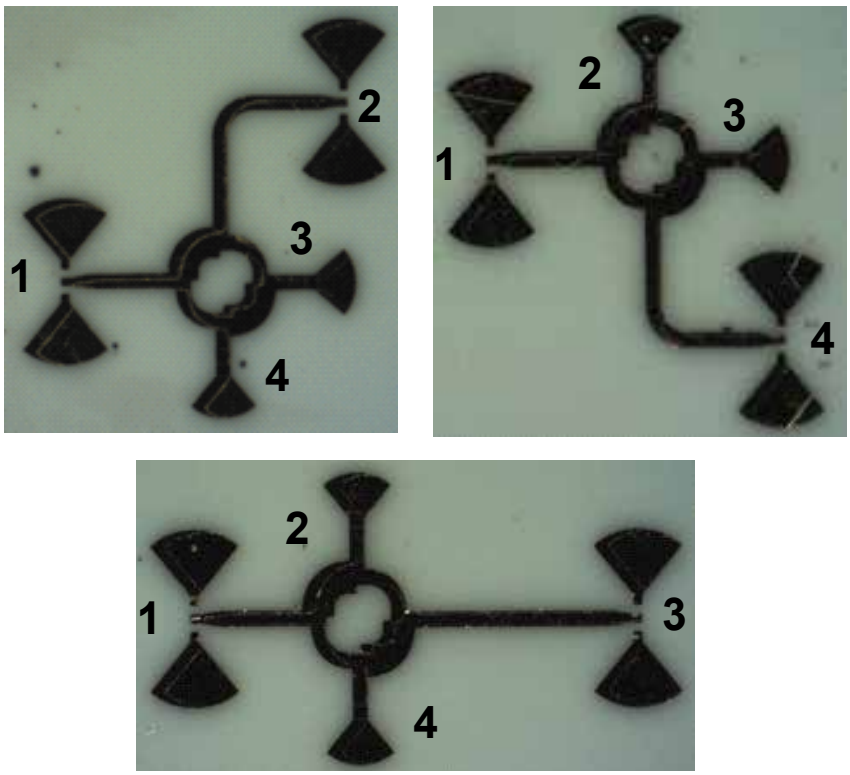

Fig. 12. MHMIC 90º hybrid coupler.

Figure 13 shows that the transmission measured phase of S_{12} and S_{13} is roughly 90°, as known for the hybrid couplers, over 4 GHz of bandwidth. Figure 14 shows that the isolation (S_{23}) and return loss (S_{11}) are higher than -15 dB and -20 dB, respectively. The measured power splits (S_{12} & S_{13}) over the band of 4 GHz are between -3 dB to -4 dB, very close to the theoretical value of -3 dB. Due to the circuit symmetry, equal measured isolations between ports 1-4 and 2-3 are obtained, as well as the return loss at all ports, S_{ii}.

The six-port model is simulated in ADS using the S-parameters measurements results of the fabricated MHMIC hybrid coupler. A matching of more than -15 dB and isolation of -20 dB are obtained for the input ports. The quadrature (I/Q) down-converted signals, using equations (11) and (12), are obtained through harmonic balance simulations for several discrete frequency points over 4 GHz band of interest. These signals have quasi co-sinusoidal/sinusoidal shapes, as requested for I/Q down-converters. The means of quadrature signals (dotted lines) are non-zero values, and, therefore, small DC offsets appear. They can be successfully eliminated using DC blocks, as shown in figure 15.

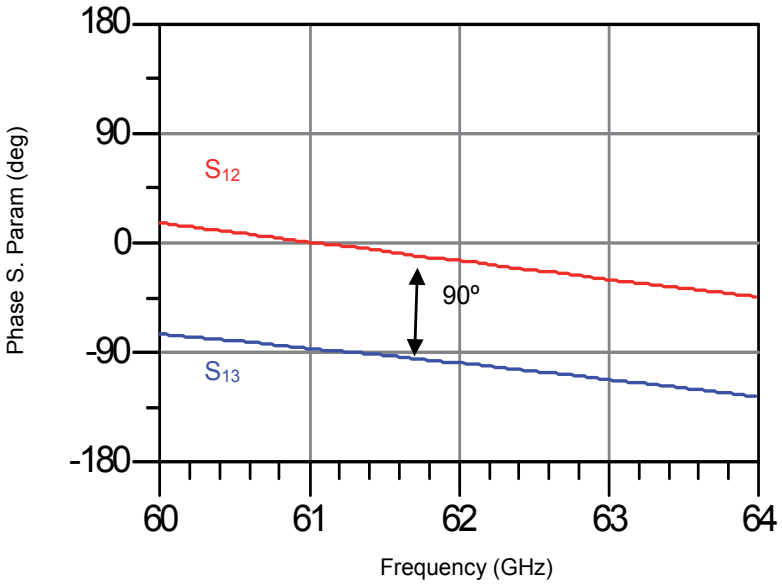

Fig. 13. S-parameters phases measurements results: Hybrid coupler.

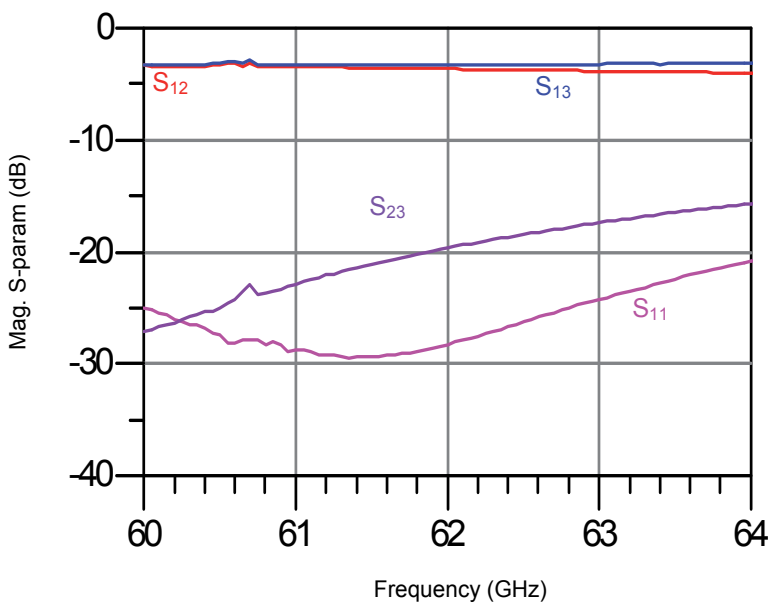

Fig. 14. Transmission, return loss, and isolation measurements results: Hybrid coupler.

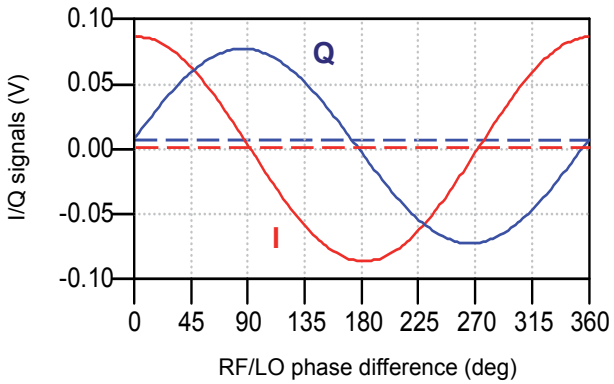

Fig. 15. Six-port harmonic balance.

4.2.2.2 60 GHz transceiver architecture for UWB

Using previous characterization results of the hybrid coupler a six-port model was built into ADS according to block diagram in Figure 7. Figure 16 shows the block diagram of a proposed wireless transceiver system working in V-band (60 GHz). The system parameters' are as follows: transmitted LO power = -25 dBm, amplifier gain (A) = +20 dB, and an antenna transmitting gain (G_T) = 10 dBi. These values are been intentionally chosen in order to obtain a transmitted signal power equal to 10 dBm (allowed by FCC for V-band communications system). The antenna receiving gain is +10 dBi, the LNA gain is +20 dB, so the six-port input signal power has a value of -38 dBm.

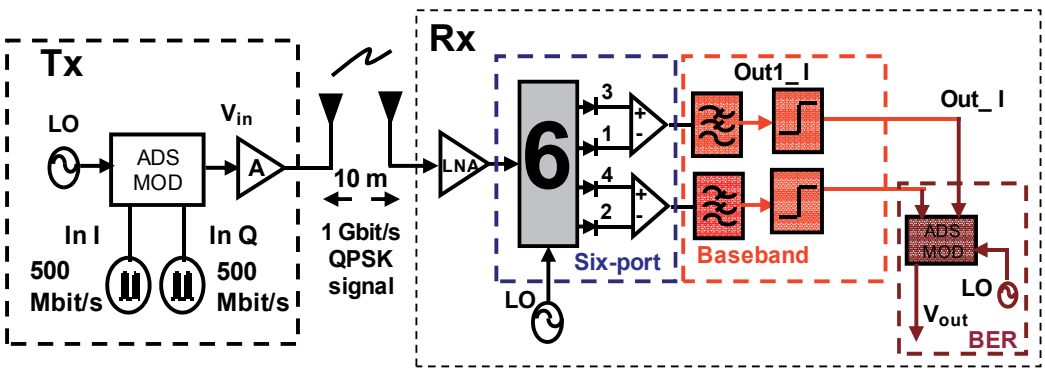

Fig. 16. 60 GHz transceiver system – UWB.

The ADS simulator is configured for an envelope simulation, at a frequency of 62 GHz, and the transmitted signals are modulated in QPSK, for 1 Gbit/s of data-rate communication. The six-port model based on the measurement results of the fabricated hybrid coupler MHMIC (discussed in the previous paragraph) and the baseband circuits are implemented in the ADS receiver model. The transmitted QPSK modulated signals are pseudo-randomly generated by ADS with a symbol rate of 500 MS / s (data rate = 1 Gbit/s). Figure 17 shows the spectrum of the transmitted QPSK signal received at the six-port receiver input. The main lobe is related to the single carrier at 62 GHz.

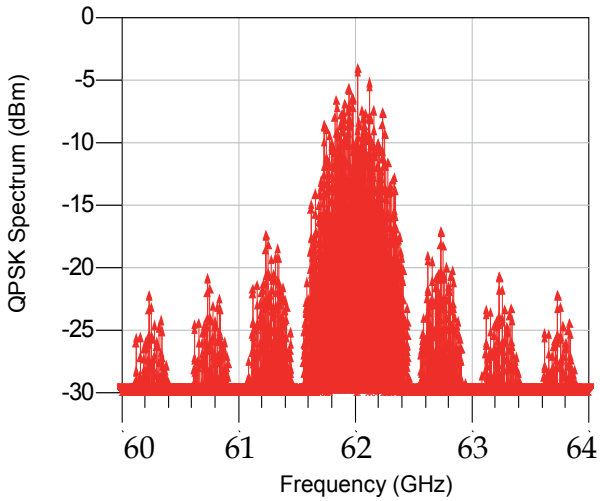

Fig. 17. QPSK spectrum of transmitted signal.

Figure 18 shows the BER variation versus energy per bit to the spectral noise density (E_b/N_0) for the same distance of 10m. Obviously, this six-port receiver architecture using the single carrier scheme has an excellent BER performance (close to the theoretical one). Using limiters in the last stage of the receiver, the output square signals are obtained, as shown in figure 19. For a bit sequence of 200 nanoseconds, the output demodulated (I) signals have the same bit sequence as those transmitted. The same conclusion is obtained for the (Q) signals.

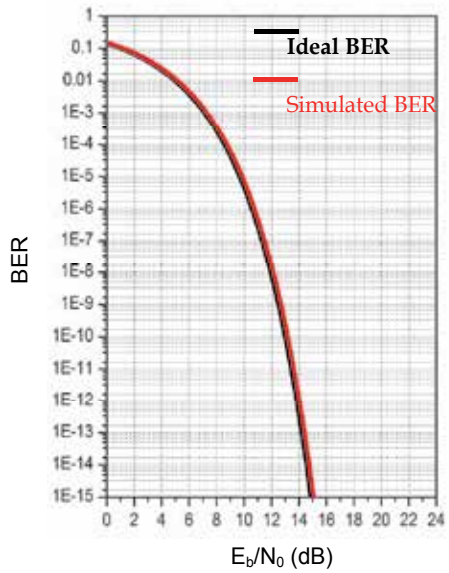

Fig. 18. BER results: QPSK signal at 1 Gbit/s

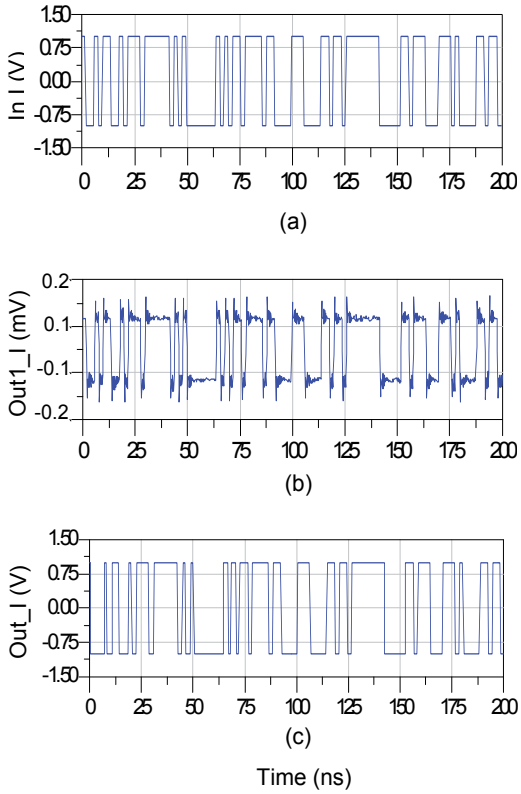

Fig. 19. Demodulation results of 1 Gbit/s QPSK pseudo-random (I) bit sequence: (a): transmitted, (b): received, after six-port, (c): demodulated, at limiter output.

5. Conclusion

The principle and the design of six-port 60 GHz transceivers dedicated to be used in future millimeter-wave UWB WLAN is presented in this chapter. It is demonstrated that the 60 GHz UWB transceiver architectures proposed can offer transceiver simplicity, high data-rate together with system miniaturization. This multiport receiver can be considered an excellent candidate for low-cost high speed future wireless communication systems.
Considerable research effort will be required to develop cost-effective, efficient and reliable designs for these wireless systems. In order to satisfy the technical requirements of wireless networks such as high data-rate and low-power consumption, it is important to design low-complexity and low-power consumption transceivers. Simple architectures are therefore requested for the future millimeter-wave UWB WLAN.

6. Acknowledgment

The authors gratefully acknowledge the financial support of the "Fonds Québecois de Recherche sur la Nature et les Technologies"(FQRNT) and the support of the "Centre de Recherche en Électronique Radiofréquence" (CREER) of Montreal, funded by the FQRNT, for the MHMIC circuit fabrication.

7. References

Cabric, D. Chen, M. Sobel, D. Wang, S. Yang, J & Brodersen, R. Novel Radio Architectures for UWB, 60 GHz and Cognitive Wireless Systems. *EURASIP Journal on Wireless Communication and Networking*, Vol. 2006, Article ID 17957, 18 pages, April 2006.

Park, C. & Rappaport, T. Short-Range Wireless Communications for Next-Generation Networks: UWB, 60 GHz Millimeter-wave WPAN and ZigBee. *IEEE Wireless Communication*, Vol. 14, Issue 4, pp. 70 -78, August 2007.

Engen, G.F. The six-port reflectometer: An alternative network analyzer. *IEEE Transactions on Microwave Theory and Techniques*, Vol. MTT-25, pp. 1077-1079, December 1977.

Yacabe, T. Xiao, F. Iwamoto, K. Ghannouchi, F. Fujii, K. & Yabe, H. Six-port based wave corellator with application to beam direction finding. *IEEE Transactions on Instrumentation and Measurement*, Vol. 50, no. 2, pp. 377-380, April 2001.

Giannetti, F. Luise, M. & Reggiannini, R. Mobile and personal communications in 60 GHz band: A survey. *Wireless Personal Communications*, Vol. 10, no. 2, pp. 207–243, 1999.

Anderson, C.R. & Rappaport, T. S. In-building wideband partition loss measurements at 2.5 and 60 GHz. *IEEE Transactions on Wireless Communications*, Vol. 3, no. 3, pp. 922–928, May 2004.

Daniels, R.C.; Murdock, J.N.; Rappaport, T.S. & Heath, R.W. 60 GHz Wireless: Up Close and Personal. *IEEE Microwave Magazine*, Vol. 11, Issue: 7, Part: Supplement. pp. 44-50. 2010.

Smulders, P; Yang, H; & Akkermans, I. On the design of Low-Cost 60 GHz Radios for Multigigabit-per-Second Transmission over Short Distances. *IEEE Communications Magazine*. 8 pages. 2007.

Smulders, P; Exploiting the 60 GHz band for wireless multimedia access: prospects and future directions. *IEEE Communication Magazine.* Vol. 40. no.1. pp.140 -147. 2002.

Collonge, S; Zaharia, G; & El Zein, G. Wideband and Dynamic Characterization of the 60 GHz Indoor Radio Propagation-future Home WLAN Architectures. *Annals of Telecommunications*. Vol. 58. N° 3-4. pp. 417-447. 2003.

Tatu, S.O. & Moldovan, E. V-band Multi-port Heterodyne Receiver for High-speed Communication Systems. *EURASIP Journal on Wireless Communication and Networking*. Vol. 2007. Article ID 34358. 7 pages. 2007.

Deparis, N.; Bendjabballah, A.; Boe, A.; Fryziel, M.; Loyez, C.; Clavier, L.; Rolland, N.; & Rolland, P.-A. Transposition of a Baseband UWB Signal at 60 GHz for High Data Rate Indoor WLAN. *Microwave and Wireless Components Letters, IEEE*. Volume 15. Issue 10. Pages: 609 – 611. 2005

Tatu, S.O.; Moldovan, E.; & Affes, S. Low-Cost Tranceiver Architectures for 60 GHz Ultra Wideband WLANs. *EURASIP Journal on Wireless Communication and Networking*. Vol. 2009. Article ID 382695. 6 pages. 2009.

Win, M. Z. and Scholtz, R. A. Ultra-wide-bandwidth time-hopping spread-spectrum impulse radio for wireless multiple-access communications. *IEEE Transactions on Communications*. Vol. 48. No. 4. pp. 679–689. 2000.

El Aabbaoui, H.; Rolland, N.; Benlarbi-Delaï, A.; Fel, N.; Allouche, V.; Leclerc, P.; Riondet, B.; & Rolland, P. A. Design of a fully HBT 40 GS/s sampling circuit for very large bandwidth non repetitive signal analysis. *IEEE Microwave Symposium Digest*. 2005.

Deparis, N.; Loyez, C.; Fryziel, M.; Boe, A.; Rolland, N.; & Rolland, P. A. Transposition of a base band ultra wide band width impulse radio signal at 60 GHz for high data

rates multiple access indoor communication systems. *34th European Microwave Conference. EuMW-ECWT*. Amsterdam, The Netherlands. 2004.

Cohn, S.B. and Weinhouse, N.P. An Automatic Microwave Phase Measurement System. *Microwave Journal*. Vol. 7. pp. 49-56. 1964.

Khaddaj Mallat, N. and Tatu, S.O. Six-port receiver in millimeter-wave systems. *Systems Man and Cybernetics (SMC), 2010 IEEE International Conference*. pp. 2693 – 2697. 2007

Tatu, S.O.; Moldovan, E.; Wu, K.; & Bosisio, R.G. Analog Signal Treatment in Six-Port Technology. *Canadian Conference on Electrical and Computer Engineering (CCECE)*. Montreal, Canada. Vol. 3. pp. 1925-1928. 2003.

Tatu, S.O. and Denidni, T.A. Millimeter-Wave Six-Port Heterodyne Receiver Concept. *IEEE MTT International Microwave Symposium*. San Fransisco, California. 2006.

Edited by Mohammad Matin

This book has addressed few challenges to ensure the success of UWB technologies and covers several research areas including UWB low cost transceiver, low noise amplifier (LNA), ADC architectures, UWB filter, and high power UWB amplifiers. It is believed that this book serves as a comprehensive reference for graduate students in UWB technologies.

ISBN 978-953-51-5560-7

Photo by PhonlamaiPhoto / iStock

IntechOpen